Lehrstuhl für Statik
der Technischen Universität München

Nonlinear Analysis of Pneumatic Membranes: "From Subgrid to Interface"

Amphon Jrusjrungkiat

Vollständiger Abdruck der von der Fakultät für Bauingenieur– und Vermessungswesen der Technischen Universität München zur Erlangung des akademischen Grades eines

Doktor–Ingenieurs

genehmigten Dissertation.

Vorsitzender:	Univ.-Prof. Dr.-Ing., Dr.-Ing. habil. G. H. Müller
Prüfer der Dissertation:	
	1. Univ.-Prof. Dr.-Ing. K.-U. Bletzinger
	2. Prof. Dr.-Ing. F. Cirak, University of Cambridge/ UK

Die Dissertation wurde am 01.07.2009 bei der Technischen Universität München eingereicht und durch die Fakultät für Bauingenieur– und Vermessungswesen am 29.10.2009 angenommen.

Nonlinear Analysis of Pneumatic Membranes: "From Subgrid to Interface"

Abstract. Literally, a pneumatic membrane structure is a gas-filled type inflatable membrane whose interaction of the surrounding membrane and the enclosed gas (fluid) determines its responses at any instance. Numerical algorithms to solve such problems are challenging due to their highly nonlinearity and nonsmoothness. Within this work, the mathematical description for continuum mechanics is used to explain three major nonlinearities involved in the inflatable membrane: wrinkling, pressure loads and contact. Based on the finite element discretization, numerical treatment and solution techniques are provided regarding numerical accuracy, robustness and stability.

First, the wrinkling phenomenon is a key characteristic of a thin membrane which reacts to compressive stresses beyond its capability by means of the local buckling "*waves*" to release excessive compressive stresses. Since geometric representation of these little waves by finite elements is costly, this work proposed two efficient wrinkling models based on modifications of material laws: the projection and plasticity analogy models. Besides deeming wrinkling as a sub-grid phenomenon beneath the scale of finite element mesh, they provide asymptotically accurate stress fields corresponding to existing wrinkles.

Secondly, influences of pressure applied to a surface of a membrane are taken into account by the deformation-dependent load definition which leads to both nominal load stiffness, caused by the change in surface normal, and additional load stiffness, originated from the change in pressure magnitude. In certain circumstances, the system matrix is turned to a fully populated one where a suitable solution technique is introduced to handle this pathological situation effectively for both quasi-static and dynamic analyses to improve the convergence rate and numerical accuracy.

Lastly, to deal with issues of large deformation contact for the inflatable membranes, a mortar-based contact formulation is derived such that the imprenetrability condition is defined in an integral manner over the contact area as well as the Lagrange multiplier interpolated by dual basis functions is used to enforce the contact conditions in the weak sense to achieve an efficient approach regarding to the robustness and accuracy. Furthermore, the discrete velocity update is introduced upon existing stable time integration methods to achieve an energy conservative solution technique for the contact problem of interest.

Various numerical simulations provide adequate proof of utilities for the presented approaches. By the capability to take into account simultaneously all mentioned nonlinear behaviors, the proposed algorithm has high potential with further developments for more complicated issues.

Mechanik und Numerik pneumatischer Tragwerke: "Von der Subnetzskala zum Interface"

Zusammenfassung. Pneumatische Membranstrukturen sind gasgefüllte Tragwerke, deren mechanisches Verhalten durch die Interaktion einer Membran mit dem darin enthaltenen Gas maßgeblich bestimmt wird. Die Entwicklung numerischer Verfahren zur Untersuchung dieser Probleme ist auf Grund der ausgeprägten Nichtlinearität und Nichtglattheit sehr komplex. Im Rahmen dieser Arbeit wird eine durchgängige kontinuumsmechanische Formulierung der drei typischen Ursachen für Nichtlinearitäten bei der Behandlung von aufgeblasenen Strukturen erarbeitet: Faltenbildung, Drucklasten und Kontakt. Darauf aufbauend wird eine numerische Lösungsstrategie mittels der Finite-Elemente-Methode und speziell formulierten Lösungsalgorithmen konzipiert.

Zunächst wird die Simulation der Faltenbildung untersucht. Diese Besonderheit von dünnen Membranstrukturen basiert auf der Tatsache, dass sich Membrane den unter Belastung potenziell auftretenden Druckspannungen durch laterales Ausweichen entziehen - sie beulen aus und bilden kurzwellige Faltenmuster. Eine exakte geometrische Erfassung dieser Deformationszustände mit einer Finite-Elemente-Diskretisierung ist sehr aufwändig, weshalb im Rahmen dieser Arbeit zwei Modellierungsansätze mittels Modifikation der konstitutiven Beziehungen vorgeschlagen werden. Dies ist zum Einen ein Projektionsverfahren und zum Anderen eine Methode, die auf der Plastizitätsanalogie beruht. Beide Herangehensweisen erfassen selbst Falten, die jenseits der Auflösung des Finite-Elemente-Netzes sind und resultieren in asymptotisch korrekten Spannunsfeldern bei gefalteten Membranen.

Daraufhin wird der durch das eingeschlossene Gas auf die Membran einwirkende Druck als deformationsabhängige Last modelliert und die theoretischen und numerischen Konsequenzen werden erörtert: Auf Grund der während des Deformationsvorgangs sich ändernden Flächennormalen und des variierenden Drucks ergeben sich zusätzliche Anteile in den Steifigkeiten des Systems. Weiterhin ist unter gewissen Umständen die Systemmatrix voll besetzt, was durch eine adäquat formulierte Lösungsstrategie wiederum eine effiziente Simulation von quasistatischen und dynamischen Analysen durch eine Verbesserung der Konvergenzrate und der numerischen Genauigkeit ermöglicht

Schließlich werden die bei aufgeblasenen Membranen häufig auftretenden Kontaktprobleme gelöst. Hierzu wird eine Mortar-basierte Formulierung hergeleitet, die zu einer integralen Erfüllung der Kontaktbeziehungen mittels Lagrangemultiplikatoren führt. Letztgenannte werden mit dualen Basisfunktionen interpoliert, was eine effiziente, robuste und genaue Behandlung der Kontaktprobleme ermöglicht. Des Weiteren wird ein diskretes Geschwindigkeitsupdate eingeführt, um die Energieerhaltung bei der Kontaktsimulation zu gewährleisten.

Die Eigenschaften und Potenziale der vorgestellten Lösungsansätze werden anhand vielfältigster Beispiele aufgezeigt und erörtert. Das durchgängige Gesamtkonzept mit der Möglichkeit, die oben genannten Einzelfragen gleichzeitig in einer Simulation zu berücksichtigen, ermöglicht detaillierte Einsichten in das mechanische Verhalten von gasgefüllten Membrantragwerken und stellt eine Grundlage für die fundierte Analyse von komplexen Pneustrukturen dar.

Contents

1 Introduction **1**

1.1 Motivation 1

1.2 Objectives and outline 5

2 Theoretical Foundation **9**

2.1 Nonlinear continuum mechanics 9

2.1.1 Differential geometry of surfaces and bodies in space 9

2.1.2 Kinematics 11

2.1.3 Constitutive equation 14

2.1.4 Dynamic equilibrium condition 16

2.1.5 Initial boundary value problem (IBVP) for elastodynamics 18

2.1.6 Weak form of IBVP for elastodynamics 18

2.2 Mechanics of membrane structures 21

2.2.1 Membrane theory 21

2.2.2 Kinematics for membrane structures 22

2.2.3 Constitutive equation for membrane structures 22

2.3 Solution strategies 25

2.3.1 Spatial discretization 25

2.3.2 Time discretization 32

2.3.3 Iterative solution algorithm 32

2.3.4 Stable time integration algorithm 33

2.4 Summary for the solution algorithm 42

3 Wrinkling Model **45**

3.1 Introduction . . . 45

3.2 Definition and theoretical background . . . 48

3.2.1 Evaluation of the state of a membrane . . . 49

3.2.2 Determination of the wrinkling direction . . . 49

3.2.3 Analogy between wrinkling and perfect plasticity for small strains . . 54

3.3 Material modification by the projection method . . . 56

3.3.1 Definition of the projection tensor . . . 57

3.3.2 Derivation of the modified stress field . . . 58

3.3.3 Incremental form of the constitutive equation . . . 60

3.4 Material modification by the plasticity analogy . . . 64

3.4.1 Rate-independent nonsmooth multisurface perfect plasticity . . . 64

3.4.2 Return mapping algorithm of multisurface plasticity in wrinkling . . . 68

3.4.3 Algorithmic tangent modulus . . . 70

3.4.4 Derivation of constraints . . . 71

3.5 Numerical experiments . . . 74

3.5.1 Pure bending of a stretched rectangular membrane . . . 74

3.5.2 Shear test of a rectangular isotropic Kapton membrane . . . 76

3.5.3 An annulus membrane under torsion . . . 82

3.5.4 Inflation of an isotropic airbag . . . 85

3.5.5 A Square membrane under corner loads . . . 87

3.6 Summary . . . 88

4 Deformation-Dependent Forces for Inflatable Membranes **91**

4.1 Inflatable membrane structures . . . 91

4.2 Governing equations of inflatable membranes coupled with enclosed fluid . . 94

4.2.1 Virtual work equation . . . 95

4.2.2 Definition of deformation-dependent forces . . . 96

4.2.3 Constitutive equation of the enclosed fluid . . . 97

4.2.4 Geometric representation via boundary integral of a chamber . . . 98

4.2.5 Derivation of virtual work for each specific case . . . 99

4.3 Linearization . . . 100

4.3.1 Directional derivative of geometrical quantities . . . 101
4.3.2 Directional derivative of the virtual work expression due to $\Delta\mathbf{n}^*$ . . . 106
4.3.3 Directional derivative of the virtual work equation due to Δp . . . 110
4.4 Proof of conservativeness . . . 111
4.5 Discretization . . . 112
4.5.1 Load stiffness from deformation-dependent forces . . . 113
4.5.2 Extension for multichamber case . . . 115
4.6 Solution Algorithm . . . 116
4.6.1 Woodbury's formula . . . 116
4.6.2 Nonlinear equilibrium path following algorithm . . . 117
4.6.3 Time dependent analysis of deformation-dependent forces . . . 122
4.7 Numerical Experiments . . . 124
4.7.1 Inflatable membrane tube filled with air . . . 124
4.7.2 Static analysis of an air cushion with different pressure control . . . 125
4.7.3 Buckling of a gas-supported shell . . . 128
4.7.4 Dynamic analysis of an air cushion with different pressure control . . . 130
4.7.5 Dynamic analysis of a rhomboidal air cushion . . . 131
4.8 Summary . . . 132

5 Mortar-Based Contact Formulation for Inflatable Membranes 135

5.1 Introduction for large deformation contact mechanics . . . 135
5.1.1 Problem description . . . 137
5.1.2 Contact kinematics and constraints . . . 138
5.1.3 IBVP for elastodynamics with contact . . . 142
5.1.4 Weak form of IBVP for elastodynamics incorporating contact . . . 143
5.1.5 Treatment of contact constraints . . . 144
5.2 Mortar method for contact problems . . . 145
5.3 Spatial discretization for mortar-based frictionless contact . . . 149
5.3.1 Problem description . . . 149
5.3.2 Discrete dual ansatz function for Lagrange multipliers . . . 151
5.3.3 Unilateral contact . . . 154
5.3.4 Multibody contact . . . 159

5.4 Numerical integration of mortar integrals . . . 162
5.4.1 Two dimensional problems . . . 163
5.4.2 Three dimensional problems . . . 167
5.5 Active set strategy for contact boundary conditions . . . 172
5.5.1 Normal contact of a deformable body and a rigid obstacle . . . 172
5.5.2 Normal contact of two deformable bodies . . . 181
5.6 Energy conservation for time integration . . . 189
5.7 Numerical examples . . . 191
5.7.1 Contact patch test . . . 191
5.7.2 Hertzian contact problem . . . 194
5.7.3 Frictionless elastic ring impact . . . 195
5.7.4 3D contact of an inflatable ball and an elastic membrane . . . 198
5.8 Summary . . . 203

6 Conclusions **205**
6.1 Review . . . 205
6.2 Outlook . . . 207

Bibliography **211**

A Derivations for Wrinkling Model **223**
A.1 Properties of Ξ . . . 223
A.1.1 Symmetry property of Ξ . . . 223
A.1.2 Positive semidefinite property of Ξ . . . 223

B Derivations for Mortar Contact **225**
B.1 Static condensation for unilateral contact . . . 225
B.2 Basis transformation for two deformable bodies contact . . . 226
B.3 Construction of discrete dual Ansatz functions for 3D case . . . 227
B.4 Energy conservation for time integration . . . 229
B.5 Velocity update algorithm for contact problems with GEMM . . . 230
B.5.1 Problem description . . . 233
B.5.2 Post contact oscillation . . . 234
B.5.3 Influences on the total energy of the system . . . 235

List of Figures

1.1 Motivation: inflatable membranes in reality 2

2.1 Definition of surface on the curvilinear coordinates 10
2.2 Configuration and motion of a continuum 12
2.3 Tonti-diagram 17
2.4 Isoparametric concept of deformation for a four-node membrane element . . 27
2.5 Numerical solution algorithm of IBVP for elastodynamics 43

3.1 Wrinkle in a rectangular membrane 46
3.2 Illustration for wrinkled, inexact and fictitious flat surfaces 47
3.3 Principal state of membrane 48
3.4 Illustration for the rotated basis 50
3.5 Illustration for a fictitious flat surface 52
3.6 Characteristic of the wrinkling direction searching algorithm 53
3.7 Comparison of the perfect plastic process and wrinkling 56
3.8 Closest projection under the definition of the energy norm 57
3.9 Illustration for the intersection of two yield surfaces 65
3.10 Geometric representation of the closest point projection 67
3.11 Geometrical illustration of the principal stresses 73
3.12 Geometry and load condition of a flat membrane 75
3.13 Moment-curvature and wrinkled bandwidth 75
3.14 Cauchy stress on a vertical cut at the mid length of the beam-like membrane . 76
3.15 Geometry and load condition for the shear panel 77
3.16 Comparison for principal stresses of the shear panel 78
3.17 Principal stresses at GP of element 502 79
3.18 Comparison x displacement at node 42 79

3.19 Comparison of the accumulative iteration number 80
3.20 Runtime comparison 80
3.21 Geometry and load condition of the annulus membrane 82
3.22 Stress distribution of the annulus membrane 83
3.23 Accumulative number of iterations 84
3.24 Runtime comparison 84
3.25 Illustration of the fully inflated square airbag 85
3.26 Vertical displacement of point M 86
3.27 Geometry and load condition for the square Kapton membrane 88
3.28 Maximal principal stress with wrinkling model for varied load ratio T1/T2 . 89

4.1 Illustration for inflatable structures 93
4.2 An inflatable membrane filled with incompressible fluid and gas 94
4.3 Definition of pressure forces upon a membrane surface 95
4.4 Illustration of two diffrent types of pressure force 96
4.5 Comparison of different thermodynamics processes 98
4.6 Gas and hydrostatic pressure distribution in an enclosed chamber 99
4.7 Pressure distribution within a partially filled enclosed chamber 100
4.8 Illustration for the boundary normal $\mathbf{n}^s$ and tangential vector $\mathbf{t}^s$ of a chamber 103
4.9 Description for special boundary condition 107
4.10 Illustration for the boundary condition of an enclosed chamber 109
4.11 Illustration for tangential vectors at a common edge 113
4.12 Illustration for enclosed multichamber filled with gas and(or) fluid 115
4.13 Assembly of element contribution to create system matrices 117
4.14 Illustration for arclength-controlled algorithm 121
4.15 Numerical solution algorithm of quasi-elastostatic 123
4.16 Geometry and load condition for inflation of an Ogden air-filled tube 125
4.17 Deformation of the fully inflated tube subjected to an applied force 126
4.18 Influences of enclosed volume on the rate of convergence 126
4.19 Deformation of the enclosed air cushion at the cross section a-a 127
4.20 Pressure-Volume relaionship of the enclosed air cushion 128

4.21 Buckling of a gas supported rotation-free shell 129
4.22 Displacement response at the center node of the air cushion 130
4.23 Displacement response at the center node of the rhomboid air cushion 132

5.1 Motivation for contact mechanics of the inflatable membranes 136
5.2 Contact problem of two deformable bodies under large deformation. 138
5.3 Schematic representation of unregularized Coulomb friction law (1D) 140
5.4 Illustration of two deformable bodies contact 141
5.5 Illustration for typical nonconforming domain decomposition with FEM. . . . 146
5.6 Drawbacks of the node-to-segment approach. 147
5.7 Interpolation functions in 2D contact problems 152
5.8 Interpolation functions in 3D contact problems 153
5.9 Illustration for a unilateral contact problem 155
5.10 Illustration for the equivalent contact stress of a unilateral contact problem . . 156
5.11 Illustration for the equivalent contact stress of 2 deformable bodies 159
5.12 Discontinuous 2D normal vector field 163
5.13 Local searching for 2D mortar segments 164
5.14 Schematic description for the summation of 2D mortar segments 166
5.15 Average unit normal $\mathbf{n}_A$ and unit tangential vectors $\boldsymbol{\tau}_A^{\alpha}$ at node A in 3D space 168
5.16 Illustration for searching procedure of 3D mortar segments 169
5.17 Local searching and mortal integrals evaluation for 3D segments 170
5.18 Illustration of the incremental mortar gap for unilateral contact 174
5.19 Illustration for active set strategy for unilateral 175
5.20 Exact active set strategy algorithm for unilateral contact 176
5.21 Numerical solution algorithm of IBVP elastodynamics for unilateral contact . 180
5.22 Exact active set strategy algorithm for contact of two deformable bodies . . . 184
5.23 Solution algorithm of IBVP elastodynamics contact of 2 deformable bodies . . 187
5.24 Illustration for the velocity jump at contact interfaces 191
5.25 Illustration of the contact patch test 192
5.26 Deformed configuration of the contact patch test example 193
5.27 Illustration of the Hertzian contact example 195

5.28 Comparison of numerical and analytical solutions for the Hertzian problem . 196
5.29 Illustration for the impact of an elastic ring with a rigid obstacle 196
5.30 The pre- and post-contact configurations of the elastic ring with $\rho_\infty = 1.0$ . . . 197
5.31 Impact of an elastic ring with a rigid obstacle 197
5.32 Impact of the inflatable ball and elastic membrane 198
5.33 Problem descriptions for the inflatable ball and an elastic membrane 199
5.34 Deformation sequence for the elastic membrane with regular mesh 200
5.35 Displacement profile at node 1 of the inflatable ball 201
5.36 Velocity profile at node 1 of the inflatable ball 201
5.37 Acceleration profile at node 1 of the inflatable ball 202

6.1 Illustration for the multiscale wrinkling simulation 208

B.1 Geometry of the interested membrane element in the 3D space. 228
B.2 Illustration for the dual Ansatz of node 1 for a 3D membrane element. 229
B.3 Example for contact of a two dimensional box 233
B.4 Time history at the node A for (a) velocity and (b) acceleration 234
B.5 Influences of velocity update over the system total energy 236

List of Tables

2.1 Strong form of IBVP 18
2.2 Comparison of different variational principles 19
2.3 Classification of time stepping algorithms 36

3.1 Comparison of element enrichment 47
3.2 Wrinkling criteria 48
3.3 Flowchart for the projection method wrinkling model 58
3.4 Material properties for the shear panel example 77
3.5 Material properties for the PVC coated polyester 83
3.6 Material properties for the square airbag example 86
3.7 Comparison of results for the square airbag example 86
3.8 Material properties of the Kapton membrane with 4 corner tension 87

4.1 Classification of thermodynamic process 97
4.2 Conclusion for the conservativeness of load stiffness matrix 112
4.3 Summary for a two-step process controlled by different load factors 119

5.1 The KKT conditions for normal contact constraints 140
5.2 Strong form for IBVP wiht contact 142
5.3 Comparison for different regularization methods 145
5.4 Mesh details for the Hertzian example 194
5.5 Displacement norm for inflatable ball contact with membrane (regular) 202
5.6 Displacement norm for inflatable ball contact with membrane (nonregular) . 203

B.1 Classification of $\omega_A z_{N_A}$ at the end of t_{n+1}. 232

Chapter 1

Introduction

This dissertation explores mathematical explanations for the continuum problems under interests. Besides, it provides numerical treatments based on the *finite element method (FEM)* (see, e.g. Hughes [Hug00], Bathe [Bat02]) as well as the solution algorithms for three dominant nonlinearities for the inflatable membranes: The efficient wrinkling models based on the material modification approach, additional stiffness terms due to the deformation-dependent pressure loads on the membrane surfaces and finally the mortar-based formulation to determine the solution of frictionless contact problems in case of finite deformations for inflatable membranes with regard to accuracy, robustness, efficiency and rate of convergence.

The dissertation is written in the manner that the complete framework from mathematical formulations to implementation algorithms is clearly presented. Since the formulation is at first introduced in the continuum description, it allows the implementation with virtually all possibilities of desired spatial discretization. The first part of this chapter is dedicated to the motivation for this research to draw an illustration of relevant nonlinear phenomena and to describe key issues which must be taken into account during the analysis process of inflatable membranes. Then, subsequent sections will provide the state of the art for the problem of interest as well as yet unsolved problems. The outline for the whole dissertation is clarified in the final part of this chapter. Note that for the sake of brevity, this chapter will provide only an important thematic overview. Detailed discussions and literature reviews are deferred to the corresponding parts in subsequent chapters.

1.1 Motivation

Nowadays, much attention is devoted to the lightweight membrane owing to its versatile applications. An important reason is its high load carrying capacity despite comparatively low self weight. This is the main reason why it is commonly used as construction materials for large lightweight structures as well as equipments for space missions where even a small reduction in weight means significant decrease in expense. Its flexibility allows the designs with irregular shapes, thus satisfying simultaneously both mechanical and aesthetic demands. The inflatable membrane, a special type of membrane structures, gains its load carrying capacity from the interaction between the surrounding membrane and filled fluid

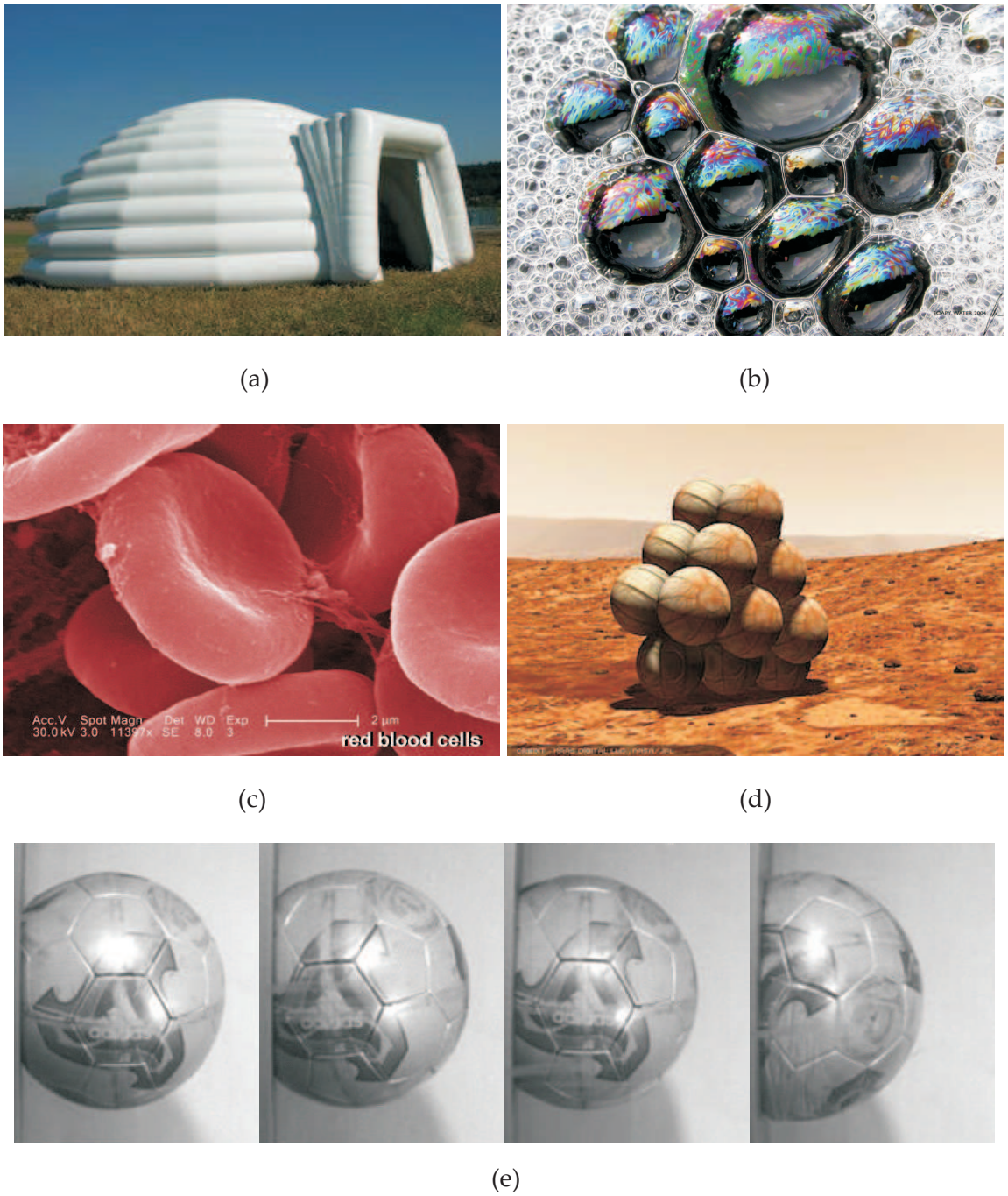

Figure 1.1: Motivation: illustration of inflatable membranes (a) inflatable habitat (http://www.FStructures.com), (b) soap bubbles (http://www.eikongraphia.com), (c) collisions among blood cells and arterial wall (http://www.smartimagebase.com) (d) Mars Exploration Rover airbags for landing protection (http://athena1.cornell.edu) and (e) collision of a soccer ball against a rigid wall (Asai *et.al.* [ASKN07]).

and/or gas. For this reason, this type of structure is usually called the "air-supported structure"

To obtain an insight into the class of interested problems, the best explanation perhaps

is considering the illustrations in Figure 1.1. Frame (a) shows an air-supported membrane structure while frame (b) displays a cluster of soap bubbles which are in equilibrium due to contact interaction between all bubbles and the air pressure inside each bubble. Noticeably, this form of bubbles is an inspiration for numerous modern architectural design, e.g. the Water Cube in Beijing, the Eden project in Cornwall, U.K., etc. Frame (c) displays collisions among blood cells flowing within the blood plasma. Each cell is formed by the cell membrane which covers the internal fluid content of the cell. Furthermore, one can imagine the contact interaction between blood cells and arterial wall. Frame (d) illustrates the Mars Exploration Rover airbags providing a protective cushion for impact with the Martian surface during the landing process (http://athena1.cornell.edu). In frame (e), a series of snapshots for a collision of a soccer ball against a rigid wall is demonstrated. This excellent example captures all aspects of nonlinearities within the scope of this dissertation: The inflatable ball is pressurized with air. Then this inflatable ball undergoes large deformation contact with the rigid wall, whereas abundant wrinkles are noticeable within the area where compressive stresses are induced near the contact zone in the right most picture. Further applications for this kind of structure are airbags in crashworthiness, pneumatic fenders working as protective devices against collision of marine vehicles and marine structures, etc. It is conceivable from this Figure that the inflatable membranes undergoing large deformation which leads to nonlinear relations between actions and responses. Of particular interest are three thematic issues of nonlinearities: the *wrinkling of membranes*, the description of *displacement-dependent forces* acting on the membrane surfaces and the *contact issues of inflatable membranes*.

First, wrinkling of a thin membrane is a local phenomenon caused by the lack of resistance against compressive stresses. To release the excessive compressive stresses, the thin membrane reacts to compressive stresses beyond its capacity by a sudden movement towards the weakest direction, perpendicular to the plane of the membrane surface at that position. Such motion is well known to the community of thin-walled structures as "buckling" which is noticeable by the profile of little waves with wavefronts being perpendicular to the direction of applied compressive stresses at that position (see Figure 1.1(e)). Although the wavelength of a wrinkle depends on material properties and dimension of the membrane in which the wrinkled situates. In general the wavelength is in the vicinity of the membrane thickness. Unless the expected size of an element is smaller than the thickness of the membrane, the simulation cannot represent the geometry of a wrinkle, i.e. the wrinkling phenomena is a sub-scale process beneath the scale of finite element grid. This inaccurate geometric representation yields the wrong kinematic relation which will be delivered to the wrong stress field via the material laws. To avoid this pathological situation, various wrinkling models stemming from either the *kinematic modification (KM)* [RDO87a, RDO87b, Rod91, KI97, KI99, LAL01, HS03, HS05c] or *material modification (MM)* [CS88, DY03, JL96, LAL01, RLVO05, RO03, Ros05, SP89, EF01], have been proposed during the last three decades. The purpose to invent these models for is employing elements with reasonable size, while the stress field is adequately accurate with regard to existing wrinkles.

Although all material modification (MM)-based works mentioned here reflects the state of the art for the MM-bases wrinkling model, most of them concern only the isotropic material except for the initiation to cope with both isotropic and orthotropic materials in [EF01].

Nevertheless, most formulations are presented in the closed form solution for a specific material law and the abrupt modifications on the constitutive law deteriorate the convergence rate. Aiming to fill this gap, the research within this dissertation develops innovative MM-based wrinkling models for both isotropic and orthotropic materials by applying the algorithmic treatment, developed for perfect plasticity process, with wrinkling due to their similarities. The algorithmically consistent modification of material leads to the good rate of convergence. Moreover, the newly developed algorithmic framework allows more freedom for the selection of desired material laws.

Another topic of interest is a decision about the description of the deformation-dependent forces acting on membrane surfaces. Intuitively, an inflatable membrane can be interpreted as a composite material where the interaction between the surrounding membrane and the enclosed fluid and/or gas dictates structural responses to an applied action. This fluid-structure interaction is in general a dynamic process. However, there exist certain situations where inertial terms can be omitted, i.e. the deformation process is remarkably slow, and thus, influences of inertial forces are negligible. With this assumption, there is no inertial forces transferred between the membrane and filled fluid at their interface. This situation is similar to the hydrostatic load case such that the applied force on the membrane surface can be derived from the pressure of fluid contacting with the membrane surface at that point. Although, a computation with this type of solid-fluid interaction is considerably simplified, any restriction must be handled with care.

This type of loading is of particular interest in finite deformation problems in three-dimensional continuum mechanics. The variational formulation of this class of problems and the question of existence of potentials is extensively investigated in the literature, for instance Buffler [Buf84] and reference therein. This issue is discussed in the context of FEM by Schweizerhof and Ramm [SR84] such that the conservativeness of the system is reflected by symmetry of the system matrix, whereas Simo *et.al.* [STW91] consider further the axi-symmetric problems. Bonet *et.al.* [BWMH00] extend the scope of work towards the pneumatic membrane–an enclosed membrane filled with gas–where pressure of the filled gas is linked to its (enclosed) volume via a suitable state equation. In the context of FEM, this additional pressure-volume law leads to a fully-populated system matrix which requires a special solving procedure. Based on this work, recently Rumpel, Schweizerhof and Haßler contribute to dramatic developments for numerical analysis of inflatable membranes in various aspects: single and multichamber gas (pneumatic) and/or fluid (hydraulic) filled inflatable membranes with a special solving algorithm for quasi-static problems [Rum03, RS03, RS04, HS05a, HS08b], stability analysis of inflatable membranes [HS07, HS08a] as well as an application with hydroforming [HS05b]. All works mentioned here concern with quasi-static problems, whereas the endeavors to expand the border towards dynamic problems are recently proposed in [HS08c, JWB08a].

On this account, the concept of deformation-dependent forces has high potential for the inflatable membranes within the scope of this work, i.e. the filled gas inside a pneumatic membrane usually has relatively low density which means that one can discard the inertial forces derived from the change in momentum of this amount of gas mass. Nevertheless, violation of this assumption may affect accuracy and numerical stability.

The last aspect is contact issues of inflatable membranes. As mentioned in Laursen [Lau92], contact problems may be mathematically interpreted as a physical system subjected to a governing variational inequality which has an important characteristic such that the solution and variational spaces are constrained by the physical constraints, which depend on the unknown solution. As a result, the mathematical description of the contact conditions significantly differs from that of typical Dirichlet and Neumann boundary conditions, whereas consideration of friction even complicates the situation. Of more immediate interest is the contact aspects: Finding an unpredictably unknown contact area at any instance of the simulation, while interpenetration between bodies is prohibited. Then, the contact pressure must be determined over the resulting contact area which can significantly evolve owing to the coupling between impenetrability constraints and the contact pressure to fulfill them. This coupling is especially difficult to deal with existing geometrical and material nonlinearities; The formulation and solution of the problems must be handled with care. In particular, the introduction of friction results in higher nonlinearities and associated algorithmic complexity.

Albeit some aspects, e.g. large deformation continuum mechanics, inelastic constitutive response and nonlinear equation solving techniques, involved in solving such problems numerically can be satisfactorily handled with the present technology, the contact issues have not been yet maturely developed. Recently, the mortar-based contact schemes have been introduced with various attractive benefits, which are superior to traditional methods in the literature and finite element softwares available in markets. The idea behind is performing integration of each contact variable over the contact surface and then this result is transferred towards corresponding discrete degree of freedoms to form up a consistent representation of the whole contact variables on one side of the discrete contact surface. Therefore, the mortar-based formulation has high potential for frictionless low speed impact-contact problems of inflatable membranes undergoing large deformation. As a result, the suitable solution technique is the implicit solution scheme which allows large incremental step for calculation and in many cases is unconditionally stable by design.

1.2 Objectives and outline

The goals of this research can be stated as follows:

- ◇ Firstly, this work aims for new and innovative MM-based wrinkling models for both isotropic and orthotropic materials with regard to accuracy, efficiency, computing expense, implementation complexity and rate of convergence. Furthermore, the algorithmic framework must be presented in a general form which is flexible for various material models.
- ◇ The second objective is to consider influences of pressure acting on the membrane surface in a systematic manner via the definition of displacement-dependent forces. This issue leads to additional load stiffness terms caused either by the change in surface normal or the change in pressure magnitude, an implicit function of the deformation of the membranes. With prescribed boundary conditions to preclude nonconservative

deformations, this work concentrates on the case of enclosed membranes filled with either gas or fluid or both of them. Since assembly the load stiffness terms may turn the system matrix to a fully populated one, an additional task in this work is developing suitable solution techniques for quasi-static as well as dynamic analysis for the problem at hands.

- ◇ The next goal is to introduce the mortar-based formulation for low-speed frictionless contact problems for inflatable membranes undergoing large deformation. The expected outcome is an accurate, robust and stable contact formula which reflects the outstanding benefits of the mortar element method. This derived formula appears to be superior to traditional treatment of contact problems. In addition, dual basis functions will be introduced for interpolation of the Lagrange multiplier field to allow local condensation of the nodal Lagrange multiplier. As a result, size of the system matrix is maintained for the whole computation. Besides, a stable implicit solution scheme is developed upon the existing time integration method with algorithmic energy conservation. By means of the post-contact discrete velocity update, the energy conservative time integration method, suitable for the contact problems of interest, is developed.

- ◇ The last issue is combining all algorithms mentioned above to form a complete tool which is capable of simulating all these phenomena simultaneously.

The presentation sequence will proceed as follows. In Chapter 2, all necessary notation and theoretical foundation are expressed to the degree which is adequate for derivations in subsequent chapters. At first, the nonlinear continuum mechanics is explained along with the differential geometry. Then, all governing equations are introduced to create both strong and weak forms of the initial boundary value problem before an introduction of the principal of virtual work and linearization. A specific case is separately described for mechanics of the membrane. The solution procedure begins by performing spatial discretization which transforms a continuous system to a discrete one, in particular for this work, composed of membrane elements. The next section presents temporal discretization as well as stable time integration methods, where in this case the *Generalized-α method* (GEN_α) [CH93] and the *Genealized Energy Momentum Method* (GEMM) [KC99, KR99] are chosen.

In Chapter 3, two wrinkling models are derived on the basis of modifications on the material law to restrict the artificial compressive stiffness of the membrane model to a level existing in reality. As the starting point, description and notation for wrinkled membranes are given along with empirical wrinkling criteria by which current state of membrane is judged. Afterwards, a crucial algorithm to determine the wrinkling direction is shown graphically as well as a discussion about similarities between the perfect plasticity and wrinkling. The first wrinkling model–*the projection method*– presented in this work is less complicated when compared with the second model–*the plasticity analogy*–which adopts the algorithmic treatment developed for the perfect plasticity. To investigate performances of the implementation, numerous benchmark examples are computed for both isotropic and orthotropic materials. At the end, a concise summary ties all contents of this chapter together.

The deformation-dependent forces, which are results of pressure applied on the membrane surface, is defined in Chapter 4. After linearization, relevant load-stiffness terms are

derived and then appended to the system of equations mentioned previously in Chapter 2. In general, the system matrix is non-symmetric due to the load stiffness terms, but it can be symmetrized by introducing specific classes of boundary conditions. The load-stiffness terms can be divided into two parts: the effect of the change of surface normal vectors and the influence from the change in pressure magnitude of the enclosed fluid. The former is local to the point of interest, the latter involves coupling of myriad degrees of freedom. In case of the enclosed inflatable membranes, the latter requires an additional state law relating the magnitude of pressure and volume of fluid enclosed within the membranes. Furthermore, assembling the latter into the system matrix yields a fully-populated matrix which can be effectively handled by the Woodbury's algorithm [Woo50]. In static case, a class of the path following scheme which takes into account advantages of the Woodbury's formula is provided. Extensions towards dynamic analysis is valid as long as the deformation process has comparatively low speed such that the negligence of inertial forces of fluid does not affect the dynamic equilibrium. Later, the idea of multi-chamber is briefly introduced before numerical benchmarks are performed to verify accuracy and proficiency of the implemented codes. Eventually, a summary is given to finalize this chapter.

Chapter 5 presents the mortar-based contact formulation for inflatable membranes in case of frictionless contact problems. At first, the overview of contact mechanics with large deformation is given along with problem descriptions. Then, a strong form for the frictionless contact formulation is described side by side with its weak counterpart for both two and three dimensional cases. Later, spatial discretization with both nominal and dual basis functions are then introduced with the highlight on the orthogonal property of the dual function on the physical space. Besides, the system of equations for unilateral and multi-body contact cases are derived. The subsequent section is dedicated to the numerical treatment of the mortar integration for each contact variable. The following section explains the algorithmic treatment for the active set strategy which is used to predefine a fixed active set of contact constraints at the beginning of each time step. Then any change in the active set is evaluated at the end of that time step to decide whether available solutions are acceptable. Two distinct numerical algorithms, which are employed to solve the contact problem at hand, are separately presented for unilateral and multi-body contact cases. In the post-processing phase, an energy conservation scheme for time integration method is performed via the discrete velocity update algorithm. Lastly, the accuracy of implemented codes is investigated by means of various benchmark examples. The robustness and efficiency of the presented method are emphasized with regard to its advantages for applications on the inflatable membranes.

The summary of this dissertation is given in chapter 6, where all major accomplishments of this work are concluded as well as highly potential aspects for future developments are supplemented.

Chapter 2

Theoretical Foundation

Within this chapter notational and conceptual theoretical background is reviewed for the physical problem of interest. Therefore, the rigorous derivation for large deformation continuum mechanics and relevant variational principles are not the intent; rather, it provides the foundation only in sufficient aspect to motivate the global equations into which the subsequent chapters are incorporated. The interested reader may consider the given references for more details.

2.1 Nonlinear continuum mechanics

Usually, the deformation of continua is defined by the kinematic relations, the balance equations and the constitutive equations. Within this section, a review of necessary nonlinear continuum mechanics theory is given. Various treatises on the topic are available for further reading, e.g. [TN92, MH83, Hol00, Mal69, BW00]. For a common understanding, the Einstein's summation convention is employed throughout this thesis where the Latin index run from 1 to 3 and the Greek from 1 to 2.

2.1.1 Differential geometry of surfaces and bodies in space

In this section the basis of differential geometry will be briefly explained. The description of differential geometry and kinematics employ the classical tensor analysis which suitably explains the processes taking place in *three-dimensional Euclidean space* $\mathbb{R}^3$ as long as space and time are decoupled.

Spatially curved surfaces in $\mathbb{R}^3$ are generally described by either a Cartesian coordinate system x_i which is spanned by orthonormal vectors $\mathbf{e}_i = \mathbf{e}^i$ or a curvilinear coordinate system θ^i. Each material point P on the surface is definitely defined by two independent *surface coordinates* or *surface parameters* θ^1 and θ^2. In general, coordinate lines, lines of constant surface coordinates, are curved lines in space. The position vector $\mathbf{r}$ of a material point P on the surface is, therefore, a vector function of the surface parameters (Figure 2.1):

$$\mathbf{r} = \mathbf{r}(\theta^1, \theta^2) \tag{2.1}$$

θ^1 and θ^2 uniquely define a specific location on the surface which is associated with a pair of coordinates (θ^1, θ^2).

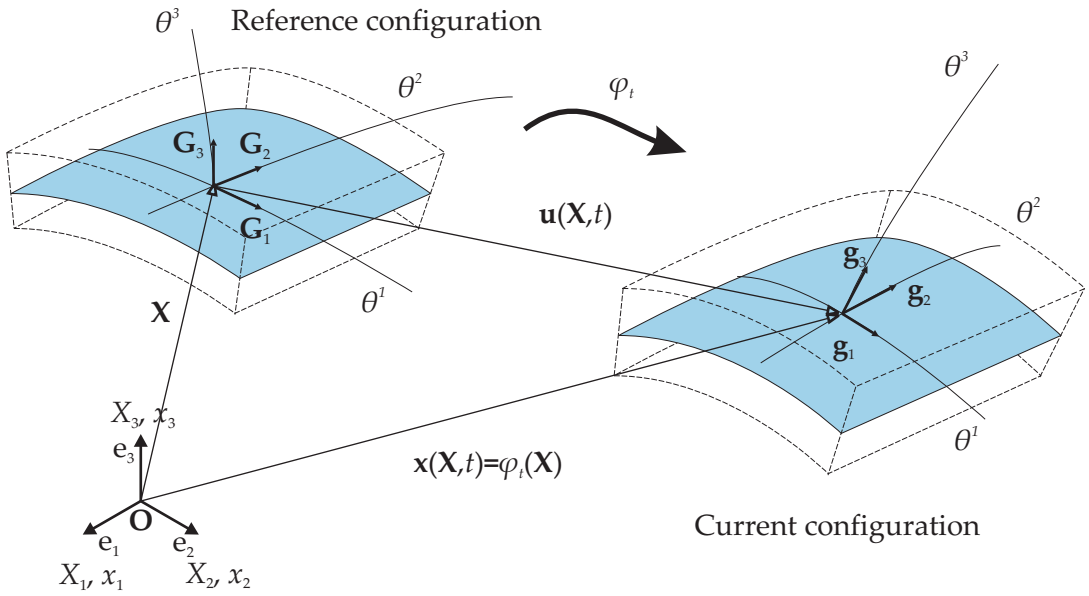

Figure 2.1: Definition of surface on the curvilinear coordinates.

Likewise, a position vector to a given point in a three dimensional body (3D) is denoted as $\mathbf{x}(\theta^1, \theta^2, \theta^3)$, where θ^3 is the parameter in the thickness-direction required to describe a three-dimensional body associated with the surface in Figure 2.1. Therefore, the body under consideration contains the aforementioned surface, its mid-surface, as a subset in the form

$$\mathbf{x}(\theta^1, \theta^2, 0) = \mathbf{x}|_{\theta^3=0} = \mathbf{r}(\theta^1, \theta^2), \qquad \theta^3 \in \left[-\frac{t(\theta^1, \theta^2)}{2}, \frac{t(\theta^1, \theta^2)}{2}\right], \tag{2.2}$$

with $t(\theta^1, \theta^2)$ being the shell thickness. *Covariant base vectors* $\mathbf{g}_1$ and $\mathbf{g}_2$ on the mid-surface are defined by differentiation of the corresponding position vectors $\mathbf{x}$ with respect to the convective coordinate in either case, viz.

$$\mathbf{g}_1 = \frac{\partial \mathbf{x}}{\partial \theta^1}; \qquad \mathbf{g}_2 = \frac{\partial \mathbf{x}}{\partial \theta^2} \quad \Rightarrow \quad \mathbf{g}_i = \mathbf{x}_{,i}\,. \tag{2.3}$$

The covariant base vectors are tangential to the corresponding coordinate lines, e.g. $\mathbf{g}_1$ is tangential to the coordinate line θ^1 where another coordinate θ^2 is constant. Covariant base vectors are in general neither orthogonal nor of unit length. The *surface normal vector* $\mathbf{g}_3$ (Figure 2.1) is defined by

$$\mathbf{g}_3 = \frac{\mathbf{g}_1 \times \mathbf{g}_2}{\|\mathbf{g}_1 \times \mathbf{g}_2\|}; \qquad \|\mathbf{g}_3\| = 1. \tag{2.4}$$

Their scalar products g_{ij}, the components of the covariant metric tensor $\mathbf{I}$ (identity tensor) which reflects the metric of the surface, i.e. the length of the covariant base vectors and the angle between them, can be expressed both in the co- and contravariant basis in the form

$$\mathbf{I} = g_{ij}\mathbf{g}^i \otimes \mathbf{g}^j = g^{ij}\mathbf{g}_i \otimes \mathbf{g}_j = \mathbf{g}^i \otimes \mathbf{g}_i = \mathbf{g}_i \otimes \mathbf{g}^i; \qquad g_{ij} = \mathbf{g}_i \cdot \mathbf{g}_j \text{ and } g^{ij} = \mathbf{g}^i \cdot \mathbf{g}^j, \tag{2.5}$$

where $\otimes$ stands for the tensor product. The contravariant metric tensor is considered as the inversion of the covariant metric tensor:

$$g^{ij} = (g_{ij})^{-1}. \tag{2.6}$$

As a dual pair of the covariant basis, the contravariant basis $\mathbf{g}^i$ are defined by

$$\mathbf{g}^i \cdot \mathbf{g}_j = \delta^i_j = \begin{cases} 1 & i = j, \\ 0 & \text{otherwise}, \end{cases} \tag{2.7}$$

with δ^i_j being the *Kronecker delta*. Eq. (2.7) informs that the contravariant basis $\mathbf{g}^i$ is the dual basis of the covariant basis $\mathbf{g}_j$ such that both of them are orthogonal to each other. Since $\mathbf{g}_3$ is orthogonal to both $\mathbf{g}_1$ and $\mathbf{g}_2$, therefore it results in $\mathbf{g}^3 = \mathbf{g}_3$ and $\left\|\mathbf{g}^3\right\|$=1. The contravariant basis are alternatively defined by partial derivative of the corresponding convective coordinate with respect to the position vector $\mathbf{x}$, viz.

$$\mathbf{g}^1 = \frac{\partial \theta^1}{\partial \mathbf{x}}; \qquad \mathbf{g}^2 = \frac{\partial \theta^2}{\partial \mathbf{x}} \quad \Rightarrow \quad \mathbf{g}^i = \frac{\partial \theta^i}{\partial \mathbf{x}}. \tag{2.8}$$

The co- and contravariant components and base vectors are transformed into each other by use of the metric tensors:

$$A_i = g_{ij} A^j; \quad B^i = g^{ij} B_j; \quad \mathbf{g}_i = g_{ij} \mathbf{g}^j; \quad \mathbf{g}^i = g^{ij} \mathbf{g}_j. \tag{2.9}$$

The differential piece of area *da* is defined as the vector parallelogram which is given by the covariant base vector $\mathbf{g}_1$ and $\mathbf{g}_2$. An infinitesimal area content *da* is given along side the total area *a* in term of the surface coordinates by

$$da = \|\mathbf{g}_1 \times \mathbf{g}_2\| \, d\theta^1 d\theta^2 = j d\theta^1 d\theta^2 \;\Rightarrow\; a = \int_{\theta^1} \int_{\theta^2} j d\theta^1 d\theta^2 = \int_{\theta^1} \int_{\theta^2} \|\mathbf{g}_1 \times \mathbf{g}_2\| \, d\theta^1 d\theta^2. \tag{2.10}$$

2.1.2 Kinematics

Motion and deformation

This section discusses the motion and deformation of continua. The exact definition of bodies is necessary to describe the motion of continua. The notation used in this thesis is summarized in Figure 2.2, which describes a solid body in $\mathbb{R}^{n_{sd}}$, where $n_{sd} = 2$ and $n_{sd} = 3$ stand for a two and three dimensional Euclidean space, respectively. A deformable body $\mathcal{B}$ as shown in Figure 2.2 can be described by a set of points which are in a region of the *Euclidean space* $\mathbb{R}^3$. The body is imagined as being a composition of a (continuous) set of particles (or material points), represented by $\mathrm{P} \in \mathcal{B}$. This body is bounded by the boundary defined by $\partial\mathcal{B}$. As the body $\mathcal{B}$ moves in space from one instance in time to another, it occupies sequence of geometric region named Ω_t. At a specific time $t \in [0, T]$, the regions occupied by the body $\mathcal{B}$ are known as the configuration of $\mathcal{B}$ at the time t. The region $\Omega = \Omega_0$ with the point X corresponding to a fixed *reference time* is considered as the *reference configuration* (or *undeformed configuration*) of the body $\mathcal{B}$. The region at *initial time* $t = 0$ is referred to as the *initial configuration*. For simplicity, we assume that the initial configuration coincides with the reference configuration. A point defined by the position vector $\mathbf{X} \in \Omega$ has the position occupied by a particle $\mathrm{P} \in \mathcal{B}$ at time $t = 0$. As the image of a particle $\mathrm{P} \in \mathcal{B}$, the position vector $\mathbf{X} = X^i \mathbf{e}_i \in \Omega$ is in $\mathbb{R}^3$ with respect to the origin $\mathbf{O}$ (see Figure 2.2). We label X^i,

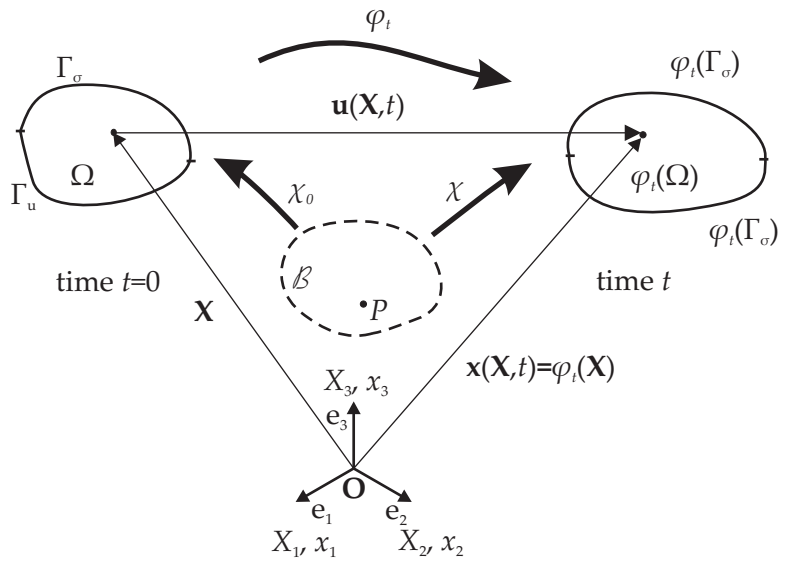

Figure 2.2: Configuration and motion of a continuum.

i=1,2,3, as the *material* (or *referential*) coordinate of point X and $\mathbf{e}_i$ stands for an orthogonal basis in Ω with origin at **O**.

Now, we assume that the body $\mathcal{B}$ moves from the region Ω to a new region Ω_t at a subsequent time $t \in \mathbb{R}^+$. The configuration of the body $\mathcal{B}$ at this time t is named the *current configuration* or *deformed configuration*. A typical point described by a *current position vector* $\mathbf{x} \in \Omega_t$ is the position occupied by a particle $\mathrm{P} \in \mathcal{B}$ at time $t \in \mathbb{R}^+$. The placement of the body $\mathcal{B}$ is described by $\chi_t(\mathcal{B}) = \{\chi(\mathrm{P},t)|\mathrm{P} \in \mathcal{B}\}$. We assume the map $\mathbf{X} = \chi(\mathrm{P},0) = \chi_0(\mathrm{P})$ is a one-to-one mapping $\chi_0 : \mathrm{P} \in \mathcal{B} \rightarrow \mathbf{X} \in \Omega$. The position of a particle $\mathrm{P} \in \mathcal{B}$ in the current configuration Ω_t is defined by the map $\mathbf{x} = \chi(\mathrm{P},t)$ which creates the region $\varphi_t(\Omega)$ at time t. The motion φ of body $\mathcal{B}$ is the temporal series of configuration $\chi_t : \mathcal{B} \rightarrow \mathbb{R}^3$ which is described by

$$\mathbf{x} = \chi\left[\chi_0^{-1}(\mathbf{X}),t\right] = \varphi(\mathbf{X},t), \qquad \Rightarrow \qquad x^i = \varphi^i(X^A,t), \tag{2.11}$$

For the *material description*, often referred to *Lagrangian description*, the convective coordinates are fixed to the surface geometry (Figure 2.1). During the deformation, the attention is paid to what happens with a moving particle, a fixed material point to which the observer is attached. This means that a motion (or other quantities) is characterized with respect to the material coordinate θ^i of a material point in the reference configuration. The *material displacement field* of a typical particle $\mathrm{P} \in \mathcal{B}$ relating its position $\mathbf{X}$ in Ω and its position $\mathbf{x}$ in $\varphi_t(\Omega)$ at time t (see Figure 2.2) can be expressed as the displacement vector:

$$\mathbf{u}(\mathbf{X},t) = \mathbf{x}(\mathbf{X},t) - \mathbf{X} = \varphi(\mathbf{X},t) - \mathbf{X}. \tag{2.12}$$

Note that we use the small letter $\mathbf{u}$ to avoid a conflict with the symbol $\mathbf{U}$ for the *right stretch tensor*. The velocity and the acceleration fields are derived by the material time derivative of

the displacement field in eq. (2.12) such that

$$\mathbf{V}(\mathbf{X},t) = \frac{\mathrm{D}\mathbf{x}(\mathbf{X},t)}{\mathrm{D}t} = \frac{\partial \mathbf{x}(\mathbf{X},t)}{\partial t}\Big|_{\mathbf{X}} = \dot{\mathbf{x}}(\mathbf{X},t) = \dot{\varphi}(\mathbf{X},t), \tag{2.13}$$

$$\mathbf{A}(\mathbf{X},t) = \frac{\mathrm{D}\mathbf{V}(\mathbf{X},t)}{\mathrm{D}t} = \frac{\partial^2 \mathbf{x}(\mathbf{X},t)}{\partial t^2}\Big|_{\mathbf{X}} = \ddot{\mathbf{x}}(\mathbf{X},t) = \ddot{\varphi}(\mathbf{X},t). \tag{2.14}$$

On the convective curvilinear coordinate mentioned in section 2.1.1, the surface coordinates (θ^1, θ^2) stick to the surface geometry and stay invariant during the deformation (Figure 2.1). The line element $d\mathbf{X}$ and $d\mathbf{x}$ are described on this coordinate by $d\mathbf{X}(\theta^1,\theta^2) = \theta^i \mathbf{G}_i = \theta_i \mathbf{G}^i$ and $d\mathbf{x}(\theta^1,\theta^2) = \theta^i \mathbf{g}_i = \theta_i \mathbf{g}^i$, respectively. The co- and contravariant base vectors $\mathbf{G}_i$ and $\mathbf{G}^i$ in the reference configuration Ω stem from the differentiation of $\mathbf{X}$ with respect to the surface coordinates. We adopt all convention in section 2.1.1 with additional notations that lowercase letters refer to quantities based on the current configuration while uppercase letters associate with quantities based on the reference configuration.

A transformation map between a material line element $d\mathbf{X} \in \Omega$ and the corresponding spatial line element $d\mathbf{x} \in \varphi_t(\Omega)$ requires the definition of the *deformation gradient tensor* $\mathbf{F}$:

$$\mathbf{F} = \mathrm{GRAD}\mathbf{x} = \frac{\partial \mathbf{x}}{\partial \theta^i} \otimes \frac{\partial \theta^i}{\partial \mathbf{X}} = \mathbf{g}_i \otimes \mathbf{G}^i,\ \mathbf{F}^T = \mathbf{G}^i \otimes \mathbf{g}_i,\ \mathbf{F}^{-1} = \mathbf{G}_i \otimes \mathbf{g}^i,\ \mathbf{F}^{-T} = \mathbf{g}^i \otimes \mathbf{G}_i. \tag{2.15}$$

Therefore, tangent vectors in Ω is associated with the tangent vector in $\varphi_t(\Omega)$ by

$$\mathbf{g}_i = \mathbf{F}\mathbf{G}_i, \quad \mathbf{G}_i = \mathbf{F}^{-1}\mathbf{g}_i, \quad \mathbf{g}^i = \mathbf{F}^{-T}\mathbf{G}^i, \quad \mathbf{G}^i = \mathbf{F}^T\mathbf{g}^i. \tag{2.16}$$

To preserve the continuous structure in Ω during the deformation, the mapping eq. (2.15) has to be one-to-one, i.e. $\mathbf{F}$ cannot be singular which is equivalent to the condition

$$J = \frac{dv}{dV} = \det\mathbf{F} \neq 0, \tag{2.17}$$

where J defines the *Jacobian determinant*. This positive scalar describes the ratio between the current differential volume dv and the reference differential volume dV of material. Furthermore, to exclude self-penetration of the body, J has to be greater than 0. A transformation between the differential area in the current configuration da with the current unit normal vector $\mathbf{n}$ and its corresponding area in the reference configuration dA with the reference unit normal vector $\mathbf{N}$ is possible with the help of the Nanson's formula (see, e.g. [Hol00]):

$$\mathbf{n}da = \det\mathbf{F}\mathbf{F}^{-T}\mathbf{N}dA. \tag{2.18}$$

Strain mearsure

To close this section, we introduce a commonly used, symmetric and objective material strain measure, the Green-Lagrange strain tensor (GL):

$$\mathbf{E} = \frac{1}{2}(\mathbf{F}^T\mathbf{F} - \mathbf{I}) = \frac{1}{2}(\mathbf{G}^i \otimes \mathbf{g}_i \cdot \mathbf{g}_j \otimes \mathbf{G}^j - G_{ij}\mathbf{G}^i \otimes \mathbf{G}^j) = \frac{1}{2}(g_{ij} - G_{ij})\mathbf{G}^i \otimes \mathbf{G}^j. \tag{2.19}$$

Obviously, the GL strain tensor is based on the initial configuration Ω where $\mathbf{C} = \mathbf{F}^T\mathbf{F}$ is the *right Cauchy-Green tensor*. The identity tensor $\mathbf{I}$, introduced in eq. (2.5), can be defined in the

reference configuration by replacing current co-and contravariant base vectors $\mathbf{g}_i, \mathbf{g}^i$ by their counterpart $\mathbf{G}_i, \mathbf{G}^i$ in the refernce configuration such that

$$\mathbf{I} = G_{ij}\mathbf{G}^i \otimes \mathbf{G}^j = G^{ij}\mathbf{G}_i \otimes \mathbf{G}_j = \mathbf{G}^i \otimes \mathbf{G}_i = \mathbf{G}_i \otimes \mathbf{G}^i, \tag{2.20}$$

where $G_{ij} = \mathbf{G}_i \cdot \mathbf{G}_j$ and $G^{ij} = \mathbf{G}^i \cdot \mathbf{G}^j$ are co- and contravariant components of the metric tensor in the undeformed configuration.

2.1.3 Constitutive equation

Stress measure

The stress measure describes the amount of force taking place in the interior part of material per unit area while it interacts with the neighboring material during the deformation. In this section we introduce a common stress measure, the Cauchy stress tensor

$$\boldsymbol{\sigma}(\mathbf{x}, t) = \sigma^{ij}\mathbf{g}_i \otimes \mathbf{g}_j = \boldsymbol{\sigma}^T(\mathbf{x}, t), \tag{2.21}$$

which is a symmetric stress tensor defined on the current configuration. The Cauchy's stress theorem postulates a relation between the Cauchy traction $\mathbf{t}$ and the unit normal vector $\mathbf{n}$ of an arbitrary surface area da:

$$\boldsymbol{\sigma}(\mathbf{x}, t)\mathbf{n} = \mathbf{t}(\mathbf{x}, t, \mathbf{n}). \tag{2.22}$$

In general, all quantities defined in the current configuration in eq. (2.22) are related to relevant quantities in the initial configuration via the *pull back* operation (see, e.g. [MH83]), and thus, with the help of the Nanson's formula in eq. (2.18) the First Piola-Kirchhoff stress tensor (PK1) is expressed by

$$\mathbf{P} = \det\mathbf{F}\boldsymbol{\sigma}\mathbf{F}^{-T} = \det\mathbf{F}\sigma^{ij}\mathbf{g}_i \otimes \mathbf{G}_j = P^{ij}\mathbf{g}_i \otimes \mathbf{G}_j. \tag{2.23}$$

The PK1 stress tensor $\mathbf{P}$ is regularly non symmetric and it is called a *two-field tensor* where one base vector lies in $\varphi_0(\mathcal{B})$ and the other in $\varphi_t(\mathcal{B})$. Deemed as a pseudo stress vector, the Piola traction $\mathbf{T}$ is defined by

$$\mathbf{PN} = \mathbf{T} \tag{2.24}$$

where $\mathbf{N}$ is the unit normal vector of an area dA which is the corresponding area on the undeformed configuration for the area da of eq. (2.22). With some manipulation, a symmetric stress tensor known as the the second Piola-Kirchhoff stress tensor (PK2) based on the initial configuration $\varphi_0(\mathcal{B})$ is defined by

$$\mathbf{S} = \mathbf{F}^{-1}\mathbf{P} = \det\mathbf{F}\mathbf{F}^{-1}\boldsymbol{\sigma}\mathbf{F}^{-T} = S^{ij}\mathbf{G}_i \otimes \mathbf{G}_j. \tag{2.25}$$

Despite an unphysical stress measure, the PK2 stress tensor plays a key role in the constitutive theory where the PK2 stress is an energetic conjugate of the GL strain tensor in eq. (2.19). Double contraction of an energetic conjugate pair, e.g. PK2 stress tensor and the GL strain tensor, yields the strain energy stored within a deformable body during deformation, viz.

$$\mathbf{S} : \mathbf{E} = S^{ij}\mathbf{G}_i \otimes \mathbf{G}_j : E_{kl}\mathbf{G}^k \otimes \mathbf{G}^l = S^{ij}E_{kl}\delta_i^k\delta_j^l = S^{ij}E_{ij}. \tag{2.26}$$

Material law

This section defines an energetic link between the measures of stress and strain mentioned above by means of a constitutive equation. The constitutive law is created to approximate observed physical behaviors of materials under interest. In this work, a material is postulated to be hyper elastic with the existence of the Helmholtz free-energy function Ψ defined per unit volume. For the case that $\Psi = \Psi(\mathbf{F})$, the Helmholtz free-energy function is referred to as the strain-energy function $\mathbf{W}^{int}$. Since the scope of this work is mainly related to large deformation with small strain, at first, the *St. Venant-Kirchoff material*, a generalized version of linear elastic laws for nonlinear material, is presented for the simplest material law. The existence of Ψ indirectly reflects a path independent stress-strain relation. In general, the hyperelastic material is explained by

$$\mathbf{S} = \frac{\partial \Psi(\mathbf{E})}{\partial \mathbf{E}} \quad \text{with} \quad \mathbf{S} = S^{ij}\mathbf{G}_i \otimes \mathbf{G}_j. \tag{2.27}$$

The fourth order elasticity tensor is derived from a strain-energy function Ψ via

$$\mathbb{C} = \frac{\partial \mathbf{S}(\mathbf{E})}{\partial \mathbf{E}} = \frac{\partial^2 \Psi(\mathbf{E})}{\partial \mathbf{E} \partial \mathbf{E}} \quad \text{with} \quad \mathbb{C} = C^{ijkl}\mathbf{G}_i \otimes \mathbf{G}_j \otimes \mathbf{G}_k \otimes \mathbf{G}_l, \tag{2.28}$$

where elastic moduli C^{ijkl} are constant for this model. The St. Venant-Kirchoff model relates the PK2 stress tensor and the GL strain tensor such that

$$\mathbf{S} = \mathbb{C} : \mathbf{E} \quad \text{with} \quad S^{ij} = C^{ijkl}E_{kl}. \tag{2.29}$$

Basically, the fourth order tensor $\mathbb{C}$ has $3^4 = 81$ independent coefficients. The symmetries of stress and strain tensors and the major symmetry of $\mathbb{C}$, mentioned in [MH83, Mal69], decrease the number of independent elastic constants to 21. By employing the Voigt notation (see [BLM00]), we can convert the symmetric fourth-order constitutive tensor to a constitutive matrix:

$$[\mathbb{C}] = \begin{bmatrix} \mathbb{C}^{1111} & \mathbb{C}^{1122} & \mathbb{C}^{1133} & \mathbb{C}^{1123} & \mathbb{C}^{1113} & \mathbb{C}^{1112} \\ & \mathbb{C}^{2222} & \mathbb{C}^{2233} & \mathbb{C}^{2223} & \mathbb{C}^{2213} & \mathbb{C}^{2212} \\ & & \mathbb{C}^{3333} & \mathbb{C}^{3323} & \mathbb{C}^{3313} & \mathbb{C}^{3312} \\ & & & \mathbb{C}^{2323} & \mathbb{C}^{2313} & \mathbb{C}^{2312} \\ & \textit{symm.} & & & \mathbb{C}^{1313} & \mathbb{C}^{1312} \\ & & & & & \mathbb{C}^{1212} \end{bmatrix}. \tag{2.30}$$

For an isotropic material, which has no preferred orientation directions, components of the tensor of elastic modulus $\mathbb{C}$ are invariant with respect to any rectangular Cartesian coordinate system. Therefore, we can express the tensor of elastic modulus by

$$\mathbb{C} = \lambda \mathbf{I} \otimes \mathbf{I} + 2\mu \mathbb{I} \quad \text{with} \quad C^{ijkl} = \lambda G^{ij}G^{kl} + \mu(G^{ik}G^{jl} + G^{il}G^{jk}). \tag{2.31}$$

The fourth-order symmetric identity tensor $\mathbb{I}$ has components $I_{ijkl} = G^{ik}G^{jl} + G^{il}G^{jk}$, and as a result, the PK2 stress tensor in eq. (2.29) can be rewritten to

$$\mathbf{S} = \lambda \mathrm{tr}(\mathbf{E})\mathbf{I} + 2\mu\mathbf{E}. \tag{2.32}$$

Two Lame's constants λ and μ can be expressed in term of physical constants, Young's modulus E, Poisson's ratio μ and bulk modulus κ:

$$\lambda = \frac{\nu E}{(1+\nu)(1-2\nu)}, \qquad \mu = \frac{E}{2(1+\nu)}, \qquad \kappa = \frac{E}{3(1-2\nu)}. \tag{2.33}$$

Unfortunately, the St. Venant-Kirchoff material is suitable only for the case of small strain. In the case of large strain, various model are available, e.g. the *Ogden* model [Ogd72, Ogd97] postulates that the strain energy is a function of the principal stretches λ_α of the right Cauchy-Green tensor $\mathbf{C}$ by

$$\Psi = \Psi(\lambda_1, \lambda_2, \lambda_3) = \sum_{p=1}^{N} \frac{\mu_p}{\alpha_p}(\lambda_1^{\alpha_p} + \lambda_2^{\alpha_p} + \lambda_3^{\alpha_p} - 3) \tag{2.34}$$

This model is suitable for incompressible rubber like material where the material parameters α_p and μ_p must fulfill the consistency condition with the shear modulus μ such that

$$2\mu = \sum_{p=1}^{N} \mu_p \alpha_p \qquad \text{with} \qquad \mu_p \alpha_p > 0, \qquad p = 1, \dots N. \tag{2.35}$$

From eq. (2.34), the *Mooney-Rivlin* model is obtained by setting $N = 2$, $\alpha_1 = 2$, $\alpha_2 = -2$ and the *Neo-Hookean* model is recovered with $N = 1$, $\alpha_1 = 2$ (see [Hol00]). Moreover, anisotropic materials play a key role in reality, in particular for membranes structures, e.g. [Rai03, Jar04].

2.1.4 Dynamic equilibrium condition

The boundary of Ω denoted by $\partial\Omega$ is divided into two regions: Dirichlet boundary Γ_u and Neumann boundary Γ_σ which are specified by

$$\begin{aligned} \Gamma_u \cup \Gamma_\sigma &= \partial\Omega, \\ \Gamma_u \cap \Gamma_\sigma &= \varnothing. \end{aligned} \tag{2.36}$$

From the local momentum balance (see, e.g. [MH83, Hol00]), the strong form of the dynamic equilibrium condition (Cauchy's first equation of motion) for the finite deformation boundary value problem in the spatial configuration of a space-time referential domain $(\Omega \times [0, T]) \in \mathbb{R}^4$ is written by

$$\begin{aligned} \mathrm{div}\sigma + \mathbf{b} = \rho\mathbf{a} \quad &\text{on} \quad \varphi_t(\Omega), \\ \varphi_t = \bar{\varphi}_t \quad &\text{on} \quad \varphi_t(\Gamma_u), \\ \mathbf{t} = \bar{\mathbf{t}} \quad &\text{on} \quad \varphi_t(\Gamma_\sigma) \end{aligned} \tag{2.37}$$

where $\bar{\varphi}_t \in \Gamma_u \times (0, T) \to \mathbb{R}^{n_{sd}}$ is prescribed location for points on the Dirichlet boundary Γ_u, while $\bar{\mathbf{t}} \in \Gamma_\sigma \times (0, T) \to \mathbb{R}^{n_{sd}}$ is prescribed Cauchy traction on the Neumann boundary Γ_σ. In eq. (2.37), ρ and $\mathbf{a}$ are the density and acceleration in the current configuration and $\mathbf{b}$ stands for the current body force per unit volume. Besides, it is supplemented with the initial conditions at $t = 0$:

$$\begin{aligned} \dot{\varphi}|_{t=0} = \mathbf{V}_0 \quad &\text{on} \quad \bar{\Omega}, \\ \varphi|_{t=0} = \varphi_0 = \mathcal{I} \quad &\text{on} \quad \bar{\Omega}, \end{aligned} \tag{2.38}$$

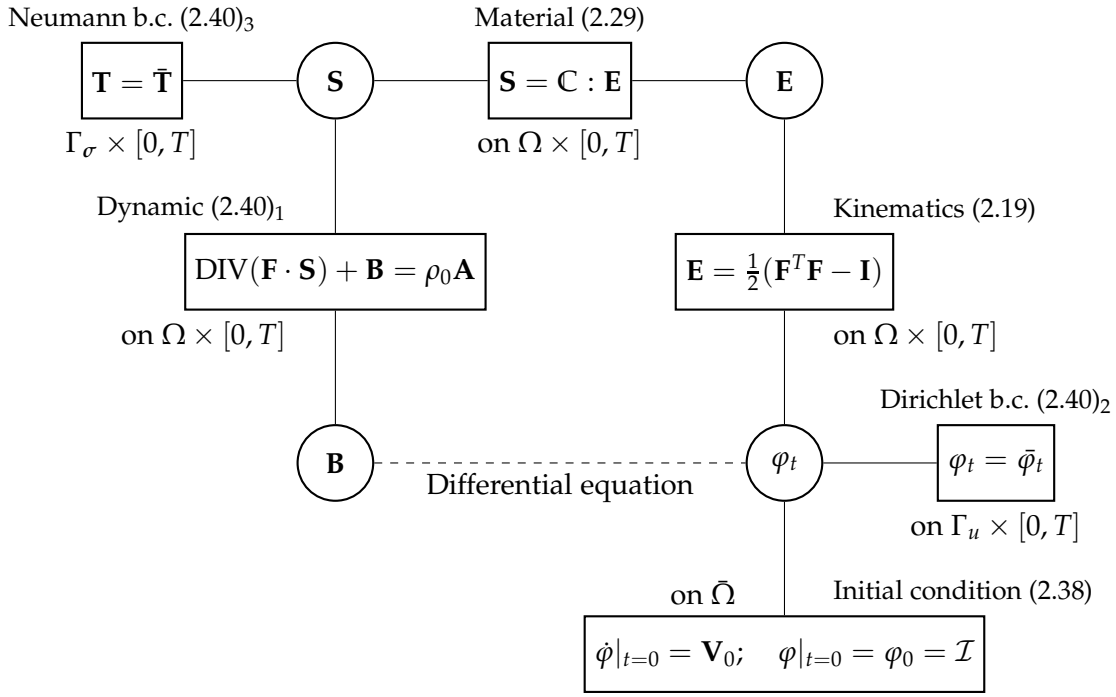

Figure 2.3: Tonti-Diagram for the strong form of IBVP for elastodynamics.

where $\mathcal{I}$ is the identity mapping for the assumption that the reference configuration and the configuration at $t = 0$ are coincident and $\bar{\Omega}$ is the closure, or inclusion of the boundary, of the open set Ω. With the help of the local momentum balance, eq. (2.37) can be pointwise considered in the reference configuration Ω by

$$\begin{aligned} \mathrm{DIV}\mathbf{P} + \mathbf{B} &= \rho_0 \mathbf{A}, \quad \text{on} \quad \Omega \times [0, T], \\ \varphi_t &= \bar{\varphi}_t \quad \text{on} \quad \Gamma_u \times [0, T], \\ \mathbf{T} = \mathbf{P}\mathbf{N} &= \bar{\mathbf{T}} \quad \text{on} \quad \Gamma_\sigma \times [0, T], \end{aligned} \tag{2.39}$$

where $\rho_0 = \det\mathbf{F}\rho$ is the density in the reference configuration, $\mathbf{B} = \det\mathbf{F}\mathbf{b}$ represents the body force per unit volume in the reference configuration Ω. $\mathbf{P}$ is the PK1 stress tensor from eq. (2.23) and $\mathbf{A}$ is the reference acceleration in eq. (2.14). We use the notation DIV for the divergence operator applied in reference coordinates. Following eq. (2.25), the transformation of eq. (2.39) yields

$$\begin{aligned} \mathrm{DIV}(\mathbf{F} \cdot \mathbf{S}) + \mathbf{B} &= \rho_0 \mathbf{A}, \quad \text{on} \quad \Omega \times [0, T], \\ \varphi_t &= \bar{\varphi}_t \quad \text{on} \quad \Gamma_u \times [0, T], \\ \mathbf{T} = \mathbf{F}\mathbf{S}\mathbf{N} &= \bar{\mathbf{T}} \quad \text{on} \quad \Gamma_\sigma \times [0, T]. \end{aligned} \tag{2.40}$$

Moreover, the initial boundary condition in eq. (2.38) is a supplement for both eqs. (2.39) and (2.40).

2.1.5 Initial boundary value problem (IBVP) for elastodynamics

For the solution of continuum mechanics, the contributions of eqs. (2.19), (2.29) and (2.37)-(2.40) are summarized in Table 2.1 to establish a strong form of the initial boundary value problem for elastodynamics. The Tonti's diagram in Figure 2.3 illustrates overall links between each field equations. This formation constitutes a nonlinear system of hyperbolic type partial differential equations [Hug00]. Since it is well known that the analytical solution for this type of equations exists only for very limited cases, hence an approximate solution by numerical methods is preferable. To achieve this goal, a variational principle is employed to turn a strong form into its weak counterpart which is the basis for the FEM.

2.1.6 Weak form of IBVP for elastodynamics

Since the weak formulation of momentum balance equation is the basis for FEM, therefore, the strong form in section 2.1.5 must be transformed into a variational form (weak form) with the help of an energy principle. The simplest one among others, the *principle of virtual work (PVW)*, often known as principle of virtual displacement, is widely used to derive the pure-displacement-based finite element formula. Nevertheless, there exist various number of alternative variational formulations with all possible combinations of weak and strong satisfaction of the field equations and boundary conditions, e.g. the Hellinger-Reissner principle or the Hu-Washizu principle, etc. A comparison of three different variational principles from [Bis99] is shown in Table 2.2. Because this work concerns with the displacement based FEM, thus the next section focuses solely on PVW as the main method to derive FEM while details for other variational principles are available in [Was, TN92] for example.

2.1.6.1 Principle of virtual work

The principle of virtual work (PVW) is the basis for the derivation of the displacement-based FEM, where only the displacement field is chosen as a single variation parameter. The principal idea is to fulfill the dynamic equilibrium equation and the force boundary condition in eq. (2.40) in the weak sense as seen in Table 2.2. Besides, subsidiary conditions: the kinematic, the constitutive equations and the displacement boundary condition, will be

Table 2.1: Strong form for the initial boundary value problem for elastodynamics.

Dynamic equilibrium equation	$\mathrm{DIV}(\mathbf{F}\cdot\mathbf{S})+\mathbf{B}=\rho_0\mathbf{A}, \quad \text{on} \quad \Omega\times[0,T]$
Kinematics (Green-Lagrange strain)	$\mathbf{E}=\frac{1}{2}(\mathbf{F}^T\mathbf{F}-\mathbf{I})=\frac{1}{2}(g_{ij}-G_{ij})\mathbf{G}^i\otimes\mathbf{G}^j$
Constitutive equation	$\mathbf{S}=\mathbb{C}:\mathbf{E}$
Dirichlet boundary condition	$\boldsymbol{\varphi}_t=\bar{\boldsymbol{\varphi}}_t \quad \text{on} \quad \Gamma_u\times[0,T]$
Neumann boundary condition	$\mathbf{T}=\mathbf{FSN}=\bar{\mathbf{T}} \quad \text{on} \quad \Gamma_\sigma\times[0,T]$
Initial condition (at $t=0$)	$\dot{\varphi}\vert_{t=0}=\mathbf{V}_0$ on $\bar{\Omega}$; $\quad\varphi\vert_{t=0}=\varphi_0=\mathcal{I}$ on $\bar{\Omega}$

Table 2.2: Comparison for different variational principles.

Principle	Variables	Euler-Lagrange equations(weak)	Subsidiary conditions (strong)
Virtual work	$\mathbf{u}$	equilibrium force bc.	kinematic equation constitutive equation displacement bc.
Hellinger-Reissner	$\mathbf{u}, \sigma$	equilibrium kinematic equation force bc. displacement bc.	constitutive equation
Hu-Washizu	$\mathbf{u}, \sigma, \epsilon$	equilibrium kinematic equation constitutive equation force bc. displacement bc.	

satisfied in a strong manner. The solution space $\mathcal{C}_t$ for each $t \in (0, T)$ is defined by

$$\mathcal{C}_t = \left\{ \varphi_t : \bar{\Omega} \to \mathbb{R}^{n_{sd}} | \varphi_t \in H^1(\Omega), \varphi_t = \bar{\varphi}_t \text{ on } \Gamma_u \right\}, \tag{2.41}$$

where the *Sobolev space* $H^1(\Omega)$ consists of all vector valued functions over Ω whose values and first derivatives are square integrable over the domain. In general, the space $\mathcal{C}_t$ depends upon t because of the prescribed motion boundary condition $\bar{\varphi}_t$ on Γ_u. Additionally, the weighting function $\delta\varphi$ defined on $\bar{\Omega}$ is a subset of the weighting space $\mathcal{V}$ holding such properties:

$$\mathcal{V} = \left\{ \delta\varphi : \bar{\Omega} \to \mathbb{R}^{n_{sd}} | \delta\varphi \in H^1(\Omega), \delta\varphi = \mathbf{0} \text{ on } \Gamma_u \right\}. \tag{2.42}$$

The variational form is developed by multiplying the governing differential eq. $(2.40)_1$ with an arbitrary weighting function $\delta\varphi \in \mathcal{V}$ and performing integration over the domain Ω by considering the boundary condition eq. $(2.40)_3$ and taking into account the fact that $\delta\varphi = \mathbf{0}$ on Γ_u. With these operations, the outcome is the weak form of the problem:

$$G(\varphi_t, \delta\varphi) = -\delta W = \int_\Omega \rho_0 \mathbf{A} \cdot \delta\varphi d\Omega + \int_\Omega \mathbf{S} : \delta\mathbf{E} d\Omega - \int_\Omega \mathbf{B} \cdot \delta\varphi d\Omega - \int_{\Gamma_\sigma} \bar{\mathbf{T}} \cdot \delta\varphi d\Gamma = 0. \tag{2.43}$$

In addition, the solution is subjected to weak form of the initial boundary conditions:

$$\int_\Omega \delta\varphi \cdot [\varphi|_{t=0} - \varphi_0] d\Omega = 0 \quad \text{and} \quad \int_\Omega \delta\varphi \cdot [\dot{\varphi}|_{t=0} - \mathbf{V}_0] d\Omega = 0. \tag{2.44}$$

One may verify that the strong and weak forms have an equivalent solution. For more details, the reader can consult [Hug00]. The PVW postulates that virtual work of the system δW consists of contributions from inertial forces δW_{dyn}, internal forces δW_{int} and external forces δW_{ext} such that

$$G(\varphi_t, \delta\varphi) = -\delta W = -\delta W_{dyn} - \delta W_{int} - \delta W_{ext} = 0. \tag{2.45}$$

Hence, each term in eq. (2.45) is described by

$$G_{dyn}(\varphi_t, \delta\varphi) = -\delta W_{dyn} = \int_\Omega \rho_0 \mathbf{A} \cdot \delta\varphi d\Omega, \tag{2.46}$$

$$G_{int}(\varphi_t, \delta\varphi) = -\delta W_{int} = \int_\Omega \mathbf{S} : \delta\mathbf{E} d\Omega, \tag{2.47}$$

$$G_{ext}(\varphi_t, \delta\varphi) = -\delta W_{ext} = -\int_\Omega \mathbf{B} \cdot \delta\varphi d\Omega - \int_{\Gamma_\sigma} \bar{\mathbf{T}} \cdot \delta\varphi d\Gamma. \tag{2.48}$$

Note that the external virtual work $\delta W_{ext} = \delta W_{ded} \cup \delta W_{fol} \cup \delta W_{con}$ can be decomposed into influences from deformation-independent forces δW_{ded}, deformation-dependent forces δW_{fol} and contact forces δW_{con}. The last two contributions are discussed in subsequent chapters 4 and 5, respectively.

2.1.6.2 Linearization

Naturally, the weak form IBVP in eq. (2.43) must be solved iteratively due to various sources of nonlinearity, e.g. geometric nonlinearities, material nonlinearities, or nonlinearities from constrained boundary conditions as in contact. With an eye toward the Newton-Raphson solution algorithm, consistent linearization of the mathematical model is necessary to maintain the best convergence rate. Mathematical details can be found for example in [MH83]. Schematically, to use the Newton-Raphson strategy with eq. (2.43), one starts at a deformation state φ_t^k at which the body under investigation is in equilibrium and solves a linearized problem:

$$\mathbf{LIN}(G(\varphi_t, \delta\varphi)) = G(\varphi_t^k, \delta\varphi) + \Delta G(\varphi_t^k, \delta\varphi) = 0 \tag{2.49}$$

for $\Delta\varphi$, where a quantity $\Delta(\cdot)$ stands for the directional derivative of $(\cdot)$in the direction of $\Delta\varphi$:

$$\Delta G(\varphi_t^k, \delta\varphi) = DG(\varphi_t^k, \delta\varphi) \cdot \Delta\varphi = \frac{\partial G(\varphi_t^k, \delta\varphi)}{\partial\varphi} \cdot \Delta\varphi = \frac{d}{d\alpha}\Big|_{\alpha=0} G(\varphi_t^k + \alpha\Delta\varphi, \delta\varphi) \tag{2.50}$$

which defines a linear map in $\Delta\varphi$. The approximate of φ_t is then updated along

$$\varphi_t^{k+1} = \varphi_t^k + \Delta\varphi. \tag{2.51}$$

Iterations on k are continued until the configuration increment $\Delta\varphi$ becomes smaller than a prescribed tolerance, and this is the situation that the nonlinear problem eq. (2.45) is deemed to be solved. With an assumption of displacement-independent external forces, linearization of eq. (2.43) is expressed by

$$\begin{aligned}\Delta G(\varphi_t^k, \delta\varphi) =& \Delta \int_\Omega \rho_0 \mathbf{A} \cdot \delta\varphi d\Omega + \Delta \int_\Omega \mathbf{S} : \delta\mathbf{E} d\Omega - \Delta \int_\Omega \mathbf{B} \cdot \delta\varphi d\Omega - \Delta \int_{\Gamma_\sigma} \bar{\mathbf{T}} \cdot \delta\varphi d\Gamma \\ =& \int_\Omega \rho_0 \Delta\mathbf{A} \cdot \delta\varphi d\Omega + \int_\Omega \left(\Delta\mathbf{S} : \delta\mathbf{E} + \mathbf{S} : \Delta\delta\mathbf{E}\right) d\Omega - \int_\Omega \Delta\mathbf{B} \cdot \delta\varphi d\Omega - \int_{\Gamma_\sigma} \Delta\bar{\mathbf{T}} \cdot \delta\varphi d\Gamma.\end{aligned} \tag{2.52}$$

2.2 Mechanics of membrane structures

Owing to the objective to analyze pneumatic membrane structures, this section provides a brief overview about the model which is suitable to describe mechanical behaviors of membrane structures. In general, a membrane is a member in the class of continua. Thus, the theory of continuum mechanics in section 2.1 is inherently valid for mechanics of membranes while the governing equations for general continua in previous section are significantly simplified due to the assumptions for membrane structures.

2.2.1 Membrane theory

As seen in Figure 2.1, a membrane is considered as a surface structure due to the high slenderness ratio between its thickness h and the dimension in the perpendicular plane of the thickness. From a mechanical point of view, a membrane is a thin-walled structure with extremely low bending stiffness which destines its load-carrying behaviors such that the membrane significantly deforms under forces applied perpendicular to its mid-surface to another configuration in which a balance between the applied forces and stresses developed within the tangential plane of the membrane mid-surface is held. Based on this characteristic, the following assumptions are introduced:

- ◇ The membrane is extremely thin with constant thickness h during the deformation. In doing so, we neglect the poison's effect which relates the in-plane deformation with that of the thickness direction. For this reason, shear strains associated with the thickness direction vanish
$$E_{13} = E_{23} = 0. \tag{2.53}$$
- ◇ The distribution of normal stresses in the tangential plane of the mid-surface is constant over the thickness.
- ◇ The plane stress condition is assumed on the mid-plane of the membrane where all stress components with respect to the thickness direction are neglected, viz.
$$S^{i3} = S^{3i} = 0 \quad \text{and} \quad \sigma^{i3} = \sigma^{3i} = 0. \tag{2.54}$$

Geometry of a membrane is conveniently described by the convective surface coordinates (θ^1, θ^2) on its midplane. Therefore, the concept of differential geometry for surfaces in section 2.1.1 is valid for the membrane mid-surface which means that all geometrical fields defined on the membrane are functions of the surface coordinates (θ^1, θ^2) on the membrane mid-surface. As a result, the displacement field in eq. (2.12) can be rewritten to

$$\mathbf{u}(\theta^1, \theta^2, t) = \mathbf{x}(\theta^1, \theta^2, t) - \mathbf{X}(\theta^1, \theta^2) = \varphi(\theta^1, \theta^2, t) - \mathbf{X}(\theta^1, \theta^2). \tag{2.55}$$

From this equation, the independence of the field quantities from the surface coordinate θ^3 in the thickness direction is thus illuminated. This issue is mentioned in [Bis99] as semi-discretization in the thickness direction while field quantities in other two directions are

still continuous. This pre-operation in the thickness direction makes pre-integration of the weak form in eq. (2.43) over the thickness h. Consequently, a three dimensional integration domain in eq. (2.43) is degenerated into the two dimensional mid-surface of the membrane itself. Owing to the assumption of constant thickness h we can transform the volume ratio in eq. (2.17) with the help of eq. (2.10) into

$$hda = \det\mathbf{F} h dA \quad \Rightarrow \quad da = \det\mathbf{F} dA \quad \Rightarrow \quad \det\mathbf{F} = J = \frac{\|\mathbf{g}_1 \times \mathbf{g}_2\| \, d\theta^1 d\theta^2}{\|\mathbf{G}_1 \times \mathbf{G}_2\| \, d\theta^1 d\theta^2}. \tag{2.56}$$

2.2.2 Kinematics for membrane structures

In this section, we can simplify the kinematics for three-dimensional continua in section 2.1.2 into the two dimensional version on the mid-surface of a membrane. With all assumptions mentioned above, we can rewrite the GL strain tensor in eq. (2.19) for the membrane mid-surface, viz

$$\mathbf{E} = \frac{1}{2}(\mathbf{F}^T\mathbf{F} - \mathbf{I}) = \frac{1}{2}(\mathbf{G}^\alpha \otimes \mathbf{g}_\alpha \cdot \mathbf{g}_\beta \otimes \mathbf{G}^\beta - G_{\alpha\beta}\mathbf{G}^\alpha \otimes \mathbf{G}^\beta) = \frac{1}{2}(g_{\alpha\beta} - G_{\alpha\beta})\mathbf{G}^\alpha \otimes \mathbf{G}^\beta, \tag{2.57}$$

as well as the variation of eq. (2.57):

$$\begin{aligned}\delta\mathbf{E} &= \frac{1}{2}(\delta\mathbf{F}^T\mathbf{F} + \mathbf{F}^T\delta\mathbf{F}) = \frac{1}{2}(\mathbf{G}^\alpha \otimes \delta\mathbf{g}_\alpha \cdot \mathbf{g}_\beta \otimes \mathbf{G}^\beta + \mathbf{G}^\alpha \otimes \mathbf{g}_\alpha \cdot \delta\mathbf{g}_\beta \otimes \mathbf{G}^\beta) \\ &= \frac{1}{2}(\delta\mathbf{g}_\alpha \cdot \mathbf{g}_\beta + \mathbf{g}_\alpha \cdot \delta\mathbf{g}_\beta)\mathbf{G}^\alpha \otimes \mathbf{G}^\beta,\end{aligned} \tag{2.58}$$

and the directional derivative of eq. (2.58):

$$\begin{aligned}\Delta\delta\mathbf{E} &= \frac{1}{2}(\delta\mathbf{F}^T\Delta\mathbf{F} + \Delta\mathbf{F}^T\delta\mathbf{F}) = \frac{1}{2}(\mathbf{G}^\alpha \otimes \delta\mathbf{g}_\alpha \cdot \Delta\mathbf{g}_\beta \otimes \mathbf{G}^\beta + \mathbf{G}^\alpha \otimes \Delta\mathbf{g}_\alpha \cdot \delta\mathbf{g}_\beta \otimes \mathbf{G}^\beta) \\ &= \frac{1}{2}(\delta\mathbf{g}_\alpha \cdot \Delta\mathbf{g}_\beta + \Delta\mathbf{g}_\alpha \cdot \delta\mathbf{g}_\beta)\mathbf{G}^\alpha \otimes \mathbf{G}^\beta.\end{aligned} \tag{2.59}$$

Due to the lack of bending stiffness, a membrane is incapable of withstand forces in the out-of-plane direction (thickness direction). Consequently, a pretension is required to generate the initial stiffness within the membrane to which the state of self-equilibrium due to the prescribed pretension is attained before the out-of-plane forces can be introduced. In general, the pretension can be imposed within the membrane either by the mechanical approach or by the pneumatic approach. The interested readers may look [Lew03] for explanations. A procedure to find out this self-equilibrated configuration for the membrane is called "*form finding*" (see, for instance, in [Ble98, WB05, Wüc06]). Then, this self-equilibrated configuration, which is the outcome of the form finding procedure, is used as the reference configuration for further loading process.

2.2.3 Constitutive equation for membrane structures

Likewise, we can replace the constitutive equations for three-dimensional continua in section 2.1.3 by an alternative for the membrane structures in this section. With the imposed

pretension, a total PK2 stress tensor $\mathbf{S}$ within a membrane is a combination of the PK2 prestress tensor $\mathbf{S}_{pre}$ and the elastic PK2 stress tensor $\mathbf{S}_{el}$ with regard to the reference configuration (the self-equilibrated configuration of prestress):

$$\mathbf{S} = \mathbf{S}_{pre} + \mathbf{S}_{el} = \mathbf{S}_{pre} + \mathbb{C}_{2D} : \mathbf{E} \quad \text{or} \quad S^{\alpha\beta} = S^{\alpha\beta}_{pre} + S^{\alpha\beta}_{el} = S^{\alpha\beta}_{pre} + C^{\alpha\beta\tau\upsilon}_{2D} E_{\tau\upsilon}. \tag{2.60}$$

where the elastic PK2 stress tensor $\mathbf{S}_{el}$ is determined by the degenerated version of the St. Venant-Kirchoff model from eq. (2.29) which relates the PK2 stress tensor and the GL strain tensor for the mid-plane of a membrane such that

$$\mathbf{S}_{el} = \mathbb{C}_{2D} : \mathbf{E} \quad \text{with} \quad S^{\alpha\beta}_{el} = C^{\alpha\beta\tau\upsilon}_{2D} E_{\tau\upsilon}, \tag{2.61}$$

with constant 2D elastic moduli $C^{\alpha\beta\gamma\upsilon}_{2D}$ for this model. In reality, a membrane is made of either an isotropic material or an anisotropic, in particular, orthotropic material. In the rest of this section, we provide models for both types of membrane material. From the same reason as for eq. (2.7), the co-and contravariant components of metric tensor in the undeformed configuration relevant to the thickness direction are written by

$$\mathbf{G}^{3\alpha} = \mathbf{G}^{\alpha 3} = \mathbf{G}_{3\alpha} = \mathbf{G}_{\alpha 3} = 0 \quad \text{and} \quad \mathbf{G}^{33} = \mathbf{G}_{33} = 1. \tag{2.62}$$

From the constitutive tensor in eq. (2.29), the state of plane stress in eqs. (2.54) and (2.53) leads to

$$S^{33}_{el} = 0 = \mathbb{C}^{33kl} E_{kl} \quad \Rightarrow \quad E_{33} = -\frac{(\mathbb{C}^{3311} E_{11} + \mathbb{C}^{3322} E_{22})}{\mathbb{C}^{3333}}. \tag{2.63}$$

Therefore, the two-dimensional constitutive tensor $\mathbb{C}_{2D}$ for the mid-plane of a membrane in eq. (2.61) is rewritten for the plane stress condition via

$$C^{\alpha\beta\tau\upsilon}_{2D} = C^{\alpha\beta\tau\upsilon} - \frac{C^{\alpha\beta 33} C^{33\tau\upsilon}}{C^{3333}}. \tag{2.64}$$

Instead of the state of plane stress in 2.64, the state of plane strain is accomplished by $C^{\alpha\beta\tau\upsilon}_{2D} = C^{\alpha\beta\tau\upsilon}$. Note that in the rest of this thesis the subscript $2D$ of the constitutive tensor for the mid-surface of a membrane is neglected since the reader can recognize from the context of equations. Furthermore, the constitutive equation for a plane stress condition is defined with Voigt notation by

$$\{\mathbf{S}\} = \{\mathbf{S}_{el}\} + \{\mathbf{S}_{pre}\} = [\mathbb{C}]\{\mathbf{E}\} + \{\mathbf{S}_{pre}\} \tag{2.65}$$

with $\{\mathbf{S}\} = [S^{11}, S^{22}, S^{12}]^T$, $\{\mathbf{E}\} = [E_{11}, E_{22}, 2E_{12}]^T$, $\{\mathbf{S}_{pre}\} = [S^{11}_{pre}, S^{22}_{pre}, S^{12}_{pre}]^T$,

$$[\mathbb{C}] = \begin{bmatrix} \mathbb{C}^{1111} - \mathbb{C}^{1133}\frac{\mathbb{C}^{3311}}{\mathbb{C}^{3333}} & \mathbb{C}^{1122} - \mathbb{C}^{1133}\frac{\mathbb{C}^{3322}}{\mathbb{C}^{3333}} & \mathbb{C}^{1112} - \mathbb{C}^{1133}\frac{\mathbb{C}^{3312}}{\mathbb{C}^{3333}} \\ \mathbb{C}^{2211} - \mathbb{C}^{2233}\frac{\mathbb{C}^{3311}}{\mathbb{C}^{3333}} & \mathbb{C}^{2222} - \mathbb{C}^{2233}\frac{\mathbb{C}^{3322}}{\mathbb{C}^{3333}} & \mathbb{C}^{2212} - \mathbb{C}^{2233}\frac{\mathbb{C}^{3312}}{\mathbb{C}^{3333}} \\ \mathbb{C}^{1211} - \mathbb{C}^{1233}\frac{\mathbb{C}^{3311}}{\mathbb{C}^{3333}} & \mathbb{C}^{1222} - \mathbb{C}^{1233}\frac{\mathbb{C}^{3322}}{\mathbb{C}^{3333}} & \mathbb{C}^{1212} - \mathbb{C}^{1233}\frac{\mathbb{C}^{3312}}{\mathbb{C}^{3333}} \end{bmatrix} \tag{2.66}$$

At this point, we introduce a local Cartesian basis with the definition:

$$\mathbf{i}_1 = \frac{\mathbf{G}_1}{\|\mathbf{G}_1\|}, \quad \mathbf{i}_3 = \mathbf{G}_3 = \frac{\mathbf{G}_1 \times \mathbf{G}_2}{\|\mathbf{G}_1 \times \mathbf{G}_2\|}, \quad \mathbf{i}_2 = \frac{\mathbf{i}_3 \times \mathbf{i}_1}{\|\mathbf{i}_3 \times \mathbf{i}_1\|} \tag{2.67}$$

2.2.3.1 Isotropic material model for membrane structures

For this kind of material, ETFE(Ethylen tetrafluoroethylene) foil is a prevalent example which is mainly used nowadays for pneumatic structures with small span. ETFE is light and extremely thin around 50-200 μm [Mor00, MB02]. Substituting the Lame's constant of eq. (2.33) into eq. (2.66), one obtains the closed form for an isotropic material model under the state of plane stress on the local Cartesian basis in eq. (2.67):

$$\{\bar{\mathbf{S}}_{el}\} = \left[\bar{\mathbb{C}}\right]\{\bar{\mathbf{E}}\} \quad \Rightarrow \quad \begin{Bmatrix} \bar{S}^{11}_{el} \\ \bar{S}^{22}_{el} \\ \bar{S}^{12}_{el} \end{Bmatrix} = \frac{E}{1-\nu^2}\begin{bmatrix} 1 & \nu & 0 \\ \nu & 1 & 0 \\ 0 & 0 & \frac{1-\nu}{2} \end{bmatrix}\begin{Bmatrix} \bar{E}_{11} \\ \bar{E}_{22} \\ 2\bar{E}_{12} \end{Bmatrix}, \tag{2.68}$$

where the quantities with overbar are based on the local Cartesian basis in eq. (2.67).

2.2.3.2 Orthotropic material model for membrane structures

Another popular membrane material is the fiber composite fabric, e.g. Polyvinyl chloride (PVC) coated polyester fabrics or Polyetrafluoroethylene (PTFE) coated glass fiber fabrics. This kind of material gains increased importance due to new developments of fiber materials such as glass, carbon or aramid fibers which are embedded in a less stiff matrix material. The combination results in anisotropic behavior of the fiber composite material whose mechanical characteristics depend strongly on the orientation of embedded fibers. Obviously, fiber directions destine preferred directions for this material. According to the manufacturing process, the majority of fiber composite materials for membrane structures have two families of fiber orthogonally interwoven to each other. For this reason, they are classified into the class of orthotropic materials.

This section introduces a simple phenomenological orthotropic constitutive model which is suitable for orthotropic membrane materials on the macroscopic scale. Based on the bilateral tensile testing in [MR95], this constitutive model is created to approximate the underlying microscopic properties in terms of macroscopic material parameters. Under the state of plane stress, the closed form of an orthotropic material model whose preferred fiber directions coinciding with the local Cartesian basis in eq. (2.67) can be described by

$$\begin{Bmatrix} \bar{S}^{k}_{el} \\ \bar{S}^{s}_{el} \\ \bar{S}^{ks}_{el} \end{Bmatrix} = \frac{1}{1-\nu_{ks}\nu_{sk}}\begin{bmatrix} E_k & \nu_{ks}E_k & 0 \\ \nu_{sk}E_s & E_s & 0 \\ 0 & 0 & (1-\nu_{ks}\nu_{sk})\cdot G \end{bmatrix}\begin{Bmatrix} \bar{E}_{k} \\ \bar{E}_{s} \\ 2\bar{E}_{ks} \end{Bmatrix} \tag{2.69}$$

with the symmetry condition $\frac{\nu_{ks}}{\nu_{sk}} = \frac{E_s}{E_k}$ where E_k and E_s are the Young's modulus in the k and s direction, respectively. The Poison's ratio ν_{sk} and ν_{ks} relate the axial strain in the s and k direction and vice versa, while G denotes shear modulus. Note that subscripts of all stresses and strains are related to their corresponding fiber directions. Furthermore, quantities with overbar are based on the local Cartesian basis which coincide to each orthogonal fiber direction. For further reading, Raible [Rai03] proposed an anisotropic model for membrane structures by introducing structural tensors, while its applications are presented in [Jar04].

2.3 Solution strategies

To acquire an approximate solution of the nonlinear elastodynamics IBVP in eq. (2.43) by FEM, the entity in eq. (2.49) must be in a spatial discret form where a continuum is approximated by its discrete counterpart. As a result, the semidiscrete formulation is assumed, as mentioned in [Hug00]. At first, a continuous weak form of the governing equations is spatially discretized into a semidiscrete weak form which maintains temporal continuity of nodal displacements. The outcome is a nonlinear set of ordinary differential equations, which can be integrated in time with any time integration algorithm. Apart from the spatial and temporal discretization, this section provides information about implicit solution algorithms.

2.3.1 Spatial discretization

By considering the spatial discretization of a body Ω by a finite set of elements $\mathcal{E}^h$

$$\Omega \approx \Omega^h = \bigcup_{\forall e \in \mathcal{E}^h} \Omega^e, \tag{2.70}$$

the reference domain $\Omega \in \mathbb{R}^{n_{sd}}$ is subdivided into a number of element subdomains Ω^e, where e is an index to the specific element, running between 1 and n_{el}, where n_{el} is the total number of elements used for discretization. The superscript h designates an approximate quantity while $\bigcup$ denotes assembly process of all elements in the set $\mathcal{E}^h$. In the following section, we will index the nodes with uppercase letters A, B, C, etc. running between 1 and n_{np}, the total number of nodes in the problem. As a result, the number of degree of freedom (dof) n_{dof} is defined by $n_{dof} = n_{sd} \cdot n_{np}$. The essence of FEM lies in the discretization process which involves two important aspects: approximation of the solution space $\mathcal{C}_t$, and approximation of the weighting space $\mathcal{V}$. The approximation of both spaces is typically expressed in terms of prescribed *interpolation* or *shape* functions (see, e.g. [Hug00, Bat02, ZTZ05]) associated with a finite number of specific nodal points in the mesh. In turn, the interpolated space is finite. Here, we introduce an interpolation function N_A which is associated with a node A by a map $N_A : \bar{\Omega} \to \mathbb{R}^{n_{sd}}$. Given a time t, the finite-dimensional subspace of the solution space $\mathcal{C}_t$ in eq. (2.41) is defined by

$$\mathcal{C}_t^h = \left\{ \varphi_t^h = \sum_{B=1}^{n_{np}} N_B(\mathbf{X}) \mathbf{d}_B(t) |\ \varphi_t^h \approx \bar{\varphi}_t(\mathbf{X}) \text{ on } \mathbf{X} \in \Gamma_u \right\} \tag{2.71}$$

where $\mathbf{d}_B$ is a n_{sd}-vector containing the coordinates of nodal point B at time t. Given a prescribed set of nodal interpolation functions $N_B, B = 1, \ldots, n_{np}$, the discrete solution space $\mathcal{C}_t^h$ must approximately satisfy the displacement boundary condition on Γ_u. For the (Bubnov-) Galerkin FEM, the weighting space $\mathcal{V}$ in eq. (2.42) is interpolated with the same interpolation functions as were used to approximate $\mathcal{C}_t^h$. Accordingly, the finite-dimensional weighting space $\mathcal{V}^h$ can be expressed via

$$\mathcal{V}^h = \left\{ \delta\varphi^h = \sum_{A=1}^{n_{np}} N_A \mathbf{c}_A |\ \delta\varphi^h(\mathbf{X}) = \mathbf{0} \text{ on } \mathbf{X} \in \Gamma_u \right\}. \tag{2.72}$$

In these equations, $\mathbf{c}_A$ stands for a n_{sd}-vector containing the nodal constants of nodal point A. Otherwise arbitrary, the only restriction on $\delta\varphi^h$ is that it must approximately satisfy the homogeneous boundary condition on Γ_u. Discretization of the weak form in eq. (2.43) yields the discrete nonlinear equations:

$$G(\varphi_t^h, \delta\varphi^h) = -\delta W = \int_{\Omega^h} \rho_0 \mathbf{A}^h \cdot \delta\varphi^h d\Omega + \int_{\Omega^h} \mathbf{S}^h : \delta\mathbf{E}^h d\Omega - \int_{\Omega^h} \mathbf{B} \cdot \delta\varphi^h d\Omega - \int_{\Gamma_\sigma^h} \bar{\mathbf{T}} \cdot \delta\varphi^h d\Gamma = 0. \tag{2.73}$$

Furthermore, the initial conditions in eq. (2.44) are simplified in the discrete case by

$$\mathbf{d}_B(0) = \varphi_0(\mathbf{X}_B) \quad \text{and} \quad \dot{\mathbf{d}}_B(0) = \mathbf{V}_0(\mathbf{X}_B); \quad B = 1, \ldots, n_{np}, \tag{2.74}$$

where $\mathbf{X}_B$ are the reference coordinates of node B. We can express the nodal vector $\mathbf{c}_A$ and $\mathbf{d}_B$ in terms of their components via

$$\mathbf{c}_A = \{c_{iA}\} \quad \mathbf{d}_B = \{d_{jB}\}; \quad i, j = 1, \ldots, n_{sd}. \tag{2.75}$$

Furthermore, the concept of *ID* array is used to assign the corresponding *global degree of freedom number P* in the problem to the global node number A and spatial dimension number i such that

$$\overbrace{P}^{\text{global dof number}} = ID(\overbrace{i}^{\text{spatial indices}}, \overbrace{A}^{\text{global node number}}). \tag{2.76}$$

Likewise, the element *id* array concept relates the *local element degree of freedom number p* to the local element node number a and spatial dimension number i in the form

$$\overbrace{p}^{\text{local element dof number}} = id(\overbrace{i}^{\text{spatial indices}}, \overbrace{a}^{\text{local element node number}}). \tag{2.77}$$

Because the membrane element is used within this work as the basis for spatial discretization, in the following section we provide details of such kind of elements.

2.3.1.1 Membrane element

At a given time t, the FEM requires that a field variable is approximated over a finite element Ω^e described in Figure 2.4. A reference element on the parametric space $\Omega^\square$ is related to its corresponding element on the physical space by

$$\mathbf{J}_e = \text{GRAD}_{\boldsymbol{\theta}} \mathbf{X} = \frac{\partial \mathbf{X}^{h(e)}}{\partial \boldsymbol{\theta}}; \qquad \mathbf{j}_e = \text{GRAD}_{\boldsymbol{\theta}}\, \varphi^{h(e)} = \frac{\partial \varphi^{h(e)}(\mathbf{X}^{h(e)}, t)}{\partial \boldsymbol{\theta}} \tag{2.78}$$

where $\mathbf{J}_e$ is the deformation gradient between an element in the parametric space $\Omega^\square$ and its corresponding element (reference element) in the physical space Ω^e, whereas $\mathbf{j}_e$ represents the deformation gradient between the same element in the parametric space $\Omega^\square$ and the corresponding element (current element) in the physical space $\varphi^{h(e)}(\Omega^e)$, respectively. For the isoparametric concept, an approximate solution field, i.e. motion, $\varphi^{h(e)}(\mathbf{X}, \mathbf{t})$, an approximate weighting field, i.e. the variation of motion, $\delta\varphi^{h(e)}(\mathbf{X}, t)$, an approximated velocity

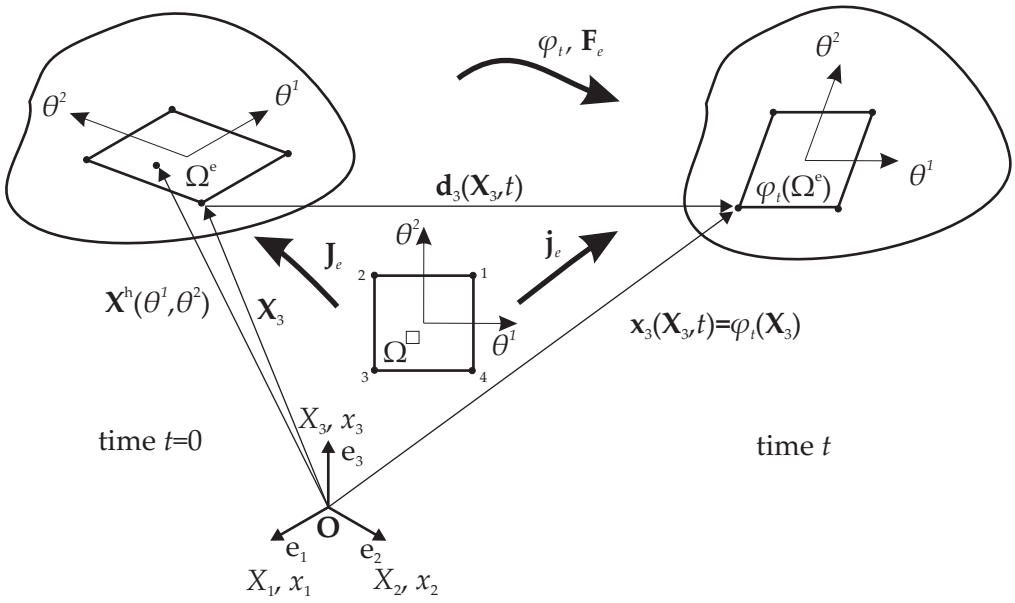

Figure 2.4: Isoparametric description for deformation of a four-node membrane element.

field $\dot{\varphi}^{h(e)}(\mathbf{X},t)$ and an approximate acceleration field $\ddot{\varphi}^{h(e)}(\mathbf{X},t)$ within an element Ω^e can be defined by the same shape function such that

$$\varphi^{h(e)} = \sum_{a=1}^{n_{nod}} N_a(\theta^1,\theta^2)\mathbf{d}_a, \tag{2.79}$$

$$\delta\varphi^{h(e)} = \sum_{a=1}^{n_{nod}} N_a(\theta^1,\theta^2)\mathbf{c}_a, \tag{2.80}$$

$$\dot{\varphi}^{h(e)} = \sum_{a=1}^{n_{nod}} N_a(\theta^1,\theta^2)\dot{\mathbf{d}}_a, \tag{2.81}$$

$$\ddot{\varphi}^{h(e)} = \sum_{a=1}^{n_{nod}} N_a(\theta^1,\theta^2)\ddot{\mathbf{d}}_a, \tag{2.82}$$

where n_{nod} is the number of nodes within an element Ω^e. One observes that shape functions $N_a(\theta^1,\theta^2)$, defined on Ω^e, are independent of time. As a consequence, the material time derivative is applied merely on the nodal value $\mathbf{d}_a$ of $\varphi^{h(e)}$ for an example.

We can relate the local field within an element Ω^e in eq. (2.79) and eq. (2.80) to the global field of the whole domain Ω in eq. (2.71) and eq. (2.72), respectively, via

$$(\ldots)_t \approx (\ldots)_t^h = \bigcup_{e=1}^{n_{el}} (\ldots)_t^{h(e)}. \tag{2.83}$$

To avoid confusion, the indicator for independent parameters $(\mathbf{X},t)$ will be shown only when necessary. With the definition at hand, the discrete virtual work of the system in eq. (2.45) can be considered as the sum of contributions from each finite element such that

$$G^h = G^h_{dyn} + G^h_{int} + G^h_{ext} = \bigcup_{e=1}^{n_{el}} G^{h(e)}_{dyn} + \bigcup_{e=1}^{n_{el}} G^{h(e)}_{int} + \bigcup_{e=1}^{n_{el}} G^{h(e)}_{ext}. \tag{2.84}$$

From eq. (2.46), the approximate virtual work from the inertial force G^h_{dyn} can be described by an assembly of elementwise contributions, viz.

$$\begin{aligned}
G^h_{dyn} &= \bigcup_{e=1}^{n_{el}} G^{h(e)}_{dyn} = \bigcup_{e=1}^{n_{el}} \int_{\Omega^e} \rho_0 \delta\varphi^h \cdot \mathbf{A}^h d\Omega, \\
&= \bigcup_{e=1}^{n_{el}} \int_{\Omega^e} \rho_0 (\sum_{a=1}^{n_{nod}} N_a(\theta^1,\theta^2)\mathbf{c}_a) \cdot (\sum_{b=1}^{n_{nod}} N_b(\theta^1,\theta^2)\ddot{\mathbf{d}}_b) d\Omega, \\
&= \bigcup_{e=1}^{n_{el}} \sum_{a=1}^{n_{nod}} \sum_{b=1}^{n_{nod}} \mathbf{c}_a \cdot [\int_{A^e} \rho_0 N_a(\theta^1,\theta^2) N_b(\theta^1,\theta^2) d\Omega] \ddot{\mathbf{d}}_b, \\
&= \bigcup_{e=1}^{n_{el}} \sum_{a=1}^{n_{nod}} \sum_{b=1}^{n_{nod}} \mathbf{c}_a \cdot m_{ab} \ddot{\mathbf{d}}_b \quad \text{or} \quad \bigcup_{e=1}^{n_{el}} \sum_{a=1}^{n_{nod}} \sum_{b=1}^{n_{nod}} \mathbf{c}_a^T \mathbf{m}_{ab} \ddot{\mathbf{d}}_b,
\end{aligned} \tag{2.85}$$

where m_{ab} is the component of the element mass matrix $\mathbf{m}_{ab} = \delta_{ij} m_{ab}$ for node a and b. By summing up all nodal constant vectors $(\ldots)_b$ into an element constant vector $(\ldots)^{(e)} = \sum_{b=1}^{n_{nod}} (\ldots)_b$, the consistent element mass matrix $\mathbf{m}^{(e)} = \sum_{a=1}^{n_{nod}} \sum_{b=1}^{n_{nod}} \mathbf{m}_{ab}$ is achieved. Eq. (2.85) is described by

$$G^h_{dyn} = \bigcup_{e=1}^{n_{el}} \left(\mathbf{c}^{(e)T} \mathbf{m}^{(e)} \ddot{\mathbf{d}}^{(e)} \right) = \bigcup_{e=1}^{n_{el}} \mathbf{c}^{(e)T} \bigcup_{e=1}^{n_{el}} \mathbf{m}^{(e)} \bigcup_{e=1}^{n_{el}} \ddot{\mathbf{d}}^{(e)} = \mathbf{c}^T \mathbf{M} \ddot{\mathbf{d}}, \tag{2.86}$$

where $\mathbf{M}$ is the *system mass matrix* with constant components during deformation. The n_{dof}-vector $\mathbf{d}$ contains nodal coordinates (in general unknown) which are the degree of freedom of the system while the n_{dof}-vector $\mathbf{c}$ holds the variation of each corresponding degree of freedom in $\mathbf{d}$.

With an assumption that the body force $\mathbf{B}$ and the prescribed traction $\bar{\mathbf{T}}$ are not subjected to discretization, the approximate virtual work from the external forces G^h_{ext} turns to

$$\begin{aligned}
G^h_{ext} &= \bigcup_{e=1}^{n_{el}} G^{h(e)}_{ext} = -\bigcup_{e=1}^{n_{el}} \int_{\Omega^e} \delta\varphi^h \cdot \mathbf{B} d\Omega - \bigcup_{e=1}^{n_{el}} \int_{\Gamma^e_\sigma} \delta\varphi^h \cdot \bar{\mathbf{T}} d\Gamma, \\
&= -\bigcup_{e=1}^{n_{el}} \int_{\Omega^e} (\sum_{a=1}^{n_{nod}} N_a(\theta^1,\theta^2)\mathbf{c}_a) \cdot \mathbf{B} d\Omega - \bigcup_{e=1}^{n_{el}} \int_{\Gamma^e_\sigma} (\sum_{a=1}^{n_{nod}} N_a(\theta^1,\theta^2)\mathbf{c}_a) \cdot \bar{\mathbf{T}} d\Gamma, \\
&= -\bigcup_{e=1}^{n_{el}} \sum_{a=1}^{n_{nod}} \mathbf{c}_a \cdot [\int_{A^e} N_a(\theta^1,\theta^2) \mathbf{B} d\Omega + \int_{\Gamma^e_\sigma} N_a(\theta^1,\theta^2) \bar{\mathbf{T}} d\Gamma] = -\bigcup_{e=1}^{n_{el}} \sum_{a=1}^{n_{nod}} \mathbf{c}_a \cdot \mathbf{f}^{ext}_a(t), \\
&= -\bigcup_{e=1}^{n_{el}} \left(\mathbf{c}^{(e)} \cdot \mathbf{f}^{ext(e)} \right) = -\bigcup_{e=1}^{n_{el}} \mathbf{c}^{(e)} \cdot \bigcup_{e=1}^{n_{el}} \mathbf{f}^{ext(e)}(t) = -\mathbf{c} \cdot \mathbf{f}^{ext}(t) = -\mathbf{c}^T \mathbf{f}^{ext}(t),
\end{aligned} \tag{2.87}$$

where the n_{dof}-external force vector $\mathbf{f}^{ext}(t)$ consists of time dependent applied external forces (known) on each corresponding degree of freedom of $\mathbf{d}$. Although, the dependence of the external force vector $\mathbf{f}^{ext}(t)$ on the system degree of freedom $\mathbf{d}$ is neglected in this chapter, this matter is one of the central topics for this thesis. Therefore chapter 4 is dedicated to explain this issue in details.

For internal forces contribution in eq. (2.47), the GL strain tensor depends nonlinearly on the configuration map $\varphi(\mathbf{X}, t)$. With the discretization of φ in eq. (2.79), the discrete nodal coordinates, the system degree of freedom $\mathbf{d}$, become independent parameters. Thus, the variation of the GL strain tensor for the discrete problems is expressed by

$$\delta\mathbf{E}(\varphi) = \frac{\partial \mathbf{E}(\varphi)}{\partial \varphi}\delta\varphi \quad \approx \quad \delta\mathbf{E}^h(\varphi) = \frac{\partial \mathbf{E}^h(\mathbf{d})}{\partial \mathbf{d}}\delta\mathbf{d} = \frac{\partial \mathbf{E}^h(\mathbf{d})}{\partial \mathbf{d}}\mathbf{c} = \mathbf{E}^h{}_{,\mathbf{d}}\,\mathbf{c}. \tag{2.88}$$

As a result, the approximate version G^h_{int} of the virtual work from internal forces in eq. (2.47) is written by

$$\begin{aligned}
G^h_{int} &= \bigcup_{e=1}^{n_{el}} G^{h(e)}_{int} = \bigcup_{e=1}^{n_{el}} \int_{\Omega^e} \mathbf{S}^h : \delta\mathbf{E}^h d\Omega, \\
&= \bigcup_{e=1}^{n_{el}} \int_{\Omega^e} \mathbf{S}^h : \mathbf{E}^h{}_{,\mathbf{d}^{(e)}}\,\mathbf{c}^{(e)} d\Omega, \\
&= \bigcup_{e=1}^{n_{el}} [\int_{A^e} \mathbf{S}^h : \mathbf{E}^h{}_{,\mathbf{d}^{(e)}}\, d\Omega] \cdot \mathbf{c}^{(e)}, \\
&= \bigcup_{e=1}^{n_{el}} \left(\mathbf{f}^{int(e)}(\mathbf{d}) \cdot \mathbf{c}^{(e)}\right) = \bigcup_{e=1}^{n_{el}} \mathbf{f}^{int(e)}(\mathbf{d}) \cdot \bigcup_{e=1}^{n_{el}} \mathbf{c}^{(e)} = \mathbf{f}^{int}(\mathbf{d}) \cdot \mathbf{c} = \mathbf{c}^T \mathbf{f}^{int}(\mathbf{d}),
\end{aligned} \tag{2.89}$$

where the n_{dof}-internal force vector $\mathbf{f}^{int}(\mathbf{d})$ consists of the equivalent internal forces on each corresponding degree of freedom of $\mathbf{d}$. Combining eqs. (2.86) with (2.87) and (2.89) yields a set of nonlinear ordinary differential equations of the form

$$\mathbf{c}^T[\mathbf{M}\ddot{\mathbf{d}} + \mathbf{f}^{int}(\mathbf{d}) - \mathbf{f}^{ext}(t)] = \mathbf{0}. \tag{2.90}$$

This equation must hold for any n_{dof}-vector $\mathbf{c}$ which satisfies the homogeneous boundary condition imposed on $\delta\varphi$ in eq. (2.72). Since the variation of nodal coordinates $\mathbf{c}$ is arbitrary, therefore the fulfillment of eq. (2.90) is achieved by enforcing the terms within the bracket to be zero. Thus, we can express the *discrete equation of motion* by

$$\mathbf{M}\ddot{\mathbf{d}} + \mathbf{f}^{int}(\mathbf{d}) = \mathbf{f}^{ext}(t). \tag{2.91}$$

In structural dynamics, the *viscous damping matrix* $\mathbf{C}$ is usually added to eq. (2.91) such that

$$\mathbf{M}\ddot{\mathbf{d}} + \mathbf{C}\dot{\mathbf{d}} + \mathbf{f}^{int}(\mathbf{d}) = \mathbf{f}^{ext}(t). \tag{2.92}$$

A particularly convenient form of $\mathbf{C}$ is the *Rayleigh damping matrix* which is a linear combination of the scaled mass matrix and the scaled stiffness matrix. However, this work neglects the influences of damping. Thus, the rest of this thesis concerns only with the discrete equation of motion in eq. (2.91). For the interested readers, various textbook in structural dynamics are available, e.g. [Hug00, CP93].

2.3.1.2 Tangential stiffness matrix for membrane elements

By neglecting the inertial forces contribution from eq. (2.84), the discrete virtual work of a static system created by the membrane finite elements is recovered as

$$G^h = G^h_{int} + G^h_{ext}, \tag{2.93}$$

which is nonlinear in terms of the discretization parameters $\mathbf{d}$, the degree of freedom of the system. Dealing with the non-linear problem at hand requires an iterative solution scheme, in particular, the Newton-Raphson iterative solution algorithm. As the basis for the Newton-Raphson method, linearization of the discrete virtual work in eq. (2.93), based on the continuous version in section 2.1.6.2, must be executed such that

$$\mathbf{LIN}(G^h(\mathbf{d}_t, \delta\mathbf{d})) = G^h_{int}(\mathbf{d}^k_t, \delta\mathbf{d}) + \Delta G^h_{int}(\mathbf{d}^k_t, \delta\mathbf{d}) + G^h_{ext}(\mathbf{d}^k_t, \delta\mathbf{d}) + \Delta G^h_{ext}(\mathbf{d}^k_t, \delta\mathbf{d}) = 0. \quad (2.94)$$

In general, the external force vector $\mathbf{f}^{ext}$ may depend on the nodal displacement $\mathbf{u}$, in other words, nodal coordinate $\mathbf{d}$. As mentioned in section 2.1.6.1, this chapter adopts an assumption that $\mathbf{f}^{ext}$ is independent of nodal displacements. Therefore, $\Delta G^h_{ext}(\mathbf{d}^k_t, \delta\mathbf{d}) = 0$ and it is dropped out from the equation. With eqs. (2.87) and (2.89), eq. (2.94) can be rewritten to

$$\mathbf{c} \cdot \frac{\partial \mathbf{f}^{int}(\mathbf{d})}{\partial \mathbf{d}}\Big|_{\mathbf{d}^k_t} \Delta\mathbf{d} = \mathbf{c} \cdot \left(\mathbf{f}^{ext}(t) - \mathbf{f}^{int}(\mathbf{d}^k_t)\right) \quad (2.95)$$

within this equation the parameter t stands for a pseudo-time parameter acting as the control parameter over applied external forces for the system of equations in a static case. Therefore, the $n_{dof} + 1$ unknowns for this system of equations are the n_{dof}-vector of incremental change in the nodal coordinate $\Delta\mathbf{d}$ and the pseudo-time parameter t. Dropping out the variation $\mathbf{c}$, which is arbitrary, yields the algebraic structural equation:

$$\underbrace{\frac{\partial \mathbf{f}^{int}(\mathbf{d})}{\partial \mathbf{d}}\Big|_{\mathbf{d}^k_t}}_{\mathbf{K}_T} \Delta\mathbf{d} = \underbrace{\mathbf{f}^{ext}(t) - \mathbf{f}^{int}(\mathbf{d}^k_t)}_{\mathbf{f}} \quad \Rightarrow \quad \mathbf{K}_T \Delta\mathbf{d} = \mathbf{f} \quad \text{or} \quad K_{T_{PQ}} \Delta d_Q = f_P, \quad (2.96)$$

where $\mathbf{K}_T$ is the tangential stiffness matrix and $\mathbf{f}$ stands for the out-of-balance force vector. From eqs. (2.47) and (2.89), the internal virtual work of the discrete domain Ω^h in eq. (2.93) composed of membrane finite elements can be described via

$$G^h_{int}(\mathbf{d}, \mathbf{c}) = \mathbf{c} \cdot \mathbf{f}^{int}(\mathbf{d}) = \int_{\Omega^h} [\mathbf{S}^h : \delta\mathbf{E}^h] d\Omega. \quad (2.97)$$

For further derivation, variation of the deformation gradient $\mathbf{F}$ with respect to each dof of the nodal coordinates vector $\mathbf{d}$ must be performed such that

$$\delta\mathbf{F} = \frac{\partial \mathbf{F}}{\partial d_P} \delta d_P = \delta\mathbf{g}_\alpha \otimes \mathbf{G}^\alpha = \frac{\partial \mathbf{g}_\alpha}{\partial d_P} \delta d_P \otimes \mathbf{G}^\alpha; \quad P = 1, \ldots, n_{dof} \quad (2.98)$$

with

$$\delta\mathbf{g}_\alpha = \delta\mathbf{x}_{,\alpha} = \frac{\partial \mathbf{g}_\alpha}{\partial d_P} \delta d_P = \mathbf{g}_{\alpha,P}\, \delta d_P = \sum_{a=1}^{n_{nod}} N_{a,\alpha} \frac{\partial \mathbf{d}_a}{\partial d_P} \delta d_P; \quad P = 1, \ldots, n_{dof} \quad (2.99)$$

where d_P is the P^{th} dof of the discretized problem. With the help of eqs. (2.58), (2.59), and (2.98) the directional derivative of $G^h_{int}(\mathbf{d}, \mathbf{c})$ from eq. (2.97) in the direction of the change

in nodal coordinate $\Delta\mathbf{d}$ can be described by

$$\begin{aligned}\Delta G^h_{int}(\mathbf{d},\mathbf{c}) &= \mathbf{c}\cdot\Delta\mathbf{f}^{int}(\mathbf{d}) = \mathbf{c}\cdot\frac{\partial\mathbf{f}^{int}(\mathbf{d})}{\partial\mathbf{d}}\Delta\mathbf{d},\\ &= \int_{\Omega^h}[\Delta\mathbf{S}^h:\delta\mathbf{E}^h+\mathbf{S}^h:\Delta\delta\mathbf{E}^h]d\Omega = \int_{\Omega^h}[\Delta\mathbf{E}^h:\mathbb{C}:\delta\mathbf{E}^h+\mathbf{S}^h:\Delta\delta\mathbf{E}^h]d\Omega,\\ &= \int_{\Omega^h}[\frac{\partial\mathbf{E}^h}{\partial d_Q}\Delta d_Q:\mathbb{C}:\frac{\partial\mathbf{E}^h}{\partial d_P}\delta d_P+\mathbf{S}^h:\frac{\partial\mathbf{E}^h}{\partial d_Q\partial d_P}\delta d_P\Delta d_Q]d\Omega;\ P,Q=1,\dots,n_{dof},\\ &= \int_{\Omega^h}[\mathbf{E}^h{}_{,Q}\,\Delta d_Q:\mathbb{C}:\mathbf{E}^h{}_{,P}\,\delta d_P+\mathbf{S}^h:\mathbf{E}^h{}_{,PQ}\,\delta d_P\Delta d_Q]d\Omega;\ P,Q=1,\dots,n_{dof}\end{aligned}\tag{2.100}$$

with

$$\mathbf{E}^h{}_{,P} = \frac{1}{2}(\mathbf{g}_{\alpha,P}\cdot\mathbf{g}_\beta+\mathbf{g}_\alpha\cdot\mathbf{g}_{\beta,P})\mathbf{G}^\alpha\otimes\mathbf{G}^\beta;\quad P=1,\dots,n_{dof},\tag{2.101}$$

$$\mathbf{E}^h{}_{,PQ} = \frac{1}{2}(\mathbf{g}_{\alpha,P}\cdot\mathbf{g}_{\beta,Q}+\mathbf{g}_{\alpha,Q}\cdot\mathbf{g}_{\beta,P})\mathbf{G}^\alpha\otimes\mathbf{G}^\beta;\quad P,Q=1,\dots,n_{dof}.\tag{2.102}$$

By looking at eq. (2.99), one finds that $\mathbf{E}^h{}_{,PQ}$ is independent of nodal coordinates. With eq. (2.102), each component of the tangential stiffness $\mathbf{K}_T$ in eq. (2.96) is demonstrated by

$$K_{T_{PQ}} = \overbrace{h\int_{A^h}\mathbf{E}^h{}_{,Q}:\mathbb{C}:\mathbf{E}^h{}_{,P}\,dA}^{K_{e+u_{PQ}}}+\overbrace{h\int_{A^h}\mathbf{S}^h:\mathbf{E}^h{}_{,PQ}\,dA}^{K_{g_{PQ}}}\tag{2.103}$$

with

$$K_{e+u_{PQ}} = \frac{1}{4}h\int_{A^h}\left[(\mathbf{g}_{\alpha,Q}\cdot\mathbf{g}_\beta+\mathbf{g}_\alpha\cdot\mathbf{g}_{\beta,Q})C^{\alpha\beta\gamma\eta}(\mathbf{g}_{\gamma,P}\cdot\mathbf{g}_\eta+\mathbf{g}_\gamma\cdot\mathbf{g}_{\eta,P})\right]dA,\tag{2.104}$$

$$K_{g_{PQ}} = \frac{1}{2}h\int_{A^h}\left[S^{\alpha\beta}(\mathbf{g}_{\alpha,P}\cdot\mathbf{g}_{\beta,Q}+\mathbf{g}_{\alpha,Q}\cdot\mathbf{g}_{\beta,P})\right]dA\tag{2.105}$$

or in the matrix form:

$$\mathbf{K}_T = \mathbf{K}_{e+u}+\mathbf{K}_g\tag{2.106}$$

where $\mathbf{K}_{e+u}$ is the elastic and initial displacement stiffness matrix and $\mathbf{K}_g$ represents the geometric stiffness matrix. Furthermore, the internal force vector $\mathbf{f}^{int}$ is summarized to

$$\mathbf{f}^{int}(\mathbf{d}) = h\int_{A^h}\mathbf{S}^h:\mathbf{E}^h{}_{,\mathbf{d}}\,dA,\tag{2.107}$$

or

$$f^{int}_P(\mathbf{d}) = h\int_{A^h}\mathbf{S}^h:\mathbf{E}^h{}_{,P}\,dA = \frac{1}{2}h\int_{A^h}S^{\alpha\beta}(\mathbf{g}_{\alpha,P}\cdot\mathbf{g}_\beta+\mathbf{g}_\alpha\cdot\mathbf{g}_{\beta,P})dA.\tag{2.108}$$

With the information at hand, the change in nodal coordinate $\Delta\mathbf{d}$ within one iteration step is achieved by solving eq. (2.96). More details for the Newton-Raphson iterative solution algorithm is given in subsequent section 2.3.3.

2.3.2 Time discretization

In this section, the issue of generating numerical solutions from spatially discrete problems is examined. From eq. (2.41), we can observe that the time is still continuous for spatial discretized problems which is usually called *semidiscrete FEM*, since the spatial discretization is performed while the time is still continuous. Therefore, the approximation procedure in time for the discret equation of motion in eq. (2.91) must be performed with two problem classes of interest: Firstly, the inertial terms are maintained for a dynamic problem which focuses on temporal accuracy and stability. Secondly, for a static case inertial effects are negligible when compared with external and internal forces. Within this section, the time discretization is explained for a general dynamic problem which has a static problem as a special case. Various articles about the topic are available for example in [Hug00, Hul04, Kuh96].

For the dynamic problem at hand, solution $\mathbf{d}(t)$ over some interval $[0, T]$ of time t under interest must be determined. Subdivision of the interval $[0, T]$ into a series of typical time interval leads to

$$[0, T] = \bigcup_{n=0}^{N-1} [t_n, t_{n+1}] \,, \tag{2.109}$$

where n stands for the index of time steps or intervals. N is the total number of time interval. We assume that $t_0 = 0$ and $t_N = T$, but all time intervals are unnecessary equal. The algorithm can be summarized for a time interval $[t_n, t_{n+1}]$ in terms of the corresponding time step $\Delta t := t_{n+1} - t_n$. As a starting point, the semidiscrete equation of motion in eq. (2.91) must be discretrized in time and the result is a fully-discrete equation of motion at a generalized midpoint $t_{n+1-\alpha_{f,m}}$ within the interval $t \in [t_n, t_{n+1}]$ such that

$$\mathbf{M}\ddot{\mathbf{d}}_{n+1-\alpha_m}(\ddot{\mathbf{d}}_{n+1}(\mathbf{d}_{n+1})) + \mathbf{f}^{int}(\mathbf{d}_{n+1-\alpha_f}(\mathbf{d}_{n+1})) = \mathbf{f}^{ext}_{n+1-\alpha_f}, \tag{2.110}$$

where all subscripts denote their corresponding generalized time station. The algorithmic parameters α_f and α_m work as time shift which will be described further in the next section. This fully-discrete non-linear system of equation is an implicit function of unknown nodal coordinate $\mathbf{d}_{n+1} = \mathbf{d}(t_{n+1})$ at the end of the corresponding time step. From this point of departure, we can proceed further in the next section with an introduction about the main idea of iterative algorithms to pursue the solution of eq. (2.110).

2.3.3 Iterative solution algorithm

This section provides a framework to solve the non-linear system of equation in eq. (2.110) for unknowns at the time t_{n+1}. With an eye toward the Newton-Raphson method, we rewrite the fully-discrete equation of motion in eq. (2.110) into the nonlinear effective structural equation:

$$\mathbf{G}(\mathbf{d}_{n+1}) \equiv \mathbf{M}\ddot{\mathbf{d}}_{n+1-\alpha_m}(\ddot{\mathbf{d}}_{n+1}(\mathbf{d}_{n+1})) + \mathbf{f}^{int}(\mathbf{d}_{n+1-\alpha_f}(\mathbf{d}_{n+1})) - \mathbf{f}^{ext}_{n+1-\alpha_f} = \mathbf{0}, \tag{2.111}$$

which must be solved iteratively within the time interval $t \in [t_n, t_{n+1}]$. Iterative predictor and corrector of eq. (2.111) must be created to determine the solution (nodal coordinate) $(\mathbf{d}_{n+1})$ at the end of corresponding time step. First, the known nodal coordinate $\mathbf{d}_n$ at

the end of the last converged time step t_n is defined as the starting position for iteration of the current time step $\mathbf{d}_{n+1}^0$ where the superscript represents iteration number k. At the starting point $\mathbf{d}_{n+1}^0 := \mathbf{d}_n$ where the equation of motion is fulfilled, the predictor, denoted by the iteration number $k = 0$, is created by a projection of a linear approximation of the solution vector, as mentioned in eq. (2.49), into a specific direction. As a result, the linearization of eq. (2.111) is acquired along

$$\mathbf{LIN}(\mathbf{G}(\mathbf{d}_{n+1}^k)) = \mathbf{G}(\mathbf{d}_{n+1}^k) + \Delta\mathbf{G}(\mathbf{d}_{n+1}^k) = \mathbf{G}(\mathbf{d}_{n+1}^k) + \frac{\partial \mathbf{G}(\mathbf{d}_{n+1})}{\partial \mathbf{d}_{n+1}}\Big|_{\mathbf{d}_{n+1}^k} \Delta\mathbf{d}_{n+1}^k = \mathbf{0}. \quad (2.112)$$

We approximate eq. (2.111) at iteration $k+1$ of the current time step by a Taylor's series expansion:

$$\mathbf{G}(\mathbf{d}_{n+1}^{k+1}) = \mathbf{LIN}(\mathbf{G}(\mathbf{d}_{n+1}^k)) + \mathcal{O}(\mathbf{d}_{n+1}^k) = \mathbf{0} \quad (2.113)$$

where $\mathcal{O}$ is the higher order terms of the Taylor's series. By truncating eq. (2.113) after the linear term, one obtains the updated solution, viz.

$$\mathbf{d}_{n+1}^{k+1} = \mathbf{d}_{n+1}^k + \Delta\mathbf{d}_{n+1}^k. \quad (2.114)$$

Then an update $k := k+1$ must be performed. With a corrector step ($k > 0$), iteration on k over eqs. (2.113) and (2.114) continues until the *Euclidean norm* $\left\|\mathbf{G}(\mathbf{d}_{n+1}^k)\right\|$ is less than a prescribed tolerance, or $\left\|\Delta\mathbf{d}_{n+1}^k\right\|$ is smaller than some tolerance, or the *energy norm* $\mathbf{G}(\mathbf{d}_{n+1}^k) \cdot \Delta\mathbf{d}_{n+1}^k$ is smaller than a specific tolerance. With the converged solution $\mathbf{d}_{n+1}^k$, an approximate solution at time t_{n+1} is set up by $\mathbf{d}_{n+1} := \mathbf{d}_{n+1}^k$. Then, the whole system is updated and the iterative predictor-corrector procedure is applied to the next time step until the end of the time interval of interest.

2.3.4 Stable time integration algorithm

Several time-stepping algorithms have been proposed to solve the incremental problem in eq. (2.110) either explicit or implicit methods with regard to computational cost. An implicit method involves a direct solution of a matrix system of linear equations. As such the discrete solution would require a factorization of some form of a matrix which is a combination of the mass, damping, and stiffness matrices. On the other hand, an explicit method is one for which solution of the dynamic states does not need factorization of a combination between the damping and stiffness matrices. At most, a factorization of the mass matrix is required. However, to maintain the numerical stability [Hul04] the timestep size Δt for the explicit method must be smaller than the critical timestep Δt_{cr} size of the problem, usually rather small. Problems of structural dynamics can be divided depending on the timescale of interest into relatively low-frequency problems and high frequency problems. For the low-frequency problems, accuracy is required for the long wavelength response of structures. In contrary, the second class of problems with high-frequency, wave propagation type problems, usually including impact-contact problems, require a much smaller time step sizes to capture the rapid change in structural responses. This practical consideration reflects suitabilities of unconditionally stable implicit time integration method for the low-frequency problems. Likewise, the high-frequency problem should be associated with the explicit one.

Because the aim of this work is to utilize the implicit time integration method for contact problems under interest, the explicit method is deliberately omitted within this section.

The road map of development as well as problems and requirements to develop a stable time integration algorithm can be traced back to the first-order accuracy of the traditional Newmark methods [New59], the early successful development of structural elastodynamics, with high-frequency dissipation. This trailblazer is then followed by series of the second-order schemes including the classical HHT method from Hilber *et al*. [HHT77], the ϑ-Wilson method from Wilson [Wil], and the works from Chung and Hulbert [CH93]. It is particularly desirable to have controllable numerical dissipation in the higher frequency modal components because the higher modes of semidiscrete structural equations are artifacts of the spatial discretization.

Never before the mid of 80s had there been a great effort beyond the scope of linear dynamics. Afterwards, there exist persistent striving towards an unconditionally stable scheme for nonlinear problems due to many reports about the unsatisfactoriness of all the time integration methods mentioned above. For instance, Kuhl and Ramm [KR96, KR99] experienced that the unconditional dissipativity of these schemes is not maintained in the nonlinear regime. In particular, Armero and Romero [AR01b, AR01a] showed that the linear dissipative schemes not only cause numerical instabilities, but also lead to distorted responses of the long-term phase dynamics due to the lack of conservation of angular momentum, a fundamental law of physics. For this reason, developments of high-frequency dissipative algorithm for nonlinear dynamics gain increasing interest. Based on a stress modification method proposed in [AP99], Kuhl and Ramm [KR99] generalized the original energy-momentum algorithm of Simo and Tarnow [ST94] with an outcome of unconditionally energy decay and conservation of momenta. However, Armero and Romero [AR01b] showed that the method is not dissipative in the high-frequency in addition to limited first-order accuracy. Recently, Armero and Romero [AR01a, AR01b] proposed a family of first and second-order accurate integration methods for nonlinear elastodynamics, the so-called *Energy-Dissipative, Momentum-Conserving* (EDMC) scheme. These algorithms encapsulate the energy-momentum conservation and high-frequency dissipation by preserving exactly the linear and angular momentum with a controllable algorithmic dissipation. The development of this method for nonlinear shells is available in [RA02].

Of particular importance for structural dynamics, the quality of a time integration algorithm is measurable by following attributes:

- ◇ *Stability*: stability measure requires that the numerical solution remain uniformly bounded for all values of time step number $n = 1, \ldots, N$. An algorithm is said to be unconditional stable if the stability bound holds regardless of the time step size, while the algorithm is conditionally stable if stability imposes a restriction on the value of the time step size.
- ◇ *Accuracy*: the order of the convergence rate.
- ◇ *Numerical dispersion and numerical dissipation* are measured via the algorithmic damping ratio and relative period error.

- ◇ *Overshoot*: the computed solutions significantly exceed (overshot) the exact solution such that overshoot behavior may adversely impact the local accuracy of the solution in particular for nonlinear dynamics.

- ◇ *Starting conditions* are of practical importance for any time integration algorithm.

For more details about the topic, [Hul04, Hug00] should be consulted. In linear structural dynamics, the criterion for unconditionally stability is easily fulfilled from most algorithms. Therefore, the main concern is the order of accuracy. Let $\mathbf{A}$ be an amplification matrix whose spectral radius $\rho(\mathbf{A})$ is defined in [Hug00] by

$$\rho(\mathbf{A}) = \max_i |\lambda_i(\mathbf{A})|, \tag{2.115}$$

where $\lambda_i(\mathbf{A})$ and $\overline{\lambda_i(\mathbf{A})}$ stand for the eigenvalue of $\mathbf{A}$ and its complex conjugate, respectively and the modulus $|\lambda_i(\mathbf{A})| = (\lambda_i(\mathbf{A})\overline{\lambda_i(\mathbf{A})})^{1/2}$. The stability condition to prevent amplification of $\mathbf{A}^n$ as n becomes large can be written by

$$\rho(\mathbf{A}) \leq 1, \tag{2.116}$$

$$|\lambda(\mathbf{A})| \leq 1 \quad \text{when} \quad n > 1, \tag{2.117}$$

where n stands for multiplicity of the eigenvalue $\lambda_i(\mathbf{A})$. The conditions in eq. (2.117) define a *spectrally stable* $\mathbf{A}$ which reflects unconditionally stable algorithm for a linear problem [CH93]. The spectral radius also is a measure of numerical dissipation; a smaller spectral radius value corresponds to higher numerical dissipation.

While sufficient for linear systems, it has been long observed that the linear notion of stability cannot guarantee stability for nonlinear problems, where the main interest is focused on the numerical stability of the algorithms. Even nowadays the unconditionally stable time integration method for nonlinear problems is still a topic of ongoing research [AR99, KR99, RA02, HB08]. Conservation of total energy, in the absence of physical damping and for conservative loading, is considered as a natural norm for stability of a time integration algorithm for nonlinear structural dynamics. In a nonlinear regime, a sufficient condition for conservation or decay of the total energy within one time step is expressed in [BS75] by

$$U_{n+1} - U_n + K_{n+1} - K_n \leq \Delta W^{ext} \tag{2.118}$$

where U_n and U_{n+1} are the strain energy at the beginning and the end of the time step, respectively, while K_n and K_{n+1} stands for the corresponding kinetic energies and W^{ext} represents work done by external forces within the time step.

In general, we can roughly classify the algorithm to satisfy the energy criterion of eq. (2.118) into four groups as mentioned in Table 2.3. Among various implicit time integration algorithms for the incremental nonlinear elastodynamics problem of eq. (2.110), this thesis provides only two variants of interest due to their unconditional stability and energy conservation aspects: the *Generalized-α method* (GEN_α) [CH93] and the *Generalized Energy Momentum Method* (GEMM) [KC99, KR99].

Table 2.3: Classification of time stepping algorithms satisfying the stability criterion in eq. (2.118) with controllable numerical dissipation for high frequency modes.

Category	Time integration algorithms
Numerical dissipation	Newmark [New59] HHT [HHT77] ϑ-Wilson method [Wil] Generalized-α [CH93]
Enforced conservation of energy	Constraint Energy Method [HCL78] Constraint Energy Momentum [Kuh96, KR96]
Algorithmic conservation of energy	Energy Momentum [ST94] Modified Energy Momentum [AP98, AP99, CGJ97] Generalized Energy Momentum [KC99, KR99]
Energy dissipative, momentum conserving	Energy Dissipative, Momentum Conserving [RA02, AR01a, AR01b]

2.3.4.1 Generalized alpha method

Classified as the numerical dissipation group according to Table 2.3, the *Generalized-α method* (GEN$_\alpha$) [CH93] is developed as a generalized version for the Newmark family algorithms: Newmark method [New59], Hilber-α method [HHT77] and Bossak-α method [WBZ81] with controllable numerical dissipation in the high-frequency modes while minimizing undesirable low-frequency dissipation. Though it is unconditionally stable in the linear regime, this integration scheme is totally lost in the non-linear problems which leads to an unstable time integration for a longtime computation due to accumulative dissipativity.

Given the known state vector $\mathbf{d}_n, \dot{\mathbf{d}}_n, \ddot{\mathbf{d}}_n$ at the starting time t_n for the interval $t \in [t_n, t_{n+1}]$, the unknown state vectors $\mathbf{d}_{n+1}, \dot{\mathbf{d}}_{n+1}, \ddot{\mathbf{d}}_{n+1}$ at the end of this time step t_{n+1} are available by solving the fully-discrete equation of motion in eq. (2.110) implicitly. As the beginning, unknown nodal coordinates and velocity vectors at the end of the corresponding time step are approximated by the Newmark method via

$$\mathbf{d}_{n+1}(\ddot{\mathbf{d}}_{n+1}) = \mathbf{d}_n + \Delta t \dot{\mathbf{d}}_n + \frac{1-2\beta}{2}\Delta t^2 \ddot{\mathbf{d}}_n + \beta \Delta t^2 \ddot{\mathbf{d}}_{n+1}, \tag{2.119}$$

$$\dot{\mathbf{d}}_{n+1}(\ddot{\mathbf{d}}_{n+1}) = \dot{\mathbf{d}}_n + (1-\gamma)\Delta t \ddot{\mathbf{d}}_n + \gamma \Delta t \ddot{\mathbf{d}}_{n+1}. \tag{2.120}$$

By reducing the set of unknown to a single value of the nodal coordinate at the end of the corresponding time step $\mathbf{d}_{n+1}$, the velocity $\dot{\mathbf{d}}_{n+1}$ and acceleration $\ddot{\mathbf{d}}_{n+1}$ at the end of time step are approximated by

$$\dot{\mathbf{d}}_{n+1}(\mathbf{d}_{n+1}) = \frac{\gamma}{\beta \Delta t}(\mathbf{d}_{n+1} - \mathbf{d}_n) - \frac{\gamma - \beta}{\beta}\dot{\mathbf{d}}_n - \frac{\gamma - 2\beta}{2\beta}\Delta t \ddot{\mathbf{d}}_n. \tag{2.121}$$

$$\ddot{\mathbf{d}}_{n+1}(\mathbf{d}_{n+1}) = \frac{1}{\beta \Delta t^2}(\mathbf{d}_{n+1} - \mathbf{d}_n) - \frac{1}{\beta \Delta t}\dot{\mathbf{d}}_n - \frac{1-2\beta}{2\beta}\ddot{\mathbf{d}}_n. \tag{2.122}$$

Modified structural equation

In this section, the definition of the *modified structural equation of motion* in eq. (2.110) is explained. From the GEN_α description, a generalized state vector of the interval $t \in [t_n, t_{n+1}]$ is a linear combination between the corresponding state vector at the beginning t_n and at the end t_{n+1} of the timestep by user-defined algorithmic parameters α_m and α_f, respectively:

$$\ddot{\mathbf{d}}_{n+1-\alpha_m} = (1-\alpha_m)\ddot{\mathbf{d}}_{n+1} + \alpha_m \ddot{\mathbf{d}}_n, \tag{2.123}$$

$$\dot{\mathbf{d}}_{n+1-\alpha_f} = (1-\alpha_f)\dot{\mathbf{d}}_{n+1} + \alpha_f \dot{\mathbf{d}}_n, \tag{2.124}$$

$$\mathbf{d}_{n+1-\alpha_f} = (1-\alpha_f)\mathbf{d}_{n+1} + \alpha_f \mathbf{d}_n, \tag{2.125}$$

$$\mathbf{f}^{ext}_{n+1-\alpha_f} = (1-\alpha_f)\mathbf{f}^{ext}_{n+1} + \alpha_f \mathbf{f}^{ext}_n. \tag{2.126}$$

With an exception for a state vector of the internal forces $\mathbf{f}^{int}(\mathbf{d}_{n+1-\alpha_f}(\mathbf{d}_{n+1}))$, there are two possible interpretations for the internal forces at the generalized time $t_{n+1-\alpha_f}$:

- ◇ *classical internal force* $\mathbf{f}^{int}(\mathbf{d}_{n+1-\alpha_f}(\mathbf{d}_{n+1}))$ for GEN_α is the convex combination of two state vectors at each bound (see, e.g. [KR96]) as in the case of the external forces in eq. (2.126):
$$\mathbf{f}^{int}(\mathbf{d}_{n+1-\alpha_f}(\mathbf{d}_{n+1})) = (1-\alpha_f)\mathbf{f}^{int}_{n+1} + \alpha_f \mathbf{f}^{int}_n \tag{2.127}$$
- ◇ *algorithmic internal force* $\mathbf{f}^{int}(\mathbf{d}_{n+1-\alpha_f})$ for GEMM is determined at the generalized midpoint nodal coordinate $\mathbf{d}_{n+1-\alpha_f}$ (see, e.g. [KC99, HBRW07]):
$$\mathbf{f}^{int}(\mathbf{d}_{n+1-\alpha_f}(\mathbf{d}_{n+1})) = \mathbf{f}^{int}((1-\alpha_f)\mathbf{d}_{n+1} + \alpha_f \mathbf{d}_n). \tag{2.128}$$

For a linear case, both approaches in eqs. (2.127) and (2.128) are identical.

Effective structural equation and linearization

Substituting eq. (2.122) with the help of eq. (2.123) into the modified structural equation of motion eq. (2.110) yields a fully discrete nonlinear algebraic system of equations so-called *"the effective structural equation"* :

$$\begin{aligned}\mathbf{G}(\mathbf{d}_{n+1}) = \mathbf{0} &\equiv \mathbf{M}\ddot{\mathbf{d}}_{n+1-\alpha_m}(\ddot{\mathbf{d}}_{n+1}(\mathbf{d}_{n+1})) + \mathbf{f}^{int}(\mathbf{d}_{n+1-\alpha_f}(\mathbf{d}_{n+1})) - \mathbf{f}^{ext}_{n+1-\alpha_f}, \\ &\equiv \frac{1-\alpha_m}{\beta\Delta t^2}\mathbf{M}\mathbf{d}_{n+1} - \mathbf{h}(\mathbf{d}_n, \dot{\mathbf{d}}_n, \ddot{\mathbf{d}}_n) + \mathbf{f}^{int}(\mathbf{d}_{n+1-\alpha_f}(\mathbf{d}_{n+1})) - \mathbf{f}^{ext}_{n+1-\alpha_f},\end{aligned} \tag{2.129}$$

where the known values evaluated at t_n, the beginning of the corresponding time step, is collected in the vector $\mathbf{h}(\mathbf{d}_n, \dot{\mathbf{d}}_n, \ddot{\mathbf{d}}_n)$:

$$\mathbf{h}(\mathbf{d}_n, \dot{\mathbf{d}}_n, \ddot{\mathbf{d}}_n) = \mathbf{M}\left[\frac{1-\alpha_m}{\beta\Delta t^2}\mathbf{d}_n + \frac{1-\alpha_m}{\beta\Delta t}\dot{\mathbf{d}}_n + \frac{1-\alpha_m-2\beta}{2\beta}\ddot{\mathbf{d}}_n\right]. \tag{2.130}$$

Obviously, the effective structural equation in eq. (2.129) is nonlinear in the nodal coordinate solution $\mathbf{d}_{n+1}$; it must be solved with an iterative method explained in section 2.3.3. Therefore, this section focuses on consistent linearization of the effective structural equation

which is required for the Newton-Raphson iterative algorithm. According to eqs. (2.112)-(2.113), the Taylor expansion of eq. (2.129), truncated after linear terms, gives

$$\mathbf{G}(\mathbf{d}_{n+1}^{k+1}) \approx \mathbf{G}(\mathbf{d}_{n+1}^{k}) + \Delta\mathbf{G}(\mathbf{d}_{n+1}^{k})) = \mathbf{G}(\mathbf{d}_{n+1}^{k}) + \frac{\partial \mathbf{G}(\mathbf{d}_{n+1})}{\partial \mathbf{d}_{n+1}}\Big|_{\mathbf{d}_{n+1}^{k}} \Delta\mathbf{d}_{n+1}^{k} = \mathbf{0} \tag{2.131}$$

and the outcome is the *effective iterative structural equation*:

$$\frac{\partial \mathbf{G}(\mathbf{d}_{n+1})}{\partial \mathbf{d}_{n+1}}\Big|_{\mathbf{d}_{n+1}^{k}} \Delta\mathbf{d}_{n+1}^{k} = -\mathbf{G}(\mathbf{d}_{n+1}^{k}) \quad \Rightarrow \quad \mathbf{K}_T^{eff}\Delta\mathbf{d}_{n+1}^{k} = \mathbf{f}^{eff}(\mathbf{d}_{n+1}^{k}). \tag{2.132}$$

The incremental solution of current iteration $\Delta\mathbf{d}_{n+1}^{k}$ is defined in eq. (2.114) and $\mathbf{K}_T^{eff}$ stands for *the effective tangential stiffness matrix* which is defined with the help of eqs. (2.127) and (2.129) by

$$\begin{aligned}\mathbf{K}_T^{eff}(\mathbf{d}_{n+1}^{k}) &= \frac{\partial \mathbf{G}(\mathbf{d}_{n+1})}{\partial \mathbf{d}_{n+1}}\Big|_{\mathbf{d}_{n+1}^{k}} = \frac{\partial \mathbf{G}(\mathbf{d}_{n+1}^{k})}{\partial \mathbf{d}_{n+1}} = \frac{1-\alpha_m}{\beta\Delta t^2}\mathbf{M} + \frac{\partial \overbrace{\mathbf{f}^{int}(\mathbf{d}_{n+1-\alpha_f}(\mathbf{d}_{n+1}^{k}))}^{eq.\ (2.127)}}{\partial \mathbf{d}_{n+1}}, \\ &= \frac{1-\alpha_m}{\beta\Delta t^2}\mathbf{M} + (1-\alpha_f)\underbrace{\frac{\partial \mathbf{f}^{int}(\mathbf{d}_{n+1}^{k})}{\partial \mathbf{d}_{n+1}}}_{\mathbf{K}_T(\mathbf{d}_{n+1}^{k})},\end{aligned} \tag{2.133}$$

while the derivative of the internal forces leads to the tangential stiffness matrix $\mathbf{K}_T(\mathbf{d}_{n+1}^{k})$ (see, e.g. [ZT05, Wri01]) which formerly was derived in the section 2.3.1 for the spatial discretization. Note that an abbreviation $\frac{\partial \mathbf{G}(\mathbf{d}_{n+1}^{k})}{\partial \mathbf{d}_{n+1}} = \frac{\partial \mathbf{G}(\mathbf{d}_{n+1})}{\partial \mathbf{d}_{n+1}}|_{\mathbf{d}_{n+1}^{k}}$ is employed for the sake of brevity. Additionally, *the effective force vector* or *the effective RHS* $\mathbf{f}^{eff} = -\mathbf{G}(\mathbf{d}_{n+1}^{k})$ from eq. (2.129) can be described by

$$\mathbf{f}^{eff}(\mathbf{d}_{n+1}^{k}) = \mathbf{f}_{n+1-\alpha_f}^{ext} - \overbrace{\mathbf{f}^{int}(\mathbf{d}_{n+1-\alpha_f}(\mathbf{d}_{n+1}^{k}))}^{eq.\ (2.127)} - \frac{1-\alpha_m}{\beta\Delta t^2}\mathbf{M}\mathbf{d}_{n+1} + \mathbf{h}(\mathbf{d}_n, \dot{\mathbf{d}}_n, \ddot{\mathbf{d}}_n) \tag{2.134}$$

where the internal forces $\mathbf{f}^{int}$ and external forces $\mathbf{f}^{ext}$ are given in eqs. (2.127) and (2.126), respectively. For simplicity, one can rewrite the iterative effective structural equation in eq. (2.132) in a compact form:

$$\mathbf{K}_T^{eff}\Delta\mathbf{d} = \mathbf{f}^{eff}. \tag{2.135}$$

According to [CH93], the GEN$_\alpha$ method maintains the unconditionally stable, second order accurate algortithm with optimal control of high-frequency and low-frequency dissipation when the relation between Newmark parameters β, γ and shift parameters α_m, α_f is defined by

$$\alpha_m = \frac{2\rho_\infty - 1}{\rho_\infty + 1}, \quad \alpha_f = \frac{\rho_\infty}{\rho_\infty + 1}, \quad \gamma = \frac{1}{2} - \alpha_m - \alpha_f, \quad \beta = \frac{1}{4}(1 - \alpha_m + \alpha_f)^2. \tag{2.136}$$

Apparently, a single control parameter $\rho_\infty \leq 1$ is the user-specified value of the spectral radius to control the high-frequency dissipation as explained in eq. (2.115). The optimal GEN$_\alpha$ method allows the degree of high-frequency dissipation ranging from the no dissipation case (ρ_∞=1) to the asymptotic annihilation case (ρ_∞=0) while the numerical dissipation case with $\rho_\infty \in [0.85, 0.95]$ is proved to be adequately stable for various applications.

2.3.4.2 Generalized energy momentum method

According to Kuhl and Crisfield [KC99], the *Energy-Momentum Method* (EMM) [ST94] is second order accurate while the total energy as well as linear and angular momentum are preserved within a time step. Albeit, the algorithm seems to be stable for the non-linear elastodynamics, Kuhl and Ramm [KR96] observed convergence problems with high-frequency modes. For this reason, an extension of the method to the generalized version took place. The Generalized Energy Momentum Method (GEMM), stemming from a simple modification of the classical Mid-Point Rule (see, e.g. [Hug00]), is developed by Kuhl and Ramm [KR99, KC99] within the framework of the (GEN_α) method. As a consequence, it allows at the same time conservation or decay of the total energy and controllable numerical dissipation of unwanted high frequency response. The key difference between these two methods is the definition of internal forces at the generalized time $\mathbf{f}^{int}(\mathbf{d}_{n+1-\alpha_f}(\mathbf{d}_{n+1}))$. While GEN_α uses the classical convex combination internal forces in eq. (2.127), the algorithmic internal forces mentioned in eq. (2.128) are employed in case of GEMM. Since the definition of algorithmic internal forces causes modifications in element formulation, the evaluation of the internal virtual work δW_{int} for GEMM is explained within this section.

Algorithmic internal forces

From eq. (2.89), the algorithmic internal forces is derived from the internal virtual work of the discrete domain Ω^h created by membrane finite elements at the generalized mid-point configuration $t_{n+1-\alpha_f}$ within a time step:

$$G_{int}^{h,GEMM}\Big|_{n+1-\alpha_f} = \int_{\Omega^h} [\mathbf{S}^h : \delta\mathbf{E}^h]_{n+1-\alpha_f} d\Omega. \tag{2.137}$$

Now, one must decide about variation of the GL strain tensor $\delta\mathbf{E}^h$ and its energetic conjugate variable $\mathbf{S}^h$ at $t_{n+1-\alpha_f}$. Simo and Tarnow [ST94] proved the exact energy conservation of the St Venant-Kirchhoff model in case of EMM by "*evaluating the constitutive relation with the average of the strains and not the strain of the average configuration*." This idea is used by Kuhl and Ramm [KR99, KC99] as a basis to develop the internal virtual work for GEMM. In that work, the constitutive relation is evaluated with the average GL strain at the generalized mid-point configuration $\mathbf{E}^h_{n+1-\alpha_f} = (1-\alpha_f)\mathbf{E}^h_{n+1} + \alpha_f \mathbf{E}^h_n$ by

$$\begin{aligned}
G_{int}^{h,GEMM}\Big|_{n+1-\alpha_f} &= \int_{\Omega^h} \delta\mathbf{E}^h(\mathbf{d}_{n+1-\alpha_f}) : \mathbb{C} : \mathbf{E}^h_{n+1-\alpha_f} d\Omega, \\
&= \int_{\Omega^h} \delta\mathbf{E}^h(\mathbf{d}_{n+1-\alpha_f}) : \mathbb{C} : ((1-\alpha_f)\mathbf{E}^h_{n+1} + \alpha_f \mathbf{E}^h_n) d\Omega, \\
&= \int_{\Omega} \delta\mathbf{E}^h(\mathbf{d}_{n+1-\alpha_f}) : ((1-\alpha_f)\mathbf{S}^h_{n+1} + \alpha_f \mathbf{S}^h_n) d\Omega, \\
&= \int_{\Omega^h} \delta\mathbf{E}^h(\mathbf{d}_{n+1-\alpha_f}) : \mathbf{S}^h_{n+1-\alpha_f} d\Omega
\end{aligned} \tag{2.138}$$

where the PK2 stress tensor $\mathbf{S}^h_{n+1-\alpha_f}$ is a convex combination of stress tensor at the beginning and the end of the time interval $(1-\alpha_f)\mathbf{S}^h_{n+1} + \alpha_f \mathbf{S}^h_n$ while the virtual GL strain tensor is determined at the generalized mid-point configuration $\delta\mathbf{E}^h(\mathbf{d}_{n+1-\alpha_f}) = \delta\mathbf{E}^h((1-\alpha_f)\mathbf{d}^h_{n+1} + \alpha_f \mathbf{d}^h_n)$. These definitions agree with Armero and Petőcz [AP98].

Linearization of the internal virtual work for GEMM

To realize the Newton-Raphson iterative solution method as mentioned in section 2.3.3, one requires the partial derivative of the discrete internal virtual work in eq. (2.138) with respect to the nodal coordinate at the end of the interested time interval $\mathbf{d}_{n+1}$. To minimize confusion, we define abbreviations for time stations at which each state variable is evaluated such that

$$\begin{aligned}
[\circ]_n &:= [\circ](\mathbf{d}_n) \text{ evaluated at } t_n, \\
[\circ]_{n1} &:= [\circ](\mathbf{d}_{n+1}) \text{ evaluated at } t_{n+1}, \\
[\circ]_{n\alpha} &:= (1-\alpha_f)[\circ]_{n1} + \alpha_f [\circ]_n \text{ convex combination at } t_{n+1-\alpha_f}, \\
[\circ]|_{n\alpha} &:= [\circ](\mathbf{d}_{n\alpha}) \text{ evaluated at } \mathbf{d}_{n+1-\alpha_f}.
\end{aligned} \tag{2.139}$$

The discrete virtual GL strain tensor evaluated at the generalized mid-point configuration is explained by

$$\delta\mathbf{E}^h(\mathbf{d}_{n\alpha}) = \frac{\partial \mathbf{E}^h(\mathbf{d}_{n\alpha})}{\partial \mathbf{d}_{n\alpha}} \delta\mathbf{d}_{n\alpha} = \mathbf{E}^h(\mathbf{d}_{n\alpha})_{,\mathbf{d}_{n\alpha}} \, \delta\mathbf{d}_{n\alpha} \tag{2.140}$$

where $\delta\mathbf{E}^h(\mathbf{d}_{n\alpha})$ depends linearly on $\mathbf{d}_{n\alpha}$, or in other words, on $\mathbf{d}_{n1}$. From eq. (2.50), the directional derivative of eq. (2.140) in the direction of $\Delta\mathbf{d}_{n1}$ can be written in the form

$$\Delta\delta\mathbf{E}^h(\mathbf{d}_{n\alpha}) = \frac{\partial \delta\mathbf{E}^h((1-\alpha_f)\mathbf{d}_{n1} + \alpha_f \mathbf{d}_n)}{\partial \mathbf{d}_{n1}} \Delta\mathbf{d}_{n1} = (1-\alpha_f)\Delta[\delta\mathbf{E}^h(\mathbf{d}_{n\alpha})](\mathbf{d}_{n1}). \tag{2.141}$$

Inserting eq. (2.141) in eq. (2.138), one obtains the directional derivative of $G^{h,GEMM}_{int}\Big|_{n\alpha}$ in the direction of $\Delta\mathbf{d}_{n1}$

$$\begin{aligned}
\Delta G^{h,GEMM}_{int}\Big|_{n\alpha} &= \int_{\Omega^h} \Delta\delta\mathbf{E}^h(\mathbf{d}_{n\alpha}) : \mathbf{S}^h_{n\alpha} + \delta\mathbf{E}^h(\mathbf{d}_{n\alpha}) : \Delta\mathbf{S}^h_{n\alpha} d\Omega, \\
&= \int_{\Omega^h} (1-\alpha_f)\Delta[\delta\mathbf{E}^h(\mathbf{d}_{n\alpha})](\mathbf{d}_{n1}) : \mathbf{S}^h_{n\alpha} + \delta\mathbf{E}^h(\mathbf{d}_{n\alpha}) : (1-\alpha_f)\Delta\mathbf{S}^h_{n1} d\Omega, \\
&= (1-\alpha_f) \int_{\Omega^h} \Delta[\delta\mathbf{E}^h(\mathbf{d}_{n\alpha})](\mathbf{d}_{n1}) : \mathbf{S}^h_{n\alpha} + \delta\mathbf{E}^h(\mathbf{d}_{n\alpha}) : \Delta\mathbf{S}^h_{n1} d\Omega.
\end{aligned} \tag{2.142}$$

By considering the variation w.r.t. the P^{th} dof $d_{n\alpha P}$ and the directional derivative w.r.t. Q^{th} dof d_{n1Q}, one can rewrite eq. (2.142) w.r.t $d_{n\alpha P}$ and d_{n1Q} by

$$\Delta G^{h,GEMM}_{int}\Big|_{n\alpha PQ} = \delta d_{n\alpha P}(1-\alpha_f) \int_{\Omega^h} \begin{bmatrix} [\mathbf{E}^h(\mathbf{d}_{n\alpha})_{,d_{n\alpha P}}](\mathbf{d}_{n1})_{,d_{n1Q}} : \mathbf{S}^h_{n\alpha} \\ +\mathbf{E}^h(\mathbf{d}_{n\alpha})_{,d_{n\alpha P}} : \mathbb{C}_{n1} : \mathbf{E}^h_{n1,d_{n1Q}} \end{bmatrix} d\Omega \Delta d_{n1Q} \tag{2.143}$$

with the definition of PQ referred to eq. (2.76). By an analogy to section 2.3.1, the tangential stiffness matrix for GEMM is demonstrated by

$$\mathbf{K}_T^{GEMM} = (1-\alpha_f)\left[\mathbf{K}_{e+u}^{GEMM} + \mathbf{K}_g^{GEMM}\right] \tag{2.144}$$

where $\mathbf{K}_{e+u}^{GEMM}$ is the elastic and initial displacement stiffness matrix with its PQ components:

$$K_{e+u_{PQ}}^{GEMM} = h \int_{A^h} \mathbf{E}^h(\mathbf{d}_{n\alpha})_{,d_{n\alpha P}} : \mathbb{C}_{n1} : \mathbf{E}^h_{n1,d_{n1Q}}\, dA \tag{2.145}$$

and the PQ component of the geometric stiffness matrix $\mathbf{K}_g^{GEMM}$ is provided by

$$\begin{aligned} K_{g_{PQ}}^{GEMM} &= h \int_{A^h} [\mathbf{E}^h(\mathbf{d}_{n\alpha})_{,d_{n\alpha P}}](\mathbf{d}_{n1})_{,d_{n1Q}} : \mathbf{S}^h_{n\alpha} dA \\ &= h \int_{A^h} \mathbf{E}^h{}_{,_{PQ}} : \mathbf{S}^h_{n\alpha} dA. \end{aligned} \tag{2.146}$$

Noticeably, the geometric stiffness matrix $\mathbf{K}_{g_{PQ}}^{GEMM}$ is symmetric since $[\mathbf{E}^h(\mathbf{d}_{n\alpha})_{,d_{n\alpha P}}](\mathbf{d}_{n1})_{,d_{n1Q}}$ is independent of the deformation of membrane elements, i.e. there exists only the derivative of shape functions. Therefore, it can be collapsed to $\mathbf{E}^h{}_{,_{PQ}}$ as in the case of the geometric stiffness matrix $K_{g_{PQ}}$ in eq. (2.105). In contrary, the elastic and initial displacement stiffness matrix $\mathbf{K}_{e+u}^{GEMM}$ is nonsymmetric due to the fact that $\mathbf{E}^h(\mathbf{d}_{n\alpha})_{,d_{n\alpha P}}$ and $\mathbf{E}^h_{n1,d_{n1Q}}$ are evaluated at different state of time, i.e. $t_{n+1-\alpha f}$ and t_{n+1}, respectively.

To facilitate this complexity, Kuhl and Ramm [KR99] suggested a symmetrized approximation of $\mathbf{K}_{e+u}^{GEMM}$ related to the GEN$_\alpha$ via

$$K_{e+u_{PQ}}^{GEMM} \approx \bar{K}_{e+u_{PQ}}^{GEMM} = h \int_{A^h} \mathbf{E}^h(\mathbf{d}_{n\alpha})_{,d_{n\alpha P}} : \mathbb{C}_{n1} : \mathbf{E}^h(\mathbf{d}_{n\alpha})_{,d_{n\alpha Q}}\, dA. \tag{2.147}$$

However, the symmetrized elastic and initial displacement stiffness matrix $\bar{\mathbf{K}}_{e+u}^{GEMM}$ deteriorates the convergence rate of GEMM as reported in Kuhl and Ramm [KR99].

Effective structural equation for GEMM

The procedure to derive the effective structural equation for GEMM is quite similar to that of the GEN$_\alpha$ in the section 2.3.4.1 with the exception that the definition of the internal force vector at the generalized midpoint configuration in eq. (2.128) must be used for the effective structural equation in eq. (2.129) in lieu of eq. (2.127). Based on eq. (2.133), the effective tangential stiffness matrix for GEMM is then expressed with

$$\begin{aligned} \mathbf{K}_T^{eff}(\mathbf{d}_{n+1}^k) &= \frac{\partial \mathbf{G}(\mathbf{d}_{n+1})}{\partial \mathbf{d}_{n+1}}\Big|_{\mathbf{d}_{n+1}^k} = \frac{\partial \mathbf{G}(\mathbf{d}_{n+1}^k)}{\partial \mathbf{d}_{n+1}} = \frac{1-\alpha_m}{\beta \Delta t^2}\mathbf{M} + \frac{\partial \overbrace{\mathbf{f}^{int}(\mathbf{d}_{n+1-\alpha_f}(\mathbf{d}_{n+1}^k))}^{eq.\ (2.128)}}{\partial \mathbf{d}_{n+1}} \\ &= \frac{1-\alpha_m}{\beta \Delta t^2}\mathbf{M} + \underbrace{\mathbf{K}_T^{GEMM}}_{eq.\ (2.144)} \end{aligned} \tag{2.148}$$

and the effective force vector $\mathbf{f}^{eff} = -\mathbf{G}(\mathbf{d}^k_{n+1})$ from eq. (2.129) is shown by

$$\mathbf{f}^{eff}(\mathbf{d}^k_{n+1}) = \mathbf{f}^{ext}_{n+1-\alpha_f} - \overbrace{\mathbf{f}^{int}(\mathbf{d}_{n+1-\alpha_f}(\mathbf{d}^k_{n+1}))}^{eq.\ (2.128)} - \frac{1-\alpha_m}{\beta\Delta t^2}\mathbf{M}\mathbf{d}_{n+1} + \mathbf{h}(\mathbf{d}_n, \dot{\mathbf{d}}_n, \ddot{\mathbf{d}}_n). \tag{2.149}$$

With the help of eq. (2.140), the internal force vector $\mathbf{f}^{int}(\mathbf{d}_{n+1-\alpha_f}(\mathbf{d}^k_{n+1}))$ in eq. (2.149) can be derived from eq. (2.138) such that

$$\mathbf{f}^{int}(\mathbf{d}_{n\alpha}) = h \int_{A^h} \mathbf{E}^h(\mathbf{d}_{n\alpha})_{,\mathbf{d}_{n\alpha}} : \mathbf{S}^h_{n\alpha} dA \tag{2.150}$$

with

$$f^{int}_P(\mathbf{d}_{n\alpha}) = h \int_{A^h} \mathbf{E}^h(\mathbf{d}_{n\alpha})_{,d_{n\alpha P}} : \mathbf{S}^h_{n\alpha} dA. \tag{2.151}$$

As a generalized version of EMM, the high-frequency dissipation of GEMM is controllable by the user-defined spectral radius $\rho_\infty \leq 1$ with the special case when $\rho_\infty = 1$ according to eq. (2.136), EMM is recovered.

2.4 Summary for the solution algorithm

As the closing remark, we summarize the algorithmic setup to solve IBVP for elastodynamics of section 2.3 in Figure 2.5.

Initialize: set intitial time step number $(n = 0)$ and initial conditions $\left(\mathbf{d}_0; \dot{\mathbf{d}}_0 \Rightarrow \ddot{\mathbf{d}}_0\right)$

Loop over all time steps $(n_T = T/\Delta t)$

Predictor step $(k = 0)$

GEN_α { $\mathbf{K}_T^{eff}(\mathbf{d}_{n+1}^0) = \frac{1-\alpha_m}{\beta\Delta t^2}\mathbf{M} + (1-\alpha_f)\mathbf{K}_T(\mathbf{d}_{n+1}^0)$ (2.133)

GEMM { $\mathbf{K}_T^{eff}(\mathbf{d}_{n+1}^0) = \frac{1-\alpha_m}{\beta\Delta t^2}\mathbf{M} + \mathbf{K}_T^{GEMM}(\mathbf{d}_{n+1}^0)$ (2.148)

$\mathbf{f}^{eff}(\mathbf{d}_{n+1}^0) = \mathbf{f}_{n+1-\alpha_f}^{ext} - \mathbf{f}^{int}(\mathbf{d}_{n+1-\alpha_f}(\mathbf{d}_{n+1}^0)) - \frac{1-\alpha_m}{\beta\Delta t^2}\mathbf{M}\mathbf{d}_{n+1}^0 + \mathbf{h}(\mathbf{d}_n, \dot{\mathbf{d}}_n, \ddot{\mathbf{d}}_n)$ (2.134);(2.149)

$\Delta\mathbf{d}_{n+1,\sum}^0 = \left(\mathbf{K}_T^{eff}\right)^{-1}\mathbf{f}^{eff}(\mathbf{d}_{n+1}^0)$

$\mathbf{d}_{n+1}^1 = \mathbf{d}_{n+1}^0 + \Delta\mathbf{d}_{n+1,\sum}^0$

Set up $k = 1$

Newton-Raphson correction iteration:

GEN_α

$\mathbf{K}_T^{eff}(\mathbf{d}_{n+1}^k) = \frac{1-\alpha_m}{\beta\Delta t^2}\mathbf{M} + (1-\alpha_f)\mathbf{K}_T(\mathbf{d}_{n+1}^k)$ (2.133)

$\mathbf{f}^{eff}(\mathbf{d}_{n+1}^k) = \mathbf{f}_{n+1-\alpha_f}^{ext} - \mathbf{f}^{int}(\mathbf{d}_{n+1-\alpha_f}(\mathbf{d}_{n+1}^k)) - \frac{1-\alpha_m}{\beta\Delta t^2}\mathbf{M}\mathbf{d}_{n+1}^k + \mathbf{h}(\mathbf{d}_n, \dot{\mathbf{d}}_n, \ddot{\mathbf{d}}_n)$ (2.134)

GEMM

$\mathbf{K}_T^{eff}(\mathbf{d}_{n+1}^k) = \frac{1-\alpha_m}{\beta\Delta t^2}\mathbf{M} + \mathbf{K}_T^{GEMM}(\mathbf{d}_{n+1}^k)$ (2.148)

$\mathbf{f}^{eff}(\mathbf{d}_{n+1}^k) = \mathbf{f}_{n+1-\alpha_f}^{ext} - \mathbf{f}^{int}(\mathbf{d}_{n+1-\alpha_f}(\mathbf{d}_{n+1}^k)) - \frac{1-\alpha_m}{\beta\Delta t^2}\mathbf{M}\mathbf{d}_{n+1}^k + \mathbf{h}(\mathbf{d}_n, \dot{\mathbf{d}}_n, \ddot{\mathbf{d}}_n)$ (2.149)

$\Delta\mathbf{d}_{n+1}^k = \left(\mathbf{K}_T^{eff}\right)^{-1}\mathbf{f}^{eff}(\mathbf{d}_{n+1}^k)$

$\Delta\mathbf{d}_{n+1,\sum}^k = \Delta\mathbf{d}_{n+1,\sum}^{k-1} + \Delta\mathbf{d}_{n+1}^k$

$\mathbf{d}_{n+1}^{k+1} = \mathbf{d}_{n+1}^0 + \Delta\mathbf{d}_{n+1,\sum}^k$

$\Delta\mathbf{d}_{n+1,\sum}^k$: Sum of incremental change of nodal coordinate till end of iteration k of step $n+1$

$\Leftarrow$ Set up $k = k+1$ until convergence

Update change of nodal coordiate after convergence $\mathbf{d}_{n+1} = \mathbf{d}_{n+1}^{k+1}$

$\dot{\mathbf{d}}_{n+1}(\mathbf{d}_{n+1}) = \frac{\gamma}{\beta\Delta t}(\mathbf{d}_{n+1} - \mathbf{d}_n) - \frac{\gamma-\beta}{\beta}\dot{\mathbf{d}}_n - \frac{\gamma-2\beta}{2\beta}\Delta t\ddot{\mathbf{d}}_n$ (2.121)

$\ddot{\mathbf{d}}_{n+1}(\mathbf{d}_{n+1}) = \frac{1}{\beta\Delta t^2}(\mathbf{d}_{n+1} - \mathbf{d}_n) - \frac{1}{\beta\Delta t}\dot{\mathbf{d}}_n - \frac{1-2\beta}{2\beta}\ddot{\mathbf{d}}_n$ (2.122)

$\Leftarrow$ Set up $n = n+1$ until $n+1 = n_T$

Figure 2.5: Numerical solution algorithm of IBVP for elastodynamics.

Chapter 3

Wrinkling Model

With the advent of the light-weight structure era, thin membranes increasingly gain indispensable roles in diverse engineering disciplines from space down to underwater. However, the unique characteristic, the scarce amount of compressive stiffness, causes numerical simulations of the wrinkling within thin membranes nontrivial. To deal with such problems, wrinkling models based on either kinematics modifications (KM) or material modification (MM) are preferable to costly computations with unnecessarily refined meshes. The MM-based wrinkling model considers wrinkling as an analogue to perfect plasticity, and as a consequence, total strains within a wrinkled membrane can be additively decomposed into an elastic part and a wrinkling part. For applications of both isotropic and orthotropic materials, two alternative MM-based wrinkling models, the projection method and the plasticity analogy, are proposed within the context of this chapter. The outcome is the modified constitutive tensor which represents only the elastic strain energy.

3.1 Introduction

Owing to a high ratio of load carrying capacity to self weight, membranes are widely used in various applications. Nevertheless, a membrane can readily buckle due to its low bending stiffness, or in other words, compressive stresses in a membrane are faded out by local instabilities in the form of the out-of-plane "waves". Usually called wrinkles (see Figure 3.1(a) and (d)), these waves lie along the perpendicular direction to compressive stresses. Because the membrane theory is based purely on the in-plane stiffness, it is unable to reproduce the exact deformation patterns. For this reason, an incorrect strain field in Figure 3.2 as well as a fictitious stress field, e.g. artificial compressive stresses, may exist when the original elastic material is used. This aspect is deemed as an important pitfall of the membrane theory.

In general, there are at present two possibilities to deal with such kind of problems: First, an extensively refined mesh with thin-shell elements to resolve even the geometry of a tiniest wrinkle in details (see, e.g. [Miy00, WP06a]), but the discrete solution with shell elements proves to be mesh dependent as seen in Figure 3.1(b)-(d). In fact, extremely dense meshes are required to recreate the actual wrinkle patterns. Secondly, the element enrichment technique was introduced for the computation, or in other words, the mechanical model consists of enriched membrane elements to avoid an extensively refined mesh. A comparison of two prevalent enrichment techniques nowadays is given

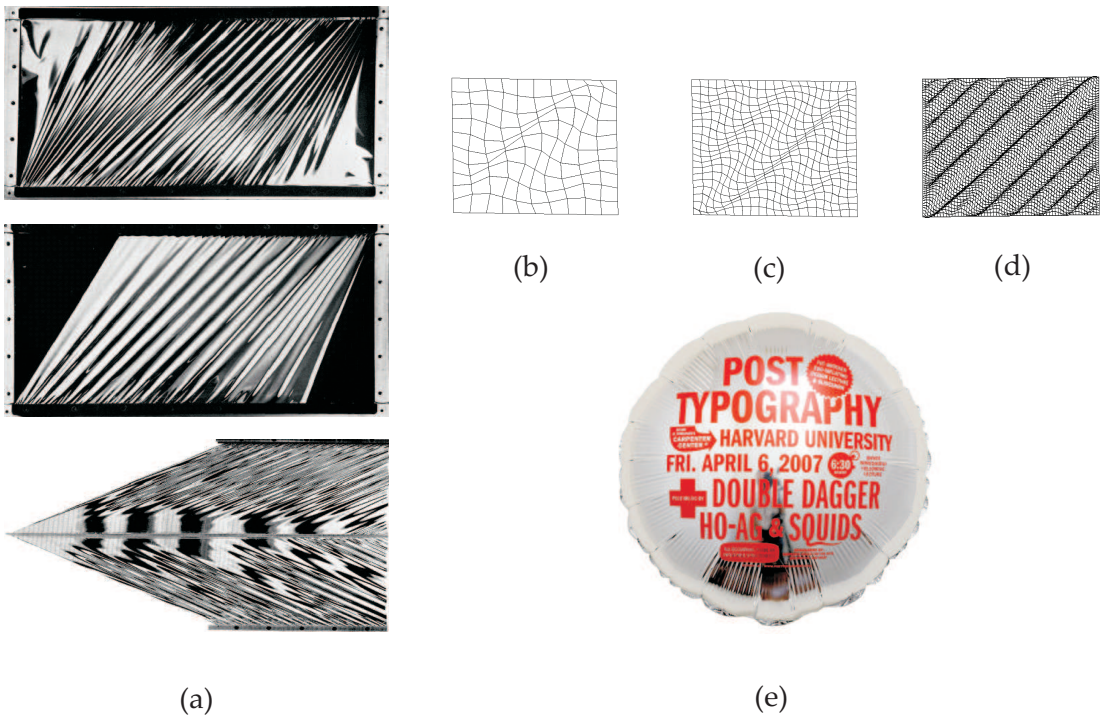

Figure 3.1: Wrinkle pattern in a rectangular membrane and mesh dependency in numerical analysis with shell elements for (a) experiment from [Man70] (b) 100 elements (c) 400 elements and (d) 3600 elements and (e) wrinkles within an inflatable foil balloon (http://www.posttypography.com/).

in Table 3.1: The first approach is based on modifications on the kinematic relation (KM) by superimposing a term concerning wrinkling to a nominal deformation gradient $\mathbf{F}$. This modification takes into account a fact that wrinkles cause shortening of the average plane of a membrane due to compressive stresses. For more details, one can consult, e.g. [RDO87a, RDO87b, Rod91, KI97, KI99, LAL01, HS03, HS05c].

The second possibility, the main focus of this chapter, is based on a local modification of the stress-strain relationship (MM) within an element to get rid of all compressive stresses. This is reasonable, since the focus of the corresponding simulations is on the "global" stress and displacement field, and therefore, the description of a single wrinkle is discarded. In turn, the model allows the use of elements which are bigger than the expected wavelength of a wrinkle. With regard to the global stress field, this approach is not less "precise" than the shell counterpart. Additionally, the wrinkling model is element independent and it is applicable as well for orthotropic materials. There exist numerous papers concerning this topic, e.g. Miyazaki [Miy06] presented an approach to adjust material parameters in the wrinkling direction for isotropic materials and applied this approach with the stiffness reduction model in dynamic analysis. Jarasjarungkiat [Jar04] experienced convergence problem for the membrane elements embedded with a simplified wrinkling model without proper numerical treatments. Further details for this topic are available in [CS88, DY03, JL96, LAL01, RLVO05, RO03, Ros05, SP89] which focus on isotropic materials whereas Epstein and Forcinito [EF01] introduced a complete theory of wrinkling based

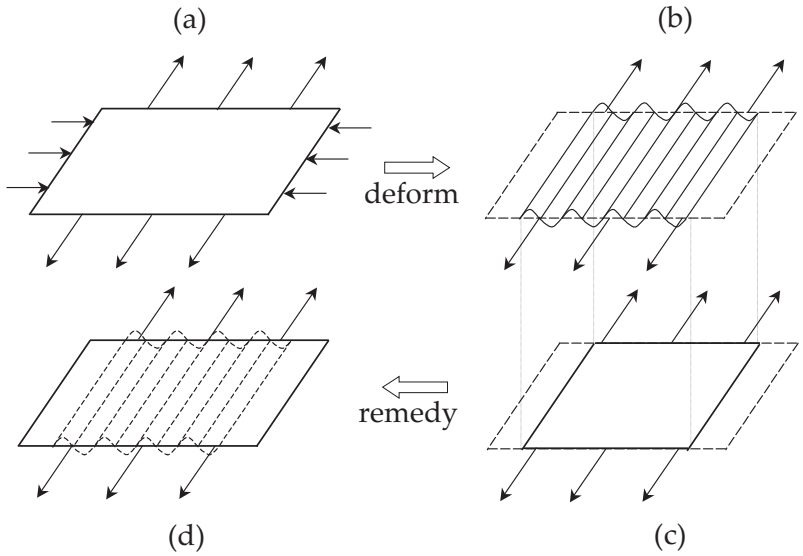

Figure 3.2: Illustration for (a) initial surface under tensile stress and compressive stress (b) actual wrinkled surface (compressive stress disappear) (c) inexact deformation in membrane theory (only in plane contraction) (d) fictitious flat surface (compensate the incorrect kinematic relation).

Table 3.1: Comparison for kinematic and material modification element enrichment techniques.

Compared items	Kinematics modification (KM)	Material modification (MM)
Able to represent exact geometry of wrinkles	No	No
Modification source	Deformation gradient $\mathbf{F}$	Constitutive tensor $\mathbb{C}$

on the notion of the relaxed energy function for anisotropic elastic membranes. This theory is considered as a particular case of a general theory of saturated elasticity. Related works with extended scope towards orthotropic materials can be found in, e.g. Valdes [VOC05] and Jarasjarungkiat *et al.* [JWB08b].

Both approaches share a common objective to minimize strain energy in a wrinkled membrane. Their equality can be roughly sketched by observing the modified strain energy density $\tilde{\Pi}$ in eq. (3.1), which is defined on the reference configuration in Voigt's notation as

$$\tilde{\Pi} = \frac{1}{2}\left\{\tilde{\mathbf{E}}\right\}^T [\mathbb{C}] \left\{\tilde{\mathbf{E}}\right\} = \frac{1}{2}\left\{\mathbf{E}\right\}^T \mathbf{\Phi}^T [\mathbb{C}] \mathbf{\Phi} \left\{\mathbf{E}\right\} = \frac{1}{2}\left\{\mathbf{E}\right\} \left[\tilde{\mathbb{C}}\right] \left\{\mathbf{E}\right\}; \qquad \left\{\tilde{\mathbf{E}}\right\} = \mathbf{\Phi}\left\{\mathbf{E}\right\} \tag{3.1}$$

where $\mathbf{E}$ stands for the GL strain tensor given in eq. (2.19). With the transformation matrix $\mathbf{\Phi}$, the modified GL strain tensor $\tilde{\mathbf{E}}$ in presence of wrinkles is achieved along with the modified constitutive tensor $\tilde{\mathbb{C}}$. A comparison among different element enrichment methods is available in Miyazaki [Miy06].

We close this introductory section with the outline of this chapter: In the next Section 3.2, we introduce the criteria to evaluate the state of a membrane which is followed by an algorithm to search for the wrinkling direction. Then the similarity between wrinkling and

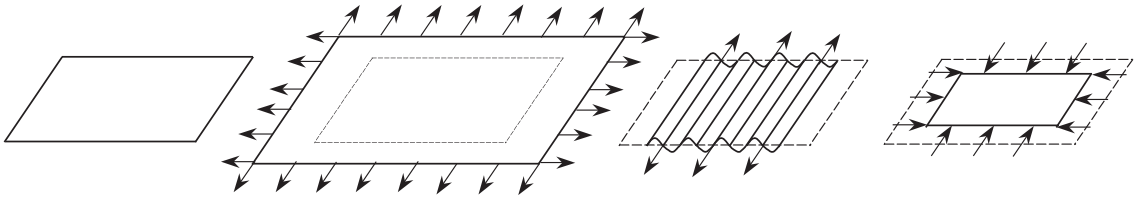

(a) (b) (c) (d)

Figure 3.3: Principal status of a membrane (a) undeformed state (b) taut (c) wrinkled (d) slack.

Table 3.2: Summary of wrinkling criteria.

Membrane state	Principal stress criteiron	Principal strain criterion	Mixed criterion
Taut	$S_{min} > 0$	$E_{min} > 0$	$S_{min} > 0$
Wrinkled	$S_{min} \leq 0$ and $S_{max} > 0$	$E_{min} \leq 0$ and $E_{max} > 0$	$S_{min} \leq 0$ and $E_{max} > 0$
Slack	$S_{min} \leq 0$ and $S_{max} \leq 0$	$E_{min} \leq 0$ and $E_{max} \leq 0$	$E_{max} \leq 0$

perfect plasticity for small elastic strain is mentioned while section 3.3 discusses concepts of the material modification by the projection method in which the definition of the projection tensor is clarified. Later in that section, the main idea to determine the modified stress field due to wrinkling is highlighted and then the derivation of the constitutive equation in an incremental form for wrinkled membranes is demonstrated. In section 3.4, an alternative model–plasticity analogy–to modify material properties for a wrinkled membrane is presented. Afterwards, section 3.5 is dedicated to various numerical examples to verify efficiency of the proposed model by means of benchmark examples from literature. This Chapter is concluded by a short summary with a supplement for a proof of symmetry and positive semi-definiteness of the modified constitutive tensor in the appendix A.1.

3.2 Definition and theoretical background

As shown in Figure 3.3, three states of a membrane are basically distinguished during deformation: taut, wrinkled or slack. To determine the current state of a membrane, one requires a wrinkling criterion. In table 3.2, three available wrinkling criteria are given. The mixed criterion, verified in [Pag04, RLVO05] as the most accurate state diagnosis, is employed within this work. To gain an insight into the approach, the MM-based model adopts such assumptions: (i) Membranes are very thin and have negligible flexural stiffness. (ii) Despite a small amount of compression, a membrane can readily buckle, i.e. wrinkle, to release excessive compressive stresses beyond its capacity. (iii) The load carrying behavior can be modeled under the state of plane stress. The main idea for the wrinkling model is to soften compressive stiffness of materials in the direction which wrinkles occur. In the derived model, any path dependence is neglected according to the justification in [WP06a, WP06b, WP06c].

3.2.1 Evaluation of the state of a membrane

As mentioned in [KI97, KI99, HS03, HS05c, LJS01], wrinkling information of a membrane is available on the undeformed configuration. Since the original constitutive tensor $\mathbb{C}$ in eq. (2.61) cannot represent the actual stress field within a wrinkled membrane, therefore, the total PK2 stress obtained from the constitutive equation in eq. (2.60) is interpreted as *the fictitious PK2 stress tensor* $\mathbf{S}_{fic} = S_{fic}^{\alpha\beta}\mathbf{G}_\alpha \otimes \mathbf{G}_\beta$:

$$\mathbf{S}_{fic} = \mathbf{S}_{pre} + \mathbf{S}_{el} = \mathbf{S}_{pre} + \mathbb{C}_{2D} : \mathbf{E} \quad \text{or} \quad S_{fic}^{\alpha\beta} = S_{pre}^{\alpha\beta} + S_{el}^{\alpha\beta} = S_{pre}^{\alpha\beta} + C_{2D}^{\alpha\beta\tau\upsilon}E_{\tau\upsilon}. \tag{3.2}$$

As a consequence, the constitutive equation in the Voigt's notation in eq. (2.65) is turned to

$$\left\{\mathbf{S}_{fic}\right\} = \left\{\mathbf{S}_{el}\right\} + \left\{\mathbf{S}_{pre}\right\} = \left[\mathbb{C}\right]\left\{\mathbf{E}\right\} + \left\{\mathbf{S}_{pre}\right\}. \tag{3.3}$$

These tensors can be based on a Cartesian basis described in Figure 3.4 under the state of plane stress in Voigt's notation where the transformation of stress and strain components from an arbitrary Cartesian basis $(\bullet)$ defined on the basis $\mathbf{A}_\alpha$to a rotated one $(\hat{\bullet})$defined on the basis $\hat{\mathbf{A}}_\alpha$ in Figure 3.4 by a mathematically positive angle α can be written as

$$\left\{\hat{\mathbf{E}}\right\} = \mathbf{T}^{-T}\left\{\mathbf{E}\right\},\ \mathbf{T}^{T}\left\{\hat{\mathbf{E}}\right\} = \left\{\mathbf{E}\right\};\quad \mathbf{T}^{T} = \begin{bmatrix} c^2 & s^2 & -cs \\ s^2 & c^2 & cs \\ 2cs & -2cs & c^2 - s^2 \end{bmatrix} = \begin{bmatrix} \mathbf{U}_1 & \mathbf{U}_2 & \mathbf{U}_3 \end{bmatrix}, \tag{3.4}$$

$$\left\{\hat{\mathbf{S}}\right\} = \mathbf{T}\left\{\mathbf{S}\right\},\ \mathbf{T}^{-1}\left\{\hat{\mathbf{S}}\right\} = \left\{\mathbf{S}\right\};\quad \mathbf{T}^{-1} = \begin{bmatrix} c^2 & s^2 & -2cs \\ s^2 & c^2 & 2cs \\ cs & -cs & c^2 - s^2 \end{bmatrix} = \begin{bmatrix} \mathbf{n}_1 & \mathbf{n}_2 & \mathbf{n}_3 \end{bmatrix}, \tag{3.5}$$

which c stands for cosα and s represents sinα, respectively (see Figure 3.4). Obviously, $\mathbf{U}_i$ is the transformation vector that maps a stress $\{\mathbf{S}\}$ in an arbitrary Cartesian basis to the component $\hat{S}_i$ of the stress $\left\{\hat{\mathbf{S}}\right\}$ in the rotated basis. Similarly, $\mathbf{n}_j$ is the transformation vector that transforms a strain $\{\mathbf{E}\}$ in an arbitrary Cartesian basis to the component $\hat{E}_j$ of the strain $\left\{\hat{\mathbf{E}}\right\}$ in the rotated basis. Generally, $\mathbf{U}_i$ and $\mathbf{n}_j$ are conjugate to each other in such the way that

$$\mathbf{U}_i \cdot \mathbf{n}_j = \delta_{ij} = \begin{cases} 1 & i = j \\ 0 & i \neq j \end{cases} \tag{3.6}$$

$$\mathbf{n}_i \times \mathbf{n}_j = \epsilon_{ijk}\mathbf{U}_k;\ \mathbf{U}_i \times \mathbf{U}_j = \epsilon_{ijk}\mathbf{n}_k;\quad \text{with}\quad \epsilon_{ijk} = \begin{cases} 1 & \text{cyclic } i,j,k \\ -1 & \text{anticyclic } i,j,k \\ 0 & \text{otherwise} \end{cases} \tag{3.7}$$

From eq. (3.5), the constitutive tensor on the rotated axis is expressed by $\hat{\mathbb{C}}$

$$\begin{aligned} &\left\{\hat{\mathbf{S}}\right\} = \left[\hat{\mathbb{C}}\right]\left\{\hat{\mathbf{E}}\right\} \Rightarrow \mathbf{T}\left\{\mathbf{S}\right\} = \left[\hat{\mathbb{C}}\right]\mathbf{T}^{-T}\left\{\mathbf{E}\right\} \Rightarrow \left\{\mathbf{S}\right\} = \mathbf{T}^{-1}\left[\hat{\mathbb{C}}\right]\mathbf{T}^{-T}\left\{\mathbf{E}\right\}, \\ &\left[\mathbb{C}\right] = \mathbf{T}^{-1}\left[\hat{\mathbb{C}}\right]\mathbf{T}^{-T} \Rightarrow \mathbf{T}\left[\mathbb{C}\right]\mathbf{T}^{T} = \left[\hat{\mathbb{C}}\right]. \end{aligned} \tag{3.8}$$

3.2.2 Determination of the wrinkling direction

An accurate wrinkling direction plays a key role for an efficient wrinkling model. For an isotropic material this issue is trivial due to the coincidence between the principal stress and

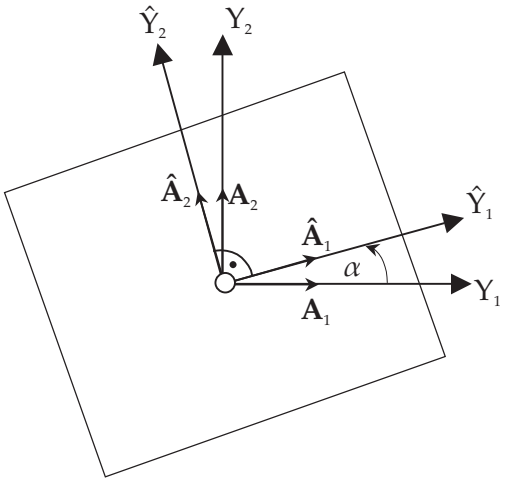

Figure 3.4: Illustration for an arbitrary Cartesian basis and its corresponding rotated basis.

principal strain directions. In contrary, the wrinkling direction in case of an orthotropic material is achieved by solving a nonlinear equation system, e.g. algorithms proposed in [KI99, LAL01]. This work presents a simple algorithm which is derived by an observation on the characteristic of the feasible solution. Based on [RDO87b], the algorithm considers only the average membrane deformation by removing wrinkles from the midplane of the membrane as illustrated in Figure 3.2 and Figure 3.5. With an assumption that the uniaxial tension direction $\mathbf{t}$ is perpendicular to the wrinkling direction $\mathbf{w}$ in the current configuration, thus the modified deformation gradient $\tilde{\mathbf{F}}$ is described by

$$\tilde{\mathbf{F}} = (\mathbf{I} + \beta \mathbf{w} \otimes \mathbf{w})\, \mathbf{F}, \tag{3.9}$$

where $\mathbf{I}$ is the identity tensor, and the scalar value $\beta > 0$ represents the amount of elongation when a wrinkled surface is stretched to create a fictitious flat plane (see Figure 3.5). The nominal deformation gradient $\mathbf{F}$ accounts for the deformation of an infinitesimal area (abcd) from the reference configuration Ω_0 to the deformed configuration Ω(abcd). The curved surface (abcd) represents a wrinkled surface around a point on Ω. When the infinitesimal plane (abcd) is located at an integration point of a finite element as shown in Figure 3.5, continuum and discrete definitions of this wrinkled surface (abcd) are pointwise identical. Moreover, the fictitious flat surface (abc´d´) is the outcome when the curved surface (abcd) is stretched to get rid of all wrinkles, while the corresponding motion $\mathbf{I} + \beta \mathbf{w} \otimes \mathbf{w}$ from the curved surface (abcd) to fictitious flat surface (abc´d´) is illustrated in the Figure. In the fictitious flat surface (abc'd'), the modified GL strain, based on the contravariant basis $\mathbf{G}^\alpha$, of the fictitious flat surface (abc´d´) can be written by

$$\begin{aligned} \tilde{\mathbf{E}} &= \frac{1}{2}\left(\tilde{\mathbf{F}}^T\tilde{\mathbf{F}} - \mathbf{I}\right) = \frac{1}{2}\left[(\mathbf{F} + \beta \mathbf{w} \otimes \mathbf{w}\mathbf{F})^T (\mathbf{F} + \beta \mathbf{w} \otimes \mathbf{w}\mathbf{F}) - \mathbf{I}\right], \\ &= \mathbf{E} + \frac{1}{2}\beta\,(2+\beta)\,\mathbf{w}_0 \otimes \mathbf{w}_0 \end{aligned} \tag{3.10}$$

where $\mathbf{w} = w_\alpha \mathbf{g}^\alpha$; $\mathbf{w}_0 = \mathbf{w}\mathbf{F} = \mathbf{F}^T\mathbf{w} = \mathbf{G}^\alpha \otimes \mathbf{g}_\alpha \cdot w_\beta \mathbf{g}^\beta = w_\alpha \mathbf{G}^\alpha$. In this equation, a correlation between $\mathbf{w}$ and $\mathbf{w}_0$ must be clarified. Since in the current configuration the wrinkling direction vector $\mathbf{w}$ is orthogonal to the uniaxial tension direction $\mathbf{t}$, both vectors form

the wrinkling axes $(\mathbf{t}, \mathbf{w})$ in the current configuration, whereas $\mathbf{t}$ and $\mathbf{w}$ are unit vectors, i.e. $\|\mathbf{t}\| = \|\mathbf{w}\| = 1$. The pull-back of the wrinkling direction vector $\mathbf{w}$ is $\mathbf{w}_0$ which is defined on the contravariant basis in the undeformed configuration $\mathbf{G}^\alpha$. An orthogonal vector pair $\mathbf{t}_0$, $\mathbf{w}_0$ constitutes an orthogonal wrinkling basis in the undeformed configuration whereas $\mathbf{t}_0$ is not the result from a pull-back of $\mathbf{t}$. To prevent confusion, the notation used in subsequent sections should be mentioned: As illustrated in Figure 3.5, any variable without any mark $(\bullet)$ is a nominal variable on the material axes $(\mathbf{A}_1, \mathbf{A}_2)$ whereas a variable $(\tilde{\bullet})$ is a variable which is modified by the wrinkling model. On the material basis $(\mathbf{A}_1, \mathbf{A}_2)$[1], the modified GL strain tensor $\tilde{\mathbf{E}}$ in eq. (3.10) and its energetic conjugate $\tilde{\mathbf{S}}$ on the reference configuration are described by

$$\begin{aligned} \left\{\tilde{\mathbf{E}}\right\} &= \{\mathbf{E}\} + \frac{1}{2}\beta\left(2+\beta\right)\|\mathbf{w}_0\|^2\begin{bmatrix} s^2 & c^2 & -2cs \end{bmatrix}^T = \{\mathbf{E}\} + \mu\mathbf{U}_2, \\ \left\{\tilde{\mathbf{S}}\right\} &= [\mathbb{C}]\left\{\tilde{\mathbf{E}}\right\} + \left\{\mathbf{S}_{pre}\right\} \end{aligned} \tag{3.11}$$

where $\mathbf{U}_2$ is the transformation vector of stress towards the wrinkling direction $\mathbf{w}_0$ as mentioned in eq. (3.5) and illustrated in Figure 3.4 and Figure 3.5. Obviously, $\mu = \frac{1}{2}\beta\left(2+\beta\right)\|\mathbf{w}_0\|^2$ represents the amount of wrinkling, while c and s stand for $\cos\theta$ and $\sin\theta$, respectively. The angle θ is an angle of rotation that is measured counter-clockwise from the local Cartesian basis in the reference configuration $(\mathbf{A}_1, \mathbf{A}_2)$ to an orthogonal basis formed by the wrinkling axes $(\mathbf{t}_0, \mathbf{w}_0)$. The wrinkling direction vector in the reference configuration is given by $\mathbf{w}_0 = -\|\mathbf{w}_0\|\sin\theta\mathbf{A}_1 + \|\mathbf{w}_0\|\cos\theta\mathbf{A}_2 = w_{0\alpha}\mathbf{A}_\alpha$. By stretching edge cd to edge c'd' to form the fictitious flat surface in Figure 3.5, the corresponding wrinkling direction vector on this surface is $\boldsymbol{\omega}$, and the corresponding uniaxial tension vector on the same surface is $\boldsymbol{\tau}$. During a strain free movement to remove wrinkles from the surface, a uniaxial tension state of the Cauchy stress is invariant. Consequently, after wrinkles vanish, the fictitious flat surface is still under the state of uniaxial tension.

Here, $\boldsymbol{\tau}$ and $\boldsymbol{\omega}$ are introduced in order to differentiate them from $\mathbf{t}$ and $\mathbf{w}$ with an aim to make a specific wrinkling basis $(\boldsymbol{\tau}, \boldsymbol{\omega})$ for the fictitious flat surface (abc´d´). While $\mathbf{t}$ is equivalent to $\boldsymbol{\tau}$, $\mathbf{w}$ is not necessarily equivalent to $\boldsymbol{\omega}$. With the help of eq. (3.9), when the contravariant definition of the vector $\mathbf{w}_0 = w_0^\alpha\mathbf{G}_\alpha$ is introduced, one can write $\boldsymbol{\omega} = \tilde{\mathbf{F}}\mathbf{w}_0 = \left(\mathbf{I} + \beta\mathbf{w}\otimes\mathbf{w}\right)\mathbf{F}\mathbf{w}_0 = \left(\mathbf{I} + \beta\mathbf{w}\otimes\mathbf{w}\right)\mathbf{w} = (1+\beta)\mathbf{w}$. Obviously, $\boldsymbol{\omega}$ is collinear to $\mathbf{w}$ and the normalized $\boldsymbol{\omega}$ is equivalent to $\mathbf{w}$. Note that for an orthonormal basis, the contravariant and covariant base vectors are identical $\mathbf{w}^\alpha = \mathbf{w}_\alpha$.

On the wrinkling axes of the fictitious flat surface $(\boldsymbol{\tau}, \boldsymbol{\omega})$, push-forward of the modified PK2 stress tensor on the mid-surface of the membrane $\tilde{\mathbf{S}} = \tilde{S}^{\alpha\beta}\mathbf{G}_\alpha\otimes\mathbf{G}_\beta$ is described with respect to the curvilinear coordinate by

$$\tilde{\sigma} = \left(det\tilde{\mathbf{F}}\right)^{-1}\tilde{\mathbf{F}}\tilde{\mathbf{S}}\tilde{\mathbf{F}}^T, \quad \boldsymbol{\tau}_0 = \tilde{\mathbf{F}}^T\boldsymbol{\tau} = \boldsymbol{\tau}\tilde{\mathbf{F}}, \quad \mathbf{w}_0 = \tilde{\mathbf{F}}^T\boldsymbol{\omega} = \boldsymbol{\omega}\tilde{\mathbf{F}}, \tag{3.12}$$

where the pull-back $\boldsymbol{\tau}_0$ of $\boldsymbol{\tau}$ is given in eq. $(3.12)_2$, as well as the pull-back of $\boldsymbol{\omega}$ is $\mathbf{w}_0$ in eq. $(3.12)_3$. Although $\mathbf{t}$ is orthogonal to $\mathbf{w}$, It is unnecessary that $\boldsymbol{\tau}_0$ is always orthogonal to $\mathbf{w}_0$ (see Figure 3.5) The uniaxial tension state of the modified Cauchy stress tensor is equivalent to

$$\boldsymbol{\omega}\cdot\tilde{\sigma}\boldsymbol{\omega} = 0 \quad \text{and} \quad \boldsymbol{\tau}\cdot\tilde{\sigma}\boldsymbol{\omega} = 0. \tag{3.13}$$

[1]On the Cartesian coordinate the covariant and contravariant basis are identical $(\mathbf{A}_\alpha = \mathbf{A}^\alpha)$.

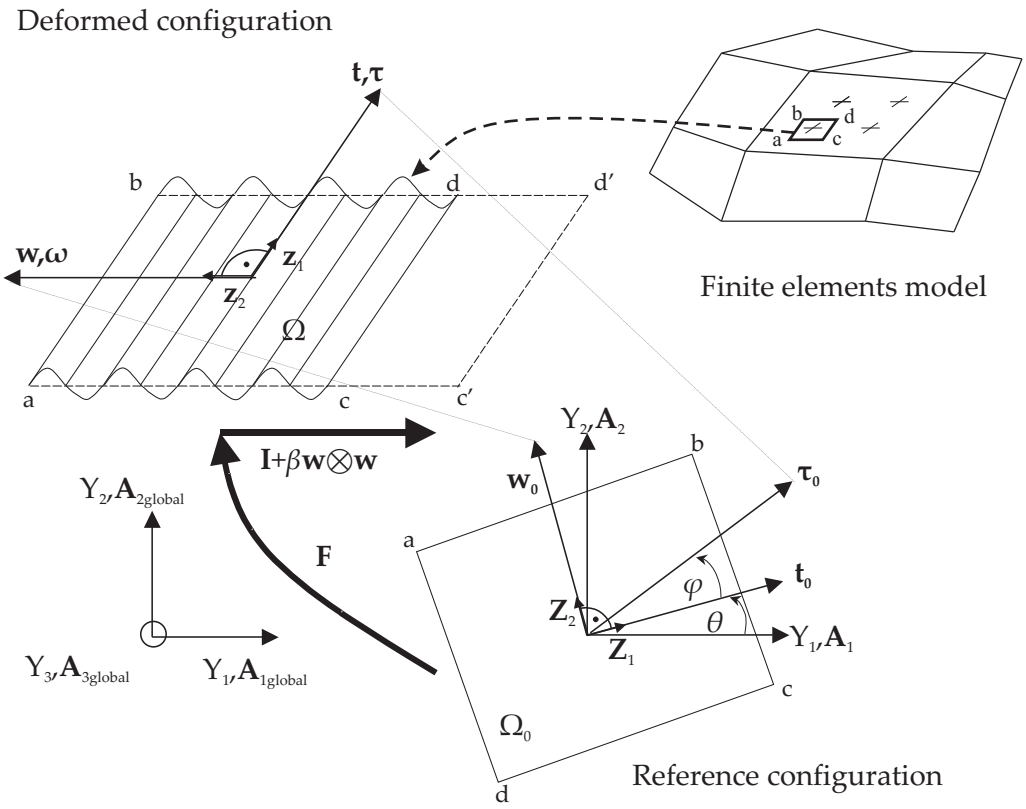

Figure 3.5: Illustration for fictitious flat surface, wrinkled surface and their coordinate systems.

Eq. $(3.13)_{1,2}$ describe that the axial stress in the direction of $\boldsymbol{\omega}$ and the in-plane shear stress vanish, respectively. Inserting 3.12 in 3.13 yields

$$\mathbf{w}_0 \cdot \tilde{\mathbf{S}}\mathbf{w}_0 = 0 \quad \text{and} \quad \boldsymbol{\tau}_0 \cdot \tilde{\mathbf{S}}\mathbf{w}_0 = 0. \tag{3.14}$$

Apparently, in eq. (3.14), the uniaxial tension state of the Cauchy stress in eq. (3.13) is equivalent to the vanishing of the modified PK2 stress in the axial direction of $\mathbf{w}_0$ and the in plane shear stress spanned by $(\boldsymbol{\tau}_0, \mathbf{w}_0)$. Under the state of plane stress, the uniaxial tension in eq. (3.13) can be expressed on the local Cartesian basis in the fictitious flat surface by

$$\begin{aligned} \boldsymbol{\omega} \cdot \tilde{\boldsymbol{\sigma}}\boldsymbol{\omega} &= \|\boldsymbol{\omega}\| \, \mathbf{z}_2 \cdot \tilde{\sigma}^{\alpha\beta} \mathbf{z}_\alpha \otimes \mathbf{z}_\beta \, \|\boldsymbol{\omega}\| \, \mathbf{z}_2 = \tilde{\sigma}^{22} = 0, \\ \boldsymbol{\tau} \cdot \tilde{\boldsymbol{\sigma}}\boldsymbol{\omega} &= \|\boldsymbol{\tau}\| \, \mathbf{z}_1 \cdot \tilde{\sigma}^{\alpha\beta} \mathbf{z}_\alpha \otimes \mathbf{z}_\beta \, \|\boldsymbol{\omega}\| \, \mathbf{z}_2 = \tilde{\sigma}^{12} = 0, \end{aligned} \tag{3.15}$$

where an orthonormal basis $(\mathbf{z}_1, \mathbf{z}_2)$ is defined in the direction of the wrinkling axes $(\boldsymbol{\tau}, \boldsymbol{\omega})$ whereas its counterpart eq. (3.14) on the local Cartesian basis $(\mathbf{Z}_1, \mathbf{Z}_2)$ in the undeformed configuration is written by

$$\begin{aligned} \mathbf{w}_0 \cdot \tilde{\mathbf{S}}\mathbf{w}_0 &= \|\mathbf{w}_0\| \, \mathbf{Z}_2 \cdot \tilde{S}^{\alpha\beta} \mathbf{Z}_\alpha \otimes \mathbf{Z}_\beta \, \|\mathbf{w}_0\| \, \mathbf{Z}_2 = \tilde{S}^{22} = 0, \\ \boldsymbol{\tau}_0 \cdot \tilde{\mathbf{S}}\mathbf{w}_0 &= (\|\boldsymbol{\tau}_0\| \cos\varphi \mathbf{Z}_1 + \|\boldsymbol{\tau}_0\| \sin\varphi \mathbf{Z}_2) \cdot \tilde{S}^{\alpha\beta} \mathbf{Z}_\alpha \otimes \mathbf{Z}_\beta \, \|\mathbf{w}_0\| \, \mathbf{Z}_2 = 0, \\ &= \|\boldsymbol{\tau}_0\| \, \|\mathbf{w}_0\| \cos\varphi \tilde{S}^{12} + \|\boldsymbol{\tau}_0\| \, \|\mathbf{w}_0\| \sin\varphi \underbrace{\tilde{S}^{22}}_{0} = 0 \quad \Rightarrow \quad \tilde{S}^{12} = 0. \end{aligned} \tag{3.16}$$

Here φ is an angle of rotation, measured counter-clockwisely from an orthonormal basis $(\mathbf{Z}_1, \mathbf{Z}_2)$ in the direction of the wrinkling axes $(\mathbf{t}_0, \mathbf{w}_0)$ to the direction of $\boldsymbol{\tau}_0$, the pull-back

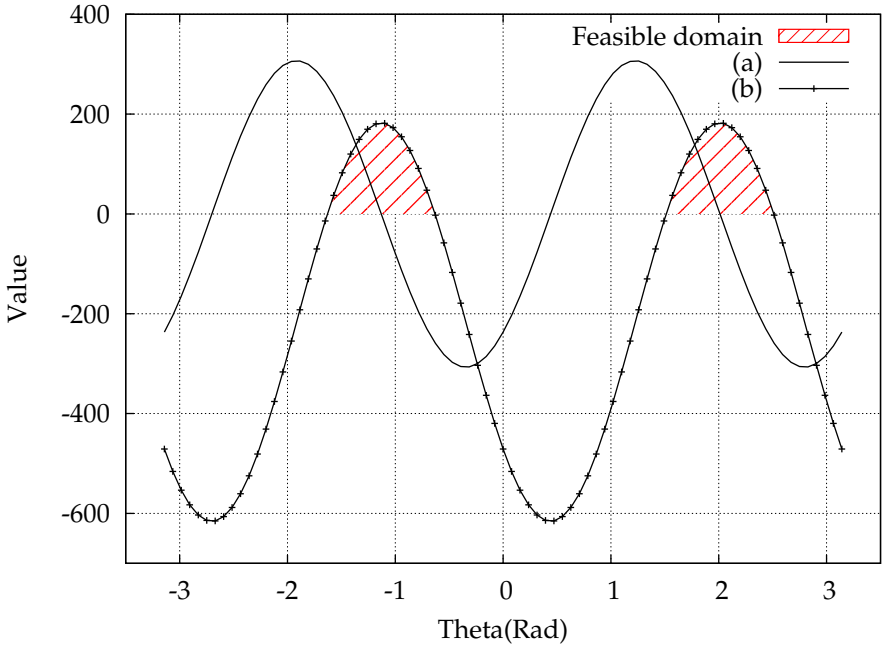

Figure 3.6: Illustration for (a) characteristic solution of uniaxial tension state in eq. (3.19) and (b) uniaxial tension constraint g_1.

of $\boldsymbol{\tau}$. Apparently, eq. $(3.16)_2$ is only valid if $\boldsymbol{\tau}_0$ is linearly independent of $\mathbf{w}_0$. It is noteworthy to emphasize that eqs. (3.15) and (3.16) are equivalent, i.e. the uniaxial tension conditions in eq. (3.15) in the current configuration can be transformed to the uniaxial tension conditions of eq. (3.16) in the reference configuration. As a result, the uniaxial condition in the wrinkling axes $(\mathbf{t}_0, \mathbf{w}_0)$ can be expressed by the modified PK2 stress tensor on the material axes $(\mathbf{A}_1, \mathbf{A}_2)$ with the help of the transformation vectors $\mathbf{U}_2$ and $\mathbf{U}_3$ from eq. (3.4) such that

$$\tilde{S}^{22} = 0 \Rightarrow \tilde{S}_2 = \mathbf{U}_2^T \left\{\tilde{\mathbf{S}}\right\} = 0 \quad \tilde{S}^{12} = 0 \Rightarrow \tilde{S}_3 = \mathbf{U}_3^T \left\{\tilde{\mathbf{S}}\right\} = 0 \tag{3.17}$$

where vector $\mathbf{U}_3$ is interpreted as the transformation vector towards the shear stress of the wrinkling axis $(\mathbf{t}_0, \mathbf{w}_0)$. Then substituting eq. (3.11) into eq. (3.17) yields

$$\mu = -\mathbf{U}_2^T \left\{\mathbf{S}\right\} / \mathbf{U}_2^T \left[\mathbb{C}\right] \mathbf{U}_2, \tag{3.18}$$

$$\mathbf{U}_2^T \left[\mathrm{C}\right] \mathbf{U}_2 \left(\mathbf{U}_3^T \left\{\mathbf{S}\right\}\right) - \mathbf{U}_2^T \left[\mathrm{C}\right] \mathbf{U}_3 \left(\mathbf{U}_2^T \left\{\mathbf{S}\right\}\right) = 0. \tag{3.19}$$

Eqs. (3.18) and (3.19) contribute to a system of nonlinear equations, which can be solved numerically for the wrinkling direction θ, e.g. by the Newton method. By the way, the solution, having local minima within the range of angle 0 to π, is not unique. For instance, the line (a) in Figure 3.6, has two roots of eq. (3.19) in the range of 0 to π. Thus, an additional constraint is required to preclude plunging into unfeasible local minima and to find a unique root within the feasible domain. A possible constraint is the uniaxial tension condition in the case that wrinkle occurs. For this reason, a condition $\tilde{S}^{11} \geq 0 \Rightarrow \tilde{S}_1 = \mathbf{U}_1^T \left\{\tilde{\mathbf{S}}\right\} \geq 0$ is chosen as the additional constraint g_1 depicted by the line (b) in Figure 3.6. Therefore, the feasible domain in the range of 0 to π is uniquely defined by the fulfillment of g_1. Whenever the solution of Newton methods falls outside the feasible domain, a shift parameter will

move the predicted phase angle either forward or backward by $\pi/2$, and as a result, the unique root in the feasible domain is achieved. Other roots are periodical with the period of π. Moreover, numerical proofs show the efficiency with regard to computational cost.

3.2.3 Analogy between wrinkling and perfect hypoelastoplasticity for small strains

Within this section, similarities between wrinkling and perfect hypoelastoplasticity (see [BLM00, SH98]) are discussed. For a hypoelastic-plastic model, an additive decomposition of the strain tensor $\mathbf{E}$ into an elastic part $\mathbf{E}^e$ and a plastic part $\mathbf{E}^p$ is assumed. Under normal conditions, membranes undergo large deformation within the small elastic strain regime. For this reason, *the rate-independent hypoelastic-plastic model*, which is typically used when elastic strains are small compared to plastic strains, is considered as a suitable choice. For small strains, the energy error is insignificant and hypoelastic descriptions of the elastic response are often adequate. In turn, this model is not recommended for the case of large elastic strains. Wrinkling is related to the elastic-plastic process as follows:
(i). An analogy between the wrinkling strain $\mathbf{E}^w$ and the plastic strain $\mathbf{E}^p$ is adopted as

$$\mathbf{E} = \mathbf{E}^e + \mathbf{E}^p; \qquad \mathbf{E}^p \cong \mathbf{E}^w. \tag{3.20}$$

(ii). When wrinkles occur, compressive stiffness in the direction of those wrinkles vanishes suddenly. This phenomenon resembles a perfect plastic process without any hardening. An illustration in Figure 3.7a represents the relation between stress and strain for a 1D perfect plastic process while $\partial \mathrm{E}_\sigma$ denotes the boundary of an elastic domain. Nearby, Figure 3.7b depicts a 1D wrinkling process of a tension structure, e.g. a membrane. In this figure, one observes that a constraint on the condition of no-compressive stress can be fulfilled by either the Lagrange multiplier or the penalty method (see [BLM00]). Obviously, these figures exhibit a resemblance between wrinkling in a membrane and the perfect plastic process.
(iii). With a known wrinkling direction, the corresponding modified stress field is determined in such a way that the plastic flow direction $\mathbf{r}$ and the wrinkling direction $\mathbf{w}_0$ (see Figure3.5) are identical ($\mathbf{r} \approx f_{\mathbf{S}} = \mathbf{w}_0$) where $f_{\mathbf{s}}$ is the gradient of the yield function in a stress space. According to [BLM00, SH98], the concept of a rate-independent hypoelastic-plastic adopted wrinkling model for small strains can be summarized as in the following:

- ◇ Additive decomposition of strain rate into an elastic part and a plastic (wrinkling) part:

$$\dot{\mathbf{E}} = \dot{\mathbf{E}}^e + \dot{\mathbf{E}}^w. \tag{3.21}$$

- ◇ Relation between stress rate and elastic strain rate:

$$\dot{\mathbf{S}} = \mathbb{C} : \dot{\mathbf{E}}^e = \mathbb{C} : (\dot{\mathbf{E}} - \dot{\mathbf{E}}^w). \tag{3.22}$$

- ◇ Plastic, i.e. wrinkling, flow rule:

$$\dot{\mathbf{E}}^w = \dot{\lambda}\mathbf{r}(\mathbf{S}). \tag{3.23}$$

◇ Yield, i.e. wrinkling, condition:

$$f(\mathbf{S}) = 0. \tag{3.24}$$

◇ Loading-unloading conditions:

$$\dot{\lambda} \geq 0, \quad f \leq 0, \quad \dot{\lambda} f = 0. \tag{3.25}$$

◇ Plastic, i.e. wrinkling, rate parameter (from consistency condition):

$$\dot{\lambda} = \frac{f_{\mathbf{S}} : \mathbb{C} : \dot{\mathbf{E}}}{f_{\mathbf{S}} : \mathbb{C} : \mathbf{r}}. \tag{3.26}$$

◇ Relation between stress rate and strain rate:

$$\dot{\mathbf{S}} = \mathbb{C}^{epw} : \dot{\mathbf{E}}. \tag{3.27}$$

◇ Continuum elasto-plastic tangent modulus for wrinkling:

$$\mathbb{C}^{epw} = \mathbb{C} - \frac{(\mathbb{C} : \mathbf{r}) \otimes (f_{\mathbf{S}} : \mathbb{C})}{f_{\mathbf{S}} : \mathbb{C} : \mathbf{r}}, \tag{3.28}$$

which is symmetric if plastic, i.e. wrinkling, flow is associative $\mathbb{C} : \mathbf{r} \approx f_{\mathbf{S}} : \mathbb{C}$ where $\mathbf{r}$ is the plastic flow (wrinkling) direction and $f_{\mathbf{S}}$ is the gradient of yield (wrinkling) function in the stress space.

Because objectivity requirements are not relevant for the small-strain setting, the material time derivative of the relevant stress rate $\dot{\mathbf{S}}$ and strain rate $\dot{\mathbf{E}}$ replaces the rate-of-deformation (see [BLM00]). With this similitude, wrinkling can be deemed as an analogue to the perfect plastic process. Therefore, the well-developed computational algorithms for perfect plasticity are feasibly applicable to wrinkling in a thin membrane. In the case of wrinkling, the continuum elasto-plastic adopted wrinking constitutive tensor $\mathbb{C}^{epw}$ in eq. (3.28) can be rewritten as

$$[\mathbb{C}^{epw}] = [\mathbb{C}] - \frac{[\mathbb{C}]\,\mathbf{w}_0\mathbf{w}_0^T\,[\mathbb{C}]}{\mathbf{w}_0^T\,[\mathbb{C}]\,\mathbf{w}_0} \tag{3.29}$$

where $[\mathbb{C}]$ is the original constitutive tensor in Voigt notation. For an isotropic material[2], the closed form of eq. (3.29), compared to eq. (2.68), can be described by

$$[\mathbb{C}^{epw}] = \frac{E}{1-\nu^2}\left(\begin{bmatrix} 1 & \nu & 0 \\ \nu & 1 & 0 \\ 0 & 0 & \frac{1-\nu}{2} \end{bmatrix} - \begin{bmatrix} \nu^2 & \nu & 0 \\ \nu & 1 & 0 \\ 0 & 0 & 0 \end{bmatrix}\right) = \left(\begin{bmatrix} E & 0 & 0 \\ 0 & 0 & 0 \\ 0 & 0 & \frac{E}{2(1+\nu)} \end{bmatrix}\right) \tag{3.30}$$

An important difference between plastic strain and wrinkling strain must be discussed: It is well known that the plastic strain is irreversible while this is not the case for the wrinkling strain which is a result of a reversible process without any dissipation. During wrinkling, both the stress field within the membrane and total stiffness of the membrane evolves with respect to formation of wrinkles. An algorithm for the plastic evolution can therefore suitably describe the change in stress fields which affects the stiffness of the membrane in the next calculation step. In contrast to plastic deformation, only the strain information referred to the reference configuration is required to determine the actual state of a membrane in each iteration step whereas historical information of wrinkling evolution in the last iteration step can be discarded.

[2]The wrinkling direction coincides with the direction of the minimal principal stress.

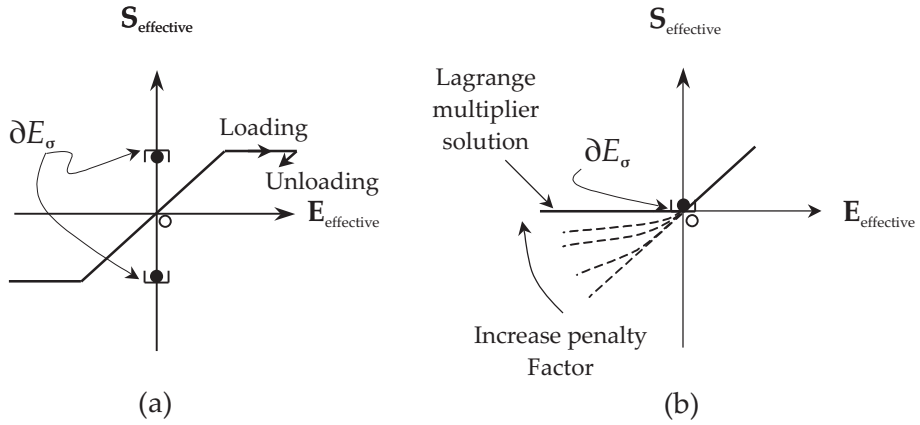

Figure 3.7: Comparison of the perfect plastic process and wrinkling.

3.3 Material modification by the projection method

In [JWB08b], Jarasjarungkiat *et al.* presented a simplified MM-based wrinkling model. Although the model is simple and readily implemented, it inherits a convergence problem due to a lack of consistent linearization on the constitutive tensor. Their further work [JWB09a] a wrinkling model based on an analogy between wrinkling and perfect plasticity, which is also provided in the next section 3.4, circumvents the convergence problems encountered in [JWB08b] because the model is consistently linearized. However, the employed return mapping algorithm (see [SH98]) is time-consuming. For these reasons, developments of an innovative wrinkling model should take into account both rate of convergence and computational time

Recently, Akita *et al*. [ANNP07] proposed a simple wrinkling model by the definition of a projection technique which maps the original constitutive matrix to a modified one which is used to determine the modified stress field within a wrinkled membrane. Based on [ANNP07, JWB08b, JWB09b], this section adopts the elastoplasticity concept with the aim at an innovative wrinkling model possesses a good balance between the rate of convergence and the computational effort by extending the work of [ANNP07] for both isotropic and orthotropic materials to compute the modified stress field within a wrinkled membrane. In contrast to [JWB08b], this model maintains the incremental terms caused by a consistent linearization, and as a consequence, a better rate of convergence is achieved. With an analogy to perfect plasticity, total strain within a wrinkled membrane is subdivided into an elastic part and a wrinkling part according to the additive strain decomposition technique. The projection model removes the wrinkling strain part, which has zero strain energy, from the total strain. As a consequence, the outcome is a modified constitutive tensor which represents only the energy of the elastic strain part. The potential of the proposed wrinkling model is verified via various numerical benchmarks in section 3.5. While the model combines a good rate of convergence with low computational cost, the implementation is simple.

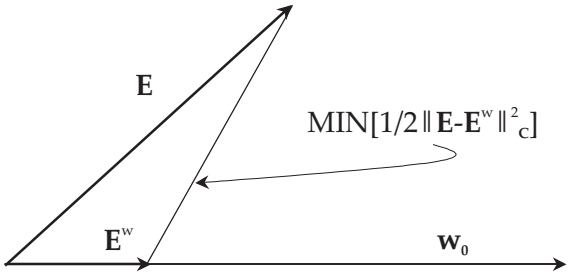

Figure 3.8: Illustration for the closest projection under the definition of the energy norm $\frac{1}{2}\left\|\mathbf{E}^e\right\|_{\mathbb{C}}^2$.

3.3.1 Definition of the projection tensor

To illustrate the concept of the projection method, the projection tensor will be introduced within this section. With eq. (3.11) and help from eq. (3.18), the modified stress field without prestress $\mathbf{S}_{pre} = \mathbf{0}$ is rewritten to

$$\begin{aligned}
\left\{\tilde{\mathbf{S}}\right\} &= [\mathbb{C}]\left\{\tilde{\mathbf{E}}\right\} = [\mathbb{C}]\left\{\mathbf{E}\right\} + \mu\,[\mathbb{C}]\,\mathbf{U}_2, \\
&= [\mathbb{C}]\left\{\mathbf{E}\right\} - [\mathbb{C}]\,\mathbf{U}_2\mathbf{U}_2^T\,[\mathbb{C}]\left\{\mathbf{E}\right\}/\mathbf{U}_2^T\,[\mathbb{C}]\,\mathbf{U}_2, \\
&= [\mathbb{C}]\left(\left\{\mathbf{E}\right\} - \mathbf{U}_2\mathbf{U}_2^T\,[\mathbb{C}]\left\{\mathbf{E}\right\}/\mathbf{U}_2^T\,[\mathbb{C}]\,\mathbf{U}_2\right), \\
&= [\mathbb{C}]\left\{\mathbf{E} - \mathbf{E}^w\right\} = [\mathbb{C}]\left\{\mathbf{E}^e\right\}, \\
&= [\mathbb{C}]\left(\mathbf{I} - \mathbf{U}_2\mathbf{U}_2^T\,[\mathbb{C}]/\mathbf{U}_2^T\,[\mathbb{C}]\,\mathbf{U}_2\right)\left\{\mathbf{E}\right\} = [\mathbb{C}]\,\mathbf{P}\left\{\mathbf{E}\right\},
\end{aligned} \tag{3.31}$$

where $\mathbf{E}$, $\mathbf{E}^w$ and $\mathbf{E}^e$ are the total strain, the wrinkling strain and the elastic strain, respectively, whereas $\mathbf{P}$ stands for the projection tensor that projects the total strain on to the elastic strain space. Remarkably, one observes a close relationship between the modified constitutive tensor via the projection tensor in eq. (3.31) and the continuum elasto-plastic adopted wrinkling constitutive tensor $[\mathbb{C}^{epw}]$ in eq. (3.29). Then, energy norm of the elastic strain part is introduced by

$$\frac{1}{2}\left\|\mathbf{E}^e\right\|_{\mathbb{C}}^2 = \frac{1}{2}\left\{\mathbf{E}^e\right\}^T[\mathbb{C}]\left\{\mathbf{E}^e\right\} = \frac{1}{2}\left\{\mathbf{E} - \mathbf{E}^w\right\}^T[\mathbb{C}]\left\{\mathbf{E} - \mathbf{E}^w\right\} \tag{3.32}$$

The actual elastic strain $\mathbf{E}^e$ is interpreted as the solution of the minimization of strain energy:

$$\mathbf{E}^e = \mathrm{ARG}\left\{\mathrm{MIN}\left[\frac{1}{2}\left\|\mathbf{E}^e\right\|_{\mathbb{C}}^2\right]\right\} = \mathrm{ARG}\left\{\mathrm{MIN}\left[\frac{1}{2}\left\{\mathbf{E} - \mathbf{E}^w\right\}^T[\mathbb{C}]\left\{\mathbf{E} - \mathbf{E}^w\right\}\right]\right\} \tag{3.33}$$

where the constitutive tensor $\mathbb{C} = 4\partial^2\Psi\left(\mathbf{C}\right)/\partial\mathbf{C}\partial\mathbf{C}$, which is defined by the second order partial derivative of the elastic potential Ψ with respect to the right Cauchy-Green tensor $\mathbf{C}$, is assumed to be constant and positive definite. The energy norm of the elastic strain $\frac{1}{2}\left\|\mathbf{E}^e\right\|_{\mathbb{C}}^2$ in eq. (3.32) is geometrically interpreted as the closest projection of the total strain $\mathbf{E}$ on to the direction of the wrinkling strain $\mathbf{E}^w$ along the definition of $\left\|\circ\right\|_{\mathbb{C}}^2$ (see Figure 3.8). For this reason, the solution $\mathbf{E}^e$ has to fulfill the minimal energy norm $\frac{1}{2}\left\|\mathbf{E}^e\right\|_{\mathbb{C}}^2$ for a wrinkled membrane. Table 3.3 illustrates the flowchart for the projection method wrinkling model.

Table 3.3: Flowchart for the projection method wrinkling model.

Initialize: set initial equilibrium iteration number $(i_n = i_0 = 0)$		
Loop over equilibrium iteration $(i_n = i_n + 1)$		
From nominal total strain $\{\mathbf{E}\}$ and nominal constitutive tensor $[\mathbb{C}]$, determine stress $\{\mathbf{S}\}$		
Find principal stress $\left(S^{max}, S^{min}\right)$ and principal strain (E_{max}, E_{min})		
Evaluate the state of membrane via the wrinkling criteria in table 3.2		
TAUT no modification $[\mathbb{C}_{mod}] = [\mathbb{C}]$	SLACK $[\mathbb{C}_{mod}] = \varpi\,[\mathbb{C}]\,;\ \varpi \to 0$	WRINKLED find wrinkling direction via (3.19) setup transformation matrix via (3.5) $[\mathbb{C}_{mod}] = \left[^{\Delta}\mathbb{C}\right]$ from (3.60)
$\Leftarrow$ RETURN $[\mathbb{C}_{mod}]$		

3.3.2 Derivation of the modified stress field

Because in reality compressive stress of a membrane is not absolute zero, thus, it is reasonable to prescribe an allowable compressive stress S_{alw} within the membrane. Thus, eq. (3.17) can be modified to

$$\geq \tilde{S}_2 = \mathbf{U}_2^T\left\{\tilde{\mathbf{S}}\right\} = S_{alw} \quad \tilde{S}_3 = \mathbf{U}_3^T\left\{\tilde{\mathbf{S}}\right\} = 0 \tag{3.34}$$

Eq. $(3.34)_2$ is interpretable as a projection of the modified PK2 stress $\tilde{\mathbf{S}}$ with the help of the transformation vector $\mathbf{U}_2$ towards the wrinkling direction $\mathbf{w}_0$ (see Figure 3.5). For isotropic material, this argument is valid as well for the projection of the nominal stress tensor onto the wrinkling direction. By decomposing the fictitious stress into an elastic part and a prestress as described in eq. (3.3), eqs. (3.18) and (3.19) can be rewritten to

$$\mu = S_{alw} - \mathbf{U}_2^T\left(\left[\mathbb{C}\right]\{\mathbf{E}\} + \left\{\mathbf{S}_{pre}\right\}\right)/\mathbf{U}_2^T\left[\mathbb{C}\right]\mathbf{U}_2, \tag{3.35}$$

$$\mathbf{U}_2^T\left[\mathbb{C}\right]\mathbf{U}_2\left(\mathbf{U}_3^T\left(\left[\mathbb{C}\right]\{\mathbf{E}\} + \left\{\mathbf{S}_{pre}\right\}\right)\right) + \mathbf{U}_3^T\left[\mathbb{C}\right]\mathbf{U}_2\left(S_{alw} - \mathbf{U}_2^T\left(\left[\mathbb{C}\right]\{\mathbf{E}\} + \left\{\mathbf{S}_{pre}\right\}\right)\right) = 0 \tag{3.36}$$

In case that S_{alw} vanishes, eq. (3.19) is recovered. Alternatively, when the allowable compressive stress concept is used, a small amount of compressive stiffness can be allowed via a penalty parameter ρ. By an extension of the modified deformation gradient approach, the state of uniaxial tension on the wrinkling axes $(\mathbf{t}_0,\ \mathbf{w}_0)$ according to eq. (3.34) is redefined to

$$\begin{aligned} &\tilde{S}_2 = \mathbf{U}_2^T\left\{\tilde{\mathbf{S}}\right\} = S_{alw} = \rho\mathbf{U}_2^T\left[\mathbb{C}\right]\{\mathbf{E}\} \quad \Rightarrow \quad \rho = S_{alw}/\mathbf{U}_2^T\left[\mathbb{C}\right]\{\mathbf{E}\} \\ &\tilde{S}_3 = \mathbf{U}_3^T\left\{\tilde{\mathbf{S}}\right\} = 0 \end{aligned} \tag{3.37}$$

Similar to eqs. (3.35) and (3.36), one obtains

$$\mu = -\frac{(1-\rho)\,\mathbf{U}_2^T\left[\mathbb{C}\right]\{\mathbf{E}\} + \mathbf{U}_2^T\left\{\mathbf{S}_{pre}\right\}}{\mathbf{U}_2^T\left[\mathbb{C}\right]\mathbf{U}_2}, \tag{3.38}$$

$$\mathbf{U}_2^T\left[\mathbb{C}\right]\mathbf{U}_2\left(\mathbf{U}_3^T\left(\left[\mathbb{C}\right]\{\mathbf{E}\} + \left\{\mathbf{S}_{pre}\right\}\right)\right) = \mathbf{U}_3^T\left[\mathbb{C}\right]\mathbf{U}_2\left((1-\rho)\,\mathbf{U}_2^T\left[\mathbb{C}\right]\{\mathbf{E}\} + \mathbf{U}_2^T\left\{\mathbf{S}_{pre}\right\}\right) \tag{3.39}$$

By substituting eq. (3.38) in eq. (3.11), the modified PK2 stress tensor in presence of wrinkles is obtained by

$$
\begin{aligned}
\left\{\tilde{\mathbf{S}}\right\} &= [\mathbb{C}]\left\{\tilde{\mathbf{E}}\right\} + \left\{\mathbf{S}_{pre}\right\} = [\mathbb{C}]\left(\{\mathbf{E}\} + \mu\mathbf{U}_2\right) + \left\{\mathbf{S}_{pre}\right\}, \\
&= [\mathbb{C}]\left(\{\mathbf{E}\} - \frac{\left((1-\rho)\,\mathbf{U}_2^T\,[\mathbb{C}]\,\{\mathbf{E}\} + \mathbf{U}_2^T\left\{\mathbf{S}_{pre}\right\}\right)\mathbf{U}_2}{\mathbf{U}_2^T\,[\mathbb{C}]\,\mathbf{U}_2}\right) + \left\{\mathbf{S}_{pre}\right\}, \\
&= [\mathbb{C}]\left(\left(\mathbf{I} - \frac{(1-\rho)\,\mathbf{U}_2\mathbf{U}_2^T\,[\mathbb{C}]}{\mathbf{U}_2^T\,[\mathbb{C}]\,\mathbf{U}_2}\right)\{\mathbf{E}\} - \frac{\mathbf{U}_2\mathbf{U}_2^T\left\{\mathbf{S}_{pre}\right\}}{\mathbf{U}_2^T\,[\mathbb{C}]\,\mathbf{U}_2}\right) + \left\{\mathbf{S}_{pre}\right\}, \\
&= [\mathbb{C}]\left(\left(\mathbf{I} - \frac{\mathbf{U}_2\mathbf{U}_2^T\,[\mathbb{C}]}{\mathbf{U}_2^T\,[\mathbb{C}]\,\mathbf{U}_2}\right)\{\mathbf{E}\} + \frac{\rho\mathbf{U}_2\mathbf{U}_2^T\,[\mathbb{C}]}{\mathbf{U}_2^T\,[\mathbb{C}]\,\mathbf{U}_2}\{\mathbf{E}\} - \frac{\mathbf{U}_2\mathbf{U}_2^T\left\{\mathbf{S}_{pre}\right\}}{\mathbf{U}_2^T\,[\mathbb{C}]\,\mathbf{U}_2}\right) + \left\{\mathbf{S}_{pre}\right\}, \\
&= [\mathbb{C}]\left(\underbrace{\left(\mathbf{I} - \frac{\mathbf{U}_2\mathbf{U}_2^T\,[\mathbb{C}]}{\mathbf{U}_2^T\,[\mathbb{C}]\,\mathbf{U}_2}\right)}_{\mathbf{P}}\{\mathbf{E}\} + \underbrace{\frac{S_{alw}\mathbf{U}_2}{\mathbf{U}_2^T\,[\mathbb{C}]\,\mathbf{U}_2}}_{\mathbf{M}} - \underbrace{\frac{\mathbf{U}_2\mathbf{U}_2^T\left\{\mathbf{S}_{pre}\right\}}{\mathbf{U}_2^T\,[\mathbb{C}]\,\mathbf{U}_2}}_{\mathbf{O}}\right) + \left\{\mathbf{S}_{pre}\right\}, \\
&= [\mathbb{C}]\left\{\mathbf{P}\,\{\mathbf{E}\} + \mathbf{M} - \mathbf{O}\right\} + \left\{\mathbf{S}_{pre}\right\}.
\end{aligned}
\tag{3.40}
$$

Here, $\mathbf{P}$ is the projection tensor that projects a nominal GL strain tensor $\mathbf{E}$ onto a modified one in presence of wrinkles, but this tensor deals only with the hypoelastoplastic part as described in section 3.3.1 which considers only the pure elastic stress field. The tensor $\mathbf{M}$ is related to the prescribed allowable compressive stress S_{alw} whereas $\mathbf{O}$ is the compensation tensor for the influence of prestress on the wrinkling direction.

An alternative of eq. (3.40) can be explained by the definition of a modified constitutive tensor $\boldsymbol{\Xi}$. For this purpose, we define an additional equation:

$$
\gamma\mathbf{U}_2^T\,[\mathbb{C}]\,\{\mathbf{E}\} = \mathbf{U}_2^T\left\{\mathbf{S}_{pre}\right\} \tag{3.41}
$$

where γ stands for a reduction factor which is used to compensate the prestress S_{pre} within the membrane. Thus, eq. $(3.40)_4$ can be rewritten as:

$$
\begin{aligned}
\left\{\tilde{\mathbf{S}}\right\} &= [\mathbb{C}]\left\{\tilde{\mathbf{E}}\right\} + \left\{\mathbf{S}_{pre}\right\}, \\
&= [\mathbb{C}]\left(\left(\mathbf{I} - \frac{\mathbf{U}_2\mathbf{U}_2^T\,[\mathbb{C}]}{\mathbf{U}_2^T\,[\mathbb{C}]\,\mathbf{U}_2}\right)\{\mathbf{E}\} + \frac{\rho\mathbf{U}_2\mathbf{U}_2^T\,[\mathbb{C}]}{\mathbf{U}_2^T\,[\mathbb{C}]\,\mathbf{U}_2}\{\mathbf{E}\} - \frac{\gamma\mathbf{U}_2\mathbf{U}_2^T\,[\mathbb{C}]\,\{\mathbf{E}\}}{\mathbf{U}_2^T\,[\mathbb{C}]\,\mathbf{U}_2}\right) + \left\{\mathbf{S}_{pre}\right\}, \\
&= [\mathbb{C}]\left(\left(\mathbf{I} - \frac{(1-\rho+\gamma)\,\mathbf{U}_2\mathbf{U}_2^T\,[\mathbb{C}]}{\mathbf{U}_2^T\,[\mathbb{C}]\,\mathbf{U}_2}\right)\right)\{\mathbf{E}\} + \left\{\mathbf{S}_{pre}\right\}, \\
&= [\mathbb{C}]\left(\left(\mathbf{I} - j\frac{\mathbf{U}_2\mathbf{U}_2^T\,[\mathbb{C}]}{\mathbf{U}_2^T\,[\mathbb{C}]\,\mathbf{U}_2}\right)\right)\{\mathbf{E}\} + \left\{\mathbf{S}_{pre}\right\}, \\
&= [\mathbb{C}]\underbrace{(\mathbf{I} - \mathbf{H})}_{\boldsymbol{\Phi}}\{\mathbf{E}\} + \left\{\mathbf{S}_{pre}\right\}, \\
&= [\mathbb{C}]\,\boldsymbol{\Phi}\,\{\mathbf{E}\} + \left\{\mathbf{S}_{pre}\right\} = \boldsymbol{\Xi}\,\{\mathbf{E}\} + \left\{\mathbf{S}_{pre}\right\}.
\end{aligned}
\tag{3.42}
$$

After some arrangement, a scalar factor j is the modification factor whose magnitude is adjustable between 0 and 1. This value corresponds to the degree of modification for the constitutive tensor in such a way that the original constitutive tensor is recovered when j

disappears. In contrary, as the magnitude of j is tuned up, a modified constitutive tensor (see Figure 3.7b) emerges with the recovery of eq. (3.31) when j reaches unity. Here $\mathbf{\Phi}$ is the projection tensor that projects a nominal GL strain tensor $\mathbf{E}$ onto a modified one $\tilde{\mathbf{E}}$ with the presence of wrinkles. This modified strain includes both influences of the prescribed allowable compressive stress with factor ρ and the reduction factor γ, which accounts for the effects of prestress, on the wrinkling direction. $\mathbf{\Xi}$ stands for a modified constitutive tensor which maps a nominal GL strain tensor $\mathbf{E}$ onto a modified PK2 stress field with regard to wrinkles. In the appendix A.1, symmetry and positive semi-definiteness properties of $\mathbf{\Xi}$ are proven.

3.3.3 Incremental form of the constitutive equation

Before proceeding further, geometrical explanations of eq. (3.5) should be discussed. According to Figures 3.2, 3.4 and 3.5, the PK2 stress on the wrinkling axes $(\mathbf{t}_0, \mathbf{w}_0)$ in the reference configuration can be described by

$$\{\mathbf{S}\} = \mathbf{T}^{-1}\left\{\hat{\mathbf{S}}\right\} = \hat{S}^1\mathbf{n}_1 + \hat{S}^2\mathbf{n}_2 + \underbrace{\hat{S}^3\mathbf{n}_3}_{0} \tag{3.43}$$

where $\mathbf{n}_1$, $\mathbf{n}_2$ are the transformation vectors mentioned in eq. (3.5) which map the strain $\{\mathbf{E}\}$ in an arbitrary Cartesian basis to the component $\hat{E}^1, \hat{E}^2$ of the strain $\left\{\hat{\mathbf{E}}\right\}$ in the rotated basis, i.e. the wrinkling axes $(\mathbf{t}_0, \mathbf{w}_0)$, respectively. Obviously, on the wrinkling axes $(\mathbf{t}_0, \mathbf{w}_0)$ the shear stress $\hat{S}^3$ in eq. (3.43) vanishes. Furthermore, the cross product of these two vectors is a bi-orthogonal vector, which points out of the plane of the undeformed configuration in Figure 3.5. This vector is interpreted as the transformation vector towards the shear stress of the wrinkling axis $(\mathbf{t}_0, \mathbf{w}_0)$.

$$\mathbf{U}_3 = \mathbf{n}_1 \times \mathbf{n}_2 \tag{3.44}$$

From eq. (3.5), the rate from of $\mathbf{U}_2$ can be written by

$$\dot{\mathbf{U}}_2 = \frac{\partial \mathbf{U}_2}{\partial \theta}\dot{\theta} = -2\mathbf{U}_3\dot{\theta} \tag{3.45}$$

A close look shows that eq. $(3.34)_2$ is automatically satisfied in the wrinkling direction. This argument can be proven readily by the convergence of the wrinkling direction searching algorithm of eqs. (3.17)-(3.19)which can be interpreted as the vanishing of the projected modified stress in eq. $(3.37)_2$ onto the axis of shear stress in the wrinkling axis $(\mathbf{t}_0, \mathbf{w}_0)$. This condition as seen in eq. $(3.34)_2$ is chosen as an auxiliary function f. By performing time derivative of eq. $(3.34)_2$, one obtains

$$\dot{\overline{\mathbf{U}_3^T\left\{\widetilde{\mathbf{S}}\right\}}} = \dot{\overline{\mathbf{U}_3^T\left([\mathbb{C}]\left\{\widetilde{\mathbf{E}}\right\} + \{\mathbf{S}_{pre}\}\right)}} = 0 = \dot{f}\left(\theta, \{\mathbf{E}\}\right) = \frac{\partial f}{\partial \theta}\dot{\theta} + \frac{\partial f}{\partial \{\mathbf{E}\}}\{\dot{\mathbf{E}}\} \tag{3.46}$$

From eq. (3.46), the rate from of θ is obtained by

$$\dot{\theta} = -\left(\frac{\partial f}{\partial \{\mathbf{E}\}} \Big/ \frac{\partial f}{\partial \theta}\right)\{\dot{\mathbf{E}}\} = -\left(\frac{\mathbf{U}_3^T[\mathbb{C}]\,\mathbf{P}}{\mathbf{U}_{3,\theta}^T\left\{\widetilde{\mathbf{S}}\right\} + \mathbf{U}_3^T\left\{\widetilde{\mathbf{S}}\right\}_{,\theta}}\right)\{\dot{\mathbf{E}}\},$$
$$= \left(\frac{\mathbf{U}_3^T[\mathbb{C}]\,\mathbf{P}}{(\mathbf{U}_1-\mathbf{U}_2)^T\left\{\widetilde{\mathbf{S}}\right\} - \mathbf{U}_3^T\left\{\widetilde{\mathbf{S}}\right\}_{,\theta}}\right)\{\dot{\mathbf{E}}\} \tag{3.47}$$

where $\left\{\tilde{\mathbf{S}}\right\}$ is determined by eq. (3.40) with the help from eq. (3.38). Moreover, the denominators are defined in eq. (3.48) with the help of eq. (3.49) by

$$\left\{\tilde{\mathbf{S}}\right\}_{,\theta} = \left([\mathbb{C}]\left\{\tilde{\mathbf{E}}\right\} + \left\{\mathbf{S}_{pre}\right\}\right)_{,\theta} = [\mathbb{C}]\left(\mu_{,\theta}\mathbf{U}_2 + \mu\mathbf{U}_{2,\theta}\right) = [\mathbb{C}]\left(\mu_{,\theta}\mathbf{U}_2 - 2\mu\mathbf{U}_3\right), \tag{3.48}$$

$$\mu_{,\theta} = \frac{\left(2\mathbf{U}_2^T[\mathbb{C}]\,\mathbf{U}_2\mathbf{U}_3^T\left([\mathbb{C}]\{\mathbf{E}\} + \{\mathbf{S}_{pre}\}\right) - \mu\mathbf{U}_2^T[\mathbb{C}]\,\mathbf{U}_2\left(\mathbf{U}_2^T[\mathbb{C}]\,\mathbf{U}_2\right)_{,\theta}\right)}{\left(\mathbf{U}_2^T[\mathbb{C}]\,\mathbf{U}_2\right)^2},$$
$$= \frac{2\left(\mathbf{U}_3^T\left([\mathbb{C}]\{\mathbf{E}\} + \{\mathbf{S}_{pre}\}\right) + \mu\left(\mathbf{U}_3^T[\mathbb{C}]\,\mathbf{U}_2 + \mathbf{U}_2^T[\mathbb{C}]\,\mathbf{U}_3\right)\right)}{\mathbf{U}_2^T[\mathbb{C}]\,\mathbf{U}_2} \tag{3.49}$$

The incremental form of the constitutive equation is obtained by performing a time derivative of eq. (3.40) as in the following

$$\dot{\left\{\tilde{\mathbf{S}}\right\}} = [\mathbb{C}]\left\{\dot{\mathbf{P}}\{\mathbf{E}\} + \mathbf{P}\{\dot{\mathbf{E}}\} + \dot{\mathbf{M}} - \dot{\mathbf{O}}\right\} + \underbrace{\{\dot{\mathbf{S}}_{pre}\}}_{0} \tag{3.50}$$

where the time derivative of constant prestress $\mathbf{S}_{pre}$ vanishes. The time derivative of the projection tensor $\mathbf{P}$ is explained by:

$$\dot{\mathbf{P}} = -\overline{\left(\frac{\mathbf{U}_2\mathbf{U}_2^T[\mathbb{C}]}{\mathbf{U}_2^T[\mathbb{C}]\,\mathbf{U}_2}\right)^{\cdot}} = -\left(\frac{\mathbf{U}_2^T[\mathbb{C}]\,\mathbf{U}_2\left(\overline{\mathbf{U}_2\mathbf{U}_2^T[\mathbb{C}]}\right)^{\cdot} - \mathbf{U}_2\mathbf{U}_2^T[\mathbb{C}]\left(\overline{\mathbf{U}_2^T[\mathbb{C}]\,\mathbf{U}_2}\right)^{\cdot}}{\left(\mathbf{U}_2^T[\mathbb{C}]\,\mathbf{U}_2\right)^2}\right). \tag{3.51}$$

For the sake of brevity, the first and second terms in eq. (3.51) are expanded with the help of eq. (3.45) to

$$\overline{\mathbf{U}_2\mathbf{U}_2^T[\mathbb{C}]}^{\cdot} = \dot{\mathbf{U}}_2\mathbf{U}_2^T[\mathbb{C}] + \mathbf{U}_2\dot{\mathbf{U}}_2^T[\mathbb{C}],$$
$$= -2\left(\mathbf{U}_3\mathbf{U}_2^T[\mathbb{C}] + \mathbf{U}_2\mathbf{U}_3^T[\mathbb{C}]\right)\dot{\theta},$$
$$= -2\left(\mathbf{U}_3\mathbf{U}_2^T[\mathbb{C}] + \mathbf{U}_2\mathbf{U}_3^T[\mathbb{C}]\right)\left(\frac{\mathbf{U}_3^T[\mathbb{C}]\,\mathbf{P}}{(\mathbf{U}_1-\mathbf{U}_2)^T\left\{\widetilde{\mathbf{S}}\right\} - \mathbf{U}_3^T\left\{\widetilde{\mathbf{S}}\right\}_{,\theta}}\right)\{\dot{\mathbf{E}}\}, \tag{3.52}$$

$$\overline{\mathbf{U}_2^T[\mathbb{C}]\,\mathbf{U}_2}^{\cdot} = \dot{\mathbf{U}}_2^T[\mathbb{C}]\,\mathbf{U}_2 + \mathbf{U}_2^T[\mathbb{C}]\,\dot{\mathbf{U}}_2,$$
$$= -2\left(\mathbf{U}_3^T[\mathbb{C}]\,\mathbf{U}_2 + \mathbf{U}_2^T[\mathbb{C}]\,\mathbf{U}_3\right)\dot{\theta},$$
$$= -2\left(\mathbf{U}_3^T[\mathbb{C}]\,\mathbf{U}_2 + \mathbf{U}_2^T[\mathbb{C}]\,\mathbf{U}_3\right)\left(\frac{\mathbf{U}_3^T[\mathbb{C}]\,\mathbf{P}}{(\mathbf{U}_1-\mathbf{U}_2)^T\left\{\widetilde{\mathbf{S}}\right\} - \mathbf{U}_3^T\left\{\widetilde{\mathbf{S}}\right\}_{,\theta}}\right)\{\dot{\mathbf{E}}\}. \tag{3.53}$$

Therefore, eq. (3.51) can be rewritten by

$$\dot{\mathbf{P}} = \frac{2\left(\mathbf{U}_2^T[\mathbb{C}]\mathbf{U}_2\left(\mathbf{U}_3\mathbf{U}_2^T[\mathbb{C}] + \mathbf{U}_2\mathbf{U}_3^T[\mathbb{C}]\right) - \mathbf{U}_2\mathbf{U}_2^T[\mathbb{C}]\left(\mathbf{U}_3^T[\mathbb{C}]\mathbf{U}_2 + \mathbf{U}_2^T[\mathbb{C}]\mathbf{U}_3\right)\right)\dot{\theta}}{\left(\mathbf{U}_2^T[\mathbb{C}]\mathbf{U}_2\right)^2} \tag{3.54}$$

Multiplying eq. (3.54) with $\mathbf{E}$ yields:

$$\begin{aligned}\dot{\mathbf{P}}\{\mathbf{E}\} &= \frac{2}{\kappa}\begin{pmatrix}\left(\mathbf{U}_3\mathbf{U}_3^T[\mathbb{C}]\mathbf{P}\right)\left(\mathbf{U}_2^T[\mathbb{C}]\mathbf{U}_2\right)\mathbf{U}_2^T[\mathbb{C}]\{\mathbf{E}\} + \left(\mathbf{U}_2\mathbf{U}_3^T[\mathbb{C}]\mathbf{P}\right)\cdot \\ \left(\mathbf{U}_2^T[\mathbb{C}]\mathbf{U}_2\mathbf{U}_3^T[\mathbb{C}]\{\mathbf{E}\} - \mathbf{U}_2^T[\mathbb{C}]\{\mathbf{E}\}\left(\mathbf{U}_3^T[\mathbb{C}]\mathbf{U}_2 + \mathbf{U}_2^T[\mathbb{C}]\mathbf{U}_3\right)\right)\end{pmatrix}\{\dot{\mathbf{E}}\} \\ &= \mathbf{R}_1\{\dot{\mathbf{E}}\}\end{aligned} \tag{3.55}$$

where $\kappa = \left(\mathbf{U}_2^T[\mathbb{C}]\mathbf{U}_2\right)^2\left(\left(\mathbf{U}_1-\mathbf{U}_2\right)^T\left\{\widetilde{\mathbf{S}}\right\} - \mathbf{U}_3^T\left\{\widetilde{\mathbf{S}}\right\}_{,\theta}\right)$. From the first two terms of eq. (3.50), one obtains

$$\dot{\mathbf{P}}\{\mathbf{E}\} + \mathbf{P}\{\dot{\mathbf{E}}\} = \left(\mathbf{P}+\mathbf{R}_1\right)\{\dot{\mathbf{E}}\}. \tag{3.56}$$

From eqs. (3.40), (3.53), the third term of eq. (3.50) is expandable as

$$\begin{aligned}\dot{\mathbf{M}} &= S_{alw}\frac{\mathbf{U}_2^T[\mathbb{C}]\mathbf{U}_2\dot{\mathbf{U}}_2 - \mathbf{U}_2\dot{\overline{\left(\mathbf{U}_2^T[\mathbb{C}]\mathbf{U}_2\right)}}}{\left(\mathbf{U}_2^T[\mathbb{C}]\mathbf{U}_2\right)^2} \\ &= \frac{2}{\kappa}\begin{pmatrix}\left(\mathbf{U}_3\mathbf{U}_3^T[\mathbb{C}]\mathbf{P}\right)\left(\mathbf{U}_2^T[\mathbb{C}]\mathbf{U}_2\right)\left(-S_{alw}\right) \\ +\left(\mathbf{U}_2\mathbf{U}_3^T[\mathbb{C}]\mathbf{P}\right)\left(\mathbf{U}_3^T[\mathbb{C}]\mathbf{U}_2 + \mathbf{U}_2^T[\mathbb{C}]\mathbf{U}_3\right)S_{alw}\end{pmatrix}\{\dot{\mathbf{E}}\} \\ &= \mathbf{R}_2\{\dot{\mathbf{E}}\}\end{aligned} \tag{3.57}$$

From eqs. (3.40), (3.52) and (3.53), the fourth term of eq. (3.50) can be described by

$$\begin{aligned}\dot{\mathbf{O}} &= \frac{\mathbf{U}_2^T[\mathbb{C}]\mathbf{U}_2\dot{\overline{\mathbf{U}_2\mathbf{U}_2^T\{\mathbf{S}_{pre}\}}} - \mathbf{U}_2\mathbf{U}_2^T\{\mathbf{S}_{pre}\}\dot{\overline{\left(\mathbf{U}_2^T[\mathbb{C}]\mathbf{U}_2\right)}}}{\left(\mathbf{U}_2^T[\mathbb{C}]\mathbf{U}_2\right)^2}, \\ &= \frac{2}{\kappa}\begin{pmatrix}\left(\mathbf{U}_3\mathbf{U}_3^T[\mathbb{C}]\mathbf{P}\right)\left(\mathbf{U}_2^T[\mathbb{C}]\mathbf{U}_2\right)\left(-\mathbf{U}_2^T\{\mathbf{S}_{pre}\}\right) + \left(\mathbf{U}_2\mathbf{U}_3^T[\mathbb{C}]\mathbf{P}\right)\cdot \\ \left(-\mathbf{U}_2^T\{\mathbf{S}_{pre}\}\mathbf{U}_2^T[\mathbb{C}]\mathbf{U}_2 + \left(\mathbf{U}_3^T[\mathbb{C}]\mathbf{U}_2 + \mathbf{U}_2^T[\mathbb{C}]\mathbf{U}_3\right)\mathbf{U}_2^T\{\mathbf{S}_{pre}\}\right)\end{pmatrix}\{\dot{\mathbf{E}}\}, \\ &= \mathbf{R}_3\{\dot{\mathbf{E}}\}.\end{aligned} \tag{3.58}$$

From eq. (3.50) with the help of eqs. (3.56)-(3.58), one obtains

$$\begin{aligned}\dot{\widetilde{\mathbf{S}}} &= [\mathbb{C}]\{\dot{\mathbf{P}}\{\mathbf{E}\} + \mathbf{P}\{\dot{\mathbf{E}}\} + \dot{\mathbf{M}} - \dot{\mathbf{O}}\} + \underbrace{\{\dot{\mathbf{S}}_{pre}\}}_{0}, \\ &= [\mathbb{C}]\{\mathbf{P}+\mathbf{R}_1+\mathbf{R}_2+\mathbf{R}_3\}\{\dot{\mathbf{E}}\} = [\mathbb{C}]\boldsymbol{\Theta}\{\dot{\mathbf{E}}\} = \left[{}^{\Delta}\mathbb{C}\right]\{\dot{\mathbf{E}}\},\end{aligned} \tag{3.59}$$

where ${}^{\Delta}\mathbb{C}$ is the incremental constitutive tensor which will be employed in the elastic stiffness matrix in the context of FEM. This tensor maps an incremental strain tensor $\dot{\mathbf{E}}$ onto the relevant incremental stress tensor with regard to existing wrinkles. In an explicit form, ${}^{\Delta}\mathbb{C}$ can be written as

$$\begin{aligned}\left[{}^{\Delta}\mathbb{C}\right] &= [\mathbb{C}]\{\mathbf{P}+\mathbf{R}_1+\mathbf{R}_2+\mathbf{R}_3\} = [\mathbb{C}]\boldsymbol{\Theta}, \\ &= [\mathbb{C}]\left[\mathbf{P} + \frac{2}{\kappa}\begin{pmatrix}\left(\mathbf{U}_3\mathbf{U}_3^T[\mathbb{C}]\mathbf{P}\right)\mathbf{U}_2^T[\mathbb{C}]\mathbf{U}_2\left(\mathbf{U}_2^T[\mathbb{C}]\{\mathbf{E}\} - S_{alw} + \mathbf{U}_2^T\{\mathbf{S}_{pre}\}\right) \\ +\left(\mathbf{U}_2\mathbf{U}_3^T[\mathbb{C}]\mathbf{P}\right)\begin{pmatrix}\left(\mathbf{U}_3^T[\mathbb{C}]\mathbf{U}_2 + \mathbf{U}_2^T[\mathbb{C}]\mathbf{U}_3\right)\cdot \\ \left(-\mathbf{U}_2^T[\mathbb{C}]\{\mathbf{E}\} + S_{alw} - \mathbf{U}_2^T\{\mathbf{S}_{pre}\}\right) \\ +\mathbf{U}_2^T[\mathbb{C}]\mathbf{U}_2\left(\mathbf{U}_3^T\left([\mathbb{C}]\{\mathbf{E}\} + \{\mathbf{S}_{pre}\}\right)\right)\end{pmatrix}\end{pmatrix}\right].\end{aligned} \tag{3.60}$$

Eq. (3.60) is valid for both isotropic and orthotropic materials when the wrinkling direction $\mathbf{w}_0$ is available. Specifically, the vector $\mathbf{U}_2$ is coplanar and orthogonal to vector $\mathbf{U}_1$ which is the transformation vector of a stress towards the uniaxial tension direction as described in eq. (3.5) and Figure 3.4.

For an isotropic problem, this situation means that the first principal direction of the total stress field $\mathbf{S}_{el} + \mathbf{S}_{pre}$ coincides to that of the strain field as well as the wrinkling direction. As a result, the modified stress field in eq. (3.40) and the incremental constitutive tensor in eq. (3.60) are significatnly simplified. This is observable by looking at the term $\mathbf{U}_3^T \left([\mathbb{C}] \{\mathbf{E}\} + \{\mathbf{S}_{pre}\} \right)$ as the projection of the original stress field onto the shear stress direction of the wrinkling axes $(\mathbf{t}_0, \mathbf{w}_0)$ which in turn is, for the isotropic case, the principal strain as well as the principal stress direction. Undoubtedly, the shear stress on this direction disappears and so does the last line of eq. (3.60). Furthermore, the constitutive tensor for isotropic material is invariant. Thus its off-diagonal components in the third row and column vanish, so do $\left(\mathbf{U}_3^T [\mathbb{C}] \mathbf{U}_2 + \mathbf{U}_2^T [\mathbb{C}] \mathbf{U}_3 \right)$ in the second and third line of eq. (3.60). With the same reason as above, a close look at the first line of eq. (3.60) yields

$$\mathbf{U}_3 \mathbf{U}_3^T [\mathbb{C}] \mathbf{P} = \mathbf{U}_3 \mathbf{U}_3^T [\mathbb{C}] \left(\mathbf{I} - \frac{\mathbf{U}_2 \mathbf{U}_2^T [\mathbb{C}]}{\mathbf{U}_2^T [\mathbb{C}] \mathbf{U}_2} \right) = \mathbf{U}_3 \mathbf{U}_3^T [\mathbb{C}] \tag{3.61}$$

On this account, eq. (3.60) can be written for the isotropic case by

$$\left[{}^{\Delta}\mathbb{C} \right] = [\mathbb{C}] \left[\mathbf{P} + \frac{2}{\kappa} \left(\mathbf{U}_3 \mathbf{U}_3^T [\mathbb{C}] \right) \mathbf{U}_2^T [\mathbb{C}] \mathbf{U}_2 \left(\mathbf{U}_2^T [\mathbb{C}] \{\mathbf{E}\} - S_{alw} + \mathbf{U}_2^T \{\mathbf{S}_{pre}\} \right) \right]. \tag{3.62}$$

For a comparison purpose, the allowable compressive stress in a membrane and prestress are assumed to vanish, the modified stress field in eq. (3.40) and the wrinkling factor in eq. (3.35) are reduced to

$$\{\tilde{\mathbf{S}}\} = [\mathbb{C}] \mathbf{P} \{\mathbf{E}\}, \qquad \mu = \frac{-\mathbf{U}_2^T [\mathbb{C}] \{\mathbf{E}\}}{\mathbf{U}_2^T [\mathbb{C}] \mathbf{U}_2}. \tag{3.63}$$

For an isotropic material, vanishing of the projected nominal stress field onto the shear stress axis with regard to the wrinkling direction is chosen as an auxiliary function instead of eq. $(3.34)_2$ such that

$$f(\theta, \{\mathbf{E}\}) = \mathbf{U}_3^T \{\mathbf{S}\} = 0 \tag{3.64}$$

Thus, the rate form of eq. (3.64) leads to

$$\begin{aligned} \dot{f}(\theta, \{\mathbf{E}\}) = \dot{\overline{\mathbf{U}_3^T \{\mathbf{S}\}}} = 0 = \dot{\overline{\mathbf{U}_3^T [\mathbb{C}] \{\mathbf{E}\}}} = \frac{\partial f}{\partial \theta} \dot{\theta} + \frac{\partial f}{\partial \{\mathbf{E}\}} \{\dot{\mathbf{E}}\}, \\ \Rightarrow \dot{\theta} = - \left(\frac{\partial f}{\partial \{\mathbf{E}\}} \Big/ \frac{\partial f}{\partial \theta} \right) \{\dot{\mathbf{E}}\} = \left\{ \frac{\mathbf{U}_3^T [\mathbb{C}]}{(\mathbf{U}_1 - \mathbf{U}_2)^T [\mathbb{C}] \{\mathbf{E}\}} \right\} \{\dot{\mathbf{E}}\}. \end{aligned} \tag{3.65}$$

Thus κ in eq. (3.62) is changed to:

$$\kappa = \left(\mathbf{U}_2^T [\mathbb{C}] \mathbf{U}_2 \right)^2 (\mathbf{U}_1 - \mathbf{U}_2)^T [\mathbb{C}] \{\mathbf{E}\} \tag{3.66}$$

From eqs. (3.63)-(3.66), the incremental constitutive tensor in eq. (3.62) can be rewritten by

$$\begin{aligned}\left[{}^{\Delta}\mathbb{C}\right] &= [\mathbb{C}]\left(\mathbf{P} + \frac{2\left(\mathbf{U}_3\mathbf{U}_3^T[\mathbb{C}]\right)\mathbf{U}_2^T[\mathbb{C}]\{\mathbf{E}\}}{\mathbf{U}_2^T[\mathbb{C}]\mathbf{U}_2^T\left(\mathbf{U}_1-\mathbf{U}_2\right)^T[\mathbb{C}]\{\mathbf{E}\}}\right),\\ &= [\mathbb{C}]\mathbf{P} + \frac{2\mathbf{U}_2^T[\mathbb{C}]\{\mathbf{E}\}\left([\mathbb{C}]\mathbf{U}_3\mathbf{U}_3^T[\mathbb{C}]\right)}{\mathbf{U}_2^T[\mathbb{C}]\mathbf{U}_2^T\left(\mathbf{U}_1-\mathbf{U}_2\right)^T[\mathbb{C}]\{\mathbf{E}\}},\\ &= [\mathbb{C}]\mathbf{P} + \alpha[\mathbb{C}]\mathbf{U}_3\mathbf{U}_3^T[\mathbb{C}]. \end{aligned} \tag{3.67}$$

Eq. (3.67) is exactly equivalent to $\widetilde{\mathbb{C}}_{inc}$ which is mentioned in [ANNP07] for an isotropic material. With the help of eq. (3.5) the explicit form of eq. (3.67) is given by

$$\left[{}^{\Delta}\mathbb{C}\right] = [\mathbb{C}]\mathbf{P} + \frac{2(1+\nu)}{E}\left(\frac{\epsilon^I\nu+\epsilon^{II}}{\epsilon^I-\epsilon^{II}}\right)[\mathbb{C}]\mathbf{U}_3\mathbf{U}_3^T[\mathbb{C}] \tag{3.68}$$

where $\{\mathbf{E}\} = \epsilon^I\mathbf{U}_1 + \epsilon^{II}\mathbf{U}_2$; $\epsilon^I, \epsilon^{II}$ are the maximal and minimal principal strains respectively.

3.4 Material modification by the plasticity analogy

This section is intended to create a more robust wrinkling model for both isotropic and orthotropic materials. The wrinkling model in this section is motivated by the work of Ziegler *et al.* [Zie01, ZWB03] who proposed a MM-based wrinkling model by adopting the solution algorithm from the perfect plasticity where the equilibrium equation is augmented with constraints of no-compressive stresses and used the return mapping algorithm to determine solution which fulfills these constraints. The algorithm is consistently linearized; therefore, it holds the quadratic rate of convergence. In this model, vanishing of the compressive stress in the corresponding wrinkling direction is considered as an additional constraint on the governing equation. To assert an overview of necessary relations for later use, reviews for relevant theories of plasticity are given in following sections. For further reading, [BLM00, SH98] are recommended.

3.4.1 Rate-independent nonsmooth multisurface perfect plasticity and closest point projection algorithm

As mentioned in section 3.2.3, wrinkling is considered as a similar problem to the rate-independent perfect plasticity. If two constraints on the principal compressive stresses are defined, obviously, constraint surfaces intersect each other nonsmoothly. This situation leads to singular points or corners at the boundary of the "elastic" domain ∂E_σ (see Figure 3.9) where an iterative procedure plays a key role to determine the current active set of constraints. With the same assumption as in the section 3.3, this model is suitable only for a membrane deforming within the small elastic strain regime. Since, this so-called *plasticity analogy wrinkling model* just adopts the idea of computational inelasticity to get rid of emerging artificial compressive stresses, restrictions from the *actual* plasticity is relaxed in this model. To follow the conventional notation from *hypoelastic-plastic model* in [SH98], within

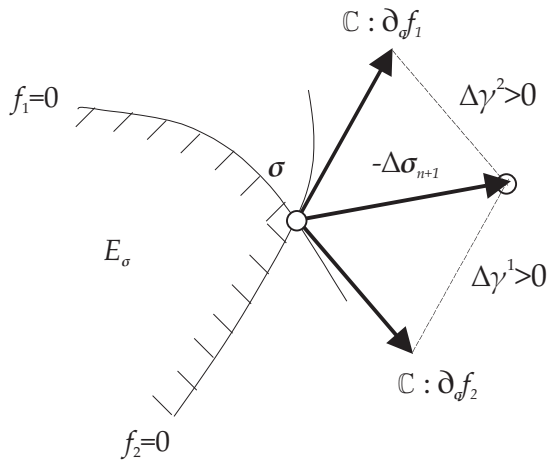

Figure 3.9: Geometric illustration at the intersection of two yield surfaces ($J_{act} = (1, 2)$) at the corner points $\sigma \in \partial E_\sigma$

.

this section, dummy symbols of stress measure and strain measure are designated by σ and ϵ, respectively. Thus, the actually used stress and strain measures are recovered just by a substitution.

Wrinkling is related to an elastic-plastic process as follows: Along the line of eq. (3.20), in the *hypoelastic-plastic model*, an additive decomposition of the strain tensor ϵ into an elastic part ϵ^e and a plastic part ϵ^p is assumed. Therefore, the wrinkling strain ϵ^w is used in place of a plastic strain ϵ^p in the rest of this subsection to illustrate how the algorithm for plasticity can be applied to wrinkling of a membrane. We consider a temporal discretization of the interval $[0, T] \subset \mathbb{R}$ of interest, and let ϵ_n, ϵ_n^w be the initial value of the total strain and wrinkling strain at $t_n \in [0, T]$. Given an incremental displacement field $\Delta\mathbf{u} : \Omega \to \mathbb{R}^3$ where $\Omega \subset \mathbb{R}^{n_{sd}}$ is the reference configuration of the body of interest and n_{sd} is the space dimension of the Euclidean space as mentioned in section 2.1.2. Applications of an implicit backward Euler scheme leads to the following evolution equations:

◇ Additive decomposition of a total strain tensor ϵ:

$$\epsilon = \epsilon^e + \epsilon^w. \tag{3.69}$$

◇ Elastic stress-strain relationship:

$$\sigma = \nabla\Psi\left(\epsilon^e\right) = \nabla\Psi\left(\epsilon - \epsilon^w\right); \quad \Psi \text{ stands for the elastic potential.} \tag{3.70}$$

◇ Associative flow rule:

$$\dot{\epsilon}^w = \sum_{\alpha=1}^{m} \gamma^\alpha \partial_\sigma f_\alpha\left(\sigma\right) \tag{3.71}$$

where γ^α is the sliprate and $f_\alpha\left(\sigma\right)$ are $m \geq 1$ constraint functions intersecting possibly nonsmoothly (see Figure 3.9).

◇ Yield, i.e. wrinkling, and loading/unloading conditions:

$$\begin{aligned} \gamma^{\alpha} f_{\alpha}(\boldsymbol{\sigma}) &= 0, \\ \gamma^{\alpha} \dot{f}_{\alpha}(\boldsymbol{\sigma}) &= 0, \\ \gamma^{\alpha} &\geq 0, \\ f_{\alpha}(\boldsymbol{\sigma}) &\leq 0. \end{aligned} \tag{3.72}$$

Eqs. (3.69)-(3.72) result in a nonlinear coupled system of equations for the unknown state variables $\boldsymbol{\epsilon}_{n+1}$, $\boldsymbol{\epsilon}^{w}_{n+1}$ at the time t_{n+1} :

$$\begin{aligned} \boldsymbol{\epsilon}_{n+1} &= \boldsymbol{\epsilon}_{n} + \nabla^{s}(\Delta \mathbf{u}), \\ \boldsymbol{\sigma}_{n+1} &= \nabla \Psi(\boldsymbol{\epsilon}_{n+1} - \boldsymbol{\epsilon}^{w}_{n+1}), \\ \boldsymbol{\epsilon}^{w}_{n+1} &= \boldsymbol{\epsilon}^{w}_{n} + \sum_{\alpha=1}^{m} \Delta\gamma^{\alpha} \partial_{\sigma} f_{\alpha}(\boldsymbol{\sigma}_{n+1}). \end{aligned} \tag{3.73}$$

Here, the *plastic, i.e. wrinkling, slip* is setup as $\Delta\gamma^{\alpha} := \Delta t \gamma^{\alpha}$. The discrete Kuhn Tucker condition takes the form

$$\begin{aligned} f_{\alpha}(\boldsymbol{\sigma}_{n+1}) &\leq 0, \\ \Delta\gamma^{\alpha} &\geq 0, \\ \Delta\gamma^{\alpha} f_{\alpha}(\boldsymbol{\sigma}_{n+1}) &= 0. \end{aligned} \tag{3.74}$$

A trial state is obtained by *freezing* plastic, i.e. wrinkling, flow in the interval $[t_n, t_{n+1}]$. Therefore, by setting $\Delta\gamma^{\alpha} = 0$ in eq. (3.74), one obtains

$$\begin{aligned} &\boldsymbol{\epsilon}^{w}_{n+1} := \boldsymbol{\epsilon}^{w}_{n} \quad \Rightarrow \quad \boldsymbol{\epsilon}^{e^{trial}}_{n+1} := \boldsymbol{\epsilon}_{n+1} - \boldsymbol{\epsilon}^{w}_{n}, \\ &\boldsymbol{\sigma}^{trial}_{n+1} := \nabla \Psi\left(\boldsymbol{\epsilon}^{e^{trial}}\right), \qquad f^{trial}_{\alpha,n+1}\left(\boldsymbol{\sigma}^{trial}_{n+1}\right) = f_{\alpha}\left(\boldsymbol{\sigma}^{trial}_{n+1}\right). \end{aligned} \tag{3.75}$$

The converged solution is characterized as the argument of the minimization problem

$$\boldsymbol{\sigma}_{n+1} = \mathrm{ARG}\left\{ \underset{\boldsymbol{\tau} \in E_{\sigma}}{\mathrm{MIN}} \left[\xi(\boldsymbol{\tau}) \right] \right\} \tag{3.76}$$

where $\xi(\boldsymbol{\tau})$ represents the energy norm of the projection from the trial state $\boldsymbol{\sigma}^{trial}_{n+1}$ onto the current stress $\boldsymbol{\sigma}^{(k)}_{n+1}$ (see Figure 3.10). For this reason, the solution $\boldsymbol{\sigma}_{n+1}$ has to fulfill the minimal energy norm $\xi(\boldsymbol{\tau})$, geometrically interpreted as the closest projection of the current stress $\boldsymbol{\sigma}^{(k)}_{n+1}$ from the trial one $\boldsymbol{\sigma}^{trial}_{n+1}$ as

$$\xi(\boldsymbol{\tau}) := \frac{1}{2} \left\| \boldsymbol{\sigma}^{trial}_{n+1} - \boldsymbol{\tau} \right\|^{2}_{\mathbb{C}^{-1}} = \frac{1}{2} \left[\boldsymbol{\sigma}^{trial}_{n+1} - \boldsymbol{\tau} \right] : \mathbb{C}^{-1} : \left[\boldsymbol{\sigma}^{trial}_{n+1} - \boldsymbol{\tau} \right], \tag{3.77}$$

where $\mathbb{C} := \boldsymbol{\nabla}^{2}\Psi$ is assumed to be constant and positive definite and $\boldsymbol{\tau}$ stands for the current stress $\boldsymbol{\sigma}^{(k)}_{n+1}$. Furthermore, the projection has to lay on one or more boundary surfaces of the *elastic domain* E_{σ}. This requirement is enforced by including the yield, i.e. wrinkling, surface as constraints on eq. (3.77). Hence, the Lagrangian functional is obtained by

$$L(\boldsymbol{\tau}, \gamma^{\alpha}) := \xi(\boldsymbol{\tau}) + \sum_{\alpha \in J_{act}} \Delta\gamma^{\alpha} f_{\alpha}(\boldsymbol{\tau}). \tag{3.78}$$

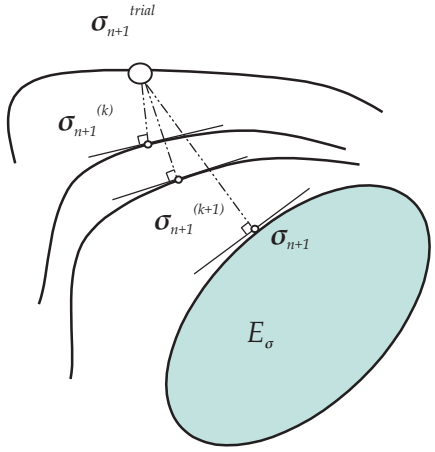

Figure 3.10: Geometric illustration for the closest point projection onto the yield surface.

where $J_{act} \subseteq \{1,\dots,m\}$ is the set of indices associated with the active constraints at the unknown solution σ_{n+1}; $J_{act} := \{\alpha \in \{1,\dots,m\} \,|f_\alpha(\sigma_{n+1}) > 0\}$. Then, by taking derivatives of eq. (3.78) with respect to $\sigma, \Delta\gamma^\alpha$ one obtains

$$\begin{aligned}
\partial_\sigma L &= \mathbb{C}^{-1} : \left[\sigma_{n+1}^{(k)} - \sigma_{n+1}^{trial}\right] + \sum_{\alpha\in J_{act}} \Delta\gamma^\alpha \partial_\sigma f_\alpha\left(\sigma_{n+1}^{(k)}\right) = 0,\\
\partial^2_{\sigma\sigma} L &= \mathbb{C}^{-1} + \sum_{\alpha\in J_{act}} \Delta\gamma^\alpha \partial^2_{\sigma\sigma} f_\alpha\left(\sigma_{n+1}^{(k)}\right) = 0,\\
\partial_{\Delta\gamma^\alpha} L &= f_\alpha\left(\sigma_{n+1}^{(k)}\right) = 0,\\
\partial^2_{\sigma\Delta\gamma^\alpha} L &= \partial^2_{\Delta\gamma^\alpha\sigma} L = \partial_\sigma f_\alpha\left(\sigma_{n+1}^{(k)}\right),\\
\partial^2_{\Delta\gamma^\alpha\Delta\gamma^\alpha} L &= 0.
\end{aligned} \tag{3.79}$$

With the discrete Kuhn Tucker conditions $\Delta\gamma^\alpha \geq 0$ and $\Delta\gamma^\alpha f_\alpha\left(\sigma_{n+1}^{(k)}\right) = 0$, eq. (3.79) can be grouped in a matrix form as follows

$$\boldsymbol{\nabla} L^{(k)} = \begin{bmatrix} \partial_\sigma L^{(k)} \\ \partial_{\Delta\gamma^\alpha} L^{(k)} \end{bmatrix} = \begin{bmatrix} \mathbb{C}^{-1} : \left[\sigma_{n+1}^{(k)} - \sigma_{n+1}^{trial}\right] + \sum_{\alpha\in J_{act}} \Delta\gamma^\alpha \partial_\sigma f_\alpha\left(\sigma_{n+1}^{(k)}\right) \\ f_\alpha\left(\sigma_{n+1}^{(k)}\right) \end{bmatrix} = \mathbf{0} \tag{3.80}$$

$$\begin{aligned}
\boldsymbol{\nabla}^2 L^{(k)} &= \begin{bmatrix} \partial^2_{\sigma\sigma} L^{(k)} & \partial^2_{\sigma\Delta\gamma^\alpha} L^{(k)} \\ \partial^2_{\Delta\gamma^\alpha\sigma} L^{(k)} & \partial^2_{\Delta\gamma^\alpha\Delta\gamma^\alpha} \end{bmatrix},\\
&= \begin{bmatrix} \mathbb{C}^{-1} + \sum_{\alpha\in J_{act}} \Delta\gamma^\alpha \partial^2_{\sigma\sigma} f_\alpha\left(\sigma_{n+1}^{(k)}\right) & \partial_\sigma f_\alpha\left(\sigma_{n+1}^{(k)}\right) \\ \left(\partial_\sigma f_\alpha\left(\sigma_{n+1}^{(k)}\right)\right)^T & \mathbf{0} \end{bmatrix}.
\end{aligned} \tag{3.81}$$

A decision about the set of active constraints $J_{act} := \{\alpha \in \{1,\dots,m\} \,|f_\alpha(\sigma_{n+1}) > 0\}$, which is usually not known, will be discussed in subsection 3.4.2. With some algebraic operations, linearization of eq. (3.80) leads to

$$\boldsymbol{\nabla} L^{(k+1)} = \boldsymbol{\nabla} L^{(k)} + \boldsymbol{\nabla}^2 L^{(k)} \begin{bmatrix} \Delta\sigma \\ \Delta\left(\Delta\gamma^\alpha\right) \end{bmatrix} = \mathbf{0} \;\Rightarrow\; \begin{bmatrix} \Delta\sigma \\ \Delta\left(\Delta\gamma^\alpha\right) \end{bmatrix} = -\left[\boldsymbol{\nabla}^2 L^{(k)}\right]^{-1} \boldsymbol{\nabla} L^{(k)}. \tag{3.82}$$

With the help of eq. (3.80) and eq. (3.81), the first line in eq. (3.82) can be expanded and then solved for $\Delta\boldsymbol{\sigma}$ by

$$\begin{aligned}\partial^2_{\boldsymbol{\sigma}\boldsymbol{\sigma}} L^{(k)} : \Delta\boldsymbol{\sigma} + \partial^2_{\boldsymbol{\sigma}\Delta\gamma^\alpha} L^{(k)} \cdot \Delta\left(\Delta\gamma^\alpha\right) &= -\partial_{\boldsymbol{\sigma}} L^{(k)}, \\ \Delta\boldsymbol{\sigma} = -\left[\partial^2_{\boldsymbol{\sigma}\boldsymbol{\sigma}} L^{(k)}\right]^{-1} : \left(\sum_{\alpha\in J_{act}} \partial^2_{\boldsymbol{\sigma}\Delta\gamma^\alpha} L^{(k)} \cdot \Delta\left(\Delta\gamma^\alpha\right) + \partial_{\boldsymbol{\sigma}} L^{(k)}\right).\end{aligned} \tag{3.83}$$

By differentiating the consistency condition $f^{(k)}_{\alpha,n+1} = 0$, one obtains $df^{(k)}_{\alpha,n+1} = \partial_{\boldsymbol{\sigma}} f^{(k)}_{\alpha,n+1} : \Delta\boldsymbol{\sigma} = 0,\ \alpha \in J^{(k)}_{act}$. As a result, the algorithmic consistency condition takes the form

$$f^{(k+1)}_{\alpha,n+1} = f^{(k)}_{\alpha,n+1} + \partial_{\boldsymbol{\sigma}} f^{(k)}_{\alpha,n+1} : \Delta\boldsymbol{\sigma} = 0. \tag{3.84}$$

Pre-multiplying eq. $(3.83)_2$ with $\partial_{\boldsymbol{\sigma}} f^{(k)}_{\alpha,n+1}$ and substituting the result in eq. (3.84), one achieves the change in plastic, i.e. wrinkling, slip with the help of eqs. (3.80) and (3.81) as

$$\Delta\left(\Delta\gamma^\beta\right) = \sum_{\alpha\in J_{act}} \frac{f^{(k)}_{\alpha,n+1} - \partial_{\boldsymbol{\sigma}} f^{(k)}_{\alpha,n+1} : \left[\partial^2_{\boldsymbol{\sigma}\boldsymbol{\sigma}} L^{(k)}\right]^{-1} : \partial_{\boldsymbol{\sigma}} L^{(k)}}{\partial_{\boldsymbol{\sigma}} f^{(k)}_{\alpha,n+1} : \left[\partial^2_{\boldsymbol{\sigma}\boldsymbol{\sigma}} L^{(k)}\right]^{-1} : \partial^2_{\boldsymbol{\sigma}\Delta\gamma^\beta} L^{(k)}}. \tag{3.85}$$

Therefore, the solution of the Lagrangian functional in eq. (3.78) is interpreted as the closest point projection of the trial state $\boldsymbol{\sigma}^{trial}_{n+1}$ onto *the boundary of elastic domain* $\partial E_{\boldsymbol{\sigma}}$ as illustrated in Figure 3.10.

3.4.2 Application of the Return Mapping Algorithm of Multisurface Perfect Plasticity in wrinkling

To solve this problem, a decision about the current active constraints is required. Hence, we follow the procedure from [SH98] in which the current active set of constraints J^{trial}_{act} is updated during an iterative process. Consistency is restored by enforcing the constraint $f_\alpha\left(\boldsymbol{\sigma}_{n+1}\right)$ with the nonnegative Lagrange multiplier $\Delta\gamma^{\alpha^{(k)}}$ in eq. (3.74) for all $\alpha \in J_{act}$. This procedure together with the return mapping algorithm are successfully employed for perfect plasticity with a summary as follows:

(i) Compute the elastic predictor

$$\begin{aligned}\boldsymbol{\sigma}^{trial}_{n+1} &= \mathbb{C} : \left(\boldsymbol{\epsilon}_{n+1} - \boldsymbol{\epsilon}^{w}_{n+1}\right) \\ f^{trial}_{\alpha,n+1} &= f_\alpha\left(\boldsymbol{\sigma}^{trial}_{n+1}\right); \quad \forall\alpha \in \{1,\dots,m\}\end{aligned}$$

(ii) Check for the occurrence of the plastic process (wrinkling)

if $f^{trial}_{\alpha,n+1} \le 0$ for $\forall\alpha \in \{1,\dots,m\}$ **then**
$\forall\,(\bullet)_{n+1} = (\bullet)^{trial}_{n+1}$ (no active constraint, only elastic process)
exit wrinkling subroutine
else
$J^{(0)}_{act} := \left(\alpha \in \{1,\dots,m\}\,; f^{trial}_{\alpha,n+1} > 0\right)$ (plastic process, i.e., wrinkling)

$\boldsymbol{\epsilon}_{n+1}^{w(0)} = \boldsymbol{\epsilon}_n^w, \quad \Delta\gamma^{\alpha(0)} = 0$ freezing the plastic process (wrinkling)
goto (iii)
end if

(iii) Evaluate flow rule residuals of eq. $(3.79)_1$

$$\boldsymbol{\sigma}_{n+1}^{(k)} = \mathbb{C} : \left(\boldsymbol{\epsilon}_{n+1} - \boldsymbol{\epsilon}_{n+1}^{w(k)}\right)$$
$$R_{n+1}^{(k)} = \mathbb{C}^{-1} : \left(\boldsymbol{\sigma}_{n+1}^{(k)} - \boldsymbol{\sigma}_{n+1}^{trial}\right) + \sum_{\beta \in J_{act}} \Delta\gamma^{\beta(k)} \left\{\partial_\sigma f_\beta\right\}_{n+1}^{(k)}$$

(iv) Check convergence $f_{\alpha,n+1}^{(k)} = f_\alpha\left(\boldsymbol{\sigma}_{n+1}^k\right)$, for $\alpha \in J_{act}^k$
if $(f_{\alpha,n+1}^{(k)} <$ **TOL1** for $\forall \alpha \in J_{act}^k)$ and $(\left\|R_{n+1}^{(k)}\right\| <$ **TOL2**) **then**
Find algorithmic elastoplastic tangent moduli $\mathbb{C}_{alg}$ from eq. (3.94)
exit
end if

(v) Compute elastic moduli and consistent tangent moduli (see eq. (3.85))

$$G_{\alpha\beta,n+1}^{(k)} := \partial_\sigma f_{\alpha,n+1}^{(k)} : \left[\partial_{\sigma\sigma}^2 L_{n+1}^{(k)}\right]^{-1} : \partial_\sigma f_{\beta,n+1}^{(k)}$$
$$G_{n+1}^{\alpha\beta(k)} := G_{\alpha\beta,n+1}^{(k)^{-1}}$$
$$\left[\mathbb{C}_{n+1}^{(k)}\right]^{-1} := \left[\boldsymbol{\nabla}^2\Psi\left(\boldsymbol{\epsilon}_{n+1} - \boldsymbol{\epsilon}_{n+1}^{w(k)}\right)\right]^{-1}$$

(vi) Find the increment plastic (wrinking) slip in eq. (3.85) and update the set of active constraints

$$\Delta\left(\Delta\gamma_{n+1}^{\beta(k)}\right) := \sum_{\alpha \in J_{act}} G_{n+1}^{\alpha\beta(k)} \left\{f_{\alpha,n+1}^{(k)} - \partial_\sigma f_{\alpha,n+1}^{(k)} : \left[\partial_{\sigma\sigma}^2 L^{(k)}\right]^{-1} : \partial_\sigma L^{(k)}\right\}$$
$$\widetilde{\Delta}\left(\Delta\gamma_{n+1}^{\beta(k+1)}\right) = \Delta\gamma_{n+1}^{\beta(k)} + \Delta\left(\Delta\gamma_{n+1}^{\beta(k)}\right)$$

if $\widetilde{\Delta}\left(\Delta\gamma_{n+1}^{\beta(k+1)}\right) < 0,\ \beta \in J_{act}$ **then**
Reset and update set of active constraint $\beta \in J_{act}^{k+1} := \left\{\beta \in J_{act}^k | \widetilde{\Delta}\left(\Delta\gamma_{n+1}^{\beta(k+1)}\right) > 0\right\}$
goto (iii)
else
goto (vii)
end if

(vii) Obtain increments in stress (see eq. (3.83))

$$\Delta\boldsymbol{\sigma}_{n+1}^{(k)} = -\left[\partial_{\sigma\sigma}^2 L_{n+1}^{(k)}\right]^{-1} : \left(\sum_{\alpha \in J_{act}} \partial_{\sigma\Delta\gamma^\alpha}^2 L_{n+1}^{(k)} \cdot \Delta\left(\Delta\gamma^\alpha\right) + \partial_\sigma L_{n+1}^{(k)}\right)$$

(viii) Update plastic (wrinkling) strain, plastic (wrinkling) slip and stress tensor

$$\begin{aligned}\boldsymbol{\epsilon}_{n+1}^{w(k+1)} &= \boldsymbol{\epsilon}_{n+1}^{w(k)} + \Delta\boldsymbol{\epsilon}_{n+1}^{w(k)} = \boldsymbol{\epsilon}_{n+1}^{w(k)} - \mathbb{C}^{-1} : \Delta\boldsymbol{\sigma}_{n+1}^{(k)},\\ \Delta\gamma_{n+1}^{\alpha(k+1)} &= \Delta\gamma_{n+1}^{\alpha(k)} + \Delta\left(\Delta\gamma_{n+1}^{\alpha(k)}\right);\ \alpha \in J_{act}^{n+1},\\ \boldsymbol{\sigma}_{n+1}^{(k+1)} &= \boldsymbol{\sigma}_{n+1}^{(k)} + \Delta\boldsymbol{\sigma}_{n+1}^{(k)}\end{aligned}$$

set $k \leftarrow k+1$ **goto** (iii)

3.4.3 Algorithmic tangent modulus

A consistently linearized elastoplastic tangent modulus is available by enforcing the consistency condition on the discrete algorithmic level. This consistent modulus gives a smooth transition from an elastic state to a plastic state, i.e. wrinkling. Derivation of the algorithmic tangent modulus with the fully implicit backward Euler scheme is given as follows: First, differentiating eqs. $(3.73)_2$ and $(3.73)_3$ yields

$$d\boldsymbol{\sigma}_{n+1} = \mathbb{C} : \left(d\boldsymbol{\epsilon}_{n+1} - d\boldsymbol{\epsilon}_{n+1}^{w}\right), \tag{3.86}$$

$$d\boldsymbol{\epsilon}_{n+1}^{w} = \sum_{\alpha\in 1}^{m} \left(d\left(\Delta\gamma^{\alpha}\right)\partial_{\sigma} f_{\alpha,n+1} + \Delta\gamma^{\alpha} d\left(\partial_{\sigma} f_{\alpha,n+1}\right)\right). \tag{3.87}$$

By combining eqs. (3.86) and (3.87), one obtains

$$\begin{aligned}\mathbb{C}^{-1} : d\boldsymbol{\sigma}_{n+1} &= d\boldsymbol{\epsilon}_{n+1} - \sum_{\alpha\in 1}^{m}\left(d\left(\Delta\gamma^{\alpha}\right)\partial_{\sigma} f_{\alpha}\left(\boldsymbol{\sigma}_{n+1}\right) + \Delta\gamma^{\alpha}\left(\partial_{\sigma\sigma}^{2} f_{\alpha}\left(\boldsymbol{\sigma}_{n+1}\right)\right) : d\boldsymbol{\sigma}_{n+1}\right),\\ d\boldsymbol{\sigma}_{n+1} &= \boldsymbol{\Xi}_{n+1} : \left[d\boldsymbol{\epsilon}_{n+1} - \sum_{\alpha\in 1}^{m}\left(d\left(\Delta\gamma^{\alpha}\right)\partial_{\sigma} f_{\alpha}\left(\boldsymbol{\sigma}_{n+1}\right)\right)\right],\end{aligned} \tag{3.88}$$

in which $\boldsymbol{\Xi}_{n+1}$ is an algorithmic moduli expressed by

$$\boldsymbol{\Xi}_{n+1} = \left[\mathbb{C}^{-1} + \sum_{\alpha\in 1}^{m}\left(\Delta\gamma^{\alpha}\left(\partial_{\sigma\sigma}^{2} f_{\alpha}\left(\boldsymbol{\sigma}_{n+1}\right)\right)\right)\right]^{-1}. \tag{3.89}$$

By differentiating $f_{\alpha}\left(\boldsymbol{\sigma}_{n+1}\right) = 0$, the algorithmic consistency condition takes the form in which $\boldsymbol{\Xi}_{n+1}$ is an algorithmic moduli expressed by

$$df_{\alpha}\left(\boldsymbol{\sigma}_{n+1}\right) = \partial_{\sigma} f_{\alpha}\left(\boldsymbol{\sigma}_{n+1}\right) : d\boldsymbol{\sigma}_{n+1} = 0; \quad \alpha \in J_{act}. \tag{3.90}$$

Then, substituting eq. $(3.88)_2$ in eq. (3.90) yields

$$d\left(\Delta\gamma_{n+1}^{\beta}\right) = \sum_{\alpha\in J_{act}} \frac{\partial_{\sigma} f_{\alpha}\left(\boldsymbol{\sigma}_{n+1}\right) : \boldsymbol{\Xi}_{n+1} : d\boldsymbol{\epsilon}_{n+1}}{g_{\alpha\beta,n+1}}; \quad \beta \in J_{act}, \tag{3.91}$$

with

$$g_{\alpha\beta,n+1} = \partial_{\sigma} f_{\alpha}\left(\boldsymbol{\sigma}_{n+1}\right) : \boldsymbol{\Xi}_{n+1} : \partial_{\sigma} f_{\beta}\left(\boldsymbol{\sigma}_{n+1}\right). \tag{3.92}$$

By substituting eq. (3.91) in eq. $(3.88)_2$, one obtains

$$\begin{aligned} d\boldsymbol{\sigma}_{n+1} &= \boldsymbol{\Xi}_{n+1} : \left[d\boldsymbol{\epsilon}_{n+1} - \sum_{\alpha,\beta \in J_{act}} \frac{\partial_\sigma f_\alpha \left(\boldsymbol{\sigma}_{n+1}\right) : \boldsymbol{\Xi}_{n+1} : d\boldsymbol{\epsilon}_{n+1} \partial_\sigma f_\beta \left(\boldsymbol{\sigma}_{n+1}\right)}{g_{\alpha\beta,n+1}} \right], \\ &= \boldsymbol{\Xi}_{n+1} : d\boldsymbol{\epsilon}_{n+1} - \left[\sum_{\alpha,\beta \in J_{act}} \frac{\boldsymbol{\Xi}_{n+1} : \partial_\sigma f_\beta \left(\boldsymbol{\sigma}_{n+1}\right) \otimes \partial_\sigma f_\alpha \left(\boldsymbol{\sigma}_{n+1}\right) : \boldsymbol{\Xi}_{n+1}}{g_{\alpha\beta,n+1}} \right] : d\boldsymbol{\epsilon}_{n+1}, \\ &= \left[\boldsymbol{\Xi}_{n+1} - \sum_{\alpha,\beta \in J_{act}} \frac{\boldsymbol{\Xi}_{n+1} : \partial_\sigma f_\beta \left(\boldsymbol{\sigma}_{n+1}\right) \otimes \partial_\sigma f_\alpha \left(\boldsymbol{\sigma}_{n+1}\right) : \boldsymbol{\Xi}_{n+1}}{g_{\alpha\beta,n+1}} \right] : d\boldsymbol{\epsilon}_{n+1}, \\ &= \mathbb{C}^{alg} : d\boldsymbol{\epsilon}_{n+1}, \end{aligned} \tag{3.93}$$

where the algorithmic tangent modulus $\mathbb{C}^{alg}$ is defined by

$$\mathbb{C}^{alg} = \left[\boldsymbol{\Xi}_{n+1} - \sum_{\alpha,\beta \in J_{act}} \frac{\boldsymbol{\Xi}_{n+1} : \partial_\sigma f_\beta \left(\boldsymbol{\sigma}_{n+1}\right) \otimes \partial_\sigma f_\alpha \left(\boldsymbol{\sigma}_{n+1}\right) : \boldsymbol{\Xi}_{n+1}}{g_{\alpha\beta,n+1}} \right]. \tag{3.94}$$

Apparently, in case of no active constraint, $\mathbb{C}^{alg} = \mathbb{C}$. Thus, the consistent algorithmic tangent modulus depends significantly on the set of active constraints.

3.4.4 Derivation of constraints

The constraint functions $f_\alpha \left(\boldsymbol{\sigma}_{n+1}, \theta\right)$ and their derivatives, which are functions of the stress tensor and the wrinkling direction , are required for a constrained minimization algorithm. Since all compressive stresses will be eliminated by the formation of wrinkles, the vanishing of compressive stresses in the direction of wrinkles is a feasible choice for the constraints.

3.4.4.1 Constraints for isotropic material

Due to the fact that the wrinkling direction of an isotropic material always coincides with the minimal principal stress direction, the constraint functions $f_\alpha \left(\boldsymbol{\sigma}_{n+1}\right) \leq 0$ depend only on the stress measure dummy $\boldsymbol{\sigma}$. The total PK2 stress tensor during the return mapping iteration step k has the form

$$\mathbf{S} = \mathbf{S}_{el} + \mathbf{S}_{pre} = \boldsymbol{\sigma}_{n+1}^{(k)}, \tag{3.95}$$

whereas the converged result can be stated as

$$\widetilde{\mathbf{S}} = \widetilde{\mathbf{S}}_{el} + \mathbf{S}_{pre} = \boldsymbol{\sigma}_{n+1}, \tag{3.96}$$

when the constrained minimization problem in eq. (3.78) is fulfilled. Note that the subscript $n+1$ is omitted for simplicity. For this reason, the constraint functions on the condition of no-compressive stresses are defined by

$$\sigma_I \geq 0 \quad \Rightarrow \quad f_1 = -\sigma_I \leq 0 \qquad ; \qquad \sigma_{II} \geq 0 \quad \Rightarrow \quad f_2 = -\sigma_{II} \leq 0 \tag{3.97}$$

where σ_I and σ_{II} stand for the maximal and minimal principal stresses, respectively. Under the state of two dimensional plane stress, illustrated in Figure 3.11, the principal stresses are defined by

$$\sigma_{I,II} = \frac{1}{2}\varsigma^T \{\sigma\} \pm \sqrt{\frac{1}{2}\{\sigma\}^T \mathbf{P} \{\sigma\}}, \tag{3.98}$$

$$\text{with} \qquad \{\sigma\} = \begin{Bmatrix} \sigma_{11} \\ \sigma_{22} \\ \sigma_{12} \end{Bmatrix}, \qquad \varsigma = \begin{Bmatrix} 1 \\ 1 \\ 0 \end{Bmatrix}, \qquad \mathbf{P} = \begin{bmatrix} \frac{1}{2} & \frac{-1}{2} & 0 \\ \frac{-1}{2} & \frac{1}{2} & 0 \\ 0 & 0 & 2 \end{bmatrix}.$$

Hence, the constraint functions and their derivatives can be written by

$$f_{1,2} = \frac{-1}{2}\varsigma^T \{\sigma\} \mp \sqrt{\frac{1}{2}\{\sigma\}^T \mathbf{P} \{\sigma\}} \qquad \text{1:=uppersign, 2:=lowersign,} \tag{3.99}$$

$$\{\partial_\sigma f_{1,2}\} = \frac{-1}{2}\varsigma \mp \frac{\frac{1}{2}\mathbf{P}\{\sigma\}}{\sqrt{\frac{1}{2}\{\sigma\}^T \mathbf{P} \{\sigma\}}},$$

$$\left[\partial^2_{\sigma\sigma} f_1\right] = \frac{-1}{2}\left(\frac{\mathbf{P}}{\sqrt{\frac{1}{2}\{\sigma\}^T \mathbf{P} \{\sigma\}}} - \frac{\frac{1}{2}\mathbf{P}\{\sigma\}\{\sigma\}^T \mathbf{P}}{\sqrt[3]{\frac{1}{2}\{\sigma\}^T \mathbf{P} \{\sigma\}}}\right) = \frac{-\mathbf{P}}{2z} + \frac{\mathbf{P}\{\sigma\}\{\sigma\}^T \mathbf{P}}{4z^3},$$

$$\left[\partial^2_{\sigma\sigma} f_2\right] = \frac{\mathbf{P}}{2z} - \frac{\mathbf{P}\{\sigma\}\{\sigma\}^T \mathbf{P}}{4z^3}; \quad \text{with } z = \sqrt{\frac{1}{2}\{\sigma\}^T \mathbf{P} \{\sigma\}}.$$

In addition to eq. $(3.97)_2$, an idea of an allowable compressive stress S_{alw} can be adopted. This issue is inspired by the too conservative result of the no-compressive stress constraint when it is compared with the shell solution. Additionally, the no-compressive stress condition may result in an ill-conditioned stiffness matrix as reported in [RLVO05]. Therefore, the condition of no-compressive stress in eq. $(3.97)_2$ is changed according to eq. (3.34) to

$$\sigma_{II} \geq S_{alw} \quad \Rightarrow \quad f_2 = -\sigma_{II} + S_{alw} \leq 0. \tag{3.100}$$

3.4.4.2 Constraints for orthotropic material

Determination of the wrinkling direction in an orthotropic material is nontrivial as discussed in [JWB08b]. Furthermore, the corresponding compressive stresses to this direction depend on both the stress measure σ and the wrinkling direction θ from section 3.2.2. For this reason, the condition of no-compressive stresses on the wrinkling direction can be used as constraint functions . The current total PK2 stress tensor and the modified one are defined as in eqs. (3.95)-(3.96), but additional conditions concerning the direction of wrinkles for orthotropic materials are required. Due to the state of uniaxial tension on the wrinkling axes in eqs. (3.17)-(3.19), constraint functions can be defined with the aid of eq. (3.5) such that

$$\begin{aligned} \mathbf{U}_1^T \{\mathbf{S}\} \geq 0 \quad &\Rightarrow \quad f_1 = -\mathbf{U}_1^T \{\mathbf{S}\} \leq 0, \\ \mathbf{U}_2^T \{\mathbf{S}\} \geq 0 \quad &\Rightarrow \quad f_2 = -\mathbf{U}_2^T \{\mathbf{S}\} \leq 0. \end{aligned} \tag{3.101}$$

From section 3.2.2, the first constraint–uniaxial tension–is always satisfied when the wrinkling direction is available. Thus, only the second constraint, the condition of no-compressive stress in the wrinkling direction $\mathbf{w}_0$ in Figure 3.5, is required. With the help

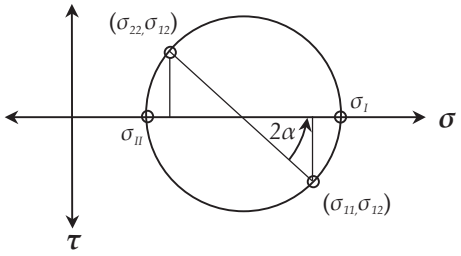

Figure 3.11: Geometrical illustration of the principal stresses.

of eqs. (3.18)-(3.19), derivatives of eq. $(3.101)_2$ can be described via

$$\begin{aligned}
\{\partial_\sigma f_2\} &= -\left(\frac{\partial \mathbf{U}_2}{\partial\theta}\left\{\frac{\partial\theta}{\partial\sigma}\right\}^T\right)\{\mathbf{S}\}+\mathbf{U}_2,\\
\left[\partial^2_{\sigma\sigma} f_2\right] &= \frac{-2\partial\mathbf{U}_2}{\partial\theta}\frac{\partial\theta}{\partial\sigma}^T+\left(\frac{\partial^2\mathbf{U}_2}{\partial\theta^2}\frac{\partial\theta}{\partial\sigma}^T\right)\frac{\partial\theta}{\partial\sigma}^T\{\mathbf{S}\}+\left(\frac{\partial\mathbf{U}_2}{\partial\theta}\frac{\partial^2\theta}{\partial\sigma^2}^T\right)\{\mathbf{S}\},
\end{aligned} \tag{3.102}$$

where

$$\begin{aligned}
\frac{\partial\theta}{\partial\sigma} &= A^{-1}\left(\frac{\mathbf{U}_3^T[\mathbb{C}]\,\mathbf{U}_2}{\mathbf{U}_2^T[\mathbb{C}]\,\mathbf{U}_2}\mathbf{U}_2-\mathbf{U}_3\right),\quad \frac{\partial^2\theta}{\partial\sigma^2}=-A^{-1}\left(\mathbf{M}_d+\mathbf{M}_e+\mathbf{M}_f\right),\\
A &= \frac{\partial\mathbf{U}_3^T}{\partial\theta}\{\mathbf{S}\}+\mu\mathbf{U}_2^T[\mathbb{C}]\frac{\partial\mathbf{U}_3}{\partial\theta}+\mu\mathbf{U}_3^T[\mathbb{C}]\frac{\partial\mathbf{U}_2}{\partial\theta}+\mathbf{U}_3^T[\mathbb{C}]\,\mathbf{U}_2\frac{\partial\mu}{\partial\theta},\\
\frac{\partial\mu}{\partial\theta} &= \frac{-1}{\mathbf{U}_2^T[\mathbb{C}]\,\mathbf{U}_2}\left(\frac{\partial\mathbf{U}_2^T}{\partial\theta}\{\mathbf{S}\}+2\mu\mathbf{U}_2^T[\mathbb{C}]\frac{\partial\mathbf{U}_2}{\partial\theta}\right),\quad \frac{\partial\mu}{\partial\sigma}=\frac{-\mathbf{U}_2}{\mathbf{U}_2^T[\mathbb{C}]\,\mathbf{U}_2},\\
\frac{\partial^2\mu}{\partial\theta^2} &= \frac{-1}{\mathbf{U}_2^T[\mathbb{C}]\,\mathbf{U}_2}\left(\frac{\partial^2\mathbf{U}_2^T}{\partial\theta^2}\{\mathbf{S}\}+4\frac{\partial\mu}{\partial\theta}\mathbf{U}_2^T[\mathbb{C}]\frac{\partial\mathbf{U}_2}{\partial\theta}+2\mu\frac{\partial\mathbf{U}_2}{\partial\theta}^T[\mathbb{C}]\frac{\partial\mathbf{U}_2}{\partial\theta}+2\mu\mathbf{U}_2^T[\mathbb{C}]\frac{\partial^2\mathbf{U}_2}{\partial\theta^2}\right),\\
\frac{\partial^2\mu}{\partial\theta\partial\sigma} &= \frac{-1}{\mathbf{U}_2^T[\mathbb{C}]\,\mathbf{U}_2}\left(\frac{\partial\mathbf{U}_2}{\partial\theta}+2\left(\frac{\partial\mathbf{U}_2}{\partial\theta}^T[\mathbb{C}]\,\mathbf{U}_2\right)+\frac{\partial\mu}{\partial\theta}\right),\\
\mathbf{M}_d &= \frac{\partial\mathbf{U}_3}{\partial\theta}\frac{\partial\theta}{\partial\sigma}^T+\left(\mathbf{U}_2^T[\mathbb{C}]\frac{\partial\mathbf{U}_3}{\partial\theta}+\frac{\partial\mathbf{U}_2}{\partial\theta}^T[\mathbb{C}]\,\mathbf{U}_3\right)\frac{\partial\theta}{\partial\sigma}\frac{\partial\mu}{\partial\sigma}^T+\mathbf{U}_3^T[\mathbb{C}]\,\mathbf{U}_2\frac{\partial\theta}{\partial\sigma}\frac{\partial^2\mu}{\partial\theta\partial\sigma}^T,\\
\mathbf{M}_e &= \left(\begin{array}{l}\mu\left(3\frac{\partial\mathbf{U}_2}{\partial\theta}^T[\mathbb{C}]\frac{\partial\mathbf{U}_3}{\partial\theta}+2\mathbf{U}_2^T[\mathbb{C}]\frac{\partial^2\mathbf{U}_3}{\partial\theta^2}+\mathbf{U}_3^T[\mathbb{C}]\frac{\partial^2\mathbf{U}_2}{\partial\theta^2}\right)\\ +\frac{\partial\mu}{\partial\theta}\left(3\mathbf{U}_2^T[\mathbb{C}]\frac{\partial\mathbf{U}_3}{\partial\theta}+2\mathbf{U}_3^T[\mathbb{C}]\frac{\partial\mathbf{U}_2}{\partial\theta}\right)+\frac{\partial^2\mu}{\partial\theta^2}\mathbf{U}_3^T[\mathbb{C}]\,\mathbf{U}_2\end{array}\right)\frac{\partial\theta}{\partial\sigma}\frac{\partial\theta}{\partial\sigma}^T,\\
\mathbf{M}_f &= \frac{\partial\mathbf{U}_3}{\partial\theta}\frac{\partial\theta}{\partial\sigma}^T+\left(\mathbf{U}_2^T[\mathbb{C}]\frac{\partial\mathbf{U}_3}{\partial\theta}+\frac{\partial\mathbf{U}_2}{\partial\theta}^T[\mathbb{C}]\,\mathbf{U}_3\right)\frac{\partial\mu}{\partial\sigma}\frac{\partial\theta}{\partial\sigma}^T+\mathbf{U}_3^T[\mathbb{C}]\,\mathbf{U}_2\frac{\partial^2\mu}{\partial\theta\partial\sigma}\frac{\partial\theta}{\partial\sigma}^T.
\end{aligned}$$

Along the line of eq. (3.100), the idea of an allowable compressive stress S_{alw} changes the condition of no-compressive stress in eq. $(3.101)_2$ to

$$\mathbf{U}_2^T\{\mathbf{S}\}\geq S_{alw}\quad\Rightarrow\quad f_2=-\mathbf{U}_2^T\{\mathbf{S}\}+S_{alw}\leq 0. \tag{3.103}$$

3.5 Numerical experiments

In this section, various numerical examples are performed to scrutinize the presented wrinkling model. In the first example, a well-known beam-like membrane under pure bending is computed to compare numerical results and the analytical one. The second example deals with the shear test of a planar rectangular Kapton membrane. Results of the presented model are compared to the literature to demonstrate its effectiveness. Moreover, abilities of the model to handle an orthotropic material is investigated in the third example of an annulus membrane under torsion. Then an application of the presented model with a curved membrane is explored in the fourth example of an inflatable square airbag. Eventually, the evolution of wrinkle trajectories is demonstrated in the last simulation of a planar square membrane applied by corner loads with varying load ratio.

3.5.1 Pure bending of a stretched rectangular membrane

In order to validate the implemented code, the benchmark example given in [MHW$^+$85] is reproduced here for a comparison between the analytical solution and the numerical result. This simple example was employed as a benchmark for numerous authors, e.g. [ANNP07, LAL01]. A rectangular membrane as shown in Figure 3.12(a) is uniformly pretensioned with a normal stress σ_0 in the x and y directions. The height of the membrane and its thickness are denoted by h and t respectively. After applying the pretension, an in-plane bending moment M is applied on both vertical edges. As a consequence of increasing the magnitude of M, the wrinkled zone expands upwardly from the lower edge. The analytical solution of the wrinkled bandwidth b is presented by Steigmann and Pipkin [SP89] via

$$\frac{b}{h} = \begin{Bmatrix} 0 & ; \frac{M}{Ph} < \frac{1}{6} & (taut) \\ \frac{3M}{Ph} - \frac{1}{2} & ; \frac{1}{6} \leq \frac{M}{Ph} < \frac{1}{2} & (partly\ wrinkled) \end{Bmatrix}. \tag{3.104}$$

For excessively high loads with $\frac{M}{Ph} > \frac{1}{2}$, the entire surface is occupied by wrinkles which results in instability problems. With the curvature κ, the moment-curvature relation of a beam-like membrane can be expressed in the form

$$\frac{2M}{Ph} = \begin{Bmatrix} \frac{1}{3}\frac{Eth^2}{2P}\kappa & ; \frac{Eth^2}{2P}\kappa \leq 1 \\ 1 - \frac{2}{3}\sqrt{\frac{2P}{Eth^2\kappa}} & ; \frac{Eth^2}{2P}\kappa > 1 \end{Bmatrix} \tag{3.105}$$

where E is the elastic modulus of the membrane. Furthermore, the ratio of a resulting stress in x-direction σ_x with respect to a pretension stress σ_0 is given in [MHW$^+$85] by

$$\frac{\sigma_x}{\sigma_0} = \begin{Bmatrix} 2\left(\frac{y}{h} - \frac{b}{h}\right) / \left(1 - \frac{b}{h}\right)^2 & ; \frac{b}{h} < \frac{y}{h} \leq 1 \\ 0 & ; 0 \leq \frac{y}{h} \leq \frac{b}{h} \end{Bmatrix}. \tag{3.106}$$

Due to symmetry, only the right half of the membrane is modeled by bilinear quadrilateral finite elements as depicted in Figure 3.12(b). A symmetric boundary condition is defined on the left boundary where displacement in x-direction is prescribed while the movement in y-direction is allowed except for the node at the middle of the edge. The upper and lower

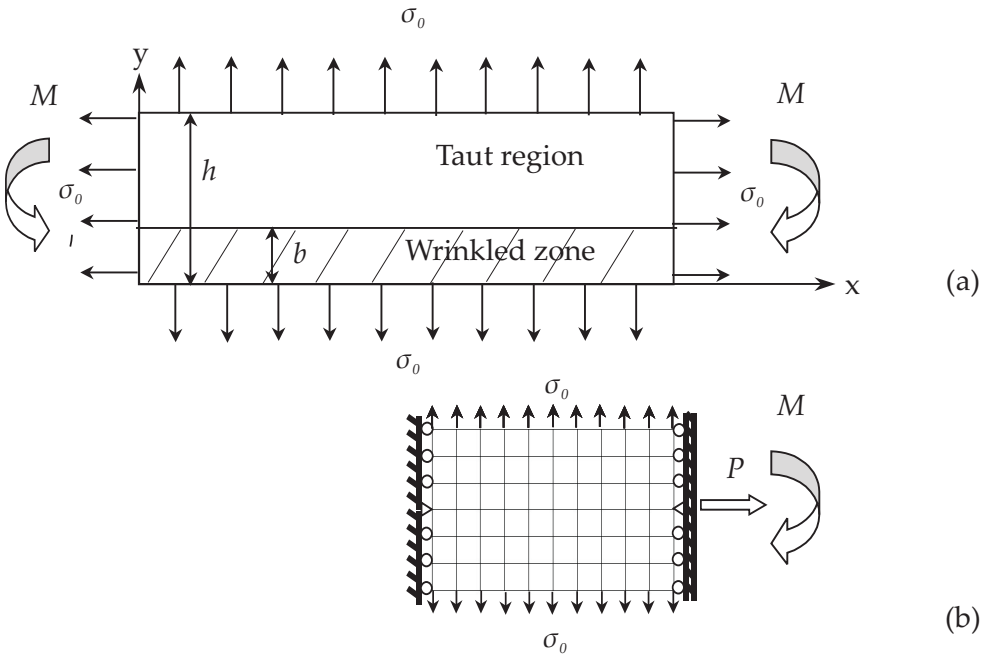

Figure 3.12: Geometry and load condition of a flat membrane subjected to pure bending moment and its discrete model for a simulation.

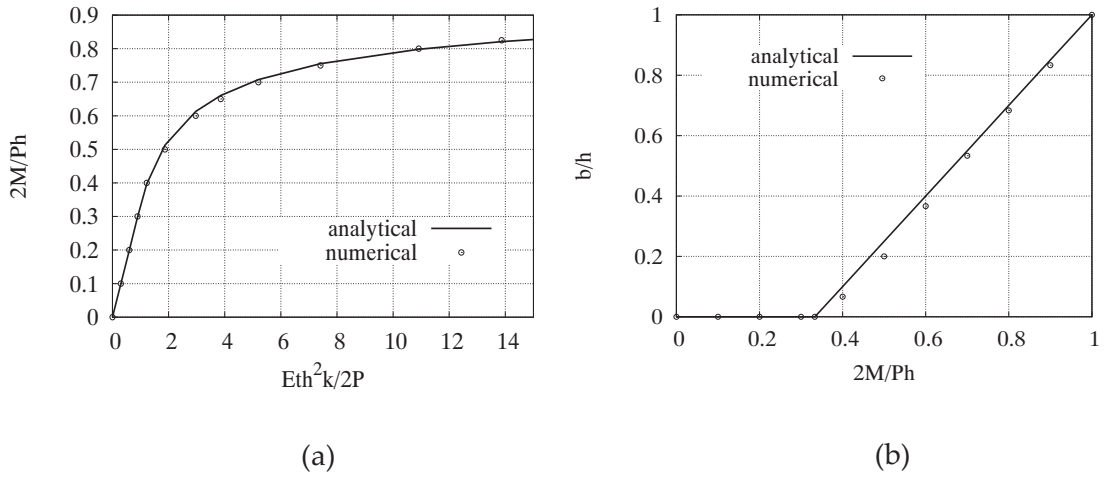

Figure 3.13: Illustration for (a) moment-curvature and (b) wrinkled bandwidth.

edges are subjected to a uniform pretension σ_0. To maintain a uniform rotation, the right boundary is attached to a very stiff beam upon which the external loads P and moment M are applied. Due to a fact that even the extremely thin membrane can hold a small amount of compressive stress, a variable called *allowable compressive stress*, assigned at -1.0e-6, is introduced in this problem. At first, the computation is conducted by applying the pretension axial force $P = \sigma_0 ht$ and σ_0 until the equilibrium state is achieved. Then, a bending moment M on the stiff beam at the right edge is gradually increased in each load step. According to [MHW$^+$85], the curvature of the finite elements model for this beam under pure bending

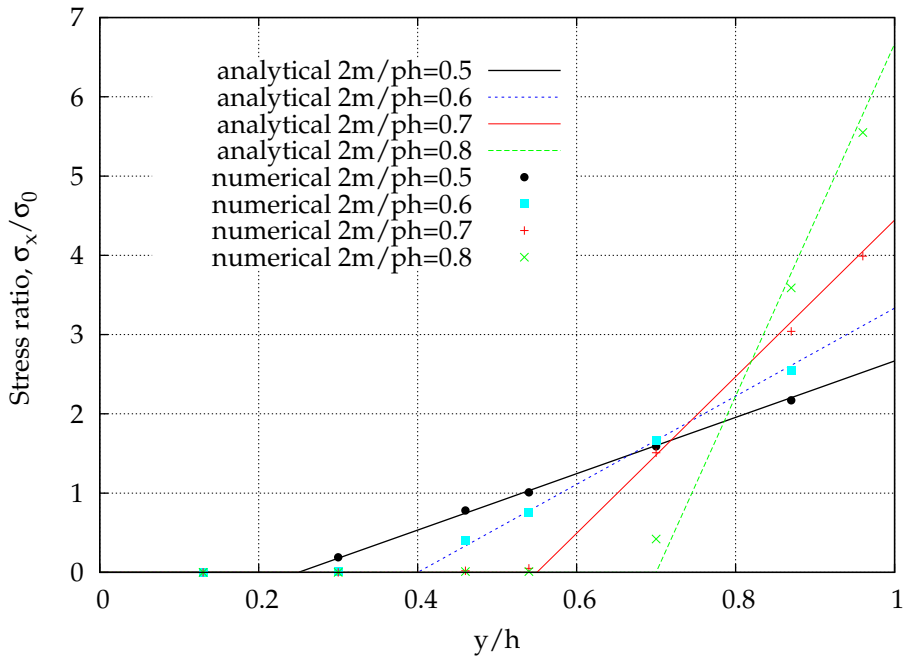

Figure 3.14: Cauchy stress on a vertical cut at the mid length of the finite elements model for the beam-like membrane.

is computed from an assumption that the displacement in y-direction is a parabolic function of the distance in x-direction. A comparison between the numerical result and the analytical solution for the moment-curvature relation in eq. (3.105) of this beam-like membrane is provided in Figure 3.13(a). In Figure 3.13(b), the wrinkle bandwidth from eq. (3.104) as proposed in [MHW$^+$85] is plotted. Results of the presented model can come close to the analytical solution with good accuracy. To avoid the *St.-Venant's boundary effect*, sampling points for wrinkled bandwidth and stresses are chosen as suggested in [LAL01] at the mid length of the finite elements model in Figure 3.12. Furthermore, Figure 3.14 compares the ratio between the Cauchy stress in x-direction to prestress $\frac{\sigma_x}{\sigma_0}$ along a vertical cut at the mid length of the finite elements model. Over a wide range of moment M, a good compatibility between the analytical solution in eq. (3.106) and the numerical one is observable. From these reasons, one can conclude that the proposed wrinkling model can efficiently represent the nonlinear behavior of the wrinkled membrane with a good agreement between the analytical solution and the numerical one. Note that results from the projection method in section 3.3 and the plasticity analogy model in section 3.4 are asymtotically identical within this example.

3.5.2 Shear test of a rectangular isotropic Kapton membrane

A benchmark example proposed in [RTLW05, WP06c] is chosen to verify the proposed wrinkling model. In Figure 3.15, A 2D rectangular membrane is fixed at the lower edge while the upper one is allowed to move only in the horizontal direction. Within the Figure, geometry and load conditions for this isotropic Kapton membrane are given while Table 3.4 provides

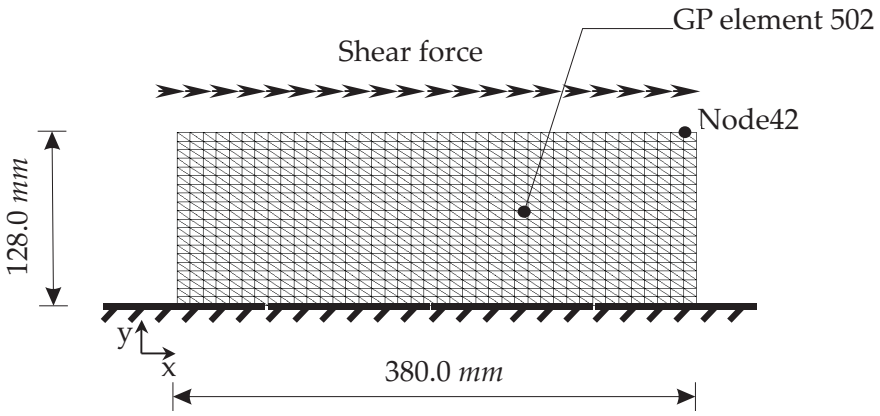

Figure 3.15: Geometry and load condition of the rectangular shear panel.

Table 3.4: Material properties for shear panel Kapton membrane.

Thickness, $t(\mu m)$	25
Young's Modulus, $E(N/mm^2)$	3500
Poisson's ratio, ν	0.31
Density, $\rho(kg/mm^3)$	1.5e-6
Prestress, $S_{pre}(N/mm^2)$	(0.0,1.5,0.0)
Allowable compressive stress $S_{alw}(N/mm^2)$	-1.0e-6
Node42	(x=370.5 ,y=128.0)
GP of element502	(x=262.83 ,y=68.27)

material properties. A vertical prestress of 1.5 N/mm^2 is prescribed to introduce the initial stiffness. This problem is discretized by 1600 linear triangular membrane elements for a nonlinear static analysis. Initially, the flat membrane is loaded by a prestress of magnitude 1.5 N/mm^2 in the y direction. Then, the pretension is held constant while the upper edge is gradually displaced in the horizontal direction with displacement control until the horizontal displacement in the x-direction at node 42 reaches $+3$ mm. Both vertical edges of the membrane are reinforced by cable elements with the Young's Modulus E of 2.1e+6 N/mm^2 and the cross sectional area of 0.50 mm^2. These cables are under prestress of 500 N/mm^2 to avoid unidentified boundary conditions at the free edges of the membrane. For a comparison, three models–pure membrane elements, membrane elements with an embedded wrinkling model and rotational free shell elements [LWKU07]–are performed, respectively. Influences of an imperfection are taken into account by specifying a distributed load of 1.0e-6 N/mm^2 in the normal direction to the membrane surface.

This example demonstrates an ability to represent the average stress field within a wrinkled membrane on the macroscopic scale, the major advantage of the model. Therefore, the mesh resolution employed in this example is not fine enough to gain a complete wrinkle pattern in details. For this reason, the rotation free shell solution in this example is intentionally not refined to mimic similarly the finest scale wrinkle pattern as in [WP06c]. Since the *allowable compressive stress* is material dependent, additional investigations are required to figure

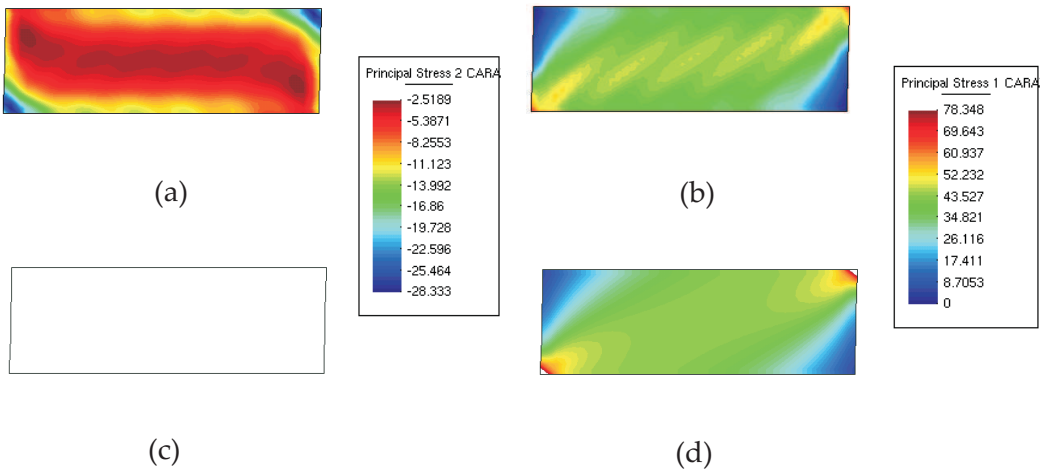

Figure 3.16: Comparison of principal stresses for membranes with imperfection for (a) S_2 rotation free shell (b) S_1 rotation free shell (c) S_2 membrane with wrinkling model and (d) S_1 membrane with wrinkling model.

out an optimal choice for this lower limit for each individual material. Note that within this contribution the original linear elastic membrane is named "wrink0". The symbol "wrink1" is referred to the simplified wrinkling model presented in [JWB08b] while "wrink2" stands for the plasticity analogy wrinkling model from section 3.4 and [JWB09b] whereas "wrink3" is the wrinkling model derived from the projection method in section 3.3 and [JWB09a]. Furthermore, "shell Wong" denotes results of the shell solution from [WP06c] whereas "shell" stands for results of the rotation-free shell [LWKU07].

In Figure 3.16, stress contours for an imperfect membrane which is simulated by either the rotation free shell model or the presented wrinkling model are compared. One observes that the minimal principal stress of the wrinkling model in Figure 3.16(c) is more conservative than the shell counterpart in Figure 3.16(a) since the allowable compressive stress in this model is defined at -1.0e-6 N/mm^2. However, as mentioned above, the resolution of the shell model is not fine enough to represent the finest wrinkle pattern. Thereafter, a deviation of the stress distribution from the exact solution is expected. In other words, the compressive stresses in the shell model should converge to a small amount below zero when the mesh is extensively refined. A comparison of the maximal principal stress in Figure 3.16(b) and (d) shows a good agreement for the average stress field of both models.

Figure 3.17 shows stress plots for a perfect structure (pf) and the same structure with imperfection (ip). Within this figure, one observes that artificial compressive stress at the integration point of element 502 (see Figure 3.15) is diminished due to the wrinkling model (S2 wrink3) for both pf case and ip case. In contrast to the pure membrane model (S1 wrink0 pf) and the shell competitor (S1 shell pf), when the projection wrinkling model (S1 wrink3 pf) is used for a perfect structure, the maximal principal stress is increased due to stress redistribution. It is noteworthy that the perfect structure does not show buckling but nonlinear deformation.

Interestingly, in the case of an imperfect structure, both the pure membrane (S1 wrink0

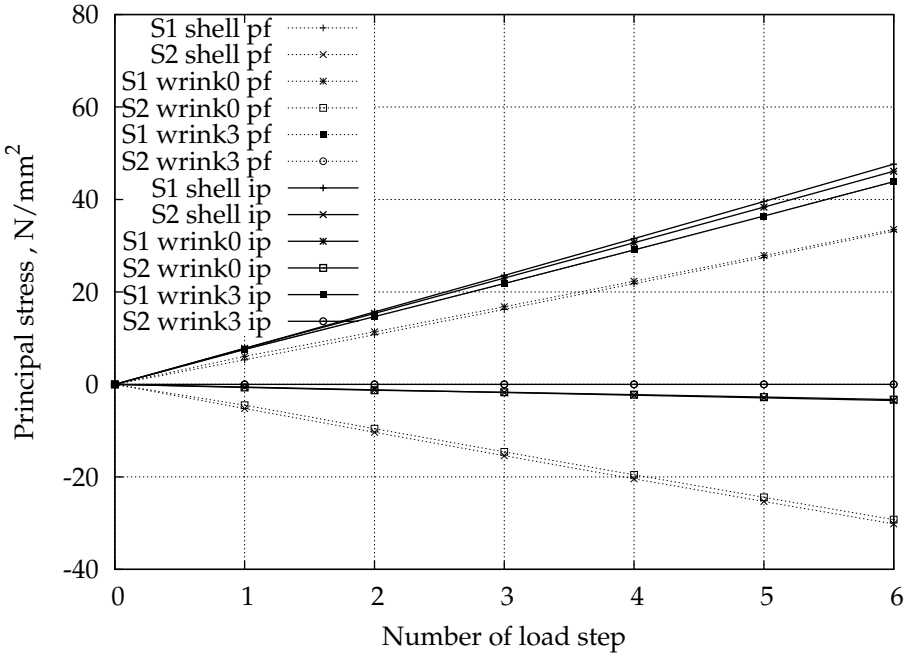

Figure 3.17: Comparison on principal stresses at the GP of element 502 for perfect and imperfect membranes.

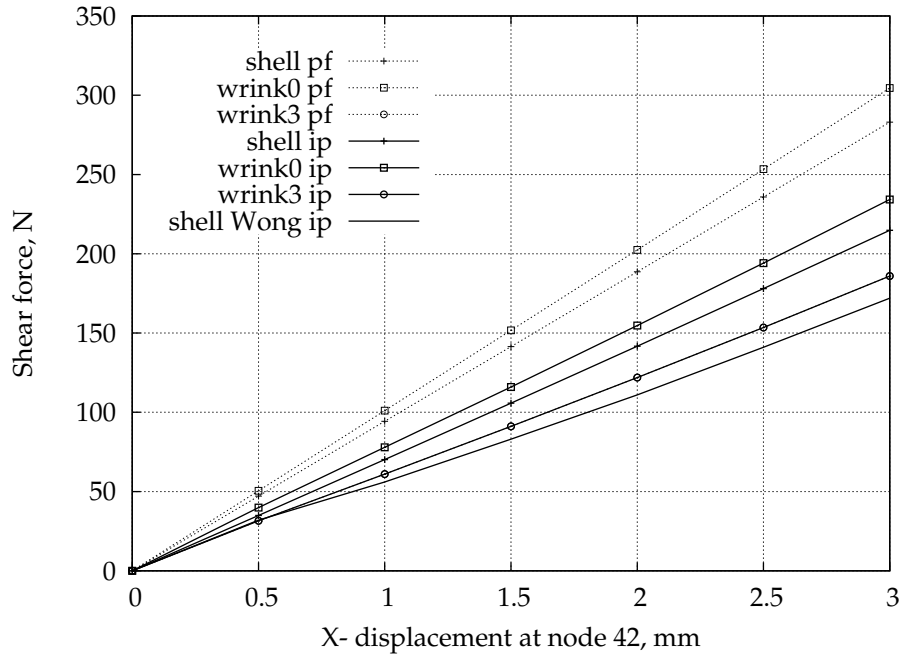

Figure 3.18: Comparison on x displacement-shear force at node 42 of the Kapton isotropic rectangular membrane for perfect and imperfect membranes.

ip) and the shell elements (S1 shell ip) are subjected to local buckling, and as a result, their behaviors are quite close to the wrinkling model (S1 wrink3 ip). However, there are some observable differences which are caused by reasons as follows:

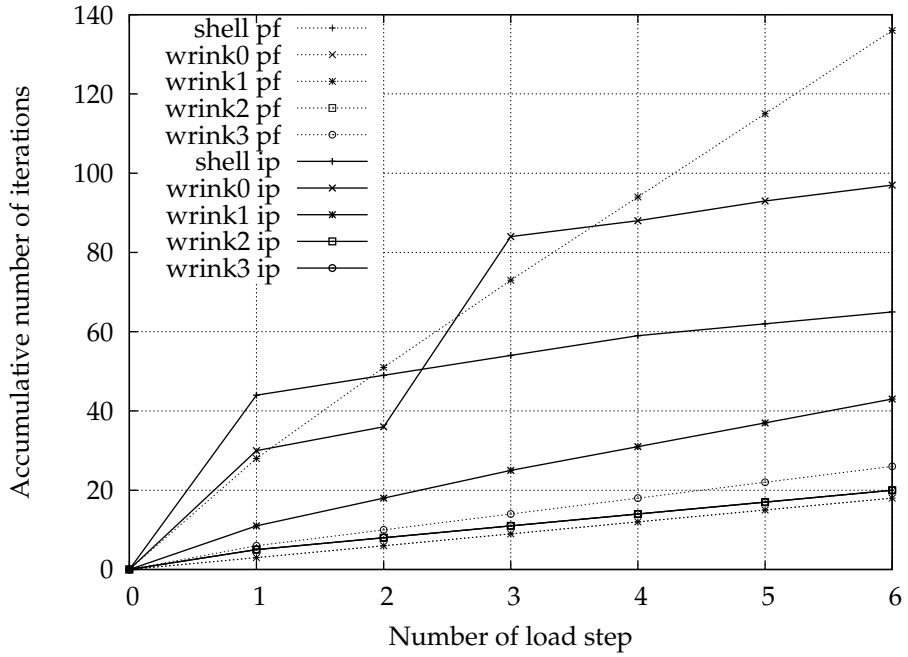

Figure 3.19: Accumulative number of iteration for the Kapton isotropic rectangular membrane for perfect and imperfect membranes.

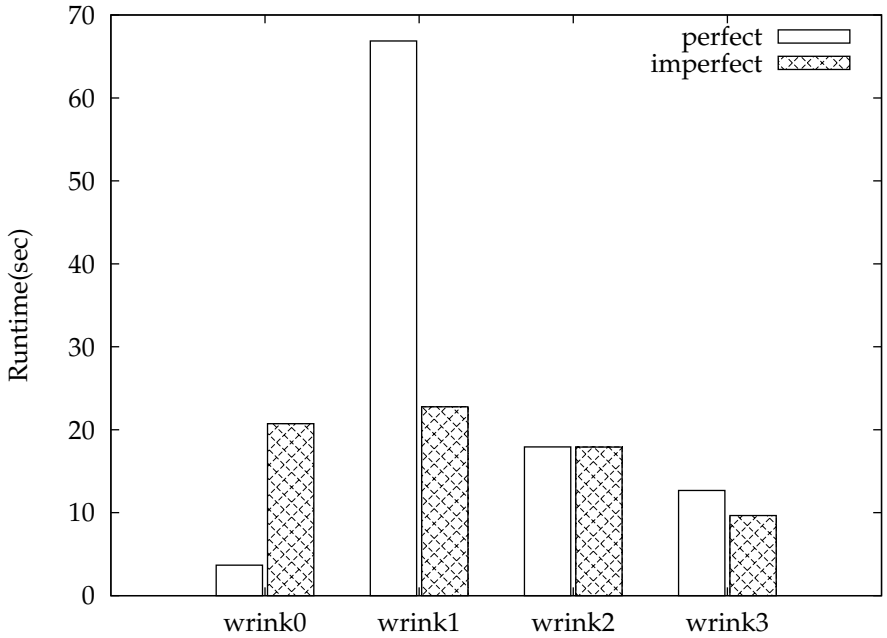

Figure 3.20: Comparison on runtime the Kapton isotropic rectangular membrane under the specified shear force.

(i) The allowable compressive stress -1.0e-6 N/mm^2 in the wrinkling model is too conservative, which eliminates all compressive stresses, whereas the other two approaches maintain a small amount of compressive stiffness. This material-dependent issue requires further investigations.

(ii) Mesh resolutions for the shell and pure membrane models are not fine enough. Therefore, they can neither simulate the finest wrinkles nor reveal the real internal forces of the structure, which leads to an artificial compressive stiffness within the membrane. Consequently, the membrane behaves too stiff as one can observe from the maximal principal stress for the shell (S1 shell) and the pure membrane competitor (S1 wrink0). The difference in the minimal principal stress between the imperfect membrane (S2 wrink3 ip) and the perfect one (S2 wrink3 pf) is insignificant. Thus, this evidence reveals insensitivity of the model wrink3 to imposed imperfections.

In Figure 3.18, the shear force is plotted versus displacement in the x direction at the upper edge for the perfect membrane (pf) and the imperfect one (ip). It can be concluded that the original linear elastic perfect membrane (wrink0 pf) and the perfect shell (shell pf) are too stiff due to the artificial compressive stiffness, while the wrinkling model (wrink3 pf) softens this over-stiff behavior. Because of arbitrary local buckling, results from the imperfect pure membrane (wrink0 ip) and the imperfect shell (shell ip) exhibit certain relaxation whereas the wrinkling model solution for the imperfect structure is nearly identical to the perfect one. It is noteworthy that amongst three simulations for the imperfect structure the wrinkling model solution is the closest approximation for the thin shell solution in [WP06c] (shell Wong ip). Differences between them are attributed to additional reasons as follows:

- ◇ The imposed imperfection in this example is different from that of [WP06c].
- ◇ A stabilization factor of 4.5 was used with ABAQUS in [WP06c], which may cause a deviation from the exact solution.
- ◇ The number of shell elements used in [WP06c] is higher than what is used in this example at the factor of around 4.35.
- ◇ Cable elements on both vertical boundaries influence the whole stiffness of the membrane in this example. Moreover, a similarity between results of wrink3 and that of wrink2, which are not plotted here, demonstrates the potential of wrink3 to reproduce the solution of wrink2 with a good accuracy.

In Figure 3.19, the accumulative number of equilibrium iterations for the perfect (pf) and imperfect (ip) membranes are shown, respectively. One observes that the wrinkling model considers wrinkles as a nonlinear material response instead of geometrically nonlinear effect, e.g. buckling. Therefore, differences in the number of iterations is insignificant among the perfect structure with the wrinkling model (wrink3 pf), the imperfect structure with the wrinkling model (wrink3 ip), the perfect shell structure (shell pf) and the perfect pure membrane structure (wrink0 pf). On the other hand, an imperfect shell (shell ip) experiences certain difficulty to reach equilibrium in the first few incremental steps but exhibits numerically stable behavior in the postbuckling regime whereas the pure membrane (wrink0 ip) shows severe convergence problems which may lead to arbitrary deformation patterns due to the lack of bending rigidity. Amongst three versions of the wrinkling models, wrink1 without stabilization in the perfect membrane (wrink1 pf) is subjected to a severe convergence problem while this situation is alleviated in the imperfect case (wrink1 ip).

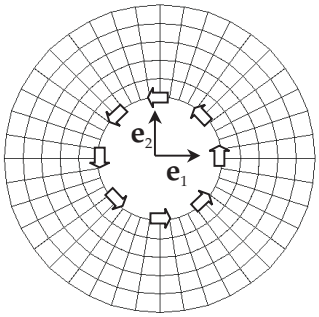

Figure 3.21: Geometry and load at the inner edge of the annulus membrane.

It is valuable to mention that the projection method in wrink3 presented here does not employ any iteration for the fictitious local nonlinear material behaviour in contrast to the return mapping algorithm used in wrink2. Therefore, wrink3 requires a higher number of global equilibrium iterations (wrink3 pf) than that of the wrink2 (wrink2 pf). Besides, the difference of results for imperfect structures between wrink3 ip and wrink2 ip are hardly visible. However, the higher number of the global iterations is compensated by less computational effort in each iteration step. This statement is documented in the runtime comparison for different models in Figure 3.20 on a single CPU Pentium4 computer with the clock speed of 3.2GHz and 512 Mb main memory. Obviously, the runtime of wrink3 is less than wrink2 around 29.28% for a perfect case and by 46.09% for an imperfect one. To sum up, the proposed model wrink3 can very well approximate the solutions of the consistently linearized model wrink2 by at the same time considerably reduced computational costs.

3.5.3 An annulus membrane under torsion

An annulus membrane given in [Rod91] is repeated here to compare results of the presented wrinkling model with those reported in that work. A membrane is attached to a rigid disk at the inner edge and a fixed guard ring at the outer edge as illustrated in Figure 3.21. The inner rigid disk is rotated counter clockwise until 10° is reached. The outer radius is 12.5 m while the inner one is 5.0 m. According to [Rod91], the membrane has a normalized thickness of 1.0 m. For the isotropic case, the Elasticity modulus E is 1.0e+5 Pa and Poisson's ratio ν is specified to 0.45. For the orthotropic case, the annulus membrane from the isotropic case is reused, but all dimensions are scaled down to centimetre. The orthotropic PVC coated polyester TYP I EH 2158, L1/1 from [MR95] is chosen for the linear orthotropic model from [LAL01] which is rewritten in eq. (3.107), where $\nu_{12}E_1 = \nu_{21}E_2$ and G=0.385e+5 Pa. The first fiber direction is assumed to coincide with $\mathbf{e}_1$ in the undeformed mesh with material parameters given in table 3.5. In both cases, the membrane is discretized by 200 bilinear quadrilateral membrane elements with four integration points each and analyzed by a nonlinear static analysis.

$$\begin{bmatrix} S^{11} \\ S^{22} \\ S^{12} \end{bmatrix} = \begin{bmatrix} 1/E_1 & -\nu_{12}/E_2 & 0 \\ -\nu_{21}/E_1 & 1/E_2 & 0 \\ 0 & 0 & 1/\mathrm{G} \end{bmatrix}^{-1} \cdot \begin{bmatrix} E_{11} \\ E_{22} \\ 2E_{12} \end{bmatrix} \tag{3.107}$$

Table 3.5: Material properties of the orthotropic PVC coated polyester TYP I EH 2158, L1/1membrane.

Thickness, $t(cm)$	1.0
Young's Modulus in $\mathbf{e}_1$ direction, $E_1(N/cm)$	3827.0
Young's Modulus in $\mathbf{e}_2$ direction, $E_2(N/cm)$	1926.0
Poisson's ratio, ν_{12}	0.13
Shear modulus, G (N/cm)	100.0
Density, $\rho(g/m)$	774.0
Prestress, $S_{pre}(N/cm)$	1.0e-6
Allowable compressive stress $S_{alw}(N/cm)$	-1.0e-4

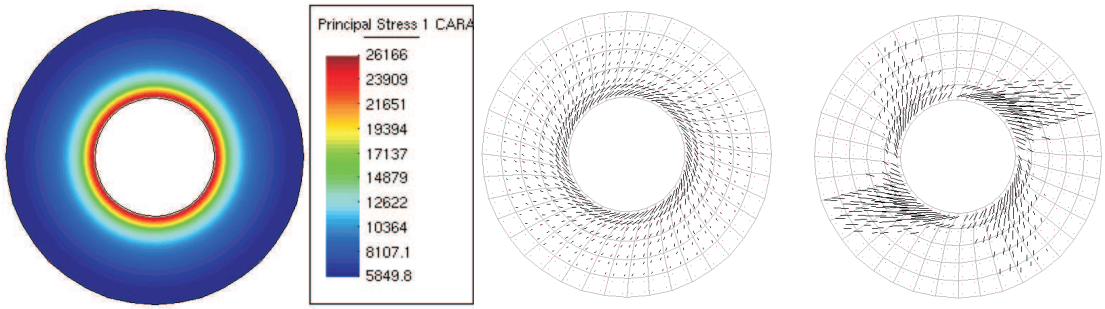

Figure 3.22: Stress distribution of the annulus membranes under specified torsion for (a) isotropic material: maximal principal stresses (b) wrinkle trajectories for isotropic material and (c) wrinkle trajectories for orthotropic material.

For the isotropic case, wrinkles develop uniformly except for the taut zone near the outer edge. The distribution of the principal stresses in Figure 3.22(a) experiences rotational symmetry of the major principal stress with the maximum value 26,166 Pa within the high concentration zone near the inner edge. This result is compatible with those reported in [LAL01, Rod91]. Elimination of artificial compressive stiffness causes redistribution of the stress field within the membrane which is noticeable by the increase of the maximal principal stress. Moreover, numerous wrinkles are developed near the highly distorted inner edge as seen in Figure 3.22(b). From Figure 3.23, one can conclude that all wrinkling models escalate the number of iterations compared to the pure membrane elements without wrinkling model (wrink0). Amongst all three wrinkling models, the rate of convergence in case of wrink2 is superior to the others while wrink1 requires the highest number of iterations to achieve equilibrium. However, due to the return mapping algorithm, wrink2 requires longer computation in each iteration step as one conceives the idea from a comparison on the runtime in Figure 3.24. The runtime of wrink3 is around 16.07% less than wrink2 with the same hardware of the section 3.5.2.

For the orthotropic case in Figure 3.22(c), wrinkle trajectories are not uniform as in the isotropic case, but rather concentrated along the direction of the stiffer fiber due to the higher

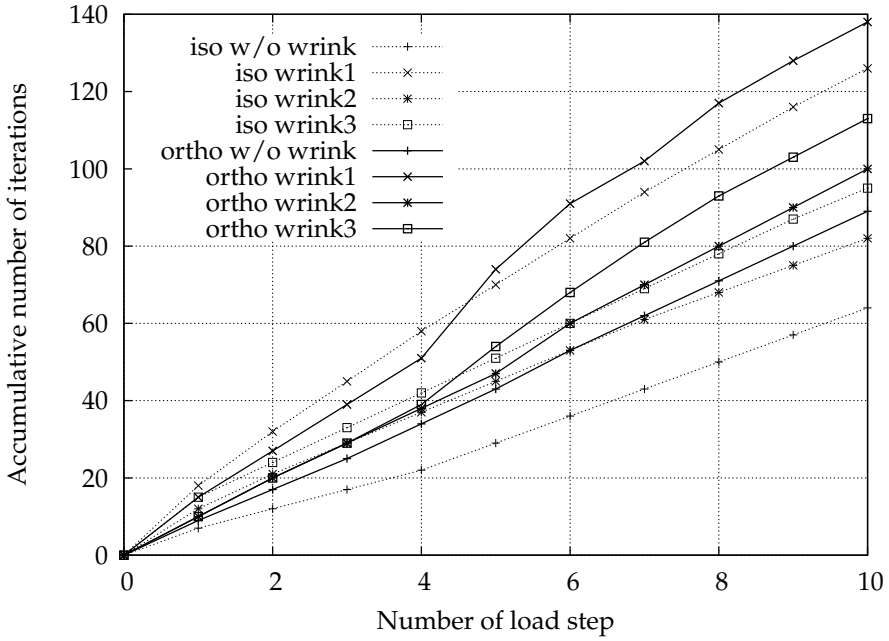

Figure 3.23: Comparison of accumulative number of iterations for isotrotpic and orthotropic materials.

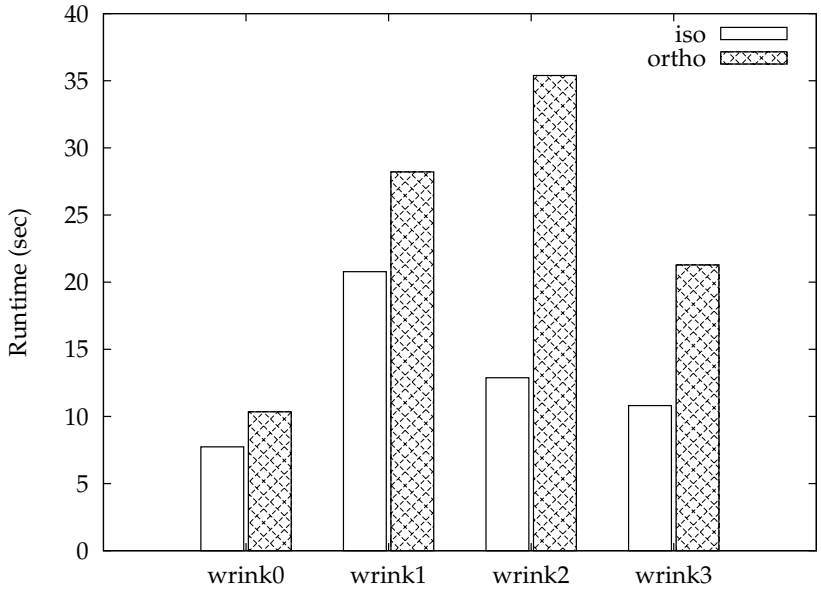

Figure 3.24: Comparison of runtime for isotrotpic and orthotropic materials.

uniaxial stress in this direction. Similarly, the maximal stress concentrates near the inner edge with the maximum of 946.72 N/cm along the direction of the stiffer fibre, i.e. the horizontal direction. When looking at the accumulative number of equilibrium iterations in Figure 3.23, we observe similar results to those of the isotropic case. However, the jump at load step 5 is attributed to the non uniform shear deformation of the orthotropic material whose

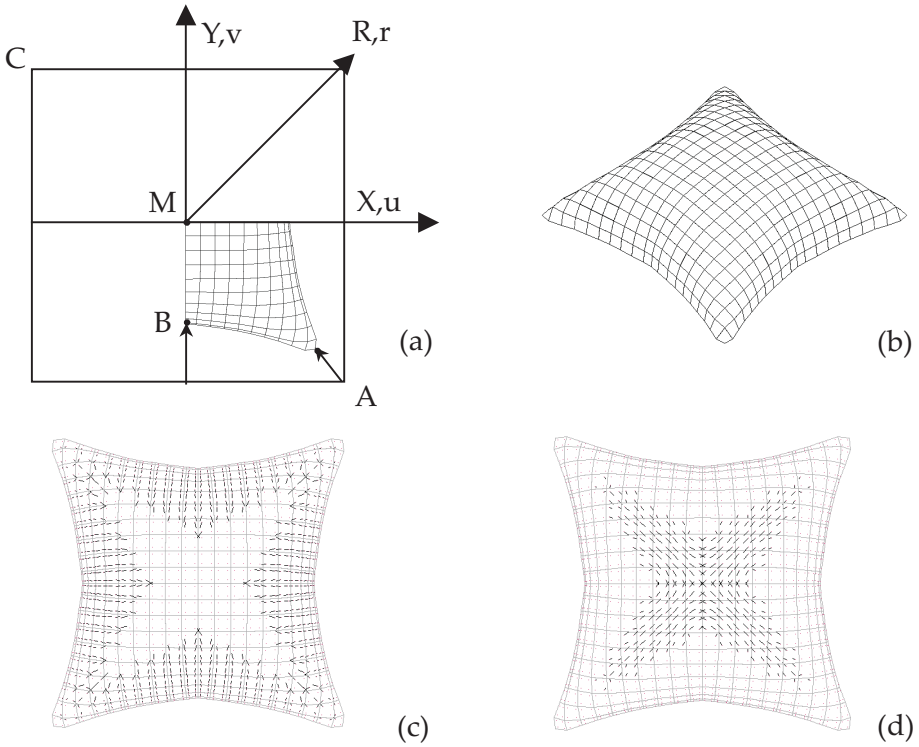

Figure 3.25: Illustration of the fully inflated square airbag for (a) coordinate system and geometry (b) isometric view of the inflated airbag (c) wrinkle trajectories and (d) taut area.

stiffness and poisson's ratio are different in each direction. The non uniform shear deformation causes difficulties to define the exact wrinkling direction for the algorithm mentioned in section 3.2.2, and as a result, the number of equilibrium iterations to achieve convergence is higher. By supplanting wrink2 by wrink3, a 39.87% reduction in the runtime is observable in Figure 3.24.

3.5.4 Inflation of an isotropic airbag

In this example, an application of the proposed wrinkling model (wrink3) under the deformation-dependent forces [HS05a, JWB07, JWB08a] is investigated. Initially, a flat square isotropic membrane is gradually inflated by a constant pressure until its magnitude reaches 5 kPa (see Figure 3.25(a) and (b)). Due to its symmetry, only a quarter of the square air bag is simulated. An extension of this example to an orthotropic material is reported in [JWB09b]. Bilinear quadrilateral membrane elements are used for the spatial discretization with the nonlinear static solution technique. According to [CS88, KI99, Zie01], this problem is initially discretized with 16 elements, and then, the refinement ascends consecutively to 25, 64 and 100 elements.

With the wrinkling model (wrink3), artificial compressive stresses are dispersed from the membrane where the state of uniaxial tension is demonstrated by the wrinkle trajectories in Figure 3.25(c). Nearby, Figure 3.25(d) exhibits taut zone (biaxial tension) which is

Table 3.6: Material properties for the square airbag example.

thickness, $t(cm)$	0.06
Lenght(AC) (cm)	120
Young's Modulus, $E(kN/cm^2)$	58.7
Poisson's ratio, ν	0.4
Allowable compressive stress $S_{alw}(N/m^2)$	-1.0e-4

Table 3.7: Comparison of results from literature and present work on different level of mesh refinement.

No.element	16				25			64				100	
P=present work	[CS88]	[Zie01]	[KI99]	P	[CS88]	[KI99]	P	[CS88]	[Zie01]	[KI99]	P	[Zie01]	P
$w_M(cm)$	20.90	21.50	21.50	21.49	21.70	21.60	21.59	20.50	21.60	21.40	21.657	21.60	21.669
$r_A(cm)$	5.70	9.70	6.08	9.72	6.30	5.94	8.82	4.70	7.40	5.80	7.38	6.90	6.92
$u_B(cm)$	10.18	12.00	11.70	12.02	11.03	11.70	12.15	13.01	12.20	11.90	12.27	12.30	12.37
$\sigma_M(kN/cm^2)$	0.34	0.36	-	0.324	0.35	-	0.36	0.35	0.37	-	0.38	0.37	0.3814

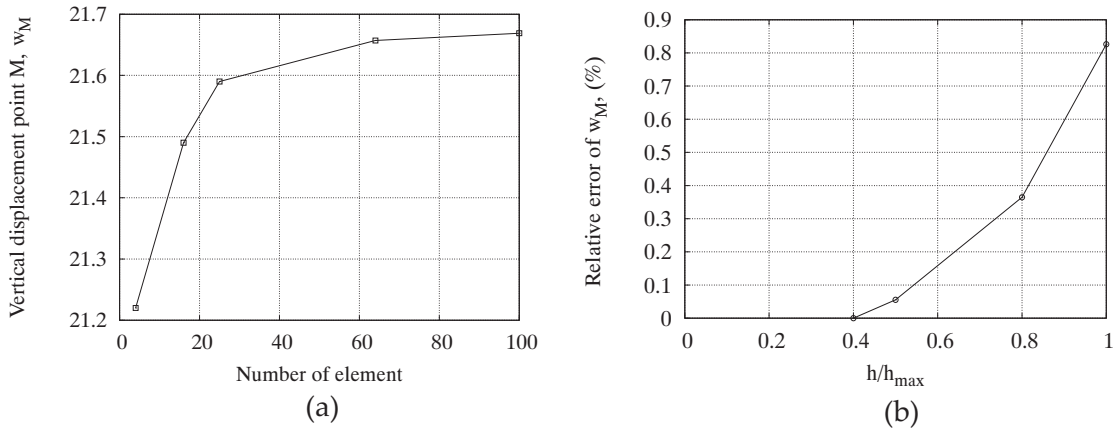

Figure 3.26: Vertical displacement of point M.

located along both diagonals of the airbag. This result is compatible with the wrinkle zone observed in the experiments from [CS88]. In Table 3.7 and Figure 3.26(a), the vertical displacement of point M converges to 21.669 cm while the maximal principal stress reaches to 0.3814 kN/cm^2 during mesh refinement. These results agree with those of other groups. In other words, the movement of the membrane is impeded by the artificial compressive stiffness. In Figure 3.26(b), relative error of the vertical displacement at point M versus the relative element size is plotted. From this Figure, one can deduce that the wrinkling model maintains the convergence rate of $O(h^2)$ as the size of element h is reduce by $1/2$, the error is decreased by the factor of $1/4$. It is noteworthy to mention that the result from this example is closely identical to that of wrink2 which is not shown here.

Table 3.8: Material properties for Kapton membrane under 4 corner tension.

Thickness, $t(\mu m)$	25
Young's Modulus, $E(N/mm^2)$	3500
Poisson's ratio, ν	0.31
Density, $\rho(kg/mm^3)$	1.5e-6
Prestress, $S_{pre}(N/mm^2)$	(1.0e-6, 1.0e-6,0.0)
Allowable compressive stress $S_{alw}(N/mm^2)$	-1.0e-6

3.5.5 A Square membrane under corner loads

The last example demonstrates a capability of the proposed model to investigate the evolution of wrinkles in a flat square isotropic membrane. Besides, numerical results will be compared with results from the experiment by Wong and Pellegrino [WP06c]. An extension to an orthotropic material is straightforward. This square membrane is pulled at its four corners by two diagonal pairs of equal and opposite forces (T1 and T2 in Figure 3.27). Geometry, material and load parameters, shown in Figure 3.27, are complied with those given in [WP06c] for a comparison purpose. All edges are reinforced with cable elements just to prevent convergence problem due to unidentified boundary conditions. To prevent rigid body motions, the center point of this membrane is fixed and the out-of-plane displacement (z direction) at all edges is restrained. This membrane is discretized by 900 bilinear quadrilateral membrane elements with three translational dof per node and analyzed by a nonlinear static analysis. In this example, the loading process is subdivided into three stages. In the first stage, the square flat membrane is isotropically prestressed to create initial stiffness within the flat membrane. In the second phase, a pair of symmetric loads T1=T2=5N are prescribed at all corners. Then, in the third stage T2 is maintained constant at 5N while T1 is increased up to 20 N with the final load ratio of T1/T2=4. The last two load stages are carried out as a follow-on to the first stage according to those defined in [WP06c].

In Figure 3.28, wrinkle trajectories are plotted with different load ratios (T1/T2). As depicted from Figure 3.28(a), the wrinkle trajectories are symmetric and concentrated near each corner of the membrane as long as the load ratio is unity. When T1 is increased to 10 N while T2 is kept constant, the wrinkle trajectories are intensified and head towards the major diagonal which is the direction of the stronger applied force T1. Later, with increased load ratio T1/T2, more wrinkles are developed along the major diagonal. Finally, when the load ratio reached 4 and T1 arrived 20 N, wrinkles are highly concentrated along the major diagonal whereas the wrinkles in the minor diagonal, i.e. along the direction of T2, are also increased. All these results agree well with the thin shell solutions investigated in [WP06c]. Thus, this evidence substantiates the potential of this model to detect roughly wrinkled zones on a macroscopic level without the need to resolve them in details. In the following, the modified stress field due to the wrinkling model is explained. In Figure 3.28(a)-(d), the maximal principal stress within the membrane is shown with increased load ratio T1/T2. When T1 is raised, the magnitude of the uniaxial tensile stress along the major diagonal is escalated. From the contour plot, the magnitude of the major principal stress is in the

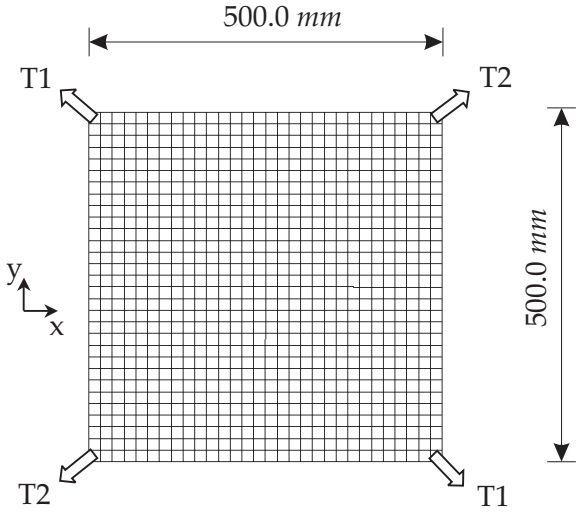

Figure 3.27: Geometry and load condition for the square Kapton© membrane.

range of 0 to 6 N/mm^2 which is comparable to that of [WP06c]. One can conclude that the modified stress field caused by the wrinkling model agrees quite well with the thin shell solution.

On the other hand, the minimal principal stress is an outcome of a specific allowable compressive stress. Since a nearly nonnegative stress field is expected in reality, a reasonable value for the allowable compressive stress requires further experiments. However, the contour plot of the minimal principal stress in Figure 3.28(a)-(d) within the range between 1.0 and -2.0 N/mm^2 shows a qualitative agreement to that in [WP06c]. When the load ratio is unity, the minimal principal stress field is axi-symmetric. In that case, the membrane is occupied by wrinkles (see Figure 3.28(a) except for the circular taut (bi-axial tension) zone radiated from the center. When T1 is increased, the taut zone is bisected along the major diagonal in Figure 3.28(b). With increasing load ratio, both taut zones are stretched in parallel to the major diagonal with contraction in the direction of the minor diagonal (see Figure 3.28(c) and 3.28(d)).

3.6 Summary

The projection-based wrinkling model is derived on the basis of a projection method which projects the original total strain, determined by the kinematic relationship, onto the elastic strain space and neglects the influences of the zero energy wrinkling strain part. The model has a potential to suppress artificial compressive stresses within the membrane. As a result, the wrinkling model embedded membrane has more freedom to move with less constraints from the artificial stiffness.

This model improves the simplified wrinkling model in [JWB08b] by augmenting the incremental term of the constitutive tensor, and as a consequence, the rate of convergence is improved while the number of equilibrium iterations is reduced. Thus the convergence

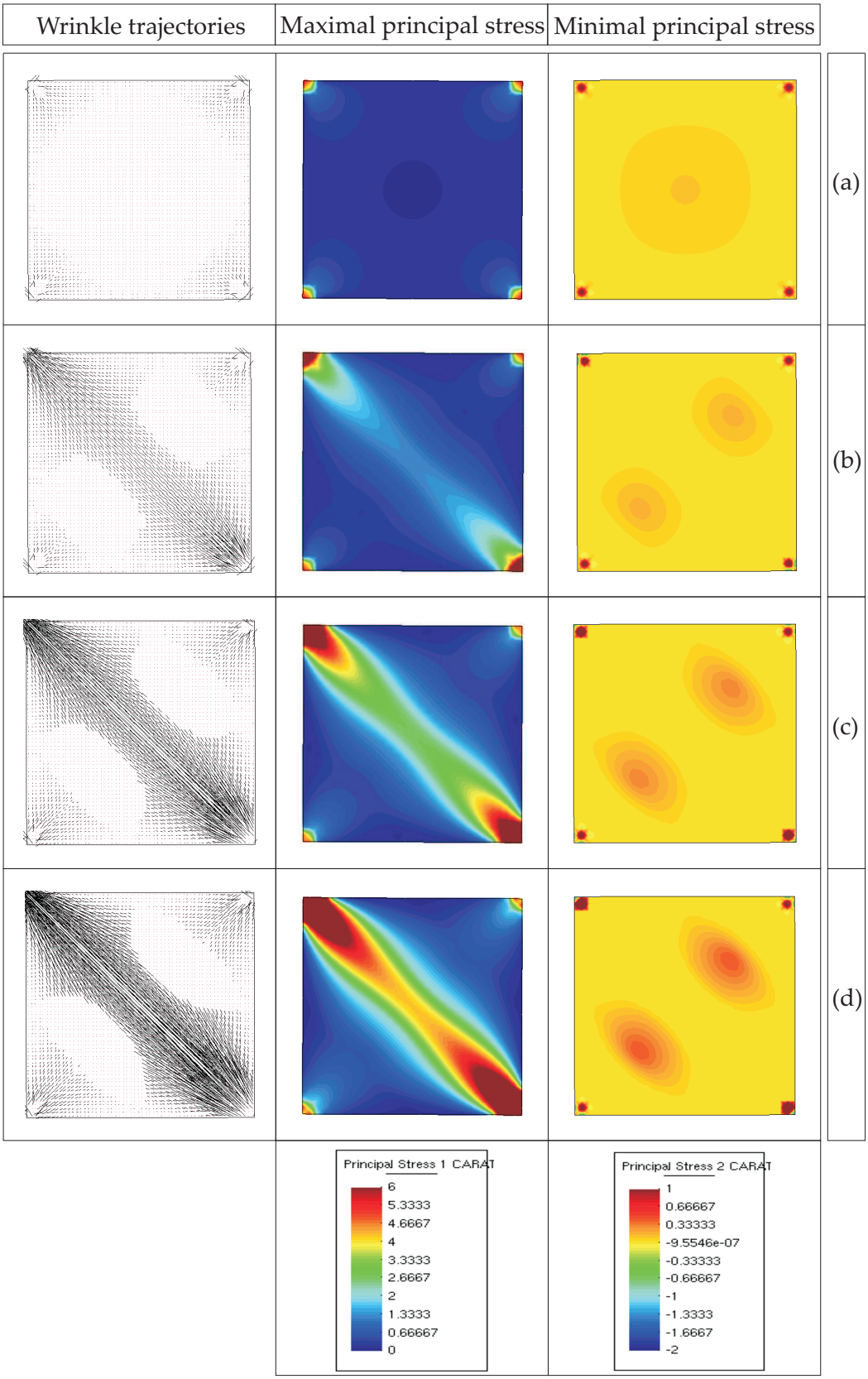

Figure 3.28: Comparison of the wrinkle trajectories, the maximal and the minimal principal stress with wrinkling model for different load ratio (T1/T2) for (a) T1/T2=1 (b) T1/T2=2 (c) T1/T2=3 and (d) T1/T2=4.

problem found due to the lack of linearization in [JWB08b] is remedied in an approximate way and a smoother transition from the elastic (i.e., taut) to plastic (i.e., wrinkled) state is achieved. Compared with the plasticity analogy wrinkling model in [JWB09a], the projection-based wrinkling model is deemed as an approximate version since the proposed model is less accurate and it requires a higher number of equilibrium iteration steps to reach the equilibrium. However, without the return mapping algorithm as in the plasticity analogy model the projection-based model requires less computational time to cope with fictitious material nonlinearity. Hence, this model fulfills the aim of a balance between the accuracy and simplicity for both isotropic and orthotropic materials. The excellent performance of the newly developed model is demonstrated with convincing numerical results and the corresponding runtime.

As a limit of use, both models are applicable only within the range of the small elastic strain and it is not recommended for large elastic strain deformation due to the assumption of an additive strain decomposition. On the other hand, this is an opportunity for further development as seen in the recent publication by Mosler [Mos08]. A reasonable choice of an allowable compressive stress S_{alw} requires further investigations for an insight into an actual compressive stiffness of each membrane material.

Chapter 4

Deformation-Dependent Forces for Inflatable Membranes

This chapter provides the finite element formulation of a class of deformation-dependent forces for inflatable membrane structures. Such important load case is prevalent in reality, e.g. wind, gas and fluid pressure. However, the deformation-dependent forces are usually neglected in computations; they are often replaced by other deformation-independent forces for the sake of simplicity. By doing so, one can neither monitor the actual characteristic of the problem nor rely on the obtained results. This chapter studies influences of the pressure of a gas and/or a fluid filled in an inflatable structure undergoing large deformation. In contrast to the assumption that the fluid and/or a gas filled in the chambers has constant pressure for a conventional *finite element analysis (FEA)*, this study reveals important features that the enclosed fluid and/or gas provides additional stiffness to the inflatable structure and the convergence rate is significantly improved by considering influences of the enclosed fluid and/or gas.

4.1 Inflatable membrane structures

Inflatable structures have gained more and more popularity in recent years for a wide variety of architectural and engineering applications (see Figure 4.1), for instance, the translucent roof spanning over a vast area, foldable and/or portable structures, smart and adaptive structures, protective equipments, extremely light vehicles, balloons and light air ships, etc.

From the mechanical point of view, an inflatable membrane structure can be considered as a gas and/or fluid supported membrane structure. The interaction between the filled fluid and its surrounding membranes plays a key role for whole stiffness of this structure, in particular for an inflatable membrane with a highly-pressurized gas or a high density fluid. This interaction can be directly computed by means of a complete modeling of both solid and fluid domains. However, the method leads to a coupled problem between the fluid and membrane under large deformation which can be solved by employing state of the art techniques. Both fields are coupled at their interface where information from one field is transfered to another, while at the same time, compatibility conditions are not violated. Despite a realistic and reliable approach, the computation is rapidly becoming prohibitive. Alternatively, for a preliminary investigation, modeling of the fluid domain

is avoidable by an introduction of the deformation-dependent forces, which always act in the perpendicular direction to a body coming into contact with the fluid. More precisely, the pressure of an enclosed fluid is varied along the change of its volume which is directly linked to deformation of the surrounding membrane. Influences of fluid pressure on the membrane is determined by surface integrals over the interface area where the fluid and membrane touch each other. As a result, the pressure exerted on the membrane surface can be computed analytically with the mesh-free description on the fluid domain. By doing so, complexities in fluid-membrane interface coupling is considerably alleviated. This simple idea is useful in various applications, in particular, for a static or quasi-static case as reported by Rumpel and Schweizerhof [RS03]. A comprehensive study of the deformation dependent pressure load under special boundary conditions based on FEM can be found in Schweizerhof and Ramm [SR84]. Simo *et al.* [STW91] proposed an axis-symmetric formula for pressure boundary loading. Later, Wriggers [Wri01] provides a general expression for the deformation-dependent forces.

Typically, the fluid pressure can be related to the variation in fluid volume by a suitable state equation. For the enclosed membrane of interest, special boundary conditions mentioned in [SR84] are utilized to preclude the skew symmetric boundary terms with the aim at a symmetric load stiffness matrix based on the pure-displacement description. Assembling this symmetric load stiffness matrix results in the symmetric system stiffness matrix which indirectly indicates conservativeness of the system. This load stiffness matrix is composed of various terms. Some of them are attributed to the change in direction of pressure forces acting on the membrane surface while the others are caused by the change in pressure magnitude of the enclosed fluid. Later, this load stiffness matrix is appended to the stiffness matrices mentioned in eq. (2.106). This merging yields in many cases a fully-populated system matrix. With the help of the Woodbury's formula [Woo50], the inverse of this fully-populated system matrix is achieved via an update scheme for each update tensor without additional factorization on the system matrix. In addition, a modified arclength method is introduced for a quasi-static case to identify the critical load of a fluid-filled membrane.

Within this chapter, we restrict ourselves to an inflatable membrane filled with either an incompressible fluid with free surface or a gas or both of them in each chamber. For further reading, interested readers can consult [Rum03, RS04, HS08b]. The objective of this chapter is to investigate influences of the variation in volume, or more precisely, pressure of an enclosed fluid and/or a gas on the stiffness of the surrounding membrane with the focus on the coupled stiffness between the enclosed fluid and/or gas and its surrounding membrane. Both time-independent and time-dependent problems are examined, while numerical examples demonstrate not only efficiency of the model but also the necessity to consider the volume (pressure) variation in addition to the change in surface normal vector. This study reveals an important feature that the pressure of an enclosed fluid provides additional stiffness to the inflatable structure, analogous to a membrane on elastic springs. The result of this study emphasizes the necessity to take into account influences of the enclosed fluid volume-pressure, usually neglected, to the total stiffness of an inflatable membrane, especially in case of a highly pressurized gas and a high density fluid. Moreover, an inclusion of this enclosed volume effects significantly improves the convergence rate.

As a closing remark, we concisely outline this chapter. At first, the next section pro-

Figure 4.1: Applications of inflatable structures (a) hot air ballon (http://images.google.de) (b) rescue shelter supported by inflatable beams (http://www.gumotex-rescue-systems.cz) (c) pneumatic membrane roof for Eden Project, Cornwall, UK (d) space communication antenna with 6.4 m inflatable ring and 5 m inflatable reflector (http://www.abc.net.au) (e) inflatable packaging (http://www.inflatablepackaging.com) (f) air cushions cladding of the Alliance arena (http://www.allianz-arena.de) and (g) large span air house (http://images.google.de)

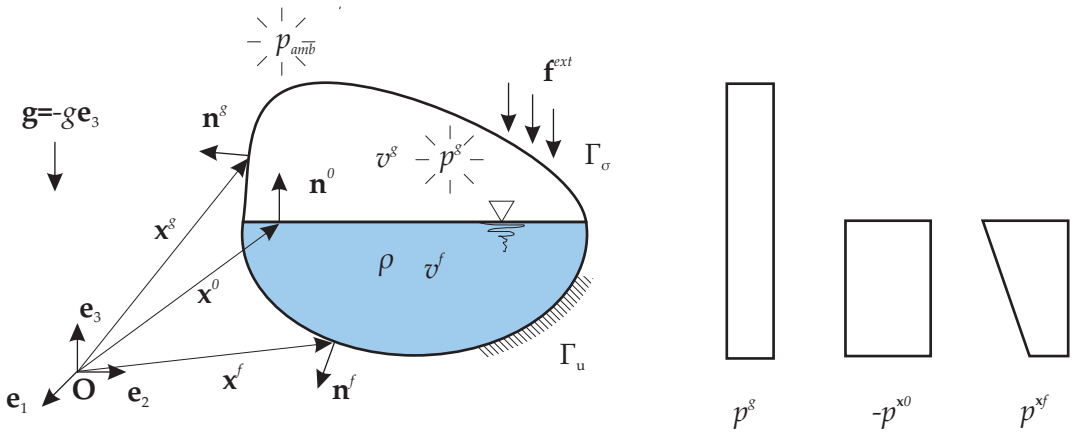

Figure 4.2: An inflatable membrane filled with incompressible fluid and gas.

vides a clear definition of pressure loads. Then, the basis for displacement-based FEM is derived based on the PVW of the pressure forces for a curved surface in the three-dimensional space. Later, linearization is performed to create the incremental equilibrium equations. By discretization, an algebraic system of equations is available for the Newton-type solution method. At this point, there exist a load-stiffness matrix caused by the deformation-dependent forces from the gas and/or fluid within each enclosed chamber. By investigating symmetry of the load-stiffness matrix, the conservativeness of these pressure forces is approved. Note that this work does not intend to prove the existence of potential, in general, the internal energy and gravitational potential, of the system, see e.g. [Buf84, Sew67]. Then a special solution algorithm by the arclength method is introduced for a quasi-static analysis, before an extension to time-dependent problems with the Generalized-α method (GEN$_\alpha$) and the Generalized Energy Momentum Method (GEMM). Eventually, the chapter is concluded by chosen numerical examples and summary.

4.2 Governing equations of inflatable membranes coupled with enclosed fluid

For an incompressible fluid with free fluid surface and overpressure gas as seen in Figure 4.2, pressure at the wet membrane surface below the free fluid surface is stated by:

$$p^f = -p^{\mathbf{x}^0} + p^{\mathbf{x}^f} + p^g; \quad p^{\mathbf{x}^0} = \rho \mathbf{g} \cdot \mathbf{x}^0; \quad p^{x^f} = \rho \mathbf{g} \cdot \mathbf{x}^f; \quad p^g = \frac{P_0 V_0^k}{V^k}. \tag{4.1}$$

Referred to the reference level at the origin $\mathbf{0}$ of the Cartesian coordinate in Figure 4.2, $p^{\mathbf{x}^0}$ is the pressure due to the fluid depth at the free fluid surface above the reference level. $p^{\mathbf{x}^f}$ is the pressure at a point within the fluid domain due to the local fluid depth measured from the reference level. Subtracting $p^{\mathbf{x}^0}$ from $p^{\mathbf{x}^f}$ of the same position yields for that position the hydrostatic pressure caused by the enclosed fluid within the membrane. Moreover, p^g is the gas pressure and $\mathbf{n}^0$ is an outward unit normal vector at the free fluid surface while $\mathbf{n}^g$ and $\mathbf{n}^f$ are ones above and below the free fluid surface, respectively.

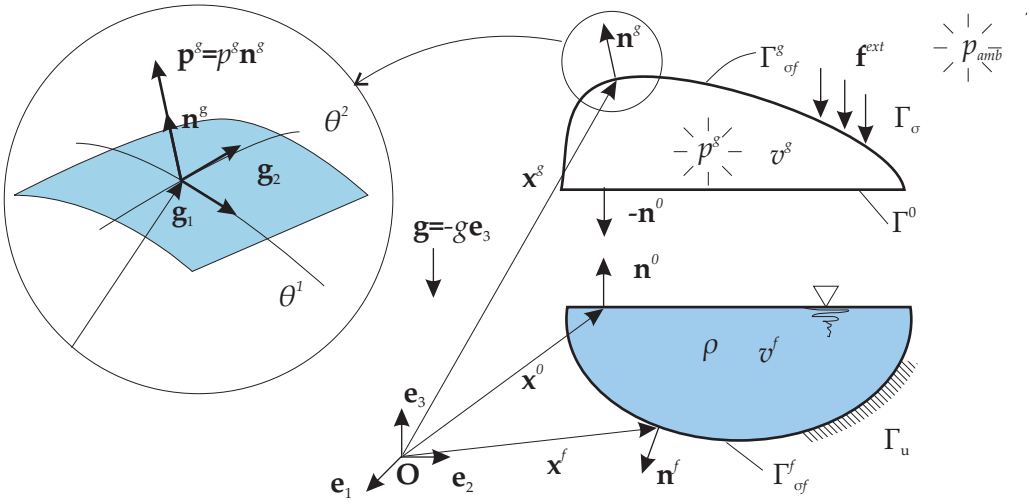

Figure 4.3: Definition of pressure forces upon a membrane surface.

4.2.1 Virtual work equation

Within this section, the virtual work of the deformation-dependent forces for a single chamber i is introduced. An extension to the case of multi chambers is mentioned later in section 4.5.2 which is considered as a sum of all individual chamber filled with gas and/or fluid $\sum_{i=1}^{n_b}$ where n_b is the number of all chambers filled with gas and/or fluid.

As mentioned in eq. (2.45) the total virtual work is composed of the inertial force contribution δW_{dyn}, the internal force contribution δW_{int} and the external force contribution δW_{ext} such that $G(\varphi_t, \delta\varphi) = -\delta W = -\delta W_{dyn} - \delta W_{int} - \delta W_{ext} = 0$. This section extensively explains the deformation-dependent contribution of the external virtual work $\delta W_{fol} \in \delta W_{ext}$ which is mentioned in section 2.1.6.1. According to the problem at hand in Figure 4.2, the follower force virtual work consists of a contribution from gas δW^g_{fol} and another contribution from fluid δW^f_{fol}. With the definition of pressure given in eq. (4.1), the virtual work from deformation-dependent forces of an arbitrary state of current enclosed volume $v(\mathbf{x})$ can be described by means of the corresponding volume-dependent, or in other words, deformation-dependent fluid pressure $p = p(v(\mathbf{x}))$ which is exerted perpendicularly to the current interface area $a(\mathbf{x})$ between fluid and membrane, viz.

$$\delta W_{fol} = \int\limits_{\varphi_t\left(\Gamma_{\sigma f}\right)} p\mathbf{n}\cdot\delta\varphi da = \overbrace{\int\limits_{\varphi_t\left(\Gamma^g_{\sigma f}\right)} p^g\mathbf{n}^g\cdot\delta\varphi da}^{\delta W^g_{fol}} + \overbrace{\int\limits_{\varphi_t\left(\Gamma^f_{\sigma f}\right)} p^f\mathbf{n}^f\cdot\delta\varphi da}^{\delta W^f_{fol}} \tag{4.2}$$

where $\Gamma_{\sigma f}$ is the reference interface area of $a(\mathbf{x})$ with the current position vector $\mathbf{x}\left(\theta^1,\theta^2\right)$ to the mid-plane of the membrane, the outward unit normal vector $\mathbf{n} = \mathbf{x}_{,\theta^1}\times\mathbf{x}_{,\theta^2} / \|\mathbf{x}_{,\theta^1}\times\mathbf{x}_{,\theta^2}\|$ and a current differential interface area $da = d\theta^1 d\theta^2 \|\mathbf{x}_{,\theta^1}\times\mathbf{x}_{,\theta^2}\|$. Thus, eq. (4.2) can be rewritten to

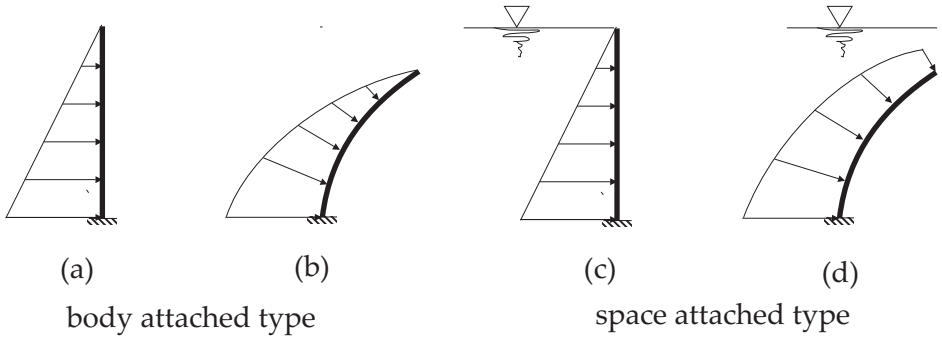

Figure 4.4: Illustration of two different types of deformation-dependent pressure forces: body attached type (a) undeformed configuration (b) deformed configuration and space attached type (c) undeformed configuration (d) deformed configuration.

$$\delta W_{fol} = \int_{\theta^2}\int_{\theta^1} p\mathbf{n}^* \cdot \delta\varphi \; d\theta^1 d\theta^2 = \int_{\theta^2}\int_{\theta^1} p^g \mathbf{n}^{*g} \cdot \delta\varphi \; d\theta^1 d\theta^2 + \int_{\theta^2}\int_{\theta^1} p^f \mathbf{n}^{*f} \cdot \delta\varphi \; d\theta^1 d\theta^2 \tag{4.3}$$

with the nonnormalized surface normal vector $\mathbf{n}^* = \mathbf{x}_{,\theta^1} \times \mathbf{x}_{,\theta^2}$. Furthermore, for a proportional load case, one can describe the pressure magnitude p in eq. (4.2) by

$$p = \lambda \bar{p} \tag{4.4}$$

where $\bar{p} = \bar{p}(\mathbf{x}) = \bar{p}(\varphi_t(\mathbf{X}))$ stands for the load distribution over the current loaded surface a which depends on the coordinate of the current configuration $\mathbf{x} = \varphi_t(\mathbf{X})$ and λ is the load multiplier at each time step. Note that a positive value of p means that the pressure vector $\mathbf{p}$ points into the direction of the normal vector $\mathbf{n}$ at that position.

4.2.2 Definition of deformation-dependent forces

Before proceeding further, definition of the pressure forces $\mathbf{p} = p\mathbf{n}$ in eq. (4.2) must be clarified. Usually, the deformation-dependent pressure forces are classified w.r.t. their dependency on the state of current configuration due to the change in direction of the unit normal vector $\mathbf{n}$, magnitude of the pressure p and the current loaded area da. Figure 4.4 shows two distinct types of the deformation-dependent pressure forces: the body attached type and the space attached type.

4.2.2.1 Body attached deformation-dependent forces

The pressure magnitude p depends only on the coordinate of the reference configuration $\mathbf{X}$ while the normal vector $\mathbf{n}$ changes its direction along the deformation of structures which must be determined at the current configuration $\mathbf{x} = \varphi_t(\mathbf{X})$ as depicted in Figure 4.4 (a,b):

$$\mathbf{p} = p\mathbf{n}(\varphi_t(\mathbf{X})) \tag{4.5}$$

Table 4.1: Classification of thermodynamic process.

Isothermal process:	$dT = 0$	$p_1 V_1 = p_2 V_2$
Isobaric process:	$dp = 0$	$V_1/V_2 = T_1/T_2$
Isochoric process:	$dV = 0$	$p_1/p_2 = T_1/T_2$
Adiabatic process:	$dQ = 0$	$p_1 V_1^\kappa = p_2 V_2^\kappa$

4.2.2.2 Space attached deformation-dependent forces

As illustrated in Figure 4.4 (c,d), both the distribution of the pressure magnitude p and the normal vector $\mathbf{n}$ are functions of the current configuration $\mathbf{x} = \varphi_t(\mathbf{X})$:

$$\mathbf{p} = p(\varphi_t(\mathbf{X}))\,\mathbf{n}(\varphi_t(\mathbf{X})) \tag{4.6}$$

As mentinoned by Schweizerhof [SR84], most pressure load in reality can be identified as space attached type but they are often assumed to be body attached type for the sake of simplicity. However, such simplified analysis with the body attached type load must be handled with care due to the fact that the artificial nonsymmetry may emerge in stiffness matrices, or artificial flutter for the physical meaning. In the worst case, the analysis result is utterly inadmissible.

4.2.3 Constitutive equation of the enclosed fluid

In fact, the absolute pressure $p = p_{amb} + p_{gau}$ at any point within an enclosed fluid is a combination of the ambient pressure p_{amb} and the pressure difference or gauge pressure p_{gau}between the enclosed fluid and the surrounding pressure outside the enclosed fluid volume. In what follows, necessary background in thermodynamics will be introduced. From classical thermodynamics, e.g. [Kau02], the absolute value of the state variables is required in the equation of state, e.g. the thermal equation of state for an ideal gas is given by

$$pV = nRT \tag{4.7}$$

where V is the enclosed volume, n stands for number of moles (the number of atoms in exactly 12 g of the isotope ^{12}C is chosen as the standard, resulting in 6.02214e+23 molecules/mol), T is the absolute temperature (Kelvin, K), R is particular gas constant (R=287.15KJ/kgK for air) or in general a function of temperature. For further use in this work, assumptions for thermodynamics process of the enclosed volume are adopted: (i) The thermodynamic states are assumed in the state of equilibrium. (ii) State variables are constant over the whole enclosed volume. (iii) In an enclosed chamber filled by both gas and fluid, a unique part of fluid and a unique part of gas are contacted at an interface where the pressure of gas and fluid are in equilibrium $p^f = p^g$. In general, thermodynamic processes are classified as shown in Table 4.1 with a graphical illustration in Figure 4.5.

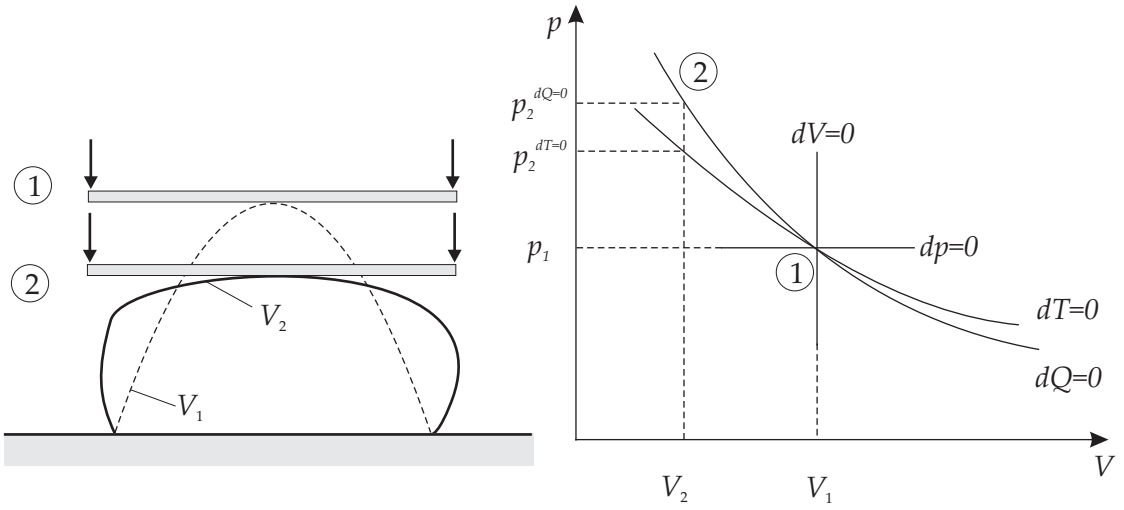

Figure 4.5: Comparison of different thermodynamics processes for an enclosed volume from [Rai03].

4.2.3.1 Pneumatic model under adiabatic state equation (Poisson's law)

A relationship between the gas pressure p^g and its corresponding state of volume v^g at an instance can be defined on the basis of the initial gas pressure P_0^g and the initial gas volume V_0^g according to the adiabatic state of thermodynamics such that

$$p^g = P_0^g \left(\frac{V_0^g}{v^g} \right)^{\kappa}. \tag{4.8}$$

For $\kappa = 1$, the simplified Boyle's law describing isothermal behavior of an ideal gas is recovered as mentioned by Bonet *et al.* [BWMH00] whereas the isentropic exponent $\kappa = 1.4$ is used for a two-atomic gas as mentioned by Baehr [Bae05] and Haßler and Schweizerhof [HS08b].

4.2.3.2 Hydraulic model (Hooke's law)

A relationship between the volume change of an enclosed fluid and the exerted fluid pressure can be determined by the Hooke's law:

$$p^f = \frac{V_0^f - v^f}{V_0^f} K \tag{4.9}$$

where V_0^f and v^f stand for the reference and current fluid volume, respectively while K is the bulk modulus of the fluid.

4.2.4 Geometric representation via boundary integral of an enclosed chamber

Furthermore, the enclosed volume of a chamber v_i is determined by

$$v_i = \frac{1}{3} \int_{\theta^2} \int_{\theta^1} \mathbf{x} \cdot \mathbf{n}^* d\theta^1 d\theta^2 \tag{4.10}$$

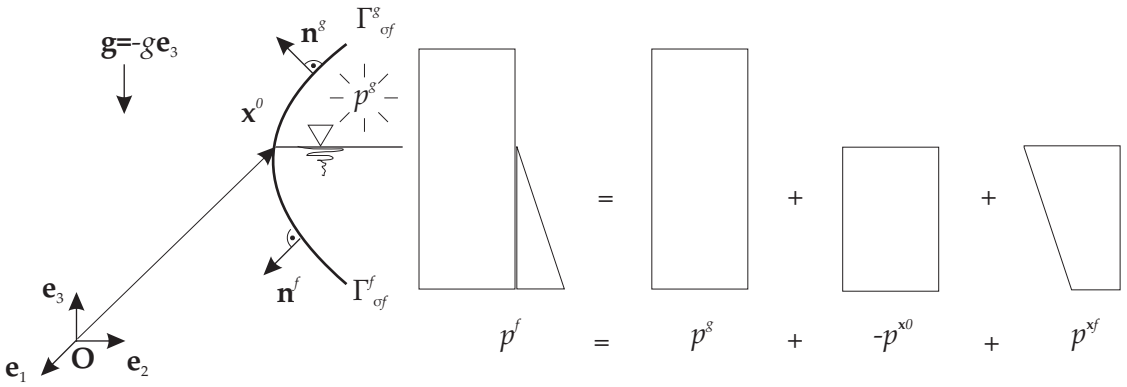

Figure 4.6: Gas pressure and hydrostatic pressure distribution in an enclosed chamber filled with gas and an incompressible fluid.

which is calculated over the membrane surface of the chamber i. The enclosed gas volume of a chamber v_i^g above the fluid free surface $\mathbf{x}_0$ in Figure 4.3 is determined by

$$v_i^g = \frac{1}{3}\int_{g\theta^2}\int_{g\theta^1} \mathbf{x}^g \cdot \mathbf{n}^{*g} d\theta^1 d\theta^2 - \frac{1}{3}\int_{0\theta^2}\int_{0\theta^1} \mathbf{x}^0 \cdot \mathbf{n}^{*0} d\theta^1 d\theta^2, \tag{4.11}$$

whereas the enclosed fluid volume of the same chamber v_i^g below the fluid free surface $\mathbf{x}_0$ is found via

$$v_i^f = \frac{1}{3}\int_{f\theta^2}\int_{f\theta^1} \mathbf{x}^f \cdot \mathbf{n}^{*f} d\theta^1 d\theta^2 + \frac{1}{3}\int_{0\theta^2}\int_{0\theta^1} \mathbf{x}^0 \cdot \mathbf{n}^{*0} d\theta^1 d\theta^2. \tag{4.12}$$

4.2.5 Derivation of virtual work for each specific case

With the help of eqs. (4.1) and (4.3), the virtual work equation of the deformation-dependent forces of an enclosed chamber filled with differnt combination of gas and an incompressible fluid is demonstrated within this section.

4.2.5.1 Incompressible fluid with free fluid surface and overpressure gas

In this case, the pressure at an arbitrary position of the membrane surface above the free fluid surface in Figure 4.6 is defined by the gas pressure p^g while the pressure at any point on the wet membrane surface below the free fluid surface is determined by p^f in eq. (4.1). Then, by substituting (4.1) into (4.3), the virtual work equation of the deformation-dependent forces of an enclosed chamber partially filled by an incompressible fluid with free fluid surface and overpressure gas is available:

$$\begin{aligned} -G_{fol}(\varphi_t^k, \delta\varphi) = \delta W_{fol} &= \int_{\theta^2}\int_{\theta^1} p\mathbf{n}^* \cdot \delta\varphi \, d\theta^1 d\theta^2 \\ &= \int_{g\theta^2}\int_{g\theta^1} p^g \mathbf{n}^{*g} \cdot \delta\varphi^g \, d\theta^1 d\theta^2 + \int_{f\theta^2}\int_{f\theta^1} \left(-p^{\mathbf{x}^0} + p^{\mathbf{x}^f} + p^g\right) \mathbf{n}^{*f} \cdot \delta\varphi^f \, d\theta^1 d\theta^2 \end{aligned} \tag{4.13}$$

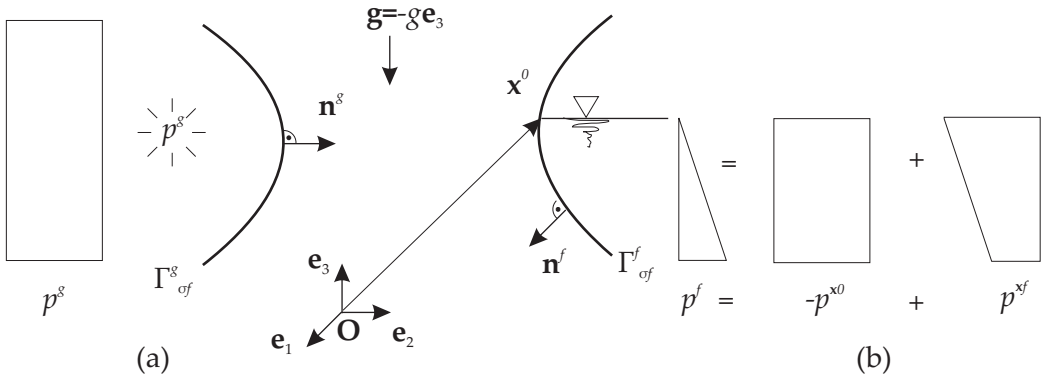

Figure 4.7: Pressure distribution on the membrane in case of (a) gas pressure distribution in an enclosed chamber filled with gas (b) hydrostatic pressure distribution in an enclosed chamber partially filled with an incompressible fluid.

4.2.5.2 Incompressible fluid with free fluid surface

Illustrated in Figure 4.7(b), the overpressure gas p^g is diminished and then eq. (4.13) is turned into

$$-G_{fol}(\varphi_t^k, \delta\varphi) = \int_{\theta^2}\int_{\theta^1} p\mathbf{n}^* \cdot \delta\varphi^f \, d\theta^1 d\theta^2 = \int_{f\theta^2}\int_{f\theta^1} \left(-p^{\mathbf{x}^0} + p^{\mathbf{x}^f}\right) \mathbf{n}^{*f} \cdot \delta\varphi^f \, d\theta^1 d\theta^2 \tag{4.14}$$

4.2.5.3 Pure gas filled chamber

From Figure 4.7(a), any arbitrary position of the membrane surface is under the enclosed gas pressure p^g and the virtual work equation in eq. (4.13) is reduced to

$$-G_{fol}(\varphi_t^k, \delta\varphi) = \int_{\theta^2}\int_{\theta^1} p\mathbf{n}^* \cdot \delta\varphi^g \, d\theta^1 d\theta^2 = \int_{g\theta^2}\int_{g\theta^1} p^g \mathbf{n}^{*g} \cdot \delta\varphi^g \, d\theta^1 d\theta^2. \tag{4.15}$$

4.3 Linearization

To solve the nonlinear system of equation in (4.3) with the Newton-Raphson algorithm mentioned in section 2.1.6.2, consistent linearization of the virtual work equation is required. With the help of (2.49), a linearized form of the virtual work equation for deformation-dependent forces in eq. (4.3) is expressed by

$$\mathbf{LIN}(G_{fol}(\varphi_t, \delta\varphi)) = G_{fol}(\varphi_t^k, \delta\varphi) + \Delta G_{fol}(\varphi_t^k, \delta\varphi) \tag{4.16}$$

where the directional derivative $\Delta G_{fol}(\varphi_t^k, \delta\varphi)$ is defined with

$$
\begin{aligned}
-\Delta G_{fol}(\varphi_t^k, \delta\varphi) &= \int_{\theta^2}\int_{\theta^1} \Delta p \mathbf{n}^* \cdot \delta\varphi \, d\theta^1 d\theta^2 + \int_{\theta^2}\int_{\theta^1} p \Delta \mathbf{n}^* \cdot \delta\varphi \, d\theta^1 d\theta^2 \\
&= \overbrace{\int_{^g\theta^2}\int_{^g\theta^1} \Delta p^g \mathbf{n}^{*g} \cdot \delta\varphi^g \, d\theta^1 d\theta^2 + \int_{^f\theta^2}\int_{^f\theta^1} \Delta p^f \mathbf{n}^{*f} \cdot \delta\varphi^f \, d\theta^1 d\theta^2}^{-\Delta G_{fol}^{\Delta p}} \\
&\quad + \overbrace{\int_{^g\theta^2}\int_{^g\theta^1} p^g \Delta \mathbf{n}^{*g} \cdot \delta\varphi^g \, d\theta^1 d\theta^2 + \int_{^f\theta^2}\int_{^f\theta^1} p^f \Delta \mathbf{n}^{*f} \cdot \delta\varphi^f \, d\theta^1 d\theta^2}^{-\Delta G_{fol}^{\Delta \mathbf{n}}},
\end{aligned} \tag{4.17}
$$

where $\Delta G_{fol}^{\Delta \mathbf{n}}$ represents linearization over the change of unit normal vector while $\Delta G_{fol}^{\Delta p}$ stands for linearization over the change in pressure.

With a close look at the boundary terms, Figure 4.8(a) introduces a boundary normal vector $\mathbf{n}^s$ and a boundary tangential vector $\mathbf{t}^s$ on the differential arclength ds of the boundary s for a chamber. From this Figure, the boundary normal vector $\mathbf{n}^s$ and the tangential one $\mathbf{t}^s$ on the boundary s can be defined on the Cartesian coordinate system such that

$$
\begin{bmatrix} \mathbf{n}^s \\ \mathbf{t}^s \end{bmatrix} = \begin{bmatrix} n_{\theta^1}^s & n_{\theta^2}^s \\ -n_{\theta^2}^s & n_{\theta^1}^s \end{bmatrix} \begin{bmatrix} \mathbf{x}_{,1} \\ \mathbf{x}_{,2} \end{bmatrix} \tag{4.18}
$$

4.3.1 Directional derivative of geometrical quantities

In this section, the directional derivative in the direction of the change in the configuration $\Delta\varphi$ of all geometrical quantities, required in subsequent sections, are provided.

4.3.1.1 Directional derivative of enclosed gas volume

First of all, the directional derivative of the enclosed gas volume for a chamber i in eq. (4.11) can be described by

$$
\begin{aligned}
\Delta v_i^g &= \frac{1}{3}\int_{^g\theta^2}\int_{^g\theta^1} \left[\Delta \mathbf{x}^g \cdot \mathbf{n}^{*g} + \mathbf{x}^g \cdot \Delta \mathbf{n}^{*g}\right] d\theta^1 d\theta^2 - \frac{1}{3}\int_{^0\theta^2}\int_{^0\theta^1} \left[\Delta \mathbf{x}^0 \cdot \mathbf{n}^{*0} + \mathbf{x}^0 \cdot \Delta \mathbf{n}^{*0}\right] d\theta^1 d\theta^2 \\
&= \Delta v_i^{g\Delta \mathbf{x}^g} + \Delta v_i^{g\Delta \mathbf{n}^{*g}} - \Delta v_i^{g\Delta \mathbf{x}^0} - \Delta v_i^{g\Delta \mathbf{n}^{*0}}.
\end{aligned} \tag{4.19}
$$

Note that the normal vector of the free fluid surface $\mathbf{n}^{*0}$ in Figure 4.2 is deformation-independent and it always points to the direction of the unit normal basis $\mathbf{e}_3$. From eq. (4.19), we can establish an equation

$$
\Delta v_i^{g\Delta \mathbf{n}^{*g}} = \frac{1}{3}\int_{^g\theta^2}\int_{^g\theta^1} \left[\mathbf{x}^g \cdot \Delta \mathbf{n}^{*g}\right] d\theta^1 d\theta^2 = \frac{1}{3}\int_{^g\theta^2}\int_{^g\theta^1} \mathbf{x}^g \cdot \left(\Delta \mathbf{x}_{,1}^g \times \mathbf{x}_{,2}^g + \mathbf{x}_{,1}^g \times \Delta \mathbf{x}_{,2}^g\right) d\theta^1 d\theta^2. \tag{4.20}
$$

With integration by part, eq. (4.20) is turned to

$$\begin{aligned}\Delta v_i^{g\Delta\mathbf{n}^{*g}} =& \frac{1}{3}\int\limits_{g\theta^2}\int\limits_{g\theta^1}\begin{bmatrix}-\mathbf{x}_{,1}^g\cdot\left(\Delta\mathbf{x}^g\times\mathbf{x}_{,2}^g\right)-\mathbf{x}^g\cdot\left(\Delta\mathbf{x}^g\times\mathbf{x}_{,21}^g\right)\\ -\mathbf{x}_{,2}^g\cdot\left(\mathbf{x}_{,1}^g\times\Delta\mathbf{x}^g\right)-\mathbf{x}^g\cdot\left(\mathbf{x}_{,12}^g\times\Delta\mathbf{x}^g\right)\end{bmatrix}d\theta^1d\theta^2\\ &+\frac{1}{3}\int\limits_{gs}\left[\mathbf{x}^g\cdot\left(\Delta\mathbf{x}^g\times\mathbf{x}_{,2}^g\,n_{\theta^1}^s\right)-\mathbf{x}^g\cdot\left(\Delta\mathbf{x}^g\times\mathbf{x}_{,1}^g\,n_{\theta^2}^s\right)\right]ds.\end{aligned}\tag{4.21}$$

By the help of eq. (4.18), one can reduce eq. (4.21) to

$$\begin{aligned}\Delta v_i^{g\Delta\mathbf{n}^{*g}} =& \frac{1}{3}\int\limits_{g\theta^2}\int\limits_{g\theta^1}\begin{bmatrix}-\mathbf{x}_{,1}^g\cdot\left(\Delta\mathbf{x}^g\times\mathbf{x}_{,2}^g\right)\\ -\mathbf{x}_{,2}^g\cdot\left(\mathbf{x}_{,1}^g\times\Delta\mathbf{x}^g\right)\end{bmatrix}d\theta^1d\theta^2+\frac{1}{3}\int\limits_{gs}\left[\left(\mathbf{x}^g\times\Delta\mathbf{x}^g\right)\cdot\mathbf{t}^{sg}\right]ds\\ =&\frac{2}{3}\int\limits_{g\theta^2}\int\limits_{g\theta^1}\Delta\mathbf{x}^g\cdot\mathbf{n}^{*g}d\theta^1d\theta^2+\frac{1}{3}\int\limits_{gs}\left(\mathbf{x}^g\times\Delta\mathbf{x}^g\right)\cdot\mathbf{t}^{sg}ds\end{aligned}\tag{4.22}$$

Furthermore, the last term in eq. (4.19) can be expanded to

$$\Delta v_i^{g\Delta\mathbf{n}^{*0}} =\frac{1}{3}\int\limits_{0\theta^2}\int\limits_{0\theta^1}\left[\mathbf{x}^0\cdot\Delta\mathbf{n}^{*0}\right]d\theta^1d\theta^2=\frac{1}{3}\int\limits_{0\theta^2}\int\limits_{0\theta^1}\mathbf{x}^0\cdot\left(\Delta\mathbf{x}_{,1}^0\times\mathbf{x}_{,2}^0+\mathbf{x}_{,1}^0\times\Delta\mathbf{x}_{,2}^0\right).\tag{4.23}$$

By applying the integration by part, eq. (4.23) is turned to

$$\begin{aligned}\Delta v_i^{g\Delta\mathbf{n}^{*0}} =& \frac{1}{3}\int\limits_{0\theta^2}\int\limits_{0\theta^1}\begin{bmatrix}-\mathbf{x}_{,1}^0\cdot\left(\Delta\mathbf{x}^0\times\mathbf{x}_{,2}^0\right)-\mathbf{x}^0\cdot\left(\Delta\mathbf{x}^0\times\mathbf{x}_{,21}^0\right)\\ -\mathbf{x}_{,2}^0\cdot\left(\mathbf{x}_{,1}^0\times\Delta\mathbf{x}^0\right)-\mathbf{x}^0\cdot\left(\mathbf{x}_{,12}^0\times\Delta\mathbf{x}^0\right)\end{bmatrix}d\theta^1d\theta^2\\ &+\frac{1}{3}\int\limits_{0s}\left[\mathbf{x}^0\cdot\left(\Delta\mathbf{x}^0\times\mathbf{x}_{,2}^0\,n_{\theta^1}^s\right)-\mathbf{x}^0\cdot\left(\Delta\mathbf{x}^0\times\mathbf{x}_{,1}^0\,n_{\theta^2}^s\right)\right]ds.\end{aligned}\tag{4.24}$$

Similarly, with the help from eq. (4.18), one can transform eq. (4.24) to

$$\begin{aligned}\Delta v_i^{g\Delta\mathbf{n}^{*0}} =& \frac{1}{3}\int\limits_{0\theta^2}\int\limits_{0\theta^1}\begin{bmatrix}-\mathbf{x}_{,1}^0\cdot\left(\Delta\mathbf{x}^0\times\mathbf{x}_{,2}^0\right)\\ -\mathbf{x}_{,2}^0\cdot\left(\mathbf{x}_{,1}^0\times\Delta\mathbf{x}^0\right)\end{bmatrix}d\theta^1d\theta^2+\frac{1}{3}\int\limits_{0s}\left[\left(\mathbf{x}^0\times\Delta\mathbf{x}^0\right)\cdot\mathbf{t}^{s0}\right]ds,\\ =&\frac{2}{3}\int\limits_{0\theta^2}\int\limits_{0\theta^1}\Delta\mathbf{x}^0\cdot\mathbf{n}^{*0}d\theta^1d\theta^2+\frac{1}{3}\int\limits_{0s}\left(\mathbf{x}^0\times\Delta\mathbf{x}^0\right)\cdot\mathbf{t}^{s0}ds.\end{aligned}\tag{4.25}$$

Substituting eqs.(4.22) and (4.25) in eq. (4.19) yields

$$\begin{aligned}\Delta v_i^g =& \int\limits_{g\theta^2}\int\limits_{g\theta^1}\Delta\mathbf{x}^g\cdot\mathbf{n}^{*g}d\theta^1d\theta^2-\int\limits_{0\theta^2}\int\limits_{0\theta^1}\Delta\mathbf{x}^0\cdot\mathbf{n}^{*0}d\theta^1d\theta^2\\ &\underbrace{+\frac{1}{3}\int\limits_{gs}\left(\mathbf{x}^g\times\Delta\mathbf{x}^g\right)\cdot\mathbf{t}^{sg}ds-\frac{1}{3}\int\limits_{0s}\left(\mathbf{x}^0\times\Delta\mathbf{x}^0\right)\cdot\mathbf{t}^{s0}ds}_{0}.\end{aligned}\tag{4.26}$$

Note that at the gas-free fluid surface interface in an enclosed chamber filled by both gas and fluid which is depicted in Figure 4.8(b), the boundary terms in eq. (4.26) cancel each other due to following reasons:

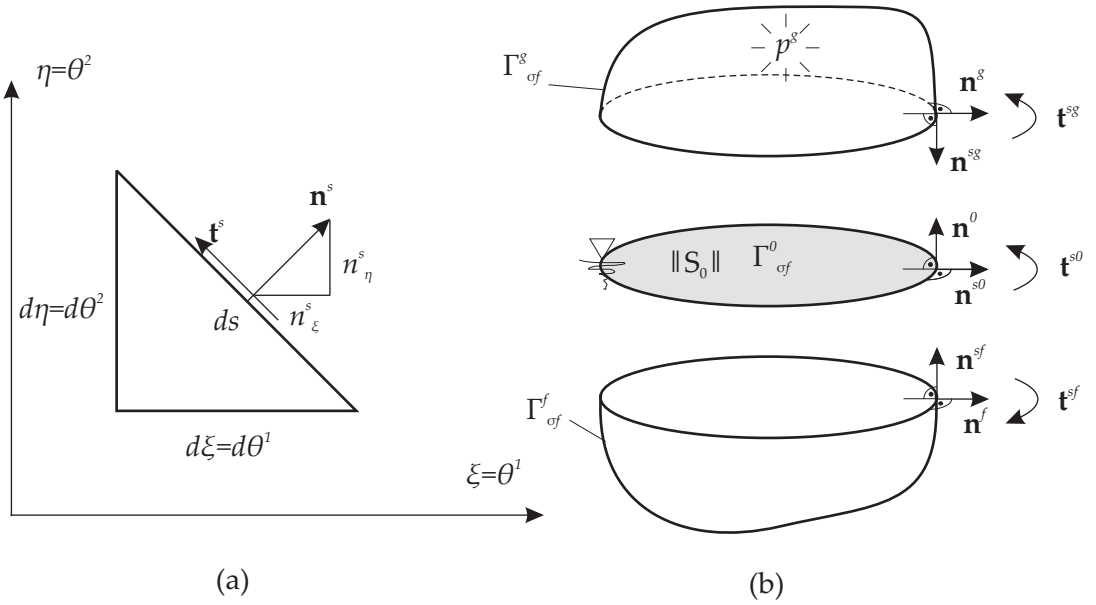

Figure 4.8: Illustration of the boundary normal vector $\mathbf{n}^s$ and the boundary tangential vector $\mathbf{t}^s$ (a) for general definition and (b) on differnt parts–gas $\Gamma^g_{\sigma f}$, fluid $\Gamma^f_{\sigma f}$ and free surface $\Gamma^0_{\sigma f}$–of a chamber partially filled with gas and fluid.

- ◇ The gas boundary normal vector $\mathbf{n}^{sg}$ and the free fluid surface boundary normal vector $\mathbf{n}^{s0}$ are perpendicular to each other (see Figure 4.8(b))
- ◇ The gas boundary tangential vector $\mathbf{t}^{sg}$ and the free fluid surface boundary tangential vector $\mathbf{t}^{s0}$ point into the same directions $\mathbf{t}^{sg} = \mathbf{t}^{s0}$
- ◇ By an assumption of stick interface between gas and free fluid surface within an enclosed chamber, the current postion vector and directional derivative at the interface is unique $\Delta\mathbf{x}^g = \Delta\mathbf{x}^0$, $\mathbf{x}^g = \mathbf{x}^0$

4.3.1.2 Directional derivative of enclosed fluid volume

Similarly, the directional derivative of the enclosed fluid volume of a chamber i in eq. (4.12) is described by

$$\begin{aligned}\Delta v_i^f &= \frac{1}{3}\int_{f\theta^2}\int_{f\theta^1}\left[\Delta\mathbf{x}^f\cdot\mathbf{n}^{*f}+\mathbf{x}^f\cdot\Delta\mathbf{n}^{*f}\right]d\theta^1 d\theta^2+\frac{1}{3}\int_{0\theta^2}\int_{0\theta^1}\left[\Delta\mathbf{x}^0\cdot\mathbf{n}^{*0}+\mathbf{x}^0\cdot\Delta\mathbf{n}^{*0}\right]d\theta^1 d\theta^2\\ &= \Delta v_i^{f\Delta\mathbf{x}^f}+\Delta v_i^{f\Delta\mathbf{n}^{*f}}+\Delta v_i^{f\Delta\mathbf{x}^0}+\Delta v_i^{f\Delta\mathbf{n}^{*0}}.\end{aligned} \tag{4.27}$$

From eq. (4.27), one can set up an equation

$$\Delta v_i^{f\Delta\mathbf{n}^{*f}} = \frac{1}{3}\int_{f\theta^2}\int_{f\theta^1}\left[\mathbf{x}^f\cdot\Delta\mathbf{n}^{*f}\right]d\theta^1 d\theta^2 = \frac{1}{3}\int_{f\theta^2}\int_{f\theta^1}\mathbf{x}^f\cdot\left(\Delta\mathbf{x}^f_{,1}\times\mathbf{x}^f_{,2}+\mathbf{x}^f_{,1}\times\Delta\mathbf{x}^f_{,2}\right)d\theta^1 d\theta^2. \tag{4.28}$$

By applying the integration by part, eq. (4.28) is transformed into

$$\begin{aligned}\Delta v_i^{f\Delta\mathbf{n}^{*f}} =& \frac{1}{3}\int_{f_{\theta^2}}\int_{f_{\theta^1}} \begin{bmatrix} -\mathbf{x}_{,1}^f \cdot \left(\Delta\mathbf{x}^f \times \mathbf{x}_{,2}^f\right) - \mathbf{x}^f \cdot \left(\Delta\mathbf{x}^f \times \mathbf{x}_{,21}^f\right) \\ -\mathbf{x}_{,2}^f \cdot \left(\mathbf{x}_{,1}^f \times \Delta\mathbf{x}^f\right) - \mathbf{x}^f \cdot \left(\mathbf{x}_{,12}^f \times \Delta\mathbf{x}^f\right) \end{bmatrix} d\theta^1 d\theta^2 \\ &+ \frac{1}{3}\int_{f_s} \left[\mathbf{x}^f \cdot \left(\Delta\mathbf{x}^f \times \mathbf{x}_{,2}^f\, n_{\theta^1}^s\right) - \mathbf{x}^f \cdot \left(\Delta\mathbf{x}^f \times \mathbf{x}_{,1}^f\, n_{\theta^2}^s\right)\right] ds, \\ =& \frac{2}{3}\int_{f_{\theta^2}}\int_{f_{\theta^1}} \Delta\mathbf{x}^f \cdot \mathbf{n}^{*f} d\theta^1 d\theta^2 + \frac{1}{3}\int_{f_s} \left(\mathbf{x}^f \times \Delta\mathbf{x}^f\right) \cdot \mathbf{t}^{sf} ds. \end{aligned} \tag{4.29}$$

Obviously, the change in fluid volume due to the change in normal vector of the free fluid surface $\Delta v_i^{f\Delta\mathbf{n}^{*0}}$ of eq. (4.27) is identical to the change in gas volume due to the same parameter $\Delta v_i^{g\Delta\mathbf{n}^{*0}}$ in eq. (4.25):

$$\Delta v_i^{f\Delta\mathbf{n}^{*0}} = \Delta v_i^{g\Delta\mathbf{n}^{*0}} \tag{4.30}$$

Substituting eqs.(4.29) and (4.30) in eq. (4.27) yields a compact equation:

$$\begin{aligned}\Delta v_i^f =& \int_{f_{\theta^2}}\int_{f_{\theta^1}} \Delta\mathbf{x}^f \cdot \mathbf{n}^{*f} d\theta^1 d\theta^2 + \int_{0_{\theta^2}}\int_{0_{\theta^1}} \Delta\mathbf{x}^0 \cdot \mathbf{n}^{*0} d\theta^1 d\theta^2 \\ &\underbrace{+\frac{1}{3}\int_{f_s} \left(\mathbf{x}^f \times \Delta\mathbf{x}^f\right) \cdot \mathbf{t}^{sf} ds + \frac{1}{3}\int_{0_s} \left(\mathbf{x}^0 \times \Delta\mathbf{x}^0\right) \cdot \mathbf{t}^{s0} ds}_{0}. \end{aligned} \tag{4.31}$$

Remarkbly, at the wetted membrane-free fluid surface interface in an enclosed chamber filled by both gas and fluid which is depicted in Figure 4.8(b), the boundary terms in eq. (4.31) vanish due to following observations:

- ◇ The wetted membrane boundary normal vector $\mathbf{n}^{sf}$ and the free fluid surface boundary normal vector $\mathbf{n}^{s0}$ are perpendicular to each other (see Figure 4.8(b))
- ◇ The wetted membrane boundary tangential vector $\mathbf{t}^{sf}$ and the free fluid surface boundary tangential vector $\mathbf{t}^{s0}$ point into opposite directions $\mathbf{t}^{sf} = -\mathbf{t}^{s0}$
- ◇ By an assumption of stick interface between wetted membrane and free fluid surface within an enclosed chamber, the current postion vector and directional derivative at at the interface is unique $\Delta\mathbf{x}^f = \Delta\mathbf{x}^0,\ \mathbf{x}^g = \mathbf{x}^0$

Due to the fact that there is no change in volume of an incompressible fluid $\Delta v_i^f = 0$, eq. (4.31) is equivalent to

$$\int_{f_{\theta^2}}\int_{f_{\theta^1}} \Delta\mathbf{x}^f \cdot \mathbf{n}^{*f} d\theta^1 d\theta^2 = -\int_{0_{\theta^2}}\int_{0_{\theta^1}} \Delta\mathbf{x}^0 \cdot \mathbf{n}^{*0} d\theta^1 d\theta^2. \tag{4.32}$$

Since the fluid domain is not discretized, therefore, we adopt an assumption that the whole free fluid surface in Figure 4.8(b) homogeneously moves along the direction of its unit normal vector $\Delta\mathbf{x}^0 = \Delta x^0 \mathbf{n}^0$. As a result, eq. (4.32) is expandable by

$$\begin{aligned}
\int_{f\theta^2}\int_{f\theta^1} \Delta\mathbf{x}^f \cdot \mathbf{n}^{*f} d\theta^1 d\theta^2 &= -\int_{0\theta^2}\int_{0\theta^1} \Delta x^0 \mathbf{n}^0 \cdot \mathbf{n}^{*0} d\theta^1 d\theta^2 = -\int_{0\theta^2}\int_{0\theta^1} \Delta x^0 \left\|\mathbf{n}^{*0}\right\| d\theta^1 d\theta^2, \\
&= -\Delta x^0 \int_{0\theta^2}\int_{0\theta^1} \left\|\mathbf{x}_{,1}^0 \times \mathbf{x}_{,2}^0\right\| d\theta^1 d\theta^2 = -\Delta x^0 \left\|S_0\right\|, \\
\Rightarrow \Delta x^0 &= \frac{-1}{\|S_0\|} \int_{f\theta^2}\int_{f\theta^1} \Delta\mathbf{x}^f \cdot \mathbf{n}^{*f} d\theta^1 d\theta^2,
\end{aligned} \tag{4.33}$$

where $\|S_0\|$ depicted in Figure 4.8 stands for the free fluid surface area and the scalar Δx^0 is the change in free fluid surface level along the direction of its unit normal vector $\mathbf{n}^0$.

4.3.1.3 Directional derivative for the enclosed gas pressure

Pneumacit model for enclosed gas pressure

The directional derivative of gas pressure p_i^g in an enclosed gas chamber i from the pneumatic model eq. (4.8) is determined by

$$\Delta p_i^g = -\kappa P_{i0}^g \left(V_{i0}^g\right)^\kappa \left(v_i^g\right)^{-\kappa-1} \Delta v_i^g = -\kappa \frac{p_i^g}{v_i^g} \Delta v_i^g. \tag{4.34}$$

With the help of eqs. (4.26) and (4.32), we can rewrite the directional derivative of gas pressure from eq. (4.34) to

$$\begin{aligned}
\Delta p_i^g &= -\kappa \frac{p_i^g}{v_i^g} \left[\int_{g\theta^2}\int_{g\theta^1} \Delta\mathbf{x}^g \cdot \mathbf{n}^{*g} d\theta^1 d\theta^2 - \int_{0\theta^2}\int_{0\theta^1} \Delta\mathbf{x}^0 \cdot \mathbf{n}^{*0} d\theta^1 d\theta^2 \right], \\
&= -\kappa \frac{p_i^g}{v_i^g} \left[\int_{g\theta^2}\int_{g\theta^1} \Delta\mathbf{x}^g \cdot \mathbf{n}^{*g} d\theta^1 d\theta^2 + \int_{f\theta^2}\int_{f\theta^1} \Delta\mathbf{x}^f \cdot \mathbf{n}^{*f} d\theta^1 d\theta^2 \right].
\end{aligned} \tag{4.35}$$

Hydraulic model for enclosed gas pressure

Likewise, the directional derivative of gas pressure p_i^g in the enclosed gas chamber i from the hydraulic model eq. (4.9) is described with

$$\Delta p_i^g = \frac{-K}{V_{i0}^g} \Delta v_i^g = \frac{-K}{V_{i0}^g} \left[\int_{g\theta^2}\int_{g\theta^1} \Delta\mathbf{x}^g \cdot \mathbf{n}^{*g} d\theta^1 d\theta^2 + \int_{f\theta^2}\int_{f\theta^1} \Delta\mathbf{x}^f \cdot \mathbf{n}^{*f} d\theta^1 d\theta^2 \right]. \tag{4.36}$$

4.3.1.4 Directional derivative of the free fluid pressure

From the definition of the fluid head in eq. (4.1), the directional derivative of the pressure from the highest fluid head in an enclosed chamber partially filled with gas and fluid as illustrated in Figure 4.2 can be written with the help of eq. (4.33) by

$$\Delta p_i^{\mathbf{x}^0} = \Delta\rho\mathbf{g}\cdot\mathbf{x}^0 + \rho\mathbf{g}\cdot\Delta\mathbf{x}^0 = 0 + \rho\mathbf{g}\cdot\Delta\mathbf{x}^0 = \frac{-\rho\mathbf{g}\cdot\mathbf{n}^{\mathbf{0}}}{\|S_0\|}\int_{f\theta^2}\int_{f\theta^1}\Delta\mathbf{x}^f\cdot\mathbf{n}^{*f}d\theta^1 d\theta^2. \tag{4.37}$$

Note that in case of an incompressible fluid with conservation of mass the density is unaltered $\Delta\rho = \Delta\left(\frac{m}{v}\right) = 0$.

4.3.1.5 Directional derivative of the pressure on a point of the wetted membrane due to local fluid head

In the same fashion, the directional derivative of the pressure at a point on the wetted membrane surface solely caused by the local depth of fluid below the free surface in an enclosed chamber partially filled with gas and fluid in eq. (4.1) can be derived by

$$\Delta p_i^{\mathbf{x}^f} = \Delta\rho\mathbf{g}\cdot\mathbf{x}^f + \rho\mathbf{g}\cdot\Delta\mathbf{x}^f = 0 + \rho\mathbf{g}\cdot\Delta\mathbf{x}^f. \tag{4.38}$$

4.3.1.6 Directional derivative of the pressure on the wetted membrane below free fluid surface

The directional derivative of the pressure at arbitrary point on the wetted membrane surface below the free surface in an enclosed chamber partially filled with gas and fluid in eq. (4.1) is described by

$$\Delta p^f = -\underbrace{\Delta p^{\mathbf{x}^0}}_{(4.37)} + \underbrace{\Delta p^{\mathbf{x}^f}}_{(4.38)} + \underbrace{\Delta p^g}_{(4.35)\text{or }(4.36)}. \tag{4.39}$$

4.3.2 Directional derivative of the virtualwork equation due to change in normal vector $\Delta\mathbf{n}^*$

From (4.17), the directional derivative of the virtual work due to the change of normal vector $\Delta\mathbf{n}^*$ in the direction of $\Delta\varphi$ is a combination of contributions from gas and fluid:

$$-\Delta G_{fol}^{\Delta\mathbf{n}} = -\Delta G_{fol}^{\Delta\mathbf{n}^g} - \Delta G_{fol}^{\Delta\mathbf{n}^f} \tag{4.40}$$

where the gas contribution is expanded to

$$\begin{aligned}
-\Delta G_{fol}^{\Delta\mathbf{n}^g} &= \int_{g\theta^2}\int_{g\theta^1} p^g\Delta\mathbf{n}^{*g}\cdot\delta\varphi^g\, d\theta^1 d\theta^2 = \int_{g\theta^2}\int_{g\theta^1} p^g\Delta\left(\mathbf{x}_{,1}^g\times\mathbf{x}_{,2}^g\right)\cdot\delta\varphi^g\, d\theta^1 d\theta^2,\\
&= \int_{g\theta^2}\int_{g\theta^1} p^g\left(\Delta\mathbf{x}_{,1}^g\times\mathbf{x}_{,2}^g + \mathbf{x}_{,1}^g\times\Delta\mathbf{x}_{,2}^g\right)\cdot\delta\varphi^g\, d\theta^1 d\theta^2,\\
&= \int_{g\theta^2}\int_{g\theta^1}\left[p^g\left(\left(\mathbf{x}_{,2}^g\times\delta\varphi^g\right)\cdot\Delta\mathbf{x}_{,1}^g + \left(\delta\varphi^g\times\mathbf{x}_{,1}^g\right)\cdot\Delta\mathbf{x}_{,2}^g\right)\right] d\theta^1 d\theta^2.
\end{aligned} \tag{4.41}$$

With integration by part, eq. (4.41) is transformed to

$$-\Delta G_{fol}^{\Delta \mathbf{n}^g} = \int_{g\theta^2}\int_{g\theta^1} \begin{bmatrix} -p^g{}_{,1}\left(\mathbf{x}^g_{,2} \times \delta\varphi^g\right) \cdot \Delta\mathbf{x}^g - p^g\left(\mathbf{x}^g_{,2} \times \delta\varphi^g\right)_{,1} \cdot \Delta\mathbf{x}^g \\ -p^g{}_{,2}\left(\delta\varphi^g \times \mathbf{x}^g_{,1}\right) \cdot \Delta\mathbf{x}^g - p^g\left(\delta\varphi^g \times \mathbf{x}^g_{,1}\right)_{,2} \cdot \Delta\mathbf{x}^g \end{bmatrix} d\theta^1 d\theta^2 + \int_{g_s} p^g \left[(\delta\varphi^g \times \Delta\mathbf{x}^g) \cdot \mathbf{x}^g_{,2}\, n^s_{\theta^1} - (\delta\varphi^g \times \Delta\mathbf{x}^g) \cdot \mathbf{x}^g_{,1}\, n^s_{\theta^2} \right] ds. \tag{4.42}$$

Due to the fact that the gas pressure is assumed to be constant within a chamber, therefore, derivative of gas pressure w.r.t. surface coordinates vanish $p^g{}_{,\theta^\alpha} = 0$. With the help of eq. (4.18), one can reduce eq. (4.42) to

$$\begin{aligned} -\Delta G_{fol}^{\Delta \mathbf{n}^g} &= \int_{g\theta^2}\int_{g\theta^1} \begin{bmatrix} -p^g\left(\mathbf{x}^g_{,2} \times \delta\varphi^g\right)_{,1} \cdot \Delta\mathbf{x}^g \\ -p^g\left(\delta\varphi^g \times \mathbf{x}^g_{,1}\right)_{,2} \cdot \Delta\mathbf{x}^g \end{bmatrix} d\theta^1 d\theta^2 + \int_{g_s} p^g\,(\Delta\mathbf{x}^g \times \mathbf{t}^{sg}) \cdot \delta\varphi^g\, ds, \\ &= \int_{g\theta^2}\int_{g\theta^1} \begin{bmatrix} -p^g\left(\mathbf{x}^g_{,2} \times \delta\varphi^g{}_{,1}\right) \cdot \Delta\mathbf{x}^g \\ -p^g\left(\delta\varphi^g{}_{,2} \times \mathbf{x}^g_{,1}\right) \cdot \Delta\mathbf{x}^g \end{bmatrix} d\theta^1 d\theta^2 + \int_{g_s} p^g\,(\Delta\mathbf{x}^g \times \mathbf{t}^{sg}) \cdot \delta\varphi^g\, ds, \\ &= \int_{g\theta^2}\int_{g\theta^1} p^g \delta \underbrace{\left(\varphi^g{}_{,1} \times \mathbf{x}^g_{,2}\right)}_{\mathbf{n}^{*g}} \cdot \Delta\mathbf{x}^g\, d\theta^1 d\theta^2 + \int_{g_s} p^g\,(\Delta\mathbf{x}^g \times \mathbf{t}^{sg}) \cdot \delta\varphi^g\, ds, \\ &= \int_{g\theta^2}\int_{g\theta^1} p^g \delta\mathbf{n}^{*g} \cdot \Delta\mathbf{x}^g\, d\theta^1 d\theta^2 + \int_{g_s} p^g\,(\Delta\mathbf{x}^g \times \mathbf{t}^{sg}) \cdot \delta\varphi^g\, ds. \end{aligned} \tag{4.43}$$

Schweizerhof and Ramm [SR84] and Rumpel and Schweizerhof [RS03, RS04] showed that the boundary terms can be dropped out from the linearized equation in eq. (4.43) if one of

(i) Fixed boundary condition $\Delta\mathbf{x}^s = \mathbf{0}$

(ii) No loading p on complete boundary $s : p|_s = 0$

(iii) The boundary displacement is allowed only in parallel to the considered boundary $s : \Delta\mathbf{x}^s || \mathbf{t}^s \rightarrow \Delta\mathbf{x}^s \times \mathbf{t}^s = \mathbf{0}$.

(iv) The boundary displacement component in the perpendicular direction to the tangential vector $\mathbf{t}^s$ is fixed: $(\Delta\mathbf{x}^s \times \mathbf{t}^s) \cdot \delta\varphi^g = \mathbf{0}$ which yields zero virutal work from the boundary terms which means that all three vectors are coplanar, e.g. the sliding boundary.

(v) There is no boundary which reflects the enclosed chamber filled with gas or fluid.

(vi) The sum of virtual work at the boundary becomes zero. The fulfillment of this condition is regularly not assured and usually not known in advance.

(vii) The physical boundary is not clearly defined. So, the boundary integration over this undefined boundary is unavailable.

Figure 4.9: Description for special boundary condition to discard the boundary terms.

the following conditions given in Figure 4.9 and illustrated in Figure 4.10 are valid. Now, the contribution from fluid in eq. (4.40) can be expanded to

$$\begin{aligned}
-\Delta G_{fol}^{\Delta \mathbf{n}^f} &= \int_{f\theta^2}\int_{f\theta^1} p^f \Delta \mathbf{n}^{*f} \cdot \delta\varphi^f d\theta^1 d\theta^2 = \int_{f\theta^2}\int_{f\theta^1} p^f \Delta \left(\mathbf{x}_{,1}^f \times \mathbf{x}_{,2}^f\right) \cdot \delta\varphi^f \; d\theta^1 d\theta^2, \\
&= \int_{f\theta^2}\int_{f\theta^1} p^f \left(\Delta\mathbf{x}_{,1}^f \times \mathbf{x}_{,2}^f + \mathbf{x}_{,1}^f \times \Delta\mathbf{x}_{,2}^f\right) \cdot \delta\varphi^f \; d\theta^1 d\theta^2, \\
&= \int_{f\theta^2}\int_{f\theta^1} \left[p^f \left(\left(\mathbf{x}_{,2}^f \times \delta\varphi^f\right) \cdot \Delta\mathbf{x}_{,1}^f + \left(\delta\varphi^f \times \mathbf{x}_{,1}^f\right) \cdot \Delta\mathbf{x}_{,2}^f\right)\right] \; d\theta^1 d\theta^2. \qquad (4.44)
\end{aligned}$$

By applying integration by part, eq. (4.44) can be rewritten to

$$\begin{aligned}
-\Delta G_{fol}^{\Delta \mathbf{n}^f} = &\int_{f\theta^2}\int_{f\theta^1} \begin{bmatrix} -p^f{}_{,1} \left(\mathbf{x}_{,2}^f \times \delta\varphi^f\right) \cdot \Delta\mathbf{x}^f - p^f \left(\mathbf{x}_{,2}^f \times \delta\varphi^f\right)_{,1} \cdot \Delta\mathbf{x}^f \\ -p^f{}_{,2} \left(\delta\varphi^f \times \mathbf{x}_{,1}^f\right) \cdot \Delta\mathbf{x}^f - p^f \left(\delta\varphi^f \times \mathbf{x}_{,1}^f\right)_{,2} \cdot \Delta\mathbf{x}^f \end{bmatrix} \; d\theta^1 d\theta^2, \\
&+ \int_{f_S} p^f \left[\left(\delta\varphi^f \times \Delta\mathbf{x}^f\right) \cdot \mathbf{x}_{,2}^f \, n_{\theta^1}^{sf} - \left(\delta\varphi^f \times \Delta\mathbf{x}^f\right) \cdot \mathbf{x}_{,1}^f \, n_{\theta^2}^{sf}\right] \; ds. \qquad (4.45)
\end{aligned}$$

The derivative of pressure at an arbitrary position of the wetted membrane surface p^f in eq. (4.1) with respect to each surface coordinate θ^α is written by

$$p^f{}_{,\alpha} = -p^{\mathbf{x}^0}{}_{,\alpha} + p^{\mathbf{x}^f}{}_{,\alpha} + p^g{}_{,\alpha} = 0 + \left(\rho\mathbf{g} \cdot \mathbf{x}^f\right)_{,\alpha} + 0 = \overbrace{\rho_{,\alpha}}^{0} \mathbf{g} \cdot \mathbf{x}^f + \rho\mathbf{g} \cdot \mathbf{x}^f{}_{,\alpha} \qquad (4.46)$$

Note that derivative of the gas pressure p^g which is assumed to be uniform within a chamber vanishes as well as the constant free fluid head $p^{\mathbf{x}^0}$ at an instance of time t w.r.t the surface coordinate θ^α. Moreover, the conservation of mass for an incompressible fluid causes a constant fluid density $\rho v^f = \rho_0 V_0^f$, $v^f = V_0^f \rightarrow \rho = \rho_0$. With the help of eqs. (4.18) and (4.46) one can rewrite eq. (4.45) by

$$\begin{aligned}
-\Delta G_{fol}^{\Delta \mathbf{n}^f} &= \int_{f\theta^2}\int_{f\theta^1} \begin{bmatrix} -p^f{}_{,1} \left(\mathbf{x}_{,2}^f \times \delta\varphi^f\right) \cdot \Delta\mathbf{x}^f \\ -p^f{}_{,2} \left(\delta\varphi^f \times \mathbf{x}_{,1}^f\right) \cdot \Delta\mathbf{x}^f \\ +p^f \delta \left(\varphi^f{}_{,1} \times \mathbf{x}_{,2}^f\right) \cdot \Delta\mathbf{x}^f \end{bmatrix} \; d\theta^1 d\theta^2 + \int_{f_S} p^f \left(\Delta\mathbf{x}^f \times \mathbf{t}^{sf}\right) \cdot \delta\varphi^f \; ds, \\
&= \int_{f\theta^2}\int_{f\theta^1} \begin{bmatrix} -\rho\mathbf{g} \cdot \mathbf{x}^f{}_{,1} \left(\mathbf{x}_{,2}^f \times \delta\varphi^f\right) \cdot \Delta\mathbf{x}^f \\ -\rho\mathbf{g} \cdot \mathbf{x}^f{}_{,2} \left(\delta\varphi^f \times \mathbf{x}_{,1}^f\right) \cdot \Delta\mathbf{x}^f \\ +p^f \delta\mathbf{n}^{*f} \cdot \Delta\mathbf{x}^f \end{bmatrix} \; d\theta^1 d\theta^2 + \int_{f_S} p^f \left(\Delta\mathbf{x}^f \times \mathbf{t}^{sf}\right) \cdot \delta\varphi^f \; ds, \\
&= \int_{f\theta^2}\int_{f\theta^1} \begin{bmatrix} \rho\mathbf{g} \cdot \delta\varphi^f \left(\mathbf{x}_{,1}^f \times \mathbf{x}_{,2}^f\right) \cdot \Delta\mathbf{x}^f \\ -\rho\mathbf{g} \cdot \Delta\mathbf{x}^f \left(\mathbf{x}_{,1}^f \times \mathbf{x}_{,2}^f\right) \cdot \delta\varphi^f \\ +p^f \delta\mathbf{n}^{*f} \cdot \Delta\mathbf{x}^f \end{bmatrix} \; d\theta^1 d\theta^2 + \int_{f_S} p^f \left(\Delta\mathbf{x}^f \times \mathbf{t}^{sf}\right) \cdot \delta\varphi^f \; ds. \qquad (4.47)
\end{aligned}$$

By combining eq. (4.41) with eq. (4.43), we obtain

$$-\Delta G_{fol}^{\Delta \mathbf{n}^g} = \frac{1}{2}\int_{g\theta^2}\int_{g\theta^1} p^g \left[\Delta\mathbf{n}^{*g} \cdot \delta\varphi^g + \delta\mathbf{n}^{*g} \cdot \Delta\mathbf{x}^g\right] \; d\theta^1 d\theta^2 + \frac{1}{2}\int_{g_S} p^g \left(\Delta\mathbf{x}^g \times \mathbf{t}^{sg}\right) \cdot \delta\varphi^g \; ds. \qquad (4.48)$$

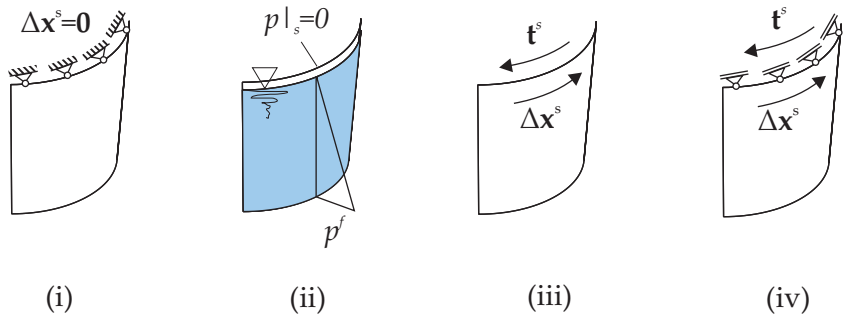

Figure 4.10: Illustration for boundary conditions of an enclosed chamber (i) $\Delta\mathbf{x}^s = \mathbf{0}$, (ii) $s : p|_s = 0$, (iii) $\Delta\mathbf{x}^s || \mathbf{t}^s \rightarrow \Delta\mathbf{x}^s \times \mathbf{t}^s = \mathbf{0}$ and (iv) $(\Delta\mathbf{x}^s \times \mathbf{t}^s) \cdot \delta\varphi^g = \mathbf{0}$.

Obviously, the domain term in eq. (4.48) is symmetric while the skew symmetric property of the boundary term is proven by

$$(\Delta\mathbf{x}^g \times \mathbf{t}^{sg}) \cdot \delta\varphi^g = (\mathbf{t}^{sg} \times \delta\varphi^g) \cdot \Delta\mathbf{x}^g = -(\delta\varphi^g \times \mathbf{t}^{sg}) \cdot \Delta\mathbf{x}^g \tag{4.49}$$

Besides, combining eqs., (4.44) and (4.47) yields

$$-\Delta G_{fol}^{\Delta\mathbf{n}^f} = \frac{1}{2}\int_{f\theta^2}\int_{f\theta^1} \begin{bmatrix} \rho\mathbf{g} \cdot \delta\varphi^f \mathbf{n}^{*f} \cdot \Delta\mathbf{x}^f \\ -\rho\mathbf{g} \cdot \Delta\mathbf{x}^f \mathbf{n}^{*f} \cdot \delta\varphi^f \\ +p^f \delta\mathbf{n}^{*f} \cdot \Delta\mathbf{x}^f \\ +p^f \Delta\mathbf{n}^{*f} \cdot \delta\varphi^f \end{bmatrix} d\theta^1 d\theta^2 + \frac{1}{2}\int_{fs} p^f \left(\Delta\mathbf{x}^f \times \mathbf{t}^{sf}\right) \cdot \delta\varphi^f \, ds. \tag{4.50}$$

Similar to eq. (4.49), the boundary term of eq. (4.50) shows its skew symmetric property:

$$\left(\Delta\mathbf{x}^f \times \mathbf{t}^{sf}\right) \cdot \delta\varphi^f = \left(\mathbf{t}^{sf} \times \delta\varphi^f\right) \cdot \Delta\mathbf{x}^f = -\left(\delta\varphi^f \times \mathbf{t}^{sf}\right) \cdot \Delta\mathbf{x}^f. \tag{4.51}$$

Remarkably, the first domain term $\rho\mathbf{g} \cdot \delta\varphi^f \mathbf{n}^{*f} \cdot \Delta\mathbf{x}^f - \rho\mathbf{g} \cdot \Delta\mathbf{x}^f \mathbf{n}^{*f} \cdot \delta\varphi^f$ manifests its skew symmetric property while another term $p^f \delta\mathbf{n}^{*f} \cdot \Delta\mathbf{x}^f + p^f \Delta\mathbf{n}^{*f} \cdot \delta\varphi^f$ is symmetric. At the interface between gas and fluid in an enclosed chamber depicted in Figure 4.8(b), one observes following issues:

- ◇ The pressure of gas and fluid are in equilibrium $p^f = p^g$ as mentioned in section 4.2.3.
- ◇ The gas boundary normal vector $\mathbf{n}^{sg}$ and the fluid boundary normal vector $\mathbf{n}^{sf}$ point into opposite directions $\mathbf{n}^{sg} = -\mathbf{n}^{sf}$.
- ◇ The gas boundary tangential vector $\mathbf{t}^{sg}$ and the fluid boundary tangential vector $\mathbf{t}^{sf}$ point into opposite directions $\mathbf{t}^{sg} = -\mathbf{t}^{sf}$.
- ◇ Variation and directional derivative at the interface is unique $\Delta\mathbf{x}^g = \Delta\mathbf{x}^f$, $\delta\varphi^g = \delta\varphi^f$.

Thus, an addition of the boundary integral term of gas in (4.48) and fluid in (4.50) yields

$$\begin{aligned} \Rightarrow &= \frac{1}{2}\int_{g=f_S} p^{g=f} \left[(\Delta\mathbf{x}^g \times \mathbf{t}^{sg}) \cdot \delta\varphi^g + \left(\Delta\mathbf{x}^f \times \mathbf{t}^{sf}\right) \cdot \delta\varphi^f\right] ds, \\ &= \frac{1}{2}\int_{g=f_S} p^{g=f} \left[(\Delta\mathbf{x}^g \times \mathbf{t}^{sg}) \cdot \delta\varphi^g - (\Delta\mathbf{x}^g \times \mathbf{t}^{sg}) \cdot \delta\varphi^g\right] ds = 0, \end{aligned} \tag{4.52}$$

which means that the boundary term of gas in eq. (4.48) and that of the fluid in eq. (4.50) mutually cancel each other. At this point, the directional derivative $-\Delta G_{fol}^{\Delta \mathbf{n}} = -\Delta G_{fol}^{\Delta \mathbf{n}^g} - \Delta G_{fol}^{\Delta \mathbf{n}^f}$ in eq. (4.40) is obtainable by an addition of eqs. (4.48) and (4.50), viz.

$$\left.\begin{aligned} -\Delta G_{fol}^{\Delta \mathbf{n}} = \frac{1}{2} \int_{g\theta^2} \int_{g\theta^1} p^g \left[\Delta \mathbf{n}^{*g} \cdot \delta \varphi^g + \delta \mathbf{n}^{*g} \cdot \Delta \mathbf{x}^g \right] \, d\theta^1 d\theta^2 \end{aligned}\right\} \Rightarrow -\Delta G_{fol}^{\Delta \mathbf{n}^g}$$

$$\left.\begin{aligned} + \frac{1}{2} \int_{f\theta^2} \int_{f\theta^1} \begin{bmatrix} \rho \mathbf{g} \cdot \delta \varphi^f \mathbf{n}^{*f} \cdot \Delta \mathbf{x}^f - \rho \mathbf{g} \cdot \Delta \mathbf{x}^f \mathbf{n}^{*f} \cdot \delta \varphi^f \\ + p^f \delta \mathbf{n}^{*f} \cdot \Delta \mathbf{x}^f + p^f \Delta \mathbf{n}^{*f} \cdot \delta \varphi^f \end{bmatrix} d\theta^1 d\theta^2 \end{aligned}\right\} \Rightarrow -\Delta G_{fol}^{\Delta \mathbf{n}^f}, \quad (4.53)$$

where the first term of $-\Delta G_{fol}^{\Delta \mathbf{n}^f}$ causes eq.(4.53) nonsymmetric.

4.3.3 Directional derivative of the virtual work equation due to the change in pressure Δp

The directional derivative of the virtual work in eq. (4.17) due to the change of pressure Δp in the direction of $\Delta \varphi$ is as well composed of contributions from gas and fluid such that

$$-\Delta G_{fol}^{\Delta p} = -\Delta G_{fol}^{\Delta p^g} - \Delta G_{fol}^{\Delta p^f}, \quad (4.54)$$

where the enclosed gas contribution with the pneumatic model in eq. (4.35) can be explained by

$$\begin{aligned} -\Delta G_{fol}^{\Delta p^g} &= \int_{g\theta^2} \int_{g\theta^1} \Delta p^g \mathbf{n}^{*g} \cdot \delta \varphi^g d\theta^1 d\theta^2, \\ &= -\kappa \frac{p_i^g}{v_i^g} \begin{bmatrix} \int_{g\theta^2} \int_{g\theta^1} \mathbf{n}^{*g} \cdot \Delta \mathbf{x}^g d\theta^1 d\theta^2 \\ + \int_{f\theta^2} \int_{f\theta^1} \mathbf{n}^{*f} \cdot \Delta \mathbf{x}^f d\theta^1 d\theta^2 \end{bmatrix} \int_{g\theta^2} \int_{g\theta^1} \mathbf{n}^{*g} \cdot \delta \varphi^g d\theta^1 d\theta^2, \\ &= -\kappa \frac{p_i^g}{v_i^g} \begin{bmatrix} \int_{g\theta^2} \int_{g\theta^1} \mathbf{n}^{*g} \cdot \Delta \mathbf{x}^g d\theta^1 d\theta^2 \int_{g\theta^2} \int_{g\theta^1} \mathbf{n}^{*g} \cdot \delta \varphi^g d\theta^1 d\theta^2 \\ + \int_{f\theta^2} \int_{f\theta^1} \mathbf{n}^{*f} \cdot \Delta \mathbf{x}^f d\theta^1 d\theta^2 \int_{g\theta^2} \int_{g\theta^1} \mathbf{n}^{*g} \cdot \delta \varphi^g d\theta^1 d\theta^2 \end{bmatrix}. \end{aligned} \quad (4.55)$$

Likewise, the fluid contribution of eq. (4.54) can be expanded according to eq. (4.39) or indirectly eqs. (4.35), (4.37) and (4.38) to

$$\begin{aligned} -\Delta G_{fol}^{\Delta p^f} &= \int_{f\theta^2} \int_{f\theta^1} \Delta p^f \mathbf{n}^{*f} \cdot \delta \varphi^f \, d\theta^1 d\theta^2, \\ &= -\kappa \frac{p_i^g}{v_i^g} \begin{bmatrix} \int_{g\theta^2} \int_{g\theta^1} \mathbf{n}^{*g} \cdot \Delta \mathbf{x}^g d\theta^1 d\theta^2 \int_{f\theta^2} \int_{f\theta^1} \mathbf{n}^{*f} \cdot \delta \varphi^f d\theta^1 d\theta^2 \\ + \int_{f\theta^2} \int_{f\theta^1} \mathbf{n}^{*f} \cdot \Delta \mathbf{x}^f d\theta^1 d\theta^2 \int_{f\theta^2} \int_{f\theta^1} \mathbf{n}^{*f} \cdot \delta \varphi^f d\theta^1 d\theta^2 \end{bmatrix} \\ &\quad + \frac{\rho \mathbf{g} \cdot \mathbf{n}^0}{\|S_0\|} \int_{f\theta^2} \int_{f\theta^1} \mathbf{n}^{*f} \cdot \Delta \mathbf{x}^f d\theta^1 d\theta^2 \int_{f\theta^2} \int_{f\theta^1} \mathbf{n}^{*f} \cdot \delta \varphi^f \, d\theta^1 d\theta^2 \\ &\quad + \rho \mathbf{g} \cdot \Delta \mathbf{x}^f \int_{f\theta^2} \int_{f\theta^1} \mathbf{n}^{*f} \cdot \delta \varphi^f d\theta^1 d\theta^2. \end{aligned} \quad (4.56)$$

Therefore, combining eqs. (4.53), (4.55) and (4.56) recalls the directional derivative $\Delta G_{fol}(\varphi_t^k, \delta\varphi)$ in eq. (4.17), viz.

$$-\Delta G_{fol}(\varphi_t^k, \delta\varphi) = \underbrace{-\Delta G_{fol}^{\Delta \mathbf{n}^g} - \Delta G_{fol}^{\Delta \mathbf{n}^f}}_{eq.\ (4.53)} \underbrace{-\Delta G_{fol}^{\Delta p^g}}_{eq.\ (4.55)} \underbrace{-\Delta G_{fol}^{\Delta p^f}}_{eq.\ (4.56)}. \tag{4.57}$$

4.4 Proof of conservativeness

As an early proposed work, Sewell [Sew67] checked the existence global potential as an indicator for the conservativeness for the case of distributed loads. Then in Bufler [Buf84] conditions for conservative problems, i.e. the existence of a potential, for generalized nonuniform pressure loading are provided. Note that the existence of potential is derived based on the linearized incremental energy expression without the higher order terms. For nonlinear finite element analysis, Schweizerhof and Ramm [Sch82, SR84] mentioned that the conservativeness of the problem under interest in case of large deformation is indirectly indicated by the symmetry of the linearized virtual work equations. For this reason, eq. (4.57) is rearranged to emphasize its symmetry with a remark that the non symmetric term of $-\Delta G_{fol}^{\Delta \mathbf{n}^f}$ in eq. (4.53) vanishes after it is combined with the last term of $-\Delta G_{fol}^{\Delta p^f}$ in eq. (4.56).

$$\begin{aligned}
-\Delta G_{fol}(\varphi_t^k, \delta\varphi) =& \frac{1}{2} \int_{g\theta^2} \int_{g\theta^1} p^g \left[\Delta \mathbf{n}^{*g} \cdot \delta\varphi^g + \delta \mathbf{n}^{*g} \cdot \Delta \mathbf{x}^g\right] d\theta^1 d\theta^2 \\
&+ \frac{1}{2} \int_{f\theta^2} \int_{f\theta^1} \begin{bmatrix} \rho \mathbf{g} \cdot \delta\varphi^f \mathbf{n}^{*f} \cdot \Delta \mathbf{x}^f + \rho \mathbf{g} \cdot \Delta \mathbf{x}^f \mathbf{n}^{*f} \cdot \delta\varphi^f \\ + p^f \delta \mathbf{n}^{*f} \cdot \Delta \mathbf{x}^f + p^f \Delta \mathbf{n}^{*f} \cdot \delta\varphi^f \end{bmatrix} d\theta^1 d\theta^2 \\
&- \kappa \frac{p_i^g}{v_i^g} \left[\int_{g\theta^2} \int_{g\theta^1} \mathbf{n}^{*g} \cdot \Delta \mathbf{x}^g d\theta^1 d\theta^2 \int_{g\theta^2} \int_{g\theta^1} \mathbf{n}^{*g} \cdot \delta\varphi^g d\theta^1 d\theta^2 \right] \\
&- \kappa \frac{p_i^g}{v_i^g} \left[\begin{array}{l} \int_{g\theta^2} \int_{g\theta^1} \mathbf{n}^{*g} \cdot \Delta \mathbf{x}^g d\theta^1 d\theta^2 \int_{f\theta^2} \int_{f\theta^1} \mathbf{n}^{*f} \cdot \delta\varphi^f d\theta^1 d\theta^2 \\ + \int_{f\theta^2} \int_{f\theta^1} \mathbf{n}^{*f} \cdot \Delta \mathbf{x}^f d\theta^1 d\theta^2 \int_{f\theta^2} \int_{f\theta^1} \mathbf{n}^{*f} \cdot \delta\varphi^f d\theta^1 d\theta^2 \end{array} \right] \\
&- \kappa \frac{p_i^g}{v_i^g} \left[\int_{f\theta^2} \int_{f\theta^1} \mathbf{n}^{*f} \cdot \Delta \mathbf{x}^f d\theta^1 d\theta^2 \int_{f\theta^2} \int_{f\theta^1} \mathbf{n}^{*f} \cdot \delta\varphi^f d\theta^1 d\theta^2 \right] \\
&+ \frac{\rho \mathbf{g} \cdot \mathbf{n^0}}{\|S_0\|} \int_{f\theta^2} \int_{f\theta^1} \mathbf{n}^{*f} \cdot \Delta \mathbf{x}^f d\theta^1 d\theta^2 \int_{f\theta^2} \int_{f\theta^1} \mathbf{n}^{*f} \cdot \delta\varphi^f \, d\theta^1 d\theta^2.
\end{aligned} \tag{4.58}$$

As a result, symmetry of eq. (4.58) is maintained and this evidence indirectly reflects the conservativeness of the enclosed membrane filled with gas and/or fluid under interest. To close this section, a conclusion, given by Schweizerhof and Ramm [SR84], about the conservativeness of the deformation-dependent pressure forces for both the body attached and space attached type is summarized in Table 4.2.

Table 4.2: Conclusion for the conservativeness of load stiffness matrix with symmetry (Sym) and non-symmetry (Nsym) from [SR84].

Load stiffness portion		body attached	space attached
domain terms	nonuniform pressure	Nsym	Sym
	uniform pressure	Sym	Sym
boundary terms	arbitrary b.c.	Nsym	NSym
	special b.c. in Figure 4.9	Sym	Sym

4.5 Discretization

To transform a continuous system into a discrete one as mentioned in section 2.3.1, the virtual work equation in eq. (4.58) must be spatially discretized by membrane elements introduced in section 2.3.1.1. By recalling the configuration map $\mathbf{x} = \varphi(\mathbf{X}, t)$ and its discrete field description from eqs. (2.79) and (2.80), one can rewrite the variation of the discrete configuration map such that

$$\delta\varphi^h = \frac{\partial\varphi^h}{\partial\mathbf{d}}\delta\mathbf{d} = \varphi^h_{,\mathbf{d}}\,\delta\mathbf{d} \quad \text{or} \quad \frac{\partial\varphi^h}{\partial d_P}\delta d_P = \varphi^h_{,_P}\,\delta d_P; \qquad P = 1,\dots,n_{dof}, \tag{4.59}$$

where $\mathbf{d}$ is the nodal value of the discrete configuration map φ^h, i.e. the degree of freedoms (dof) of the system. With an isoparametric concept, the discrete form of the virtual work equation for deformation-dependent forces in eq (4.58) for a single chamber i is stated by

$$\begin{aligned}
-\Delta G^h_{fol} &= \bigcup_{e=1}^{n_{el}} G^{h(e)}_{fol}(\varphi^k_t, \delta\varphi); \quad P,Q = 1,\dots,n_{dof},\\
&= -\kappa\frac{p^g_i}{v^g_i}\left[\bigcup_{e=1}^{n_{el}}\int_{_g\theta^{2(e)}}\int_{_g\theta^{1(e)}} \mathbf{n}^{*g}\cdot\varphi^{hg}_{,_Q}\,\Delta d_Q d\theta^1 d\theta^2 \bigcup_{e=1}^{n_{el}}\int_{_g\theta^{2(e)}}\int_{_g\theta^{1(e)}} \mathbf{n}^{*g}\cdot\varphi^{hg}_{,_P}\,\delta d_P d\theta^1 d\theta^2\right]\\
&\quad -\kappa\frac{p^g_i}{v^g_i}\left[\begin{array}{l}\bigcup_{e=1}^{n_{el}}\int_{_g\theta^{2(e)}}\int_{_g\theta^{1(e)}} \mathbf{n}^{*g}\cdot\varphi^{hg}_{,_Q}\,\Delta d_Q d\theta^1 d\theta^2 \bigcup_{e=1}^{n_{el}}\int_{_f\theta^{2(e)}}\int_{_f\theta^{1(e)}} \mathbf{n}^{*f}\cdot\varphi^{hf}_{,_P}\,\delta d_P d\theta^1 d\theta^2\\ +\bigcup_{e=1}^{n_{el}}\int_{_f\theta^{2(e)}}\int_{_f\theta^{1(e)}} \mathbf{n}^{*f}\cdot\varphi^{hf}_{,_Q}\,\Delta d_Q d\theta^1 d\theta^2 \bigcup_{e=1}^{n_{el}}\int_{_g\theta^{2(e)}}\int_{_g\theta^{1(e)}} \mathbf{n}^{*g}\cdot\varphi^{hg}_{,_P}\,\delta d_P d\theta^1 d\theta^2\end{array}\right]\\
&\quad -\kappa\frac{p^g_i}{v^g_i}\left[\bigcup_{e=1}^{n_{el}}\int_{_f\theta^{2(e)}}\int_{_f\theta^{1(e)}} \mathbf{n}^{*f}\cdot\varphi^{hf}_{,_Q}\,\Delta d_Q d\theta^1 d\theta^2 \bigcup_{e=1}^{n_{el}}\int_{_f\theta^{2(e)}}\int_{_f\theta^{1(e)}} \mathbf{n}^{*f}\cdot\varphi^{hf}_{,_P}\,\delta d_P d\theta^1 d\theta^2\right]\\
&\quad +\frac{\rho\mathbf{g}\cdot\mathbf{n}^{\mathbf{0}}}{\|S_0\|}\left[\bigcup_{e=1}^{n_{el}}\int_{_f\theta^{2(e)}}\int_{_f\theta^{1(e)}} \mathbf{n}^{*f}\cdot\varphi^{hf}_{,_Q}\,\Delta d_Q d\theta^1 d\theta^2 \bigcup_{e=1}^{n_{el}}\int_{_f\theta^{2(e)}}\int_{_f\theta^{1(e)}} \mathbf{n}^{*f}\cdot\varphi^{hf}_{,_P}\,\delta d_P\, d\theta^1 d\theta^2\right]\\
&\quad +\frac{1}{2}\bigcup_{e=1}^{n_{el}}\int_{_g\theta^{2(e)}}\int_{_g\theta^{1(e)}} p^g\left[\mathbf{n}^{*g}_{,_Q}\,\Delta d_Q\cdot\varphi^{hg}_{,_P}\,\delta d_P + \mathbf{n}^{*g}_{,_P}\,\delta d_P\cdot\varphi^{hg}_{,_Q}\,\Delta d_Q\right] d\theta^1 d\theta^2\\
&\quad +\frac{1}{2}\bigcup_{e=1}^{n_{el}}\int_{_f\theta^{2(e)}}\int_{_f\theta^{1(e)}}\left[\begin{array}{c}\rho\mathbf{g}\cdot\varphi^{hf}_{,_P}\,\delta d_P\;\mathbf{n}^{*f}\cdot\varphi^{hf}_{,_Q}\,\Delta d_Q\\ +\rho\mathbf{g}\cdot\varphi^{hf}_{,_Q}\,\Delta d_Q\;\mathbf{n}^{*f}\cdot\varphi^{hf}_{,_P}\,\delta d_P\\ +p^f\mathbf{n}^{*f}_{,_P}\,\delta d_P\cdot\varphi^{hf}_{,_Q}\,\Delta d_Q + p^f\mathbf{n}^{*f}_{,_Q}\,\Delta d_Q\cdot\varphi^{hf}_{,_P}\,\delta d_P\end{array}\right] d\theta^1 d\theta^2,
\end{aligned} \tag{4.60}$$

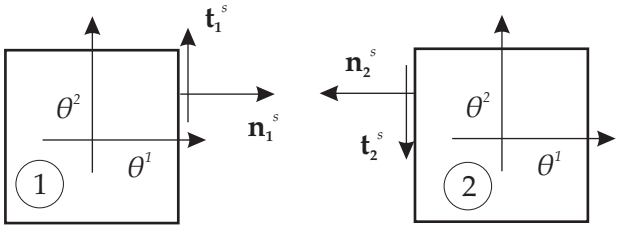

Figure 4.11: Illustration for tangential vectors of two adjacent element sharing a common edge.

where d_P and d_Q are the P^{th} and Q^{th} dof of the discrete system, respectively. In this equation, the summation $\cup_{e=1}^{n_{el}}$ is only summed over all elements belong to the chamber i under interest. For numerical integration of each membrane element of a partially filled chamber, in certain cases there is some element which is not completely wetted. This situation may influence the accuracy of integration due to some missing integration point. This pathological circumstance may be circumvented by employing the idea of the level set method [OS88] which is widely used to impose discontinuities within an element. It is noteworthy to mention the vanishing of the element boundary terms which are the element-level version of eqs.(4.48) and (4.50). For two adjacent elements sharing a common edge as drawn in Figure 4.11, one observes that the edge tangential vector of element1 $\mathbf{t}_1^s$ at the common edge points into an opposite direction of the edge tangential vector of element2 $\mathbf{t}_2^s$. Thus, the summation of the boundary terms in eq. (4.48) at this common edge can be expressed by

$$\begin{aligned}\frac{1}{2}\int\limits_{g_S(e)} p^g\left(\Delta\mathbf{x}^g\times\mathbf{t}^{sg}\right)\cdot\delta\varphi^g ds &= \frac{1}{2}\int\limits_{g_S(e)} p^g\left(\Delta\mathbf{x}^g\times\mathbf{t}_1^{sg}\right)\cdot\delta\varphi^g ds + \frac{1}{2}\int\limits_{g_S(e)} p^g\left(\Delta\mathbf{x}^g\times\mathbf{t}_2^{sg}\right)\cdot\delta\varphi^g ds\\ &= \frac{1}{2}\int\limits_{g_S(e)} p^g\left(\Delta\mathbf{x}^g\times\mathbf{t}_1^{sg}\right)\cdot\delta\varphi^g ds - \frac{1}{2}\int\limits_{g_S(e)} p^g\left(\Delta\mathbf{x}^g\times\mathbf{t}_1^{sg}\right)\cdot\delta\varphi^g ds\\ &= 0\end{aligned} \tag{4.61}$$

with an assumption of a continuous load function over the common edge. Likewise, the vanishing of eq. (4.50) at a common edge of two adjacent elements is fulfilled via

$$\frac{1}{2}\int\limits_{f_S(e)} p^f\left(\Delta\mathbf{x}^f\times\mathbf{t}^{sf}\right)\cdot\delta\varphi^f ds = 0. \tag{4.62}$$

For this reason, the skew symmetric boundary terms of two adjacent elements sharing a common edge cancel each other when they are assembled into the system stiffness matrices and all of them are discarded from eq. (4.60).

4.5.1 Load stiffness from deformation-dependent forces

From the discrete virtual work equation of a static system with membrane finite elements in eq. (2.93), the contribution from deformation-dependent forces is a member in the class of the external virtual work $G_{fol}^h \in G_{ext}^h$. With the same procedure in section 2.3.1.2, the *load*

stiffness matrix $\mathbf{K}_l$ caused by the deformatin-dependent forces can be added to the system matrix in eq. (2.106) such that

$$\mathbf{K}_T = \mathbf{K}_{e+u} + \mathbf{K}_g - \mathbf{K}_l, \tag{4.63}$$

where each component of the load stiffness matrix $\mathbf{K}_l$ for a single chamber i is determined by

$$\begin{aligned}
K_{l_{PQ}} = & \left[\begin{array}{c} \frac{1}{2} \int\limits_{g\theta^2} \int\limits_{g\theta^1} p^g \left[\mathbf{n}^{*g}_{,Q} \cdot \varphi^{hg}_{,P} + \mathbf{n}^{*g}_{,P} \cdot \varphi^{hg}_{,Q} \right] d\theta^1 d\theta^2 \\ + \frac{1}{2} \int\limits_{f\theta^2} \int\limits_{f\theta^1} \left[\begin{array}{c} \rho \mathbf{g} \cdot \varphi^{hf}_{,P} \ \mathbf{n}^{*f} \cdot \varphi^{hf}_{,Q} \\ + \rho \mathbf{g} \cdot \varphi^{hf}_{,Q} \ \mathbf{n}^{*f} \cdot \varphi^{hf}_{,P} \\ + p^f \mathbf{n}^{*f}_{,P} \cdot \varphi^{hf}_{,Q} + p^f \mathbf{n}^{*f}_{,Q} \cdot \varphi^{hf}_{,P} \end{array} \right] d\theta^1 d\theta^2 \end{array} \right] \Bigg\} K^0_{l_{PQ}} \\
& + \frac{\rho \mathbf{g} \cdot \mathbf{n}^0}{\|S_0\|} \int\limits_{f\theta^2} \int\limits_{f\theta^1} \mathbf{n}^{*f} \cdot \varphi^{hf}_{,Q} \, d\theta^1 d\theta^2 \int\limits_{f\theta^2} \int\limits_{f\theta^1} \mathbf{n}^{*f} \cdot \varphi^{hf}_{,P} \, d\theta^1 d\theta^2 \Bigg\} \beta^0 (b_Q b_P) \\
& - \kappa \frac{p^g_i}{v^g_i} \left[\int\limits_{g\theta^2} \int\limits_{g\theta^1} \mathbf{n}^{*g} \cdot \varphi^{hg}_{,Q} \, d\theta^1 d\theta^2 \int\limits_{g\theta^2} \int\limits_{g\theta^1} \mathbf{n}^{*g} \cdot \varphi^{hg}_{,P} \, d\theta^1 d\theta^2 \right] \Bigg\} \beta^1 (a_Q a_P) \\
& - \kappa \frac{p^g_i}{v^g_i} \left[\begin{array}{c} \int\limits_{g\theta^2} \int\limits_{g\theta^1} \mathbf{n}^{*g} \cdot \varphi^{hg}_{,Q} \, d\theta^1 d\theta^2 \int\limits_{f\theta^2} \int\limits_{f\theta^1} \mathbf{n}^{*f} \cdot \varphi^{hf}_{,P} \, d\theta^1 d\theta^2 \\ + \int\limits_{f\theta^2} \int\limits_{f\theta^1} \mathbf{n}^{*f} \cdot \varphi^{hf}_{,Q} \, d\theta^1 d\theta^2 \int\limits_{g\theta^2} \int\limits_{g\theta^1} \mathbf{n}^{*g} \cdot \varphi^{hg}_{,P} \, d\theta^1 d\theta^2 \end{array} \right] \Bigg\} \beta^1 (a_Q b_P + b_Q a_P) \\
& - \kappa \frac{p^g_i}{v^g_i} \left[\int\limits_{f\theta^2} \int\limits_{f\theta^1} \mathbf{n}^{*f} \cdot \varphi^{hf}_{,Q} \, d\theta^1 d\theta^2 \int\limits_{f\theta^2} \int\limits_{f\theta^1} \mathbf{n}^{*f} \cdot \varphi^{hf}_{,P} \, d\theta^1 d\theta^2 \right] \Bigg\} \beta^1 (b_Q b_P).
\end{aligned} \tag{4.64}$$

For the sake of brevity, the summation symbol over each element in eq. (4.60) is dropped out from eq. (4.64). Therefore, each term in eq. (4.64) which is written in the global structure level is then referred back to the corresponding term on the element level in eq. (4.60). With further rearrangement, the load stiffness matrix in eq. (4.64) can be concisely written by

$$\mathbf{K}_l = \mathbf{K}^0_l + \beta^0 \mathbf{b} \otimes \mathbf{b} + \beta^1 \mathbf{a} \otimes \mathbf{a} + \beta^1 (\mathbf{a} \otimes \mathbf{b} + \mathbf{b} \otimes \mathbf{a}) + \beta^1 \mathbf{b} \otimes \mathbf{b}. \tag{4.65}$$

The so called load-stiffness matrix $\mathbf{K}_l$ is composed of two portions: (i) First, $\mathbf{K}^0_l$ reflects influences of the change in the normal vector $\Delta \mathbf{n}^*$ of a chamber filled with gas and/or fluid. (ii) Secondly, influences of the change in pressure Δp within each chamber filled with gas and/or fluid is transmitted to the main stiffness matrix of the membrane during the deformation via various update tensors, the rest of eq. (4.65). In this equation, $\mathbf{a}$ and $\mathbf{b}$ play the roles of update vectors for the enclosed gas and fluid volume, while β^0 and β^1 are the fluid pressure gradient and the gas pressure gradient, respectively. Obviously, the coupling of the gas and fluid domain via the gas volume and the fluid depth variation is expressed in term: $\beta^1 (\mathbf{a} \otimes \mathbf{b} + \mathbf{b} \otimes \mathbf{a})$. Besides, the deformation-dependent force vector, being a member of the external force $\mathbf{f}^{fol}(t) \in \mathbf{f}^{ext}(t)$ in eq. (2.96), can be explained with the help of eq. (4.13) by

$$\begin{aligned}
f^{fol}_P(t) &= \int\limits_{\theta^2} \int\limits_{\theta^1} p \mathbf{n}^* \cdot \varphi^h_{,P} \, d\theta^1 d\theta^2 \\
&= \int\limits_{g\theta^2} \int\limits_{g\theta^1} p^g \mathbf{n}^{*g} \cdot \varphi^{hg}_{,P} \, d\theta^1 d\theta^2 + \int\limits_{f\theta^2} \int\limits_{f\theta^1} \left(p^{\mathbf{x}^f} - p^{\mathbf{x}^0} + p^g \right) \mathbf{n}^{*f} \cdot \varphi^{hf}_{,P} \, d\theta^1 d\theta^2.
\end{aligned} \tag{4.66}$$

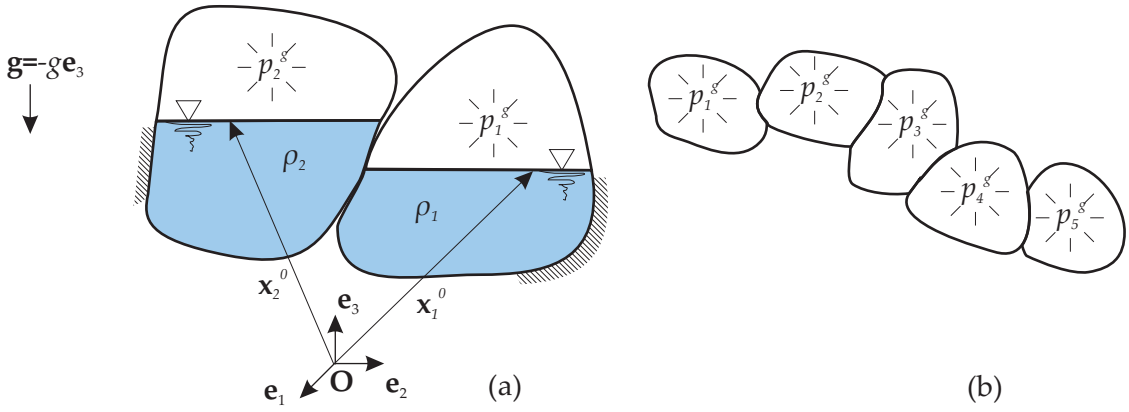

Figure 4.12: Illustration for multichamber enclosed membrane filled with gas and(or) fluid.

Based on eqs. (2.96), (4.63)-(4.66), the algebraic system of equation can be set up in a compact form, viz.

$$\begin{aligned} \mathbf{K}_T \Delta\mathbf{d} &= \mathbf{f}^{ext}(t) - \mathbf{f}^{int}(\mathbf{d}_t) = \mathbf{f} \\ \left[\mathbf{K}_{e+u} + \mathbf{K}_g - \mathbf{K}_l\right] \Delta\mathbf{d} &= \mathbf{f}^{ded}(t) + \mathbf{f}^{fol}(t) - \mathbf{f}^{int}(\mathbf{d}_t) \end{aligned} \tag{4.67}$$

where $\mathbf{f}$ is the out-of-balance force vector introduced in eq. (2.96) and $\mathbf{f}^{ded}$ is the deformation-independent portion of $\mathbf{f}^{ext}(t)$ as mentioned in section 2.1.6.1. Substituting (4.65) in (4.67), we obtain the system of equations for a single chamber i by

$$\left[\mathbf{K}_{e+u} + \mathbf{K}_g - \left(\mathbf{K}_l^0 + \beta^0 \mathbf{b}\otimes\mathbf{b} + \beta^1 \begin{bmatrix} \mathbf{a}\otimes\mathbf{a} \\ +\mathbf{b}\otimes\mathbf{b} \\ +\mathbf{a}\otimes\mathbf{b} \\ +\mathbf{b}\otimes\mathbf{a} \end{bmatrix}\right)\right] \Delta\mathbf{d} = \begin{bmatrix} \mathbf{f}^{ded}(t) - \mathbf{f}^{int}(\mathbf{d}_t) \\ +\mathbf{f}^{fol}(t) \end{bmatrix}. \tag{4.68}$$

The symmetry of this stiffness matrix reflects the conservativeness of this structure as described in section 4.4 under such follower forces due to special boundary conditions mentioned in section 4.3.1.1. Introduced in [RS03], the interaction of the enclosed gas and fluid are transferred towards the membrane surface via the update tensors from gas $\mathbf{a}\otimes\mathbf{a}$ and the update vector from the fluid $\mathbf{b}\otimes\mathbf{b}$. Note that the mixed terms $\mathbf{a}\otimes\mathbf{b}$ and $\mathbf{b}\otimes\mathbf{a}$ designate the coupling of the enclosed gas and fluid.

4.5.2 Extension for multichamber case

An extension of the derived formula for the single chamber problem to the multichamber membrane (see Figure 4.12) can be accomplished by a summation of all contributions from each single chamber i to create the system of all chambers n_b. Therefore, the algebraic system of equations in eq. (4.68) is changed to

$$\left[\mathbf{K}_{e+u} + \mathbf{K}_g - \sum_{i=1}^{n_b} \left(\mathbf{K}_l^0 + \beta^0 \mathbf{b}\otimes\mathbf{b} + \beta^1 \begin{bmatrix} \mathbf{a}\otimes\mathbf{a} \\ +\mathbf{b}\otimes\mathbf{b} \\ +\mathbf{a}\otimes\mathbf{b} \\ +\mathbf{b}\otimes\mathbf{a} \end{bmatrix}\right)_i\right] \Delta\mathbf{d} = \begin{bmatrix} \mathbf{f}^{ded}(t) - \mathbf{f}^{int}(\mathbf{d}_t) \\ +\sum_{i=1}^{n_b} \mathbf{f}_i^{fol}(t) \end{bmatrix} \tag{4.69}$$

4.6 Solution Algorithm

By introducing the update tensors, typical sparse system stiffness matrix $\mathbf{K}_{e+u} + \mathbf{K}_g - \mathbf{K}_l^0$ evolves into a fully-populated one whose factorization requires enormous efforts and extensive storage memory. This circumstance is a catastrophe for a direct solver. As a matter of fact, the sensitivity of the inverse of a matrix due to a certain change in a column of the matrix have caught significant attentions due to various emerging applications. Thereby, the objective of this section is not only to avoid factorization of the system matrix due to the update tensors, but also to reuse the inverse of the system matrix which requires factorization only once and for all within an iteration step. Therefore, this technique has a key benefit to reduce computational efforts significantly.

4.6.1 Woodbury's formula

For the reason mentioned above, we employ the Woodbury's formula [Woo50] which is the block-matrix solution [Pre92] for a specific form of a system of equations:

$$\left(\mathbf{A} + \sum_{k=1}^{p} \mathbf{u_k} \otimes \mathbf{v_k}\right) \Delta\mathbf{d} = \left(\mathbf{A} + \mathbf{U}\mathbf{V}^T\right) \Delta\mathbf{d} = \mathbf{f} \tag{4.70}$$

with $\mathbf{U} = \left[\{\mathbf{u}_1\} \dots \{\mathbf{u}_p\}\right]$ and $\mathbf{V} = \left[\{\mathbf{v}_1\} \dots \{\mathbf{v}_p\}\right]$. The formula relates the inverse of a modified matrix which is perturbed by the updated tensors $\sum_{k=1}^{p} \mathbf{u_k} \otimes \mathbf{v_k}$ to the inverse of an original matrix $\mathbf{A}$, or in other words, this algorithm updates the inverse of the original matrix $\mathbf{A}^{-1}$ with the help of auxiliary matrices:

$$\mathbf{Z}^{n_{dof} \times p} = \left[\left\{\mathbf{A}^{-1}\mathbf{u}_1\right\} \dots \left\{\mathbf{A}^{-1}\mathbf{u}_p\right\}\right], \tag{4.71}$$

$$\mathbf{H}^{p \times p} = \left[\mathbf{I} + \mathbf{V}^T\mathbf{Z}\right]^{-1}, \tag{4.72}$$

$$\mathbf{A}\mathbf{y} = \mathbf{f}. \tag{4.73}$$

Eventually, the solution is determined by

$$\Delta\mathbf{d} = \mathbf{y} - \mathbf{Z}\left[\mathbf{H}\left(\mathbf{V}^T\mathbf{y}\right)\right]. \tag{4.74}$$

For interested readers, Haßler and Schweizerhof [HS08b] discussed the aspect of memory requirements and performance of this solution method and Hager [Hag89] provided an overview of various methods for updating the inverse of a matrix. As well in that work, Woodbury's formula is generalized to a class for the inverse of the *Schur complement* (see [Cot74]).

If matrix $\mathbf{A}$ has a convenient structure–sparse, factorized into a convenient form–then the linear systems in eqs. (4.71) and (4.73) can be rapidly solved. In case that the number of update vectors p is small, then the rank of the modification matrix $\mathbf{U}\mathbf{V}^T$ is as well small relative to the dimension of matrix $\mathbf{A}$. As a result, the system of p linear equations $\mathbf{H}\left(\mathbf{V}^T\mathbf{y}\right)$ is solved quickly. For summary, the modification formula is effective in case that the coefficient

For each iteration step:

Assembly global stiffness matrix $\mathbf{K}_{e+u} + \mathbf{K}_g$ and global RHS force vector $\mathbf{f}$ (2.106); (2.96)

Loop over all chambers i $\sum_{i=1}^{n_b}$; initialize $(i = 1)$

- Loop over all elements of a chamber i $(\sum_{e=1}^{n_{el(i)}})$; initialize $(e = 1)$
  - Volume contribution from an element $v_i^{(e)} = \frac{1}{3} \int_{\theta^2} \int_{\theta^1} \mathbf{x} \cdot \mathbf{n}^* d\theta^1 d\theta^2$ (4.10)
  - Sum volume for a chamber $v_i = v_i + v_i^{(e)}$ (4.10)
- $\Leftarrow$ $e = e + 1$
- Update pressure for a chamber i; $p_i = p_i(v_i, V_i, P_i, K_i)$ (4.9) or (4.8)
- Loop over all elements of a chamber i $(\sum_{e=1}^{n_{el(i)}})$; initialize $(e = 1)$
  - Element load stiffness from $\Delta\mathbf{n}$: $\mathbf{K}_{l_i}^{0(e)}$ (4.64)
  - Element load vector: $\mathbf{f}_i^{fol(e)}$ (4.66)
  - Element update vectors: $\mathbf{a}_i^{(e)}$ and $\mathbf{b}_i^{(e)}$ (4.64)
  - Assembly $\mathbf{K}_{l_i}^{0(e)}$ to system matrix: $\mathbf{K}_T = \mathbf{K}_T + \mathbf{K}_{l_i}^{0(e)}$ (4.68)
  - Assembly $\mathbf{f}_i^{fol(e)}$ to global RHS vector: $\mathbf{f} = \mathbf{f} + \mathbf{f}_i^{fol(e)}$ (4.68)
  - Assembly $\mathbf{a}_i^{(e)}$ and $\mathbf{b}_i^{(e)}$ to global ones: $\mathbf{a} = \mathbf{a} + \mathbf{a}_i^{(e)}$ and $\mathbf{b} = \mathbf{b} + \mathbf{b}_i^{(e)}$ (4.68)
- $\Leftarrow$ $e = e + 1$
- $\Leftarrow$ Set up $i = i + 1$ until $i + 1 = n_b$

Figure 4.13: Assembly of element contribution to create system matrices.

matrix for a linear system can be expressed as the sum of a "nice" matrix and a small rank perturbation. Note that matrices **U** and **V** must be chosen carefully since an inappropriate choice can lead to an ill-conditioned matrix **H** of eq. (4.72) for which the computed result is useless. For more details about the topic, interested readers may look in Hager [Hag89]. For a vivid explanation, the assembly process for each element to create the system matrices is provided in Figure 4.13.

4.6.2 Nonlinear equilibrium path following algorithm

The loss of stability is a very important issue in nonlinear structural mechanics, in particular the very thin structures with high slenderness ratio like shells and membranes. In order to detect the situation where structures lose their stability, various general purpose solution procedures which are effective to trace along the equilibrium path have been proposed. One of which is the *arclength-controlled algorithm*, see e.g. Riks [Rik79, Ram80, Cri81].

Discussions of arclength-controlled method with the problem of Fluid-Structure interaction are well worth considering. Rumpel and Schweizerhof [Rum03, RS03, RS04] provided a technique to apply the arclength-controlled algorithm to follow the equilibrium path for the volume-dependent pressure loading from gas and fluid for nonlinear FE analysis of thin-walled structures. For the problem of an enclosed membrane filled with gas and/or fluid presented in this chapter, all terms of the deformation-dependent load stiffness $\mathbf{K}_l$ in eq. (4.65) influence the critical point of the pure membrane stiffness $\mathbf{K}_{e+u} + \mathbf{K}_g$. At the critical point, the system is singular and significantly deformed. In many cases, it results in a convergence problem. The arclength-controlled algorithm is an effective measurement for the critical load of the system by tracing along the equilibrium path beyond the critical point towards the postcritical regime. However, the postcritical numerical results, e.g. the postbuckling load-displacement equalibrium path, are not meaningful from the mechanical point of view due to the facts that there exists a question whether the inertial forces provoked by movements of the structure and fluid masses after buckling is still negligible from the equilibrium equation.

In general, the nonlinear path following algorithms are roughly categorized into three groups: the load controlled algorithm, the displacement controlled algorithm and the arclength controlled algorithm. A brief overview for all of them is provided in the following sections with an emphasis on the arclength method due to its advantages to handily deal with singular systems of equations at the critical points. The main idea of all algorithms is to augment the original system of equation in eq. (4.68) or (4.69) by an additional discrete constraint equation:

$$g(\varphi_t^h(\mathbf{X}), \lambda_t) = 0 \tag{4.75}$$

with the objective of increasing the number of equations to an adequate degree for solving all system unknowns which are a combination of the incremental change of the system degree of freedom $\Delta\mathbf{d}$ and an additional pseudo-time unknown. Physically interpreted as the control parameter for the load factor $\lambda(t)$ of the applied external force $\mathbf{f}^{ext}$ in eq.(2.95), the pseudo-time parameter is the static counterpart for the real time parameter t for the dynamic case in eqs. (2.91) and (2.92). Therefore, the augmented discrete system of equations based on the virtual work of a static system for membrane finite elements in eq. (2.93) and the constraint equation in eq. (4.75) can be written by

$$\begin{aligned} G^h(\mathbf{d}_t, \delta\mathbf{d}, \lambda_t) &= G^h_{int}(\mathbf{d}_t, \delta\mathbf{d}) + G^h_{ext}(\mathbf{d}_t, \delta\mathbf{d}, \lambda_t) = 0 \\ &= G^h_{int}(\mathbf{d}_t, \delta\mathbf{d}) + G^h_{ded}(\lambda_t) + G^h_{fol}(\mathbf{d}_t, \delta\mathbf{d}, \lambda_t) = 0 \qquad (4.76) \\ g(\mathbf{d}_t, \lambda_t) &= 0. \qquad (4.77) \end{aligned}$$

With eqs. (2.87) and (2.89), an expansion of the discrete virtual work equation in (4.76) can be expressed by

$$\begin{aligned} -\delta\mathbf{d} \cdot \mathbf{f}(\mathbf{d}_t, \lambda_t) &= \delta\mathbf{d} \cdot (\mathbf{f}^{int} - \mathbf{f}^{ext}) = 0 \\ -\mathbf{f}(\mathbf{d}_t, \lambda_t) &= \mathbf{f}^{int}(\mathbf{d}_t) - \mathbf{f}^{ext}(\mathbf{d}_t, \lambda_t) = 0 \\ -\mathbf{f}(\mathbf{d}_t, \lambda_t) &= \mathbf{f}^{int}(\mathbf{d}_t) - \mathbf{f}^{ded}(\lambda_t) - \mathbf{f}^{fol}(\mathbf{d}_t, \lambda_t) = 0, \end{aligned} \tag{4.78}$$

where the n_{dof}-vector $\mathbf{f}$ is the out-of-balance force vector on the right side of eq. (4.67). Note that the external force is a combination of the deformation-independent force $\mathbf{f}^{ded}$ and the

Table 4.3: A summary for a two-step process controlled by different load factors in each step.

Step	Description	Control of $\mathbf{f}^{ded}$	Control of $\mathbf{f}^{fol}$
1	Inflating the cushion by gas pressure	none	λ^{fol}
2	Applying deformation-independent forces	λ^{ded}	state eqs. (4.8),(4.9)

deformation-dependent force $\mathbf{f}^{fol}$ with $\mathbf{f}^{ext} = \mathbf{f}^{ded} + \mathbf{f}^{fol}$ as mentioned in section 2.3.1.2. Furthermore, the deformation-dependent force can be either a function of only the current nodal position $\mathbf{f}^{fol}(\mathbf{d}_t)$, e.g. exerting an external applied force upon an enclosed membrane filled with gas whose pressure is regulated by the state equation, or a function of both the current nodal position and the load factor $\mathbf{f}^{fol}(\mathbf{d}_t, \lambda_t)$, e.g. inflation of a cushion. As a basis for the Newton-Raphson method, linearization of the vector $\mathbf{f}$ in (4.78) yields

$$\begin{aligned}
\mathbf{LIN}(-\mathbf{f}(\mathbf{d}_t, \lambda_t)) = -\mathbf{f}(\mathbf{d}_t^k, \lambda_t^k) - \Delta\mathbf{f}(\mathbf{d}_t^k, \lambda_t^k) = 0 \\
\Rightarrow -\Delta_{\mathbf{d}}\mathbf{f}(\mathbf{d}_t^k, \lambda_t^k) - \Delta_\lambda \mathbf{f}(\mathbf{d}_t^k, \lambda_t^k) = \mathbf{f}(\mathbf{d}_t^k, \lambda_t^k) \\
-\mathbf{f}_{,\mathbf{d}}\,(\mathbf{d}_t^k, \lambda_t^k)\Delta\mathbf{d} - \mathbf{f}_{,\lambda}\,(\mathbf{d}_t^k, \lambda_t^k)\Delta\lambda = \mathbf{f}(\mathbf{d}_t^k, \lambda_t^k)
\end{aligned} \tag{4.79}$$

According to eq. (4.78), one can expand $-\mathbf{f}_{,\mathbf{d}}\,(\mathbf{d}_t^k, \lambda_t^k)\Delta\mathbf{d}$ and $-\mathbf{f}_{,\lambda}\,(\mathbf{d}_t^k, \lambda_t^k)\Delta_\lambda$ in eq. (4.79) to

$$-\mathbf{f}_{,\mathbf{d}}\,(\mathbf{d}_t^k, \lambda_t^k) = \underbrace{\frac{\partial \mathbf{f}^{int}(\mathbf{d})}{\partial \mathbf{d}}\Big|_{\mathbf{d}_t^k}}_{\mathbf{K}_{e+u}+\mathbf{K}_g \text{ eq. (2.106)}} - \underbrace{\frac{\partial \mathbf{f}^{fol}(\mathbf{d}, \lambda)}{\partial \mathbf{d}}\Big|_{\mathbf{d}_t^k, \lambda_t^k}}_{\mathbf{K}_l \text{ eq. (4.65)}} = \underbrace{\mathbf{K}_{e+u} + \mathbf{K}_g - \mathbf{K}_l}_{\text{see eq. (4.67)}}, \tag{4.80}$$

$$-\mathbf{f}_{,\lambda}\,(\mathbf{d}_t^k, \lambda_t^k) = -\frac{\partial \mathbf{f}^{ded}(\lambda)}{\partial \lambda}\Big|_{\lambda_t^k} - \frac{\partial \mathbf{f}^{fol}(\mathbf{d}, \lambda)}{\partial \lambda}\Big|_{\mathbf{d}_t^k, \lambda_t^k}. \tag{4.81}$$

In the case of $-\mathbf{f}_{,\lambda}$ in eq. (4.81), there exist two questions whether the external force vector $\mathbf{f}^{ded}$ and $\mathbf{f}^{fol}$ are proportional to the load factor $\lambda(t)$ and whether $\mathbf{f}^{ded}$ and $\mathbf{f}^{fol}$ are controlled by different load factors, e.g. λ^{ded} and λ^{fol}.

Table 4.3 demonstrates an example of a loading control process for the gas cushion under interest. At first, this enclosed membrane is incrementally inflated by the gas pressure regulated by the load factor for the gas λ^{fol} until it reaches the fully inflated state. Then, the gas pressure inside the cushion is regulated by the state equation either the pneumatic law or the hydraulic law described in section 4.2.3 while a deformation-independent external applied force which is controlled by its own load factor λ^{ded} is gradually exerted on the gas cushion.

Likewise, linearization of the constraint equation (4.77) leads to

$$\begin{aligned}
\mathbf{LIN}\,(g(\mathbf{d}_t, \lambda_t)) = g(\mathbf{d}_t^k, \lambda_t^k) + \Delta g(\mathbf{d}_t^k, \lambda_t^k) = 0, \\
\Rightarrow \Delta_{\mathbf{d}} g(\mathbf{d}_t^k, \lambda_t^k) + \Delta_\lambda g(\mathbf{d}_t^k, \lambda_t^k) = -g(\mathbf{d}_t^k, \lambda_t^k), \\
g_{,\mathbf{d}}\,(\mathbf{d}_t^k, \lambda_t^k)\Delta\mathbf{d} + g_{,\lambda}\,(\mathbf{d}_t^k, \lambda_t^k)\Delta\lambda = -g(\mathbf{d}_t^k, \lambda_t^k).
\end{aligned} \tag{4.82}$$

With a combination of eq.(4.79) and eq. (4.82), the algebraic system of equations for eq.(4.76), augmented by the constraint function from eq.(4.77), can be written in the matrix form:

$$\begin{bmatrix} -\mathbf{f}_{,\mathbf{d}}\,(\mathbf{d}_t^k, \lambda_t^k) & -\mathbf{f}_{,\lambda}\,(\mathbf{d}_t^k, \lambda_t^k) \\ g_{,\mathbf{d}}\,(\mathbf{d}_t^k, \lambda_t^k) & g_{,\lambda}\,(\mathbf{d}_t^k, \lambda_t^k) \end{bmatrix} \begin{Bmatrix} \Delta\mathbf{d} \\ \Delta\lambda \end{Bmatrix} = \begin{Bmatrix} \mathbf{f}(\mathbf{d}_t^k, \lambda_t^k) \\ -g(\mathbf{d}_t^k, \lambda_t^k) \end{Bmatrix} \tag{4.83}$$

for which the incremental change of nodal coordinate $\Delta\mathbf{d}$ and the incremetal change in load factor $\Delta\lambda$ is solved. We can now solve first for $\Delta\lambda$ and subsequently for $\Delta\mathbf{d}$. The result may be presented by rearrange the first line of eq.(4.83) to

$$\Delta\mathbf{d} = -\left(\mathbf{f}_{,\mathbf{d}}\right)^{-1}\mathbf{f} - \left(\mathbf{f}_{,\mathbf{d}}\right)^{-1}\mathbf{f}_{,\lambda}\,\Delta\lambda. \tag{4.84}$$

Substituting eq. (4.84) in the second line of eq.(4.83) yields

$$\Delta\lambda = \frac{g_{,\mathbf{d}}\cdot\left(\mathbf{f}_{,\mathbf{d}}\right)^{-1}\mathbf{f} - g}{g_{,\lambda} - g_{,\mathbf{d}}\cdot\left(\mathbf{f}_{,\mathbf{d}}\right)^{-1}\mathbf{f}_{,\lambda}}. \tag{4.85}$$

After $\Delta\lambda$ is obtained, then backsubstituion of $\Delta\lambda$ in eq.(4.84) gives the incremental change in nodal coordinate $\Delta\mathbf{d}$. Note that independent parameters are dropped out to avoid ambiguities. In case that the update tensors in eq. (4.68) or (4.69) exist, the Woodbury's formula in eq. (4.70) is employed to find out $\left(\mathbf{f}_{,\mathbf{d}}\right)^{-1}\mathbf{f}$ and $\left(\mathbf{f}_{,\mathbf{d}}\right)^{-1}\mathbf{f}_{,\lambda}$ of eqs.(4.85) and (4.84), respectively. Note that this partitioned update process is performed on the structure level where all relevant structure level vectors are created by assembling the contribution from each element (see Figure 4.13). At this point, the only one left to define is the constraint function for each path-following algorithm. Thus, the following subsections are dedicated to briefly discuss this issue.

4.6.2.1 Load controlled algorithm

◇ Constraint:

$$\begin{aligned} &g(\mathbf{d}_t^k, \lambda_t^k) = \lambda_t^k - \bar{\lambda}_t = 0 \quad \Rightarrow \quad \Delta\lambda = 0, \\ &\Rightarrow g_{,\mathbf{d}}\left(\mathbf{d}_t^k, \lambda_t^k\right) = 0, \quad g_{,\lambda}\left(\mathbf{d}_t^k, \lambda_t^k\right) = 1. \end{aligned} \tag{4.86}$$

◇ Predictor: iteration number $k = 0$

$$g(\mathbf{d}_t^0, \lambda_t^0) = \lambda_t^0 - \bar{\lambda}_t = 0, \tag{4.87}$$

where $\bar{\lambda}_t$ is the prescribed load factor for the current time step t.

4.6.2.2 Displacement controlled algorithm

◇ Constraint:

$$\begin{aligned} &g(\mathbf{d}_t^k, \lambda_t^k) = {d_P}_t^k - \bar{d}_{Pt} = 0, \\ &\Rightarrow g_{,\mathbf{d}}\left(\mathbf{d}_t^k, \lambda_t^k\right) = g_{,d_Q}\left(\mathbf{d}_t^k, \lambda_t^k\right) = \delta_P^Q \begin{cases} 1 & P = Q \\ 0 & \text{otherwise} \end{cases}, \quad g_{,\lambda}\left(\mathbf{d}_t^k, \lambda_t^k\right) = 0. \end{aligned} \tag{4.88}$$

◇ Predictor: iteration number $k = 0$

$$g(\mathbf{d}_t^0, \lambda_t^0) = {d_P}_t^0 - \bar{d}_{Pt} = 0, \tag{4.89}$$

where $\bar{d}_{Pt}$ is the prescribed nodal coordinate of the P^{th}-dof for the current time step t.

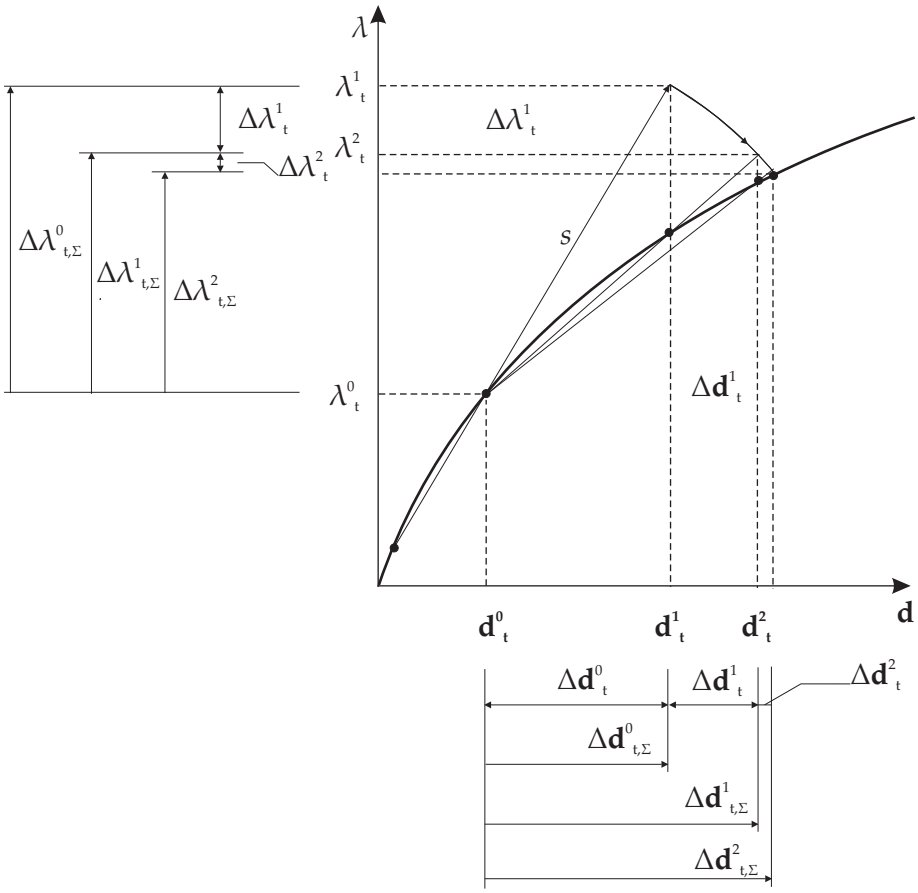

Figure 4.14: Illustration for arclength-controlled algorithm.

4.6.2.3 Arclength controlled algorithm

◇ Constraint:

$$g(\mathbf{d}_t^k, \lambda_t^k) = \Delta\mathbf{d}_{t,\sum}^k \cdot \Delta\mathbf{d}_{t,\sum}^k + \left(\Delta\lambda_{t,\sum}^k\right)^2 - \bar{s}^2 = 0,$$
$$\Rightarrow g_{,\mathbf{d}}\left(\mathbf{d}_t^k, \lambda_t^k\right) = 2\Delta\mathbf{d}_{t,\sum}^k, \quad g_{,\lambda}\left(\mathbf{d}_t^k, \lambda_t^k\right) = 2\Delta\lambda_{t,\sum}^k. \tag{4.90}$$

◇ Predictor: iteration number $k = 0$

$$g(\mathbf{d}_t^0, \lambda_t^0) = \Delta\mathbf{d}_{t,\sum}^0 \cdot \Delta\mathbf{d}_{t,\sum}^0 + \left(\Delta\lambda_{t,\sum}^0\right)^2 - \bar{s}^2 = 0 \tag{4.91}$$

$$\text{with} \qquad \Delta\mathbf{d}_{t,\sum}^0 = \overline{\Delta\mathbf{d}}_t^0 \tag{4.92}$$

$$\text{and} \qquad \Delta\lambda_{t,\sum}^0 = \overline{\Delta\lambda}_t^0 \tag{4.93}$$

where $\Delta\mathbf{d}_{t,\sum}^k$ stands for the sum of incremental change of nodal coordinate vector $\mathbf{d}$ till the end of iteration k of time step t while $\mathbf{d}_t^k$ is the nodal coordinate at the beginning of iteration k of the time step t. Besides $\overline{\Delta\mathbf{d}}_t^0$ is the prescribed incremental change of nodal coordinate vector for iteration 0 of the time step t. Furthermore, $\Delta\lambda_{t,\sum}^k$ stands for the sum

of incremental change of load factor λ till the end of iteration k of time step t and λ_t^k is the value of load factor at the beginning of iteration k of the current time step t. $\overline{\Delta\lambda_t}^0$ is the prescribed incremental change of load factor for iteration 0 for the current time step t whereas $\bar{s}$ represents the prescribed radius of the desired intersection on the equilibrim path to which the calculated result converges (see Figure 4.14).

The algorithmic setup for solving the quasi-elastostatic system of equations in this section is summarized in Figure 4.15. In fact, it is well acknowledged that stability problems of thin and light-weight surface structures inevitably require a dynamic simulation to accurately represent their physical collapse process. Thus, the next section introduces an application of the presented load stiffness matrice to dynamic analysis based on the implicit time integration given in section 2.3.4.

4.6.3 Time dependent analysis of deformation-dependent forces

In this section, we are striving to apply the deformation-dependent forces concept derived in this chapter with a relatively slow time-dependent problem. Therefore, we can directly extend formulae derived for the quasi-static case to certain dynamic systems of interest. Therefore, the time integration algorithms mentioned in section 2.3.4 are still usable. However, the time step size Δt must be small enough to minimize the error from the convex combination of external force vectors in eq. (2.126) at the beginning t_n and the end of the time step t_{n+1} where $\mathbf{f}^{ext}(t)$ is comprised of the deformation-dependent forces $\mathbf{f}^{fol}(t) \in \mathbf{f}^{ext}(t)$.

According to the Generalized-α method (GEN$_\alpha$) in section 2.3.4.1, a generalized state vector of the external force in eq. (2.126) within an interval $t \in [t_n, t_{n+1}]$ is expanded for the deformation-dependent force by

$$\mathbf{f}^{ext}_{n+1-\alpha_f} = (1-\alpha_f)(\mathbf{f}^{ded}_{n+1} + \mathbf{f}^{fol}_{n+1}) + \alpha_f(\mathbf{f}^{ded}_{n} + \mathbf{f}^{fol}_{n}). \tag{4.94}$$

Therefore, the derivation for the effective structural equation in eq. (2.129) is valid as well for the problem of deformation-dependent forces under interest with an assumption that the time step size is small enough, and as a result, a linear combination of the external force in eq. (4.94) results in a negligible error for an approximation of the deformation-dependent force $\mathbf{f}^{fol}$. Hence, the effective tangential stiffness matrix in eq. (2.133) is rewritten by

$$\begin{aligned}\mathbf{K}_T^{eff}(\mathbf{d}^k_{n+1}) &= \frac{\partial \mathbf{G}(\mathbf{d}_{n+1})}{\partial \mathbf{d}_{n+1}}\Big|_{\mathbf{d}^k_{n+1}} = \frac{1-\alpha_m}{\beta\Delta t^2}\mathbf{M} + \frac{\partial \overbrace{\mathbf{f}^{int}(\mathbf{d}_{n+1-\alpha_f}(\mathbf{d}^k_{n+1}))}^{eq.\ (2.127)}}{\partial \mathbf{d}_{n+1}} - \frac{\partial \mathbf{f}^{fol}(\mathbf{d}_{n+1-\alpha_f}(\mathbf{d}^k_{n+1}))}{\partial \mathbf{d}_{n+1}}, \\ &= \frac{1-\alpha_m}{\beta\Delta t^2}\mathbf{M} + (1-\alpha_f)\underbrace{\frac{\partial \mathbf{f}^{int}(\mathbf{d}^k_{n+1})}{\partial \mathbf{d}_{n+1}}}_{\mathbf{K}_{e+u}+\mathbf{K}_g \text{ eq. (2.106)}} - \underbrace{\frac{\partial \mathbf{f}^{fol}(\mathbf{d}^k_{n+1})}{\partial \mathbf{d}_{n+1}}}_{\mathbf{K}_l \text{ eq. (4.65)}}.\end{aligned} \tag{4.95}$$

Likewise, by the help of eq. (4.94) the effective force vector in eq. (2.134) is turned to

$$\begin{aligned}\mathbf{f}^{eff}(\mathbf{d}^k_{n+1}) = &-\frac{1-\alpha_m}{\beta\Delta t^2}\mathbf{M}\mathbf{d}_{n+1} + \mathbf{h}(\mathbf{d}_n, \dot{\mathbf{d}}_n, \ddot{\mathbf{d}}_n) - \overbrace{\mathbf{f}^{int}(\mathbf{d}_{n+1-\alpha_f}(\mathbf{d}^k_{n+1}))}^{\text{eq. (2.127)}} \\ &+ (1-\alpha_f)(\mathbf{f}^{ded}_{n+1} + \mathbf{f}^{fol}_{n+1}) + \alpha_f(\mathbf{f}^{ded}_{n} + \mathbf{f}^{fol}_{n}),\end{aligned} \tag{4.96}$$

Initialize: set intitial pseudo-time step number $(n = 0)$ and initial configuration $(\mathbf{d}_0)$

Loop over all pseudo-time steps (n_T)

Predictor step $(k = 0)$

Load-controlled or displacement-controlled

$$-\mathbf{f}_{,\mathbf{d}}\,(\mathbf{d}^0_{n+1}, \lambda^0_{n+1}) = \mathbf{K}_T(\mathbf{d}^0_{n+1}) \tag{4.80}$$

$$-\mathbf{f}_{,\lambda}\,(\mathbf{d}^0_{n+1}, \lambda^0_{n+1}) = -\frac{\partial \mathbf{f}^{ded}(\lambda)}{\partial \lambda}\Big|_{\lambda^0_{n+1}} - \frac{\partial \mathbf{f}^{fol}(\mathbf{d},\lambda)}{\partial \lambda}\Big|_{\mathbf{d}^0_{n+1},\lambda^0_{n+1}} \tag{4.81}$$

$$-\mathbf{f}(\mathbf{d}^0_{n+1}, \lambda^0_{n+1}) = \mathbf{f}^{int}(\mathbf{d}^0_{n+1}) - \mathbf{f}^{ded}(\lambda^0_{n+1}) - \mathbf{f}^{fol}(\mathbf{d}^0_{n+1}, \lambda^0_{n+1}) \tag{4.78}$$

$$g(\mathbf{d}^0_{n+1}, \lambda^0_{n+1}),\ g_{,\mathbf{d}}\,(\mathbf{d}^0_{n+1}, \lambda^0_{n+1}),\ g_{,\lambda}\,(\mathbf{d}^0_{n+1}, \lambda^0_{n+1}). \tag{4.87); (4.89}$$

If update tensors exist, find $(\mathbf{f}_{,\mathbf{d}})^{-1}\,\mathbf{f}$ and $(\mathbf{f}_{,\mathbf{d}})^{-1}\,\mathbf{f}_{,\lambda}$ by Woodbury (4.70)

$$\Delta\lambda^0_{n+1,\sum} = (g_{,\mathbf{d}} \cdot (\mathbf{f}_{,\mathbf{d}})^{-1}\,\mathbf{f} - g)/(g_{,\lambda} - g_{,\mathbf{d}}\,(\mathbf{f}_{,\mathbf{d}})^{-1}\,\mathbf{f}_{,\lambda}) \tag{4.85}$$

$$\Delta\mathbf{d}^0_{n+1,\sum} = -(\mathbf{f}_{,\mathbf{d}})^{-1}\,\mathbf{f} - (\mathbf{f}_{,\mathbf{d}})^{-1}\,\mathbf{f}_{,\lambda}\,\Delta\lambda^0_{n+1,\sum} \tag{4.84}$$

Arclength-controlled

$$\Delta\lambda^0_{n+1,\sum} = \overline{\Delta\lambda}^0_{n+1}, \quad \Delta\mathbf{d}^0_{n+1,\sum} = \overline{\Delta\mathbf{d}}^0_{n+1} \tag{4.93), (4.92}$$

Update $\mathbf{d}^1_{n+1} = \mathbf{d}^0_{n+1} + \Delta\mathbf{d}^0_{n+1,\sum}, \quad \lambda^1_{n+1} = \lambda^0_{n+1} + \Delta\lambda^0_{n+1,\sum}$

Set up $k = 1$

Newton-Raphson correction iteration:

$$-\mathbf{f}_{,\mathbf{d}}\,(\mathbf{d}^k_{n+1}, \lambda^k_{n+1}) = \mathbf{K}_T(\mathbf{d}^k_{n+1}) \tag{4.80}$$

$$-\mathbf{f}_{,\lambda}\,(\mathbf{d}^k_{n+1}, \lambda^k_{n+1}) = -\frac{\partial \mathbf{f}^{ded}(\lambda)}{\partial \lambda}\Big|_{\lambda^k_{n+1}} - \frac{\partial \mathbf{f}^{fol}(\mathbf{d},\lambda)}{\partial \lambda}\Big|_{\mathbf{d}^k_{n+1},\lambda^k_{n+1}} \tag{4.81}$$

$$-\mathbf{f}(\mathbf{d}^k_{n+1}, \lambda^k_{n+1}) = \mathbf{f}^{int}(\mathbf{d}^k_{n+1}) - \mathbf{f}^{ded}(\lambda^k_{n+1}) - \mathbf{f}^{fol}(\mathbf{d}^k_{n+1}, \lambda^k_{n+1}) \tag{4.78}$$

$$g(\mathbf{d}^k_{n+1}, \lambda^k_{n+1}),\ g_{,\mathbf{d}}\,(\mathbf{d}^k_{n+1}, \lambda^k_{n+1}),\ g_{,\lambda}\,(\mathbf{d}^k_{n+1}, \lambda^k_{n+1}). \tag{4.86); (4.88); (4.90}$$

If update tensors exist, find $(\mathbf{f}_{,\mathbf{d}})^{-1}\,\mathbf{f}$ and $(\mathbf{f}_{,\mathbf{d}})^{-1}\,\mathbf{f}_{,\lambda}$ by Woodbury (4.70)

$$\Delta\lambda^k_{n+1} = (g_{,\mathbf{d}} \cdot (\mathbf{f}_{,\mathbf{d}})^{-1}\,\mathbf{f} - g)/(g_{,\lambda} - g_{,\mathbf{d}}\,(\mathbf{f}_{,\mathbf{d}})^{-1}\,\mathbf{f}_{,\lambda}) \tag{4.85}$$

$$\Delta\mathbf{d}^k_{n+1} = -(\mathbf{f}_{,\mathbf{d}})^{-1}\,\mathbf{f} - (\mathbf{f}_{,\mathbf{d}})^{-1}\,\mathbf{f}_{,\lambda}\,\Delta\lambda^k_{n+1} \tag{4.84}$$

$$\Delta\mathbf{d}^k_{n+1,\sum} = \Delta\mathbf{d}^{k-1}_{n+1,\sum} + \Delta\mathbf{d}^k_{n+1}, \quad \Delta\lambda^k_{n+1,\sum} = \Delta\lambda^{k-1}_{n+1,\sum} + \Delta\lambda^k_{n+1}$$

$$\mathbf{d}^{k+1}_{n+1} = \mathbf{d}^0_{n+1} + \Delta\mathbf{d}^k_{n+1,\sum}, \quad \lambda^{k+1}_{n+1} = \lambda^0_{n+1} + \Delta\lambda^k_{n+1,\sum}$$

$\Delta(\bullet)^k_{n+1,\sum}$: Sum of incremental change of $(\bullet)$ till the end of iteration k of time step $n+1$

$\Leftarrow$ Set up $k = k + 1$ until convergence

Update change of nodal coordiate and load factor after converge $\mathbf{d}_{n+1} = \mathbf{d}^{k+1}_{n+1},\ \lambda_{n+1} = \lambda^{k+1}_{n+1}$

$\Leftarrow$ Set up $n = n + 1$ until $n + 1 = n_T$

Figure 4.15: Numerical solution algorithm of quasi-elastostatic.

where both shift parameters are given in eq. (2.136). Likewise, the derivation for GEMM can proceed in the same fashion and for this reason, it will not be shown here. Given eqs. (4.95) and (4.96), the incremental change in nodal coordinate of the system $\Delta\mathbf{d}$ in eq. (2.135) is iteratively solved as described by the flow chart in Figure 2.5. To a certain degree the procedure is similar to the load-controlled algorithm for the pseudo-static case in section 4.6.2.3. Furthermore, one observes that the effective structural equation in eq. (4.96) has a similar form as eq (4.68) or (4.69) in case of single chamber and multi chamber, respectively. Therefore, the Woodbury's formula in section 4.6.1 is valid as well to update the inverse of system matrices of eq.(4.95) in the form:

$$\mathbf{K}_T^{eff} = \underbrace{\begin{bmatrix} \frac{1-\alpha_m}{\beta\Delta t^2}\mathbf{M} + (1-\alpha_f)(\mathbf{K}_{e+u} + \mathbf{K}_g) \\ -\sum_{i=1}^{n_b} \mathbf{K}_{l_i}^0 \end{bmatrix}}_{\mathbf{A} \text{ see eq. (4.70)}} \underbrace{- \sum_{i=1}^{n_b} \left(\beta^0 \mathbf{b}\otimes\mathbf{b} + \beta^1 \begin{bmatrix} \mathbf{a}\otimes\mathbf{a} \\ +\mathbf{b}\otimes\mathbf{b} \\ +\mathbf{a}\otimes\mathbf{b} \\ +\mathbf{b}\otimes\mathbf{a} \end{bmatrix} \right)_i}_{\sum_{k=1}^{p}(\mathbf{u_k}\otimes\mathbf{v_k}) \text{ see eq. (4.70)}} \tag{4.97}$$

4.7 Numerical Experiments

To verify the implementation, various numerical examples from literature are computed within this section.

4.7.1 Inflatable membrane tube filled with air

Aimed to validate the implementation of the inflation process of membrane elements, this example from Bonet *et.al.* [BWMH00] demonstrates a static inflation of an air-filled membrane tube as drawn in Figure 4.16. The tube is modeled by the Neo-Hookean material which provides an analytical solution to the inflation of a tube, viz.

$$\frac{pR}{\mu h} = 1 - \frac{1}{\lambda^4}, \tag{4.98}$$

where p is the inflation pressure, $\lambda = r/R$ stands for circumferential stretch ratio between the initial R and current radii r, respectively. The initial radius R is 21 cm with the thickness of H=1 cm and the Neo-Hookean material parameter $\mu = 1.0\ kg/cm^2$. The tube is inflated to a pressure of $p = 0.045\ kg/cm^2$ before the application of nodal forces with total magnitude of $F = 1.6\ kg$ over central four elements. Due to the characteristic of this tube the plane strain condition is applicable. Therefore, only a small strip of the half-cylindrical tube is meshed by 18 bilinear quadrilateral membrane elements (see Figure 4.16). A nonlinear relationship between the applied pressure and stretch under an inflation process from the initial state to the fully inflated state is demonstrated in Figure 4.16 where a good agreement between the analytical solution from eq. (4.98) and numerical results in this paper is noticeable.

Then at the fully inflated state, we investigate influences of *the enclosed volume terms (enc)* which are linked to the update tensors in eq. (4.65). After the tube is fully inflated with the enclosed air pressure of $p = 0.045\ kg/cm^2$, vertical point loads with total magnitude of

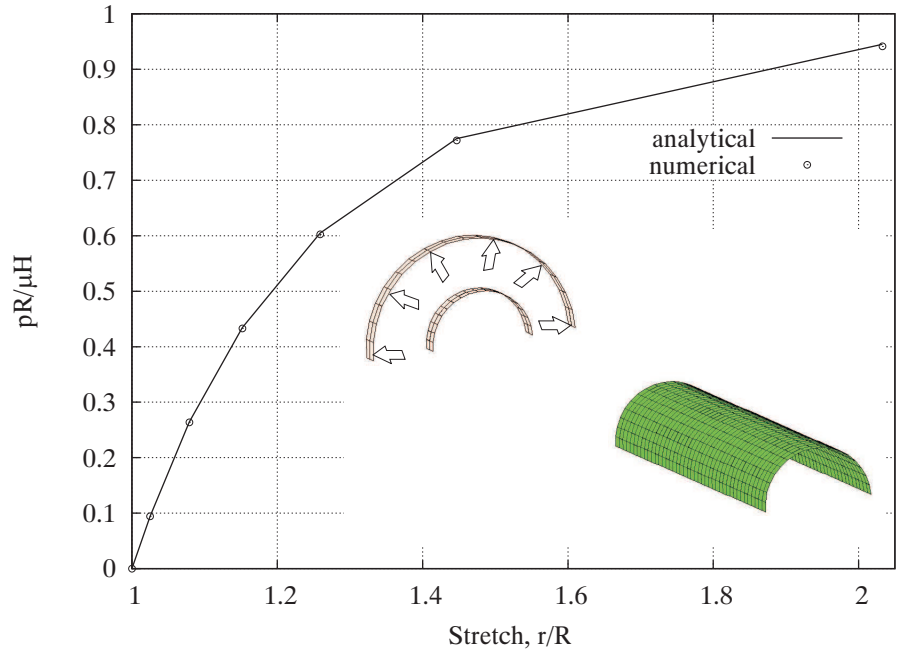

Figure 4.16: Geometry, load condition for inflation of an air-filled membrane tube modeled by the Neo-Hookean material.

$F = LF \times 1.6\ kg$ with the load factor LF over central four elements at the top of this tube are gradually applied as shown in Figure 4.17. A realistic deformation process is discernible due to the appearance of *enc*. Without *enc*, the local perturbation due to the applied forces does not interact with the enclosed gas volume, the tube suddenly displaces to another equilibrium state which cause an unrealistic collapse of gas volume under the constant air pressure (p=constant). This result emphasizes a necessity to take into account the enclosed volume terms for a more realistic simulation. In Figure 4.18, the rate of convergence of the energynorm is linear without *enc*, whereas an asymptotically quadratic convergence is obtainable in case that *enc* is included. As a conclusion, the results from this experiment agree well with those in [BWMH00].

4.7.2 Static analysis of an air cushion with different pressure control

An objective of this example is to investigate behaviors of a fully-inflated airbag which is separated into two parts: an upper membrane and a lower membrane as illustrated in Figure 4.19. We focus our study on the interaction between the upper and lower membranes via enclosed volume terms (*enc*) which is controlled by different state equations. The dimension of this airbag is defined by $6.0 \times 3.0\ m$ on the xy-plane with the thickness of $1.0\ m$. Note that we choose such large thickness to preclude a bulky deformation of the membrane. An isotropic St. Venant's material is employed with the elastic modulus of $E = 200\ kN/m$ and Poisson's ratio of $\nu = 0.45$.

First of all, to obtain the initial configuration the upper and lower flat membrane sheets are connected along their edges which are fixed for all displacements. However, this initial

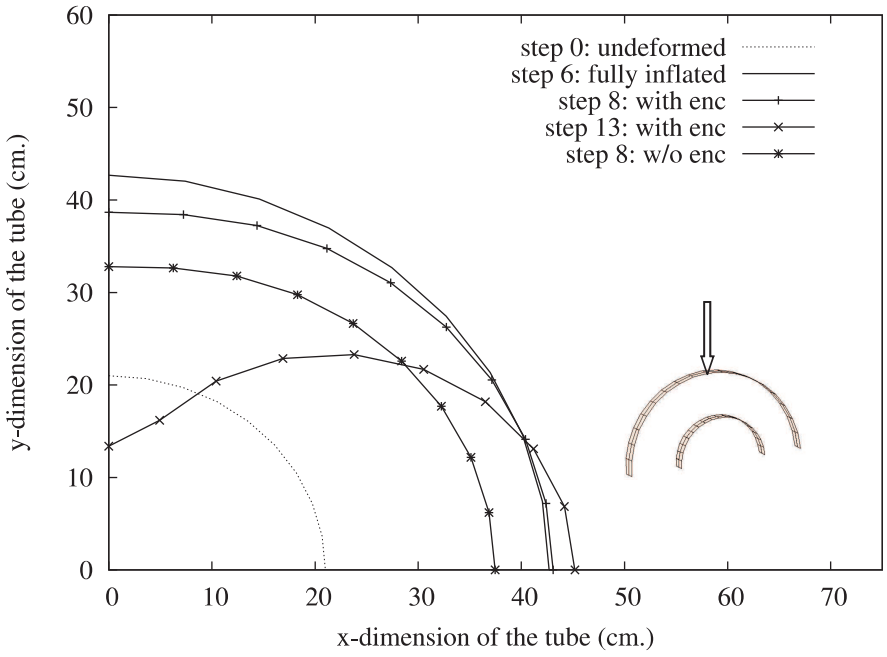

Figure 4.17: Deformation of the fully inflated membrane tube subjected to an applied force with different controls of air pressure.

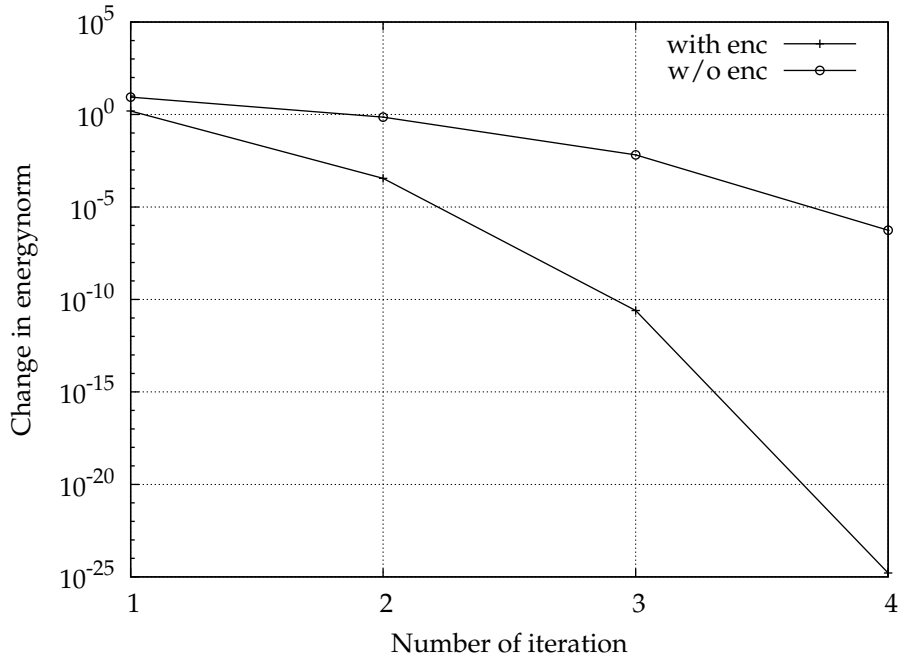

Figure 4.18: Comparison influences of enclosed volume terms on the rate of convergence for energynorm of load step 7.

configuration is not in equilibrium when the pressure of gas contained within the cushion is introduced. Therefore, we perform the form finding algorithm (see e.g. [Ble98, Wüc06]) to determine a configuration at which the prescribed pretension in the membrane is in equi-

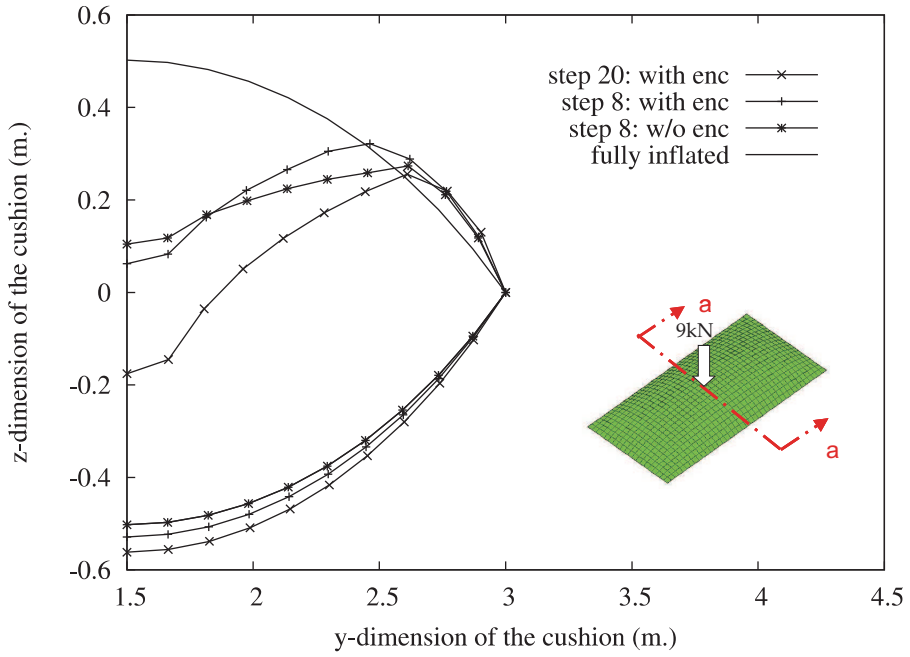

Figure 4.19: Deformation of the enclosed air cushion at the section a-a with different state controls.

librium with the applied gas pressure in the cushion. In this case, an isotropic pretension of 0.89 kN/m^2 is prescribed in the membrane, and then the enclosed gas pressure is gradually increased until $p^g = 100.4\ kN/m^2$ while the atmospheric pressure is at $p_{amb} = 100.0\ kN/m^2$. Thus, the pressure difference of $\Delta p = 0.4\ kN/m^2$ inflates the flat membrane to a fully-inflated state which is in equilibrium of the pretension and the difference Δp between pressure inside and outside the air cushion. The equilibrium configuration, the outcome of the form finding process, is then used as the initial configuration for subsequent elastostatic analysis.

At the fully-inflated (self-equilibrated) state of pressure $p = 100.4\ kN/m^2$, deformations of the upper and lower membranes reach as high as 0.5 m. at their center while the atmospheric pressure is kept at $p_{amb} = 100.0\ kN/m^2$. Then, a gradually increased force $F = LF \times 9\ kN$ acting in the z-direction with the load factor LF is applied on the node at the center of the upper membrane where the section a-a is drawn. There exist two control types over the enclosed gas pressure: the constant gas pressure p=constant which neglects *enc* and the pneumatic model pv^κ=constant from eq. (4.8) which includes *enc*.

From the cross section a-a in Figure 4.19, the deformation of the upper membrane does not influence the lower membrane in case that *enc* is neglected, i.e. there is no interaction between the deformation of the upper part and the lower part of this airbag. On the other hand, when the enclosed volume is taken into account, the enclosed gas pressure is controlled by the pneumatic model in eq. (4.8). In this case, the deformation of the upper part causes both a decrease in the amount of enclosed gas volume and an increase of the enclosed gas pressure. As a consequence, the increased gas pressure is transmitted towards the lower membrane of the airbag. Intuitively, the interaction between the deformation of the upper part and the lower part is linked via the enclosed volume terms.

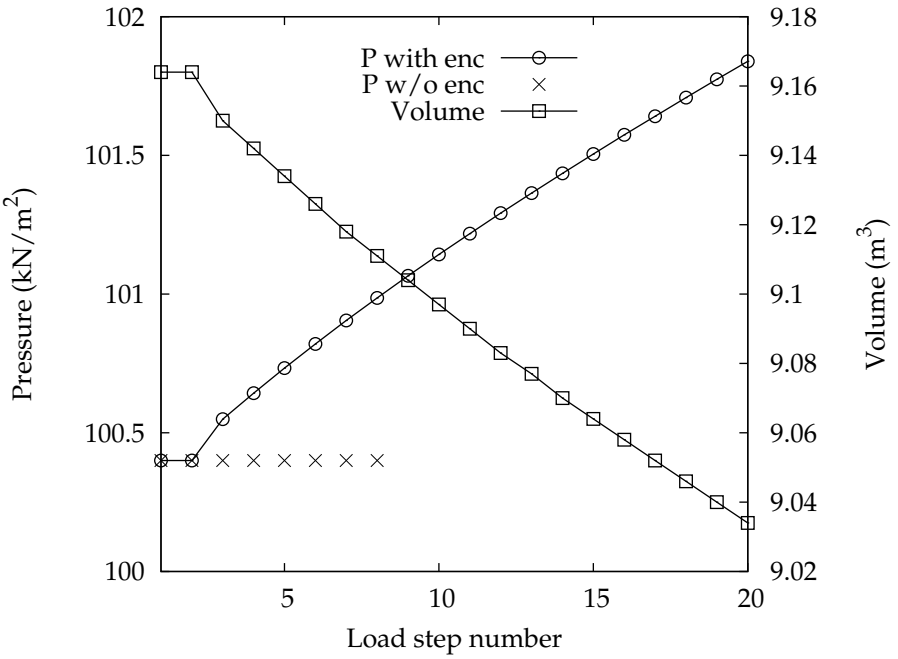

Figure 4.20: Pressure-Volume relaionship of the enclosed air cushion.

From the pressure-volume plot in Figure 4.20, we observe that the constant pressure assumption, neglecting *enc*, encounters a difficulty to converge to a state of equilibrium after load step 8 and the computation cannot proceed further. In contrary, when *enc* is taken into account, the convergence rate is significantly improved and the computation does not face with any convergence problem. This behavior is demonstrated from the continuous plot of an increase in gas pressure due to a decrease in enclosed gas volume which can very well reflect the utilized pneumatic model.

Similar to example 4.7.1, the rate of convergence in the energynorm is linear without *enc* in contrast to an asymptotically quadratic rate of convergence with the inclusion of *enc*. Thus, we can conclude from this experiment that taking into account the enclosed volume terms yields both a better rate of convergence and a more realistic simulation for the problem of interest.

4.7.3 Buckling of a gas-supported shell

In this investigation, we reproduce an example from Rumpel and Schweizerhof [RS03] by employing the rotation-free shell elements [LWKU07] to investigate the buckling of a semi-cylindrical shell which covers the top opening of a gas-filled container as shown in Figure 4.21. In particular, we focus on the coupling between the shell and the gas inside the container. The state of gas is controlled by the hydraulic model in eq. (4.9) by varying the hydraulic constant K. This semi-cylindrical shell is discretized by bilinear quadratic rotation-free shell elements with the Poisson's ratio $\nu = 0.3$, elastic modulus $E = 1.0 \times 10^5\ N/cm^2$ and thickness $t = 0.1\ cm$.

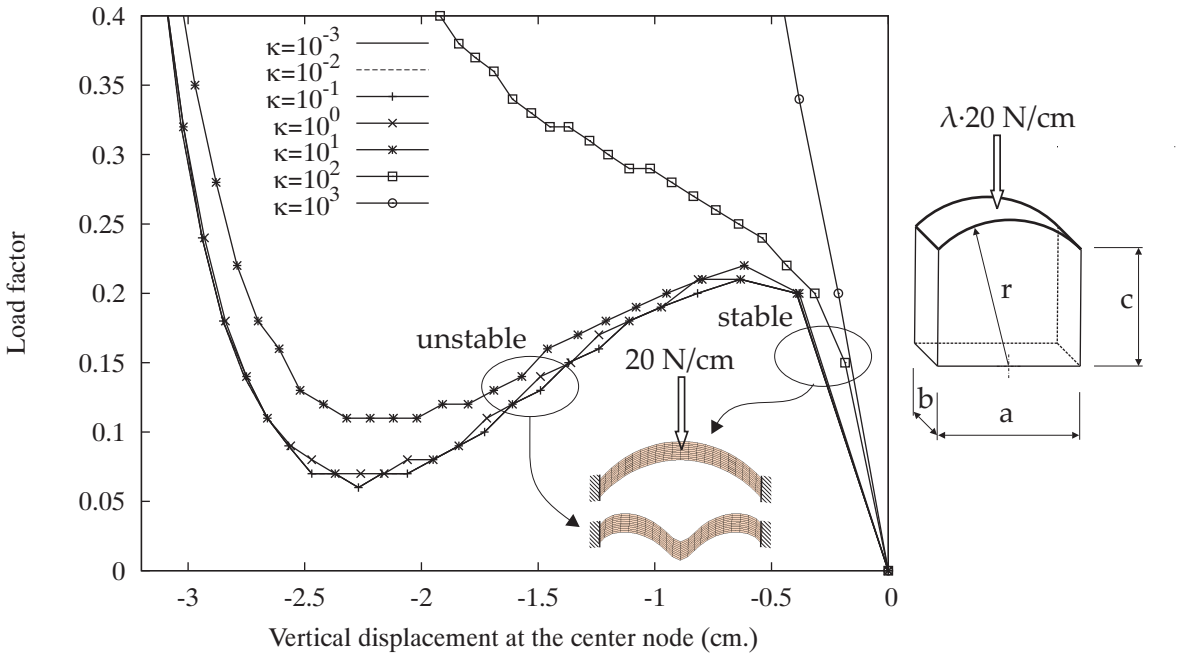

Figure 4.21: Buckling of a gas (hydraulic model) supported rotation-free shell with varying bulk modulus K; $a = 10\ cm,\ b = 5\ cm,\ c = 5\ cm$ and $r = 7\ cm$.

The shell is clamped at two straight edges whereas the other two edges are allowed to deform along the vertical direction as seen in Figure 4.21. Other walls of the container are assumed to be rigid and the container is filled by a hydraulic-type gas with varying hydraulic constant K. The top of the shell is applied by a line load $F = \lambda \cdot 20\ N/cm$ while the load factor λ is controlled by the arclength algorithm to follow the equilibrium path beyond critical points. We enforce this shell to buckle only in a symmetric mode since the critical load analysis is not the main purpose for this investigation. Figure 4.21 provides a plot between the load factor and vertical displacement at the top node of the shell upon which the line load is applied. From this plot, without the gas support or very low hydraulic constant K, the shell obviously shows a snapthrough. By increasing the hydraulic constant K, the snapthrough disappears and the relationship between load and displacement turns to be a nonlinear function. Notably, a linear relationship is represented when the hydraulic constant K is extremely high.

The outcome from this example verifies the implementation for both the path following algorithm and enclosed volume terms. Furthermore, the objective to accomplish an interaction between the shell and filled gas is fulfilled by coupling the enclosed volume terms (update tensors) in eq. (4.65) to system stiffness matrices $\mathbf{K}_{e+u} + \mathbf{K}_g - \mathbf{K}_l^0$ in eq. (4.67) or (4.68) Because of this coupling effect, the system behaves like a composite shell whose stiffness is derived from both the shell and supporting gas in case of a quasi-static analysis with slow deformation process where influences of inertial forces are negligible.

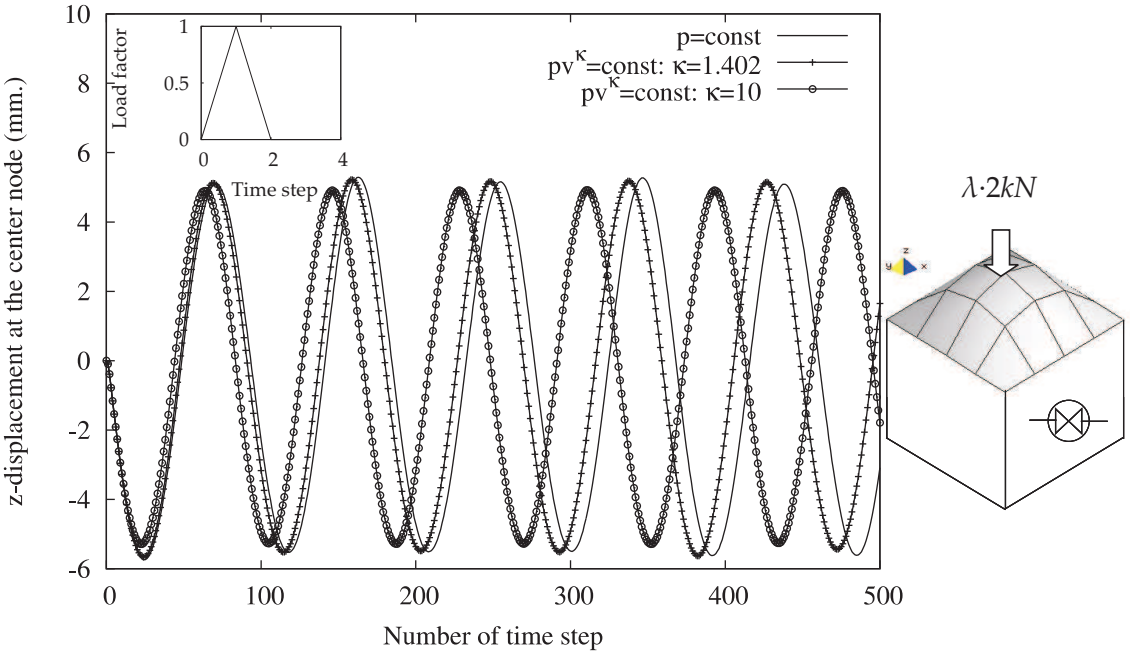

Figure 4.22: Dynamic displacement response at the center node of a closed air cushion whose pressure is controlled by (a) constant gas pressure (b) gas law with $\kappa = 1.402$ and (c) gas law with $\kappa = 10.0$.

4.7.4 Dynamic analysis of an air cushion with different pressure control

All previous experiments are restricted to a quasi-static analysis where an assumption that the deformation process is slow enough resulting in negligible influences from inertial forces is held. In this example, we are striving to apply the deformation-dependent forces concept with a relatively slow time-dependent problem. As previously introduced in section 4.6.3 the formulae derived for the quasi-static case is directly applicable to certain dynamic system of interest. However, the time step size Δt must be kept small.

In this example, we investigate an air cushion covering the top opening of a closed rigid box with the dimension of $1000 \times 1000 \times 0.2\ mm$ as illustrated in Figure 4.22. This cushion is made of a membrane material with the elastic modulus $E = 1,000\ N/mm^2$, Poisson's ratio $\nu = 0.3$, density $1.0 \times 10^{-3}\ kg/mm^3$. This problem is discretized by bilinear quadrilateral membrane elements. Then, the form finding algorithm is performed to determine a configuration at which the equilibrium between the prescribed pretension in the membrane and the applied gas pressure in the container is met. Firstly, an isotropic pretension is prescribed at 7.5 N/mm^2. Secondly, the enclosed gas pressure is gradually increased until $p^g = 0.1035\ N/mm^2$ while the atmospheric pressure is defined at $p_{amb} = 0.1\ N/mm^2$. Thus, the pressure difference of $\Delta p = 0.0035\ N/mm^2$ inflates the flat membrane to a fully-inflated state which is in equilibrium of the pretension and the pressure difference Δp. This configuration is then used as the initial configuration for a subsequent elastodynamic analysis.

At the fully-inflated state of pressure difference $\Delta p = 0.0035\ N/mm^2$ (see Figure 4.22), a nodal force $F = \lambda \times 2\ kN$ is applied at the center node in the z-direction with the load

factor λ controlled by the ramp function in Figure 4.22. The GEN_α time integration method in section 2.3.4.1 is used according to the procedure in section 4.6.3 with the time step size of $dt = 0.05\ s$ and without numerical dissipation (spectral radius $\rho = 1.0$). There are three test cases for different control on the gas pressure inside the box: (i) mostly used in practice nowadays, the constant gas pressure without enc, (ii) the pneumatic law pv^κ=constant from eq. (4.8) with $\kappa = 1.402$ (isentropic) and (iii) the pneumatic law pv^κ=constant with $\kappa = 10$.

Figure 4.22 provides a comparison on the oscillation responses for all three test cases. For the first case (i), the constant gas pressure control shows a harmonic oscillation in the plot of vertical displacement of the center node versus the timestep. In the second case (ii), the pressure control is changed to the pneumatic model with isentropic condition $\kappa = 1.402$. In this case, the center node oscillates with higher frequency than the case of constant pressure. With the last case (iii), the pneumatic model with $\kappa = 10.0$, the amplitude of the oscillation is decreased whereas the oscillated frequency is increased. Thus, one can consider the air contained in the box behaves like a spring where κ is comparable to a spring stiffness. From these results, we can conclude that different pressure control significantly influences the dynamic response of a fluid-supported membrane. Therefore, a proper pressure control must be taken into account for the problem at hand.

4.7.5 Dynamic analysis of a rhomboidal air cushion

In this last example, a rhomboidal air cushion which is installed at the Alliance arena in Munich is investigated. The cushion is made of isotropic ETFE (Ethylen tetrafluoroethylene) foil with the dimension of $4.0 \times 4.0\ m$ with the thickness of $t = 0.2\ mm$. The material properties are comprised of the elastic modulus $E = 1,045\ N/mm^2$, Poisson's ratio $\nu = 0.45$, density $1.75\ g/mm^3$. We model this cushion by 800 bilinear quadrilateral membrane elements. At first, the upper and lower flat membrane sheets are attached along their edges which are fixed for all displacements. This configuration is considered as the initial configuration for form finding which is used to figure out an equilibrium configuration between the prescribed isotropic pretension of $22.5\ N/mm^2$ in the membrane and the gas pressure of $p^g = 0.1035\ N/mm^2$ in the cushion under the atmospheric pressure of $p_{amb} = 0.10\ N/mm^2$. Then the gas pressure is gradually increased until it reaches $p^g = 0.1035\ N/mm^2$ with the pressure difference of $\Delta p = 0.0035\ N/mm^2$ between inside and outside of the cushion. This fully-inflated state is then considered as the initial configuration (see Figure 4.23) for a subsequent elastodynamic analysis.

Then, nodal forces with the total magnitude of $F = \lambda \times 25\ kN$ are applied on nine nodes around the center of the upper membrane in the z-direction with the load factor λ controlled by the ramp function in Figure 4.23. The the Generalized-α method (GEN_α) is employed for the time integration procedure as introduced in section 4.6.3 with the time step size of $dt = 0.005\ sec$ and numerical dissipation (spectral radius $\rho = 0.95$). The gas pressure filled in the box is controlled either by the constant gas pressure without the enclosed volume terms *enc* or the pneumatic law pv^κ=constant from eq. (4.8) with $\kappa = 1.402$ (isentropic). We focus on the interaction between deformation of the upper membrane and that of the lower one via *enc*.

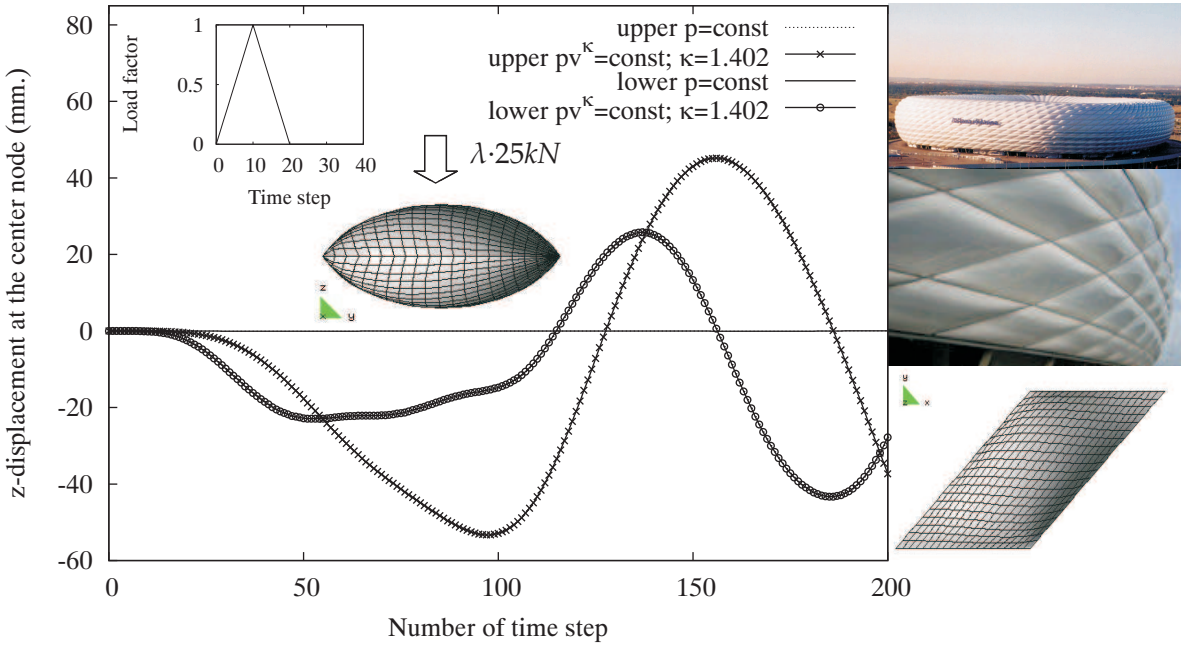

Figure 4.23: Displacement response at the center node of a rhomboidal air cushion whose pressure is controlled by (a) constant gas pressure (b) gas law with $\kappa = 1.402$ (http://www.allianz-arena.de)

Vertical oscillation of the center node on the upper and lower membrane are plotted versus step number in Figure 4.23 for both test cases. For the constant gas pressure control without *enc*, deformation of the upper membrane does not influence the lower membrane, whereas the interaction between the upper and lower membrane is observable in the case of the pneumatic law. Indeed, deformation of the upper membrane causes a decrease in the enclosed volume which elevates the enclosed gas pressure. The increased gas pressure is then transferred towards the lower membrane surface of the airbag via a coupling between enc (update tensors) in eq. (4.65) and the system stiffness matrices $\mathbf{K}_{e+u} + \mathbf{K}_g - \mathbf{K}_l^0$ from eq. (4.67) or (4.68), respectively.

4.8 Summary

This chapter provides a general framework to deal with the deformation-dependent forces acting on a surface structure, e.g. shells or membranes undergoing large displacement. The interaction between the surface structures and fluid leads to a highly nonlinear response. Roughly, the origins of nonlinearities come from two sources: Firstly, the change in the direction of pressure forces due to the fact that the fluid pressure is always acting perpendicular to the surface of a body contacting to that fluid. Secondly, the change in the pressure magnitude during the deformation.

From the numerical results, an advantage to include the change in pressure magnitude is proven in particular for an enclosed membrane filled with gas and/or fluid, e.g. an air cushion or an air bag. For such structure, the concept in this chapter has a lot of benefits: (i) The

change in fluid and/or gas pressure, caused by a variation of the enclosed fluid and/or gas volume, is transfered to the surrounding membrane by avoiding discretization of the fluid and/or gas domain. (ii) Mesh refinement for the fluid domain is unnecessary. (iii) The coupling between the fluid domain and the solid domain at their interface is avoidable. These advantages significantly simplifies the problem as well as reduces time for computation.

In detail, the variation of fluid(gas) volume and the change in fluid depth results in additional load stiffness terms so-called the enclosed volume terms written in the form of the update tensors. Although, these enclosed volume terms are in general discarded for simplicity, numerical examples within this chapter reveal the necessity to take them into account for a more realistic simulation. Influences of these enclosed volume terms, usually neglected, on the total stiffness of an inflatable membrane is indispensable in case of highly pressurized gas and high density fluid.

However, inclusion of the enclosed volume terms turns a sparse system matrix into a fully-populated one which is a bad news for both the direct solver and the amount of memory storage. In this case, the Woodbury's formula is employed with an ability to cope with such problem efficiently . It does accelerate the computation by sequential updating the last available inverse matrix without factorization. As a result, the system solution is sequentially updated with respect to each individual update tensor. To solve this nonlinear system of equations by FEM, linearization is performed. One observes that the consistent linearized enclosed volume terms lead to a quadratic convergence. Even though, it requires additional works to update the inverse matrix for each update tensor, the computational time in this case is still much less than full factorization of a fully-populated system matrix, in particular for a huge system.

For the derivation of the load stiffness from the virtual work of deformation-dependent forces, the domain terms are symmetric while the boundary terms show their skew-symmetry. Hence, for an enclosed structure which boundary terms disappear, there exist only the load stiffness from the symmetric domain terms. This symmetric property is then inherited to the discretized load stiffness matrix which reflects the conservativeness of an enclosed membrane filled with gas and/or fluid.

As shown in this chapter, an extension towards dynamic analysis requires a small amount of effort. However, the derived formulae for the deformation-dependent forces within this chapter are based on the assumption that the deformation process is adequately slow. Consequently, influences of inertial forces can be neglected. Thus, it is unsuitable for transient problem, e.g. those of high-speed fluid.

Chapter 5

Mortar-Based Contact Formulation for Inflatable Membranes

For an inflatable membrane undergoing large deformations, different parts of the membrane may come into contact with each other, e.g. self contact and multibody contact. Thus, contact realization is indispensable for such structures. Recently proven for numerous benefits, the mortar-based contact algorithm is chosen for this chapter with an objective to further simulation capabilities for inflatable membrane structures. Since this chapter focuses on this special application, basic information is provided to the level for subsequent derivation without intent for a complete review of contact mechanics. Interested readers may look at numerous literature, e.g. computation-oriented books from Wriggers [Wri02] and Laursen [Lau02] or theoretical contact mechanics by Johnsons [Joh85], etc.

5.1 Introduction for large deformation contact mechanics

Contact exists in various circumstances in reality as illustrated in Figure 5.1. One may say that life will change dramatically without contact, for example, we can imagine how an astronaut move in the space. Nevertheless, numerical realization for contact is not trivial due to its highly nonlinear and nonsmooth nature. Nowadays, contact modeling still be one of the most complicated tasks. Additionally, contact involves multifiled coupling phenomena, e.g. thermo-elastic coupling between the tire and roadway, electro-thermo coupling at the interfaces within an electronic device, etc. In the past, contact is modeled by simplified boundary conditions due to the fact that analytical solutions were usually not known. With the advent of powerful computing facilities, numerical simulations with sophisticated contact constraints are feasible. Modern simulation techniques for contact problem based on FEM have been developed with an objective to find out a robust, effective and reliable algorithm. To deal with nonlinear and nonsmooth contact problems, adaptive methods based on error-controlled FEM and mesh adaptation techniques are of great interest.

This chapter aims at a robust numerical algorithm based on the FEM for frictionless contact problems of a linear elastic inflatable membrane modeled by the St Venant material from eq. (2.27). Nonetheless, inelasticity should be taken into account in further developments for a more realistic contact simulation.

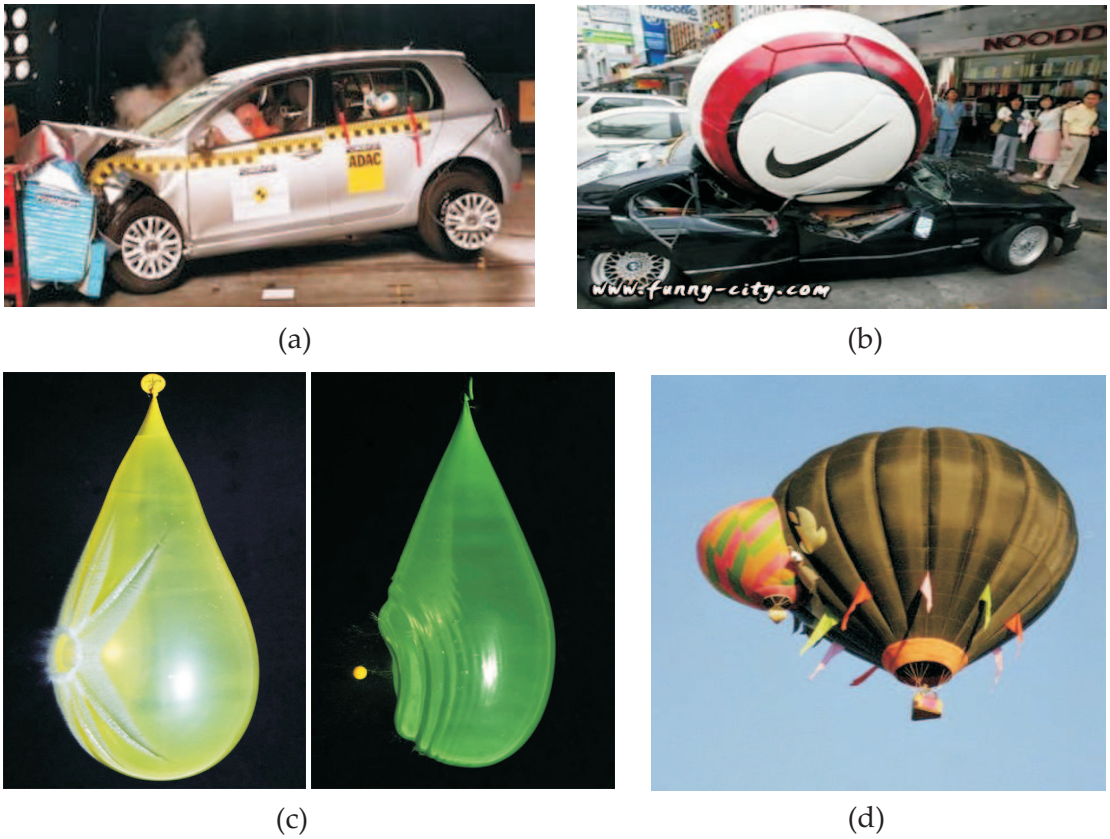

Figure 5.1: Illustration for contact problems: (a) car crash test (source: http://www.adac.de) (b) car accident (source: http://www.funny-city.com) (c) collision of a rigid ball with a water balloon and (d) mid-air collision of two hot-air balloons(source: http://images.google.de).

Due to various advantages over the collocation methods, within this chapter a mortar-based contact formulation is derived on the contact surface with suitable adjustments for both spatial and temporal discretizations. The key development is based on the following works: Puso and Laursen [PL04a, PL04b] pioneered an extension of the mortar-based segment-to-segment contact algorithm for 3D, large deformation kinematics problems. Hartmann et al. [Har07, HBRW07] employed the mortar contact formulation proposed by Hüeber and Wohlmuth [HW05] for geometrically nonlinear problems of a trilinear surface oriented hybrid shell element. Within this chapter, the derivation of the mortar-based contact formulation is based on the bilinear membrane element in section 2.3.1.1 for both two- and three-dimensional problems. Continuous approximation of the Lagrange multipliers, physically interpreted as the contact traction, yields a weak formulation of the non-penetrability condition which must be enforced to fulfill the contact constraints.

With the dual shape function introduced by Wohlmuth [Woh00], nodal contact constraints are decoupled. An introduction of the active set strategy allows the condensation of all nodal Lagrange multiplies from the system of equations. By doing so, the primary unknowns of the system are restricted to the nodal displacement dof $\Delta\mathbf{d}$ in eq. (2.94). The nodal Lagrange multipliers are recovered by performing a back substitution of the solution

for the primary unknown $\Delta\mathbf{d}$ in a variational consistent manner. This technique possesses two main advantages over traditional mortar methods: (i) the primary unknowns are only the nodal displacements $\Delta\mathbf{d}$, and therefore, the size of the system of equations is maintained. (ii) any user-defined penalty factor is omitted.

For the temporal discretization, the Generalized-α method (GEN$_\alpha$) and the Generalized Energy Momentum Method (GEMM) from section 2.3.4 are considered for time integration with an emphasis on the latter which maintains the unconditional stability for numerical problems of interest. The part of dynamic contact is elaborated by the algorithmic energy conserving strategy, the *Velocity-update method* proposed by Laursen and Love [LL02]. This algorithm is successfully employed in Hartmann [Har07] with a solid shell element for exact conservation of the total energy, while the geometric impenetrability condition is fulfilled. With such advantage, this method together with GEMM are applied to the membrane element in this chapter. Moreover, the active set is defined by a specific strategy upon the Lagrange multiplier approach. Then, a number of numerical examples are performed to evaluate the efficiency of this solution algorithm. The chapter is concluded by a brief summary. In the following subsections, the concept of large deformation contact mechanics is reviewed by following the incremental approach based on the formulation of IBVP in chapter 2.1.5. For further reading, there are numerous treatises about the topic, e.g. Laursen [Lau02], Wriggers [Wri02], Wriggers and Zavarise [WZ04] or recently Wrigger and Laursen [WL08], etc.

5.1.1 Problem description

This subsection explains contact boundary problems for two deformable bodies undergoing large deformation which includes the unilateral contact between a deformable body and a rigid obstacle as a special case. Extensions to multibody contact can be addressed in the same manner. Figure 5.2 shows a large deformation and large sliding contact problem. Here, two deformable bodies are represented by the open set $\Omega^{(1)}$ and $\Omega^{(2)}$ which reside in $\mathbb{R}^{n_{sd}}$ where n_{sd} is the number of space dimensions. To comply with the traditional slave-master concept, the $\Omega^{(1)}$ designates the *slave*, or *contactor*, body while the $\Omega^{(2)}$ stands for the *master*, or *target*, body. Even though this selection is arbitrary, it can introduce a bias into a numerical approximation by FEM. Because $\Omega^{(\alpha)}$ are assumed to be the initial positions of the bodies, thus these reference configurations produce no interactive forces if the bodies contact at time $t = 0$. The closure of $\Omega^{(\alpha)}$; $\alpha = 1, 2$, written by $\bar{\Omega}^{(\alpha)}$, is the union of the open set with its boundary $\partial\Omega^{(\alpha)}$ which can be divided into three parts: (i) The Dirichlet boundary $\Gamma_u^{(\alpha)}$; $\alpha = 1, 2$ where the displacements are prescribed. (ii) The Neumann boundary $\Gamma_\sigma^{(\alpha)}$ where the tractions are applied. (iii) The contact boundary $\Gamma_c^{(\alpha)}$ where the contact constraints are defined. In the reference configuration, the boundary $\partial\Omega^{(\alpha)}$ is defined by

$$\Gamma_u^{(\alpha)} \cup \Gamma_\sigma^{(\alpha)} \cup \Gamma_c^{(\alpha)} = \partial\Omega^{(\alpha)} \quad \text{and} \quad \Gamma_u^{(\alpha)} \cap \Gamma_\sigma^{(\alpha)} = \Gamma_\sigma^{(\alpha)} \cap \Gamma_c^{(\alpha)} = \Gamma_c^{(\alpha)} \cap \Gamma_u^{(\alpha)} = \varnothing \tag{5.1}$$

with their spatial counterparts $\gamma_u^{(\alpha)}$, $\gamma_\sigma^{(\alpha)}$ and $\gamma_c^{(\alpha)}$, respectively. Both bodies undergo motions, represented by $\varphi^{(1)}$ and $\varphi^{(2)}$, respectively. These motions move them from the reference configurations to the configuration where both bodies contact to each other. During

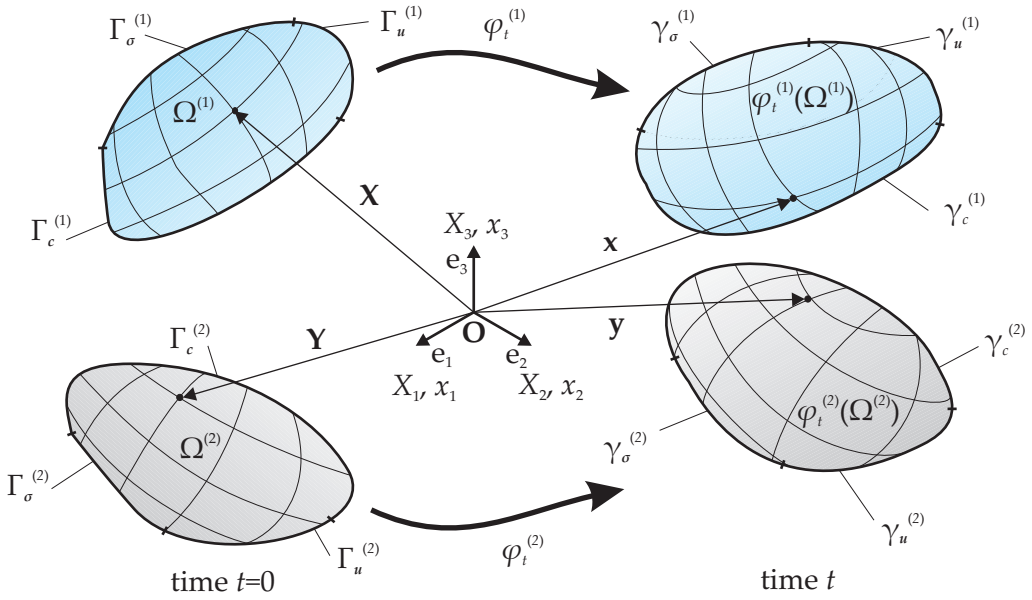

Figure 5.2: Illustration for contact problem of two deformable bodies under large deformation.

the collision, interactive forces are induced during some portion of the time interval $[0, T]$. These motions mapping are represented by

$$\varphi^{(\alpha)} : \bar{\Omega}^{(\alpha)} \times [0, T] \rightarrow \mathbb{R}^{n_{sd}+1}; \quad \alpha = 1, 2. \tag{5.2}$$

The configuration at an instance of time $t \in [0, T]$ is obtained by fixing the time argument of $\varphi_t^{(\alpha)}$; $\alpha = 1, 2$ along the convention introduced in chapter 2. Geometric objects and tensor quantities defined on the reference configuration $\Omega^{(\alpha)}$ are referred to as material objects, whereas those defined on the configuration at an instance $\varphi_t^{(\alpha)}(\Omega^{(\alpha)})$ are referred to as spatial objects. Therefore, material points of $\bar{\Omega}^{(1)}$ are denoted by $\mathbf{X}$, while material points of $\bar{\Omega}^{(2)}$ are denoted by $\mathbf{Y}$ with their spatial counterparts $\mathbf{x}$ and $\mathbf{y}$, respectively. As a result, the spatial contact boundary is designated as $\gamma_c^{(\alpha)} = \varphi_t^{(\alpha)}(\Gamma_c^{(\alpha)})$; $\alpha = 1, 2$ upon which the contact constraints are defined. Note that the superscript $^{(\alpha)}$ denotes the specific body $\Omega^{(\alpha)}$ to which the quantities are associated.

5.1.2 Contact kinematics and constraints

The main ingredient to deal with contact problems under large deformation is enforcing the contact constraints at contact boundaries of all bodies. These constraints are formulated with regard to kinematic equations suitable for large deformation and relative sliding, while at the same time, issues related to the nonlinear continuum mechanics of interfaces must be carefully handled as for nonlinear continua in chapter 2. In particular, matters concerning kinematic measure, stress measures (both material and spatial configurations), and material frame indifference must be well defined since they are correlated with interfacial parameters involved in determination of the contact conditions.

5.1.2.1 Formulation for normal contact

Basically, normal contact constraints enforce physical impenetrability conditions, while only compressive contact traction is acceptable. Although, adhesive contact may exist, within this work adhesion is excluded for simplicity. For geometric information, a point on the slave contact boundary is described by a position vector $\mathbf{X} \in \Gamma_c^{(1)}$ whose current position for an instance of time $t \in [0, T]$ is given by $\mathbf{x} = \varphi_t^{(1)}(\mathbf{X})$. Likewise, the current position of any point $\mathbf{Y} \in \Gamma_c^{(2)}$ is designated by $\mathbf{y} = \varphi_t^{(2)}(\mathbf{Y})$. The gap function $g(\mathbf{X}, t)$ is defined via

$$g(\mathbf{X}, t) = \mathbf{n} \cdot \left[\varphi_t^{(1)}(\mathbf{X}) - \varphi_t^{(2)}(\bar{\mathbf{Y}}) \right], \tag{5.3}$$

where $\mathbf{n}$ denotes the outward unit normal vector to $\gamma_c^{(1)}$ at $\mathbf{x} = \varphi_t^{(1)}(\mathbf{X})$ while $\varphi_t^{(2)}(\bar{\mathbf{Y}})$ is the current projected position on the master side of the contact point $\varphi_t^{(1)}(\mathbf{X})$ on the slave side at an instance t as illustrated in Figure 5.4(a). It is noteworthy that a special integration scheme introduced in Yang [Yan06] is employed in this work to indirectly define a pair corresponding points $\mathbf{X}$ and $\bar{\mathbf{Y}}$, whereas, in a node-to-segment approach, a contact point of the master surface identified by $\bar{\mathbf{Y}}(\mathbf{X}, t)$ is typically computed via the closest point projection method:

$$\bar{\mathbf{Y}}(\mathbf{X}, t) = \arg\min_{\mathbf{Y} \in \Gamma_c^{(2)}} \left\| \varphi_t^{(1)}(\mathbf{X}) - \varphi_t^{(2)}(\mathbf{Y}) \right\|. \tag{5.4}$$

It is convenient to choose one surface to parameterize contact, such that positions of points on this surface will be monitored with respect to the location of another surface. The parameterized surface is named the *slave*, or *contactor* surface, while another surface is called the *master*, or *target* surface. The impenetrability condition of the material point $\mathbf{X}$ relative to the master surface $\gamma_c^{(2)}$ is expressed by an inequality constraint

$$g(\mathbf{X}, t) \leq 0. \tag{5.5}$$

Besides, the condition of compressive contact traction, the normal component of contact traction, is defined by

$$\lambda_N(\mathbf{X}, t) \geq 0 \quad \text{with} \quad \lambda_N = -\boldsymbol{\lambda} \cdot \mathbf{n}, \tag{5.6}$$

which means that only compressive contact traction is permitted. $\boldsymbol{\lambda}$ stands for the Cauchy's contact traction. Thus λ_N represents the Cauchy's contact traction at the material point $\mathbf{X}$ on the slave surface $\gamma_c^{(1)}$. The gap function in eq. (5.5) is correlated to the compressive contact traction in eq. (5.6) via the *Kuhn-Tucker (KKT)* conditions such that

$$\lambda_N(\mathbf{X}, t) g(\mathbf{X}, t) = 0. \tag{5.7}$$

The physical meaning implied in eq.(5.7) is shown in Table 5.1 with the schematic illustration in Figure 5.3(a). A graphical interpretation of eqs. (5.5)-(5.7) in Figure 5.3(a) represents admissible combinations of $\lambda_N(\mathbf{X}, t)$ and $g(\mathbf{X}, t)$. Obviously, this graph not only expresses the nonsmooth contact traction $\lambda_N(\mathbf{X}, t)$ which is a nonlinear function of the gap $g(\mathbf{X}, t)$ but also emphasizes that the relation between both variables is non-unique at $g = 0$ where the graph is non-differentiable. From the numerical point of view, finding solution of this ambiguous condition in many cases requires certain regularizations (see, e.g. Wriggers [Wri02] and Laursen [Lau02]).

Table 5.1: The KKT conditions for normal contact constraints.

Description	$g(\mathbf{X}, t)$	λ_N
gap open	< 0	$= 0$
gap closed (two bodies begin to contact each other)	$= 0$	> 0
gap closed (two bodies begin to leave each other)	$= 0$	$= 0$
impenetrability is violated	> 0	> 0

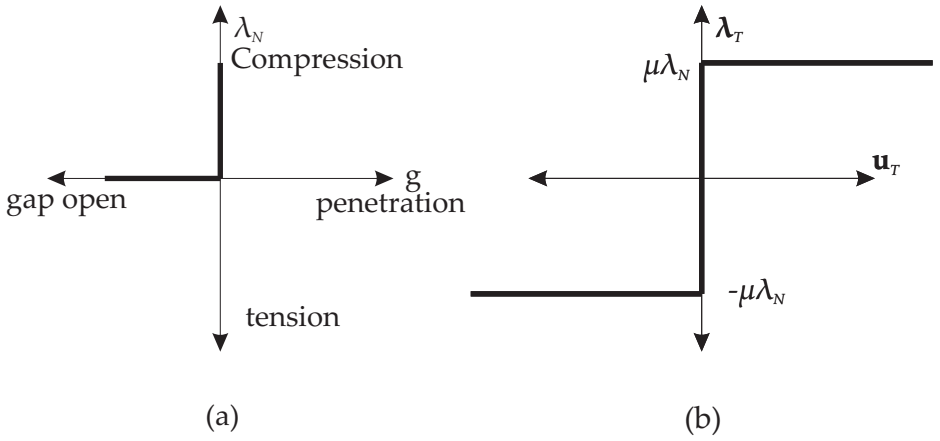

Figure 5.3: Schematic representation of (a) the impenetrability constraint for a normal contact and (b) unregularized Coulomb friction law (1D).

5.1.2.2 Formulation for frictional contact

In addition to the frictionless case, friction plays an important role at the contact interface. The attention is focused on a simple frictional model, the Coulomb friction law, to introduce basic terminologies in frictional contact. By introducing the coefficient of friction μ defined over the contact surface, one can possibly address an unregularized Coulomb friction law by satisfying the following requirements for any material point $\mathbf{X} \in \Gamma_c^{(1)}$

$$\|\boldsymbol{\lambda}_T\| \leq \mu\lambda_N, \tag{5.8}$$

where the normal and tangential components of the contact traction $\boldsymbol{\lambda}$ are denoted by $\boldsymbol{\lambda}_N = -\lambda_N \mathbf{n}$ and $\boldsymbol{\lambda}_T$, respectively. Eq. (5.8) requires that the magnitude of the tangential contact stress vector does not exceed the product of the coefficient of friction μ and the scalar-valued normal contact traction λ_N. The Coulomb law reflects two physical phenomena: First, the *sticking* case implies that the tangential slip does not appear $\mathbf{u}_T = \mathbf{0}$ as long as the tangential contact stress is smaller than the Coulomb limit. Secondly, the *slipping* case indicates the existence of the tangential slip which is collinear to the frictional stress which is induced when a spatial point $\mathbf{x} = \varphi_t^{(1)}(\mathbf{X})$ slides on the opposite surface. Both cases can briefly be expressed by

$$\mathbf{u}_T = c\boldsymbol{\lambda}_T; \quad \text{where} \quad \begin{cases} c = 0 & \text{if } \|\boldsymbol{\lambda}_T\| \leq \mu\lambda_N; \quad \text{stick,} \\ c \geq 0 & \text{if } \|\boldsymbol{\lambda}_T\| = \mu\lambda_N; \quad \text{slip} \end{cases} \tag{5.9}$$

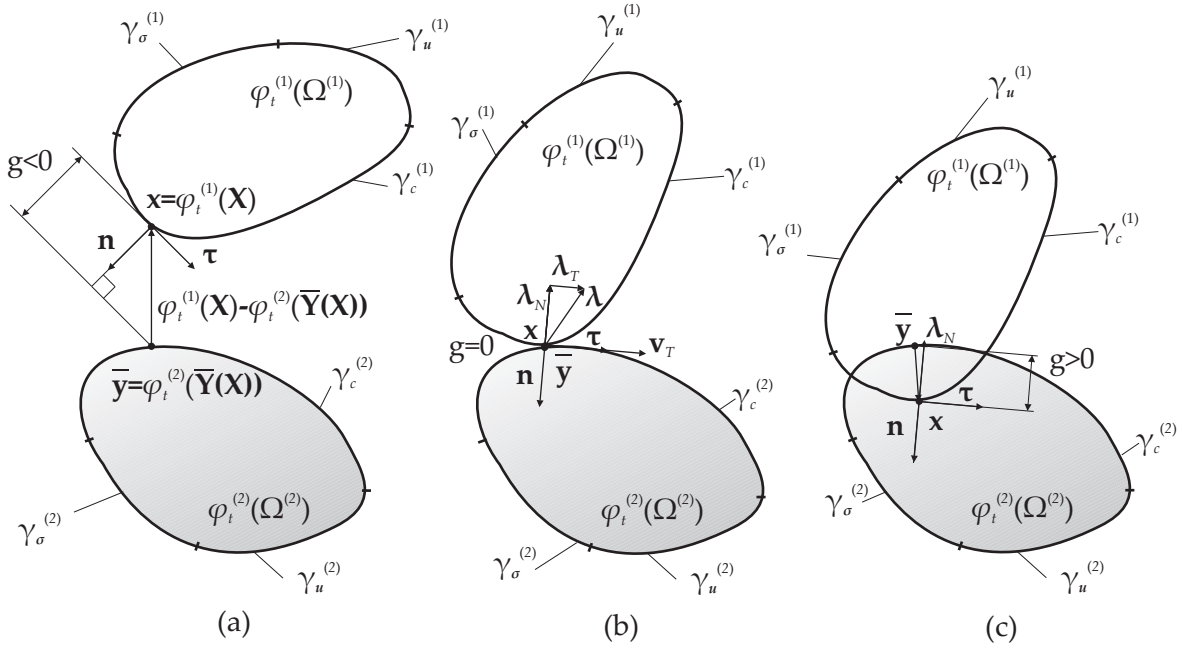

Figure 5.4: Illustration of two deformable bodies in case of (a) no contact $g < 0$ (b) contact without penetration $g = 0$ and (c) penetration $g > 0$.

with the schematic illustration for the one-dimensional problem in Figure 5.3(b). For further reading, numerous textbooks are available, e.g. Laursen [Lau02], Wriggers [Wri02], etc.

We start by defining the relative velocity of the master surface with respect to the slave surface in terms of its normal and tangential components such that

$$\begin{aligned}\mathbf{v} &= \dot{\varphi}_t^{(2)}(\bar{\mathbf{Y}}) - \dot{\varphi}_t^{(1)}(\mathbf{X}) \\ &= \mathbf{v}_N + \mathbf{v}_T = v_N \mathbf{n} + v_{T_\alpha} \boldsymbol{\tau}^\alpha,\end{aligned} \tag{5.10}$$

where $\mathbf{v}_N$ and $\mathbf{v}_T$ represent normal and tangential relative velocity vectors, respectively. v_{T_α} are covariant components of the tangential relative velocity, and $\boldsymbol{\tau}^\alpha = \partial\theta^\alpha / \partial\varphi_t^{(1)}(\mathbf{X})$ are contravariant tangential basis vectors of the slave surface in the current configuration $\gamma_c^{(1)}$(see eq. (2.3)). Similarly, the contact traction $\boldsymbol{\lambda}$ can be decomposed into the normal and tangential components via

$$\boldsymbol{\lambda} = \boldsymbol{\lambda}_N + \boldsymbol{\lambda}_T = -\lambda_N \mathbf{n} + \lambda_{T_\alpha} \boldsymbol{\tau}^\alpha, \tag{5.11}$$

where λ_{T_α} stands for the covariant components of the tangential contact traction $\boldsymbol{\lambda}_T$ with the definition of λ_N in eq. (5.6). An illustration of the relative velocity $\mathbf{v}$, the normal contact traction $\boldsymbol{\lambda}_N$ and tangential contact traction $\boldsymbol{\lambda}_T$ are provided in Figure 5.4(b) in two dimension for simplicity. With all mentioned terms, the Coulomb friction law can be expressed for the

Table 5.2: Strong form for the initial bourdary value problem of elastodynamics with contact for two deformable bodies ($\alpha = 1, 2$).

Dynamic equilibrium equation	$\left[\mathrm{DIV}(\mathbf{F}\cdot\mathbf{S}) + \mathbf{B} = \rho_0\mathbf{A}\right]^{(\alpha)}, \quad \text{on} \quad \Omega^{(\alpha)}\times[0,T]$
Kinematics (**GL** strain)	$\left[\mathbf{E} = \frac{1}{2}(\mathbf{F}^T\mathbf{F} - \mathbf{I})\right]^{(\alpha)} = \left[\frac{1}{2}(g_{ij} - G_{ij})\mathbf{G}^i\otimes\mathbf{G}^j\right]^{(\alpha)}$
Constitutive equation	$\left[\mathbf{S} = \mathbb{C} : \mathbf{E}\right]^{(\alpha)}$
Dirichlet boundary condition	$\left[\varphi_t = \bar{\varphi}_t\right]^{(\alpha)} \quad \text{on} \quad \Gamma_u^{(\alpha)}\times[0,T]$
Neumann boundary condition	$\left[\mathbf{T} = \mathbf{FSN} = \bar{\mathbf{T}}\right]^{(\alpha)} \quad \text{on} \quad \Gamma_\sigma^{(\alpha)}\times[0,T]$
Initial condition (at $t = 0$)	$\left[\dot{\varphi}\vert_{t=0} = \mathbf{V}_0\right]^{(\alpha)}$ on $\bar{\Omega}^{(\alpha)}$; $\quad \left[\varphi\vert_{t=0} = \varphi_0 = \mathcal{I}\right]^{(\alpha)}$ on $\bar{\Omega}^{(\alpha)}$
Contact conditions on slave surface $\gamma_c^{(1)}$:	
Normal contact	$g(\mathbf{X},t) \le 0; \quad \lambda_N(\mathbf{X},t) \ge 0; \quad \lambda_N(\mathbf{X},t)g(\mathbf{X},t) = 0$
Tangential contact	$\Phi(\boldsymbol{\lambda}_N,\boldsymbol{\lambda}_T) = \Vert\boldsymbol{\lambda}_T\Vert - \mu\Vert\boldsymbol{\lambda}_N\Vert$; $\mathbf{v}_T = \dot{\gamma}\frac{\boldsymbol{\lambda}_T}{\Vert\boldsymbol{\lambda}_T\Vert}; \quad \dot{\gamma} \ge 0; \quad \Phi(\boldsymbol{\lambda}_N,\boldsymbol{\lambda}_T)\dot{\gamma} = 0$

frictional contact problems of interest by

$$\Phi(\boldsymbol{\lambda}_N,\boldsymbol{\lambda}_T) = \Vert\boldsymbol{\lambda}_T\Vert - \mu\Vert\boldsymbol{\lambda}_N\Vert \le 0, \tag{5.12}$$

$$\mathbf{v}_T = \dot{\gamma}\frac{\boldsymbol{\lambda}_T}{\Vert\boldsymbol{\lambda}_T\Vert}, \tag{5.13}$$

$$\dot{\gamma} \ge 0, \tag{5.14}$$

$$\Phi(\boldsymbol{\lambda}_N,\boldsymbol{\lambda}_T)\dot{\gamma} = 0, \tag{5.15}$$

where $\Phi(\boldsymbol{\lambda}_N,\boldsymbol{\lambda}_T)$ is the slip function which can be considered as a direct analogue of the yield function in the theory of plasticity (see, e.g. [SH98]). Slip takes place when the condition in eq. (5.9) is met. In eq. (5.13), the slip velocity $\mathbf{v}_T$ is parallel to the tangential contact stress $\boldsymbol{\lambda}_T$ scaled by the slip rate $\dot{\gamma}$ or plastic multiplicator in terms of plasticity. This analogy enables both the extension of the frictional framework with other constitutive laws and a thermodynamic coupling. Note that since the expression in eqs. (5.13)-(5.15) are in the rate form, thus evaluation of frictional contact is path-dependent.

5.1.3 Initial boundary value problem (IBVP) for elastodynamics with contact

Alike section 2.1.4, the dynamic equilibrium conditions are stated with respect to the reference configuration such that

$$\begin{aligned}
\mathrm{DIV}(\mathbf{F}^{(\alpha)}\cdot\mathbf{S}^{(\alpha)}) + \mathbf{B}^{(\alpha)} &= \rho_0^{(\alpha)}\mathbf{A}^{(\alpha)} \quad \text{on} \quad \Omega^{(\alpha)}\times[0,T],\\
\varphi_t^{(\alpha)} &= \bar{\varphi}_t{}^{(\alpha)} \quad \text{on} \quad \Gamma_u^{(\alpha)}\times[0,T],\\
\mathbf{T}^{(\alpha)} = \mathbf{F}^{(\alpha)}\mathbf{S}^{(\alpha)}\mathbf{N}^{(\alpha)} &= \bar{\mathbf{T}}^{(\alpha)} \quad \text{on} \quad \Gamma_\sigma^{(\alpha)}\times[0,T],
\end{aligned} \tag{5.16}$$

where $\bar{\mathbf{T}}^{(\alpha)}$ and $\bar{\varphi}_t^{(\alpha)}$ designate the prescribed tractions and prescribed motion for each body $\Omega^{(\alpha)}$. The strong form of IBVP for elastodynamics of bulk continua in Table 2.1 is

expanded by introducing contact constraints for two deformable bodies ($\alpha = 1, 2$). To solve this system, one must satisfy the modified strong form for both bodies, while at the same time, appended contact conditions are fulfilled. These modifications are shown in Table 5.2.

5.1.4 Weak form of IBVP for elastodynamics incorporating contact

As mentioned in section 2.1.6, the weak form of IBVP is required for FEM. Rather pointwise satisfaction, the strong form of IBVP must be tranformed to the weak form which can be fulfilled in an integral sense. Along the PVW in section 2.1.6.1, we first define the solution space $\mathcal{C}_t^{(\alpha)}$ for each $t \in [0, T]$ and the weighting space $\mathcal{V}^{(\alpha)}$ involving the solution $\varphi_t^{(\alpha)}$ and the weighting function $\delta\varphi^{(\alpha)}$ for each body $\Omega^{(\alpha)}$:

$$\mathcal{C}_t^{(\alpha)} = \left\{ \varphi_t^{(\alpha)} : \bar{\Omega}^{(\alpha)} \to \mathbb{R}^{n_{sd}} | \varphi_t^{(\alpha)} \in H^1(\Omega^{(\alpha)}), \varphi_t^{(\alpha)} = \bar{\varphi}_t^{(\alpha)} \text{ on } \Gamma_u^{(\alpha)} \right\}, \tag{5.17}$$

where the *Sobolev space* $H^1(\Omega^{(\alpha)})$ consists of all vector valued functions over $\Omega^{(\alpha)}$ whose values and first derivatives are square integrable over the domain $\Omega^{(\alpha)}$.

$$\mathcal{V}^{(\alpha)} = \left\{ \delta\varphi^{(\alpha)} : \bar{\Omega}^{(\alpha)} \to \mathbb{R}^{n_{sd}} | \delta\varphi^{(\alpha)} \in H^1(\Omega^{(\alpha)}), \delta\varphi^{(\alpha)} = \mathbf{0} \text{ on } \Gamma_u^{(\alpha)} \right\}. \tag{5.18}$$

With these definitions, one can write the virtual work formulation for contact problems of two deformable bodies with the help of eq. (2.43) by

$$\begin{aligned} G(\varphi_t, \delta\varphi) =& -\delta W = \sum_{\alpha=1}^{2} G^{(\alpha)}(\varphi_t^{(\alpha)}, \delta\varphi^{(\alpha)}), \\ =& \sum_{\alpha=1}^{2} \left[\begin{array}{l} \int\limits_{\Omega^{(\alpha)}} \rho_0^{(\alpha)} \mathbf{A}^{(\alpha)} \cdot \delta\varphi^{(\alpha)} d\Omega + \int\limits_{\Omega^{(\alpha)}} \mathbf{S}^{(\alpha)} : \delta\mathbf{E}^{(\alpha)} d\Omega \\ - \int\limits_{\Omega^{(\alpha)}} \mathbf{B}^{(\alpha)} \cdot \delta\varphi^{(\alpha)} d\Omega - \int\limits_{\Gamma_\sigma^{(\alpha)}} \bar{\mathbf{T}}^{(\alpha)} \cdot \delta\varphi^{(\alpha)} d\Gamma \end{array} \right] \\ & - \sum_{\alpha=1}^{2} \int\limits_{\Gamma_c^{(\alpha)}} \mathbf{t}_c^{(\alpha)} \cdot \delta\varphi^{(\alpha)} d\Gamma = 0, \\ =& G_{dyn}(\varphi_t, \delta\varphi) + G_{int}(\varphi_t, \delta\varphi) + G_{ext}(\varphi_t, \delta\varphi) + G_c(\varphi_t, \delta\varphi), \end{aligned} \tag{5.19}$$

where definitions for the virtual work from inertial forces $G_{dyn}(\varphi_t, \delta\varphi)$, the contribution from internal forces $G_{int}(\varphi_t, \delta\varphi)$ and external forces $G_{ext}(\varphi_t, \delta\varphi)$ are provided in eqs. (2.46)-(2.48) with summation over both deformable bodies, respectively. Therefore, the main interest in the rest of this chapter is the virtual work from contact forces $G_c(\varphi_t, \delta\varphi)$ which states that contact forces must be in equilibrium along the contact interface. To implement the mortar-based contact formulation, the contact virtual work is expressed by

$$G_c(\varphi_t, \delta\varphi) = -\sum_{\alpha=1}^{2} \int\limits_{\Gamma_c^{(\alpha)}} \mathbf{t}_c^{(\alpha)} \cdot \delta\varphi^{(\alpha)} d\Gamma \quad \Rightarrow \quad -\sum_{\alpha=1}^{2} \int\limits_{\gamma_c^{(\alpha)}} \boldsymbol{\lambda}^{(\alpha)} \cdot \delta\varphi^{(\alpha)} d\gamma, \tag{5.20}$$

where $\gamma_c^{(\alpha)}$ is the contact boundary of the body $\Omega^{(\alpha)}$ in the current configuration. Obviously, the Lagrange multiplier $\boldsymbol{\lambda}^{(\alpha)}$ denotes the Cauchy's contact traction. Note that both $\boldsymbol{\lambda}^{(\alpha)}$

and $\gamma_c^{(\alpha)}$ vary along the motion mapping $\varphi_t^{(\alpha)}$ With regard to the balance of linear momentum across the mortar contact interface, the contact traction introduced on the body (2) is equal but opposite to that created on the body (1) such that

$$\boldsymbol{\lambda}^{(1)} d\gamma_c^{(1)} = -\boldsymbol{\lambda}^{(2)} d\gamma_c^{(2)}. \tag{5.21}$$

The contact traction in eq. (5.11) can be decomposed into a normal part $\boldsymbol{\lambda}_N$ and a tangential part $\boldsymbol{\lambda}_T$ such that $\boldsymbol{\lambda} = \boldsymbol{\lambda}_N + \boldsymbol{\lambda}_T$. As a result, the contact virtual work in eq. (5.20) is reformulated to

$$\begin{aligned} G_c(\varphi_t, \delta\varphi) &= -\int_{\gamma_c^{(1)}} \boldsymbol{\lambda} \cdot \left(\delta\varphi^{(1)}(\mathbf{X}) - \delta\varphi^{(2)}(\bar{\mathbf{Y}}) \right) d\gamma; \quad \text{with} \quad \boldsymbol{\lambda} = \boldsymbol{\lambda}^{(1)}, \\ &= -\int_{\gamma_c^{(1)}} (\boldsymbol{\lambda}_N + \boldsymbol{\lambda}_T) \cdot \left(\delta\varphi^{(1)}(\mathbf{X}) - \delta\varphi^{(2)}(\bar{\mathbf{Y}}) \right) d\gamma, \end{aligned} \tag{5.22}$$

Because this work focuses on the frictionless contact problems, therefore, the tangential contact stress is not interested $\boldsymbol{\lambda}_T = \mathbf{0}$. The outcome is the weak form for frictionless contact:

$$\begin{aligned} G_c(\varphi_t, \delta\varphi) &= -\int_{\gamma_c^{(1)}} \boldsymbol{\lambda}_N \cdot \left(\delta\varphi^{(1)}(\mathbf{X}) - \delta\varphi^{(2)}(\bar{\mathbf{Y}}) \right) d\gamma, \\ &= \int_{\gamma_c^{(1)}} \lambda_N \mathbf{n} \cdot \left(\delta\varphi^{(1)}(\mathbf{X}) - \delta\varphi^{(2)}(\bar{\mathbf{Y}}) \right) d\gamma, \end{aligned} \tag{5.23}$$

where the normal contact traction is denoted by $\boldsymbol{\lambda}_N = -\lambda_N \mathbf{n}$ as mentioned in eq. (5.6).

5.1.5 Treatment of contact constraints

In previous section, the weak form of IBVP for elastodynamics is given along with the constraints for frictionless contact problems. This section will introduce typical algorithms to incorporate the contact constraints into the variational formulation. Table 5.3 provides a comparison for advantages and drawbacks for five well-known mathematical algorithms originated in optimization theory to solve a constrained minimization problem as in the frictionless contact of two deformable bodies at hands. Among them, this section explains only the Lagrange multiplier method which is chosen to find the solution of the IBVP with frictionless contact constraints based on the mortar method in this chapter. Note that the dual Lagrange multiplier method with a carefully selected dual basis function is a specific case of the Lagrange multiplier method. For further details, there are numerous textbooks about the topic of enforcing contact constraints, e.g. [BLM00, Lau02, Wri02].

Lagrange multiplier method

In this method, a constraint is appended to the the weak form of IBVP, or objective function, by means of the Lagrange multiplier method. First, the contact conditions in (5.5) is

Table 5.3: Comparison pros and cons of different regularization methods.

regularization method	pros	cons
penalty	system size is maintained comparatively simple	user-defined penalty factor possibly ill-conditioned
Lagrange multiplier	exact constraint enforcement	system size is varied
Perturbed Lagrangian	good condition number stiff constraint enforcement	system size is varied
Augmented Lagrangian	system size is maintained $\cong$ exact constraint enforcement good condition number	additional iteration
Dual Lagrangian	system size is maintained exact constraint enforcement good condition number	dual function is required

multiplied with a weighting function $\delta\lambda_N$ (the virtual normal contact force) where λ_N is the Lagrange multiplier which is physically interpreted as the normal contact traction. Then, the weak form of IBVP in eq. (5.19) with the contact constrains for a frictionless contact problem is given by

$$\begin{aligned} G^{LM}(\varphi_t, \delta\varphi) =& G_{dyn}(\varphi_t, \delta\varphi) + G_{int}(\varphi_t, \delta\varphi) + G_{ext}(\varphi_t, \delta\varphi) + G_c(\varphi_t, \delta\varphi) \\ &+ \int_{\gamma_c^{(1)}} \delta\lambda_N(\mathbf{X}) g(\mathbf{X}, t) d\gamma = 0, \end{aligned} \tag{5.24}$$

where the virtual work in case of frictionless contact G_c is given in eq. (5.23). The Lagrange multiplier formulation is the basis for the mortar method which is an effective mean to transfer information among different domains with non-matching meshes for the domain decomposition approaches, especially in parallel computing. Next section will introduce the mortar method as a basis to mortar-based contact formulation.

5.2 Mortar method for contact problems

For FE applications, the IBVPs are discretized to achieve approximate solutions. In many circumstances, the number of DOF of the system reach a level that a single processor cannot handle, e.g. fluid-structure interactions, multibody contact/impact problems. To circumvent such problems, the domain decomposition technique is proposed recently with the main idea to subdivide original problems into several subdomains. It is possible to treat different subdomain with different FE discretization or even different numerical methods. The approach is effective for a problem that allows several subdomains to be coupled along their interfaces, in particular when issues of non-matching meshes come across the domain

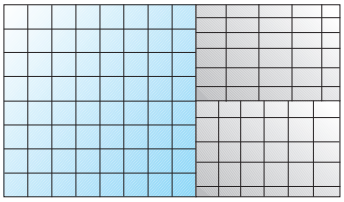

Figure 5.5: Illustration for typical nonconforming domain decomposition with FEM.

interfaces as shown in Figure 5.5. At this point, an important question arises as how to enforce the continuity of solutions across subdomain interfaces which is of great importance to gain a stable and optimal solution. In general, there are two variants to enforce constraints across nonconforming subdomains where the compatibility requirements are fulfilled either in a pointwise or in an integral manner.

Nowadays, most algorithms for nonconforming contact are based on node-to-segment approaches which enforce contact using collocation such that nodes on the *"slave side"* must not penetrate their opposing *"master side"* segments or facets. This non-penetrating condition may be enforced on the single pass method where only the slave side nodes are considered and prevented to penetrate the master side segment while the master side nodes are not under consideration. Since the single-pass method cannot pass the contact patch test [PT92], this approach is not applicable for contact problems of deformable bodies.

For this reason, the two-pass method is usually employed for contact problems of deformable bodies because the contact patch test can be considered for 2D and certain 3D mesh configurations with adequate symmetry for low order elements, e.g. bilinear quadrilateral elements. However, non-optimal rate of convergence is proven in case of the pointwise approach, i.e. the computation converges slower than what is expected from the computation with a single domain. Moreover, the two-pass method cannot satisfy patch tests with higher order element, e.g. quadratic elements. Even though, this node-to-segment approach is mostly employed nowadays, it is not robust, in particular, when implicit solution procedures are utilized to solve the non-linear equations.

The two-pass node-to-segment contact algorithms have four main drawbacks: In general, the two-pass method is prone to "lock" as shown by Puso and Laursen [PL04a]. Besides, it fails the Babuska-Brezzi (BB) condition [BF91] in addition to ill conditioning and convergence problems. All of these adverse behaviors reflect the underlying over-constraint. Furthermore, the measure of penetration for node-to-segment approach is described by the slave node gap, which is determined by the closest point projection of the slave node onto the master surface. For the frictionless case, the contact force is defined by a vector of force which is coaxial to the normal vector of the master surface at the point where the closest projection vector from a slave node intersects. As a result, the low order elements with non-smooth surface leads to jumps in the contact forces when a slave node moves from one master surface to a neighboring surface. These jumps in many cases affect convergence behavior. In case that slave nodes reach the border of the well-defined master surfaces and slide off, there exist usually jumps in the contact forces which normally result in convergence problems.

- ◇ Locking or over-constraint.
- ◇ Non-smooth contact surfaces cause jumps in contact forces when slave nodes slide between adjacent master segments due to the fact that non-penetration constraint is enforced pointwise. In many cases, this cause discontinuities or jumps in the contact forces and difficulties in convergence for implicit solution techniques.
- ◇ Even for comparatively flat contact surfaces, discrete constraints cause jumps when slave nodes slide off boundaries of a master surface.
- ◇ Inequality equations determine active and inactive constraints, e.g. gaps opening and closing, non-tensile contact traction, etc.

Figure 5.6: Drawbacks of the node-to-segment approach.

In contrary, the over-constraint is gotten rid of by design in case of the segment-to-segment contact algorithm whose contact virtual work is integrated over the contact surface by employing some interpolated scheme for the contact traction. Generally, variants of the segment-to-segment approach are different from each on how the contact traction and the projection are defined. This approach is superior to the node-to-segment schemes with regard to robustness, accuracy and rate of convergence. The jumps in contact forces for segment-to-segment approach is alleviated because penetration is measured on the weighting function, varying smoothly with perturbation, of nodal penetration over a patch of elements surrounding a node. In summary, the segment-to-segment approach deals with the first three aspects in Figure 5.6 while for the fourth issue there are several mathematical approaches which can handle this inequality constraints within the context of the computational contact mechanics.

The segment-to-segment method can be traced back to original works by Simo et al. [SWT85], Papadopoulos and Taylor [PT92] and Zavarise and Wriggers [ZW98] where the 2D contact problems with the penalty method are involved while extensions to the Lagrange multipliers method are not always stable. On the other hand, the mortar element methods was originally introduced as domain decomposition and mesh tying techniques by Bernardi et al. [Ber94], Belgacem et al. [BM94], and Wohlmuth [Woh01]. The mortar methods enforce the continuity across subdomain interfaces in an integral sense which is of great interest due to their optimal rate of convergence with suitably selected mortar spaces. With these chosen spaces, the methods satisfy the *inf-sup* conditions (see [Bat02]) in addition to the Brezzi-Babuska (BB) stability condition (see [Woh01]) for a stable discretization scheme.

Early applications of the mortar methods with contact problems, so-called mortar-based segment-to-segment contact algorithm, can be found in [BHL98, ML00]. At its early age, the mortar-based contact algorithm is restricted only to small deformation/sliding problems with comparatively flat contact surfaces. Recently, developments of mortar schemes for large deformation and/or sliding contact have gained increasing attentions: Puso and Laursen introduced a mortar-based contact scheme for large deformation frictionless contact in [PL04a] and frictional contact in [PL04b] with linear momentum conservation for

arbitrarily curved 3D surface. Numerical results show that the mortar-based segment-to-segment contact algorithm is far more robust than the node-to-segment counterpart, even though it requires more computing resources. Note that the single-pass mortar contact algorithm is biased since the Lagrange multiplier field is interpolated only over the slave side surface. However, this mortar-based algorithm passes the patch test by design unlike the single-pass node-to-segment method. Albeit the unbiased algorithm is desirable, Puso and Laursen proved that the single-pass mortar-based contact algorithm has relatively small influences on the resulting forces and stresses when the meshes on both the master and slave surfaces are adequately refined.

In general, the mortar methods are related to a saddle point problem defined on the primal unknowns and dual unknowns (Lagrange multipliers). The Lagrange multipliers are specified on one side, usually called the non-mortar side, of the interface between two subdomains. In Bernadi et al. [Ber94], a discrete Lagrange multiplier space, so-called mortar space, is presented with the advantages that the *inf-sup* condition is fulfilled while the optimal rate of convergence is held. Later, Wohlmuth [Woh00] introduced a dual Lagrange multiplier space which fulfills the bi-orthogonality property with the basis function of the trace space. Consequently, the Lagrange multipliers can be eliminated locally by a static condensation which results in a system of equations with only the primal unknowns. In Wohlmuth [Woh00], the dual mortar space is shown to maintain the optimal rate of convergence.

For the contact problems of interest, there are two requirements to be considered: First, at least the constant traction must be exactly transmitted via suitable interface coupling condition from one subdomain to its contact pair. Secondly, all subdomains which come into contact will not penetrate each other. The Lagrange multipliers, representing the contact traction between two subdomains at their contact interfaces, are interpolated by certain ansatz spaces: linear, quadratic or high-order interpolation functions.

There are several techniques to define the contact surface. One is based on using an intermediate contact surface as the reference surface at which the Lagrange multipliers are formed. This intermediate contact surface is known as the *mortar side* of the interface. Details of this method can be found in Mcdevitt and Laursen [ML00], Rebel et al. [RPF02], Yamazaki and Park [MP06] and Gonzáles et al. [GPFA08], for examples. Another method, which is introduced in mathematical literature (see, e.g. Wohlmuth [Woh00]), is derived on an assumption that one of the surfaces of the bodies in the contact interfaces is counted as the mortar side. Wohlmuth [Woh00] showed that this method together with appropriate interpolation functions for the Lagrange multipliers fulfills the Brezzi-Babuska (BB) condition. Furthermore, the Lagrange multiplier interpolation can be designed such that the local support property of the nodal basis functions is preserved. As a result, this formulation yields a stable discretization scheme with an admirable contact traction approximation.

Issues concerning consistent transmission of interface forces from one subdomain to its contact pair are related to the manner in which the traction and kinematic compatibilities are approximated across the contact interfaces. In Laursen [Lau02], an analysis of the mortar joining method is presented for convergence checks. In the context of the mortar-based formulation, the slave surface $\gamma_c^{(1)}$ is referred to as the *non-mortar* surface at which the Lagrange

multipliers are interpolated, whereas the master surface $\gamma_c^{(2)}$ is known as the *mortar* surface. Distinct differences between the "older" segment-to-segment (STS) method [SWT85] and the "younger" mortar-based method [Ber94] are the manner that the contact traction $\boldsymbol{\lambda}$ in the contact interface is interpolated and whether the contact quantities are consistently computed in an integral sense which has influences on the robustness of the method (see e.g. Wriggers [Wri02]). Nowadays, applying mortar methods for large deformation contact problems is still one of the most active research.

5.3 Spatial discretization for mortar-based frictionless contact

As mentioned in section 2.3.1, the bilinear membrane finite elements are opted to simplify derivation although higher order elements, e.g. quadratic, are as well eligible. This section begins with the description of the mortar method for frictionless contact problems. Then, the following subsection introduces discrete dual ansatz functions used to interpolate the Lagrange multiplier field within a bilinear 4-node membrane element. Finally, applications of these dual ansatz functions for unilateral and multibody contact problems are presented with the focus on the discrete form of the contact virtual work. With the underlying implicit time integrator, resulting algebraic system of equations are arranged to form the effective incremental structural equation (see eq. (2.132)) upon which the impenetrability constraints, presented in section 5.5, are enforced.

5.3.1 Problem description

The starting point for mortar-based contact problems is the interpolation of the normal contact traction $\lambda_N(\mathbf{X}, t)$ and gap function $g(\mathbf{X}, t)$ for the contact virtual work G_c and contact constraints of eq. (5.24). Because the gap function is defined by the displacement fields at the surfaces of bodies in the contact interfaces, the interpolation functions employed to interpolate the bodies can be used for this gap as well. What remains to be decided is the choice of an interpolation scheme which satisfies the BB condition for the normal contact traction λ_N. Usually, λ_N can be interpolated by either standard or dual ansatz functions.

Based on Hüber and Wohlmuth [HW05], and Hartmann [Har07], the latter approach is employed within this work due to various advantages as mentioned in Table 5.3: Contact conditions can be exactly fulfilled in the weak sense without altering the size of the system matrix. Since user-defined parameters are not involved, the problems of ill-conditioned matrix can be avoided. At this point, there is still the open question whether the dual basis functions designed for small deformation in [Woh00] are suitable for the large deformation contact problems as in this work. Similar to eq. (2.70), we start by considering the spatial discretization of bodies $\Omega^{(\alpha)}$ by using a finite set of elements $\mathcal{E}^{(\alpha)^h}$

$$\Omega^{(\alpha)} \approx \Omega^{(\alpha)^h} = \bigcup_{\forall e \in \mathcal{E}^{(\alpha)^h}} \Omega^{(\alpha)^e} \tag{5.25}$$

with $\Gamma_c^{(\alpha)^h} \in \partial\Omega^{(\alpha)^h}$ being the discrete contact surfaces. Let us introduce an interpolation function $N_A;\ A = 1, \ldots, n_{np}^{(\alpha)}$ which is associated to node A of the body $\Omega^{(\alpha)}$ by a map N_A :

$\bar{\Omega}^{(\alpha)} \rightarrow \mathbb{R}^{n_{sd}}$. Given a time t, the finite-dimensional subspace of the solution space $\mathcal{C}_t$ in (2.41) is defined by

$$\mathcal{C}_t^{(\alpha)^h} = \Big\{ \varphi_t^{(\alpha)^h} : \bar{\Omega}^{(\alpha)^h} \rightarrow \mathbb{R}^{n_{sd}} | \varphi_t^{(\alpha)^h} \in C^0(\Omega^{(\alpha)^h}); \forall e \in \mathcal{E}^{(\alpha)^h}, \quad \varphi_t^{(\alpha)^h}(\Omega^{e(\alpha)^h}) \in \mathbb{P}_N(\Omega^{e(\alpha)^h}),$$
$$\varphi_t^{(\alpha)^h} = \sum_{B=1}^{n_{np}^{(\alpha)}} N_B(\mathbf{X}) \mathbf{d}_B^{(\alpha)}(t) | \varphi_t^{(\alpha)^h} \approx \bar{\varphi}_t^{(\alpha)}(\mathbf{X}) \text{ on } \mathbf{X} \in \Gamma_u^{(\alpha)} \Big\}, \tag{5.26}$$

where $\mathbf{d}_B^{(\alpha)}$ is a n_{sd}-vector containing the coordinates of nodal points B of the body $\Omega^{(\alpha)}$ at time t. $\mathbb{P}_N(\Omega^{e(\alpha)^h})$ is the set of all polynomials on $\Omega^{e(\alpha)^h}$ of order $\leq N$. Given a prescribed set of nodal interpolation functions $N_B;\ B = 1, \ldots, n_{np}^{(\alpha)}$, the discrete solution space $\mathcal{C}_t^{(\alpha)^h}$ must approximately satisfy the displacement boundary condition on $\Gamma_u^{(\alpha)^h}$. The weighting space $\mathcal{V}$ in (2.42) for the (Bubnov-) Galerkin FEM is interpolated with the same interpolation functions as were used to approximate $\mathcal{C}_t^h$. Accordingly, the finite-dimensional weighting space $\mathcal{V}^{(\alpha)^h}$ can be expressed via

$$\mathcal{V}^{(\alpha)^h} = \Big\{ \delta\varphi^{(\alpha)^h} : \bar{\Omega}^{(\alpha)^h} \rightarrow \mathbb{R}^{n_{sd}} | \delta\varphi^{(\alpha)^h} \in C^0(\Omega^{(\alpha)^h}); \forall e \in \mathcal{E}^{(\alpha)^h}, \delta\varphi^{(\alpha)^h}(\Omega^{e(\alpha)^h}) \in \mathbb{P}_N(\Omega^{e(\alpha)^h}),$$
$$\delta\varphi^{(\alpha)^h} = \sum_{A=1}^{n_{np}^{(\alpha)}} N_A \mathbf{c}_A^{(\alpha)} | \delta\varphi^{(\alpha)^h}(\mathbf{X}) = \mathbf{0} \text{ on } \mathbf{X} \in \Gamma_u^{(\alpha)^h} \Big\}. \tag{5.27}$$

The mortar and nonmortar fields, $\varphi_t^{(\alpha)^h}(\Gamma_c^{(\alpha)^h}) \subset \mathcal{X}^{(\alpha)^h} \subset \mathcal{C}_t^{(\alpha)^h}$, and their variations, $\delta\varphi^{(\alpha)^h}(\Gamma_c^{(\alpha)^h}) \subset \mathcal{W}^{(\alpha)^h} \subset \mathcal{V}^{(\alpha)^h}$, are subset of $\mathcal{C}_t^{(\alpha)^h}$ in eq. (5.26) and $\mathcal{V}^{(\alpha)^h}$ in eq. (5.27) with restriction on the contact surface $\Gamma_c^{(\alpha)^h}$. The discrete space of the Lagrange multipliers, which is the space of contact tractions, is specified on the nonmortar (slave) side such that

$$\mathcal{M}^h = \Big\{ \boldsymbol{\lambda}^h | \boldsymbol{\lambda}^h \in C^0(\Gamma_c^{(1)^h}); \forall e \in \mathcal{P}^h, \quad \boldsymbol{\lambda}^h(\Gamma_c^{e(1)^h}) \in \mathbb{P}_N(\Gamma_c^{e(1)^h}) \Big\}, \tag{5.28}$$

where the slave surface is made of the set of nonmortar elements $\mathcal{P}^h$. The deformation, their variation and the discrete Lagrange multiplier fields on the contact surface are described by

$$\varphi_t^{(1)^h}(\mathbf{X}) = \sum_{D=1}^{n_c^s} N_D^{(1)} \left(\boldsymbol{\theta}^{(1)}(\mathbf{X}) \right) \mathbf{d}_D^{(1)}(t), \tag{5.29}$$

$$\varphi_t^{(2)^h}(\bar{\mathbf{Y}}) = \sum_{E=1}^{n_c^m} N_E^{(2)} \left(\boldsymbol{\theta}^{(2)}(\bar{\mathbf{Y}}) \right) \mathbf{d}_E^{(2)}(t), \tag{5.30}$$

$$\delta\varphi^{(1)^h}(\mathbf{X}) = \sum_{B=1}^{n_c^s} N_B^{(1)} \left(\boldsymbol{\theta}^{(1)}(\mathbf{X}) \right) \mathbf{c}_B^{(1)}, \tag{5.31}$$

$$\delta\varphi^{(2)^h}(\bar{\mathbf{Y}}) = \sum_{C=1}^{n_c^m} N_C^{(2)} \left(\boldsymbol{\theta}^{(2)}(\bar{\mathbf{Y}}) \right) \mathbf{c}_C^{(2)}, \tag{5.32}$$

$$\boldsymbol{\lambda}^h(\mathbf{X}) = \sum_{A=1}^{n_c^s} \phi_A^{(1)} \left(\boldsymbol{\theta}^{(1)}(\mathbf{X}) \right) \mathbf{z}_A, \tag{5.33}$$

where A, B, D are global nodal indices related to the slave (nonmortar) side $\Gamma_c^{(1)^h}$ while C, E are global nodal indices associated with the master (mortar) surface $\Gamma_c^{(2)^h}$.[1] The surface parameters are represented by $\boldsymbol{\theta}^{(1)}$ and $\boldsymbol{\theta}^{(2)2}$ whereas $\mathbf{z}_A$ stands for nodal value for contact tractions at slave nodes. $\mathbf{c}_D^{(1)}$ and $\mathbf{c}_E^{(2)}$ are the variations of nodal positions on the slave and master contact surfaces while $\mathbf{d}_B^{(1)}$ and $\mathbf{d}_C^{(2)}$ are nodal positions on the slave and master contact surfaces, respectively. Furthermore, n_c^s and n_c^m designate number of nodes on slave and master contact surfaces, respectively. For simplicity, we replace $\mathbf{z}_A = \boldsymbol{\lambda}_{A_N}$ for the normal contact traction at node A. Substituting eqs. (5.29)-(5.33) in eq. (5.23), one obtains the discrete virtual work for frictionless contact problems :

$$G_{cm}(\varphi_t, \delta\varphi) \approx G_{cm}^h = -\sum_{A=1}^{n_c^s}\sum_{B=1}^{n_c^s}\sum_{C=1}^{n_c^m} \mathbf{z}_A \cdot \left[n_{AB}^{(1)} \mathbf{c}_B^{(1)} - n_{AC}^{(2)} \mathbf{c}_C^{(2)} \right], \tag{5.34}$$

where $G_{cm}(\varphi_t, \delta\varphi)$ stands for the mortar version of the contact virtual work, which will be discussed in subsequent sections and the *mortar integral* n_{AB} and n_{AC} are defined by

$$n_{AB}^{(1)} = \int_{\gamma_c^{h(1)}} \phi_A^{(1)} \left(\boldsymbol{\theta}^{(1)}(\mathbf{X}) \right) N_B^{(1)} \left(\boldsymbol{\theta}^{(1)}(\mathbf{X}) \right) d\gamma, \tag{5.35}$$

$$n_{AC}^{(2)} = \int_{\gamma_c^{h(1)}} \phi_A^{(1)} \left(\boldsymbol{\theta}^{(1)}(\mathbf{X}) \right) N_C^{(2)} \left(\boldsymbol{\theta}^{(2)}(\bar{\mathbf{Y}}) \right) d\gamma. \tag{5.36}$$

5.3.2 Discrete dual ansatz function for Lagrange multipliers

This section introduces the dual ansatz function, proposed by Wohtmuth [Woh00], to approximate the Lagrange multipliers whereas alternative ansatz functions can be seen from various authors, e.g. [Lau02, YLM05, PL04a, ML00]. In the following, interpolation functiona for both the displacement fields and the Lagrange multiplier fields are provided for bilinear 4-node membrane elements in two- and three-dimensional problems, respectively.

5.3.2.1 Dual ansatz function for 2D problems

For two-dimensional contact problems, so-called *"inplane-loaded plate problems"* (see Figure 5.7), the contact boundary is composed of linear 2-node line elements connecting two adjacent nodes. On the parametric space, each line element is defined by a parameter $\theta \in [-1, 1]$. Therefore, the interpolation functions for the change of coordinates at the contact boundary are identical to the interpolation functions for displacements of the "host" bilinear 4-node element whose boundary line is considered as the contact boundary $\gamma_c^{(\alpha)}$. As a result, the displacement field on the contact boundary is interpolated by linear shape functions as shown in Figure 5.7(a). The discrete dual ansatz for the Lagrange multipliers,

[1] The superscript (1) and (2) reflect the slave and master contact surface, respectively.

[2] For the 2D problem, $\boldsymbol{\theta}^{(1)} = \theta^{1^{(1)}}$, $\boldsymbol{\theta}^{(2)} = \theta^{1^{(2)}}$, while for 3D case, $\boldsymbol{\theta}^{(1)} = \left\{\theta^{1^{(1)}}, \theta^{2^{(1)}}\right\}$, $\boldsymbol{\theta}^{(2)} = \left\{\theta^{1^{(2)}}, \theta^{2^{(2)}}\right\}$.

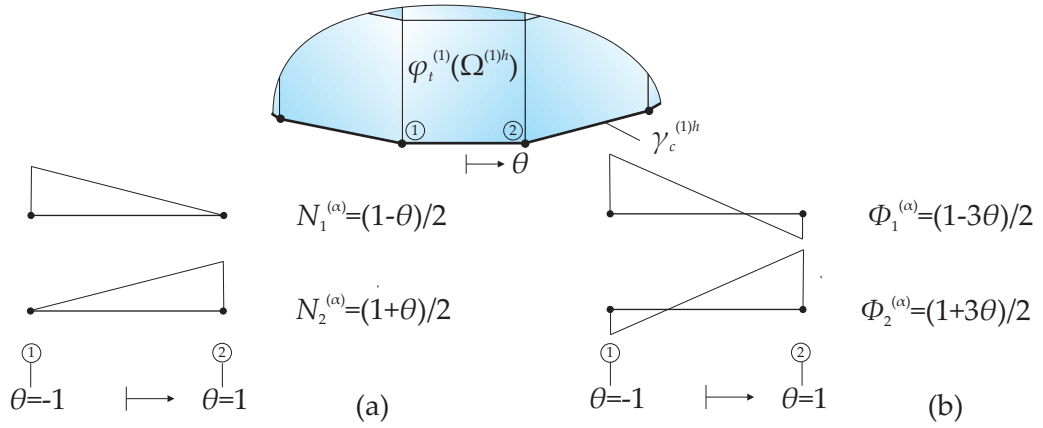

Figure 5.7: Interpolation functions in 2D contact problems for (a) displacement and (b) Lagrange multiplier fields.

parameterized on the slave side, must be chosen such that it satisfies the biorthogonality condition with the ansatz function of the displacement of the slave side in an integral manner on the "*physical contact boundary*" which means that the dual ansatz function depends on the selected FE-mesh. The biorthogonality condition for each contact element e can be described by

$$\begin{aligned} n_{AB}^{(1)} &= \int_{\gamma_c^{h(1)e}} \phi_A^{(1)} \left(\boldsymbol{\theta}^{(1)}(\mathbf{X})\right) N_B^{(1)} \left(\boldsymbol{\theta}^{(1)}(\mathbf{X})\right) d\gamma, \\ &= \delta_{AB} \int_{\gamma_c^{h(1)e}} N_B^{(1)} \left(\boldsymbol{\theta}^{(1)}(\mathbf{X})\right) d\gamma; \quad \delta_{AB} = \begin{cases} 1 & A = B, \\ 0 & \text{otherwise}, \end{cases} \end{aligned} \tag{5.37}$$

where $N_B^{(1)}(\boldsymbol{\theta}^{(1)}(\mathbf{X}))$ stands for the shape function for the displacement field on the slave contact boundary $\gamma_c^{(1)}$. In this case, the determinant of Jacobian of a transformation mapping from the parametric to physical spaces is constant, since there is only axial elongation at the contact boundary without mesh distortion. As a result, the discrete dual ansatz functions for the Lagrange multipliers are constant as demonstrated in Figure 5.7(b)

5.3.2.2 Dual ansatz function for 3D problems-undistorted mesh

For three dimensional contact problems, contact boundaries are curved surfaces in the three dimensional space composed of 4-node bilinear membrane elements (see Figure 5.8). Each membrane element is defined on the parametric space by two surface parameters $\theta^1, \theta^2 \in [-1, 1]$. Therefore, the interpolation functions for the displacement field at contact surfaces $\gamma_c^{(\alpha)}$ are identical to those of the bilinear 4-node membrane element as displayed in Figure 5.8(a). On the other hand, the discrete dual ansatz for the Lagrange multipliers, parameterized on the slave side, must fulfill the biorthogonality condition with the ansatz function of the displacement on the slave side in an integral manner on the "*physical contact boundary*"which means that the dual ansatz function depends on selected FE-mesh. Similar

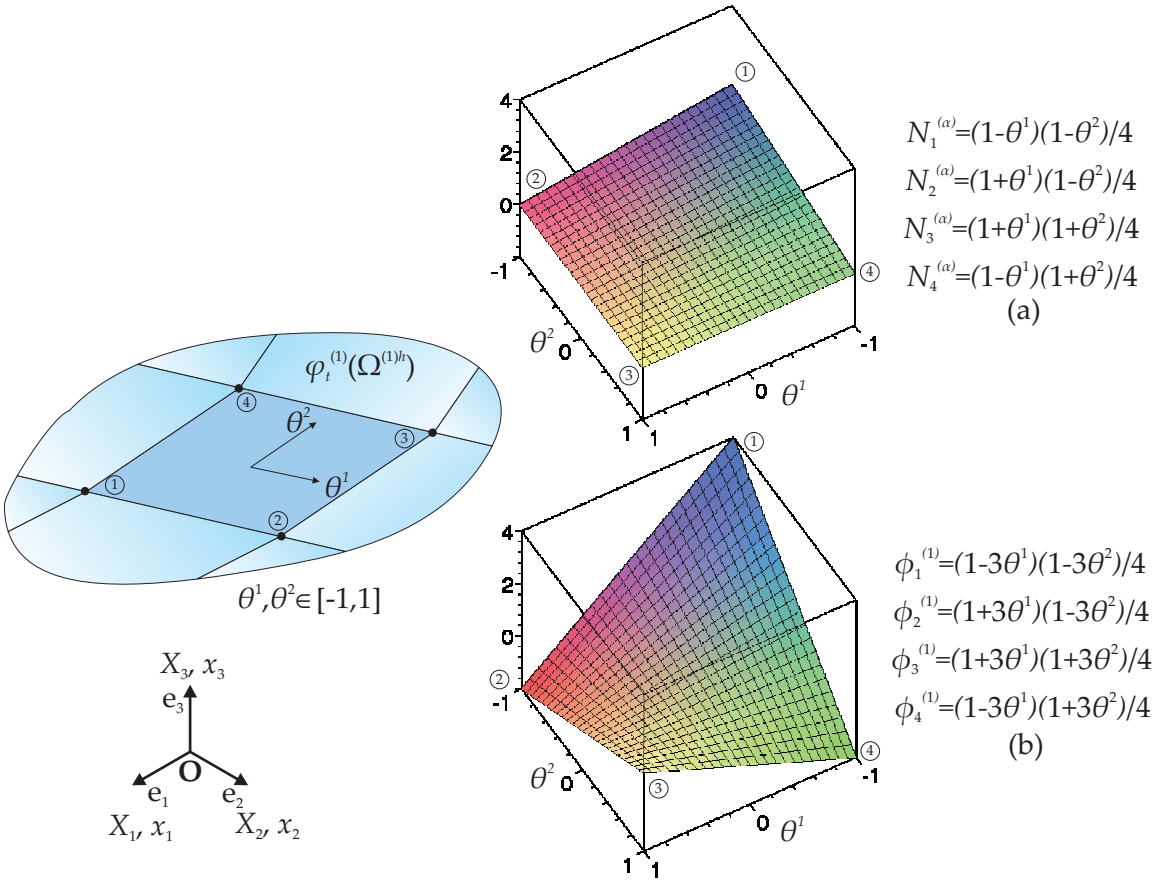

Figure 5.8: Interpolation functions in 3D contact problems for (a) displacement and (b) Lagrange multiplier fields.

to the 2D case without mesh distortion, the constant determinant of Jacobian of a transformation mapping of a contact element from the parametric space to the physical space is maintained. In Figure 5.8(b)[3], a special form of the dual ansatz functions for the Lagrange multipliers is demonstrated.

5.3.2.3 Dual ansatz function for 3D problems-arbitrary shaped elements

In this case, a main difference from an undistorted element is that the determinant of Jacobian for a transformation mapping of a contact element from the parametric space to the physical space is not constant. As mentioned in eq. (5.37), the discrete dual ansatz functions must be constructed so that the biorthogonality condition on the physical contact boundary

[3]The construction for the discrete dual ansatz function is provided in the appendix B.3.

of each contact element $\gamma_c^{h(\alpha)e}$ is satisfied:

$$n_{AB}^{(1)} = \int\limits_{\gamma_c^{h(1)e}} \phi_A^{(1)}(\boldsymbol{\theta}^{(1)}) N_B^{(1)}(\boldsymbol{\theta}^{(1)}) d\gamma = \delta_{AB} \int\limits_{\gamma_c^{h(1)e}} N_B^{(1)}(\boldsymbol{\theta}^{(1)}) d\gamma,$$
$$= \delta_{AB} \int\limits_{-1}^{1}\int\limits_{-1}^{1} N_B^{(1)}(\theta^1,\theta^2)^{(1)} j d\theta^1 d\theta^2, \tag{5.38}$$

where the determinant of Jacobian represents a ratio between the contact surface area on the parametric space and that on the physical space $j = \frac{da_{\mathbf{x}}}{dA_{\boldsymbol{\theta}}} = \|\mathbf{g}_1 \times \mathbf{g}_2\|$ (see eq. (2.10)) with the description of current covariant base vectors $\mathbf{g}_\beta$ in section 2.1.1. Then, the discrete dual ansatz function of node A for the Lagrange multipliers $\phi_A^{(1)}(\boldsymbol{\theta}^{(1)})$ is given by

$$\phi_A^{(1)}(\boldsymbol{\theta}^{(1)}) = a_{AB} N_B^{(1)}(\boldsymbol{\theta}^{(1)}) \tag{5.39}$$

which a_{AB} must be determined such that the biorthogonality condition in eq. (5.38) is fulfilled. To obtain a_{AB}, eq. (5.39) is substituted in eq. (5.38):

$$n_{AB}^{(1)} = \int\limits_{\gamma_c^{h(1)e}} \phi_A^{(1)}(\boldsymbol{\theta}^{(1)}) N_B^{(1)}(\boldsymbol{\theta}^{(1)}) d\gamma = \int\limits_{-1}^{1}\int\limits_{-1}^{1} \phi_A^{(1)}(\boldsymbol{\theta}^{(1)}) N_B^{(1)}(\boldsymbol{\theta}^{(1)}) j d\theta^1 d\theta^2,$$
$$= \int\limits_{-1}^{1}\int\limits_{-1}^{1} a_{AD} N_D^{(1)}(\boldsymbol{\theta}^{(1)}) N_B^{(1)}(\boldsymbol{\theta}^{(1)}) j d\theta^1 d\theta^2,$$
$$= a_{AD} \underbrace{\int\limits_{-1}^{1}\int\limits_{-1}^{1} N_D^{(1)}(\boldsymbol{\theta}^{(1)}) N_B^{(1)}(\boldsymbol{\theta}^{(1)}) j d\theta^1 d\theta^2}_{M_{DB}} = a_{AD} M_{DB}. \tag{5.40}$$

Noticeably, M_{DB} has a similar structure to that of the element mass matrix (see Zienkiewicz et al. [ZTZ05]). By collecting $n_{AB}^{(1)}, a_{AD}$ and M_{GB} in a matrix form, one obtains

$$\mathbf{D}_e := n_{AB}^{(1)} \in \mathbb{R}^{4\times4}, \quad \mathbf{A}_e := a_{AD} \in \mathbb{R}^{4\times4}, \quad \text{and} \quad \mathbf{M}_e := M_{DB} \in \mathbb{R}^{4\times4}, \tag{5.41}$$

which $\mathbf{D}_e$ is a diagonal matrix. With the help of eq. (5.41), the matrix form of eq. (5.40) is unveiled

$$\mathbf{A}_e \mathbf{M}_e = \mathbf{D}_e \quad \Rightarrow \quad \mathbf{A}_e = \mathbf{D}_e \mathbf{M}_e^{-1}. \tag{5.42}$$

Then, by substituting each component a_{AD} in eq. (5.39), the discrete dual ansatz functions for each node within an element is available[4].

5.3.3 Unilateral contact

As illustrated in Figure 5.9, this subsection demonstrates a comparatively simple contact problem between a deformable body $\Omega^{(1)}$ and a rigid obstacle Ω^{ob} which is the basis for contact problems of two deformable bodies in the next section. For the sake of

[4]The construct of discrete dual ansatz functions is given in the appendix B.3

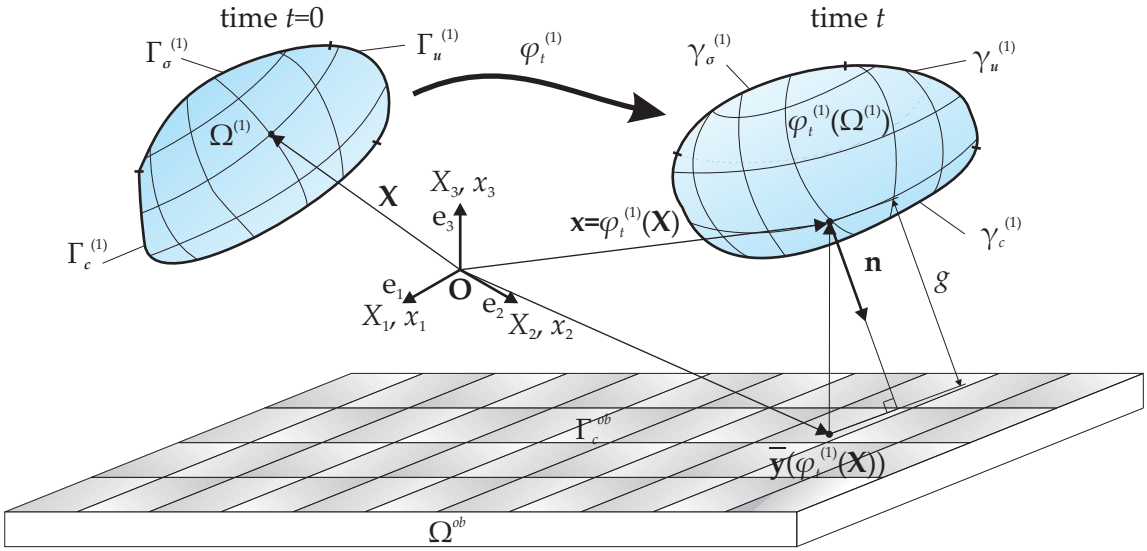

Figure 5.9: Illustration for a unilateral contact problem between a deformable body and a rigid obstacle.

brevity, only the necessary ideas are provided. The interested readers may look further in [Har07, HBRW07, Bru08]. In this case, the slave contact boundary $\gamma_c^{(1)}$ is designated to be the deformable body while the reference obstacle boundary Γ_c^{ob} is considered as the master contact boundary $\Gamma_c^{ob} = \gamma_c^{(2)}$. For each point on the slave contact surface $\varphi_t^{(1)}(\mathbf{X}) \in \gamma_c^{(1)}$, its associated projection point on the master side $\varphi_t^{(2)}(\bar{\mathbf{Y}}) \in \gamma_c^{(2)} \Rightarrow \bar{\mathbf{y}} \in \Gamma_c^{ob}$ with

$$\bar{\mathbf{y}} = \arg\min_{\mathbf{y} \in \Gamma_c^{(ob)}} \left\| \varphi_t^{(1)}(\mathbf{X}) - \mathbf{y} \right\| \tag{5.43}$$

is obtainable with the help of the closest point projection from eq. (5.4). As a result, the scalar-valued gap function from eq. (5.3) is rewritten by

$$g(\mathbf{X}, t) = \mathbf{n} \cdot \left[\varphi_t^{(1)}(\mathbf{X}) - \bar{\mathbf{y}} \right], \tag{5.44}$$

where $\mathbf{n}$ denotes the outward unit normal vector on the slave contact surface $\gamma_c^{(1)}$ at $\mathbf{x} = \varphi_t^{(1)}(\mathbf{X})$ (see Figure 5.9). Since the variation of any point on the rigid obstacle is not concerned $\delta\varphi^{(2)}(\bar{\mathbf{Y}}) = 0$, the contact virtual work from eq. (5.23) is changed to

$$G_c(\varphi_t, \delta\varphi) = \int_{\gamma_c^{(1)}} \lambda_N \mathbf{n} \cdot \delta\varphi^{(1)}(\mathbf{X}) d\gamma. \tag{5.45}$$

Obviously, the contact virtual work must be evaluated from the current configuration which means that the normal contact traction $\boldsymbol{\lambda}_N$ is referred to the physical Cauchy traction $\mathbf{t}$ exerted on the slave contact surface $\gamma_c^{(1)}$ when the body $\Omega^{(1)}$ collides with the obstacle Ω^{ob} as illustrated in Figure 5.10(a). By substituting the variation in displacement field from

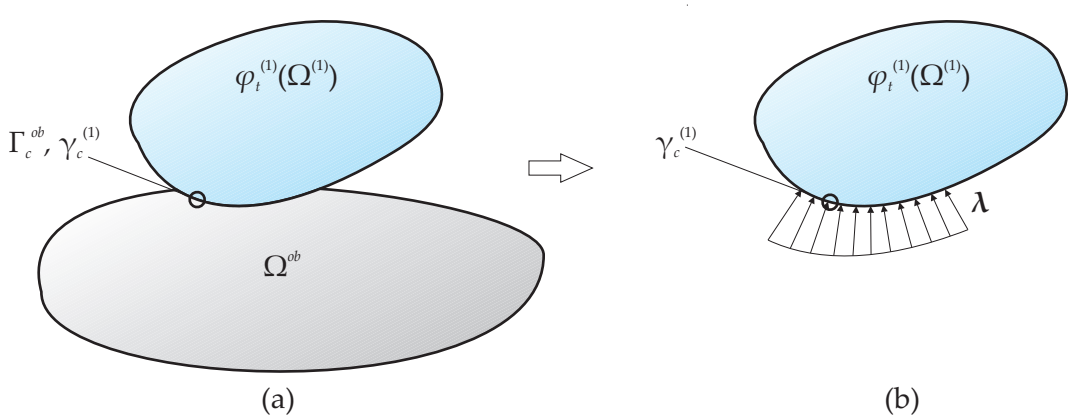

Figure 5.10: Illustration for (a) of a unilateral contact problem between a deformable body and a rigid obstacle and (b) equivalent contact stress distribution.

eq. (5.31) and the Lagrange multiplier field in eq. (5.33) into eq. (5.45), the discrete form of contact virtual work for frictionless contact in eq. (5.34) is changed to

$$G_{cm}(\varphi_t, \delta\varphi) \approx G_{cm}^h = -\sum_{A=1}^{n_c^s}\sum_{B=1}^{n_c^s} \mathbf{z}_A \cdot \left[n_{AB}^{(1)}\mathbf{c}_B^{(1)}\right] = -\sum_{A=1}^{n_c^s}\sum_{B=1}^{n_c^s} \mathbf{c}_B^{(1)} \cdot \left[n_{AB}^{(1)}\mathbf{z}_A\right]. \tag{5.46}$$

The mortar integral n_{AB} with the dual ansatz functions for the Lagrange multipliers is given in eq. (5.37) and eq. (5.38) in the two- and three-dimensional space, respectively. Note that eq. (5.46) is rearranged to facilitate the derivation. With the biorthogonality condition, eq. (5.46) can be expressed in the matrix form, viz.

$$G_{cm}^h = -\mathbf{c}^{(1)^T}\mathbf{D}_S\mathbf{z} = -\mathbf{c}^{(1)^T}\mathbf{f}^c; \quad \mathbf{c}^{(1)} = \bigcup_{B=1}^{n_c^s} \mathbf{c}_B^{(1)}, \ \mathbf{z} = \bigcup_{A=1}^{n_c^s} \mathbf{z}_A, \tag{5.47}$$

where $\mathbf{f}^c$ designates the contact force vector while the diagonal matrix $\mathbf{D}_S$ is defined by a block component for a node B on the slave contact surface $\gamma_c^{h(1)}$ such that

$$\mathbf{D}_S\left[B,B\right] = \int_{\gamma_c^{h(1)}} N_B^{(1)}\left(\boldsymbol{\theta}^{(1)}(\mathbf{X})\right) d\gamma \mathbf{I}_{n_{sd}} = n_{BB}^{(1)}\mathbf{I}_{n_{sd}}; \quad B = 1,\ldots,n_c^s, \quad n_{sd} = \{2,3\}, \tag{5.48}$$

which $\mathbf{I}_{n_{sd}}$ stands for the n_{sd}-diagonal matrix.

5.3.3.1 Semidiscrete equation of motion for unilateral contact

In this part, influences of the unilateral contact mentioned previously will be incorporated into the semi-discrete equation of motion in eq. (2.91):

$$\mathbf{M}\ddot{\mathbf{d}} + \mathbf{f}^{int}(\mathbf{d}) - \mathbf{f}^c = \mathbf{f}^{ext}(t), \tag{5.49}$$

where the n_{dof}-vector $\mathbf{c}$ containing the variation of each corresponding degree of freedom in $\mathbf{d}$ is arbitrary; it can be dropped out from the discrete virtual work. Because contact takes

place only at the slave contact boundary $\Gamma_c^{(1)} \subset \partial\Omega^{(1)}$ (see eq. (5.1)), we define a n_{dof}-vector of contact force $\mathbf{f}^c$ based on the discrete contact virtual work in eq. (5.47) such that

$$\mathbf{f}_B^c = \begin{cases} \mathbf{0} & B \notin S, \\ \mathbf{D}_S\,[B,B]\,\mathbf{z}_B & B \in S, \end{cases} \tag{5.50}$$

which the *slave node set* S stands for all nodes within the slave contact boundary $\gamma_c^{h(1)}$ while other nodes outside this set are designated with the *neutral node set* N. According to this definition, The n_{dof}-vector $\mathbf{d}$ of nodal coordinates–the degree of freedom of the system–is then separated into two groups: $\mathbf{d} = (\mathbf{d}_N, \mathbf{d}_S)^T$. Therefore, the n_{dof}-vector of contact force $\mathbf{f}^c$ is obtained by

$$\mathbf{f}^c = \bigcup_{B=1}^{n_{np}} \mathbf{f}_B^c = \mathbf{B}^c\mathbf{z} \quad \text{with} \quad \mathbf{B}^c = (\mathbf{0}, \mathbf{D}_S)^T \in \mathbb{R}^{n_{sd}\cdot n_{np} \times n_{sd}\cdot n_c^s}, \tag{5.51}$$

while n_{np} denotes the total number of nodes in the system (see section 2.3.1).

5.3.3.2 Effective incremental structural equations for unilateral contact

With the underlying implicit time integration scheme, this section employs the procedure presented in sections 2.3.4.1 and 2.3.4.2 to form the effective incremental structural equation incorporating the contact force vectors. This system of equations will be solved in each iteration by means of the GEMM of section 2.3.4.2. Similar to eq. (2.110), applying the temporal discretization on the semidiscrete equation of motion in eq. (5.49) yields a fully-discrete equation of motion at a generalized midpoint $t_{n+1-\alpha_{f,m}}$ within the interval $t \in [t_n, t_{n+1}]$:

$$\mathbf{M}\ddot{\mathbf{d}}_{n+1-\alpha_m}(\ddot{\mathbf{d}}_{n+1}(\mathbf{d}_{n+1})) + \mathbf{f}^{int}(\mathbf{d}_{n+1-\alpha_f}(\mathbf{d}_{n+1})) - \mathbf{f}^c_{n+1-\alpha_f} = \mathbf{f}^{ext}_{n+1-\alpha_f}, \tag{5.52}$$

where the generalized contact force vector $\mathbf{f}^c_{n+1-\alpha_f}$ is expressed by

$$\mathbf{f}^c_{n+1-\alpha_f} = \mathbf{B}^c\mathbf{z}_{n+1-\alpha_f}. \tag{5.53}$$

Substituting eq. (2.122) along with eq. (2.123) into the modified structural equation of motion in eq. (5.52) leads to the effective structural equation including contact forces:

$$\mathbf{G}(\mathbf{d}_{n+1}) \equiv \frac{1-\alpha_m}{\beta\Delta t^2}\mathbf{M}\mathbf{d}_{n+1} - \mathbf{h}(\mathbf{d}_n, \dot{\mathbf{d}}_n, \ddot{\mathbf{d}}_n) + \mathbf{f}^{int}(\mathbf{d}_{n+1-\alpha_f}(\mathbf{d}_{n+1})) - \mathbf{f}^c_{n+1-\alpha_f} - \mathbf{f}^{ext}_{n+1-\alpha_f} = \mathbf{0}, \tag{5.54}$$

where $\mathbf{h}(\mathbf{d}_n, \dot{\mathbf{d}}_n, \ddot{\mathbf{d}}_n)$ is given in eq. (2.130). In order to determine the nodal coordinate unknowns $\mathbf{d}_{n+1}$, the effective structural equation in (5.52), which is a nonlinear function of $\mathbf{d}_{n+1}$, must be consistently linearized according to the procedure in eq. (2.131). The outcome is the effective incremental structural equation (see eq. (2.132) for a comparison):

$$\mathbf{K}_T^{eff^c}\Delta\mathbf{d}^k_{n+1} = \mathbf{f}^{eff^c}(\mathbf{d}^k_{n+1}). \tag{5.55}$$

In this case, the expression of the effective tangential stiffness matrix for GEMM with contact $\mathbf{K}_T^{eff^c}$ is based on a combination of the effective tangential stiffness matrix for GEMM without contact $\mathbf{K}_T^{eff}$ in eq. (2.148) and influences from contact forces, viz.

$$\mathbf{K}_T^{eff^c}(\mathbf{d}_{n+1}^k) = \frac{\partial \mathbf{G}(\mathbf{d}_{n+1})}{\partial \mathbf{d}_{n+1}}\Big|_{\mathbf{d}_{n+1}^k} = \frac{\partial \mathbf{G}(\mathbf{d}_{n+1}^k)}{\partial \mathbf{d}_{n+1}} = \frac{1-\alpha_m}{\beta \Delta t^2}\mathbf{M} + \underbrace{\mathbf{K}_T^{GEMM}}_{\text{eq. (2.144)}} - \underbrace{\frac{\partial \mathbf{f}_{n+1-\alpha_f}^c}{\partial \mathbf{d}_{n+1}}}_{\approx 0}. \tag{5.56}$$

The partial derivative of the contact force vector $\frac{\partial \mathbf{f}_{n+1-\alpha_f}^c}{\partial \mathbf{d}_{n+1}} = \mathbf{B}^c \frac{\partial \mathbf{z}_{n+1-\alpha_f}}{\partial \mathbf{d}_{n+1}} \approx 0$ is neglected due to an assumption for contact problems with small deformation given in Hartmann [Har07]: The contact tractions are considered as a prescribed external surface traction to maintain the impenetrability constraints at the slave contact boundary $\gamma_c^{h(1)}$. Thus, the nodal Lagrange multipliers $\mathbf{z}$, physically interpreted as the prescribed external nodal forces on the contact boundary, will be determined after both the equilibrium state of deformation on the slave body $\Omega^{(1)}$ and the impenetrability condition on the slave contact surfaces $\gamma_c^{h(1)}$ are satisfied . For this reason, $\mathbf{z}$ is not considered as an independent parameter, and as a result, the linearization is done only with respect to the independent discrete nodal coordinate $\mathbf{d}_t$ for the current time step t. Consequenly, the effective tangential stiffness matrix for GEMM with unilateral contact in eq. (5.56) is similar to that for the case without contact in eq. (2.148). Besides, the effective force vector with contact $\mathbf{f}^{eff^c} = -\mathbf{G}(\mathbf{d}_{n+1}^k)$ is based on eq. (2.149) combined with the contact forces from eq. (5.51) such that

$$\mathbf{f}^{eff^c}(\mathbf{d}_{n+1}^k) = \mathbf{f}_{n+1-\alpha_f}^c + \mathbf{f}_{n+1-\alpha_f}^{ext} - \overbrace{\mathbf{f}^{int}(\mathbf{d}_{n+1-\alpha_f}(\mathbf{d}_{n+1}^k))}^{\text{eq. (2.128)}} - \frac{1-\alpha_m}{\beta \Delta t^2}\mathbf{M}\mathbf{d}_{n+1} + \mathbf{h}(\mathbf{d}_n, \dot{\mathbf{d}}_n, \ddot{\mathbf{d}}_n). \tag{5.57}$$

Furthermore, by moving $\mathbf{f}_{n+1-\alpha_f}^c$ to the left side of the effective incremental structural equation eq. (5.55), one obtains

$$\overbrace{\mathbf{K}_T^{eff}}^{\text{eq. (2.148)}} \Delta \mathbf{d}_{n+1}^k - \mathbf{f}_{n+1-\alpha_f}^c = \overbrace{\mathbf{f}^{eff}(\mathbf{d}_{n+1}^k)}^{\text{eq. (2.149)}}, \tag{5.58}$$

$$\begin{bmatrix} (\mathbf{K}_T^{eff})_{NN} & (\mathbf{K}_T^{eff})_{NS} & \mathbf{0} \\ (\mathbf{K}_T^{eff})_{SN} & (\mathbf{K}_T^{eff})_{SS} & -\mathbf{D}_S \end{bmatrix} \begin{bmatrix} \Delta \mathbf{d}^N \\ \Delta \mathbf{d}^S \\ \mathbf{z}_{n+1-\alpha_f} \end{bmatrix} = \begin{bmatrix} \mathbf{f}_N^{eff} \\ \mathbf{f}_S^{eff} \end{bmatrix} = \begin{bmatrix} -\mathbf{G}_N(\mathbf{d}_{n+1}^k) \\ -\mathbf{G}_S(\mathbf{d}_{n+1}^k) - \mathbf{D}_S \mathbf{z}_{n+1-\alpha_f} \end{bmatrix}. \tag{5.59}$$

When the computation converges to a balance state $\Delta \mathbf{d} \to \mathbf{0}$, the out-of-balance force vector on the neutral node set N in eq. $(5.59)_1$ reaches to the null vector $\mathbf{f}_N^{eff} \to \mathbf{0}$. The out-of-balance force vector $\mathbf{f}_S^{eff}$ on the slave node set S in eq. $(5.59)_2$ consists of the contact force vector $\mathbf{f}_S^c = \mathbf{D}_S \mathbf{z}_{n+1-\alpha_f}$ and the residual forces $-\mathbf{G}_S(\mathbf{d}_{n+1}^k)$ which will achieve the null vector once the state of balance is attained. Hence, it is valid to draw an expression $\mathbf{f}_S^{eff} \to -\mathbf{f}_S^c = -\mathbf{D}_S \mathbf{z}_{n+1-\alpha_f}$ once the computations converge. So far, we have considered only the virtual work from internal, external and contact forces without the contact constraint. For this reason, the impenetrability constraint will be introduced in section 5.5 to form a complete effective incremental structural equation including contact constraints.

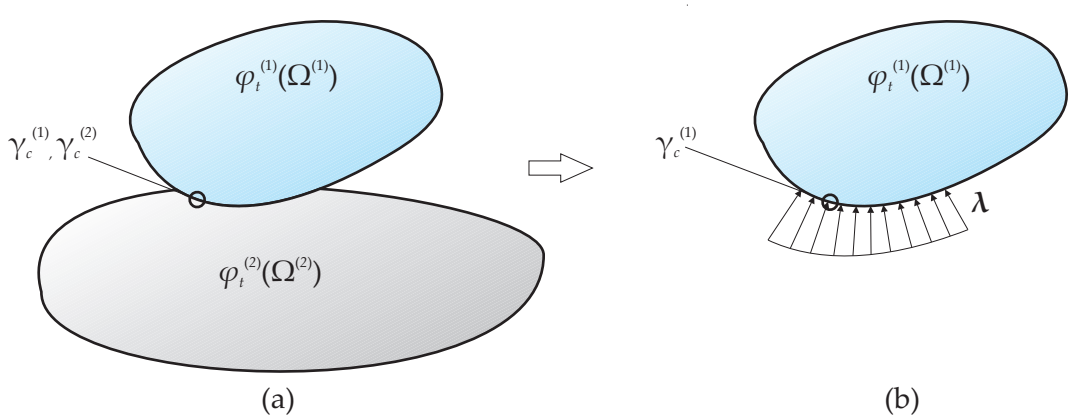

Figure 5.11: Illustration for (a) a contact problem between two deformable bodies and (b) equivalent contact stress distribution.

5.3.4 Multibody contact

Within this section, contact problems of two-deformable bodies are presented. A suitable basis transformation allows the same algebraic structure of the effective structural equation as in the case of unilateral contact in the previous section. In this case, the gap function is defined in eq. (5.3), whereas the contact virtual work, evaluated on the current slave contact boundary $\gamma_c^{(1)}$ in Figure 5.11, is similar to that of eq. (5.23):

$$G_c(\varphi_t, \delta\varphi) = \int_{\gamma_c^{(1)}} \lambda_N \mathbf{n} \cdot \left(\delta\varphi^{(1)}(\mathbf{X}) - \delta\varphi^{(2)}(\bar{\mathbf{Y}}) \right) d\gamma, \tag{5.60}$$

where the Lagrange multiplier for the frictionless case $\boldsymbol{\lambda} = \boldsymbol{\lambda}_N$ can be physically interpreted as the normal contact traction, which acts as an external surface force on the slave contact boundary $\gamma_c^{(1)}$ by the interaction between the slave body $\Omega^{(1)}$ and master body $\Omega^{(2)}$ at the contact interface. Following the procedure described for eq. (5.46) the discrete contact virtual work for frictionless contact problems of two deformable bodies is obtained such that

$$\begin{aligned} G_{cm}(\varphi_t, \delta\varphi) \approx G_{cm}^h &= -\sum_{A=1}^{n_c^s} \sum_{B=1}^{n_c^s} \sum_{C=1}^{n_c^m} \mathbf{z}_A \cdot \left[n_{AB}^{(1)} \mathbf{c}_B^{(1)} - n_{AC}^{(2)} \mathbf{c}_C^{(2)} \right], \\ &= -\left(\sum_{A=1}^{n_c^s} \sum_{B=1}^{n_c^s} \mathbf{c}_B^{(1)} \cdot \left[\underbrace{n_{AB}^{(1)}}_{\mathbf{D}_S[A,B]} \mathbf{z}_A \right] - \sum_{A=1}^{n_c^s} \sum_{C=1}^{n_c^m} \mathbf{c}_C^{(2)} \cdot \left[\underbrace{n_{AC}^{(2)}}_{\mathbf{M}_M[A,C]} \mathbf{z}_A \right] \right). \end{aligned} \tag{5.61}$$

In this equation, n_{AC} is given in eq. (5.36) whereas the mortar integrals n_{AB} is given in eq. (5.37) and eq. (5.38) in 2D and 3D, respectively. With the biorthogonality condition, the first term of eq. (5.61) ends up in the matrix $\mathbf{D}_S$ in eq. (5.48) which links the nodal Lagrange multipliers $\mathbf{z}$ with the nodal contact force vector on the slave side $\mathbf{f}_S^c$ in (5.47). For simplicity,

the matrix form of eq. (5.61) is shown via

$$G_{cm}^{h} = -\left(\mathbf{c}^{(1)^T}\mathbf{D}_S\mathbf{z} - \mathbf{c}^{(2)^T}\mathbf{M}_M^T\mathbf{z}\right) = -\mathbf{c}^T\mathbf{f}^c; \quad \mathbf{c}^{(1)} = \bigcup_{B=1}^{n_c^s}\mathbf{c}_B^{(1)}, \quad \mathbf{c}^{(2)} = \bigcup_{C=1}^{n_c^m}\mathbf{c}_C^{(2)}, \quad \mathbf{z} = \bigcup_{A=1}^{n_c^s}\mathbf{z}_A \tag{5.62}$$

with the contact force vector denoted by $\mathbf{f}^c$. Note that the n_{dof}-vector $\mathbf{c}$ containing the variation of each corresponding dof in $\mathbf{d}$ is arbitrary, and therefore, it can be dropped out from the discrete virtual work. The block diagonal coupling matrix $\mathbf{M}_M$ is defined by a block component for a node A on the slave contact surface $\Gamma_c^{(1)}$ and a node C on the master contact surface $\Gamma_c^{(2)}$ such that

$$\mathbf{M}_M[A,C] = \int_{\gamma_c^{h(1)}} \phi_A^{(1)}\left(\boldsymbol{\theta}^{(1)}(\mathbf{X})\right) N_C^{(2)}\left(\boldsymbol{\theta}^{(2)}(\bar{\mathbf{Y}})\right) d\gamma \mathbf{I}_{n_{sd}} = n_{AC}\mathbf{I}_{n_{sd}}; \quad \begin{cases} A = 1,\ldots,n_c^s, \\ C = 1,\ldots,n_c^m, \\ n_{sd} = \{2,3\}. \end{cases} \tag{5.63}$$

Intuitively, the coupling matrix $\mathbf{M}_M$ relates the nodal Lagrange multipliers $\mathbf{z}$ with the nodal contact force vector on the master side $\mathbf{f}_M^c$. In other words, the block diagonal coupling matrix $\mathbf{M}_M$ behaves like a discrete mortar layer coupling a node on the slave contact boundary $\Gamma_c^{(1)}$ with all nodes on the master contact boundary $\Gamma_c^{(2)}$ (a slave node-to-master nodes). The numerical integration of $\mathbf{M}_M$ is provided in section 5.4.1.4 and 5.4.2.3 whereas finding the inverse of the densely-populated matrix $\mathbf{M}_M$ is non-trivial and time consuming.

5.3.4.1 Semi-discrete equation of motion for contact between two deformable bodies

The semi-discrete equation of motion for contact of two deformable bodies is similar to that of the unilateral contact in eq. (5.49). Based on the discrete contact virtual work in eq. (5.62), the vector of contact force $\mathbf{f}_B^c$ at node B is defined by

$$\mathbf{f}_B^c = \begin{cases} & \mathbf{0} & B \in N\ (B \notin (S \cup M)), \\ - & \mathbf{M}_M[A,B]\,\mathbf{z}_A & B \in M, \\ & \mathbf{D}_S[B,B]\,\mathbf{z}_B & B \in S \end{cases}, \tag{5.64}$$

Obviously, the n_{dof}-vector of contact force $\mathbf{f}^c$ consists of the contact forces on the slave node set $\mathbf{f}_S^c$, master node set $\mathbf{f}_M^c$, and neutral node set $\mathbf{f}_N^c$,respectively. Likewise, the n_{dof}-vector of corresponding nodal coordinate is decomposed into $\mathbf{d} = \left(\mathbf{d}^N, \mathbf{d}^M, \mathbf{d}^S\right)^T$. Thus, $\mathbf{f}^c$ can be described by

$$\mathbf{f}^c = \bigcup_{B=1}^{n_{np}} \mathbf{f}_B^c = \mathbf{B}^c\mathbf{z} \quad \text{with} \quad \mathbf{B}^c = (\mathbf{0}, -\mathbf{M}_M^T, \mathbf{D}_S)^T \in \mathbb{R}^{n_{sd}\cdot n_{np} \times n_{sd}\cdot n_c^s} \tag{5.65}$$

5.3.4.2 Effective incremental structural equation for contact of two deformable bodies

Within this section, the effective incremental structural equation is set up at the generalized mid-point for GEMM in section 2.3.4.2. The fully-discrete equation of motion for contact problems of two deformable bodies at a generalized midpoint $t_{n+1-\alpha_{f,m}}$ within the interval

$t \in [t_n, t_{n+1}]$ is similar to that of the unilateral contact in eq. (5.52). However, differences exist in the generalized contact force vector $\mathbf{f}^c_{n+1-\alpha_f}$:

$$\mathbf{f}^c_{n+1-\alpha_f} = \mathbf{B}^c \mathbf{z}_{n+1-\alpha_f}, \tag{5.66}$$

which $\mathbf{B}^c$ is given in eq. (5.65). Following the procedure in section 5.3.3.2, one can define the effective incremental structural equation via

$$\mathbf{K}_T^{eff^c} \Delta \mathbf{d}^k_{n+1} = \mathbf{f}^{eff^c}(\mathbf{d}^k_{n+1}). \tag{5.67}$$

As described in eq. (5.56), the effective tangential stiffness matrix for GEMM incorporating contact $\mathbf{K}_T^{eff^c}$ consists of the effective tangential stiffness matrix for GEMM without contact $\mathbf{K}_T^{eff}$ in eq. (2.148) and contribution from contact forces. However, in this case, the assumption that the partial derivative of the contact force vector is negligible $\frac{\partial \mathbf{f}^c_{n+1-\alpha_f}}{\partial \mathbf{d}_{n+1}} \rightarrow \mathbf{0}$ must be used with care. Because the evaluation of the coupling matrices $\mathbf{D}_S$ and $\mathbf{M}_M$ is based on the deformed geometry at the contact interface of both bodies, both coupling matrices depend on the deformation of both bodies. As a result, typical mortar-based contact formulations for large deformation, e.g. Puso and Laursen [PL04a, PL04b], Yang *et al* [YLM05, YL07], Fischer and Wriggers [FW05a, FW05b], perform consistent linearization on the contact force vector which implies the linearization of both coupling matrices $\mathbf{D}_S$ and $\mathbf{M}_M$ w.r.t the change in nodal coordinate $\mathbf{d}_t$ for the current time step t to obtain a consistent effective tangential stiffnes matrix.

In general, the purpose of linearization is improving the convergence rate at the contact interface to the level that is close to the rate of convergence when both bodies are modeled as a single domain, even though the complexities are significantly escalated from both the formulation and computation. Within this work, linearization of the coupling matrices $\mathbf{D}_S$ and $\mathbf{M}_M$ are waived due to the same assumption for unilateral contact in section 5.3.3.2: The contact tractions are considered as a prescribed external surface traction to maintain the impenetrability constraints at the slave contact boundary $\gamma_c^{(1)h}$. Thus, the nodal Lagrange multipliers $\mathbf{z}$ will be determined after the equilibrium state of deformation on the slave body $\Omega^{(1)}$ along with the impenetrability condition at the contact interface are fulfiled. For this reason, $\mathbf{z}$ is not considered as an independent parameter and the effective tangential stiffness matrix for GEMM for contact problems of two deformable bodies in eq. (5.56) is similar to the one without contact in eq. (2.148) (compare with the unilateral contact in section 5.3.3.2).

Besides, both coupling matrices are assumed to be unchanged within an iteration step ($t^k_{n+1} \rightarrow t^{k+1}_{n+1}$). Once this assumption is held, $\mathbf{D}_S$ and $\mathbf{M}_M$ are neither unknowns nor deformation dependent. For this reason, linearization over $\mathbf{D}_S$ and $\mathbf{M}_M$ are not required $\frac{\partial \mathbf{f}^c_{n+1-\alpha_f}}{\partial \mathbf{d}_{n+1}} = \frac{\partial \mathbf{B}^c \mathbf{z}_{n+1-\alpha_f}}{\partial \mathbf{d}_{n+1}} \approx 0$. Although, the convergence is inevitably impeded by this simplification, the complexity in computation is significantly decreased in turn. To sum up, these assumptions modify the definition of the coupling matrices which can be evaluated either at the end configuration of the last iteration within the current time step according to Hartmann [Har07]:

$$\mathbf{D}_S := \mathbf{D}_S(\mathbf{d}_{n+1-\alpha_f}(\mathbf{d}^k_{n+1})) \quad \text{and} \quad \mathbf{M}_M := \mathbf{M}_M(\mathbf{d}_{n+1-\alpha_f}(\mathbf{d}^k_{n+1})) \tag{5.68}$$

or at the end configuration of the last timestep t_n^k, i.e. at the beginning of the current time step t_{n+1}^0:

$$\mathbf{D}_S := \mathbf{D}_S(\mathbf{d}_{n+1-\alpha_f}(\mathbf{d}_{n+1}^0)) \quad \text{and} \quad \mathbf{M}_M := \mathbf{M}_M(\mathbf{d}_{n+1-\alpha_f}(\mathbf{d}_{n+1}^0)). \tag{5.69}$$

Within this dissertation, the latter is employed with an acceptable rate of convergence in many cases when compared to the former. The effective force vector with contact $\mathbf{f}^{eff^c} = -\mathbf{G}(\mathbf{d}_{n+1}^k)$ is similar to that of the unilateral contact in eq. (5.57). Moving $\mathbf{f}_{n+1-\alpha_f}^c$ to the left side of the effective incremental structural equation in eq. (5.67) yields

$$\overbrace{\mathbf{K}_T^{eff}}^{(2.148)} \Delta\mathbf{d}_{n+1}^k - \mathbf{f}_{n+1-\alpha_f}^c = \overbrace{\mathbf{f}^{eff}(\mathbf{d}_{n+1}^k)}^{(2.149)}, \tag{5.70}$$

$$\begin{bmatrix} (\mathbf{K}_T^{eff})_{NN} & (\mathbf{K}_T^{eff})_{NM} & (\mathbf{K}_T^{eff})_{NS} & \mathbf{0} \\ (\mathbf{K}_T^{eff})_{MN} & (\mathbf{K}_T^{eff})_{MM} & (\mathbf{K}_T^{eff})_{MS} & \mathbf{M}_M^T \\ (\mathbf{K}_T^{eff})_{SN} & (\mathbf{K}_T^{eff})_{SM} & (\mathbf{K}_T^{eff})_{SS} & -\mathbf{D}_S \end{bmatrix} \begin{bmatrix} \Delta\mathbf{d}^N \\ \Delta\mathbf{d}^M \\ \Delta\mathbf{d}^S \\ \mathbf{z}_{n+1-\alpha_f} \end{bmatrix} = \begin{bmatrix} \mathbf{f}_N^{eff} \\ \mathbf{f}_M^{eff} \\ \mathbf{f}_S^{eff} \end{bmatrix} = \begin{bmatrix} -\mathbf{G}_N(\mathbf{d}_{n+1}^k) \\ -\mathbf{G}_M(\mathbf{d}_{n+1}^k) + \mathbf{M}_M\mathbf{z}_{n+1-\alpha_f} \\ -\mathbf{G}_S(\mathbf{d}_{n+1}^k) - \mathbf{D}_S\mathbf{z}_{n+1-\alpha_f} \end{bmatrix}, \tag{5.71}$$

where the subscript or superscript N, M, S denote the neutral, master and slave node sets, respectively. For regularization purposes, the dual Lagrange multiplier method introduced in Table 5.3 is chosen to enforce contact constraints within this work. The dual basis functions for domain decomposition from Wohlmuth [Woh00] are used for interpolation of the Lagrange multipliers by following Hüeber and Wohlmuth [HW05] who employed this dual basis function for contact problems with small deformation. In that work, a suitable active set strategy is incorporated to predefine the set of active constraints before the formation of the algebraic system of equilibrium equations is done. By doing so, the size of the system matrix is maintained and the chosen dual interpolation functions allow local elimination of the Lagrange multipliers. As a result, there exist only the primal unknowns of the change in nodal position within this context. After the primal unknowns are solved, the Lagrange multipliers are recovered in the postprocessing phase.

5.4 Numerical integration of mortar integrals

While the mortar integral in eq. (5.35) is evaluated over the slave contact boundary $\gamma_c^{(1)h}$, that of eq. (5.36) must be determined over both surfaces $\gamma_c^{(\alpha)h}$. Thus, the mortar integral $n_{AC}^{(2)}$ in eq. (5.36) is determined by subdividing the domain of integration into numerous subdomains, so-called *mortar segments* as mentioned in Yang [Yan06]. The mortar segments are detected at first by global searching and afterwards by finer local searching which is based on the definition of the continuous normal vector field, proposed by Yang [Yan06] for two dimensional problems, on the slave contact boundary $\gamma_c^{(1)h}$. In the case of three dimensional problems, the algorithm to search for mortar segments presented in Puso and Laursen [PL04a] is employed. The following sections explain procedures to create continuous normal field over the slave contact boundary which will be used later for numerical evaluation of the mortar integrals.

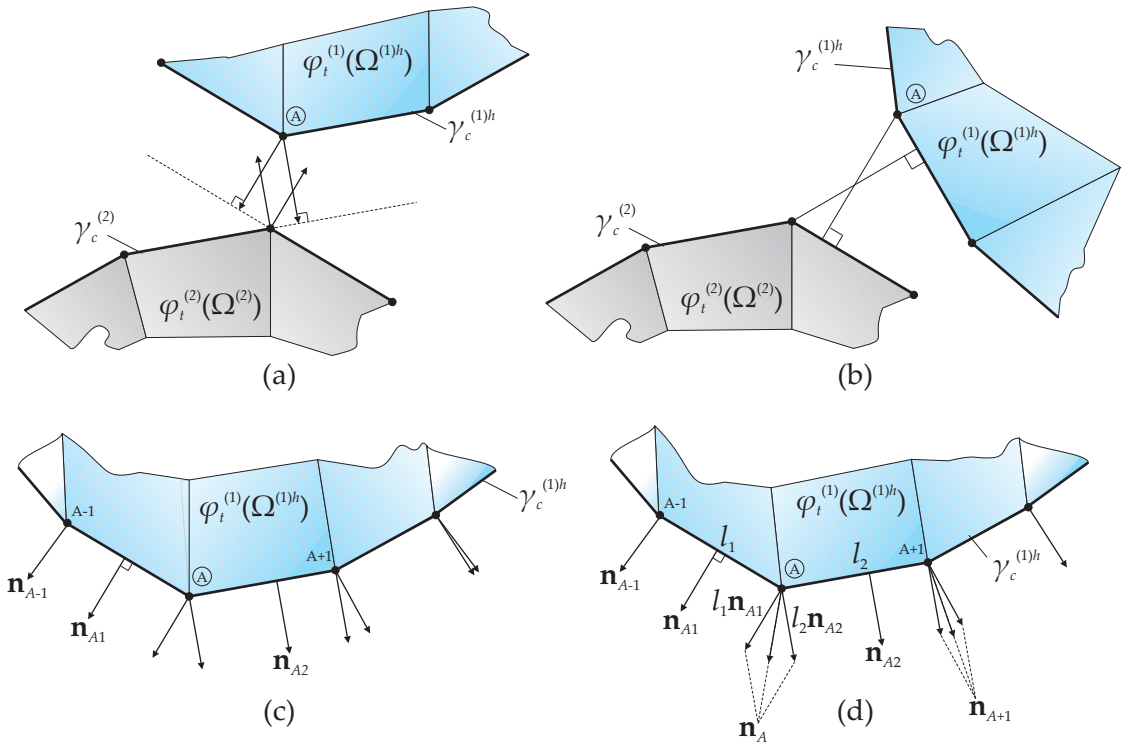

Figure 5.12: Illustration for (a) pathological mortar segment definition type a, (b) pathological mortar segment definition type b, (c) discontinuous 2D normal vector field and (d) continuous 2D normal vector field by design.

5.4.1 Two dimensional problems

5.4.1.1 Continuous normal vector field

Inevitably, discretization introduces a faceted contact geometry, which causes abrupt changes of surface normal as well as tangential vectors at a contact node. This discontinuity in many cases deteriorates the efficiency of the contact algorithm, e.g. nonunique contact pairs lead to undefined domains for mortar integral between the slave and master surfaces (see Figure 5.12). Furthermore, the definitions of nodal mortar gaps in section 5.5.1.4 and 5.5.2.5 require unique definition of normal and tangential vector fields. To obtain the continuous normal vector field, the averaging method by Yang [Yan06] as well as Linhard et al. [LWKU07] is used in this dissertation. The continuous normal field on the slave surface is based on the uniquely defined normal vector at a node $A \in S$ which is obtained by averaging the weighted outward normal vector from two adjacent elements meeting each other at a common node A (see Figure 5.12(d)). Therefore, the average outward normal vector $\mathbf{n}_A$ and tangential vectors at node A can be derived from

$$\mathbf{n}_A = \frac{l_2\mathbf{n}_{A1} + l_1\mathbf{n}_{A2}}{\|l_2\mathbf{n}_{A1} + l_1\mathbf{n}_{A2}\|} \quad \text{and} \quad \boldsymbol{\tau}_A = \mathbf{e}_3 \times \mathbf{n}_A, \tag{5.72}$$

where $\mathbf{n}_{A1}$ and $\mathbf{n}_{A2}$ represent the outward unit normal vectors defined on two elements meeting each other at node A, while The quantities l_1 and l_2 stand for the length of each

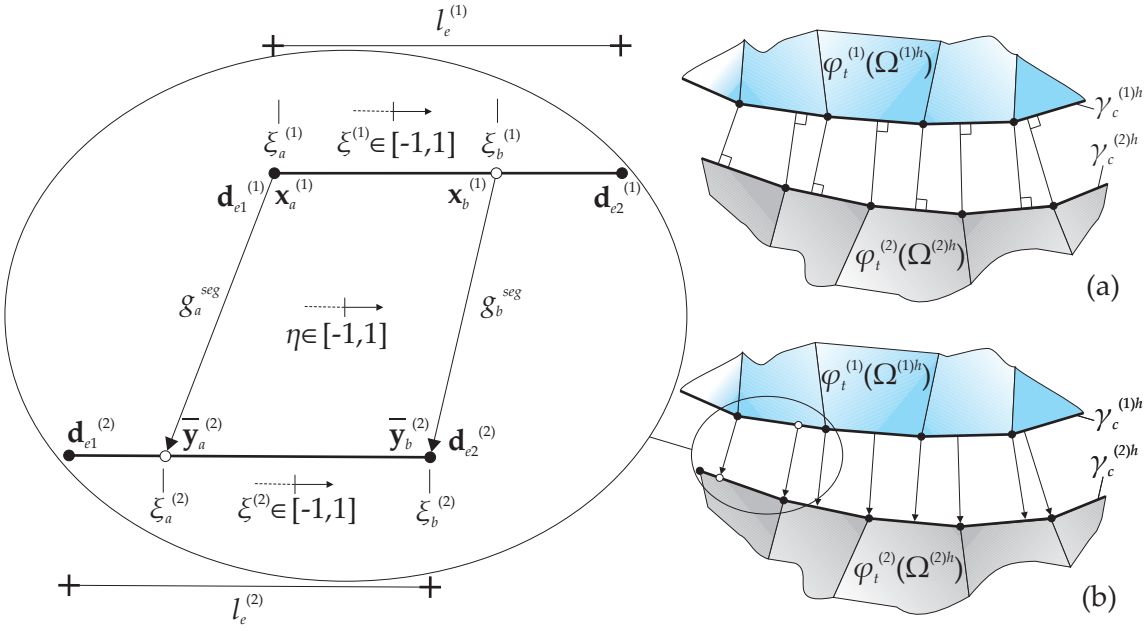

Figure 5.13: Illustration for local searching for mortar segments in 2D with (a) traditional theme based on the closest point projection and (b) continuous normal vector theme.

element, respectively. Furthermore, $\boldsymbol{\tau}_A$ is the tangential vector which is defined based on the unique nodal normal vector $\mathbf{n}_A$ and the out-of-plane (pointing toward the readers) unit vector $\mathbf{e}_3$. Afterwards, the unique nodal normal vector in eq. (5.72) is interpolated by the shape function on the slave contact boundary $\gamma_c^{(1)h}$ corresponding to node A (within this work, the linear shape function) such that

$$\mathbf{n} = \sum_{A=1}^{n_c^s} N_A^{(1)} \left(\boldsymbol{\theta}^{(1)}(\mathbf{X}) \right) \mathbf{n}_A. \tag{5.73}$$

5.4.1.2 Local searching for mortar segments

Illustrated in Figure 5.13(a), the traditional definition of a mortar segment is based on the closest point projection, e.g. McDevitt and Laursen [ML00], which is similar to the method that Papadopoulos and Taylor [PT92] used to construct contact segments. The concept is that the outward unit normal vectors on slave and master contact boundaries are projected onto the opposing surface. There are certain pathological situations which can degrade the robustness: The first problem is shown in Figure 5.12(a) where two adjacent facets meeting at a common node lead to difficulties for projections. In the figure, the projection line of a slave node onto a corner of two adjacent master elements cannot find a unique point of projection within a master element. The second case in Figure 5.12(b) shows an intersection of two projected lines from the node of each contact boundary and one must take into account overlapped mortar segments.

In contrary, this work chooses the mortar segment definition proposed by Yang [Yan06] which is consistent with the previously presented continuous normal field. As shown in Figure 5.13(b), the normal vector field of the slave side is used to accomplish both projections: master to slave and vice versa. The projection from a slave node $\mathbf{d}_A^{(1)}$ onto a master element bounded by two nodes $[\mathbf{d}_1^{(2)}, \mathbf{d}_2^{(2)}]$ is determined via the solution of

$$\left[N_1^{(2)}(\boldsymbol{\theta}^{(2)})\mathbf{d}_1^{(2)} + N_2^{(2)}(\boldsymbol{\theta}^{(2)})\mathbf{d}_2^{(2)} - \mathbf{d}_A^{(1)}\right] \times \mathbf{n}_A^{(1)} = \mathbf{0}, \tag{5.74}$$

where $\boldsymbol{\theta}^{(2)} = \theta^{1^{(2)}}$ denotes the surface coordinate of the master element onto which the the normal vector of the slave node $\mathbf{n}_A^{(1)}$ is projected. The interpolation functions $N_1^{(2)}$ and $N_2^{(2)}$ are related to the first and second nodes of the corresponding master element. Obviously, eq. (5.74) is a linear function of $\theta^{1^{(2)}}$, which can be solved by a linear solution scheme. In contrary, the projection of a master node $\mathbf{d}_C^{(2)}$ onto a slave element bounded by two nodes $[\mathbf{d}_1^{(1)}, \mathbf{d}_2^{(1)}]$ requires the solution of the nonlinear equation

$$\left[N_1^{(1)}(\boldsymbol{\theta}^{(1)})\mathbf{d}_1^{(1)} + N_2^{(1)}(\boldsymbol{\theta}^{(1)})\mathbf{d}_2^{(1)} - \mathbf{d}_C^{(2)}\right] \times \left[N_1^{(1)}(\boldsymbol{\theta}^{(1)})\mathbf{n}_1^{(1)} + N_2^{(1)}(\boldsymbol{\theta}^{(1)})\mathbf{n}_2^{(1)}\right] = \mathbf{0}, \tag{5.75}$$

where $\boldsymbol{\theta}^{(1)} = \theta^{1^{(1)}}$ stands for the surface coordinate of the slave element at which the the projection from the master node $\mathbf{d}_C^{(2)}$ is pointing. The interpolation functions $N_1^{(1)}$ and $N_2^{(1)}$ and the outward unit normal vector $\mathbf{n}_1^{(1)}$ and $\mathbf{n}_2^{(1)}$ are associated to the first and second nodes of the corresponding slave element, respectively. Furthermore, eq. (5.75) is a quadratic function of $\theta^{1^{(1)}}$, which requires iterative solution algorithm, e.g. the Newton Raphson method. After the projection points on the slave and master contact boundaries are determined from eqs. (5.74) and (5.75), numerical evaluation of mortar integrals on corresponding mortar segments can be performed.

5.4.1.3 Evaluation of the diagonal matrix $\mathbf{D}_S$

To construct the diagonal matrix $\mathbf{D}_S$ in eq. (5.48), the mortar integral for a node on the slave contact boundary $B \in S$ must be created via the determination of $n_{BB}^{(1)}$ which will later be approximated by numerical integration with the gauss integration rule (see [Cow73] for instance):

$$n_{BB}^{(1)} = \int_{\gamma_c^{(1)h}} N_B^{(1)}\left(\boldsymbol{\theta}^{(1)}(\mathbf{X})\right) d\gamma \approx \sum_{e=1}^{n_{el}^B} \left[\sum_{g=1}^{n_g} w_g N_B^{(1)}(\boldsymbol{\theta}_g^{(1)}) j_e(\boldsymbol{\theta}_g^{(1)})\right]^{(e)}. \tag{5.76}$$

This formula is valid for both two and three dimensional cases. n_g and w_g stand for the number of integration points within an element and the weight factor for the corresponding integration point, respectively, while $j_e = det(\mathbf{j}_e)$ is the determinant of the mapping of an element from the parametric space to the physical space, which is described in Figure 2.4 of section 2.3.1.1. Note that all quantities are evaluated at the position of each integration point $\boldsymbol{\theta}_g^{(1)}$ and n_{el}^B is the number of all elements sharing a common node on the slave contact boundary $B \in S$, e.g. for a 2D problem with linear elements $n_{el}^B = 2$, while for a 3D problem

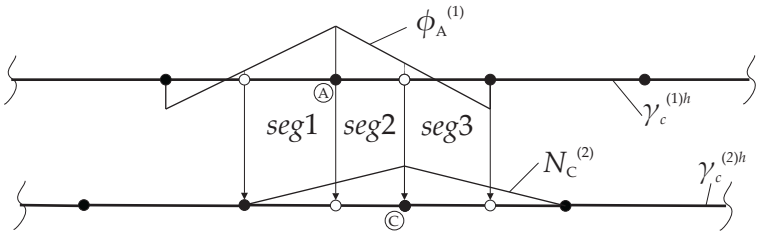

Figure 5.14: Schematic description for 2D mortar segments summation.

with bilinear elements $n_{el}^B = 4$. In case that the slave contact boundary is constructed by 2D linear elements (see Figure 5.14) having the constant determinant of element mapping j_e, Cichosz [Cic06] shows an explicit formula of $n_{BB}^{(1)}$:

$$n_{BB}^{(1)} = \frac{1}{2}\sum_{e=1}^{n_{el}^B} l_B^{(e)} \tag{5.77}$$

with $l_B^{(e)}$ being the length of an element (e) connected to a common node B.

5.4.1.4 Evaluation of the coupling matrices $\mathbf{M}_M$

To construct the coupling matrix $\mathbf{M}_M$ in eq. (5.63), the contribution $n_{AC}^{(2)}$ from nodes A and C in eq. (5.36) must be evaluated by subdividing all relevant elements into mortar segments as illustrated in Figure 5.14. The integration is then computed by summing up contributions from all segments on the entire slave contact boundar $\gamma_c^{(1)h}$:

$$n_{AC}^{(2)} = \sum^{seg} n_{AC}^{(2)^{seg}} \quad \text{with} \quad n_{AC}^{(2)^{seg}} = \int_{\gamma_c^{seg}} \phi_A^{(1)}\left(\boldsymbol{\theta}^{(1)}(\mathbf{X})\right) N_C^{(2)}\left(\boldsymbol{\theta}^{(2)}(\bar{\mathbf{Y}})\right) d\gamma, \tag{5.78}$$

where seg is the mortar segment, while γ_c^{seg} represents the contact (integration) boundary for each segment . The numerical integration of $n_{AC}^{(2)}$ requires parameterization $\eta \in [-1, 1]$ for each mortar segment. Displayed in Figure 5.13(b), four ends, two on slave side and two on master side, of a mortar segment are defined by $\theta_a^{1(1)} = \xi_a^{(1)}, \theta_b^{1(1)} = \xi_b^{(1)}, \theta_a^{1(2)} = \xi_a^{(2)}, \theta_b^{1(2)} = \xi_b^{(2)}$ where subscript a and b are referred to the start and end points of a mortar segment, respectively. Mapping of a typical mortar segment in Figure 5.13(b) between a parameter on the mortar segment η to those of slave and master contact boundaries $\xi^{(\alpha)}$ is then defined by

$$\xi^{(\alpha)} = \frac{1}{2}(1-\eta)\xi_a^{(\alpha)} + \frac{1}{2}(1+\eta)\xi_b^{(\alpha)}. \tag{5.79}$$

For this reason, the coupling mortar integral for node A and C in eq. (5.78) can be performed over η and then numerically approximated by the gauss integration rule such that

$$\begin{aligned} n_{AC}^{(2)^{seg}} &= \int_{-1}^{1} \phi_A^{(1)} \left(\xi^{(1)}(\eta)\right) N_C^{(2)} \left(\xi^{(2)}(\eta)\right) j_{seg} d\eta, \\ &\approx \sum_{g=1}^{n_g} w_g \phi_A^{(1)} \left(\xi^{(1)}(\eta_g)\right) N_C^{(2)} \left(\xi^{(2)}(\eta_g)\right) j_{seg}(\eta_g) \end{aligned} \tag{5.80}$$

with η_g being the position of an integration point in the parametric space η of a mortar segment. j_{seg}, evaluated at each integration point η_g, is the determinant of the mapping from the parametric space of a mortar segment η onto the physical space of the corresponding slave contact element $\mathbf{x}_e^{(1)^h} = \varphi_t^{(1)^h}(\mathbf{X}_e)$ to which the integration boundary γ_c^{seg} of a mortar segment belongs (see Figure 5.13(b)) such that

$$j_{seg} = \left\| \frac{\partial \varphi_t^{(1)^h}(\mathbf{X}_e)}{\partial \eta} \right\| = \left\| \frac{\partial \mathbf{x}_e^{(1)^h}}{\partial \xi^{(1)}} \right\| \frac{\partial \xi^{(1)}}{\partial \eta} \quad \text{with} \quad \varphi_t^{(1)^h}(\mathbf{X}_e) = N_1^{(1)} \mathbf{d}_{e1}^{(1)} + N_2^{(1)} \mathbf{d}_{e2}^{(1)}. \tag{5.81}$$

Note that subscript e denotes the corresponding slave contact element of the mortar segment. In particular, an explicit form of j_{seg} for a 2D linear contact element is given by

$$j_{seg} = \frac{1}{2} l_e^{(1)} \frac{1}{2} (\xi_b^{(1)} - \xi_a^{(1)}) \tag{5.82}$$

with $l_e^{(1)}$ being the length of corresponding slave contact element of the mortar segment of interest.

5.4.2 Three dimensional problems

For three dimensional problems, numerical evaluation of mortar integrals can be similarly accomplished. The mortar segments in this case are defined over two contact surfaces: slave and master. Therefore, more efforts are involved to evaluated the coupling matrix $\mathbf{M}_M$ whereas the the diagonal matrix $\mathbf{D}_S$ can be determined by eq. (5.76) on the basis of relevant elements on the slave contact boundary $\gamma_c^{(1)h}$. This section provides an overview of the procedure proposed by Puso and Laursen [PL04a] to determine the coupling mortar integral of two deformable bodies in the three dimensional space.

5.4.2.1 Continuous normal vector field

For three dimensional problems, discretization leads to faceted contact surfaces. As a result, the normal and tangential vectors are not uniquely defined, and therefore, continuous normal and tangential vector fields play a key role for a robust contact formulation. At a slave node A, an averaged normal vector $\mathbf{n}_A$ can be expressed by

$$\mathbf{n}_A = \frac{\sum_{i=1}^{n_{el}^A} w_{A_i} \mathbf{n}_{A_i}}{\left\| \sum_{i=1}^{n_{el}^A} w_{A_i} \mathbf{n}_{A_i} \right\|} \quad \text{with} \quad w_{A_i} = \frac{1}{a_{A_i}} = \frac{1}{\left\| \mathbf{g}_{1_{A_i}} \times \mathbf{g}_{2_{A_i}} \right\|}, \tag{5.83}$$

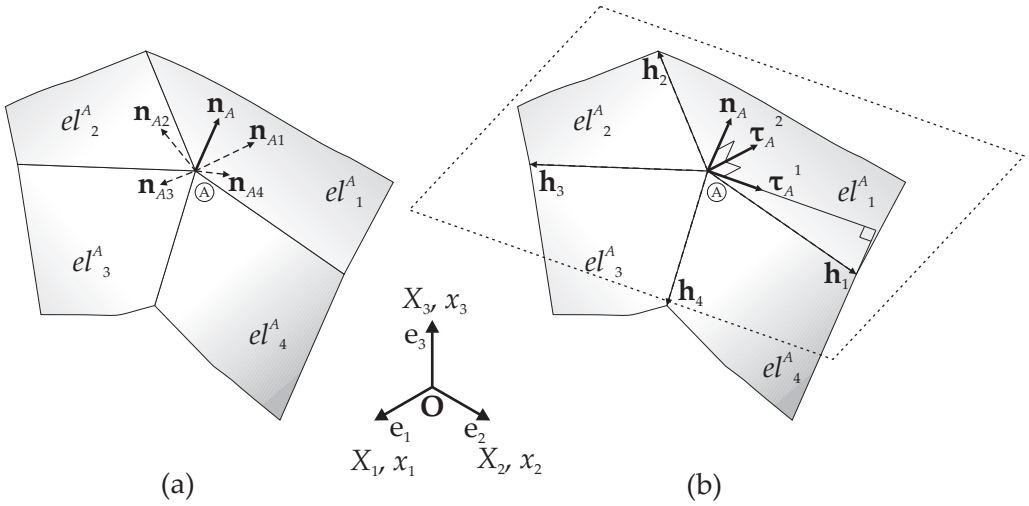

Figure 5.15: Illustration for (a) average unit normal vector $\mathbf{n}_A$ (b) unit tangential vectors $\boldsymbol{\tau}_A^\alpha$ by design at node A in the 3D space.

where $n_{el}^{(A)}$ is the number of elements meeting at a common node A, while $\mathbf{n}_{A_i}$ denotes the unit normal vector defined on the corresponding element i sharing a common node A (see Figure 5.15). The weighting factors w_{A_i} for element i sharing the common node A is chosen inversely proportional to the representative element size a_{A_i}, which is approximated by the area of the parallelogram spanned by the element base vectors at node A (for more details, see [LWKU07]). The edge vector $\mathbf{h}_i,\ i = 1, \ldots, n_{edge}$, points from node A to other neighboring nodes with n_{edge} is the number of edges meeting at node A. An arbitrary edge vector $\mathbf{e}_1$ is projected onto the plane passing node A and being orthogonal to the unit normal vector $\mathbf{n}_A$ of that node. For this reason, the tangential vector $\boldsymbol{\tau}_A^1$ at node A can be defined by

$$\boldsymbol{\tau}_A^1 = \frac{\hat{\boldsymbol{\tau}}_A^1}{\left\|\hat{\boldsymbol{\tau}}_A^1\right\|} \quad \text{with} \quad \hat{\boldsymbol{\tau}}_A^1 = \mathbf{h}_1 \cdot (\mathbf{I} - \mathbf{n}_A \otimes \mathbf{n}_A) \tag{5.84}$$

whereas another tangential vector $\boldsymbol{\tau}_A^2$ is defined by

$$\boldsymbol{\tau}_A^2 = \mathbf{n}_A \times \boldsymbol{\tau}_A^1 \quad \text{with} \quad \left\|\boldsymbol{\tau}_A^\beta\right\| = \|\mathbf{n}_A\| = 1 \quad \rightarrow \quad \boldsymbol{\tau}_A^\alpha = \boldsymbol{\tau}_{A\alpha}. \tag{5.85}$$

The result in eq. (5.85) reflects an orthonormal basis which leads to invariant covariant and contravarinat basis.

5.4.2.2 Local searching for mortar segments

Within this work, the algorithm presented by Puso and Laursen [PL04a] is adopted for local searching of mortar segments in the three dimensional space. At first, the global searching algorithm is performed to gain information about possible contact pairs and mortar segments. Figure 5.16 shows a typical mortar segment created by overlapping regions between a slave element k and a master element l. To integrate $n_{AC}^{(2)}$ in eq. (5.36), overlapping areas of the ansatz function $\phi_A^{(1)}$ defined over the slave element k and the shape function $N_C^{(2)}$

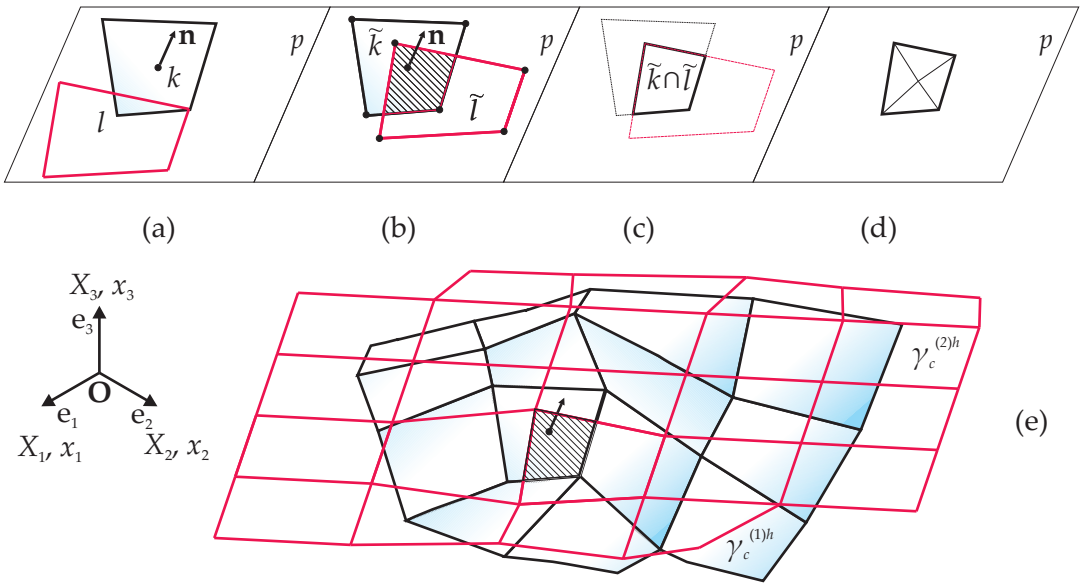

Figure 5.16: Illustration for searching procedure of mortar segments in 3D problem (a) slave element k, master element l, and plane p generated from the normal vector $\mathbf{n}$ at center of k (b) facet $\tilde{k}$ and $\tilde{l}$ constructed by projection of elements k and l onto the plane p (c) find intersection polygon of facet $\tilde{k}$ and $\tilde{l}$ ($\tilde{k} \cap \tilde{l}$) by clipping technique (d) subdivide the polygon into n_{pal} triangular pallets by radiated lines from the center towards each corner of the polygon and (e) the whole contact interfaces.

defined over the master element l must be figured out. By doing so, the quadrilateral element k is approximated by a flat quadrilateral $\tilde{k}$ generated by the normal vector at the center of element k. This flat surface $\tilde{k}$ assumes the integration surface $\gamma \approx \gamma_c^{(1)h}$ in eq. (5.36). The geometry of a slave element is approximate via $\mathbf{x}^{(1)h} = \sum_{B \in \mathcal{L}(k)} N_B^{(1)}(\boldsymbol{\theta}^{(1)}(\mathbf{X}))\mathbf{x}_B^{(1)}$ with $\mathcal{L}(k)$ being the local node set of element k. For master element l, the local node set $\mathcal{L}(l)$ defines the geometry of element l by $\mathbf{x}^{(2)h} = \sum_{C \in \mathcal{L}(l)} N_C^{(2)}(\boldsymbol{\theta}^{(2)}(\mathbf{Y}))\mathbf{x}_C^{(2)}$. Figure 5.16 illustrates the mortar segment searching algorithm for 3D problems which can be explained as follows:

- ◇ For a slave element k, a flat plane p is created as a plane that is passing through the geometric center $\mathbf{x}_c = \sum_{B \in \mathcal{L}(k)} N_B^{(1)}(\boldsymbol{\theta}^{(1)}(\mathbf{X}) = \mathbf{0})\mathbf{x}_B^{(1)}$ of element k and orthogonal to the normal vector $\mathbf{n}$ at the center $\mathbf{x}_c$ of that element (see Figure. 5.16(a)).
- ◇ Compute points $\tilde{\mathbf{x}}_A^{(1)}$ by projecting nodes $\mathbf{x}_A^{(1)}$ of element k onto the plane p (see Figure 5.16(b)). Then, the projected facet $\tilde{k}$ on the plane p is approximated via

$$\tilde{\mathbf{x}}^{(1)h} = \sum_{B \in \mathcal{L}(k)} N_A^{(1)}(\boldsymbol{\theta}^{(1)}(\mathbf{X}))\tilde{\mathbf{x}}_A^{(1)}; \quad \text{with} \quad \tilde{\mathbf{x}}_A^{(\alpha)} = \mathbf{x}_A^{(\alpha)} - \left[\mathbf{x}_A^{(\alpha)} - \mathbf{x}_c\right] \cdot \mathbf{n} \otimes \mathbf{n}. \tag{5.86}$$

- ◇ For a master element l that is close enough to the slave element k, projected points $\tilde{\mathbf{x}}_C^{(2)}$ are computed by projecting nodes $\mathbf{x}_C^{(2)}$ of element l onto the plane p (see Figure 5.16(b)). Then, the projected facet $\tilde{l}$ on the plane p is approximated via

$$\tilde{\mathbf{x}}^{(2)h} = \sum_{C \in \mathcal{L}(l)} N_C^{(2)}(\boldsymbol{\theta}^{(2)}(\mathbf{Y}))\tilde{\mathbf{x}}_C^{(2)}. \tag{5.87}$$

Initialize: set initial slave element number $(k = 1)$

Loop over all slave elements $(k \in \gamma_c^{(1)h})$

- Create flat plane p by the normal vector $\mathbf{n}$ at the center $\mathbf{x}_c$ of slave element k
- Compute points $\tilde{\mathbf{x}}_A^{(1)}$ by projecting nodes $\mathbf{x}_A^{(1)}$ of element k onto the plane p
  then create facet $\tilde{k}$ by $\tilde{\mathbf{x}}^{(1)h} = \sum_{B\in\mathcal{L}(k)} N_A^{(1)}(\boldsymbol{\theta}^{(1)}(\mathbf{X}))\tilde{\mathbf{x}}_A^{(1)}$ eq. (5.86)
- Initialize: set initial master element number $(l = 1)$
- Loop over all master elements $(l \in \gamma_c^{(2)h})$
  - (1) Perform rough searching to check whether element l close to element k (Fig. 5.16(a))
  - IF l is far from k GOTO (I)
  - (2) Compute points $\tilde{\mathbf{x}}_C^{(2)}$ by projecting nodes $\mathbf{x}_C^{(2)}$ of element l onto the plane p
    then create facet $\tilde{l}$ by $\tilde{\mathbf{x}}^{(2)h} = \sum_{C\in\mathcal{L}(l)} N_C^{(2)}(\boldsymbol{\theta}^{(2)}(\mathbf{Y}))\tilde{\mathbf{x}}_C^{(2)}$ eq. (5.87)
  - (3) Find intersection polygon $(\tilde{k}\cap\tilde{l})$, assuming integration surface γ,
    by the clipping technique [FvDF97]
  - (4) Find center of polygon and subdivide it into n_{pa} triangular pallets
    a triangle pallet pa is parametized by $\mathbf{x}_{pa}^h = \sum_{i=1}^3 N_i(\boldsymbol{\xi})\mathbf{x}_{i,pa}$ eq. (5.88)
  - (5) Locate n_g gauss points $\boldsymbol{\xi}_g$ within each triangular pallet (Fig. 5.16(d))
  - (6) To find $\boldsymbol{\theta}_g^{(1)}$ and $\boldsymbol{\theta}_g^{(2)}$ from $\mathbf{x}_{pa}(\boldsymbol{\xi}_g)\in\gamma$, perform inverse mapping
    by equating eqs. (5.86), (5.87) and (5.88): $\mathbf{x}_{pa}(\boldsymbol{\xi}_g) = \tilde{\mathbf{x}}^{(\alpha)}(\boldsymbol{\theta}_g^{(\alpha)})$ eq. (5.89)
  - (7) Find coupling mortar integrals of a pallet pa : $n_{AC(k,l)}^{(2)^{pa}}$; $\forall A\in\mathcal{L}(k)$ and $\forall C\in\mathcal{L}(l)$
    $n_{AC(k,l)}^{(2)^{pa}} \approx A^{pa}\sum_{g=1}^{n_g} w_g\phi_A^{(1)}\left(\xi^{(1)}(\boldsymbol{\theta}_g^{(1)})\right) N_C^{(2)}\left(\xi^{(2)}(\boldsymbol{\theta}_g^{(2)})\right)$ eq. (5.91)
  - (8) Add contributions from all pallets of a mortar segment (polygon) to $n_{AC}^{(2)}$
    $n_{AC}^{(2)} = n_{AC}^{(2)} + \sum_{pa=1}^{n_{pa}} n_{AC(k,l)}^{(2)^{pa}}$ eq. (5.92)
  - $\Leftarrow$ Set up $l = l+1$ (I)
- $\Leftarrow$ Set up $k = k+1$ (II)

Figure 5.17: Algorithm for local searching and mortar integral evaluation for 3D mortar segments.

- Determine the intersection polygon of the element k and l $(\tilde{k}\cap\tilde{l})$ which assumes the integration surface γ by the clipping method [FvDF97] (see Figure 5.16(c)). Then, locate the geometric center of the intersection polygon and subdivide the polygon into n_{pa} triangular pallets by radiated lines from the center of polygon to all corners (see Figure 5.16(d)). Each triangular pallet is parametized by

$$\mathbf{x}_{pa}^h = \sum_{i=1}^{3} N_i(\boldsymbol{\xi})\mathbf{x}_{i,pa} \tag{5.88}$$

with vertices $\mathbf{x}_{i,pa}(i = 1,3)$ and triangular shape function $N_i(\boldsymbol{\xi})$; $\boldsymbol{\xi} = (\xi^1,\xi^2)$, where

$N_1 = \xi_1$, $N_2 = \xi_2$ and $N_3 = 1 - \xi_1 - \xi_2$.

- ◇ Use Gauss-Radau rules [Cow73] to locate n_g gauss points $\boldsymbol{\xi}_g$ and integration weight w_g within each triangular pallet (see Figure 5.16(d)).

- ◇ To find $\boldsymbol{\theta}_g^{(1)}$ and $\boldsymbol{\theta}_g^{(2)}$ from $\mathbf{x}_{pa}(\boldsymbol{\xi}_g) \in \gamma$, the inverse mapping is performed by equating eqs. (5.86), (5.87) and (5.88) such that

$$\mathbf{x}_{pa}(\boldsymbol{\xi}_g) = \tilde{\mathbf{x}}^{(\alpha)}(\boldsymbol{\theta}_g^{(\alpha)}) \text{ , e.g. } \sum_{i=1}^{3} N_i(\boldsymbol{\xi}_g)\mathbf{x}_{i,pa} = \sum_{C=1}^{4} N_C^{(2)}(\boldsymbol{\theta}_g^{(2)})\tilde{\mathbf{x}}_C^{(2)} = \sum_{B=1}^{4} N_A^{(1)}(\boldsymbol{\theta}_g^{(1)})\tilde{\mathbf{x}}_A^{(1)}. \tag{5.89}$$

To sum up, the searching algorithm for mortar segment is summarized in Figure 5.17. A restriction for this algorithm is that the intersection polygon must be convex which results in having the geometric center within the polygon. This simplifies the numerical integration as well as the inverse mapping from the physical space of the projected plane onto the parametric space of both slave and master elements $\gamma \rightarrow \boldsymbol{\theta}^{(\alpha)}$ of the polygon. The convex polygon occurs in the following cases: (i) The slave element k is convex and not overly warped. (ii) Two element k and l are close enough to each other. (iii) The projected element $\tilde{l}$ will be convex if the normals for slave element k and master element l are relatively close.

5.4.2.3 Evaluation of the coupling matrices $\mathbf{M}_M$

Once all triangular pallets are available, the numerical integrations for mortar integrals on each pallet can be performed and then the result for each pallet is added to create the entire mortar integrals, viz.

$$n_{AC}^{(2)} = \sum^{seg} n_{AC}^{(2)^{seg}};\ n_{AC}^{(2)^{seg}} = \sum_{pa=1}^{n_{pa}} n_{AC}^{(2)^{pa}};\ n_{AC}^{(2)^{pa}} = \int_{\gamma_c^{pa}} \phi_A^{(1)}\left(\boldsymbol{\theta}^{(1)}(\mathbf{X})\right) N_C^{(2)}\left(\boldsymbol{\theta}^{(2)}(\bar{\mathbf{Y}})\right) d\gamma, \tag{5.90}$$

where γ_c^{pa} is the surface area of a triangular pallet pa. This section provides a numerical algorithm, which is a subsequent procedure of the mortar segments searching algorithm from previous section, to determine the coupling mortar integral $n_{AC}^{(2)}$ in eq. (5.36) for two deformable bodies in the three dimensional space as in the following:

- ◇ For a slave element k and a master element l, the coupling mortar integrals $n_{AC(k,l)}^{(2)^{pa}}$ of a pallet pa is computed via

$$n_{AC(k,l)}^{(2)^{pa}} \approx A^{pa} \sum_{g=1}^{n_g} w_g \phi_A^{(1)}\left(\boldsymbol{\theta}^{(1)}(\boldsymbol{\xi}_g)\right) N_C^{(2)}\left(\boldsymbol{\theta}^{(2)}(\boldsymbol{\xi}_g)\right) \ \forall A \in \mathcal{L}(k) \text{ and } \forall C \in \mathcal{L}(l) \tag{5.91}$$

with A^{pa} being the pallet area and n_g is the number of the gaussian quadrature points. $\boldsymbol{\theta}_g^{(1)}$ and $\boldsymbol{\theta}_g^{(2)}$ are the surface coordinates of the quadrature points g on the projected elements $\tilde{k}$ and $\tilde{l}$ while w_g are the integration weights. For a linear triangular pallet, the coupling mortar integral $n_{AC(k,l)}^{(2)^{pa}}$ in eq. (5.91) is a quadratic function in $\mathbf{x}$. Thus, at least

a three-point triangular integration rule [Cow73] is needed for exact integration within the pallet. Usually, 7 or 13 point integration rule is enough according to suggestions in Puso and Laursen [PL04a].

◇ Add contributions from all pallets of a mortar segment (polygon) to $n_{AC}^{(2)}$:

$$n_{AC}^{(2)} = n_{AC}^{(2)} + \sum_{pa=1}^{n_{pa}} n_{AC(k,l)}^{(2)^{pa}}. \tag{5.92}$$

For summary, the procedure to evaluate the coupling mortar integral $n_{AC}^{(2)}$ is given in Figure 5.17 (7)-(8).

5.5 Active set strategy for contact boundary conditions

In the former section, the contact virtual work is introduced without a consideration of impenetrability constraints at the contact interface. This section will complement the formulation for mortar-based contact constraints which then will be added to the effective structural equation in the previous section with the aim to fulfill compatibility conditions at the contact interface in an integral manner. To achieve the goal, the dual Lagrange multiplier method is employed for contact constraints enforcement. Additionally, the active set strategy is used to define the set of active contact nodes before the system matrices are formed. By doing so, the size of the effective incremental structural equation is constant during computation within each time step. This section introduces the active set strategy for both the unilateral contact and contact problems of two deformable bodies.

5.5.1 Normal contact of a deformable body and a rigid obstacle

As an extension of the weak form for IBVP with contact in section 5.1.4, the variational form of the impenetrability condition on the contact interface between a deformable body and a rigid obstacle must be augmented to the virtual work equation in eq. (5.19) with the help of the active set strategy in section 5.5.1.2.

5.5.1.1 Weak impenetrability condition for unilateral contact

Based on the mortar method, the impenetrability constraint is formulated in an integral manner over the geometric contact boundary $\gamma_c^{(1)}$ of the deformable body $\Omega^{(1)}$. In case of the frictionless contact, there exists only the normal component of the Lagrange multiplier appearing in the weak form of the impenetrability condition as mentioned in eq. (5.24), viz.

$$\int_{\gamma_c^{(1)}} \delta\lambda_N(\mathbf{X}) g(\mathbf{X}, t) d\gamma \leq 0 \tag{5.93}$$

with the gap function g as given in eq. (5.44). According to eq. (5.33), variation of the scalar-valued normal Lagrange multiplier fields $\delta\lambda_N(\mathbf{X})$ on the contact surface $\gamma_c^{(1)}$ can be interpolated by

$$\delta\lambda_N(\mathbf{X}) \approx \delta\lambda_N^h(\mathbf{X}) = \sum_{A=1}^{n_c^s} \phi_A^{(1)}\left(\boldsymbol{\theta}^{(1)}(\mathbf{X})\right) \delta\lambda_{A_N}, \tag{5.94}$$

where $\delta\lambda_{A_N}$ stands for the variation of the scalar-valued nodal normal Lagrange multiplier for node A. With the help of the interpolation function in eq. (5.29), substitution of eqs. (5.94) and (5.44) into the weak impenetrability condition in eq. (5.93) yields a discrete weak impenetrability condition for any $\delta\lambda_N(\mathbf{X}) \geq 0$:

$$\begin{aligned}
\int_{\gamma_c^{(1)}} \delta\lambda_N g d\gamma &\approx \int_{\gamma_c^{(1)}} \delta\lambda_N^h(\mathbf{X}) g^h(\mathbf{X},t) d\gamma \leq 0 \\
&\approx \int_{\gamma_c^{(1)}} \sum_{A=1}^{n_c^s} \phi_A^{(1)}\left(\boldsymbol{\theta}^{(1)}(\mathbf{X})\right) \delta\lambda_{A_N} \mathbf{n} \cdot \left[\sum_{D=1}^{n_c^s} N_D^{(1)}\left(\boldsymbol{\theta}^{(1)}(\mathbf{X})\right) \mathbf{d}_D^{(1)}(t) - \bar{\mathbf{y}}^h\right] d\gamma \\
&\approx \sum_{A=1}^{n_c^s} \delta\lambda_{A_N} \underbrace{\mathbf{n}_A \cdot \underbrace{\int_{\gamma_c^{h(1)}} \phi_A^{(1)}\left(\boldsymbol{\theta}^{(1)}(\mathbf{X})\right) \left[\sum_{D=1}^{n_c^s} N_D^{(1)}\left(\boldsymbol{\theta}^{(1)}(\mathbf{X})\right) \mathbf{d}_D^{(1)}(t) - \bar{\mathbf{y}}^h\right] d\gamma}_{\text{the mortar gap vector for node} A}}_{\tilde{g}_A},
\end{aligned} \tag{5.95}$$

where $\tilde{g}_A$ represents the scalar-valued mortar projected gap for node A. Therefore, the vector of mortar projected gaps for all nodes on the slave contact boundary can be created by

$$\tilde{\mathbf{g}}(\mathbf{d}^S) = \bigcup_{A=1}^{n_c^s} \tilde{g}_A \leq \mathbf{0} \quad \text{with} \quad \tilde{\mathbf{g}} \in \mathbb{R}^{n_c^s}, \tag{5.96}$$

which is the function of current nodal coordinates of the slave node set $\mathbf{d}^S$ (see Figure 5.4 along with Figure 5.18). Numerical evaluation of the mortar projected gap is postponed until section 5.5.2.5. According to the utilized implicit time integration algorithm, the mortar projected gap constraint must be fulfilled at the end of each time step such that

$$\tilde{\mathbf{g}}_{n+1} = \tilde{\mathbf{g}}(\mathbf{d}_{n+1}^S) \leq \mathbf{0}. \tag{5.97}$$

For an iterative solution method, linearization of the nonlinear mortar projected gap yields the incremental inequality condition:

$$\frac{\partial \tilde{\mathbf{g}}(\mathbf{d}_{n+1}^{Sk})}{\partial \mathbf{d}_{n+1}^S} \Delta\mathbf{d}_{n+1}^{Sk} \leq -\tilde{\mathbf{g}}_{n+1}(\mathbf{d}_{n+1}^{Sk}), \tag{5.98}$$

where the partial derivative of the mortar projected gap $\tilde{\mathbf{g}}(\mathbf{d}_{n+1}^{Sk})$ at node A in eq. (5.95) w.r.t. nodal coordinates $\mathbf{d}_{n+1}^S$ of node D when both nodes are on the slave contact surface is obtained by

$$\frac{\partial \tilde{g}_A(\mathbf{d}_{n+1}^{Sk})}{\partial (\mathbf{d}_{n+1}^S)_D} = \mathbf{n}_A^T \overbrace{\int_{\gamma_c^{h(1)}} \phi_A^{(1)}\left(\boldsymbol{\theta}^{(1)}(\mathbf{X})\right) N_D^{(1)}\left(\boldsymbol{\theta}^{(1)}(\mathbf{X})\right) d\gamma \mathbf{I}_{n_{sd}}}^{\mathbf{D}_S[A,D] \, eq. \, (5.48)}; \quad \begin{cases} D = 1, \ldots, n_c^s, \\ n_{sd} = \{2,3\}. \end{cases} \tag{5.99}$$

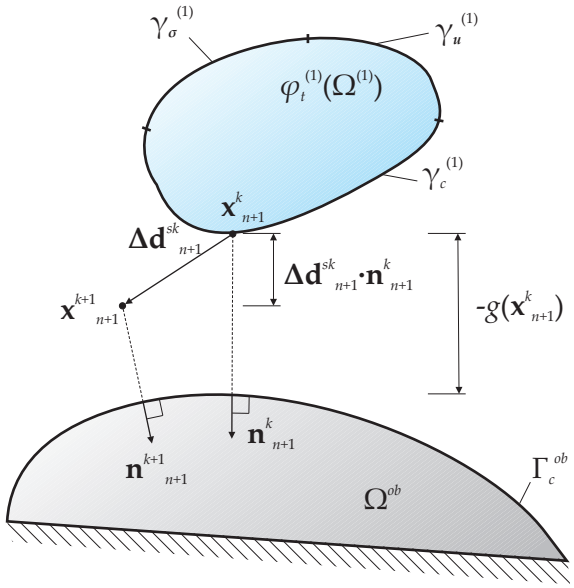

Figure 5.18: Illustration of the incremental mortar gap for unilateral contact.

By using the biorthogonality property between the dual ansatz function for the Lagrange multiplier and the interpolation functions of the displacement in section 5.3.2, the diagonal matrix $\mathbf{D}_S$ is recalled, and as a result, the incremental impenetrability condition for a node A in eq. (5.98) is transformed to $(\Delta\tilde{d}^{Sk}_{n+1})_A$ the mortar incremental change in nodal coordinate projected onto the direction of the normal vector at node $\mathbf{n}_A$ such that

$$(\Delta\tilde{d}^{Sk}_{n+1})_A = (\mathbf{n}^k_{n+1})_A \cdot \mathbf{D}_S[A,A](\Delta\mathbf{d}^{Sk}_{n+1})_A \leq -(\tilde{g}^k_{n+1})_A; \quad \text{(no summation over } A) \tag{5.100}$$

$$\text{or} \quad \Delta\tilde{\mathbf{d}}^{Sk}_{n+1} = \mathbf{n}^k_{n+1} \cdot \mathbf{D}_S \Delta\mathbf{d}^{Sk}_{n+1} \leq -\tilde{\mathbf{g}}^k_{n+1}, \tag{5.101}$$

which means that the mortar incremental change in nodal coordinate projected onto the direction of $\mathbf{n}_A$ in each iteration step $(\Delta\tilde{d}^{Sk}_{n+1})_A$ must be smaller than the mortar gap projected onto the same direction $-(\tilde{g}^k_{n+1})_A$ as illustrated in Figure 5.18. As written in eq. (5.11), the nodal Lagrange multipliers can be decomposed into a normal part and a tangential part such that $\mathbf{z}_A = \mathbf{z}_{A_N} + \mathbf{z}_{A_T}$. For the frictionless case, the tangential part vanishes $\mathbf{z}_A = \mathbf{z}_{A_N}$. Thus, the solution of the incremental effective structural equation in eq. (5.59) must simultaneously fulfill the time following discrete impenetrability conditions on the discrete slave contact boundary $\gamma_c^{h(1)}$ for a unilateral frictionless contact between a deformable body and a rigid obstacle:

$$(\Delta\tilde{d}^{Sk}_{n+1})_A \leq -(\tilde{g}^k_{n+1})_A \quad \text{(bounded mortar projected displacement)}, \tag{5.102}$$

$$z_{A_N} = -\mathbf{z}_{A_N} \cdot \mathbf{n} \geq 0 \quad \text{(compressive contact traction)}, \tag{5.103}$$

$$z_{A_N}\left[(\Delta\tilde{d}^{Sk}_{n+1})_A + (\tilde{g}^k_{n+1})_A\right] = 0 \quad \text{(KKT)}, \tag{5.104}$$

$$\mathbf{z}_{A_T} = \mathbf{0} \quad \text{(frictionless)}. \tag{5.105}$$

To proceed further, an algorithm to predetermine the active set before the computation of each time step is given in the next section.

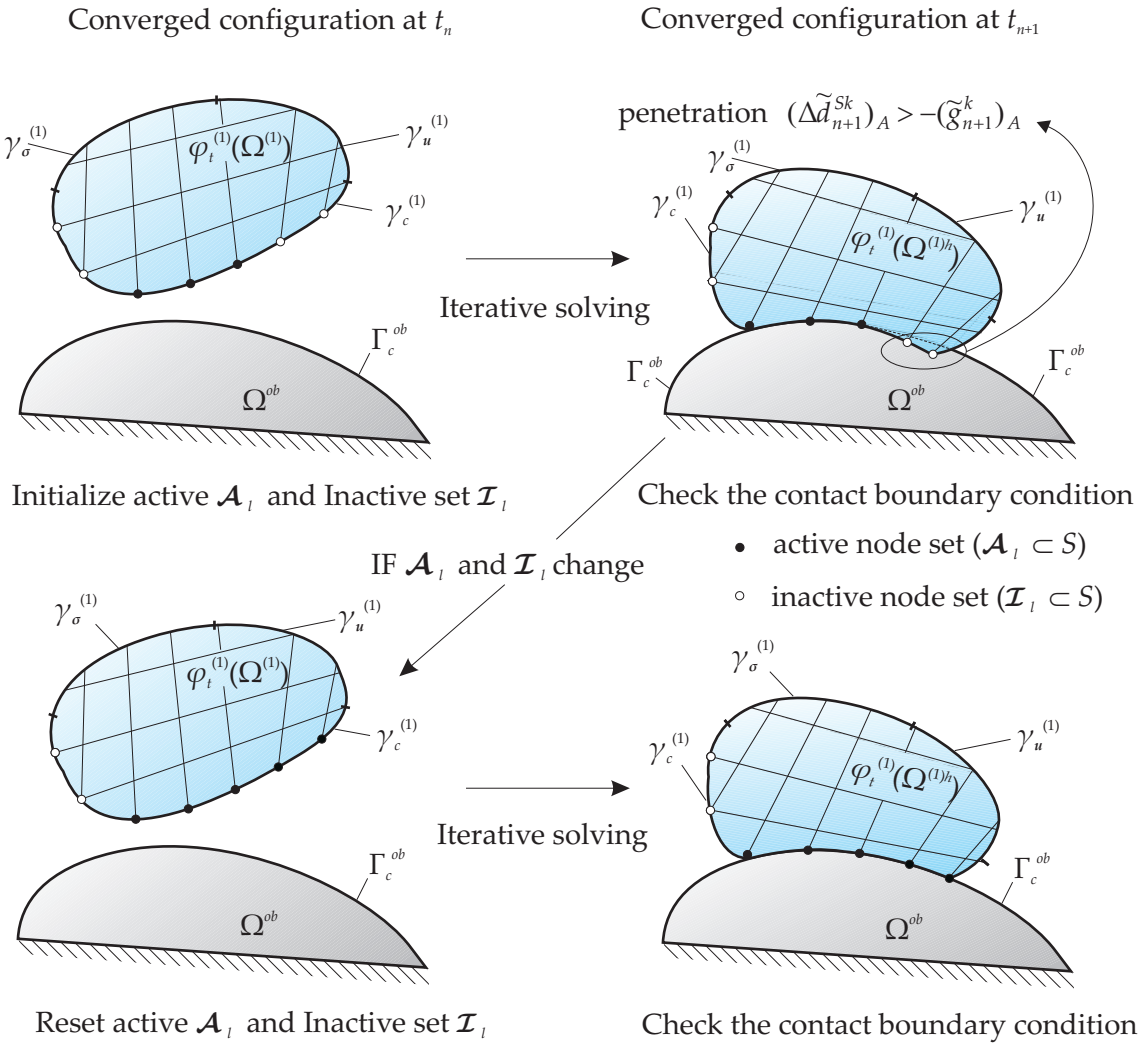

Figure 5.19: Illustration for active set strategy for unilateral contact.

5.5.1.2 Active set strategy for unilateral contact

Dealing with nonlinear impenetrability constraints defined in KKT of eq. (5.104), this chapter employs the primal-dual active set strategy (Alart and Curnier [AC91]) based on the dual Lagrange multipliers from [Woh00]. Recently, this method was successfully applied to geometrical linear multibody contact problems in [HW05], material nonlinearity contact problem in [BSSW07], and unilateral contact with large deformation in [HBRW07]. The active set strategy allows an adjustment of active contact nodes before the computation of each time step. In the postprocessing phase, the contact traction is readily recovered in a variational consistent manner from the displacement solution.

The basic idea of the method is to transform the inequality constraints in eqs. (5.102)-(5.104) to equality constraints by which the impenetrability condition for all active contact nodes are exactly fulfilled within the current time step $t \in [t_n, t_{n+1}]$. Within this work, the exact active set strategy in Hartmann [Har07] is chosen with the algorithm shown in Fig-

For time step t_{n+1}:

Initialization $\mathcal{A}_l$ and $\mathcal{I}_l$; $(l = 1)$ with $S = \mathcal{A}_l \cup \mathcal{I}_l$ and $\mathcal{A}_l \cap \mathcal{I}_l = \emptyset$

Solve the effective incremental structural equation (5.59) with boundary conditions:

$$(\Delta \tilde{d}^{Sk}_{n+1})^l_A = -(\tilde{g}^k_{n+1})^l_A \quad \forall A \in \mathcal{A}_l, \tag{5.102}$$

$$z^l_{A_N} = 0 \quad \forall A \in \mathcal{I}_l, \tag{5.103}$$

$$\mathbf{z}^l_{A_T} = \mathbf{0} \quad \forall A \in S. \tag{5.105}$$

Determine $\mathcal{A}_{l+1}$ and $\mathcal{I}_{l+1}$ such that

$$\mathcal{A}_{l+1} := \left\{ A \in S; \quad z^l_{A_N} + (\Delta \tilde{d}^{Sk}_{n+1})^l_A + (\tilde{g}^k_{n+1})^l_A > 0 \right\},$$

$$\mathcal{I}_{l+1} := \left\{ A \in S; \quad z^l_{A_N} + (\Delta \tilde{d}^{Sk}_{n+1})^l_A + (\tilde{g}^k_{n+1})^l_A \leq 0 \right\}.$$

$\Leftarrow$ IF $\mathcal{A}_{l+1} \neq \mathcal{A}_l$ or $\mathcal{I}_{l+1} \neq \mathcal{I}_l$ Set up $l = l + 1$

$\Leftarrow$ ELSEIF $\mathcal{A}_{l+1} = \mathcal{A}_l$ and $\mathcal{I}_{l+1} = \mathcal{I}_l$ Set up $n = n + 1$

Figure 5.20: Exact active set strategy algorithm for unilateral contact.

ure 5.20 along with the illustration in Figure 5.19. In these equations k denotes the number of iterations within the correction step of the Newton-type solution method for the current time step t_{n+1}, whereas the symbol l stands for the step number of the active set strategy. The starting point for this strategy is the converged configuration at the end of last time step $t^{k=0}_{n+1} = t_n$. At this initial configuration, the FE slave node set or potential contact node set S on the slave contact boundary $\gamma_c^{h(1)}$ will be subdivided ($S_l := \mathcal{A}_l \cup \mathcal{I}_l$ with $\mathcal{A}_l \cap \mathcal{I}_l = \emptyset$) into the initial active contact node set $\mathcal{A}_{l=1}$ and the initial inactive contact node set $\mathcal{I}_{l=1}$, respectively. At the active contact node set $\mathcal{A}_l$, the Dirichlet boundary condition must fulfills all impenetrability constraints while the Neumann boundary condition is prescribed at the inactive contact node set $\mathcal{I}_l$. Then the effective incremental system of equations (5.59) must be modified by additional boundary conditions corresponding to the predefined active and inactive contact node set at the beginning of the current time step $t^{k=0}_{n+1}$. Then, the modified nonlinear system of equations can be solved by iterative solution methods, e.g. Newton-type algorithms. After the state of equilibrium is achieved, the predefined active and inactive node sets will be verified whether they are valid for the available solution along the following criteria:

- ◇ A predefined active contact node with a negative discrete Lagrange multiplier $z_{A_N} < 0$ (adhesion) must be redefined as an inactive contact node for subsequent reiteration.
- ◇ A predefined inactive contact node whose balanced configuration violates the impenetrability constraint must be reset to an active contact node in the next reiteration.

As long as the change of the active set $\mathcal{A}$ and inactive set $\mathcal{I}$ in the potential contact node set S exists, the discrete geomety is set back to the configuration at the beginning of the current time step $\mathbf{d}(t^0_{n+1})$. With the new predefined active and inactive node sets, the effective incremental system of equations (5.59) will be modified by the new contact boundary conditions. The modified nonlinear system of equations must be iteratively solved until the active and

inactive contact node sets are unaltered at the end of the current time step t_{n+1}. Given the converging active and inactive contact node sets, the effective incremental structural equations can exactly be solved. Besides, an inexact active set strategy is presented in Hüber and Wohlmuth [HW05] as well as Brunssen [BSSW07] where the computation is accelerated without deterioration in the solution reliability. For the inexact algorithm, the iterative solution process stops once the evaluated active and inactive contact node sets roughly resemble to the predefined contact boundary conditions. An introduction to optimal active set strategies is given in [HW05, BSSW07].

5.5.1.3 Modified effective incremental structural equation for unilateral contact

With the known active contact node set $\mathcal{A}$ and inactive contact node set $\mathcal{I}$ from the active set strategy of the previous section, the effective incremental structural equations (5.59) must be modified w.r.t corresponding contact boundary conditions for each node in $\mathcal{A}$ and $\mathcal{I}$. As a result, the diagonal matrix $\mathbf{D}_S$ can be partitioned into

$$\mathbf{D}_S = \begin{bmatrix} \mathbf{D}^{\mathcal{I}_l} & \mathbf{0} \\ \mathbf{0} & \mathbf{D}^{\mathcal{A}_l} \end{bmatrix}. \tag{5.106}$$

Furthermore, the normal vectors of all active contact nodes in $\mathcal{A}_l$ are collected in matrix $\tilde{\mathbf{N}}_{\mathcal{A}_l} \in \mathbb{R}^{|\mathcal{A}_l| \times n_{sd}|\mathcal{A}_l|}$ where $|\mathcal{A}_l|$ is the number of active contact nodes in $\mathcal{A}_l$ such that

$$\tilde{\mathbf{N}}_{\mathcal{A}_l} = \bigcup_{A=1}^{|\mathcal{A}_l|} \tilde{\mathbf{N}}_A \mathbf{I}_{n_{sd}} \quad \text{with} \quad \tilde{\mathbf{N}}_A = \begin{bmatrix} n_{AA}^{(1)} n_{A_1} & \cdots & n_{AA}^{(1)} n_{A_{n_{sd}}} \end{bmatrix}; \; A \in \mathcal{A}_l, \tag{5.107}$$

where $\mathbf{I}_{|\mathcal{A}_l|}$ stands for a $|\mathcal{A}_l|$-diagonal matrix and the space dimensions $n_{sd} = \{2, 3\}$. $n_{AA}^{(1)}$ is the diagonal component in $\mathbf{D}_S[A, A]$ for node A in eq. (5.48) which reflects the mortar integral $n_{AB}^{(1)}$ in eqs. (5.37) and (5.38). Additionally, the normalized contravariant tangential vector (see eq.(5.11)) for node A is defined by $\mathbf{t}_A^{\varsigma} \perp \mathbf{n}_A$ and $\mathbf{t}_A^2 = \mathbf{n}_A \times \mathbf{t}_A^1$ with $\left\|\mathbf{t}_A^{\varsigma}\right\| = \|\mathbf{n}_A\| = 1$. These tangential vectors can be collected in matrices $\mathbf{T}_{\mathcal{A}_l}^{\varsigma} \in \mathbb{R}^{|\mathcal{A}_l| \times n_{sd}|\mathcal{A}_l|}$ such that

$$\mathbf{T}_{\mathcal{A}_l}^{\varsigma} = \bigcup_{A=1}^{|\mathcal{A}_l|} \mathbf{T}_A^{\varsigma} \mathbf{I}_{n_{sd}} \quad \text{with} \quad \mathbf{T}_A^{\varsigma} = \begin{bmatrix} t_{A_1}^{\varsigma} & t_{A_2}^{\varsigma} & t_{A_3}^{\varsigma} \end{bmatrix}; \quad \varsigma = (1, 2), \; A \in \mathcal{A}_l. \tag{5.108}$$

By augmenting the effective incremental structural equations (5.59) with the equality constraints, which originate from inequality constraints (5.102)-(5.105) and Figure 5.20, one obtains the modified effective incremental structural equation:

$$\begin{bmatrix} (\mathbf{K}_T^{eff})_{NN} & (\mathbf{K}_T^{eff})_{N\mathcal{I}_l} & (\mathbf{K}_T^{eff})_{N\mathcal{A}_l} & \mathbf{0} & \mathbf{0} \\ (\mathbf{K}_T^{eff})_{\mathcal{I}_l N} & (\mathbf{K}_T^{eff})_{\mathcal{I}_l\mathcal{I}_l} & (\mathbf{K}_T^{eff})_{\mathcal{I}_l\mathcal{A}_l} & -\mathbf{D}_S^{\mathcal{I}_l} & \mathbf{0} \\ (\mathbf{K}_T^{eff})_{\mathcal{A}_l N} & (\mathbf{K}_T^{eff})_{\mathcal{A}_l\mathcal{I}_l} & (\mathbf{K}_T^{eff})_{\mathcal{A}_l\mathcal{A}_l} & \mathbf{0} & -\mathbf{D}_S^{\mathcal{A}_l} \\ \mathbf{0} & \mathbf{0} & \mathbf{0} & \mathbf{I}_{n_{sd}\cdot|\mathcal{I}_l|} & \mathbf{0} \\ \mathbf{0} & \mathbf{0} & \tilde{\mathbf{N}}_{\mathcal{A}_l} & \mathbf{0} & \mathbf{0} \\ \mathbf{0} & \mathbf{0} & \mathbf{0} & \mathbf{0} & \mathbf{T}_{\mathcal{A}_l} \end{bmatrix} \begin{bmatrix} \Delta\mathbf{d}^N \\ \Delta\mathbf{d}^{\mathcal{I}_l} \\ \Delta\mathbf{d}^{\mathcal{A}_l} \\ \mathbf{z}_{n+1-\alpha_f}^{\mathcal{I}_l} \\ \mathbf{z}_{n+1-\alpha_f}^{\mathcal{A}_l} \end{bmatrix} = \begin{bmatrix} \mathbf{f}_N^{eff} \\ \mathbf{f}_{\mathcal{I}_l}^{eff} \\ \mathbf{f}_{\mathcal{A}_l}^{eff} \\ \mathbf{0} \\ -(\tilde{\mathbf{g}}_{n+1}^k)_{\mathcal{A}_l} \\ \mathbf{0} \end{bmatrix}, \tag{5.109}$$

where $\mathbf{I}_{n_{sd}\cdot|\mathcal{I}_l|}$ represents a $n_{sd}\cdot|\mathcal{I}_l|$-diagonal matrix with $|\mathcal{I}_l|$ is the number on inactive contact node in $\mathcal{I}_l$. The matrix $\mathbf{T}_{\mathcal{A}_l}=[\mathbf{T}^1_{\mathcal{A}_l},\mathbf{T}^2_{\mathcal{A}_l}]^T$ is the collective contravariant tangential basis vectors for all node in $\mathcal{A}_l$ while the $|\mathcal{I}_l|$-vector $-(\tilde{\mathbf{g}}^k_{n+1})_{\mathcal{A}_l}$ stands for the vector of mortar projected gap for all node in $\mathcal{A}_l$. Finally, the nodal Lagrange multipliers $(\mathbf{z}^{\mathcal{I}_l}_{n+1-\alpha_f},\mathbf{z}^{\mathcal{A}_l}_{n+1-\alpha_f})$ denote the nodal contact traction for potential contact node set S on the slave contact boundary $\gamma_c^{h(1)}$ at the generalized midpoint time $t_{n+1-\alpha_f}$. In eq. (5.109), the first three rows are identical to the effective incremental structural equations (5.59) whereas the fourth row informs that the contact traction does not occur at any inactive contact nodes in $\mathcal{I}_l$. For the active contact node set $\mathcal{A}_l$, the fifth row, the enforcement of the impenetrability constraint (see Figure 5.20 and eq. (5.102)), tells that the mortar projected displacement of any active contact node $A\in\mathcal{A}_l$ which is projected onto the direction of its unit normal vector must be at most equal to the mortar projected gap of that node $(\Delta\tilde{d}^{Sk}_{n+1})_{\mathcal{A}_l}=-(\tilde{g}^k_{n+1})_{\mathcal{A}_l}$. This condition guarantees that the gap between an active node A and the rigid obstacle is closed in an integral sense, and then the compressive contact traction is induced at node A. The last row is the frictionless contact condition with the vanishing of the discrete tangential contact traction ($\boldsymbol{\lambda}_{A_T}=\mathbf{z}_{A_T}=\mathbf{0}$) at node A.

As described for eq. (5.59), once the state of balance is achieved ($\Delta\mathbf{d}\rightarrow\mathbf{0}$) the out-of-balance force vector $\mathbf{f}^{eff}_S$ on the slave node set can be expressed by $\mathbf{f}^{eff}_S\rightarrow-\mathbf{f}^c_S=-\mathbf{D}_S\mathbf{z}$ where the discrete Lagrange multipliers is approximated via

$$\mathbf{z}=-\mathbf{D}_S^{-1}\mathbf{f}^{eff}_S \tag{5.110}$$

where at the state of balance the contact force vector $\mathbf{f}^c_S=\mathbf{D}_S\mathbf{z}_{n+1-\alpha_f}$ is in equilibrium with the internal force at corresponding nodes on the slave contact boundary $\gamma_c^{h(1)}$. With the static condensation procedure in Appendix B.1, a condensed form of the modified effective incremental structural equations (5.109) is achieved, viz.

$$\underbrace{\begin{bmatrix}(\mathbf{K}^{eff}_T)_{NN} & (\mathbf{K}^{eff}_T)_{N\mathcal{I}_l} & (\mathbf{K}^{eff}_T)_{N\mathcal{A}_l}\\ (\mathbf{K}^{eff}_T)_{\mathcal{I}_lN} & (\mathbf{K}^{eff}_T)_{\mathcal{I}_l\mathcal{I}_l} & (\mathbf{K}^{eff}_T)_{\mathcal{I}_l\mathcal{A}_l}\\ \mathbf{0} & \mathbf{0} & \tilde{\mathbf{N}}_{\mathcal{A}_l}\\ \mathbf{T}_{\mathcal{A}_l}(\mathbf{K}^{eff}_T)_{\mathcal{A}_lN} & \mathbf{T}_{\mathcal{A}_l}(\mathbf{K}^{eff}_T)_{\mathcal{A}_l\mathcal{I}_l} & \mathbf{T}_{\mathcal{A}_l}(\mathbf{K}^{eff}_T)_{\mathcal{A}_l\mathcal{A}_l}\end{bmatrix}}_{\mathbf{K}^{eff,mod}_T}\begin{bmatrix}\Delta\mathbf{d}^N\\ \Delta\mathbf{d}^{\mathcal{I}_l}\\ \Delta\mathbf{d}^{\mathcal{A}_l}\end{bmatrix}=\underbrace{\begin{bmatrix}\mathbf{f}^{eff}_N\\ \mathbf{f}^{eff}_{\mathcal{I}_l}\\ -(\tilde{\mathbf{g}}^k_{n+1})_{\mathcal{A}_l}\\ \mathbf{T}_{\mathcal{A}_l}\mathbf{f}^{eff}_{\mathcal{A}_l}\end{bmatrix}}_{\mathbf{f}^{eff,mod}}. \tag{5.111}$$

This system of equations must be solved in every iteration step k of the Newton-type solution method. A key advantage of this primal-dual active set strategy is reflected by the constant size of the system of equations (5.111) which must be solved within each time step. Manifestly, the system unknows are exclusively the change in nodal coordinates $\Delta\mathbf{d}$. After solution of the primal unknowns $\Delta\mathbf{d}$ is available, the discrete nodal Lagrange multipliers–the nodal contact tractions–are readily recovered during the postprocessing step in a variational consistent manner from the primal solution $\Delta\mathbf{d}$ which fulfills the impenetrability condition at the contact interface. In other words, the discrete nodal Lagrange multipliers $\mathbf{z}$ in eq. (5.110) are considered as the vector of external discrete nodal forces which are in equilibrium with the discrete nodal internal force on the slave contact boundary $\gamma_c^{h(1)}$, while the impenetrability condition on $\gamma_c^{h(1)}$ is not violated. It can be interpreted as a Dirichlet-Neumann algorithm for the nonlinear contact problem with the main idea that the contact

traction on the slave contact boundary $\gamma_c^{h(1)}$ is computed from a contact problem at the interface between the deformable body $\Omega^{h(1)}$ and the rigid obstacle Ω^{ob} with a fixed deformed state (impenetrability) of body $\Omega^{h(1)}$. Note that the mortar integral $n_{AB}^{(1)}$ in eq. (5.35), stored in the diagonal matrix $\mathbf{D}_S$, behaves as the transfer function between the displacement boundary conditions and contact tractions for the FE mesh of the deformable body $\Omega^{h(1)}$ and the rigid obstacle Ω^{ob}. However, the modification in this section leads to an unsymmetric system of equations (5.111) which requires a solver with an ability to solve the nonsymmetric matrix. This can be considered as the main drawback of the mortar-based contact formulation with the dual ansatz function for the Lagrange multipliers amongst various advantages previously mentioned. Utterly, the complete solution algorithm for the frictionless unilateral contact problem between a deformable body and a rigid obstacle is given in Figure 5.21 for the mortar-based contact formulation which satisfies the contact constraint in a weak (integral) manner over the slave contact boundary $\gamma_c^{h(1)}$.

5.5.1.4 Evaluation of the mortar gap $\tilde{g}$

The mortar projected gap $\tilde{g}_A$ of a node $A \in S$ in eq. (5.95) must be evaluated within each iteration step. For this reason, the physical gap field $\left[\sum_{D=1}^{n_c^s} N_D^{(1)}(\boldsymbol{\theta}^{(1)}(\mathbf{X}))\mathbf{d}_D^{(1)}(t) - \bar{\mathbf{y}}^h(\boldsymbol{\theta}^{(1)}(\mathbf{X}))\right]$ is weighted by the dual ansatz function for the Lagrange multiplier of node A : $\phi_A^{(1)}\left(\boldsymbol{\theta}^{(1)}(\mathbf{X})\right)$ and the result is integrated over the discrete slave contact boundary $\gamma_c^{h(1)}$ to create the mortar gap which will then be projected into the direction of normal vector of that node $\mathbf{n}_A$. Obviously in Figure 5.13(b), the discretization induces a geometric error which can be reduced to an acceptable level by mesh refinements. Because the numerical integration is performed based on the gauss integration rule to approximate the physical gap function between the discrete slave contact boundary $\gamma_c^{h(1)}$ of the deformable body $\varphi(\Omega^{h(1)})$ and the boundary of the rigid obstacle Γ_c^{ob}, the mortar gap of node A is evaluated at the quadrature points such that

$$\begin{aligned}\tilde{g}_A &\approx \mathbf{n}_A \cdot \int_{\gamma_c^{h(1)}} \phi_A^{(1)}\left(\boldsymbol{\theta}^{(1)}(\mathbf{X})\right)\left[\sum_{D=1}^{n_c^s} N_D^{(1)}\left(\boldsymbol{\theta}^{(1)}(\mathbf{X})\right)\mathbf{d}_D^{(1)}(t) - \bar{\mathbf{y}}^h\left(\boldsymbol{\theta}^{(1)}(\mathbf{X})\right)\right] d\gamma, \\ &\approx \mathbf{n}_A \cdot \sum_{e=1}^{n_{el}^A}\left[\sum_{g=1}^{n_g} w_g \phi_A^{(1)}\left(\boldsymbol{\theta}_g^{(1)}(\mathbf{X})\right)\left[\sum_{D=1}^{n_c^s} N_D^{(1)}\left(\boldsymbol{\theta}_g^{(1)}(\mathbf{X})\right)\mathbf{d}_D^{(1)}(t) - \bar{\mathbf{y}}^h\left(\boldsymbol{\theta}_g^{(1)}(\mathbf{X})\right)\right] j_e\right]^{(e)}, \end{aligned} \tag{5.112}$$

where n_g and w_g stand for the number of integration points within an element and the weight factors for the corresponding integration points, respectively. $j_e = det(\mathbf{j}_e)$ is the determinant of the mapping of an element from the parametric to the physical space, which is described in Figure 2.4 of section 2.3.1.1. Note that all quantities are evaluated at the position of each integration point $\boldsymbol{\theta}_g^{(1)}$ and n_{el}^A is the number of all elements sharing a common node on the slave contact boundary $A \in S$. Similar to section 5.4.1.3, this formula is valid for both two and three dimensional cases.

In case of a straight rigid obstacle with a linear displacment shape function $N_D^{(1)}$ and linear ansatz function for the Lagrange multipliers $\phi_A^{(1)}$ on the slave contact boundary like in

Initialize: set intitial time step number $(n = 0)$ and initial conditions $\left(\mathbf{d}_0; \dot{\mathbf{d}}_0 \Rightarrow \ddot{\mathbf{d}}_0\right)$

Loop over all time steps $(n_T = T/\Delta t)$

Initialization $\mathcal{A}_l$ and $\mathcal{I}_l$; $(l = 1)$ with $S = \mathcal{A}_l \cup \mathcal{I}_l$ and $\mathcal{A}_l \cap \mathcal{I}_l = \emptyset$

Loop over the active set strategy

Predictor step $(k = 0)$

$\mathbf{K}_T^{eff}(\mathbf{d}_{n+1}^0)$ and $\mathbf{f}^{eff}(\mathbf{d}_{n+1}^0)$ (2.133);(2.148) and (2.134);(2.149)

Modify the effective incremental structural equation

$\mathbf{K}_T^{eff,mod}(\mathbf{d}_{n+1}^0)$ and $\mathbf{f}^{eff,mod}(\mathbf{d}_{n+1}^0)$ (5.111)

$$\Delta \mathbf{d}_{n+1,\sum}^0 = \left(\mathbf{K}_T^{eff,mod}\right)^{-1} \mathbf{f}^{eff,mod}(\mathbf{d}_{n+1}^0)$$

$$\mathbf{d}_{n+1}^1 = \mathbf{d}_{n+1}^0 + \Delta \mathbf{d}_{n+1,\sum}^0$$

Set up $k = 1$

Newton-Raphson correction iteration:

$\mathbf{K}_T^{eff}(\mathbf{d}_{n+1}^k)$ and $\mathbf{f}^{eff}(\mathbf{d}_{n+1}^k)$ (2.133);(2.148) and (2.134);(2.149)

Modify the effective incremental structural equation

$\mathbf{K}_T^{eff,mod}(\mathbf{d}_{n+1}^k)$ and $\mathbf{f}^{eff,mod}(\mathbf{d}_{n+1}^k)$ (5.111)

$$\Delta \mathbf{d}_{n+1}^k = \left(\mathbf{K}_T^{eff,mod}\right)^{-1} \mathbf{f}^{eff,mod}(\mathbf{d}_{n+1}^k)$$

$$\Delta \mathbf{d}_{n+1,\sum}^k = \Delta \mathbf{d}_{n+1,\sum}^{k-1} + \Delta \mathbf{d}_{n+1}^k$$

$$\mathbf{d}_{n+1}^{k+1} = \mathbf{d}_{n+1}^0 + \Delta \mathbf{d}_{n+1,\sum}^k$$

$\Delta(\bullet)_{n+1,\sum}^k$: Sum of incremental change of $(\bullet)$ till the end of iteration k of time step t_{n+1}

$\Leftarrow$ Set up $k = k + 1$ until convergence

Determine $\mathcal{A}_{l+1}$ and $\mathcal{I}_{l+1}$; $\mathbf{z} = -\mathbf{D}_S^{-1}\mathbf{f}_S^{eff}$ (5.110)

$$\mathcal{A}_{l+1} := \left\{A \in S; \quad z_{A_N}^l + (\Delta \tilde{d}_{n+1}^{Sk})_A^l + (\tilde{g}_{n+1}^k)_A^l > 0\right\},$$

$$\mathcal{I}_{l+1} := \left\{A \in S; \quad z_{A_N}^l + (\Delta \tilde{d}_{n+1}^{Sk})_A^l + (\tilde{g}_{n+1}^k)_A^l \leq 0\right\}.$$

$\Leftarrow$ IF $\mathcal{A}_{l+1} \neq \mathcal{A}_l$ or $\mathcal{I}_{l+1} \neq \mathcal{I}_l$ Set up $l = l + 1$

Update change of nodal coordiate after convergence $\mathbf{d}_{n+1} = \mathbf{d}_{n+1}^{k+1}$

$\dot{\mathbf{d}}_{n+1}(\mathbf{d}_{n+1}), \ddot{\mathbf{d}}_{n+1}(\mathbf{d}_{n+1})$ (2.121), (2.122)

$\Leftarrow$ Set up $n = n + 1$ until $n + 1 = n_T$

Figure 5.21: Numerical solution algorithm of IBVP for elastodynamcis in unilateral contact problem between a deformable body and a rigid obstacle.

this work (see Figure 5.14), the 2-point quadrature rule is ample for exact numerical integration. However, in case of a rigid obstacle with complex geometry, more number of quadrature points are required to attain the exact numerical integration (see Cowper [Cow73], Bathe [Bat02] or Zienkiewicz [ZTZ05]).

Even though, the presentation in this section is for the two dimensional problems, extensions towards the three dimensional cases are straight forward with an emphasis that the biorthogonality of the ansatz function of the Lagrange mulitipliers and the displacement shape function must be held on the physical contact boundary $\gamma_c^{h(1)}$.

5.5.2 Normal contact of two deformable bodies

Similar to the unilateral contact in section 5.5.1, this section appends the variational form of the impenetrability condition at the contact interfaces between two deformable bodies to the virtual work equation in eq. (5.19) of section 5.1.4 with the help of the active set strategy.

5.5.2.1 Weak impenetrability condition for two deformable bodies

The mortar-based impenetrability formulation is formulated in an integral manner over the geometric contact boundary $\gamma_c^{(\alpha)}$ of both deformable bodies $\Omega^{(\alpha)}$. For the frictionless contact, only the normal component is considered within the weak impenetrability condition as mentioned in eq. (5.24) such that

$$\int_{\gamma_c^{(1)}} \delta\lambda_N(\mathbf{X}) g(\mathbf{X},t) d\gamma \leq 0 \tag{5.113}$$

with the definition of the scalar-valued gap function g from eq. (5.3). Substitution of eqs. (5.94) and (5.3) into the weak impenetrability condition in eq. (5.93) with the help of the interpolation function in eqs. (5.29) and (5.30) yields the discrete weak impenetrability condition for any $\delta\lambda_N(\mathbf{X}) \geq 0$:

$$\begin{aligned}
&\int_{\gamma_c^{(1)}} \delta\lambda_N g d\gamma \approx \int_{\gamma_c^{(1)}} \delta\lambda_N^h(\mathbf{X}) g^h(\mathbf{X},t) d\gamma \leq 0, \\
&\approx \int_{\gamma_c^{(1)}} \sum_{A=1}^{n_c^s} \phi_A^{(1)}\left(\boldsymbol{\theta}^{(1)}(\mathbf{X})\right) \delta\lambda_{A_N} \mathbf{n} \cdot \left[\sum_{D=1}^{n_c^s} N_D^{(1)}\left(\boldsymbol{\theta}^{(1)}(\mathbf{X})\right) \mathbf{d}_D^{(1)}(t) - \sum_{E=1}^{n_c^m} N_E^{(2)}\left(\boldsymbol{\theta}^{(2)}(\bar{\mathbf{Y}})\right) \mathbf{d}_E^{(2)}(t)\right] d\gamma, \\
&\approx \sum_{A=1}^{n_c^s} \delta\lambda_{A_N} \mathbf{n}_A \cdot \underbrace{\underbrace{\int_{\gamma_c^{(1)}} \phi_A^{(1)}\left(\boldsymbol{\theta}^{(1)}(\mathbf{X})\right) \left[\sum_{D=1}^{n_c^s} N_D^{(1)}\left(\boldsymbol{\theta}^{(1)}(\mathbf{X})\right) \mathbf{d}_D^{(1)}(t) - \sum_{E=1}^{n_c^m} N_E^{(2)}\left(\boldsymbol{\theta}^{(2)}(\bar{\mathbf{Y}})\right) \mathbf{d}_E^{(2)}(t)\right] d\gamma}_{\text{the mortar gap vector for node} A}}_{\tilde{g}_A},
\end{aligned} \tag{5.114}$$

where $\tilde{g}_A$ denotes the scalar-valued mortar projected gap for node A. Therefore, the vector of mortar projected gap for all nodes on the slave contact boundary is defined by

$$\tilde{\mathbf{g}}(\mathbf{d}^S, \mathbf{d}^M) = \bigcup_{A=1}^{n_c^s} \tilde{g}_A \leq \mathbf{0} \quad \text{with} \quad \tilde{\mathbf{g}} \in \mathbb{R}^{n_c^s}. \tag{5.115}$$

Obviously, $\tilde{\mathbf{g}}(\mathbf{d}^S, \mathbf{d}^M)$ is a function of nodal coordinates from both the slave and master node sets (see Figures 5.4 and 5.18) while a numerical evaluation of the mortar projected gap is postponed until section 5.5.2.5. With the implicit time integration algorithm, the impenetrability must be fulfilled at the end of each time step by enforcing a constraint over the mortar projected gap:

$$\tilde{\mathbf{g}}_{n+1} = \tilde{\mathbf{g}}(\mathbf{d}^S_{n+1}, \mathbf{d}^M_{n+1}) \leq \mathbf{0} \tag{5.116}$$

at which linearization will then be performed to achieve the incremental inequality constraint:

$$\frac{\partial \tilde{\mathbf{g}}(\mathbf{d}^{Sk}_{n+1}, \mathbf{d}^{Mk}_{n+1})}{\partial \mathbf{d}^S_{n+1}} \Delta \mathbf{d}^{Sk}_{n+1} + \frac{\partial \tilde{\mathbf{g}}(\mathbf{d}^{Sk}_{n+1}, \mathbf{d}^{Mk}_{n+1})}{\partial \mathbf{d}^M_{n+1}} \Delta \mathbf{d}^{Mk}_{n+1} \leq -\tilde{\mathbf{g}}_{n+1}(\mathbf{d}^{Sk}_{n+1}, \mathbf{d}^{Mk}_{n+1}). \tag{5.117}$$

In this equation, the first term is similar to eq. (5.99), while the partial derivative of the mortar projected gap $\tilde{\mathbf{g}}(\mathbf{d}^{Sk}_{n+1})$ at a slave node $A \in S$ in eq. (5.114) w.r.t. nodal coordinates $\mathbf{d}^M_{n+1}$ of a master node $E \in M$ is written by

$$\frac{\partial \tilde{g}_A(\mathbf{d}^{Sk}_{n+1})}{\partial (\mathbf{d}^M_{n+1})_E} = -\mathbf{n}_A^T \overbrace{\int_{\gamma_c^{h(1)}} \phi_A^{(1)} \left(\boldsymbol{\theta}^{(1)}(\mathbf{X})\right) N_E^{(2)} \left(\boldsymbol{\theta}^{(2)}(\bar{\mathbf{Y}})\right) d\gamma \mathbf{I}_{n_{sd}}}^{\mathbf{M}_M[A,E] \, eq. \, (5.63)}; \quad \begin{cases} E = 1, \ldots, n_c^m, \\ n_{sd} = \{2, 3\}. \end{cases} \tag{5.118}$$

Here, the diagonal-structure matrix for the weighted normal vector $\tilde{\mathbf{N}}_{\mathcal{A}_l} \in \mathbb{R}^{|\mathcal{A}_l| \times n_{sd}|\mathcal{A}_l|}$ is given in eq. (5.107). Thus, the incremental impenetrability inequality constraint in eq. (5.117) can be rewritten to a compact form:

$$\tilde{\mathbf{N}}_{\mathcal{A}_l} [\underbrace{\Delta \mathbf{d}^{Sk}_{n+1} - \mathbf{D}_S^{-1} \mathbf{M}_M \Delta \mathbf{d}^{Mk}_{n+1}}_{[\Delta \mathbf{d}]}] \leq -\tilde{\mathbf{g}}_{n+1}(\mathbf{d}^{Sk}_{n+1}, \mathbf{d}^{Mk}_{n+1}), \tag{5.119}$$

where the so-called "*incremental jump*" $[\Delta \mathbf{d}] = \Delta \mathbf{d}^{Sk}_{n+1} - \hat{\mathbf{M}} \Delta \mathbf{d}^{Mk}_{n+1}$ within the bracket is referred to the incremental relative change in nodal coordinates between both contact boundaries. $\hat{\mathbf{M}} = \mathbf{D}_S^{-1} \mathbf{M}_M$ is the mortar transfer matrix which links the change in nodal coordinate on the master contact boundary $\mathbf{d}^{Mk}_{n+1}$ to the change in nodal coordinate on the slave contact boundary $\mathbf{d}^{Sk}_{n+1}$. The diagonal-structure matrix $\tilde{\mathbf{N}}$ allows to decouple the incremental jump for each node A within the slave node set $A \in S$, viz.

$$[\Delta \tilde{d}^k_{n+1}]_A = (\mathbf{n}^k_{n+1})_A \cdot \mathbf{D}_S[A, A] \, [\Delta \mathbf{d}]_A \, ; \quad \text{(no summation over } A), \tag{5.120}$$

which is interpreted as the mortar incremental relative displacement at node A projected into the direction of its normal vector $(\mathbf{n}^k_{n+1})_A$. By this definition, the impenetrability constraints for each node A on the discrete slave contact boundary $\gamma_c^{h(1)}$ at the contact interfaces

between two deformable bodies are expressed by

$$[\Delta\tilde{d}^k_{n+1}]_A \leq -(\tilde{g}^k_{n+1})_A \quad \text{(bounded mortar projected relative incremental disp.)}, \tag{5.121}$$

$$z_{A_N} = -\mathbf{z}_{A_N} \cdot \mathbf{n} \geq 0 \quad \text{(compressive contact traction)}, \tag{5.122}$$

$$z_{A_N}\left[[\Delta\tilde{d}^k_{n+1}]_A + (\tilde{g}^k_{n+1})_A\right] = 0 \quad \text{(KKT)}, \tag{5.123}$$

$$\mathbf{z}_{A_T} = \mathbf{0} \quad \text{(frictionless)}, \tag{5.124}$$

which means that the mortar relative incremental change in nodal coordinate projected onto the direction of $\mathbf{n}_A$ in each iteration step $[\Delta\tilde{d}^k_{n+1}]_A$ must be smaller than the mortar gap projected onto the same direction $-(\tilde{g}^k_{n+1})_A$ as illustrated in Figure 5.18. Note that contact constraints in this case are quite similar to those of the unilateral contact in eqs. (5.102)-(5.105) with a major difference that the nodal incremental relative displacement between both contact boundaries is considered instead of the direct nodal displacement as in the case of unilateral contact.

5.5.2.2 Local basis transformation

The objective of this section is to transform the effective incremental structural equation for a contact problem of two deformable bodies into a format that is similar to that of the unilateral contact in eq. (5.59). Once the structural equation has been transformed, the available solution algorithm for the unilateral contact of the previous section can be reused. Since in this case the contact boundary conditions are functions of the incremental jump $[\Delta\mathbf{d}]$, therefore, it is reasonable to choose $[\Delta\mathbf{d}]$ as the primal unknowns instead of the change in nodal coordinated at the slave node set $\Delta\mathbf{d}^S$. In doing so, this work adopts the local basis transformation method presented in Wohlmuth and Krause [WK03] and Hartmann [Har07]. Let us introduce the transformed effective tangential stiffness matrix of $\mathbf{K}^{eff}$ denoted by $\hat{\mathbf{K}}^{eff}$ as well as the transformed effective force vector $\hat{\mathbf{f}}^{eff}$ in the transformed effective incremental structural equation:

$$\underbrace{\begin{bmatrix} \hat{\mathbf{K}}_{NN} & \hat{\mathbf{K}}_{NM} & \hat{\mathbf{K}}_{NS} & \mathbf{0} \\ \hat{\mathbf{K}}_{MN} & \hat{\mathbf{K}}_{MM} & \hat{\mathbf{K}}_{MS} & \mathbf{0} \\ \hat{\mathbf{K}}_{SN} & \hat{\mathbf{K}}_{SM} & \hat{\mathbf{K}}_{SS} & -\mathbf{D}_S \end{bmatrix}}_{\hat{\mathbf{K}}^{eff}_T} \begin{bmatrix} \Delta\mathbf{d}^N \\ \Delta\mathbf{d}^M \\ [\Delta\mathbf{d}] \\ \mathbf{z}_{n+1-\alpha_f} \end{bmatrix} = \underbrace{\begin{bmatrix} \mathbf{f}^{eff}_N \\ \mathbf{f}^{eff}_M + \hat{\mathbf{M}}^T\mathbf{f}^{eff}_S \\ \mathbf{f}^{eff}_S \end{bmatrix}}_{\hat{\mathbf{f}}^{eff}}, \tag{5.125}$$

Where the transformed effective tangential stiffness matrix $\hat{\mathbf{K}}^{eff}_T$ is expressed by

$$\hat{\mathbf{K}}^{eff}_T = \begin{bmatrix} (\mathbf{K}^{eff}_T)_{NN} & (\mathbf{K}^{eff}_T)_{NM} + (\mathbf{K}^{eff}_T)_{NS}\hat{\mathbf{M}} & (\mathbf{K}^{eff}_T)_{NS} \\ (\mathbf{K}^{eff}_T)_{MN} + \hat{\mathbf{M}}^T(\mathbf{K}^{eff}_T)_{SN} & (\mathbf{K}^{eff}_T)_{MM} + \hat{\mathbf{M}}^T(\mathbf{K}^{eff}_T)_{SM} + (\mathbf{K}^{eff}_T)_{MS}\hat{\mathbf{M}} + \hat{\mathbf{M}}^T(\mathbf{K}^{eff}_T)_{SS}\hat{\mathbf{M}} & (\mathbf{K}^{eff}_T)_{MS} + \hat{\mathbf{M}}^T(\mathbf{K}^{eff}_T)_{SS} \\ (\mathbf{K}^{eff}_T)_{SN} & (\mathbf{K}^{eff}_T)_{SM} + (\mathbf{K}^{eff}_T)_{SS}\hat{\mathbf{M}} & (\mathbf{K}^{eff}_T)_{SS} \end{bmatrix} \tag{5.126}$$

with the details of the transformation procedure in Appendix B.2. This algebraic system of equations has a similar structure as the effective incremental structural equation for unilateral contact in eq. (5.59).

For time step t_{n+1}:

Initialization $\mathcal{A}_l$ and $\mathcal{I}_l$; $(l = 1)$ with $S = \mathcal{A}_l \cup \mathcal{I}_l$ and $\mathcal{A}_l \cap \mathcal{I}_l = \emptyset$

Solve the transformed effective incremental structural equation (5.125)

with impenetrability conditions:

$$[\Delta\tilde{d}^k_{n+1}]^l_A = -(\tilde{g}^k_{n+1})^l_A \quad \forall A \in \mathcal{A}_l, \tag{5.121}$$

$$z^l_{A_N} = 0 \quad \forall A \in \mathcal{I}_l, \tag{5.122}$$

$$\mathbf{z}^l_{A_T} = \mathbf{0} \quad \forall A \in S. \tag{5.124}$$

Determine $\mathcal{A}_{l+1}$ and $\mathcal{I}_{l+1}$ such that

$$\mathcal{A}_{l+1} := \left\{ A \in S; z^l_{A_N} + [\Delta\tilde{d}^k_{n+1}]^l_A + (\tilde{g}^k_{n+1})^l_A > 0 \right\},$$
$$\mathcal{I}_{l+1} := \left\{ A \in S; z^l_{A_N} + [\Delta\tilde{d}^k_{n+1}]^l_A + (\tilde{g}^k_{n+1})^l_A \leq 0 \right\}.$$

$\Leftarrow$ IF $\mathcal{A}_{l+1} \neq \mathcal{A}_l$ or $\mathcal{I}_{l+1} \neq \mathcal{I}_l$ Set up $l = l + 1$

$\Leftarrow$ ELSEIF $\mathcal{A}_{l+1} = \mathcal{A}_l$ and $\mathcal{I}_{l+1} = \mathcal{I}_l$ Set up $n = n + 1$

Figure 5.22: Exact active set strategy algorithm for contact of two deformable bodies.

5.5.2.3 Active set strategy for contact of two deformable bodies

Alike the unilateral contact case in section 5.5.1.2, the exact active set strategy from Hartmann [Har07] is employed to predefine the active contact node set $\mathcal{A}_l$ and inactive contact node set $\mathcal{I}_l$, respectively. This subdivision on the FE slave node set or potential contact node set S on the slave contact boundary $\gamma_c^{h(1)}$ can be described by $S_l := \mathcal{A}_l \cup \mathcal{I}_l$ with $\mathcal{A}_l \cap \mathcal{I}_l = \emptyset$. Remarkably, the active set strategy for the problem at hand is similar to that of the unilateral contact in Figure 5.20. The distinct difference is the mortar projected relative incremental change in nodal coordinate $[\Delta\tilde{d}^k_{n+1}]_A$ in place of the mortar projected incremental change in nodal coordinate $(\Delta\tilde{d}^{Sk}_{n+1})_A$ within the impenetrability constraint. The active set algorithm for the contact problem of two deformable bodies is demonstrated in Figure 5.22 within a discrete time increment $[t_n, t_{n+1}]$ with k and l representing the iteration step and active set strategy step, respectively. The modified nonlinear system of equations must be iteratively solved until the active and inactive contact node sets are unaltered at the end of the current time step t_{n+1}. Then, with available active and inactive contact node sets, a solution of the effective incremental structural equation is achieved.

5.5.2.4 Modification of the transformed effective incremental structural equation for contact of two bodies

Likewise, the procedure to modify the effective incremental structural equation for contact problems of two deformable bodies is similar to that of the unilateral case in section 5.5.1.3. This section tries to avoid any repetition and mainly discusses the aspects which are not mentioned previously. With the diagonal matrix $\mathbf{D}_S \in \mathbb{R}^{n^s_c \times n_{sd} \cdot n^s_c}$ in eq. (5.106), the matrix of the mortar projected normal vector on active contact nodes $\tilde{\mathbf{N}}_{\mathcal{A}_l} \in \mathbb{R}^{|\mathcal{A}_l| \times n_{sd}|\mathcal{A}_l|}$ in eq. (5.107) and the matrix of normalized contravariant tangential vectors on the slave node

set $\mathbf{T}^c_{\mathcal{A}_l} \in \mathbb{R}^{|\mathcal{A}_l| \times n_{sd}|\mathcal{A}_l|}$ in eq. (5.108), the transformed effective incremental structural equations for contact problems of two deformable bodies in eq. (5.125) are modified according to the discrete impenetrability constraints from eqs. (5.121)-(5.124) such that

$$\begin{bmatrix} \hat{\mathbf{K}}_{NN} & \hat{\mathbf{K}}_{NM} & \hat{\mathbf{K}}_{N\mathcal{I}_l} & \hat{\mathbf{K}}_{N\mathcal{A}_l} & \mathbf{0} & \mathbf{0} \\ \hat{\mathbf{K}}_{MN} & \hat{\mathbf{K}}_{MM} & \hat{\mathbf{K}}_{M\mathcal{I}_l} & \hat{\mathbf{K}}_{M\mathcal{A}_l} & \mathbf{0} & \mathbf{0} \\ \hat{\mathbf{K}}_{\mathcal{I}_l N} & \hat{\mathbf{K}}_{\mathcal{I}_l M} & \hat{\mathbf{K}}_{\mathcal{I}_l\mathcal{I}_l} & \hat{\mathbf{K}}_{\mathcal{I}_l\mathcal{A}_l} & -\mathbf{D}^{\mathcal{I}_l} & \mathbf{0} \\ \hat{\mathbf{K}}_{\mathcal{A}_l N} & \hat{\mathbf{K}}_{\mathcal{A}_l M} & \hat{\mathbf{K}}_{\mathcal{A}_l\mathcal{I}_l} & \hat{\mathbf{K}}_{\mathcal{A}_l\mathcal{A}_l} & \mathbf{0} & -\mathbf{D}^{\mathcal{A}_l} \\ \mathbf{0} & \mathbf{0} & \mathbf{0} & \mathbf{0} & \mathbf{I}_{n_{sd}\cdot|\mathcal{I}_l|} & \mathbf{0} \\ \mathbf{0} & \mathbf{0} & \mathbf{0} & \tilde{\mathbf{N}}_{\mathcal{A}_l} & \mathbf{0} & \mathbf{0} \\ \mathbf{0} & \mathbf{0} & \mathbf{0} & \mathbf{0} & \mathbf{0} & \mathbf{T}_{\mathcal{A}_l} \end{bmatrix} \begin{bmatrix} \Delta\mathbf{d}^N \\ \Delta\mathbf{d}^M \\ [\Delta\mathbf{d}^{\mathcal{I}_l}] \\ [\Delta\mathbf{d}^{\mathcal{A}_l}] \\ \mathbf{z}^{\mathcal{I}_l}_{n+1-\alpha_f} \\ \mathbf{z}^{\mathcal{A}_l}_{n+1-\alpha_f} \end{bmatrix} = \begin{bmatrix} \mathbf{f}^{eff}_N \\ \mathbf{f}^{eff}_M + \hat{\mathbf{M}}^T \mathbf{f}^{eff}_S \\ \mathbf{f}^{eff}_{\mathcal{I}_l} \\ \mathbf{f}^{eff}_{\mathcal{A}_l} \\ \mathbf{0} \\ -(\tilde{\mathbf{g}}^k_{n+1})_{\mathcal{A}_l} \\ \mathbf{0}, \end{bmatrix} \tag{5.127}$$

where subscript or superscript M denotes the master node set on the discrete master contact boundary $\gamma_c^{h(2)}$, while $[\Delta\mathbf{d}]$ stands for the relative incremental change in nodal coordinate or incremental jump. Explanations of the system of equations (5.127) are similar to those given for eq. (5.109) except for the sixth row which informs that the mortar projected relative incremental jump $[\Delta\tilde{d}^k_{n+1}]_A$ of node A at the end of the current time step $_{n+1}$ must be equal to the mortar gap of that node which is projected onto the direction of its normal vector $-(\tilde{g}^k_{n+1})_A$. This condition results in the vanishing of the mortar projected nodal gap $-(\tilde{g}^k_{n+1})_A$ between both contact boundaries (see Figure 5.18) in the integral manner which is similar to the case of unilateral contact in eq. (5.109).

With the same reason as for eq. (5.110), at the state of balance one finds that $(\Delta\mathbf{d} \to \mathbf{0})$ as well as $([\Delta\mathbf{d}] \to \mathbf{0})$. As a result, the out-of-balance force vector $\mathbf{f}^{eff}_S$ on the slave node set from the last row of eq. (5.125) can be expressed by $\mathbf{f}^{eff}_S \to -\mathbf{f}^c_S = -\mathbf{D}_S\mathbf{z}$ where the discrete Lagrange multipliers can be approximated via

$$\mathbf{z} \approx -\mathbf{D}_S^{-1}\mathbf{f}^{eff}_S, \tag{5.128}$$

which is similar to that of the unilateral contact in eq. (5.128). At the state of balance the contact force vector $\mathbf{f}^c_S = \mathbf{D}_S\mathbf{z}_{n+1-\alpha_f}$ is in equilibrium with the internal force at corresponding nodes on the slave contact boundary $\gamma_c^{h(1)}$. Furthermore, the condensed form of eq. (5.127) is obtained by the static condensation procedure in Appendix B.1 such that

$$\underbrace{\begin{bmatrix} \hat{\mathbf{K}}_{NN} & \hat{\mathbf{K}}_{NM} & \hat{\mathbf{K}}_{N\mathcal{I}_l} & \hat{\mathbf{K}}_{N\mathcal{A}_l} \\ \hat{\mathbf{K}}_{MN} & \hat{\mathbf{K}}_{MM} & \hat{\mathbf{K}}_{M\mathcal{I}_l} & \hat{\mathbf{K}}_{M\mathcal{A}_l} \\ \hat{\mathbf{K}}_{\mathcal{I}_l N} & \hat{\mathbf{K}}_{\mathcal{I}_l M} & \hat{\mathbf{K}}_{\mathcal{I}_l\mathcal{I}_l} & \hat{\mathbf{K}}_{\mathcal{I}_l\mathcal{A}_l} \\ \mathbf{0} & \mathbf{0} & \mathbf{0} & \tilde{\mathbf{N}}_{\mathcal{A}_l} \\ \mathbf{T}_{\mathcal{A}_l}\hat{\mathbf{K}}_{\mathcal{A}_l N} & \mathbf{T}_{\mathcal{A}_l}\hat{\mathbf{K}}_{\mathcal{A}_l M} & \mathbf{T}_{\mathcal{A}_l}\hat{\mathbf{K}}_{\mathcal{A}_l\mathcal{I}_l} & \mathbf{T}_{\mathcal{A}_l}\hat{\mathbf{K}}_{\mathcal{A}_l\mathcal{A}_l} \end{bmatrix}}_{\hat{\mathbf{K}}^{eff,mod}_T} \begin{bmatrix} \Delta\mathbf{d}^N \\ \Delta\mathbf{d}^M \\ [\Delta\mathbf{d}^{\mathcal{I}_l}] \\ [\Delta\mathbf{d}^{\mathcal{A}_l}] \end{bmatrix} = \underbrace{\begin{bmatrix} \mathbf{f}^{eff}_N \\ \mathbf{f}^{eff}_M + \hat{\mathbf{M}}^T\mathbf{f}^{eff}_S \\ \mathbf{f}^{eff}_{\mathcal{I}_l} \\ -(\tilde{\mathbf{g}}^k_{n+1})_{\mathcal{A}_l} \\ \mathbf{T}_{\mathcal{A}_l}\mathbf{f}^{eff}_{\mathcal{A}_l} \end{bmatrix}}_{\hat{\mathbf{f}}^{eff,mod}}, \tag{5.129}$$

which must be solved in every iteration step k of the Newton-type solution method. The system equation in eq. (5.129) has constant size maintained throughout the computation with the change in nodal coordinates $\Delta\mathbf{d}$ and the relative incremental change in nodal coordinate $[\Delta\mathbf{d}]$ as system unknowns. Within the postprocessing state, the discrete nodal Lagrange multipliers–the nodal contact traction–are readily recovered in a variational consistent manner from the primal solution $\Delta\mathbf{d}$ and $[\Delta\mathbf{d}]$ which fulfills the impenetrability condition at

the contact interfaces in an integral manner. These discrete nodal Lagrange multipliers $\mathbf{z}$ in eq. (5.110) behave like the external discrete nodal forces that are in equilibrium with the internal discrete nodal forces on the slave contact boundary $\gamma_c^{h(1)}$.

The diagonal coupling matrix $\mathbf{D}_S$ explained in section 5.5.1.3. The mixed coupling matrix $\mathbf{M}_M$ contains the mortar integral $n_{AC}^{(2)}$ from eq. (5.36) which is the transfer function between the discrete displacement boundary conditions on the master contact boundary $\gamma_c^{h(2)}$ and discrete contact tractions on the slave contact boundary $\gamma_c^{h(1)}$. This mixed coupling matrix $\mathbf{M}_M$ links the dofs on the slave contact boundary $\gamma_c^{h(1)}$ to that on the master contact boundary $\gamma_c^{h(2)}$. Defined in accordance with active and inactive contact nodes, coupled dofs are arbitrarily altered during the computation. This issue can significantly deteriorate the solver performance, since requirements on data storage format will be varied, e.g. positions of nonzero values, once the sets of active and inactive nodes are changed. Consequently, at the beginning of each timestep the connectivity between dofs must be determined to choose the suitable data storage format which will be held during subsequent computation within that timestep. Obviously, this unpredictable connectivity of coupled dofs considerably decelerates the computation besides the requirement of a solver with an ability to solve the nonsymmetric matrices. The complete solution algorithm for the frictionless contact problem between two deformable bodies is provided in Figure 5.23.

5.5.2.5 Evaluation of the mortar gap $\tilde{g}$

To enforce the impenetrability constraint in eq. (5.129), the mortar projected gap $\tilde{g}_A$ of node $A \in S$ in eq. (5.114) must be determined for each iteration step k. As the point of departure, the physical gap field $[\sum_{D=1}^{n_c^s} N_D^{(1)}(\boldsymbol{\theta}^{(1)}(\mathbf{X}))\mathbf{d}_D^{(1)}(t) - \sum_{E=1}^{n_c^m} N_E^{(2)}(\boldsymbol{\theta}^{(2)}(\bar{\mathbf{Y}}))\mathbf{d}_E^{(2)}(t)]$ is weighted by the dual ansatz function for the Lagragne multiplier of node A : $\phi_A^{(1)}(\boldsymbol{\theta}^{(1)}(\mathbf{X}))$ and the result is integrated over the discrete slave contact boundary $\gamma_c^{h(1)}$ to created the mortar gap which will then be projected into the direction of the normal vector at that node $\mathbf{n}_A$.

Two dimensional problems

For a two dimensional problem, Figure 5.13(b) illustrates the discrete contact interface of two deformable bodies where the discretization error can be reduced with mesh refinements. With the definition of 2D mortar segments introduced in sections 5.4.1.2 and 5.4.1.4, The mortar projected gap $\tilde{g}_A$ of node $A \in S$ in eq. (5.114) is evaluated in the similar manner as the coupling mortar integrals $n_{AC}^{(2)}$ in eq. (5.78). Hence, the gauss integration rule is performed within each mortar segment to approximate the physical gap function between the discrete slave contact boundary $\gamma_c^{h(1)}$ and the discrete master contact boundary $\gamma_c^{h(2)}$. Summing up contributions from all segments on the slave contact boundary $\gamma_c^{h(1)}$ leads to the mortar projected gap $\tilde{g}_A$ of node A:

$$\tilde{g}_A = \sum^{seg} \tilde{g}_A^{seg}, \tag{5.130}$$

Initialize: set intitial time step number $(n = 0)$ and initial conditions $\left(\mathbf{d}_0; \dot{\mathbf{d}}_0 \Rightarrow \ddot{\mathbf{d}}_0\right)$

Loop over all time steps $(n_T = T/\Delta t)$

Initialization $\mathcal{A}_l$ and $\mathcal{I}_l$; $(l = 1)$ with $S = \mathcal{A}_l \cup \mathcal{I}_l$ and $\mathcal{A}_l \cap \mathcal{I}_l = \emptyset$

Loop over the active set strategy

Predictor step $(k = 0)$

$\mathbf{K}_T^{eff}(\mathbf{d}_{n+1}^0)$; $\mathbf{f}^{eff}(\mathbf{d}_{n+1}^0)$ (2.133);(2.148) and (2.134);(2.149)

Basis transformation

$\mathbf{K}_T^{eff}(\mathbf{d}_{n+1}^0) \rightarrow \hat{\mathbf{K}}_T^{eff}(\mathbf{d}_{n+1}^0)$; $\mathbf{f}^{eff}(\mathbf{d}_{n+1}^0) \rightarrow \hat{\mathbf{f}}^{eff}(\mathbf{d}_{n+1}^0)$ (5.125)

Modify the effective incremental structural equation

$\hat{\mathbf{K}}_T^{eff,mod}(\mathbf{d}_{n+1}^0)$; $\hat{\mathbf{f}}^{eff,mod}(\mathbf{d}_{n+1}^0)$ (5.129)

$$\Delta\mathbf{d}_{n+1,\sum}^0 = \left(\hat{\mathbf{K}}_T^{eff,mod}\right)^{-1} \hat{\mathbf{f}}^{eff,mod}(\mathbf{d}_{n+1}^0)$$

$$\mathbf{d}_{n+1}^1 = \mathbf{d}_{n+1}^0 + \Delta\mathbf{d}_{n+1,\sum}^0$$

Set up $k = 1$

Newton-Raphson correction iteration:

$\mathbf{K}_T^{eff}(\mathbf{d}_{n+1}^k)$; $\mathbf{f}^{eff}(\mathbf{d}_{n+1}^k)$ (2.133);(2.148) and (2.134);(2.149)

Basis transformation

$\mathbf{K}_T^{eff}(\mathbf{d}_{n+1}^0) \rightarrow \hat{\mathbf{K}}_T^{eff}(\mathbf{d}_{n+1}^0)$; $\mathbf{f}^{eff}(\mathbf{d}_{n+1}^0) \rightarrow \hat{\mathbf{f}}^{eff}(\mathbf{d}_{n+1}^0)$ (5.125)

Modify the effective incremental structural equation

$\hat{\mathbf{K}}_T^{eff,mod}(\mathbf{d}_{n+1}^0)$; $\hat{\mathbf{f}}^{eff,mod}(\mathbf{d}_{n+1}^0)$ (5.129)

$$\Delta\mathbf{d}_{n+1}^k = \left(\hat{\mathbf{K}}_T^{eff,mod}\right)^{-1} \hat{\mathbf{f}}^{eff,mod}(\mathbf{d}_{n+1}^k)$$

$$\Delta\mathbf{d}_{n+1,\sum}^k = \Delta\mathbf{d}_{n+1,\sum}^{k-1} + \Delta\mathbf{d}_{n+1}^k$$

$$\mathbf{d}_{n+1}^{k+1} = \mathbf{d}_{n+1}^0 + \Delta\mathbf{d}_{n+1,\sum}^k$$

$\Delta(\bullet)_{n+1,\sum}^k$: Sum of incremental change of $(\bullet)$ till the end of iteration k of time step t_{n+1}

$$\Delta\mathbf{d}_{n+1}^{Sk} = [\Delta\mathbf{d}_{n+1}^k] + \hat{\mathbf{M}}_{n+1}^k \Delta\mathbf{d}_{n+1}^{Mk} \quad (5.119)$$

$$\Delta\mathbf{d}_{n+1,\sum}^{Sk} = \Delta\mathbf{d}_{n+1,\sum}^{Sk-1} + \Delta\mathbf{d}_{n+1}^{Sk}$$

$$\mathbf{d}_{n+1}^{Sk+1} = \mathbf{d}_{n+1}^{S0} + \Delta\mathbf{d}_{n+1,\sum}^{Sk}$$

$\Leftarrow$ Set up $k = k + 1$ until convergence

Determine $\mathcal{A}_{l+1}$ and $\mathcal{I}_{l+1}$; $\mathbf{z} = \mathbf{D}_S^{-1}\mathbf{f}_S^{eff}$ (5.128)

$$\mathcal{A}_{l+1} := \left\{A \in S; z_{A_N}^l + [\Delta\tilde{d}_{n+1}^k]_A^l + (\tilde{g}_{n+1}^k)_A^l > 0\right\},$$

$$\mathcal{I}_{l+1} := \left\{A \in S; z_{A_N}^l + [\Delta\tilde{d}_{n+1}^k]_A^l + (\tilde{g}_{n+1}^k)_A^l \leq 0\right\}.$$

$\Leftarrow$ IF $\mathcal{A}_{l+1} \neq \mathcal{A}_l$ or $\mathcal{I}_{l+1} \neq \mathcal{I}_l$ Set up $l = l + 1$

Update change of nodal coordinate after convergence $\mathbf{d}_{n+1} = \mathbf{d}_{n+1}^{k+1}$

$\dot{\mathbf{d}}_{n+1}(\mathbf{d}_{n+1}), \ddot{\mathbf{d}}_{n+1}(\mathbf{d}_{n+1})$ (2.121), (2.122)

$\Leftarrow$ Set up $n = n + 1$ until $n + 1 = n_T$

Figure 5.23: Numerical solution algorithm of IBVP for elastodynamcis in contact problems between two deformable bodies.

where the contribution from a mortar segment *seg* is defined by

$$\tilde{g}_A^{seg} = \mathbf{n}_A \cdot \int_{\gamma_c^{seg}} \phi_A^{(1)} \left(\boldsymbol{\theta}^{(1)}(\mathbf{X})\right) \left(\sum_{D=1}^{n_c^s} N_D^{(1)} \left(\boldsymbol{\theta}^{(1)}(\mathbf{X})\right) \mathbf{d}_D^{(1)}(t) - \sum_{E=1}^{n_c^m} N_E^{(2)} \left(\boldsymbol{\theta}^{(2)}(\bar{\mathbf{Y}})\right) \mathbf{d}_E^{(2)}(t) \right) d\gamma \quad (5.131)$$

with γ_c^{seg} being the contact (integration) boundary for each segment. To perform numerical integration of $\tilde{g}_A^{seg}$, a segment *seg* must be parameterized by $\eta \in [-1,1]$ as described in Figure 5.13(b), whereas the mapping between η for each mortar segment to $\xi^{(\alpha)}$ on slave and master contact boundaries is given in eq. (5.79). The numerical integration of eq. (5.131) with the gauss integration rule is accomplished by

$$\tilde{g}_A^{seg} \approx \mathbf{n}_A \cdot \left[\sum_{g=1}^{n_g} w_g \phi_A^{(1)} \left(\xi^{(1)}(\eta_g)\right) \left[\sum_{D=1}^{n_c^s} N_D^{(1)} \left(\xi^{(1)}(\eta_g)\right) \mathbf{d}_D^{(1)} - \sum_{E=1}^{n_c^m} N_E^{(2)} \left(\xi^{(2)}(\eta_g)\right) \mathbf{d}_E^{(2)} \right] j_{seg}(\eta_g) \right] \quad (5.132)$$

with η_g being the position of an integration point in the parametric space η of a mortar segment. Similar to eq. (5.81), $j_{seg}(\eta_g)$, evaluated at each integration point η_g, is the determinant of the mapping from the parametric space of a mortar segment η onto the physical space of the corresponding slave contact element $\mathbf{x}_e^{(1)^h} = \varphi_t^{(1)^h}(\mathbf{X}_e)$ to which the integration boundary γ_c^{seg} of a mortar segment belongs (see Figure 5.13(b)). Note that subscript e denotes the corresponding slave contact element of the mortar segment. A close form of j_{seg} in case of 2D linear contact element is given in eq. (5.82).

Alternatively, $(\sum_{D=1}^{n_c^s} N_D^{(1)}(\boldsymbol{\theta}^{(1)}(\mathbf{X}))\mathbf{d}_D^{(1)}(t) - \sum_{E=1}^{n_c^m} N_E^{(2)}(\boldsymbol{\theta}^{(2)}(\bar{\mathbf{Y}}))\mathbf{d}_E^{(2)}(t))$ in eq. (5.131) representing the physical gap field within a mortar segment $\mathbf{g}^{seg}$ can be pre interpolated by shape functions within the segment via

$$\mathbf{g}^{seg} \approx \sum_{i=1}^{n_{pt}^{seg}} N_i g_i, \quad (5.133)$$

with n_{pt}^{seg} being the number of interpolation points for a mortar segment, e.g. n_{pt}^{seg}=2 for a mortar segment with 2D linear shape functions:

$$\mathbf{g}^{seg} \approx \frac{1}{2}(1-\eta)\mathbf{g}_a^{seg} + \frac{1}{2}(1+\eta)\mathbf{g}_b^{seg} \quad \text{with} \quad \begin{cases} \mathbf{g}_a^{seg} = \varphi_t^{(1)}(\mathbf{X}_a) - \varphi_t^{(2)}(\bar{\mathbf{Y}}(\mathbf{X}_a)), \\ \mathbf{g}_b^{seg} = \varphi_t^{(1)}(\mathbf{X}_b) - \varphi_t^{(2)}(\bar{\mathbf{Y}}(\mathbf{X}_b)), \end{cases} \quad (5.134)$$

where vectors $\mathbf{g}_a^{seg}$ and $\mathbf{g}_b^{seg}$ are gap vectors at the start and end points, denoted by subscript a and b, respectively, of a mortar segment *seg* which is parameterized by $\eta \in [-1,1]$ (see Figure 5.13(b)). With the help of eq. (5.134), $\tilde{g}_A^{seg}$ in eq. (5.131) with its numerical integration in eq. (5.132) can be written via

$$\tilde{g}_A^{seg} = \mathbf{n}_A \cdot \int_{\gamma_c^{seg}} \phi_A^{(1)} \left(\boldsymbol{\theta}^{(1)}(\mathbf{X})\right) \mathbf{g}^{seg} d\gamma \approx \mathbf{n}_A \cdot \left[\sum_{g=1}^{n_g} w_g \phi_A^{(1)} \left(\xi^{(1)}(\eta_g)\right) \mathbf{g}^{seg}(\eta_g) j_{seg}(\eta_g) \right]. \quad (5.135)$$

Three dimensional problems

Similar to that of the two dimensional problem in the previous section, the evaluation of the mortar gap for a three dimensional case relies on the definition of mortar segments on the projected plane p (see Figure 5.16) introduced in section 5.4.2. The mortar projected gap $\tilde{g}_A$ of node $A \in S$ in eq. (5.114) is evaluated in the similar manner as the coupling mortar integrals $n_{AC}^{(2)}$ in eq. (5.90). Hence, the gauss integration rule is performed within each triangular pallet pa to approximate the physical gap function between the discrete slave contact boundary $\gamma_c^{h(1)}$ and triangular pallet pa on one hand, and between the triangular pallet pa and the discrete master contact boundary $\gamma_c^{h(2)}$ on the other hand. Then both results at a corresponding position on the pallet pa are combined to form the physical gap between $\gamma_c^{h(1)}$ and $\gamma_c^{h(2)}$ at that position. Then summing up all contributions from each pallet yields the mortar projected gap $\tilde{g}_A$ of node A:

$$\tilde{g}_A = \sum^{seg} \tilde{g}_A^{seg}; \quad \tilde{g}_A^{seg} = \sum_{pa=1}^{n_{pa}} \tilde{g}_A^{pa}, \tag{5.136}$$

where the contribution from a triangular pallet pa is defined by

$$\tilde{g}_A^{pa} = \mathbf{n}_A \cdot \int_{\gamma_c^{pa}} \phi_A^{(1)} \left(\boldsymbol{\theta}^{(1)}(\mathbf{X})\right) \left(\sum_{D=1}^{n_c^s} N_D^{(1)} \left(\boldsymbol{\theta}^{(1)}(\mathbf{X})\right) \mathbf{d}_D^{(1)}(t) - \sum_{E=1}^{n_c^m} N_E^{(2)} \left(\boldsymbol{\theta}^{(2)}(\bar{\mathbf{Y}})\right) \mathbf{d}_E^{(2)}(t) \right) d\gamma \tag{5.137}$$

with γ_c^{pa} being the contact (integration) boundary for each pallet. To perform numerical integration of $\tilde{g}_A^{pa}$, the parameterization of a segment pa is described in eq. (5.88) while the mapping between a position on the triangular pallet $\mathbf{x}_{pa}(\boldsymbol{\xi}_g) \in \gamma$ and the corresponding slave surface coordinate $\boldsymbol{\theta}_g^{(1)}$ or master surface coordinate $\boldsymbol{\theta}_g^{(2)}$ is provided in eq (5.89). Within a pallet pa, the physical gap field of a mortar segment $\mathbf{g}^{seg} = (\sum_{D=1}^{n_c^s} N_D^{(1)}(\boldsymbol{\theta}^{(1)}(\mathbf{X}))\mathbf{d}_D^{(1)}(t) - \sum_{E=1}^{n_c^m} N_E^{(2)}(\boldsymbol{\theta}^{(2)}(\bar{\mathbf{Y}}))\mathbf{d}_E^{(2)}(t))$ in eq. (5.137) is interpolated by shape functions:

$$\mathbf{g}^{pa} \approx \sum_{i=1}^{3} N_i(\boldsymbol{\xi}) g_i \tag{5.138}$$

by the triangular shape function N_i given in eq. (5.88). Finally, with the help of eq. (5.138), the contribution $\tilde{g}_A^{pa}$ of a pallet pa on the mortar projected gap for node $A \in S$ in eq. (5.137) can be evaluated numerically by

$$\tilde{g}_A^{pa} = \mathbf{n}_A \cdot \int_{\gamma_c^{pa}} \phi_A^{(1)} \left(\boldsymbol{\theta}^{(1)}(\mathbf{X})\right) \mathbf{g}^{pa} d\gamma \approx \mathbf{n}_A \cdot \left[\sum_{g=1}^{n_g} w_g \phi_A^{(1)} \left(\boldsymbol{\theta}^{(1)}(\boldsymbol{\xi}_g)\right) \mathbf{g}^{pa}(\boldsymbol{\xi}_g) j_{pa}(\boldsymbol{\xi}_g) \right]. \tag{5.139}$$

5.6 Energy conservation for time integration

For dynamic contact-impact analysis, interactions between the numerical treatments to enforce contact constraints and behaviors of the temporal integration schemes such as those

mentioned in section 2.3.4 must be carefully considered regarding numerical accuracy and stability. To achieve this goal, the energy-momentum paradigm can be adapted to the numerical approximation of contact-impact problems for a conservative system, e.g. frictionless impact of two bodies without applied external forces. The benefits are observable by the conservation of energy, discrete linear and angular momentum. For further discussion, interested readers may look in the textbook by Laursen [Lau02].

In such problems, constraints can be introduced to the system at arbitrarily unknown spaces and times. A desirable treatment must not introduce additional energy into the system under all conditions of contact. Although the dissipative contact treatment scheme has benefits for system stability, it places limitations on the form of contact constraints which can be enforced on contact interfaces.

This section provides information for a temporally discontinuous *velocity update* scheme which is used in conjunction with an energy-momentum algorithm framework. The origin for this method can be dated back to Laursen and Love [LL02] who considered the discontinuity in time of impact phenomena. The improved integration algorithm proposed for frictionless contact in that work preserves the stability properties of exact energy and momentum conservation without inevitable violation of the impenetrability contact constraints. Whereas the discontinuous velocity update $\dot{\mathbf{d}}^c$, motivated by the discrete force and velocity waves propagating away from the contact interface into each body, is crucial for the analytical solution, such a consideration is absent from many numerical dynamic contact treatments. As a result, the introduced discrete contact velocity provides an algorithmic treatment which locally ensures exact conservation while the choice of constraints treatment is intact. Within the interested time interval $[t_n, t_{n+1}]$, impact is assumed to be taken place at the instant t_{n+c} as shown in Figure 5.24. The discrete velocity update is treated as a post convergence update in the (smooth) system velocities at the end of each time step $\dot{\mathbf{d}}^s_{n+1}$ such that the updated velocity at the end of time step $\dot{\mathbf{d}}_{n+1}$ is expressed by

$$\dot{\mathbf{d}}_{n+1} = \dot{\mathbf{d}}^s_{n+1} + \dot{\mathbf{d}}^c \tag{5.140}$$

There is no direct influence on the nonlinear solution method of the system of equations. As a result, we obtain a robust implicit algorithmic treatment for dynamic frictionless contact, suitable for large deformations. The generalized velocity update formulation for the GEN_α in section 2.3.4.1 and GEMM in section 2.3.4.2 is recently presented by Hartmann [HBRW07] by replacing $\dot{\mathbf{d}}^s_{n+1}$ in eq. (5.140) with eq. (2.121) , viz.

$$\dot{\mathbf{d}}_{n+1} = \frac{\gamma}{\beta\Delta t}(\mathbf{d}_{n+1} - \mathbf{d}_n) - \frac{\gamma-\beta}{\beta}\dot{\mathbf{d}}_n - \frac{\gamma-2\beta}{2\beta}\Delta t\ddot{\mathbf{d}}_n + \dot{\mathbf{d}}^c. \tag{5.141}$$

Inserting eq. (5.141) into the equation of motion in eq. (2.111) with the help of eq. (2.123), one obtains the equation of motion incorporating the discrete velocity update via

$$\mathbf{G}(\mathbf{d}_{n+1}) \equiv \mathbf{M}\left[\ddot{\mathbf{d}}_{n+1-\alpha_m}(\ddot{\mathbf{d}}_{n+1}(\mathbf{d}_{n+1})) - \frac{1-\alpha_m}{\gamma\Delta t}\dot{\mathbf{d}}^c\right] + \mathbf{f}^{int}(\mathbf{d}_{n+1-\alpha_f}(\mathbf{d}_{n+1})) - \mathbf{f}^{ext}_{n+1-\alpha_f} = \mathbf{0}. \tag{5.142}$$

Appendix B.4 introduces the global conservation of the total energy for a discrete system under interest whereas B.5 clarifies a procedure to determine the discrete contact velocity $\dot{\mathbf{d}}^c$ to achieve an energy conserving discrete formulation.

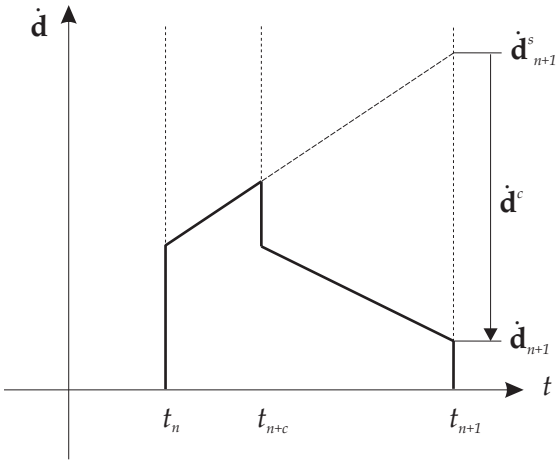

Figure 5.24: Illustration for the velocity jump at contact interfaces of a one-dimension impact.

Although, this algorithm has the advantage of energy conservation, it is not invariant under rotations. As a result, the algorithmic conservation of angular momentum is not guaranteed as mentioned in Hesch and Betsch [HB08]. Even nowadays, the development of energy-momentum schemes for mortar-based contact formulations under large deformation is still an active research field to find innovative energy-momentum algorithms.

5.7 Numerical examples

Within this section, a bunch of benchmark examples are conducted to verify the implemented code and evaluate the efficiency of the chosen model. First, a two-dimensional contact patch test is performed to answer whether the mortar-based contact formulation can recover solutions of low polynomial order. Then, the second example is the classical two-dimensional Hertzian contact problem. The third one is dedicated to a two-dimensional contact problem of a thin-walled ring with a rigid obstacle. The section is closed with a three dimensional contact problem of an inflatable sphere with a deformable rectangular membrane. Bilinear quadrilateral membrane elements with the St. Venant-Kirchoff material law from section 2.2.3 are employed in all subsequent examples.

5.7.1 A Contact patch test

As a prerequisite, the desired mortar-based contact formulation must be able to capture the low-order polynomial solutions, i.e. the contact pressure between two bodies can be properly transferred at the contact interface. In particular, if a spatially constant contact pressure is exactly transmitted from one body to another body regardless of the conformity between the meshes on either side of the contact interface, the employed contact formulation passes the patch test as described by Laursen [Lau02]. Based on the work of Simo [SWT85], the benchmark patch test example in Yang [Yan06] as well as Hartmann [Har07] is performed to examine the implementation within this work. The thematic configuration of the problem

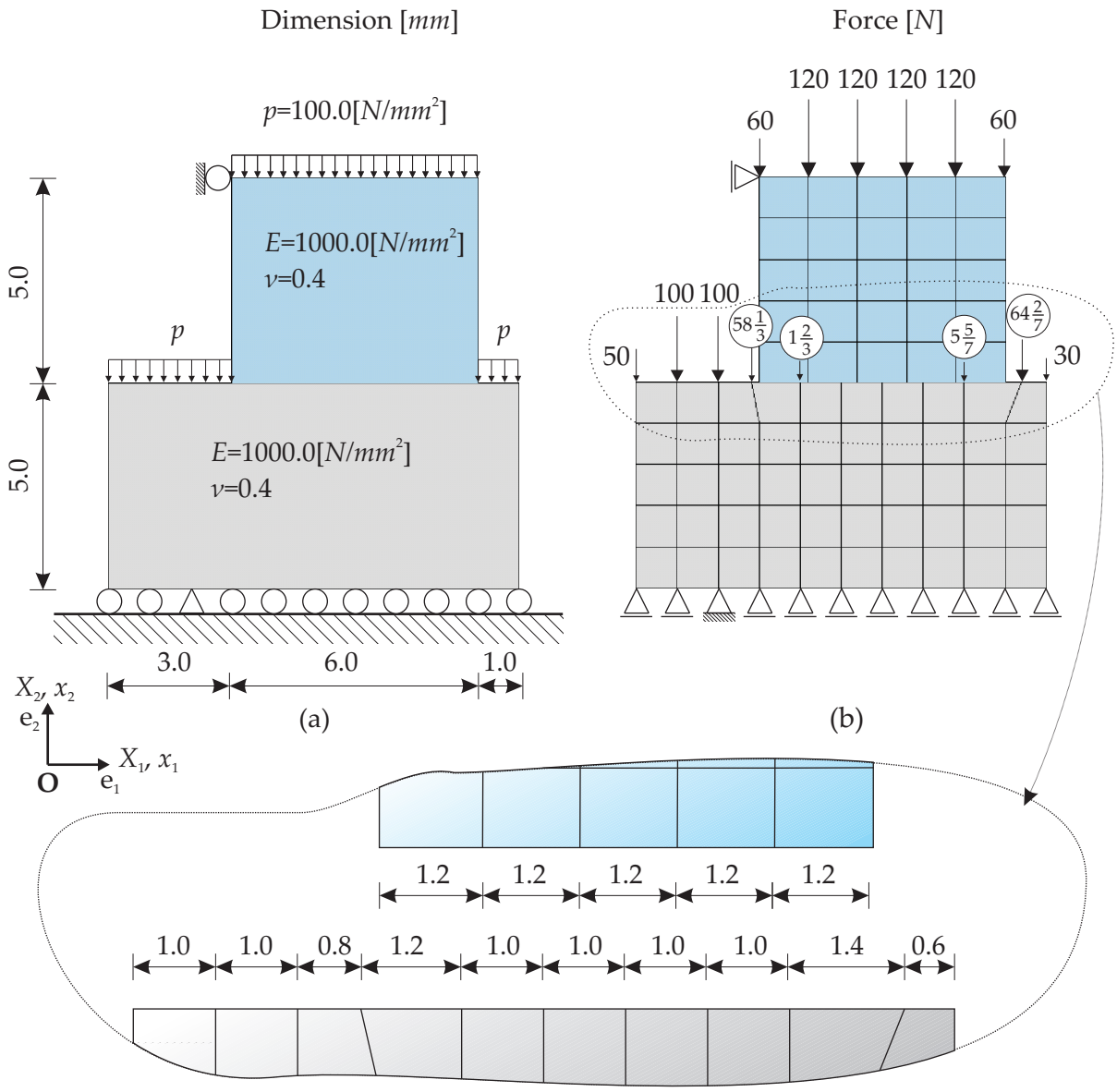

Figure 5.25: Illustration of the contact patch test example: (a) configuration and (b) mesh layout and consistent nodal loads $[N]$.

is given with the unit of *mm* in Figure 5.25(a) which corresponds to an elastic punch being pressed onto a smooth elastic foundation where the coefficient of friction is null ($\mu = 0$). A uniform, consistent load $p = 100.0\ N/mm^2$ is applied to the upper boundaries of both the punch and the foundation to introduce a constant stress over the whole domain of both bodies. Note that the applied distributed load leads to constant stress distribution over the whole domain in case that both the punch and foundation are modeled as a single domain. Therefore, the mortar-based contact formulation will pass the patch test, if and only if the stress distribution in case of two separated domains is similar to that of the single domain, i.e. the constant stress distribution over the whole domain of both bodies.

Both the punch and the foundation are modeled with an isotropic linear elastic material

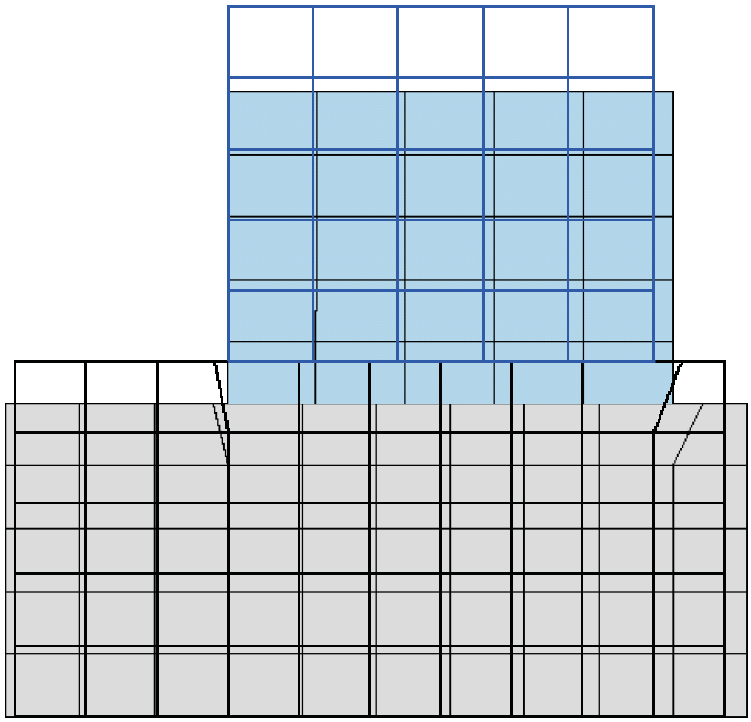

Figure 5.26: Deformed versus undeformed configuration of the contact patch test.

with the elastic modulus $E = 1000\ N/mm^2$, Poisson's ratio $\nu = 0.4$ and thickness of 1 mm. This example is simulated with 75 bilinear quadrilateral membrane elements under the state of plane stress. Selected to maintain the state of constant stress distribution, mesh layout as well as consistent nodal forces are illustrated in Figure 5.25(b). The deformed configuration is plotted along with the undeformed one in Figure 5.26 where one can observe that both bodies have an identical vertical deformation. Besides, results of this example show that the constant pressure applied onto the punch is transmitted to the elastic foundation in form of the constant stress distribution with the magnitude of 100.0 N/mm^2.

We can conclude from this example that the employed mortar-based contact formulation passes the contact patch test with the nonconforming mesh on the contact interface. Inevitably, the integration rule as well as number of integration points affect the accuracy of the solution. Within this example, the simplest two point Gauss rule is chosen for the numerical integration of linear shape functions in each mortar segment, while the discussion about an optimal number of integration point is still open for further investigation. For interested readers, an extensive study by Fischer [Fis05] is noteworthy.

Table 5.4: Mesh details for two test cases of the Hertzian contact example.

Test case	I	II	III	$\sum Elements$
(1)	10×10	40×10	40×10	1,000
(2)	25×15	80×15	80×25	3,950

5.7.2 Hertzian contact problem

In order to investigate the accuracy of the implemented contact formulation, the Hertzian linear elastic contact problem [Her81] is conducted in this example. In Figure 5.27, a parallel half cylinder with Radius $R = 8\ mm$ with infinite length along the cylindrical axis is resting on a rigid obstacle laying beneath, while a constant pressure $p = 0.625\ N/mm^2$ is applied at the upper side of the half cylinder. Geometry, material data and load condition are given in Figure 5.27(a). Indeed, the analytical solution is available only for the infinitesimal deformation, therefore, a very small applied pressure p is chosen in the similar manner to that given in Yang [Yan06]. Based on Kikuchi and Oden [KO88], Hartmann [Har07] presented the analytical contact pressure solution such that the induced pressure at the contact interface between the half cylinder and the rigid obstacle can be described by

$$\mathbf{t}_c = \frac{4pR}{\pi b^2}\sqrt{(b^2 - x^2)}, \tag{5.143}$$

which is calculated per unit length of the half cylinder, while $b = 2\sqrt{\frac{2pR^2(1-\nu^2)}{E\pi}} = 0.680641409\ mm$ stands for the effective width of the contact surface. The state of plane strain is adopted for simulations in this example with bilinear quadrilateral membrane elements. The layout of the meshes is shown in Figure 5.27(c) which is relatively fine to monitor the induced contact pressure, while corresponding design elements are shown in Figure 5.27(b). Two test cases are performed with different mesh refinement: 1,000 and 3,950 elements with details given in Table 5.4.

A comparison between the analytical solution and numerical result of nodal contact pressure is given in Figure 5.28 where a small difference is observable. A reason for this discrepancy is that the large deformation kinematics relation is used within this work, while the analytical solution is computed on the small deformation basis. Nevertheless, this difference can be subsided by mesh refinement. Moreover, Hartmann [Har07] showed that the interpolated field of the nodal contact pressure by the dual shape function has the sawtooth shape with a jump at the common node of two neighboring elements, whereas the linear shape functions yield a smooth continuous interpolated contact pressure field without the jump. Although, the mathematical proof insists that both of them have equivalent order of error, numerical results of the contact pressure reach the proximity of the analytical solution except for the end of contact region ($x \approx 0.680641409\ mm$) where a significant difference between them is recognized. This can be explained by the fact that the positions of discrete nodes, to which the consistent nodal contact forces by mortar integration are applied, are not exactly located at the end of the contact region. Therefore, a precise numerical result of contact stress within this region cannot be achieved unless the meshe in this region is extremely refined.

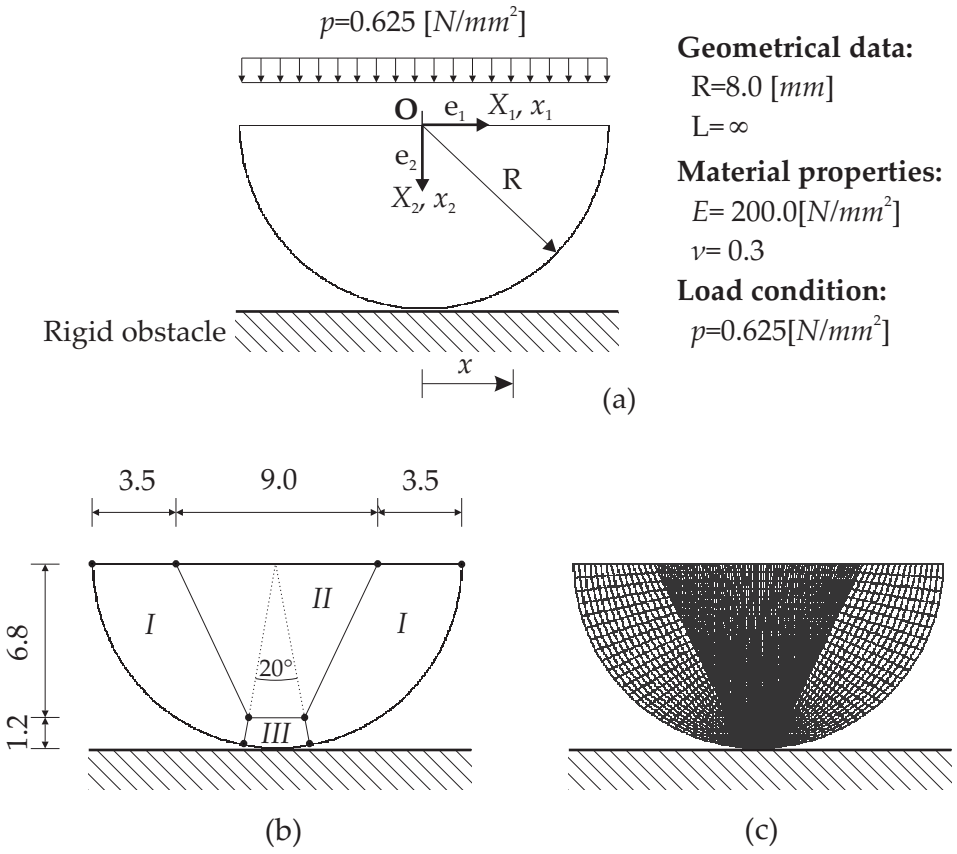

Figure 5.27: Illustration of the Hertzian contact example with (a) problem descriptions (b) design element and (c)finite element meshes.

5.7.3 Frictionless elastic ring impact

Time integration methods based on the assumption that velocity is a smooth function over time cannot deal with the abrupt change in the velocity as mentioned in appendix B.4. By exploring a rebound of a two-dimensional elastic ring from a rigid obstacle, this example demonstrates the loss in total energy due to jumps in velocity during impact. Moreover, influences of velocity update algorithm with the GEMM algorithm on the system solution is monitored while the spectral radius is defined at unity $\rho_\infty = 1$.

The example provides an insight into energy conservation of a system with potentially significant physical dissipation. Besides, its results show that an energy consistent algorithmic treatment stabilizes in a certain degree the computation without introducing numerical damping. The geometry and load condition for this example are given in Figure 5.29 which has different dimension to the similar type of example in Laursen [Lau02] and Hartmann [Har07]. An elastic ring is under a surface force $p(t)$, controlled by the time history given in Figure 5.29, in the clockwise angle of 45° from the x-axis to introduce the initial velocity before it reaches the rigid obstacle. This ring is modeled by 64 bilinear quadrilateral membrane elements with the mesh layout in Figure 5.29 under the state of plane stress and unit thickness. The computation is performed for 50 s with the time step size of 0.02 s. In Figure 5.30, the deformed state of the ring is plotted in a sequence of time $t \in [0, 50s]$,

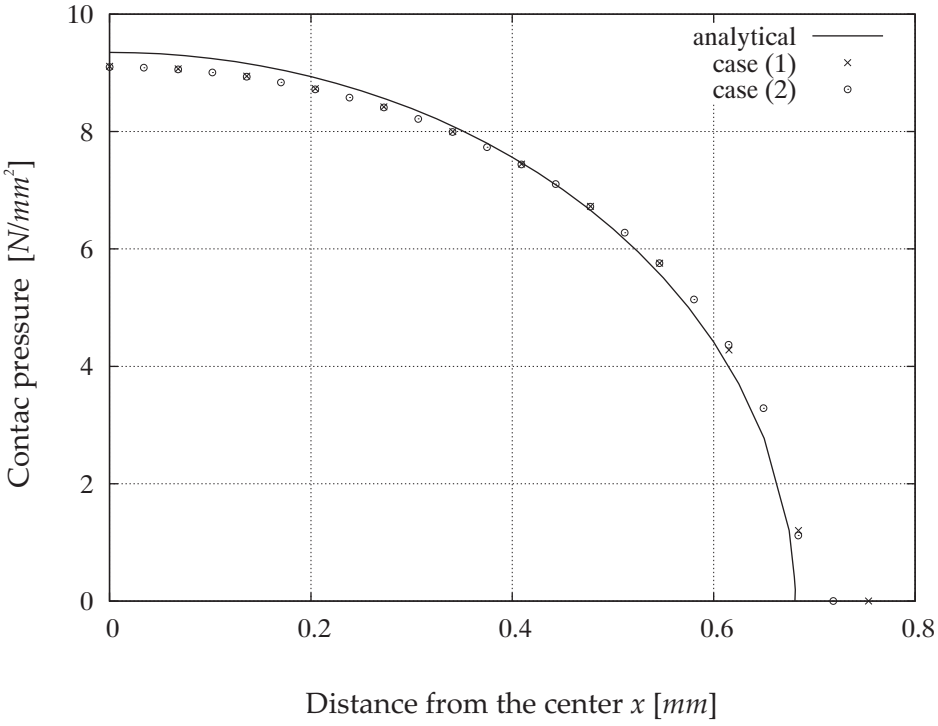

Figure 5.28: Comparison of the numerical result and the analytical solution of the nodal contact stress for the Hertzian contact example.

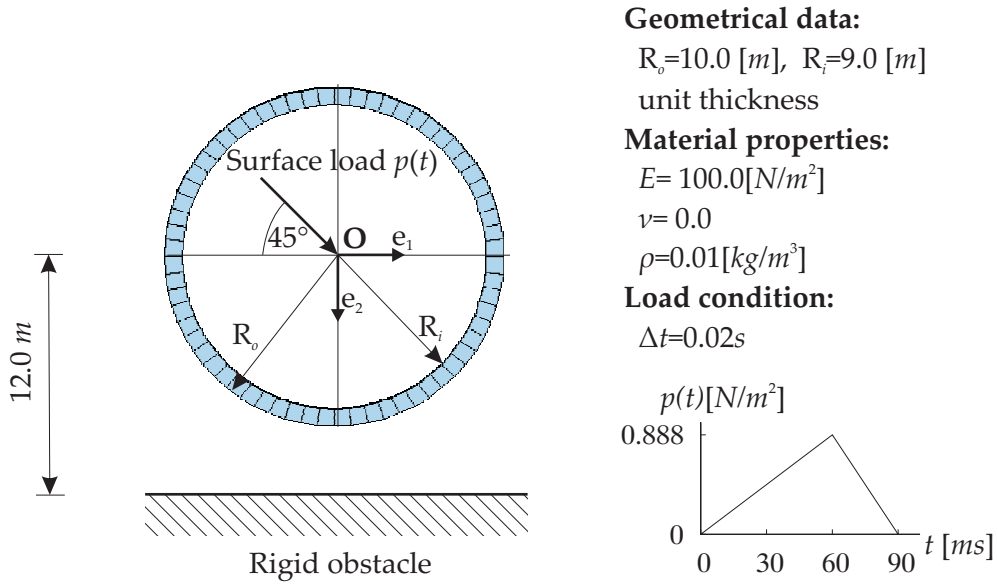

Figure 5.29: Geometry and load conditions for the impact of an elastic ring with a rigid wall.

while the plot of system energy is shown in Figure 5.31 for the time $t \in [0, 20s]$. Note that only the first 20 s, at which the contact takes place, is the point of interest, while the energy plot for $t \in [20, 50s]$, which is practically stationary, is not shown here. From Figure 5.31, the GEMM without numerical dissipation, i.e. unit spectral radius, in combination

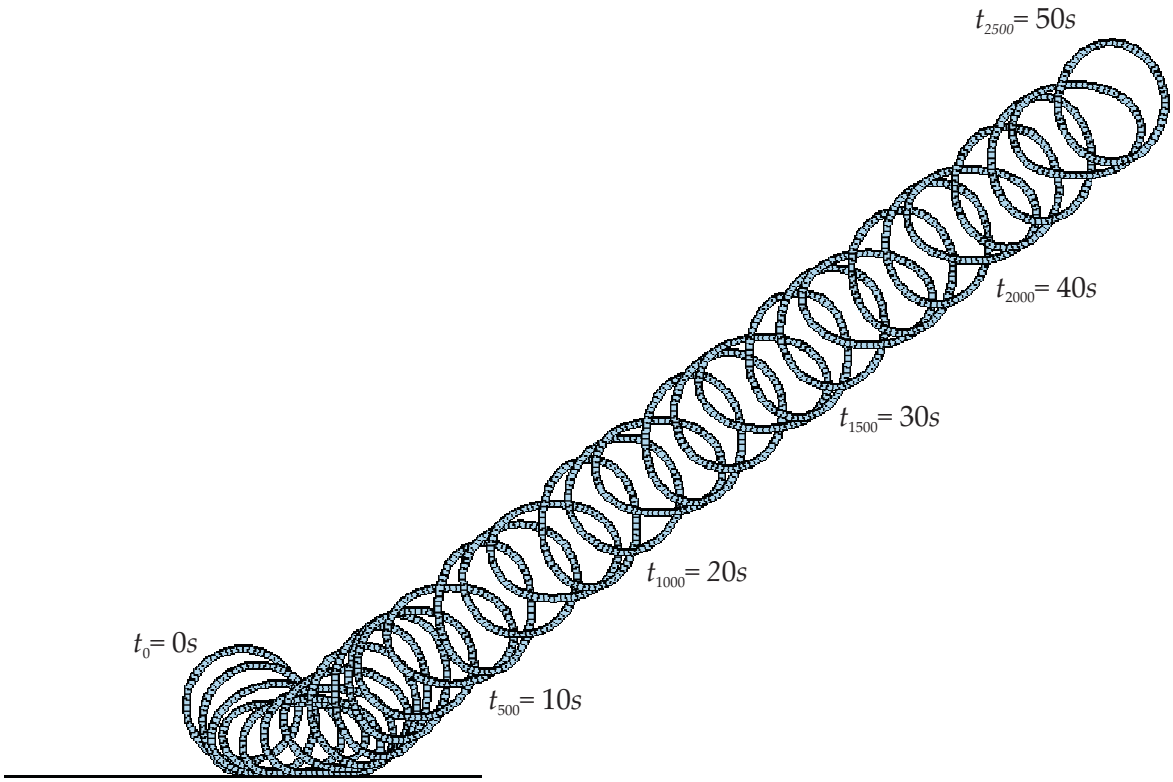

Figure 5.30: Illustration for the pre- and post-contact configurations of the elastic ring for the time $t \in [0, 50s]$ with the unity spectral radius $\rho_\infty = 1.0$.

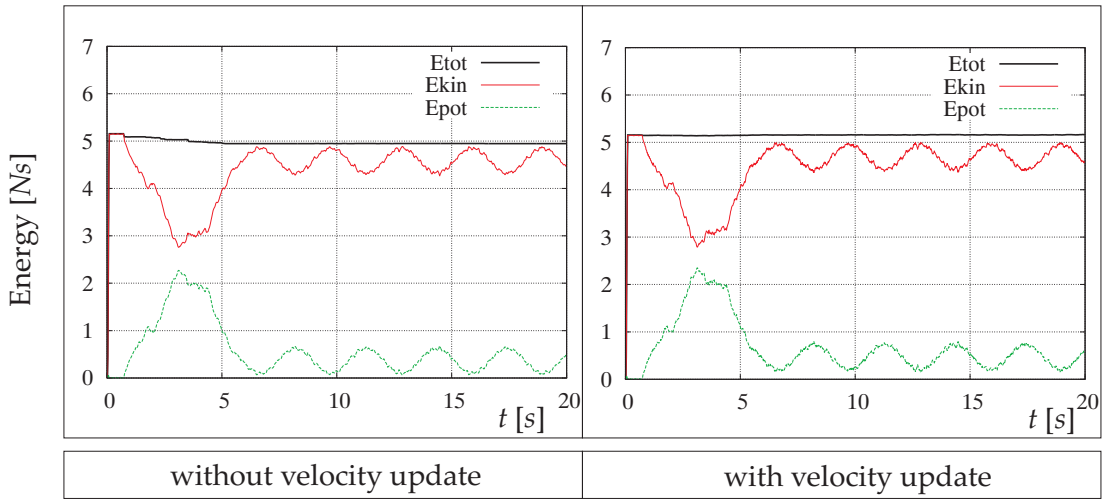

Figure 5.31: Illustration for geometry and load condition of the impact problem of an elastic ring with a rigid obstacle.

with the velocity update algorithm can conserve the total energy denoted by "Etot" whereas "Ekin" and "Epot" stand for kinetic and potential energy, respectively. In contrary, the same setting without the velocity update exhibits some loss in total energy at the magnitude of around 4%. This evidence informs that accuracy and reliability of the solution strongly de-

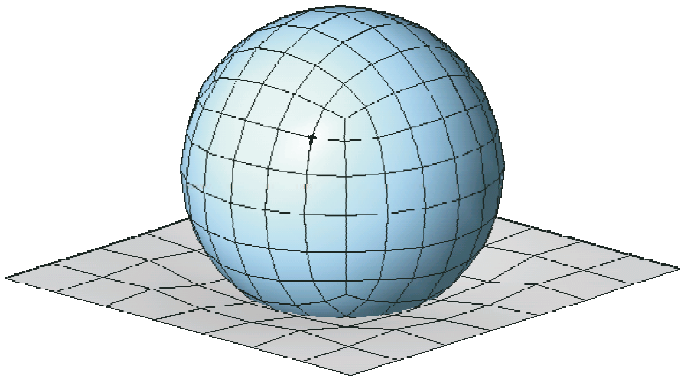

Figure 5.32: Illustration for impact problems of an inflatable ball and an elastic membrane.

pends on a suitable choice of the time integration method along with proper modifications to achieve the algorithmic treatment for energy conservation.

5.7.4 Three dimensional contact of an inflatable ball and an elastic membrane

This final example furthers an application of the mortar-based contact formulation for inflatable membranes in the three dimension as motivated in Figure 5.32. Three dimensional contact problems are much more complicated than the two dimensional contact problems since there are many parameters which must be taken into account, e.g. unique corresponding projection point of each contact node etc. Therefore, the aim of this example is to demonstrate beneficial possibilities to employ the mortar-based contact formula with the full three dimensional frictionless contact problem for inflatable membranes. Extensions towards frictional contact problems are expected for the future developments.

Figure 5.33 provides geometrical information and load conditions. Initially, the elastic ball with the initial radius R of 1.0 m is gradually inflated by the applied pressure pointing outward the ball surface during the first 4 time steps $t \in [0, 0.02s]$; $\Delta t = 5\ ms$ until the pressure magnitude reaches 4.5 N/m^2 while the ambient pressure is neglected $P_{amb} = 0$. Henceforth, the enclosed fluid pressure is controlled by the pneumatic model under the adiabatic state equation (Poisson's law) which is mentioned in section 4.2.3.1 with $\kappa = 1$ (Boyle's law). Within this example, the GEMM is used for time integration. Besides, the velocity update algorithm is activated for energy conservation in combination with the unit spectral radius $\rho_\infty = 1.0$ to guarantee the exact energy preservation. Then, a surface force $p(t)$, pointing towards the z-axis, is introduced over the whole surface of the ball. This surface force is controlled by the time history in Figure 5.33(a) to induce the initial velocity which drives the ball towards the flat elastic membrane beneath it whereas self-weight of the ball, the enclosed fluid inside the ball and the flat elastic membrane is neglected.

The inflatable ball is modeled by 96 bilinear quadrilateral membrane elements. The flat elastic membrane is modeled by 25 bilinear quadrilateral membrane elements with the isotropic pretension of 1.0 N/m^2. Both the regular mesh layout shown in Figure 5.33(b) and

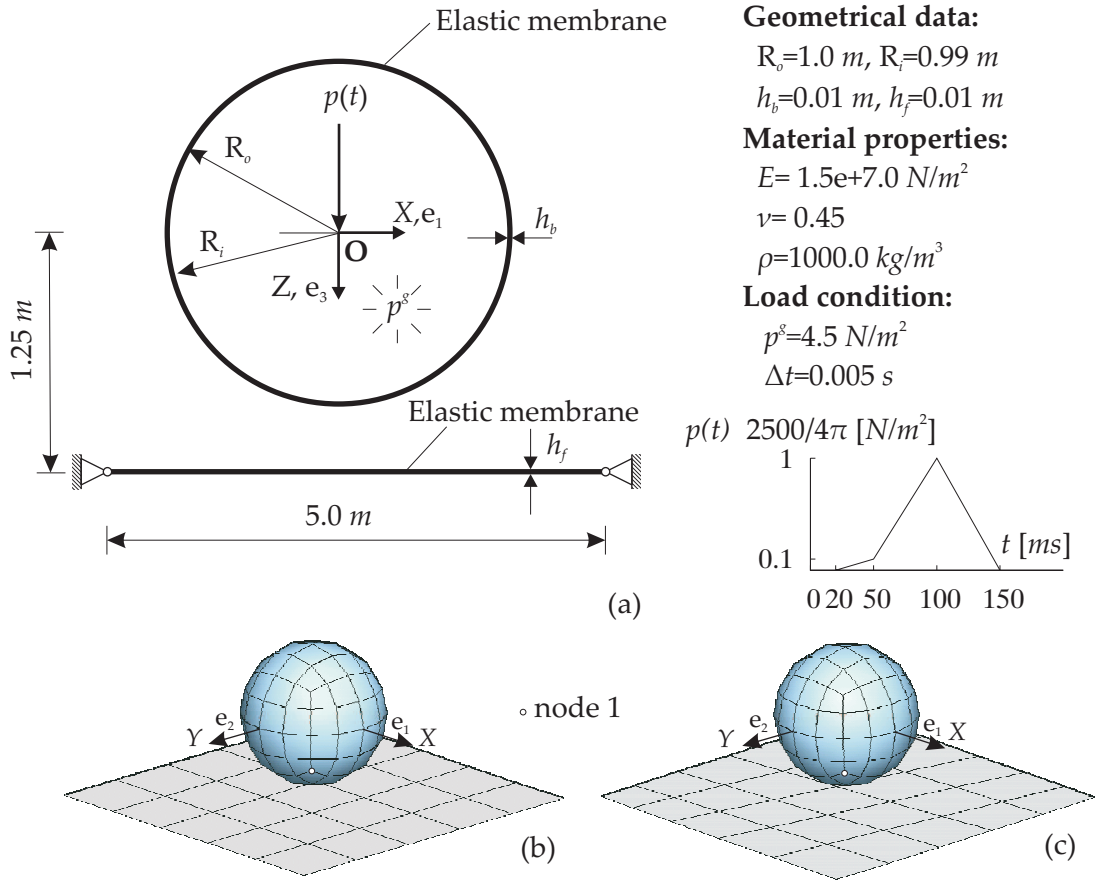

Figure 5.33: Illustration for (a) Geometry, material data and load condition of the inflatable ball and elastic membrane (b) regular mesh layout and (c) nonregular mesh layout.

nonregular mesh described in Figure 5.33(c) are investigated and the convergence performance of the employed contact formulation is investigated along with the bias of the mesh on computed results. This simulation was run with the time step size of $\Delta t = 5\ ms$. The computation is performed for 700 time steps at which the time reaches $t_{700} = 3.5\ s$. Furthermore, displacement, velocity and acceleration in the z-direction of the representative node 1 (see Figure 5.33(b) and (c)) are separately presented in Figures 5.35, 5.36 and 5.37, respectively.

Figure 5.34 captures a deformation sequence of the inflatable ball and elastic membrane with regular mesh at every 50 time steps. Because of the regular mesh layout at the contact interface, results of mortar integration are equivalently distributed to all active contact nodes on the slave side (the sphere), and thus, discrete contact tractions are introduced to the sphere in a rotational symmetric manner. This situation can be recognized by the post-contact rebound in the upright angle which is identical to the angle of attack of the ball. In case of the non-regular mesh, the rebound is quite similar to that of the regular mesh and is not plotted here. However, the mesh layout influences movements of both the ball and flat membrane in a certain degree as one can observe in Figure 5.35 where the z-displacement at node 1 in both cases are somehow different as well as the velocity and acceleration in

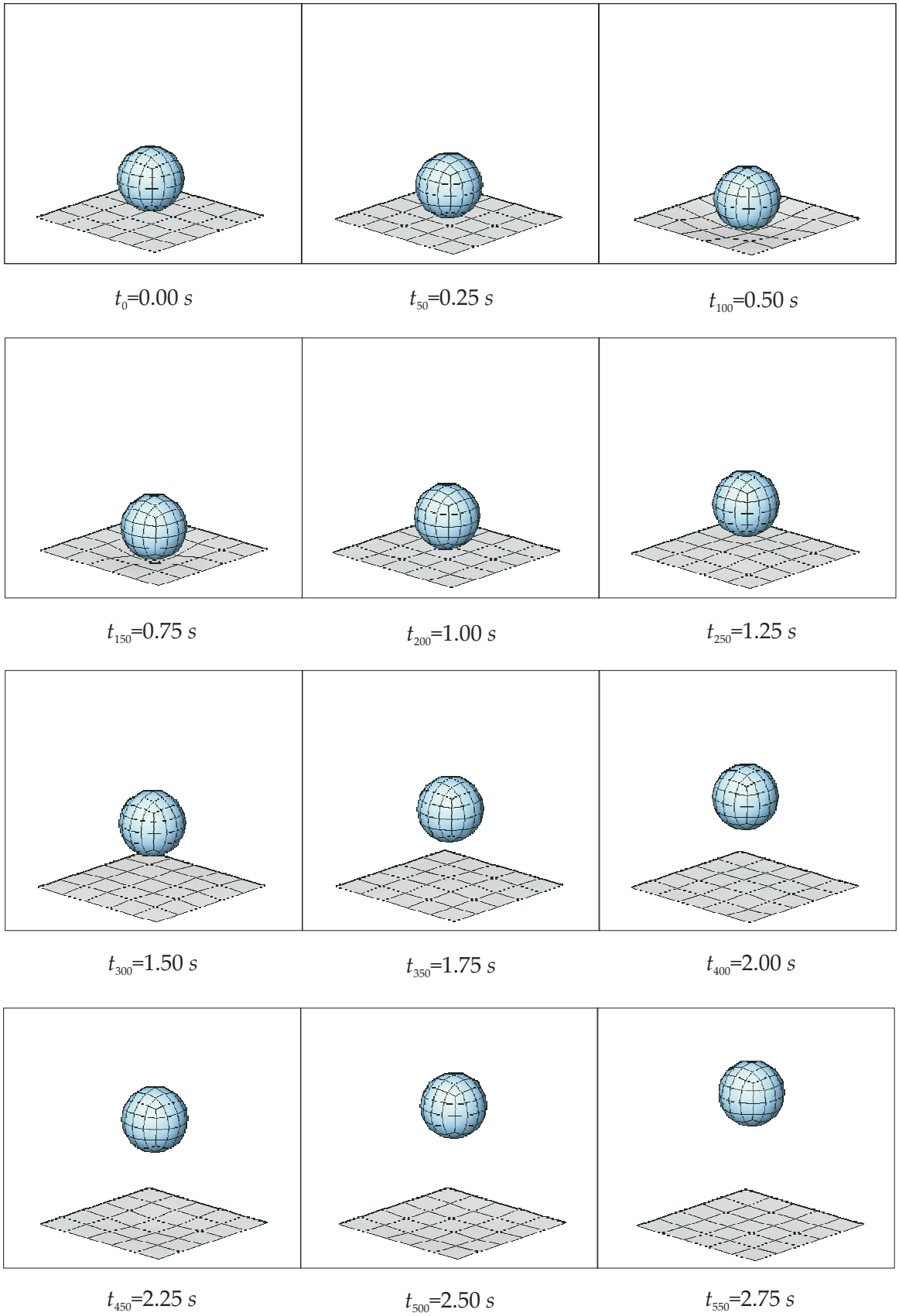

Figure 5.34: Deformation sequence in case of the elastic membrane with regular mesh.

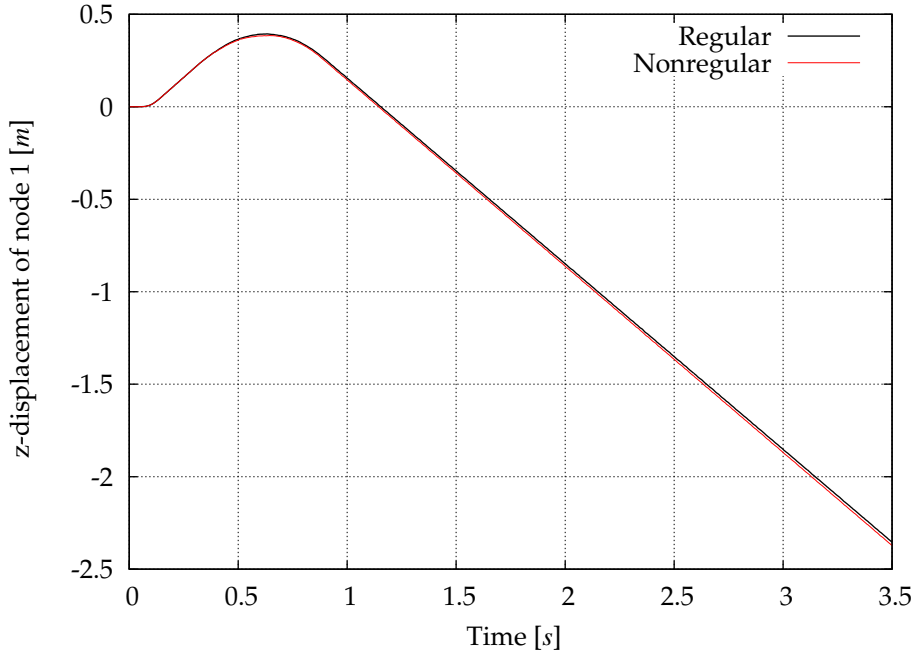

Figure 5.35: Displacement profile at node 1 for regular and nonregular meshes.

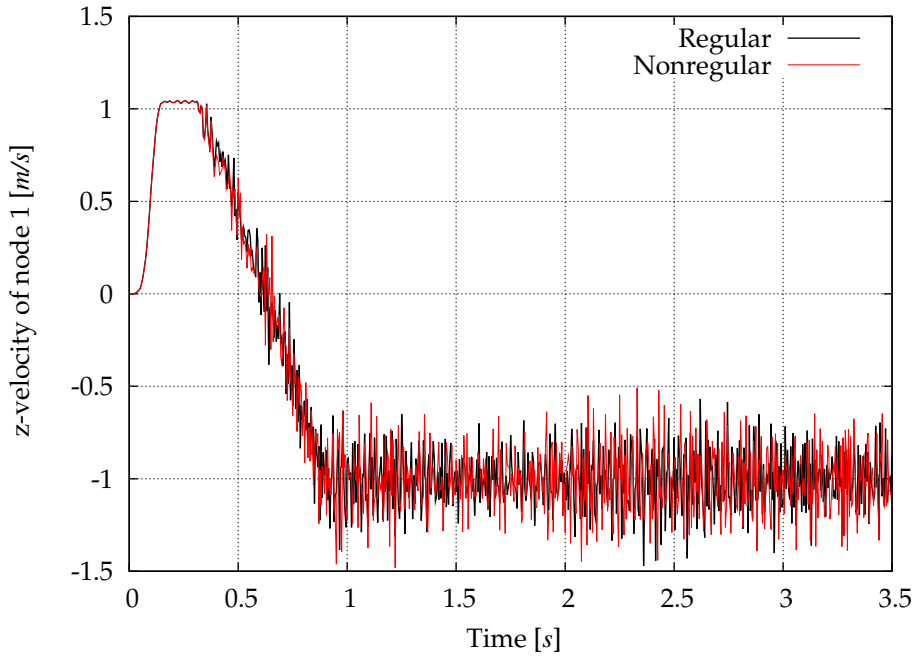

Figure 5.36: Velocity profile at node 1 for regular and nonregular meshes.

Figure 5.36 and 5.37, respectively. Such motion can be described by the fact that the non-regular meshes at the contact interface arbitrarily introduce the discrete contact tractions to each active contact nodes according to the integration domains related to each node. Thus, the discrete contact tractions on the slave side are not in a rotational symmetric form, which results in the different pathway of the post-contact rebound.

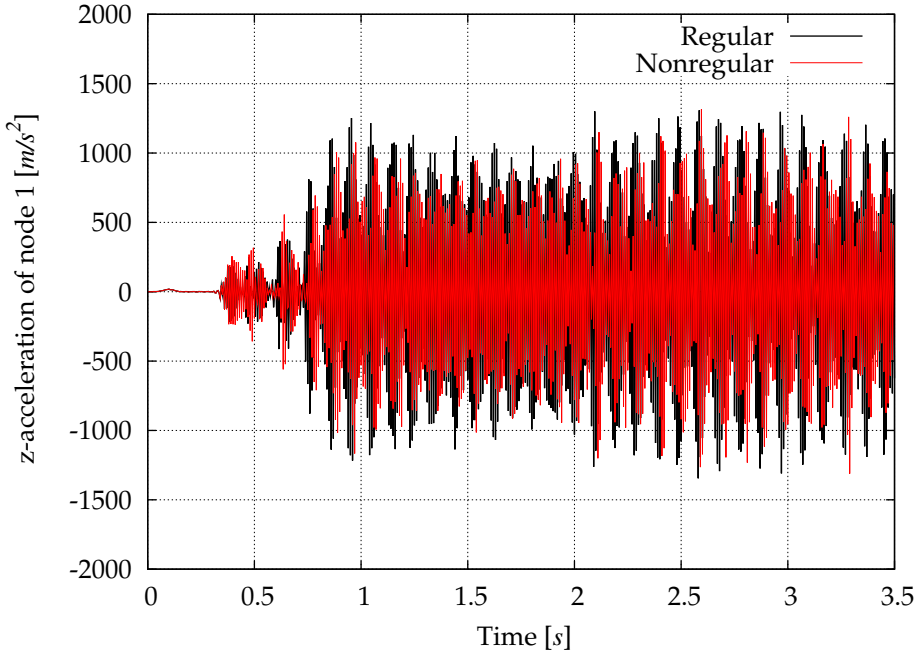

Figure 5.37: Acceleration profile at node 1 for regular and nonregular meshes.

Table 5.5: Displacement norm for the 3D contact problem of the inflatable ball and elastic membrane with regular mesh.

Iteration no.	Step76	Step100	Step125	Step150
1	0.61503E-04	0.77968E-04	0.14148E-03	0.15325E-03
2	0.38445E-05	0.48716E-05	0.84878E-05	0.93738E-05
3	0.24191E-06	0.30487E-06	0.53309E-06	0.58915E-06
4	0.15221E-07	0.19083E-07	0.33492E-07	0.37020E-07
5	0.95767E-09	0.11945E-08	0.21041E-08	0.23263E-08
6		0.10857E-09	0.13219E-09	0.12011E-09

These evidences highlight that mesh layout in the contact interface has a bias on the computed discrete contact tractions. With this information, the mesh within the contact interfaces must be handled with care for an acceptable accuracy, in particular, for three-dimensional problems. Moreover, Table 5.5 shows the convergence sequence for time steps $t_{76} = 0.38\ s, t_{100} = 0.5\ s, t_{125} = 0.625\ s, t_{150} = 0.75\ s$, respectively.

The velocity update loop performs well to conserve energy even in the three dimensional case. Furthermore, the overall computation possesses an acceptable rate of convergence in such the way that the incremental change in displacement is below the tolerance of 10^{-8} within 5-10 iterations for each time step during the instance of contact, whereas variation of the predefined active node set is around 1-5 times within a time step before the definite active node set for that time step is achieved.

However, this example is considered as an initial endeavor to combine the mortar-based

Table 5.6: Displacement norm for the 3D contact problem of the inflatable ball and elastic membrane with nonregular mesh.

Iteration no.	Step76	Step100	Step125	Step150
1	0.91449E-04	0.12582E-03	0.38157E-04	0.50485E-04
2	0.45246E-05	0.65769E-05	0.18265E-05	0.23422E-05
3	0.23792E-06	0.34466E-06	0.95122E-07	0.12202E-06
4	0.12507E-07	0.18055E-07	0.49535E-08	0.63558E-08
5	0.65744E-09	0.94584E-09	0.25795E-09	0.33105E-09

contact formulation with the algorithmic treatment of the deformation-dependent loads for inflatable membranes. Still, there are various open questions and many aspects require further developments for a generalized formulation with better performance and flexibility.

5.8 Summary

The mortar-based contact formulation for inflatable membranes is very challenging in various aspects, especially for highly curved contact surfaces. This formulation is superior to classical node-to-segment (NTS) schemes regarding robustness and numerical stability; it can readily pass through the difficulties at which NTS is unable to step over. Besides, it holds good potential for the highly nonlinear problems of large deformation contact.

Within this chapter, the efficiency of the mortar-based contact formulation with dual-shape functions is demonstrated for applications of inflatable membranes in both two- and three-dimensional contact problems. The derivation is given in details as well as various numerical examples are performed to validate the implementation and investigate its pros and contras. The investigations point out attractive properties of the mortar-based contact formulation for applications with inflatable membranes in various aspects, e.g. accuracy, efficiency, energy conservation, etc. The formulation is proven to have a good rate of convergence and it can pass the patch test for non-conforming meshes at the contact interface.

The discrete Lagrange multipliers can be condensed out of the system of equations by performing static condensation. The only unknowns of the system are displacement dofs $\mathbf{d}$. Thus, the size of system equations is unchanged throughout the computation in contrast to the traditional Lagrange multiplier method.

The GEMM is used for dynamic contact within this chapter due to its prominence as a stable time integration scheme, whereas numerical dissipation is controlled via the spectral radius ρ_∞ such that there is no numerical dissipation in case of $\rho_\infty = 1.0$. Furthermore, the velocity update algorithm is activated to conserve total energy of the system. A benefit of their combination is exhibited via stable time marching as well as total energy preservation.

Typically, the most time consuming phase for contact analysis is the searching to determine the moment when contact takes place, especially if high precision is expected. In

this work, a simple algorithm is employed, and as a result, its performance is not preferable, e.g. drastically time consuming, the potential contact node set is overwhelming. Further developments for a smarter contact searching algorithm is compulsory, for instance the tree-structure based algorithm by Yang [YL08]. Besides, the author encounters difficulties to define the unique projection point from one surface to another in the case of highly curved surfaces. Thus, more efficient projection algorithms are recommended.

Chapter 6

Conclusions

6.1 Review

Within this work, mathematical descriptions of the inflatable membrane structures undergoing finite deformation with small strain and numerical treatment based on the FEM along with effective solution algorithms have been extensively discussed with the emphasis on three distinct aspects of nonlinearity: The efficient MM-based wrinkling models, influences of the deformation-dependent forces and the mortar-based contact formulation for dynamic frictionless contact problems with implicit time integration method. The main achievements of this work are summarized in the followings:

- ◇ The mathematical formulations in Chapter 2 is written for general two- and three-dimensional continuum which has a membrane as a subset. These formulations are the main governing equations to which contributions from additional sources of nonlinearity, given in the Chapters 3, 4 and 5, are appended. Since these formulation are created in a continuum sense, then the finite element discretization with membrane elements, is postponed to the last phase before factorization. In other words, linearization is performed virtually only on the continuum formulation with the outcome of a general formulation which is not intervened by the inexactness caused by spatial discretization errors. Moreover, this generality allows for various choices of spatial discretization.

- ◇ In Chapter 3, two innovative MM-based wrinkling models–the projection model and the plasticity analogy model–are developed for both isotropic and orthotropic materials to suppress artificial compressive stresses within the membrane for both stationary and transient problems. With consistent linearization the difficulty in convergence due to an abrupt transition from an elastic (i.e. taut) to plastic (i.e. wrinkled or slack) state is diminished and the convergence rate is improved significantly. For a comparison between both models, the projection-based model is less accurate; it requires higher number of iteration steps to reach the state of equilibrium, whereas the plasticity analogy model with the return mapping algorithm uses longer computing time.

- ◇ Both wrinkling models fulfill the objective for excellent subgrid scale performance with regard to accuracy, efficiency, computing expense, implementation complexity and the convergence rate. The efficiency of the presented wrinkling models has been

demonstrated through a number of numerical benchmark examples. Results of these simulations represent potential applications of both models. Nevertheless the proposed models are suitable for a problem undergoing small elastic strain due to the assumption of the additive strain decomposition. Numerical algorithm is prepared in a general form which is flexible for various material models. An important part of the developments is that the implementation appears to be unprecedented; it play a key role as a fruitful product of this research.

- ◇ In Chapter 4, influences of pressure acting on the surface of an inflatable membrane is captured by the definition of deformation-dependent loads which nonlinearly depend on a deformation of the membrane. Two sources of nonlinearity are the change of the direction of pressure-induced force vectors and the change of pressure magnitude during the deformation process. Linearization brings out the nominal load stiffness matrix and the additional load stiffness terms so-called the enclosed volume terms written in the form of update tensors.

- ◇ For a closed membrane structure, the skew-symmetric boundary terms disappear, whereas the existing symmetric domain terms reflect conservativeness of the system. This method requires neither the discretization of the fluid (gas) domain nor interface coupling of fluid (gas) and membrane. Due to this fact, the computation is significantly simplified. The fully populated system matrix is handled efficiently by the Woodbury's solution techniques for both quasi-static and dynamic analysis. For dynamic problems, two stable implicit time integration methods–the Generalized-α method (GEN_α) and the Genealized Energy Momentum Method (GEMM)–are valid as long as the assumption of slow deformation process, which neglects inertial forces, is not violated. Consequently, the high speed deformation process is excluded from the presented method.

- ◇ From numerical investigations, inclusion of the enclosed volume terms is necessary for highly pressurized gas and high density fluid; it is proven to be advantageous in particular for an enclosed membrane filled with gas and/or fluid with regard to accuracy and rate of convergence.

- ◇ Based on [HW05, Yan06, Har07], a mortar-based contact formulation is prepared in Chapter 5 for frictionless contact problems of inflatable membranes undergoing large deformation (geometric nonlinear) in particular for low-speed contact-impact cases. For the mortar method, since the geometric impenetrability condition is formulated in an integral (weak) sense, thus its corresponding energetic conjugate–the Lagrange multiplier–which physically represents contact force must be continuously approximated in the same manner with the advantages of unlocking and robustness.

- ◇ The dual basis function is chosen to interpolate the Lagrange multiplier field such that after the active set is predefined by the active set strategy, all discrete nodal Lagrange multipliers can be eliminated from the effective incremental structural equation by static condensation. After the primal unknowns–change in nodal positions–is solved, the Lagrange multipliers can be recovered in the postprocessing phase. For contact problems of two deformable bodies, a local basis transformation is utilized to

transform the effective incremental structural equation to a transformed matrix having similar form to that of the unilateral contact and the same solution technique can be used. The dual Lagrange multiplier method can successfully enforce impenetrability constraints, while overall computation is not suffered by the penalty sensitivity. Furthermore, local condensation of the Lagrange multiplier maintains constant size of the system matrix during the computation.

- ◇ A stable implicit solution technique is developed by adding the post-contact discrete velocity update upon the existing stable GEMM time integration method to achieve the goal of algorithmic conservation of energy. From numerical investigations, this statement is valid only in the case that $\rho_\infty = 1.0$, no numerical dissipation. As mentioned in [LL02], the discrete velocity update algorithm leads to the exact energy conservation without violation on the impenetrability constraint.

- ◇ Various two- and three-dimensional numerical examples demonstrate the performance of derived formulation and implemented algorithm with regard to accuracy, robustness and stability. The presented contact formulation can pass the contact patch test with arbitrary non-conforming mesh on the contact interface such that the constant pressure is exactly transferred from one body to another regardless of mesh layout in the contact interfaces. However, the underlying mathematical background of the contact patch test should be studied in more details. By a combination of all algorithms mentioned above, a complete tool to simulate all phenomena simultaneously is achieved, while its performance is demonstrated in example 5.7.4 which indicates high potential of the algorithm for more complicated simulations when further refinements are accomplished.

6.2 Outlook

At this standing point, these accomplishments notwithstanding, there is still a number of open questions waiting for further developments as in the following:

For wrinkling model

- ◇ Extension towards the large strain regime is considered as an opportunity as mentioned by Mosler [Mos08]. A reasonable allowable compressive stress requires further investigations for the insight into an actual compressive stiffness of each membrane material.

- ◇ Another feasible aspect is development of adaptive scale separators and enhancement of wrinkling models by the variational multiscale method, which highlights its underlying multiscale characteristic, for both stationary and transient applications. The main idea is that while the analysis of effects on a global or “structural” scale are often feasible with standard membrane elements, the investigation of local effects and the corresponding influence of this “sectional scale” on the overall behavior requires

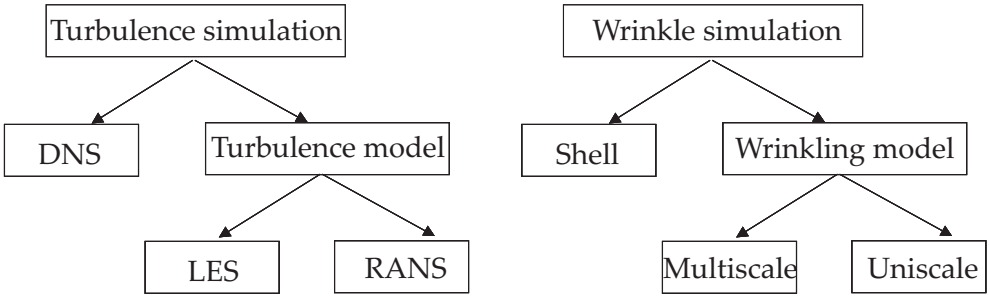

Figure 6.1: Illustration for an innovative idea to simulate wrinkled membranes by an analogy to the multiscale method for turbulence modeling.

more elaborate methods. Currently, two different approaches are used for this purpose: Either one computes with shell elements on an extremely fine mesh or membrane elements with embedded wrinkling models are used on a considerably coarser discretization. Ideally, with an introduction of a scale separator, both computational strategies should be combined by considering their respective strengths which lead to a multiscale method for wrinkled membranes.

- ◇ The wrinkling model in this chapter can be used as a subgrid-scale model for the multiscale concept demonstrated in Figure 6.1. This may be considered as a new strategy towards an improved simulation of wrinkled membranes by the finite element method as introduce by Bletzinger and Jarasjarungkiat [BJW07].

For deformation-dependent loads

- ◇ Stability analysis of inflatable membranes: A study on the stability of fluid and/or gas supported membranes with regard to influences of the enclosed fluid is still a matter of interest as recently investigated by Haßler and Schweizerhof [HS07] with the main idea that sequential update of solutions allows an investigation for stability of the inflatable membranes. Moreover, based on the implementation in this work, interaction of multichamber can be readily accomplished as a direct extension.

- ◇ From the author's opinion, another interesting aspect is an innovative model of the deformation dependent loads by taking into account influence of inertial forces. The concept of added mass may be incorporated to the idea of deformation-dependent forces within this dissertation with the outcome of an intermediate model between the fully-meshed approach and meshless approach in the fluid domain.

For contact problems

- ◇ Linearization of the contact virtual work and contact constraints for both two and three dimensional cases is attractive to improve the rate of convergence as recently published in Popp *et al.* [PGW09] and issues of frictional contact should be taken into

account as well as aspects of material nonlinearity to expand the scope of valid applications. Moreover, the solution technique presented within this work requires further improvement on algorithmic treatment for angular momentum conservation as mentioned by Hesch and Betsch [HB08].

- ◇ Transferring to the parallel computing architectures has high feasibility to reduce the calculation cost of FEM for the large contact problems. Of special challenge is the implementing aspect on the parallel architectures of the associated contact issues as in the following: Development for a better projection algorithm between highly curved contact surface, an effective contact detection and a smart contact searching algorithm are necessary to accelerate the computation as well as to deal with self-contact by tailoring too bulky overhead (see, e.g. Yang and Laursen [YL08]).
- ◇ The nonsmoothness of contact surface requires further improvements. Such nonsmoothness leads to discontinuities in both the contact constraint due to its definition and the solutions in the pathological situation. The current technology notwithstanding, extensions to higher order element with the smoother surface representation, e.g. the method of Isogeometric analysis [HCB05], possess high potential.

Bibliography

[AC91] P. Alart and A. Curnier. A mixed formulation for frictional contact problems prone to newton like solution methods. *Computer Methods in Applied Mechanics and Engineering*, 92 (3):353–375, 1991.

[ANNP07] T. Akita, K. Nakashino, C. Natori, and K.C. Park. A simple computer implementation of membrane wrinkle behaviour via a projection technique. *International Journal for Numerical Methods in Engineering*, 71(10):1231–1259, 2007.

[AP98] F. Armero and E. Petocz. Formulation and analysis for conserving algorithms for frictionless dynamic contact/impact problems. *Computer Methods in Applied Mechanics and Engineering*, 158:269–300, 1998.

[AP99] F. Armero and E. Petocz. A new dissipative time-stepping algorithm for frictional contact problems: formulation and analysis. *Computer Methods in Applied Mechanics and Engineering*, 179:151–178, 1999.

[AR99] F. Armero and I. Romero. Dissipative integration algorithms for nonlinear elastodynamics. In *European Conference on Computational Mechanics*, München, 1999.

[AR01a] F. Armero and I. Romero. On the formulation of high-frequency dissipative time-stepping algorithms for nonlinear dynamics. part i: low order methods for two model problems and nonlinear elastodynamics. *Computer Methods in Applied Mechanics and Engineering*, 190:2603–2649, 2001.

[AR01b] F. Armero and I. Romero. On the formulation of high-frequency dissipative time-stepping algorithms for nonlinear dynamics. part ii: second order methods. *Computer Methods in Applied Mechanics and Engineering*, 190:678–6824, 2001.

[ASKN07] T. Asai, K. Seo, O. Kobayashi, and H. Nunome. Identifying knuckle effect in football. *Journal of Sports Science and Medicine*, Suppl. 10:48–49, 2007.

[Bae05] H. D. Baehr. *Thermodynamik*. Springer Verlag, Berlin, 2005.

[Bat02] K.-J. Bathe. *Finite-Elemente-Methoden*. Springer-Verlag, Berlin, 2. edition, 2002.

[Ber94] Maday Y. Patera A.T. Bernardi, C. A new nonconforming approach to domain decomposition: the mortar element method. In H. Brezis and J.L. Lions, editors, *Nonlinear partial differential equations and their applications*, volume XI, pages 13–51. Pitman and Wiley, 1994.

[BF91] F. Brezzi and M. Fortin. *Mixed and Hybrid Finite Element Methods*. Springer Verlag, New York, 1991.

[BHL98] F.B. Belgacem, P. Hild, and P Laborde. The mortar finite element method for contact problems. *Mathematical and Computer Modelling*, 28:263–271, 1998.

[Bis99] M. Bischoff. *Theorie und Numerik einer dreidimensionalen Schalenformulierung*. PhD thesis, Universität Stuttgart, Stuttgart, 1999.

[BJW07] K.-U. Bletzinger, A. Jarasjarungkiat, and R. Wüchner. Wrinkling as multi-scale phenomenon in numerical analysis of membranes. In A. Ibrahimbegovic, F. Dias, H. Matthies, and P. Wriggers, editors, *Multi-scale Computational Methods for Solids and Fluids*, pages 30–36, Cachan, France, November 20-30, 2007 2007.

[Ble98] K.-U. Bletzinger. *Form finding and optimization of membranes and minimal surfaces*. Ph.D. course on Advanced Topics in Structural Optimization. Denmark, 1998.

[BLM00] T. Belytschko, W.K. Liu, and B. Moran. *Nonlinear finite elements for continua and structures*. John Wiley & Sons Ltd., Chichester, 2000.

[BM94] F. Belgacem and Y. Maday. A spectral element methodology tuned to parallel implementations. *Computer Methods in Applied Mechanics and Engineering*, 116 (1-4):59–67, 1994.

[Bru08] S. Brunssen. *Contact analysis and overlapping domain decomposition methods for dynamic and nonlinear problems*. PhD thesis, Universität Stuttgart, 2008.

[BS75] T. Belytschko and D.F. Schoeberle. On the unconditional stability of an implicit algorithm for nonlinear structural dynamics. *Journal of Applied Mechanics*, 42:865–869, 1975.

[BSSW07] Stephan Brunßen, Florian Schmid, Michael Schäfer, and Barbara Wohlmuth. A fast and robust method for contact problems by combining a primal-dual active set strategy and algebraic multigrid. *Int. J. Numer. Meth. Engrg.*, 69:524–543, 2007.

[Buf84] H. Bufler. Pressure loaded structures under large deformations. *ZAMM*, 64(7):287–295, 1984.

[BW00] Y. Başar and D. Weichert. *Nonlinear continuum mechanics of solids - Fundamental mathematical and physical concepts*. Springer-Verlag, Berlin, 2000.

[BWMH00] J. Bonet, R.D. Wood, J. Mahaney, and P. Heywood. Finite element analysis of air supported membrane structures. *Computer Methods in Applied Mechanics and Engineering*, 190:579–595, 2000.

[CGJ97] M.A. Crisfield, U. Galvanetto, and G. Jelenic. Dynamics of 3-d co-rotational beams. *Computational Mechanics*, 20:507–519, 1997.

[CH93] J. Chung and G.M. Hulbert. A time integration algorithm for structural dynamics with improved numerical dissipation: the generalized-α method. *Journal of Applied Mechanics*, 60:371–375, 1993.

[Cic06] T. Cichosz. Simulation von inkrementellen blechumformprozessen. Master's thesis, Institut für Baustatik und Baudynamik, Universität Stuttgart., 2006.

[Cot74] R.W. Cottle. Manifestations of the schur complement. *Linear Algebra Applications*, 8:189–211, 1974.

[Cow73] G.R. Cowper. Gaussian quadrature formulas for triangles. *Int. J. Numer. Methods Engrg.*, 7:405–408, 1973.

[CP93] R.W. Clough and J. Penzien. *Dynamics of structures*. McGraw-Hill, New York, 2. edition, 1993.

[Cri81] M.A. Crisfield. A fast incremental/iterative solution procedure that handels snap-through. *Computers and Structures*, 13:55–62, 1981.

[CS88] P. Contri and B.A. Schrefler. A geometrically nonlinear finite element analysis of wrinkled membrane surfaces by a no-compression material model. *Communications in Applied Numerical Methods*, 4:5–15, 1988.

[DY03] H. Ding and B. Yang. The modelling and numerical analysis of wrinkled membranes. *International Journal for Numerical Methods in Engineering*, 58:1785–1801, 2003.

[EF01] M. Epstein and M. A. Forcinito. Anisotropic membrane wrinkling: theory and analysis. *International Journal of Solids and Structures*, 38 (30-31):5253–5272, 2001.

[Fis05] K.A. Fischer. *Mortar Type Methods Applied to Nonlinear Contact Mechanics*. PhD thesis, Dissertation, Research Report F 05/2, Institut für Baumechanik und Numerische Mechanik, Universität Hannover, 2005.

[FvDF97] J.D. Foley, A. van Dam, and Hughes J.F. Feiner, S.K. *Computer Graphics, Principles and Practice.* Addison-Wesley, Reading, 1997.

[FW05a] K. Fischer and P. Wriggers. Mortar based frictional contact formulation for higher order interpolations using the moving friction cone. *Computer Methods in Applied Mechanics and Engineering*, 195:5020–5036, 2005.

[FW05b] K.A. Fischer and P. Wriggers. Frictionless 2d contact formulations for finite deformations based on the mortar method. *Computational Mechanics*, 36:226–244, 2005.

[GPFA08] J.A. González, K.C. Park, C.A. Felippa, and R. Abascal. A formulation based on localized lagrange multipliers for bem-fem coupling in contact problems. *Computer Methods in Applied Mechanics and Engineering*, 197(6-8):623–640, 2008.

[Hag89] W.H. Hager. Updating the inverse of a matrix. *Society for industrial and Applied Mechanics*, 31(2):221–239, 1989.

[Har07] S. Hartmann. *Kontaktanalyse dünnwandiger Strukturen bei großen Deformationen*. PhD thesis, Institut für Baustatik und Baudynamik der Universität Stuttgart, 2007.

[HB08] C. Hesch and P. Betsch. A mortar method for energy-momentum conserving schemes in frictionless dynamic contact problems. *International Journal for Numerical Methods in Engineering*, 2008.

[HBRW07] S. Hartmann, S. Brunssen, E. Ramm, and B.I. Wohlmuth. Unilateral non-linear dynamic contact of thin-walled structures using a primal-dual active set strategy. *International Journal for Numerical Methods in Engineering*, 70(8):883–912, 2007.

[HCB05] T.J.R. Hughes, J.A. Cottrell, and Y. Bazilevs. Isogeometric analysis: Cad, finite elements, nurbs, exact geometry and mesh refinement. *Computer Methods in Applied Mechanics and Engineering*, 194(39-41):4135–4195, 2005.

[HCL78] T.J.R. Hughes, T.K. Caughey, and W.K. Liu. Finite-element methods for nonlinear elastodynamics which conserve energy. *Journal of Applied Mechanics*, 45:366–370, 1978.

[Her81] H. Hertz. Über die berührung fester elastischer körper. *Journal für die reine und angewandte Mathematik*, 92:156–171, 1881.

[HHT77] H.M. Hilber, T.J.R. Hughes, and R.L. Taylor. Improved numerical dissipation for the time integration algorithms in structural dynamics. *Earthquake Engineering and Structural Dynamics*, 5:283–292, 1977.

[Hol00] G.A. Holzapfel. *Nonlinear solid mechanics*. John Wiley & Sons Ltd., Chichester, 2000.

[HS03] J. Hornig and H. Schoop. Closed form analysis of wrinkled membranes with linear stress-strain relation. *Computational Mechanics*, 30:259–264, 2003.

[HS05a] M. Haßler and K. Schweizerhof. Large deformation static analysis of inflatable prefolded membrane and shell structures. In B. Oñate and B. Kröplin, editors, *Structural membranes 2005*, Barcelona, Spain, 2005. CIMNE.

[HS05b] M. Hassler and K. Schweizerhof. Simulation of hydroforming of metal sheets with an efficient fe-formulation based on an analytical meshfree description of a compressible fluid. *PAMM, Proc. Appl. Math. Mech.*, 5:403–404, 2005.

[HS05c] J. Hornig and H. Schoop. Wrinkling analysis of membranes with elastic-plastic material behaviour. *Computational Mechanics*, 35:153–160, 2005.

[HS07] M Haßler and K. Schweizerhof. On the influence of fluid-structure-interactions on the stability of thin walled shell structures. *International Journal of Structural Stability and Dynamics*, 7(2):313–335, 2007.

[HS08a] M. Haßler and K. Schweizerhof. On the influence of a volume dependent pressure support on the stability of thin-walled inflatable structures. In E. Onate and B. Kröplin, editors, *Textile Composites and Inflatable Structures II*, pages 197–210, 2008.

[HS08b] M. Haßler and K. Schweizerhof. On the static interaction of fluid and gas loaded multi-chamber systems in large deformation finite element analysis. *Computer Methods in Applied Mechanics and Engineering*, 197(19-20):1725–1749, 2008.

[HS08c] M. Haßler and K. Schweizerhof. Vibration analysis of thin-walled - gas or fluid filled - structures including the effect of the inflation/filling process. In J. F. Abel and J. R. Cooke, editors, *the 6th International Conference on Computation of Shell and Spatial Structures IASS-IACM 2008: "Spanning Nano to Mega"*, 2008.

[Hug00] T.J.R. Hughes. *The finite element method - Linear static and dynamic finite element analysis*. Dover Publications, Inc., Mineola, 2000.

[Hul04] G.M. Hulbert. Computational structural dynamics. In E. Stein, R. de Borst, and T.J.R. Hughes, editors, *Encyclopedia of Computational Mechanics*, pages 169–194. John Wiley & Sons, Ltd., Chichester, 2004.

[HW05] S. Hüeber and B. Wohlmuth. A primal-dual active set strategy for non-linear multibody contact problems. *Comput. Methods Appl. Mech. Engrg.*, 194:3147–3155, 2005.

[Jar04] A. Jarasjarungkiat. The orthotropic material and wrinkling model for membrane structures. Master's thesis, Lehrstuhl für Statik, Technische Universität München, München, Germany, March 2004.

[JL96] C.H. Jenkins and J.L. Leonard. Dynamic wrinkling of viscoelastic membranes. *ASME Journal of Applied Mechanics*, 60:575–582, 1996.

[Joh85] K. Johnson. *Contact Mechanics*. Cambridge University Press, 1985.

[JWB07] A. Jarasjarungkiat, R. Wüchner, and K.-U. Bletzinger. The coupling of enclosed gas with inflatable membranes. In *Coupled Problems 2007*, pages 557–560, Santa Eulalia, Ibiza, Spain, May 21-23 2007.

[JWB08a] A. Jarasjarungkiat, R. Wüchner, and K.-U. Bletzinger. Dynamic analysis of inflatable membranes coupled with enclosed fluid. In *8th.World Congress on Computational Mechanics (WCCM8) and the 5th. European Congress on Computational Methods in Applied Sciences and Engineering (ECCOMAS 2008)*, Lido Island in Venice, Italy, 30 June - 4 July 2008. CDROM.

[JWB08b] A. Jarasjarungkiat, R. Wüchner, and K.-U. Bletzinger. A wrinkling model based on material modification for isotropic and orthotropic membranes. *Computer Methods in Applied Mechanics and Engineering*, 197:773–788, 2008.

[JWB09a] A. Jarasjarungkiat, R. Wüchner, and K.-U. Bletzinger. Efficient sub-grid scale modeling of membrane wrinkling by a projection method. *Computer Methods in Applied Mechanics and Engineering*, 198:1097–1116, 2009.

[JWB09b] A. Jarasjarungkiat, R. Wüchner, and K.-U. Bletzinger. Wrinkling modeling based on plasticity analogy. *Computer Methods in Applied Mechanics and Engineering*, 2009. (submitted).

[Kau02] M. Kaufman. *Principles of Thermodynamics*. Marcel Dekker, Inc., 2002.

[KC99] D. Kuhl and M.A. Crisfield. Energy-conserving and decaying algorithms in non-linear structural dynamics. *International Journal for Numerical Methods in Engineering*, 45:569–599, 1999.

[KI97] S. Kang and S. Im. Finite element analysis of wrinkling membranes. *ASME Journal of Applied Mechanics*, 64:263–269, 1997.

[KI99] S. Kang and S. Im. Finite element analysis of dynamic response of wrinkling membranes. *Computer Methods in Applied Mechanics and Engineering*, 173:227–240, 1999.

[KO88] N. Kikuchi and J.T. Oden. *Contact Problems in Elasticity: A Study of Variational Inequalities and Finite Element Methods*. SIAM, Philadelphia, 1988.

[KR96] D. Kuhl and E. Ramm. Constraint energy momentum algorithm and its application to non-linear dynamics of shells. *Computer Methods in Applied Mechanics and Engineering*, 136:293–315, 1996.

[KR99] D. Kuhl and E. Ramm. Generalized energy-momentum method for non-linear adaptive shell dynamics. *Computer Methods in Applied Mechanics and Engineering*, 178:343–366, 1999.

[Kuh96] D. Kuhl. *Stabile Zeitintegrationsalgorithmen in der nichtlinearen Elastodynamik dünnwandiger Tragwerke*. PhD thesis, Universität Stuttgart, Stuttgart, 1996.

[LAL01] K. Lu, M. Accorsi, and J. Leonard. Finite element analysis of membrane wrinkling. *International Journal for Numerical Methods in Engineering*, 50:1017–1038, 2001.

[Lau92] T.A. Laursen. *Formulation and treatment of frictional contact problems using finite elements*. PhD thesis, Department of mechanical engineering, School of engineering, Standford University, 1992.

[Lau02] T.A. Laursen. *Computational Contact and Impact Mechanics*. Springer, Berlin, Heidelberg, Germany, 2002.

[Lew03] W. Lewis. *Tension structures Form and behaviour*. Thomas Telford publishing, 2003.

[LJS01] X. Liu, C.H. Jenkins, and W.W. Schur. Large deflection analysis of pneumatic envelopes using a penalty parameter modified material model. *Finite Elements in Analysis and Design*, 37:233–251, 2001.

[LL02] T.A. Laursen and G.R. Love. Improved implicit integrators for transient impact problems - geometric admissibility within the conserving framework. *International Journal for Numerical Methods in Engineering*, 53 (2):245–274, 2002.

[LWKU07] J. Linhard, R. Wüchner, and Bletzinger K.-U. Upgrading membranes to shells - the ceg rotation free shell element and its application in structural analysis. *Finite Elements in Analysis and Design*, 44:63–74, 2007.

[Mal69] L.E. Malvern. *Introduction to the mechanics of a continuous medium*. Prentice-Hall, Inc., Englewood Cliffs, 1969.

[Man70] E. H. Mansfield. Load transfer via a wrinkled membrane. *Proc R Soc A*, 316:269–289, 1970.

[MB02] K. Moritz and R. Barthel. Transparente Architektur - Bauen mit ETFE-Folien. *Detail*, (12):1616–1620, 2002.

[MH83] J.E Marsden and T.J.R. Hughes. *Mathematical foundations of elastictiy*. Dover publication, New York., 1983.

[MHW+85] R.M. Miller, J. M. Hedgepeth, V. I. Weingarten, P. Das, and S. Kahyai. Finite element analysis of partly wrinkled membranes. *Computers & Structures*, 20(1-3):631–639., 1985.

[Miy00] T. Miyamura. Wrinkling on stretched circular membrane under in-plane torsion: bifurcation analyses and experiments. *Engineering Structures*, 23:1407–1425, 2000.

[Miy06] Y. Miyazaki. Wrinkle/slack model and finite element dynamics of membrane. *International Journal for Numerical Methods in Engineering*, 66:1179–1206, 2006.

[ML00] T.W. McDevitt and T.A. Laursen. A mortar-finite element formulation for frictional contact problems. *International Journal for Numerical Methods in Engineering*, 48:1525–1547, 2000.

[Mor00] K. Moritz. Membranwerkstoffe im Hochbau. *Detail*, (6):1050–1058, 2000.

[Mos08] J. Mosler. A novel variational algorithmic formulation for wrinkling at finite strains based on energy minimization: Application to mesh adaption. *Computer methods in Applied Mechanics and Engineering*, 197:1131–1146, 2008.

[MP06] Y. Miyazaki and K. C. Park. A formulation of conserving impact system based on localized lagrange multipliers. *International Journal for Numerical Methods in Engineering*, 68(1):98–124, 2006.

[MR95] R. Münsch and H.-W. Reinhardt. Zur Berechnung von Membrantragwerken aus beschichteten Geweben mit Hilfe genäherter elastischer Materialparameter. *Bauingenieur*, 70:271–275, 1995.

[New59] N.M. Newmark. A method of computation for structural dynamics. *Journal of the Engineering Mechanics Division, ASCE*, 85:67–94, 1959.

[Ogd72] R.W. Ogden. Large deformation isotopic elasticity; on the correlation of theory and experiments for incompressible rubber-like solids. In *Royal Society of London*, number 328 in A, pages 565–584, 1972.

[Ogd97] R.W. Ogden. *Non-linear elastic deformations*. Dover Publications, 1997.

[OS88] S. Osher and J. A. Sethian. Fronts propagating with curvature-dependent speed: Algorithms based on hamilton-jacobi formulations. *Journal of Computation Physics*, 79:12–49, 1988.

[Pag04] M.E. Pagitz. Computational methods for membrane structures. Master's thesis, Dept. Engng, University of Cambridge, 2004.

[PGW09] A. Popp, M.W. Gee, and W.A. Wall. A finite deformation mortar contact formulation using a primal-dual active set strategy. *International Journal for Numerical Methods in Engineering*, 79 (11):1354–1391, 2009.

[PL04a] M. Puso and T. Laursen. A mortar segment-to-segment contact method for large deformation solid mechanics. *Computer Methods in Applied Mechanics and Engineering*, 193:601–629, 2004.

[PL04b] M. Puso and T. Laursen. A mortar segment-to-segment frictional contact method for large deformations. *Computer Methods in Applied Mechanics and Engineering*, 193:4891–4913, 2004.

[Pre92] W. H. Press. *Numerical Recipe in FORTRAN*. Cambridge Press, 2 edition, 1992.

[PT92] P. Papadopoulos and R.L. Taylor. A mixed formulation for the finite element solution of contact problems. *Computer Methods in Applied Mechanics and Engineering*, 94:373–389, 1992.

[RA02] I. Romero and F. Armero. Numerical integration of the stiff dynamics of geometrically exact shells: an energy-dissipative momentum-conserving scheme. *International Journal for Numerical Methods in Engineering*, 54:1043–1086, 2002.

[Rai03] T. Raible. *Concepts for nonlinear orthotropic material modeling with applications to membrane structures*. PhD thesis, Universität Hannover, Hannover, 2003.

[Ram80] E. Ramm. Strategies for tracing the nonlinear response near limit pints. In K.J. Bathe, E. Stein, and W. Wunderlich, editors, *Europe-US-Workshop on Nonlinear Finite Elements Analysis in Structural Mechanics*, pages 63–89. Springer: Berlin, 1980.

[RDO87a] D.G. Roddeman, J. Drucker, and C.W.C. Oomens. The wrinkling of thin membranes: part i-theory. *ASME Journal of Applied Mechanics*, 54:884–887, 1987.

[RDO87b] D.G. Roddeman, J. Drucker, and C.W.C. Oomens. The wrinkling of thin membranes: part ii-numerical analysis. *ASME Journal of Applied Mechanics*, 54:888–882, 1987.

[Rik79] E. Riks. An incremental approach to the solution of snapping and buckling problems. *Internation journal of Solids and Structures*, 15:529–551, 1979.

[RLVO05] R. Rossi, M. Lazzari, R. Vitaliani, and E. Onate. Simulation of light-weight membrane structures by wrinkling model. *International Journal for Numerical Methods in Engineering*, 62 (15):2127–2153, 2005.

[RO03] R. Rossi and E. Onate. Convergence of the modified material model for wrinkling simulation of light-weight membrane structures. In B. Onate and B. Kröpin, editors, *Structural Membranes 2003*. CIMNE, 2003.

[Rod91] D.G. Roddeman. Finite element analysis of wrinkling membranes. *Communications in Applied Numerical Methods*, 7:299–307, 1991.

[Ros05] R. Rossi. *Light weight structures: Structural analysis and coupling issues*. PhD thesis, The university of Bologna, 2005.

[RPF02] G. Rebel, K.C. Park, and C.A. Felippa. A contact formulation based on localized lagrange multipliers: formulation and application to two-dimensional problems. *International Journal for Numerical Methods in Engineering*, 54(2):263–297, 2002.

[RS03] T. Rumpel and K Schweizerhof. Volume dependent pressure loading and its influence on the stability of structures. *International Journal for Numerical Methods in Engineering*, 56(2):211–238, 2003.

[RS04] T. Rumpel and K. Schweizerhof. Hydrostatic fluid loading in non-linear finite element analysis. *International Journal for Numerical Methods in Engineering*, 59:849–870, 2004.

[RTLW05] T. Raible, K. Tegeleer, S. Loehnert, and P. Wriggers. Development of a wrinkling algorithm for orthotropic membrane materials. *Computer methods in Applied Mechanics and Engineering*, 194:2550–2568, 2005.

[Rum03] T. Rumpel. *Effiziente Diskretisierung von statischen Fluid-Struktur-Problemen bei großen Deformationen*. PhD thesis, Universität Karlsruhe, 2003.

[Sch82] K. Schweizerhof. *Nichtlineare Berechnung von Tragwerken unter verformungsabhängiger Belastung mit finiten Elementen*. PhD thesis, Universität Stuttgart, Stuttgart, 1982.

[Sew67] M.J. Sewell. On configuration-dependent loading. *Archive for Rational Mechanics and Analysis*, 23:327–351, 1967.

[SH98] J.C. Simo and T.J.R. Hughes. *Computational Inelasticity*. Springer Verlag, 1998.

[SP89] D.J. Steigmann and A.C. Pipkin. Wrinkling of pressurized membranes. *ASME Journal of Applied Mechanics*, 56:624–628, 1989.

[SR84] K. Schweizerhof and E. Ramm. Displacement dependent pressure loads in nonlinear finite element analyses. *Computers & Structures*, 18(6):1099–1114, 1984.

[ST92] J.C. Simo and N. Tarnow. The discrete energy-momentum method. conserving algorithms for nonlinear elastodynamics. *Zeitschrift für Angewandte Mathematik und Physik*, 43(5):757–792, 1992.

[ST94] J.C. Simo and N. Tarnow. A new energy and momentum conserving algorithm for the nonlinear dynamics of shells. *International Journal for Numerical Methods in Engineering*, 37(15):2527–2549, 1994.

[STW91] J. C. Simo, R. L. Taylor, and P. Wriggers. A note on finite-element implementation of pressure boundary loading. *Communications in Applied Numerical Methods*, 7 (7):513–525, 1991.

[SWT85] J.C. Simo, P. Wriggers, and R.L. Taylor. A perturbed lagrangian formulation for the finite element solution of contact problems. *Computer Methods in Applied Mechanics and Engineering*, 50:163–180, 1985.

[TN92] C. Truesdell and W. Noll. *The non-linear field theories of mechanics*. Springer-Verlag, Berlin, 2nd. edition, 1992.

[VOC05] J.G. Valdes, E. Onate, and J.M. Canet. A modified material model to simulate wrinkling of orthotropic membranes at finite deformations. In B. Onate and B. Kröpin, editors, *Structural Membranes 2005*, pages 113–122. CIMNE, 2005.

[Was] K. Washizu. *Variational methods in Elasticity and Plasticity*. Pergamon.

[WB05] R. Wüchner and K.-U. Bletzinger. Stress-adapted numerical form finding of pre-stressed surfaces by the updated reference strategy. *International Journal for Numerical Methods in Engineering*, 64:143–166, 2005.

[WBZ81] W.L. Wood, M. Bossak, and O.C. Zienkiewicz. An alpha modification of Newmark's method. *International Journal for Numerical Methods in Engineering*, 15:1562–1566, 1981.

[Wüc06] R. Wüchner. *Mechanik und Numerik der Formfindung und Fluid-Struktur-Interaktion von membrantragwerken*. PhD thesis, Lehrstuhl für Statik, Technische Universität München, München, Germany, 2006.

[Wil] E. L. Wilson. A computer program for the dynamic stress analysis of underground structures. Technical report, SEL Report 68-1, University of California at Berkeley.

[WK03] B. Wohlmuth and R. Krause. Monotone methods on non-matching grids for non linear contact problems. *SIAM J. Sci. Comput.*, 25:324–347, 2003.

[WL08] P. Wriggers and T.A. Laursen, editors. *Computational Contact Mechanics(International Center for Mechanical Sciences: Courses and Lectures)*. Springer, 2008.

[Woh00] B.I. Wohlmuth. A mortar finite element method using dual spaces for the Lagrange multiplier. *SIAM J. Numer. Anal.*, 38:989–1012, 2000.

[Woh01] B. Wohlmuth. *Discretization Techniques and Iterative Solvers Based on Domain Decomposition*, volume 17. Springer, Heidelberg, 2001.

[Woo50] M. Woodbury. Inverting modified matrices. Memorandum Report 42, Statistical Research Group, Princeton University, Princeton, NJ, 1950.

[WP06a] Y.W. Wong and S. Pellegrino. Wrinkled membranes i: Experiments. *Journal of Mechanics of Materials and Structures*, 1(1):1–23, 2006.

[WP06b] Y.W. Wong and S. Pellegrino. Wrinkled membranes ii: Analytical models. *Journal of Mechanics of Materials and Structures*, 1(1):25–59, 2006.

[WP06c] Y.W. Wong and S. Pellegrino. Wrinkled membranes iii: Numerical simulations. *Journal of Mechanics of Materials and Structures*, 1(1):61–93, 2006.

[Wri01] P. Wriggers. *Nichtlineare Finite-Element-Methoden*. Springer-Verlag, Berlin, 2001.

[Wri02] P. Wriggers. *Computational Contact Mechanics*. Wiley, Chichester, UK, 2002.

[WZ04] P. Wriggers and G. Zavarise. *Computational Contact Mechanics: Encyclopedia of Computational Mechanics*, volume 2, Solids and Structures. John Wiley & Sons, Ltd., 2004.

[Yan06] B. Yang. *Mortar finite element methods for large deformationen contact mechanics*. PhD thesis, Duke University, 2006.

[YL07] B. Yang and T. A. Laursen. A large deformation mortar formulation of self contact with finite sliding. *Computer Methods in Applied Mechanics and Engineering*, 197 (6-8):756–772, 2007.

[YL08] B. Yang and T.A. Laursen. A contact searching algorithm including bounding volume trees applied to finite sliding mortar formulations. *COMPUTATIONAL MECHANICS*, 41(2):189–205, 2008.

[YLM05] B. Yang, T. Laursen, and X. Meng. Two dimensional mortar contact methods for large deformation frictional sliding. *International Journal for Numerical Methods in Engineering*, 62:1183–1225, 2005.

[Zie01] R. Ziegler. *Theorie und Numerik für den Entwurf von vorgespannten Membrantragwerken*. PhD thesis, Universität Karlsruhe(TH), 2001.

[ZT05] O.C. Zienkiewicz and R.L. Taylor. *The finite element method for solid and structural mechanics*. Elsevier Butterworth-Heinemann, Burlington, 6. edition, 2005.

[ZTZ05] O.C. Zienkiewicz, R.L. Taylor, and J.Z. Zhu. *The finite element method: its basis and fundamentals*. Elsevier Butterworth-Heinemann, Burlington, 6. edition, 2005.

[ZW98] G. Zavarise and P. Wriggers. A segment-to-segment contact strategy. *Mathematical and Computer Modelling*, 28:497–515, 1998.

[ZWB03] R. Ziegler, W. Wagner, and K.U. Bletzinger. A finite element model for the analysis of wrinkled membrane structures. *International Journal of Space Structures*, 18 (1):1–14, 2003.

Appendix A

Derivations for Wrinkling Model

This appendix provides detailed derivations and transformations that have been applied in the equations addressed below. To keep the representation throughout the text as concise as possible, some rather lengthy intermediate steps in the derivations have been deferred to the appendix.

A.1 Properties of the modified constitutive tensor, $\boldsymbol{\Xi}$

In the following, symmetry and positive semidefiniteness properties of $\boldsymbol{\Xi}$ are described in detail.

A.1.1 Symmetry property of the modified constitutive tensor, $\boldsymbol{\Xi}$

The symmetry of $\boldsymbol{\Xi}$ in (3.42) is readily proven according to [ANNP07]. We start from proving the symmetry of $\mathbf{CH}$

$$\begin{aligned}\mathbf{H}^2 &= \frac{(1-\rho+\gamma)^2\,\mathbf{U}_2\mathbf{U}_2^T\,[\mathbb{C}]}{\mathbf{U}_2^T\,[\mathbb{C}]\,\mathbf{U}_2}\cdot\frac{\mathbf{U}_2\mathbf{U}_2^T\,[\mathbb{C}]}{\mathbf{U}_2^T\,[\mathbb{C}]\,\mathbf{U}_2} = \frac{(1-\rho+\gamma)^2\,\mathbf{U}_2\mathbf{U}_2^T\,[\mathbb{C}]}{\mathbf{U}_2^T\,[\mathbb{C}]\,\mathbf{U}_2},\\ &= (1-\rho+\gamma)\,\mathbf{H} = j\mathbf{H}. \qquad \text{(A.1)}\end{aligned}$$

$$\mathbb{C}\mathbf{H} = \frac{(1-\rho+\gamma)\,[\mathbb{C}]\,\mathbf{U}_2\mathbf{U}_2^T\,[\mathbb{C}]}{\mathbf{U}_2^T\,[\mathbb{C}]\,\mathbf{U}_2} = \mathbf{H}^T\,[\mathbb{C}]^T = [\mathbb{C}\mathbf{H}]^T. \qquad \text{(A.2)}$$

Similarly to (A.2), the symmetry of the modified constitutive tensor $\boldsymbol{\Xi}$ is shown by

$$\boldsymbol{\Phi}^2 = \mathbf{I} - 2\mathbf{H} + \mathbf{H}^2. \qquad \text{(A.3)}$$

$$\boldsymbol{\Xi} = [\mathbb{C}]\,\boldsymbol{\Phi} = [\mathbb{C}]\,[\mathbf{I}-\mathbf{H}] = [\mathbb{C}] - [\mathbb{C}]\,\mathbf{H} = ([\mathbb{C}] - [\mathbb{C}]\,\mathbf{H})^T = ([\mathbb{C}]\,\boldsymbol{\Phi})^T = \boldsymbol{\Xi}^T. \qquad \text{(A.4)}$$

$$\text{(A.5)}$$

A.1.2 Positive semidefiniteness property of the modified constitutive tensor, $\boldsymbol{\Xi}$

The positive semi-definiteness of $\boldsymbol{\Xi}$ can be proved as in the following. From (3.42), let $\boldsymbol{\Psi}$ be an arbitrary vector and $[\boldsymbol{\Phi}+\mathbf{H}]\,\boldsymbol{\Psi} = \mathbf{I}\boldsymbol{\Psi}$. With the positive definiteness property of $\mathbb{C}$, pre

and post multiplying $\mathbb{C}$ by $\mathbf{\Psi}$ yields

$$\begin{aligned}\mathbf{\Psi}^T[\mathbb{C}]\mathbf{\Psi} &= \mathbf{\Psi}^T[\mathbf{\Phi}+\mathbf{H}]^T[\mathbb{C}][\mathbf{\Phi}+\mathbf{H}]\mathbf{\Psi} = \mathbf{\Psi}^T\left[\mathbf{\Phi}^T+\mathbf{H}^T\right][\mathbb{C}][\mathbf{\Phi}+\mathbf{H}]\mathbf{\Psi} > 0,\\ &= \mathbf{\Psi}^T\left[\mathbf{\Phi}^T[\mathbb{C}]\mathbf{\Phi}+\mathbf{H}^T[\mathbb{C}]\mathbf{\Phi}+\mathbf{\Phi}^T[\mathbb{C}]\mathbf{H}+\mathbf{H}^T[\mathbb{C}]\mathbf{H}\right]\mathbf{\Psi} > 0,\\ &= \mathbf{\Psi}^T\left[\mathbf{\Phi}^T[\mathbb{C}]\mathbf{\Phi}+2[\mathbb{C}](\mathbf{H}-\mathbf{H}^2)+\mathbf{H}^T[\mathbb{C}]\mathbf{H}\right]\mathbf{\Psi} > 0. \end{aligned} \tag{A.6}$$

From (A.6), the following expression is valid

$$\begin{aligned}\mathbf{\Psi}^T[\mathbb{C}]\mathbf{\Psi} &\geq \mathbf{\Psi}^T\left[\mathbf{\Phi}^T[\mathbb{C}]\mathbf{\Phi}+2[\mathbb{C}](\mathbf{H}-\mathbf{H}^2)\right]\mathbf{\Psi},\\ \mathbf{\Psi}^T\left[[\mathbb{C}]-\mathbf{\Phi}^T[\mathbb{C}]\mathbf{\Phi}+2[\mathbb{C}](\mathbf{H}-\mathbf{H}^2)\right]\mathbf{\Psi} &\geq 0,\\ \mathbf{\Psi}^T[\mathbb{C}]\left[\mathbf{I}-(\mathbf{I}-2\mathbf{H}-\mathbf{H}^2)-2(\mathbf{H}-\mathbf{H}^2)\right]\mathbf{\Psi} &\geq 0,\\ \mathbf{\Psi}^T[\mathbb{C}]\mathbf{H}^2\mathbf{\Psi} &\geq 0. \end{aligned} \tag{A.7}$$

(A.7) expresses the positive semi-definiteness of $\mathbb{C}\mathbf{H}^2$ which can be fulfilled if and only if $\mathbf{H}^2$ is positive semi-definite. Moreover, this property of $\mathbf{H}^2$ brings out that $\mathbf{H}$ is also positive semi-definite. With these evidences, $\mathbb{C}\mathbf{H}$ possesses the positive semi-definite property. All mentioned here are described by

$$\mathbf{\Psi}^T[\mathbb{C}]\mathbf{H}^2\mathbf{\Psi} \geq 0 \qquad \Rightarrow \qquad \mathbf{\Psi}^T[\mathbb{C}]\mathbf{H}\mathbf{\Psi} \geq 0. \tag{A.8}$$

With (A.8), the second term of (A.6) can be rewritten as:

$$2\mathbf{\Psi}^T[\mathbb{C}](\mathbf{H}-\mathbf{H}^2)\mathbf{\Psi} = 2\mathbf{\Psi}^T[\mathbb{C}](\mathbf{H}-j\mathbf{H})\mathbf{\Psi} = 2(1-j)\mathbf{\Psi}^T[\mathbb{C}]\mathbf{H}\mathbf{\Psi} \geq 0. \tag{A.9}$$

With (A.8), a fulfilment of (A.9) is obtainable if

$$(1-j) \geq 0 \qquad \Rightarrow \qquad 1 \geq j. \tag{A.10}$$

The condition in (A.10) agrees with the definition of the modification factor j which varies between 0 and 1. This value corresponds to the modification degree of the constitutive tensor. From (A.6) and (A.9), this expression is valid

$$\begin{aligned}\mathbf{\Psi}^T[\mathbb{C}]\mathbf{\Psi} &\geq \mathbf{\Psi}^T[\mathbb{C}]\mathbf{\Psi}-\mathbf{\Psi}^T\mathbf{\Phi}^T[\mathbb{C}]\mathbf{\Phi}\mathbf{\Psi}-\mathbf{\Psi}^T[\mathbb{C}](\mathbf{H}-\mathbf{H}^2)\mathbf{\Psi},\\ \mathbf{\Psi}^T\mathbf{H}^T[\mathbb{C}]\mathbf{H}\mathbf{\Psi}+\mathbf{\Psi}^T[\mathbb{C}](\mathbf{H}-\mathbf{H}^2)\mathbf{\Psi} &\geq 0,\\ \mathbf{\Psi}^T[\mathbb{C}]\mathbf{\Psi}-\mathbf{\Psi}^T[\mathbb{C}]\mathbf{H}^2\mathbf{\Psi}-\mathbf{\Psi}^T[\mathbb{C}](\mathbf{H}-\mathbf{H}^2)\mathbf{\Psi} &\geq 0,\\ \mathbf{\Psi}^T[\mathbb{C}](\mathbf{I}-\mathbf{H})\mathbf{\Psi} &\geq 0,\\ \mathbf{\Psi}^T[\mathbb{C}]\mathbf{\Phi}\mathbf{\Psi} \geq 0 \qquad &\Rightarrow \qquad \mathbf{\Psi}^T\mathbf{\Xi}\mathbf{\Psi} \geq 0. \end{aligned} \tag{A.11}$$

Obviously, (A.11) corroborates the positive semi definiteness of $\mathbf{\Xi}$.

Appendix B

Derivations for Mortar Contact

B.1 Static condensation for unilateral contact

This section explains the static condensation of the modified effective incremental structural equation in eq. (5.109) to obtain the condensed form as written in eq. (5.111). As the point of departure, the modified effective incremental structural equation in eq. (5.109) is given, viz.

$$\begin{bmatrix} (\mathbf{K}_T^{eff})_{NN} & (\mathbf{K}_T^{eff})_{N\mathcal{I}_l} & (\mathbf{K}_T^{eff})_{N\mathcal{A}_l} & \mathbf{0} & \mathbf{0} \\ (\mathbf{K}_T^{eff})_{\mathcal{I}_l N} & (\mathbf{K}_T^{eff})_{\mathcal{I}_l\mathcal{I}_l} & (\mathbf{K}_T^{eff})_{\mathcal{I}_l\mathcal{A}_l} & -\mathbf{D}_S^{\mathcal{I}_l} & \mathbf{0} \\ (\mathbf{K}_T^{eff})_{\mathcal{A}_l N} & (\mathbf{K}_T^{eff})_{\mathcal{A}_l\mathcal{I}_l} & (\mathbf{K}_T^{eff})_{\mathcal{A}_l\mathcal{A}_l} & \mathbf{0} & -\mathbf{D}_S^{\mathcal{A}_l} \\ \mathbf{0} & \mathbf{0} & \mathbf{0} & \mathbf{I}_{n_{sd}\cdot|\mathcal{I}_l|} & \mathbf{0} \\ \mathbf{0} & \mathbf{0} & \tilde{\mathbf{N}}_{\mathcal{A}_l} & \mathbf{0} & \mathbf{0} \\ \mathbf{0} & \mathbf{0} & \mathbf{0} & \mathbf{0} & \mathbf{T}_{\mathcal{A}_l} \end{bmatrix} \begin{bmatrix} \Delta\mathbf{d}^N \\ \Delta\mathbf{d}^{\mathcal{I}_l} \\ \Delta\mathbf{d}^{\mathcal{A}_l} \\ \mathbf{z}_{n+1-\alpha_f}^{\mathcal{I}_l} \\ \mathbf{z}_{n+1-\alpha_f}^{\mathcal{A}_l} \end{bmatrix} = \begin{bmatrix} \mathbf{f}_N^{eff} \\ \mathbf{f}_{\mathcal{I}_l}^{eff} \\ \mathbf{f}_{\mathcal{A}_l}^{eff} \\ \mathbf{0} \\ -(\tilde{\mathbf{g}}_{n+1}^k)_{\mathcal{A}_l} \\ \mathbf{0} \end{bmatrix}. \tag{B.1}$$

From the fact that the discrete nodal Lagrange multipliers or the nodal contact traction on inactive contact nodes must vanish $\mathbf{z}_{n+1-\alpha_f}^{\mathcal{I}_l} = \mathbf{0}$, the fourth row and column in eq. (B.1) can be eliminated such that

$$\begin{bmatrix} (\mathbf{K}_T^{eff})_{NN} & (\mathbf{K}_T^{eff})_{N\mathcal{I}_l} & (\mathbf{K}_T^{eff})_{N\mathcal{A}_l} & \mathbf{0} \\ (\mathbf{K}_T^{eff})_{\mathcal{I}_l N} & (\mathbf{K}_T^{eff})_{\mathcal{I}_l\mathcal{I}_l} & (\mathbf{K}_T^{eff})_{\mathcal{I}_l\mathcal{A}_l} & \mathbf{0} \\ (\mathbf{K}_T^{eff})_{\mathcal{A}_l N} & (\mathbf{K}_T^{eff})_{\mathcal{A}_l\mathcal{I}_l} & (\mathbf{K}_T^{eff})_{\mathcal{A}_l\mathcal{A}_l} & -\mathbf{D}_S^{\mathcal{A}_l} \\ \mathbf{0} & \mathbf{0} & \tilde{\mathbf{N}}_{\mathcal{A}_l} & \mathbf{0} \\ \mathbf{0} & \mathbf{0} & \mathbf{0} & \mathbf{T}_{\mathcal{A}_l} \end{bmatrix} \begin{bmatrix} \Delta\mathbf{d}^N \\ \Delta\mathbf{d}^{\mathcal{I}_l} \\ \Delta\mathbf{d}^{\mathcal{A}_l} \\ \mathbf{z}_{n+1-\alpha_f}^{\mathcal{A}_l} \end{bmatrix} = \begin{bmatrix} \mathbf{f}_N^{eff} \\ \mathbf{f}_{\mathcal{I}_l}^{eff} \\ \mathbf{f}_{\mathcal{A}_l}^{eff} \\ -(\tilde{\mathbf{g}}_{n+1}^k)_{\mathcal{A}_l} \\ \mathbf{0} \end{bmatrix}. \tag{B.2}$$

By pre-multiplying the third row of eq. (B.2) with $\mathbf{T}_{\mathcal{A}_l}$ and the vanishing of the tangential contact traction in case of frictionless contact, $\mathbf{T}_{\mathcal{A}_l}\mathbf{z}_{n+1-\alpha_f}^{\mathcal{A}_l} = \mathbf{0}$, the last row can be eliminated from eq. (B.2) such that

$$\begin{bmatrix} (\mathbf{K}_T^{eff})_{NN} & (\mathbf{K}_T^{eff})_{N\mathcal{I}_l} & (\mathbf{K}_T^{eff})_{N\mathcal{A}_l} & \mathbf{0} \\ (\mathbf{K}_T^{eff})_{\mathcal{I}_l N} & (\mathbf{K}_T^{eff})_{\mathcal{I}_l\mathcal{I}_l} & (\mathbf{K}_T^{eff})_{\mathcal{I}_l\mathcal{A}_l} & \mathbf{0} \\ \mathbf{T}_{\mathcal{A}_l}(\mathbf{K}_T^{eff})_{\mathcal{A}_l N} & \mathbf{T}_{\mathcal{A}_l}(\mathbf{K}_T^{eff})_{\mathcal{A}_l\mathcal{I}_l} & \mathbf{T}_{\mathcal{A}_l}(\mathbf{K}_T^{eff})_{\mathcal{A}_l\mathcal{A}_l} & -\mathbf{T}_{\mathcal{A}_l}\mathbf{D}_S^{\mathcal{A}_l} \\ \mathbf{0} & \mathbf{0} & \tilde{\mathbf{N}}_{\mathcal{A}_l} & \mathbf{0} \end{bmatrix} \begin{bmatrix} \Delta\mathbf{d}^N \\ \Delta\mathbf{d}^{\mathcal{I}_l} \\ \Delta\mathbf{d}^{\mathcal{A}_l} \\ \mathbf{z}_{n+1-\alpha_f}^{\mathcal{A}_l} \end{bmatrix} = \begin{bmatrix} \mathbf{f}_N^{eff} \\ \mathbf{f}_{\mathcal{I}_l}^{eff} \\ \mathbf{T}_{\mathcal{A}_l}\mathbf{f}_{\mathcal{A}_l}^{eff} \\ -(\tilde{\mathbf{g}}_{n+1}^k)_{\mathcal{A}_l} \end{bmatrix}. \tag{B.3}$$

With the vanishing of the tangential contact traction $\mathbf{T}_{\mathcal{A}_l}\mathbf{z}_{n+1-\alpha_f}^{\mathcal{A}_l} = \mathbf{0}$, it is valid to write $-\mathbf{T}_{\mathcal{A}_l}\mathbf{D}_S^{\mathcal{A}_l}\mathbf{z}_{n+1-\alpha_f}^{\mathcal{A}_l} = \mathbf{0}$. Hence, one can condense the fourth column of eq. (B.3) and then

interchanging of the third and the fourth row leads to the condensed form of the modified effective incremental structural equation as given in eq. (5.111):

$$\underbrace{\begin{bmatrix} (\mathbf{K}_T^{eff})_{NN} & (\mathbf{K}_T^{eff})_{N\mathcal{I}_l} & (\mathbf{K}_T^{eff})_{N\mathcal{A}_l} \\ (\mathbf{K}_T^{eff})_{\mathcal{I}_l N} & (\mathbf{K}_T^{eff})_{\mathcal{I}_l\mathcal{I}_l} & (\mathbf{K}_T^{eff})_{\mathcal{I}_l\mathcal{A}_l} \\ \mathbf{0} & \mathbf{0} & \tilde{\mathbf{N}}_{\mathcal{A}_l} \\ \mathbf{T}_{\mathcal{A}_l}(\mathbf{K}_T^{eff})_{\mathcal{A}_l N} & \mathbf{T}_{\mathcal{A}_l}(\mathbf{K}_T^{eff})_{\mathcal{A}_l\mathcal{I}_l} & \mathbf{T}_{\mathcal{A}_l}(\mathbf{K}_T^{eff})_{\mathcal{A}_l\mathcal{A}_l} \end{bmatrix}}_{\mathbf{K}_T^{eff,mod}} \begin{bmatrix} \Delta\mathbf{d}^N \\ \Delta\mathbf{d}^{\mathcal{I}_l} \\ \Delta\mathbf{d}^{\mathcal{A}_l} \end{bmatrix} = \underbrace{\begin{bmatrix} \mathbf{f}_N^{eff} \\ \mathbf{f}_{\mathcal{I}_l}^{eff} \\ -(\tilde{\mathbf{g}}_{n+1}^k)_{\mathcal{A}_l} \\ \mathbf{T}_{\mathcal{A}_l}\mathbf{f}_{\mathcal{A}_l}^{eff} \end{bmatrix}}_{\mathbf{f}^{eff,mod}}. \tag{B.4}$$

B.2 Basis transformation for contact of two deformable bodies

This section shows the procedure for basis transformation of the effective incremental structural equation for contact problems of two deformable bodies form eq. (5.71) with the objective to achieve the same format as for the unilateral contact in eq. (5.59). As the starting point, the effective incremental structural equation for contact problems of two deformable bodies in eq. (5.71) is given

$$\begin{bmatrix} (\mathbf{K}_T^{eff})_{NN} & (\mathbf{K}_T^{eff})_{NM} & (\mathbf{K}_T^{eff})_{NS} & \mathbf{0} \\ (\mathbf{K}_T^{eff})_{MN} & (\mathbf{K}_T^{eff})_{MM} & (\mathbf{K}_T^{eff})_{MS} & \mathbf{M}_M^T \\ (\mathbf{K}_T^{eff})_{SN} & (\mathbf{K}_T^{eff})_{SM} & (\mathbf{K}_T^{eff})_{SS} & -\mathbf{D}_S \end{bmatrix} \begin{bmatrix} \Delta\mathbf{d}^N \\ \Delta\mathbf{d}^M \\ \Delta\mathbf{d}^S \\ \mathbf{z}_{n+1-\alpha_f} \end{bmatrix} = \begin{bmatrix} \mathbf{f}_N^{eff} \\ \mathbf{f}_M^{eff} \\ \mathbf{f}_S^{eff} \end{bmatrix}. \tag{B.5}$$

With the definition of the incremental jump in displacement from eq. (5.119), the vector of incremental displacement of slave contact nodes $\Delta\mathbf{d}_{n+1}^{Sk}$ is expressed by

$$[\Delta\mathbf{d}] = \Delta\mathbf{d}_{n+1}^{Sk} - \hat{\mathbf{M}}\Delta\mathbf{d}_{n+1}^{Mk} \quad \rightarrow \quad \Delta\mathbf{d}_{n+1}^{Sk} = [\Delta\mathbf{d}] + \hat{\mathbf{M}}\Delta\mathbf{d}_{n+1}^{Mk}; \quad \hat{\mathbf{M}} = \mathbf{D}_S^{-1}\mathbf{M}_M. \tag{B.6}$$

By replacing $\Delta\mathbf{d}_{n+1}^{Sk}$ from eq. (B.6) in the first, second and third rows of eq. (B.5) yields

$$\begin{aligned} (\mathbf{K}_T^{eff})_{NN}\Delta\mathbf{d}^N + (\mathbf{K}_T^{eff})_{NM}\Delta\mathbf{d}^M + (\mathbf{K}_T^{eff})_{NS}([\Delta\mathbf{d}] + \hat{\mathbf{M}}\Delta\mathbf{d}^M) &= \mathbf{f}_N^{eff}, \\ (\mathbf{K}_T^{eff})_{NN}\Delta\mathbf{d}^N + ((\mathbf{K}_T^{eff})_{NM} + (\mathbf{K}_T^{eff})_{NS}\hat{\mathbf{M}})\Delta\mathbf{d}^M + (\mathbf{K}_T^{eff})_{NS}[\Delta\mathbf{d}] &= \mathbf{f}_N^{eff}. \end{aligned} \tag{B.7}$$

$$\begin{aligned} (\mathbf{K}_T^{eff})_{MN}\Delta\mathbf{d}^N + (\mathbf{K}_T^{eff})_{MM}\Delta\mathbf{d}^M + (\mathbf{K}_T^{eff})_{MS}([\Delta\mathbf{d}] + \hat{\mathbf{M}}\Delta\mathbf{d}^M) + \mathbf{M}_M^T\mathbf{z} &= \mathbf{f}_M^{eff}, \\ (\mathbf{K}_T^{eff})_{MN}\Delta\mathbf{d}^N + ((\mathbf{K}_T^{eff})_{MM} + (\mathbf{K}_T^{eff})_{MS}\hat{\mathbf{M}})\Delta\mathbf{d}^M + (\mathbf{K}_T^{eff})_{MS}([\Delta\mathbf{d}]) + \mathbf{M}_M\mathbf{z} &= \mathbf{f}_M^{eff}. \end{aligned} \tag{B.8}$$

$$\begin{aligned} (\mathbf{K}_T^{eff})_{SN}\Delta\mathbf{d}^N + (\mathbf{K}_T^{eff})_{SM}\Delta\mathbf{d}^M + (\mathbf{K}_T^{eff})_{SS}([\Delta\mathbf{d}] + \hat{\mathbf{M}}\Delta\mathbf{d}^M) - \mathbf{D}_S\mathbf{z} &= \mathbf{f}_S^{eff}, \\ (\mathbf{K}_T^{eff})_{SN}\Delta\mathbf{d}^N + ((\mathbf{K}_T^{eff})_{SM} + (\mathbf{K}_T^{eff})_{SS}\hat{\mathbf{M}})\Delta\mathbf{d}^M + (\mathbf{K}_T^{eff})_{SS}[\Delta\mathbf{d}] - \mathbf{D}_S\mathbf{z} &= \mathbf{f}_S^{eff}. \end{aligned} \tag{B.9}$$

respectively. Then, premultiplying eq. (B.9) with $\hat{\mathbf{M}}^T$ and adding the result with eq. (B.8), one obtains

$$\left\{ \begin{array}{c} ((\mathbf{K}_T^{eff})_{MN} + \hat{\mathbf{M}}^T(\mathbf{K}_T^{eff})_{SN})\Delta\mathbf{d}^N \\ +((\mathbf{K}_T^{eff})_{MM} + (\mathbf{K}_T^{eff})_{MS}\hat{\mathbf{M}} + \hat{\mathbf{M}}^T(\mathbf{K}_T^{eff})_{SM} + \hat{\mathbf{M}}^T(\mathbf{K}_T^{eff})_{SS}\hat{\mathbf{M}})\Delta\mathbf{d}^M \\ +((\mathbf{K}_T^{eff})_{MS} + \hat{\mathbf{M}}^T(\mathbf{K}_T^{eff})_{SS})[\Delta\mathbf{d}] + \underbrace{(\mathbf{M}_M^T - \hat{\mathbf{M}}^T\mathbf{D}_S)\mathbf{z}}_{\mathbf{M}_M^T - \mathbf{M}_M^T\mathbf{D}_S^{-1}\mathbf{D}_S = \mathbf{0};\ \text{(see eq.(5.119))}} \end{array} \right\} = \mathbf{f}_M^{eff} + \hat{\mathbf{M}}^T\mathbf{f}_S^{eff}. \tag{B.10}$$

Forming the system of equation by sorting eqs. (B.7), (B.9) and (B.10), one obtains the transformed effective incremental structural equation as shown in eq. (5.125), viz.

$$\begin{bmatrix} (\mathbf{K}_T^{eff})_{NN} & (\mathbf{K}_T^{eff})_{NM} + (\mathbf{K}_T^{eff})_{NS}\hat{\mathbf{M}} & (\mathbf{K}_T^{eff})_{NS} & \mathbf{0} \\ \begin{bmatrix} (\mathbf{K}_T^{eff})_{MN} + \\ \hat{\mathbf{M}}^T(\mathbf{K}_T^{eff})_{SN} \end{bmatrix} & \begin{bmatrix} (\mathbf{K}_T^{eff})_{MM} + \hat{\mathbf{M}}^T(\mathbf{K}_T^{eff})_{SM} + \\ (\mathbf{K}_T^{eff})_{MS}\hat{\mathbf{M}} + \hat{\mathbf{M}}^T(\mathbf{K}_T^{eff})_{SS}\hat{\mathbf{M}} \end{bmatrix} & \begin{bmatrix} (\mathbf{K}_T^{eff})_{MS} + \\ \hat{\mathbf{M}}^T(\mathbf{K}_T^{eff})_{SS} \end{bmatrix} & \mathbf{0} \\ (\mathbf{K}_T^{eff})_{SN} & (\mathbf{K}_T^{eff})_{SM} + (\mathbf{K}_T^{eff})_{SS}\hat{\mathbf{M}} & (\mathbf{K}_T^{eff})_{SS} & -\mathbf{D}_S \end{bmatrix} \begin{bmatrix} \Delta\mathbf{d}^N \\ \Delta\mathbf{d}^M \\ [\Delta\mathbf{d}] \\ \mathbf{z}_{n+1-\alpha_f} \end{bmatrix} = \begin{bmatrix} \mathbf{f}_N^{eff} \\ \mathbf{f}_M^{eff} + \hat{\mathbf{M}}^T\mathbf{f}_S^{eff} \\ \mathbf{f}_S^{eff} \end{bmatrix} \tag{B.11}$$

B.3 Construction of discrete dual ansatz functions for the Lagrange multipliers in 3D case.

As mentioned in section 5.3.2.3, this appendix explains a construction procedure of the dual Ansatz functions for the Lagrange multipliers in case of an element with arbitrary shape in the three dimensional space which is illustrated in Figure B.1. Geometry of each element on the discrete slave contact boundary $\Gamma_c^{(1)^h}$ in Figure B.1 is described on the Cartesian basis with orthonormal base vectors $\mathbf{e}_i = \mathbf{e}^i$ by interpolation from nodal positions $\varphi_t^{(1)^h}(\mathbf{X}) = \sum_{D=1}^{n_c^s} N_D^{(1)}\left(\boldsymbol{\theta}^{(1)}(\mathbf{X})\right)\mathbf{d}_D^{(1)}(t)$ as described in eq. (5.29):

$$\mathbf{x} = \begin{bmatrix} \frac{1}{2}(7 + \eta + 3\xi + 3\xi\eta) \\ \frac{1}{4}(-13 - \eta - 7\xi + \xi\eta) \\ \frac{1}{4}(5 + 3\eta - \xi + 5\xi\eta) \end{bmatrix}. \tag{B.12}$$

From the geometry in eq. (B.12), the covariant base vectors $\mathbf{g}_\alpha$ at any point on the surface from eq. (2.3) is written by

$$\mathbf{g}_1 = \frac{\partial\mathbf{x}}{\partial\xi} = \begin{bmatrix} \frac{1}{2}(3 + 3\eta) \\ \frac{1}{4}(-7 + \eta) \\ \frac{1}{4}(-1 + 5\eta) \end{bmatrix} \quad \text{and} \quad \mathbf{g}_2 = \frac{\partial\mathbf{x}}{\partial\eta} = \begin{bmatrix} \frac{1}{2}(1 + 3\xi) \\ \frac{1}{4}(-1 + \xi) \\ \frac{1}{4}(3 + 5\xi) \end{bmatrix}. \tag{B.13}$$

Thus, the discrete dual Ansatz functions from eq. (5.38) with the help of eq. (5.48) is transformed to

$$n_{BB}^{(1)} = \int_{\gamma_c^{(1)h}} N_B^{(1)}\left(\boldsymbol{\theta}^{(1)}(\mathbf{X})\right) d\gamma = \int_{-1}^{1}\int_{-1}^{1} N_B^{(1)}(\xi^{(1)}, \eta^{(1)}) \, \|\mathbf{g}_1 \times \mathbf{g}_2\| \, d\xi d\eta, \tag{B.14}$$

while the M_{DB} from eq. (5.40) is define by

$$\begin{aligned} M_{DB} &= \int_{\gamma_c^{(1)h}} N_D^{(1)}(\boldsymbol{\theta}^{(1)}) N_B^{(1)}(\boldsymbol{\theta}^{(1)}) d\gamma, \\ &= \int_{-1}^{1}\int_{-1}^{1} N_D^{(1)}(\xi^{(1)}, \eta^{(1)}) N_B^{(1)}(\xi^{(1)}, \eta^{(1)}) \, \|\mathbf{g}_1 \times \mathbf{g}_2\| \, d\xi d\eta. \end{aligned} \tag{B.15}$$

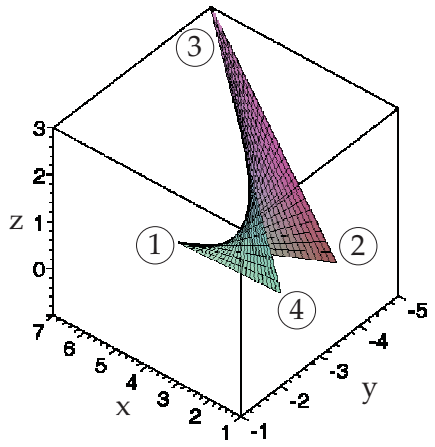

$\mathbf{x}_1$=(3,-1, 2)^T
$\mathbf{x}_2$=(3,-5,-1)^T
$\mathbf{x}_3$=(7,-5, 3)^T
$\mathbf{x}_4$=(1,-2, 1)^T

Figure B.1: An example of a membrane element at the contact interfaces in 3D problems.

By 2×2 quadrature rule, the numerical evaluation of the element matrix $\mathbf{D}_e := n_{AB}^{(1)} \in \mathbb{R}^{4\times4}$ as well as the matrix $\mathbf{M}_e := M_{DB} \in \mathbb{R}^{4\times4}$ from eq. (5.41) is available by

$$\mathbf{D}_e = \begin{bmatrix} 1.8645 & 0 & 0 & 0 \\ 0 & 3.7112 & 0 & 0 \\ 0 & 0 & 3.6265 & 0 \\ 0 & 0 & 0 & 2.0334 \end{bmatrix}, \quad \mathbf{M}_e = \begin{bmatrix} 0.5976 & 0.6172 & 0.3121 & 0.3375 \\ 0.6172 & 1.8710 & 0.9109 & 0.3121 \\ 0.3121 & 0.9109 & 1.7724 & 0.6312 \\ 0.3375 & 0.3121 & 0.6312 & 0.7524 \end{bmatrix}, \tag{B.16}$$

respectively. As a result, the transformation matrix $\mathbf{A}_e := a_{AD} \in \mathbb{R}^{4\times4}$ is calculated with

$$\mathbf{A}_e = \begin{bmatrix} 6.3567 & -2.0941 & 0.9456 & -2.7763 \\ -4.1683 & 4.0191 & -2.0018 & 1.8821 \\ 1.8392 & -1.9561 & 3.8965 & -3.2825 \\ -3.0278 & 1.0312 & -1.8405 & 5.1770 \end{bmatrix}. \tag{B.17}$$

Then, the discrete dual Ansatz functions for each node within an element is determined by $\phi_A^{(1)}(\boldsymbol{\theta}^{(1)}) = a_{AB} N_B^{(1)}(\boldsymbol{\theta}^{(1)})$ from eq. (5.39) such that

$$\begin{bmatrix} \phi_1^{(1)} \\ \phi_2^{(1)} \\ \phi_3^{(1)} \\ \phi_4^{(1)} \end{bmatrix} = \begin{bmatrix} 6.3567 & -2.0941 & 0.9456 & -2.7763 \\ -4.1683 & 4.0191 & -2.0018 & 1.8821 \\ 1.8392 & -1.9561 & 3.8965 & -3.2825 \\ -3.0278 & 1.0312 & -1.8405 & 5.1770 \end{bmatrix} \begin{bmatrix} N_1^{(1)} \\ N_2^{(1)} \\ N_3^{(1)} \\ N_4^{(1)} \end{bmatrix}. \tag{B.18}$$

In case of an undistorted element with constant determinant of jacobian j over the entire element, relevant matrices are invariant and can be expressed by

$$\mathbf{D}_e = \mathbf{I}_{4\times4}, \quad \mathbf{M}_e = \frac{1}{9}\begin{bmatrix} 4 & 2 & 1 & 2 \\ 2 & 4 & 2 & 1 \\ 1 & 2 & 4 & 2 \\ 2 & 1 & 2 & 4 \end{bmatrix}, \quad \mathbf{A}_e = \begin{bmatrix} 4 & -2 & 1 & -2 \\ -2 & 4 & -2 & 1 \\ 1 & -2 & 4 & -2 \\ -2 & 1 & -2 & 4 \end{bmatrix}. \tag{B.19}$$

Figure B.2 compares the dual Ansatz functions for a membrane element between (a) an undistorted element and (b) a distorted element.

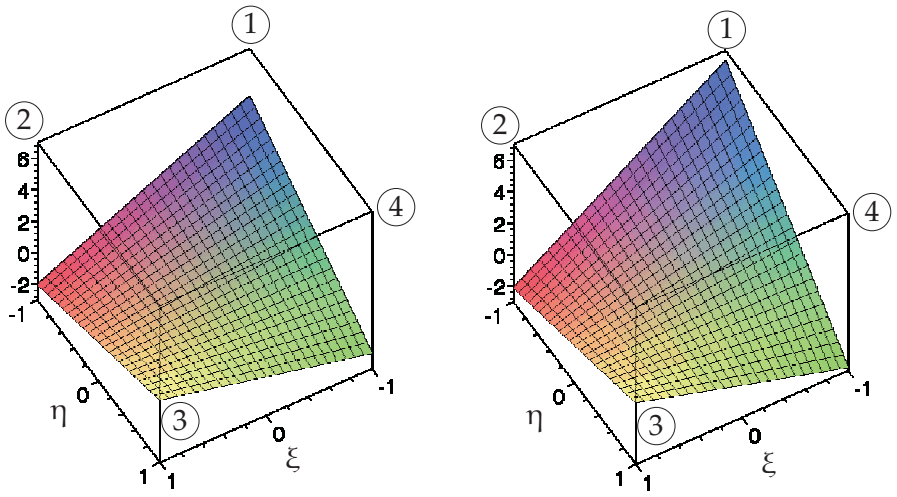

Figure B.2: Illustration for the dual Ansatz functions of node 1 in the 3D space for a membrane element for (a) an undistorted element and (b) a distorted element.

B.4 Energy conservation for time integration

The development of an energy conserving formulation is based on the general approach from Simo and Tarnow [ST92] which aims at constant algorithmic total energy of complete discrete system within a time step. For further derivation, algorithmic incremental total energy of a discrete system ΔE^{tot} is introduced along with incremental change in nodal coordinate $\Delta\mathbf{d}$ in eq. (B.20) by reformulating eq. (5.141), viz.

$$\underbrace{(\mathbf{d}_{n+1}-\mathbf{d}_n)}_{\Delta\mathbf{d}} = \underbrace{\frac{\beta\Delta t}{\gamma}\left[\dot{\mathbf{d}}_{n+1}+\frac{\gamma-\beta}{\beta}\dot{\mathbf{d}}_n+\frac{\gamma-2\beta}{2\beta}\Delta t\ddot{\mathbf{d}}_n\right]}_{\Delta\mathbf{d}^s} - \frac{\beta\Delta t}{\gamma}\dot{\mathbf{d}}^c. \tag{B.20}$$

To consider influences of the discrete contact velocity $\dot{\mathbf{d}}^c$ on the conservation of system total energy, $\dot{\mathbf{d}}^c$ in eq.(B.20) is multiplied to the equation of motion in eq. (5.142) to create incremental total system energy ΔE^{tot} without applied external forces $\mathbf{f}^{ext}_{n+1-\alpha_f}=\mathbf{0}$ within a time step Δt , viz.

$$\begin{aligned}\Delta E^{tot} &= \Delta E^{tot}_o + \Delta E^{tot}_c \stackrel{!}{=} 0,\\ &= \left[\mathbf{M}\left(\ddot{\mathbf{d}}_{n+1-\alpha_m}(\ddot{\mathbf{d}}_{n+1}(\mathbf{d}_{n+1}))-\frac{1-\alpha_m}{\gamma\Delta t}\dot{\mathbf{d}}^c\right)+\mathbf{f}^{int}(\mathbf{d}_{n+1-\alpha_f})-\mathbf{f}^c_{n+1-\alpha_f}\right]\Delta\mathbf{d}\stackrel{!}{=}0.\end{aligned} \tag{B.21}$$

With ΔE^{tot}_o and ΔE^{tot}_c being the original (witout contact) portion and contact portion of the incremental total energy, respectively. The first part, ΔE^{tot}_o, is written by

$$\Delta E^{tot}_o = \mathbf{M}\ddot{\mathbf{d}}_{n+1-\alpha_m}(\ddot{\mathbf{d}}_{n+1}(\mathbf{d}_{n+1}))\cdot\Delta\mathbf{d}^s+\mathbf{f}^{int}(\mathbf{d}_{n+1-\alpha_f})\cdot\Delta\mathbf{d}, \tag{B.22}$$

where the algorithmic internal force $\mathbf{f}^{int}(\mathbf{d}_{n+1-\alpha_f}(\mathbf{d}_{n+1}))$ is determined by the algorithmic conservation of energy methods, e.g. EMM or GEMM (see Table 2.3 in section 2.3.4). As mentioned in section 2.3.4.2, the GEMM is a controllable numerical dissipative method $\Delta E_o^{tot} \leq 0$ with a specific case of energy conservation $\Delta E_o^{tot} = 0$ when the unity spectral radius is defined $\rho_\infty = 1$. Besides, the second part ΔE_c^{tot}, the influence of the discrete contact velocity $\dot{\mathbf{d}}^c$, is written by

$$\Delta E_c^{tot} = \mathbf{M}\dot{\mathbf{d}}^c \cdot \left[-\frac{\beta \Delta t}{\gamma} \ddot{\mathbf{d}}_{n+1-\alpha_m}(\ddot{\mathbf{d}}_{n+1}(\mathbf{d}_{n+1})) - \frac{1-\alpha_m}{\gamma \Delta t} \Delta \mathbf{d}^s + \frac{\beta(1-\alpha_m)}{\gamma^2} \dot{\mathbf{d}}^c \right] - \mathbf{f}^c_{n+1-\alpha_f} \cdot \Delta \mathbf{d}. \tag{B.23}$$

From eq. (2.120), we obtain

$$\ddot{\mathbf{d}}_{n+1} = \frac{1}{\gamma \Delta t} \left(\dot{\mathbf{d}}_{n+1}(\ddot{\mathbf{d}}_{n+1}) - \dot{\mathbf{d}}_n - (1-\gamma)\Delta t \ddot{\mathbf{d}}_n \right). \tag{B.24}$$

Substitution of $\dot{\mathbf{d}}_{n+1}$ from eq. (5.141) into eq. (B.24) with the help of eq. (2.121) yields

$$\ddot{\mathbf{d}}_{n+1}(\mathbf{d}_{n+1}) = \frac{1}{\beta \Delta t^2}(\mathbf{d}_{n+1} - \mathbf{d}_n) - \frac{1}{\beta \Delta t} \dot{\mathbf{d}}_n - \frac{1-2\beta}{2\beta} \ddot{\mathbf{d}}_n + \frac{1}{\gamma \Delta t} \dot{\mathbf{d}}^c. \tag{B.25}$$

Inserting eqs. (5.140) and (B.25) in eq. (B.23), one obtains a quadratic equation

$$\Delta E_c^{tot} = \mathbf{M}\dot{\mathbf{d}}^c \cdot \left[R_1 \Delta \mathbf{d} + R_2 \dot{\mathbf{d}}_n + R_3 \ddot{\mathbf{d}}_n + R_4 \dot{\mathbf{d}}^c \right] - \mathbf{f}^c_{n+1-\alpha_f} \cdot \Delta \mathbf{d} \quad \text{with} \tag{B.26}$$

$$R_1 = \frac{2(\alpha_m - 1)}{\gamma \Delta t}, \quad R_2 = \frac{(1-\alpha_m)}{\gamma}, \quad R_3 = \frac{\Delta t}{2\gamma}(1 - \alpha_m - 2\beta), \quad R_4 = \frac{\beta(\alpha_m - 1)}{\gamma^2}.$$

B.5 Velocity update algorithm for contact problems with GEMM

To obtain the discrete contact velocity $\dot{\mathbf{d}}^c$, the total energy conservation in eq. (B.21) must be solved. In case of the unity spectral radius $\rho_\infty = 1 \rightarrow \Delta E_o^{tot} = 0$, eq. (B.21) is transformed to a homogeneous equation of eq. (B.26):

$$\Delta E^{tot} = \Delta E_c^{tot} = \mathbf{M}\dot{\mathbf{d}}^c \cdot \left[R_1 \Delta \mathbf{d} + R_2 \dot{\mathbf{d}}_n + R_3 \ddot{\mathbf{d}}_n + R_4 \dot{\mathbf{d}}^c \right] - \mathbf{f}^c_{n+1-\alpha_f} \cdot \Delta \mathbf{d} = 0. \tag{B.27}$$

At first, the generalized contact force vector $\mathbf{f}^c_{n+1-\alpha_f} \in \mathbb{R}^{n_{sd} \cdot n_{np}}$ from eq. (5.66) is rewritten such that

$$\mathbf{f}^c_{n+1-\alpha_f} = -\mathbf{B}^c \mathbf{N}_{n+1-\alpha_f} \mathbf{z}_{N_{n+1-\alpha_f}}, \tag{B.28}$$

where $\mathbf{z}_{N_{n+1-\alpha_f}}$ is the vector storing the scalar-valued normal component of the generalized discrete Lagrange multiplier at each slave node $A \in S$ with $(\mathbf{z}_{N_{n+1-\alpha_f}})_A = -\mathbf{z}_{A_{n+1-\alpha_f}} \cdot \mathbf{n}_{A_{n+1-\alpha_f}}$ (see eq. (5.6)). The matrix $\mathbf{N}_n$, evaluated at t_n, stands for the matrix storing the unit normal vector of all slave nodes $A \in S$:

$$\mathbf{N}_n = \begin{bmatrix} \mathbf{n}_{n,\{A:=S[1]\}} & & \\ & \ddots & \\ & & \mathbf{n}_{n,\{A:=S[n_c^s]\}} \end{bmatrix} \in \mathbb{R}^{n_{sd} \cdot n_c^s \times n_c^s}. \tag{B.29}$$

Then, we employ the assumption from Laursen and Love [LL02] that the discrete contact velocity $\dot{\mathbf{d}}^c$ induces an impulse $\mathbf{p}_N$ acting in the direction of the normal vector of contact boundaries at contact interfaces. This assumption considers that the contact impulse introduces momentum change which is represented by discrete contact velocity via

$$\mathbf{M}\dot{\mathbf{d}}^c = \mathbf{B}^c\mathbf{N}_{n+\alpha_N}\mathbf{p}_N, \tag{B.30}$$

where the n_c^s-vector $\mathbf{p}_N$ collects normal contact impulses at all slave node $A \in S$ with the parameter $\alpha_N \in [0,1]$ to generalize the state of normal contact impulse. According to Laursen and Love [LL02], this parameter is defined at unity $\alpha_N = 1$ within this work to guarantee the angular momentum conservation in case of multibody contact problems. Thus, eq. (B.30) is changed to

$$\dot{\mathbf{d}}^c = \mathbf{M}^{-1}\mathbf{B}^c\mathbf{N}_{n+1}\mathbf{p}_N. \tag{B.31}$$

Substitution of $\dot{\mathbf{d}}^c$ from eq. (B.31) and $\mathbf{f}^c_{n+1-\alpha_f}$ from eq. (B.28) into eq.(B.27) yields

$$\begin{aligned}
\mathbf{M}\mathbf{M}^{-1}\mathbf{B}^c\mathbf{N}_{n+1}\mathbf{p}_N \cdot \left[R_1\Delta\mathbf{d} + R_2\dot{\mathbf{d}}_n + R_3\ddot{\mathbf{d}}_n + R_4\dot{\mathbf{d}}^c\right] + \Delta\mathbf{d}\cdot\mathbf{B}^c\mathbf{N}_{n+1-\alpha_f}\mathbf{z}_N = 0,\\
R_4\mathbf{B}^c\mathbf{N}_{n+1}\mathbf{p}_N \cdot \mathbf{M}^{-1}\mathbf{B}^c\mathbf{N}_{n+1}\mathbf{p}_N + \left[R_1\Delta\mathbf{d} + R_2\dot{\mathbf{d}}_n + R_3\ddot{\mathbf{d}}_n\right]\cdot\mathbf{B}^c\mathbf{N}_{n+1}\mathbf{p}_N + \Delta\mathbf{d}\cdot\mathbf{B}^c\mathbf{N}_{n+1-\alpha_f}\mathbf{z}_N = 0,\\
\mathbf{p}_N^T\underbrace{R_4\mathbf{N}_{n+1}^T(\mathbf{B}^c)^T\mathbf{M}^{-1}\mathbf{B}^c\mathbf{N}_{n+1}}_{\boldsymbol{\Phi}}\mathbf{p}_N + \underbrace{\left[R_1\Delta\mathbf{d} + R_2\dot{\mathbf{d}}_n + R_3\ddot{\mathbf{d}}_n\right]^T\mathbf{B}^c\mathbf{N}_{n+1}}_{\boldsymbol{\psi}}\mathbf{p}_N + \underbrace{\Delta\mathbf{d}^T\mathbf{B}^c\mathbf{N}_{n+1-\alpha_f}}_{\boldsymbol{\omega}}\mathbf{z}_N = 0,
\end{aligned} \tag{B.32}$$

where $\mathbf{z}_N$ stands for an abbreviation of $\mathbf{z}_{N_{n+1-\alpha_f}}$. Thus, the quadratic equation is achieve by

$$\mathbf{p}_N^T\boldsymbol{\Phi}\mathbf{p}_N + \boldsymbol{\psi}\mathbf{p}_N + \boldsymbol{\omega}\mathbf{z}_N = 0. \tag{B.33}$$

Unfortunately, eq. (B.33) is unsolvable in the presented structure unless the coupling among slave nodes is decoupled. Hence, eq. (B.33) is reformulated for each individual slave node $A \in S$ via

$$\sum_{B=1}^{n_c^s}\left[\Phi_{AB}p_{N_B}p_{N_A}\right] + \psi_A p_{N_A} + \omega_A z_{N_A} = 0; \quad \forall A \in S, \tag{B.34}$$

which after reformulation is turned to

$$\begin{aligned}
\Phi_{AA}p_{N_A}p_{N_A} + \underbrace{\left[\sum_{B=1,B\neq A}^{n_c^s}\Phi_{AB}p_{N_B} + \psi_A\right]}_{\varsigma_A}p_{N_A} + \omega_A z_{N_A} = 0; \quad \forall A \in S,\\
\Phi_{AA}p_{N_A}^2 + \varsigma_A p_{N_A} + \omega_A z_{N_A} = 0.
\end{aligned} \tag{B.35}$$

The roots of eq. (B.35) are determined by

$$\frac{-\varsigma_A \pm \sqrt{\varsigma_A^2 - 4\Phi_{AA}\omega_A z_{N_A}}}{2\Phi_{AA}}, \tag{B.36}$$

which are two positive real numbers if and only if

$$\varsigma_A^2 - 4\Phi_{AA}\omega_A z_{N_A} > 0. \tag{B.37}$$

Table B.1: Classification of $\omega_A z_{N_A}$ at the end of the current time step t_{n+1} .

Contact description	ω_A	z_{N_A}	$\omega_A z_{N_A}$
(1) Node A is inactive within the current time step	> 0	$= 0$	$= 0$
(2) Node A becomes active within the current time step	> 0	> 0	> 0
(3) Node A becomes inactive within the current time step	< 0	$= 0$	$= 0$
(4) Node A is active the whole current time step	$= 0$	> 0	$= 0$

With a close look on eq. (B.37), $\varsigma_A^2 \geq 0$ is always positive semi definite. Moreover, since both a quadratic function of $\mathbf{B}^c\mathbf{N}_{n+1}$ and each component of the mass matrix inverse $\mathbf{M}^{-1}$ are always positive, thus the sign of Φ_{AA}, defined in eq. (B.32) is dictated by value of R_4 which is always negative (see eq. (2.136)). Eq. (B.37) is fulfilled if and only if $\omega_A z_{N_A} > 0$. The definition of ω_A is equivalent to that of the mortar incremental change in nodal coordinate projected onto the direction of the normal vector at node $\mathbf{n}_A$, $(\Delta\tilde{d}^S)_A$, in eq. (5.100) for unilateral contact and the mortar incremental relative displacement at node A projected into the direction of its normal vector $\mathbf{n}_A$, $[\Delta\tilde{d}]_A$, for contact problems of two deformable bodies in eq. (5.120) which are repeated here for simplicity:

$$\omega_A = \begin{cases} \left(\Delta\tilde{d}^S\right)_A ; \ \forall A \in S & \text{unilateral contact,} \\ \left[\Delta\tilde{d}\right]_A ; \ \forall A \in S & \text{two deformable bodies contact.} \end{cases} \tag{B.38}$$

Note that all quantities are evaluated at the end of the current time step t_{n+1} as a postprocessing procedure. To determine the sign of $\omega_A z_{N_A}$, four distinct cases are considered in Table B.1. From this Table, $\omega_A z_{N_A}$ will never be negative. As a result, roots p_{N_A} of eq. (B.35) are always two distinct real numbers one of which is a meaningful choice for normal impulse across the contact interfaces. To choose a suitable root, eq. (B.36) is reformulated with the criterion for a suitable choice proposed in Laursen and Love [LL02] and Hartmann [Har07] to

$$\begin{aligned} p_{N_A} &= \frac{-\varsigma_A \pm \sqrt{\varsigma_A^2 - 4\Phi_{AA}\omega_A z_{N_A}}}{2\Phi_{AA}} = \frac{-\varsigma_A \pm (|\varsigma_A| + \epsilon)}{2\Phi_{AA}}, \\ &= \frac{sign(\varsigma_A)}{2\Phi_{AA}}\{\epsilon, -(2\,|\varsigma_A| + \epsilon)\} \quad \text{with} \quad \epsilon > 0. \end{aligned} \tag{B.39}$$

For a physical interpretation, the normal contact impulse does not exist at an inactive slave node $A \in \mathcal{I}$, i.e. $p_{N_A} = 0$ when $\omega_A z_{N_A} = 0 \Rightarrow \epsilon = 0$. This expression is valid only for the first solution of eq. (B.39) which always has the same sign as ς_A, whereas the sign of another solution choice is always opposite to that of ς_A. For this reason, the uniqueness of the root can be ensured by a satisfaction of the condition:

$$sign(p_{N_A}) = -sign(\varsigma_A). \tag{B.40}$$

After a proper normal contact impulse p_{N_A} is obtained, the discrete contact velocity $\dot{\mathbf{d}}^c$ is determined by eq. (B.31). Eventually, the update of discrete system velocity in eq. (5.140) is performed in a postprocessing step to achieve the energy conservation goal at the end of each time step. Note that the expression $\omega_A z_{N_A} \neq 0$ is valid within the current time

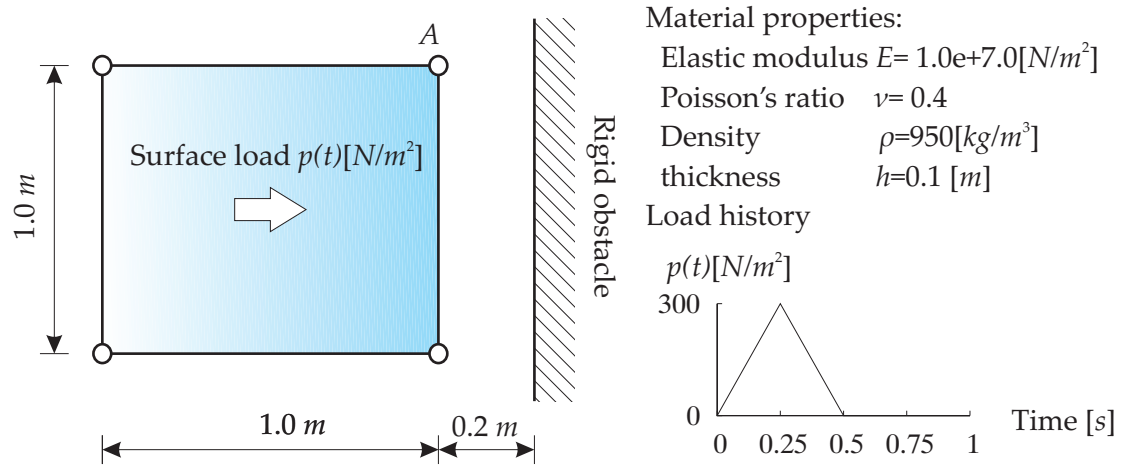

Figure B.3: Information for 2D box example: geometric, material and load informations.

step $t \in [t_n, t_{n+1}]$ only for the second case in Table B.1. Therefore, the velocity update routine is activated only in this case.

To verify the implementation and demonstrate influences of the velocity update algorithm, a simple 2D unilateral contact problem presented in [Har07] is performed.

B.5.1 Problem description

In Figure B.3, all information about the geometry, material and load is given. A planar square block is under a time-dependent surface force $p(t)$ which is controlled by the ramp function in Figure B.3 to introduce constant velocity on the block before it collides with the rigid wall. With given information, the magnitude of momentum I and velocity of the whole block $\dot{\mathbf{x}}$, induced by the load function, can be computed analytically by

$$
\begin{aligned}
I &= \frac{1}{2} \cdot 0.5[s] \cdot 1[m^2] \cdot 300[N/m^2] = 75[Ns], \\
\dot{\mathbf{x}} &= \frac{I}{M} = \frac{75[Ns]}{95[kg]} = 0.78947[m/s]; \quad \text{with} \quad M = \rho V = 950[kg/m^3] \cdot 0.1[m] \cdot 1[m^2] = 95[kg],
\end{aligned}
\tag{B.41}
$$

where M is total mass of the system. From this setting, total energy of the system before contact is derived exclusively from the applied surface force which introduces the acceleration, velocity as well as the kinetic energy to the system:

$$
E^{tot} = E^{kin} = \frac{1}{2} M \dot{\mathbf{x}}^2 = \frac{1}{2} \cdot 95[kg] \cdot (0.78947[m/s])^2 = 29.6052[Nm = Joule]. \tag{B.42}
$$

This block is then spatially discretized by a bilinear quadrilateral membrane element under the state of plane stress, while the GEMM is employed for time integration with the unity spectral radius $\rho_\infty = 1$

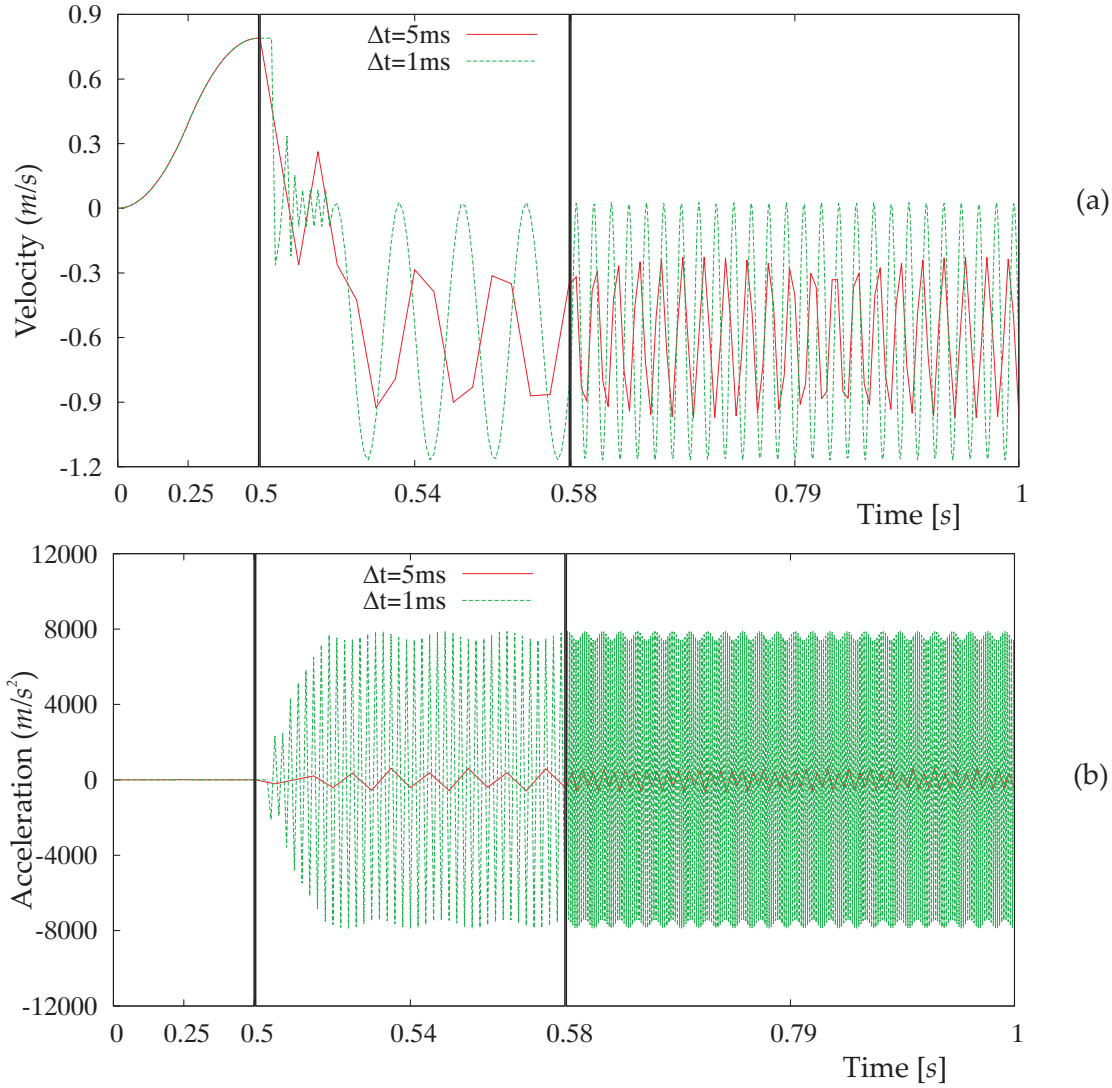

Figure B.4: Time history at the node A for (a) velocity and (b) acceleration.

B.5.2 Post contact oscillation

This problem is computed by the GEMM time integration algorithm with unit spectral radius $\rho_\infty = 1$ without the update velocity algorithm. Two simulations are performed with different time step size: $\Delta t = 5\ ms$ and $\Delta t = 1\ ms$, respectively. Figure B.4 presents the velocity and acceleration at node A of the deformable block (see Figure B.42). At node A, the velocity reaches $\dot{\mathbf{d}} = 0.79\ m/s^2$ before contact takes place.

Immediately after the block collides with the wall, the velocity at node A is suddenly dropped and fluctuated which is emphasized in the middle section of Figure B.4(a) within $t \in [0.50, 0.58]$ during which the oscillation of the velocity at node A is detected. At the same time, the acceleration at node A starts to oscillate after the collision as shown in Figure. B.4(b) . Interestingly, the computation with $\Delta t = 0.1ms$ shows a very strong oscillation with the amplitude around 8500 m/s^2. This strong oscillation significantly influences the

employed active set strategy such that the state of a slave contact node is alternated between active and inactive state within a time step. As a result, the active set loop, described in Figure 5.20 within a time step cannot converge at all. Furthermore, the acceleration , which is derived from the velocity, inherits as well this oscillation, thus resulting in an oscillation of the discrete Lagrange multipliers whose amplitude is depending on a chosen time step size Δt. This oscillation of the Lagrange multipliers has two adverse effects: First, a meaningful evaluation of the Lagrange multipliers, i.e. contact tractions, cannot be achieved. Secondly, the active set strategy encounters a convergence problem since an alternation of the Lagrange multipliers between two successive time stations leads to a persistent alternation of contact state within a time step. For this problem, Hartmann [Har07] suggested a remedy by an average of the Lagrange multipliers between two successive time stations at which the oscillation of the Lagrange multipliers occurs. This average value is considered as an approximation of contact traction which will then be used to evaluate the state of contact for the active set strategy. For more information, interested readers can consult [Har07].

B.5.3 Influences on the total energy of the system

In this section, influences of the velocity update algorithm over system total energy are investigated within the framework of the GEMM time integration with the unit spectral radius $\rho_\infty = 1$. In Figure B.5, the time history of the total, kinetic and potential energy is given for two different time steps: $\Delta t = 5\ ms$ and $\Delta t = 1\ ms$, respectively. For all cases, the computed total energy before the collision reaches the analytical solution $E^{tot} = 29.6052[Nm]$ given in section B.5.1. Without the velocity update, the total energy in Figure B.5(a) and (b) drops after the block collide with the rigid obstacle. Notably, this lost in total energy is caused by the fact that the continuous time is simplified into a sequence of discrete time stations at which the displacement, velocity and acceleration are evaluated in a discrete manner with the assumption that displacement, velocity and acceleration are continuous functions of time. Therefore, if the contact, which is a discontinuous phenomena in time, takes place at a specific point in time between two subsequent discrete time stations, which results in a sudden drop in velocity between that two subsequent time stations (see Figure 5.24), a continuous time integration algorithm cannot detect this discontinuity. Ideally, a continuous time integration algorithm can exactly detect the instance of contact when the time step reach zero $\Delta t \rightarrow 0$, and as a consequence, the loss in total energy is not concerned. However, such infinitesimal time step is impractical in reality.

On the other hand, the velocity update algorithm ameliorates this problem by conserving the system total energy in the post contact duration for both cases with different time step size. This statement is illustrated in Figure B.5(c) and (d) which are similar to those of Hartmann [Har07]. The energy plots in this Figure demonstrate the conservation properties of the method, incorporating a post-contact first-order breathing mode (see Laursen [Lau02]) as observed from the asymptotically periodic interchange of potential and kinetic energies. This breathing mode is induced in the block by the impact of the block against the rigid obstacle; it is preserved in this simulation by the energy conservation algorithm. To conclude, the velocity update algorithm, originated from Laursen and Love [LL02], is applicable for contact problems of membrane elements within the context of the GEMM time integration

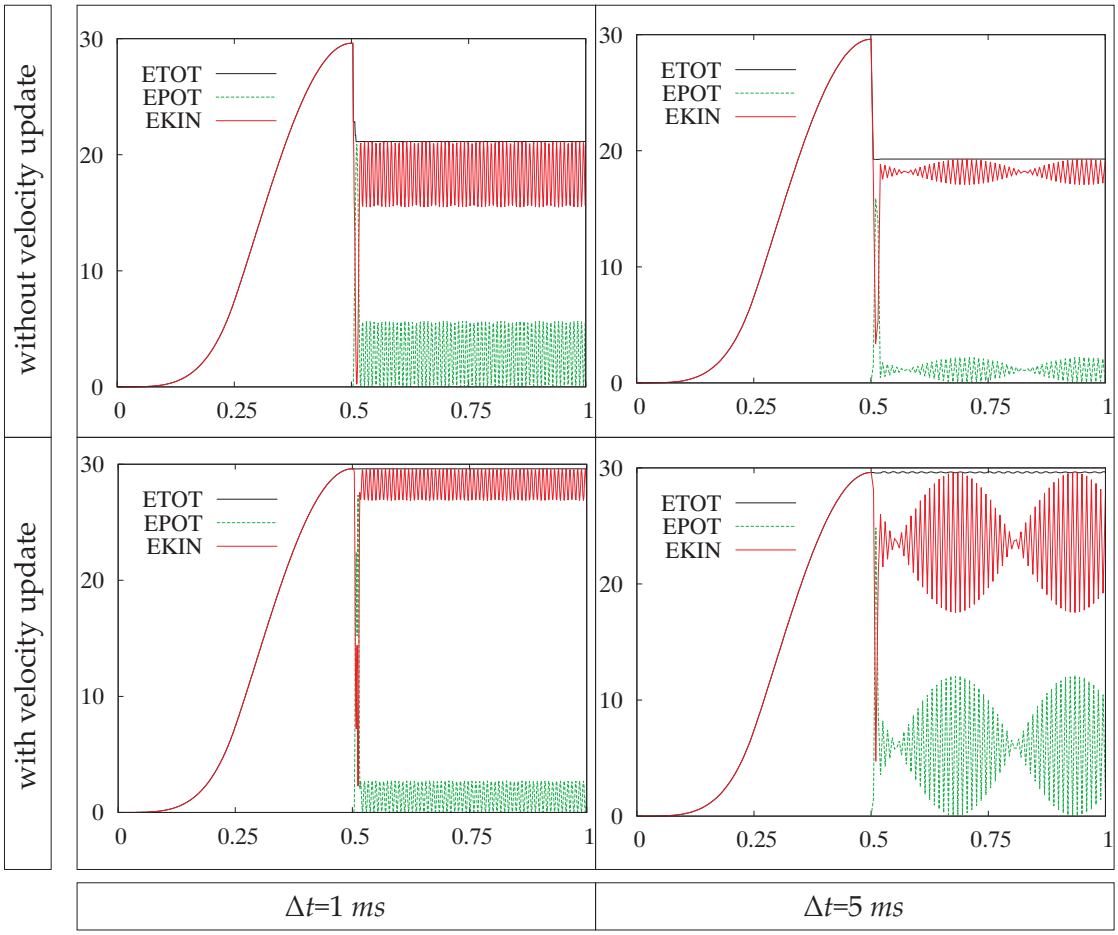

Figure B.5: Influences of velocity update over the system total energy.

algorithm. This simple example demonstrates a success to employ the velocity update algorithm with the dual mortar-based contact formulation for dynamic analysis of problems under interest.